HAL open science

Adaptive modeling of plate structures

Uroš Bohinc

▶ **To cite this version:**

Uroš Bohinc. Adaptive modeling of plate structures. Other. École normale supérieure de Cachan - ENS Cachan; Univerza v Ljubljani, 2011. English. NNT : 2011DENS0016 . tel-00675729

HAL Id: tel-00675729

https://theses.hal.science/tel-00675729v1

Submitted on 1 Mar 2012

HAL is a multi-disciplinary open access archive for the deposit and dissemination of scientific research documents, whether they are published or not. The documents may come from teaching and research institutions in France or abroad, or from public or private research centers.

L'archive ouverte pluridisciplinaire **HAL**, est destinée au dépôt et à la diffusion de documents scientifiques de niveau recherche, publiés ou non, émanant des établissements d'enseignement et de recherche français ou étrangers, des laboratoires publics ou privés.

ENSC-(n° d'ordre)

Thèse de doctorat
de L'École Normale Supérieure de Cachan

Présentée par

Monsieur Uroš BOHINC

pour obtenir le grade de

Docteur De L'École Normale Supérieure de Cachan

Domaine:

Mécanique, Gènie-Mécanique, Gènie Civil

Sujet de la thèse:

Modelisation adaptives des structures

Thèse présentee et soutenue à Ljubljana le 5 Mai 2011 devant le jury composé de:

Matjaž MIKOŠ	Université de Ljubljana Faculté de Génie civil et de Géodésie	Président de Jury
Ivica KOŽAR	Université de Rijeka Faculté de Génie civil	Rapporteur
Miran SAJE	Université de Ljubljana Faculté de Génie civil et de Géodésie	Rapporteur
Marko KEGL	Université de Maribor Faculté de mécanique	Rapporteur
Boštjan BRANK	Université de Ljubljana Faculté de Génie civil et de Géodésie	Directeur de thèse
Adnan IBRAHIMBEGOVIĆ	École Normale Supérieure de Cachan Laboratoire de Mécanique et Technologie	Co-directeur de thèse

Nom du Laboratoire LMT
ENS CACHAN/CNRS/UMR 8029/8535
61, avenue du Prsident Wilson, 94235 CACHAN CEDEX (France)

BIBLIOGRAPHIC-DOCUMENTARY INFORMATION

UDC	**519.61/.64:624.04:624.073(043.3)**
Author:	**Uroš Bohinc**
Supervisor:	**assoc. prof. Boštjan Brank**
Co-supervisor:	**prof. Adnan Ibrahimbegović**
Title:	**Adaptive analysis of plate structures**
Notes:	**289 p., 8 tab., 185 fig., 332 eq.**
Key words:	**structures, plates, plate models, finite element method, discretization error, model error, adaptivity**

Abstract

The thesis deals with adaptive finite element modeling of plate structures. The finite element modeling of plates has grown to a mature research topic, which has contributed significantly to the development of the finite element method for structural analysis due to its complexity and inherently specific issues. At present, several validated plate models and corresponding families of working and efficient finite elements are available, offering a sound basis for an engineer to choose from. In our opinion, the main problems in the finite modeling of plates are nowadays related to the adaptive modeling. Adaptive modeling should reach much beyond standard discretization (finite element mesh) error estimates and related mesh (discretization) adaptivity. It should also include model error estimates and model adaptivity, which should provide the most appropriate mathematical model for a specific region of a structure. Thus in this work we study adaptive modeling for the case of plates.

The primary goal of the thesis is to provide some answers to the questions related to the key steps in the process of adaptive modeling of plates. Since the adaptivity depends on reliable error estimates, a large part of the thesis is related to the derivation of computational procedures for discretization error estimates as well as model error estimates. A practical comparison of some of the established discretization error estimates is made. Special attention is paid to what is called equilibrated residuum method, which has a potential to be used both for discretization error and model error estimates. It should be emphasized that the model error estimates are quite hard to obtain, in contrast to the discretization error estimates. The concept of model adaptivity for plates is in this work implemented on the basis of equilibrated residuum method and hierarchic family of plate finite element models.

The finite elements used in the thesis range from thin plate finite elements to thick plate finite elements. The latter are based on a newly derived higher order plate theory, which includes through the thickness stretching. The model error is estimated by local element-wise computations. As all the finite elements, representing the chosen plate mathematical models, are re-derived in order to share the same interpolation bases, the difference between the local computations can be attributed mainly to the model error. This choice of finite elements enables effective computation of the model error estimate and improves the robustness of the adaptive modeling. Thus the discretization error can be computed by an independent procedure.

Many numerical examples are provided as an illustration of performance of the derived plate elements, the derived discretization error procedures and the derived modeling error procedure. Since the basic goal of modeling in engineering is to produce an effective model, which will produce the most accurate results with the minimum input data, the need for the adaptive modeling will always be present. In this view, the present work is a contribution to the final goal of the finite element modeling of plate structures: a fully automatic adaptive procedure for the construction of an optimal computational model (an optimal finite element mesh and an optimal choice of a plate model for each element of the mesh) for a given plate structure.

BIBLIOGRAFSKO-DOKUMENTACIJSKA STRAN

UDK	**519.61/.64:624.04:624.073(043.3)**
Avtor:	**Uroš Bohinc**
Mentor:	**izr. prof. dr. Boštjan Brank**
Somentor:	**prof. dr. Adnan Ibrahimbegović**
Naslov:	**Prilagodljivo modeliranje ploskovnih konstrukcij**
Obseg in oprema:	**289 str., 8 pregl., 185 sl., 332 en.**
Ključne besede:	**konstrukcije, metoda končnih elementov, plošče, modeli plošč, napaka diskretizacije, modelska napaka, prilagodljivost**

Izvleček

V disertaciji se ukvarjamo z različnimi vidiki modeliranja ploskovnih konstrukcij s končnimi elementi. Modeliranje plošč je nekoliko specifično in je zaradi kompleksnosti in pojavov, ki jih opisuje, bistveno prispevalo k razvoju same metode končnih elementov. Danes je na voljo več uveljavljenih modelov plošč in pripadajočih končnih elementov, ki uporabniku nudijo široko množico možnosti, iz katere lahko izbira. Prav široka možnost izbire predstavlja tudi največjo težavo, saj je težje določiti, kateri model je primernejši in tudi, katera mreža končnih elementov je za dan problem optimalna.

Glavni cilj disertacije je raziskati ključne korake v procesu prilagodljivega modeliranja plošč, ki omogoča samodejno določitev optimalnega modela za dan problem. Ker je prilagodljivo modeliranje odvisno od zanesljivih ocen napak, je večji del disertacije posvečen metodam za izračun diskretizacijske in modelske napake. Na praktičnih primerih smo preučili nekaj najbolj uveljavljenih metod za oceno napake. V nasprotju z ocenami napake diskretizacije, je modelsko napako mnogo težje določiti. Posebna pozornost je bila zato namenjena metodi *uravnoteženja rezidualov*, ki ima potencial tudi na področju ocene modelske napake. V tem smislu to delo predstavlja pomemben prispevek k področju računanja modelske napake za plošče.

Koncept prilagodljivega modeliranja ploskovnih konstrukcij je bil preskušen na hierarhični družini končnih elementov za plošče - od tankih plošč do modelov višjega reda, ki upoštevajo deformacije po debelini. Ravno dobro vzpostavljena hierarhija v družini končnih elementov se je pokazala za ključno pri zanesljivi oceni modelske napake.

Prilagodljivo modeliranje ploskovnih konstrukcije je bilo preskušeno na nekaj zahtevnejših primerih. Območje je bilo najprej modeliranjo z najbolj grobim modelom na sorazmerno redki mreži. Z uporabo informacije o napaki začetnega izračuna je bil zgrajen nov model. Primerjava izračuna na novem modelu z začetnim računom je pokazala, da je predlagan način prilagodljivega modeliranja sposoben nadzorovati porazdelitev napake, kakor tudi zajeti vse pomembnejše pojave, ki so značilni za modeliranje plošč.

INFORMATION BIBLIOGRAPHIQUE-DOCUMENTAIRE

CDU	**519.61/.64:624.04:624.073(043.3)**
Auteur:	**Uroš Bohinc**
Directeur de thèse:	**prof. Boštjan Brank**
Co-directeur de thèse:	**prof. Adnan Ibrahimbegović**
Titre:	**Modelisation adaptives des structures**
Notes:	**289 p., 8 tab., 185 fig., 332 éq.**
Mots clés:	**structures, plaques, modele de plaques, méthode éléments finis, erreur de discrétisation, erreur de modelisation, adaptativité**

Résumé

Le rapport de these traite la modélisation adaptative des plaques par la méthode des éléments finis. Le domaine de recherche sur la méthode des éléments finis de plaques a atteint une certaine maturité et a contribué d'une maniere significative au développement de la méthode des éléments finis dans un sens plus large, en apportant les réponses a des problemes tres spécifiques et complexes. A présent, on dispose de nombreux modeles de plaques et des formulations d'éléments finis correspondantes efficaces et opérationnelles, qui offrent a l'ingénieur une bonne base pour bien choisir la solution adaptée. A notre avis, les principaux problemes ouverts pour la modélisation des plaques par éléments finis sont aujourd'hui liés a la modélisation adaptative. Une modélisation adaptative devrait aller au-dela de l'estimation d'erreurs dues a la discrétisation standard (maillage éléments finis) et de l'adaptivité de maillages. Elle devrait inclure aussi l'estimation d'erreur due au modele et l'adaptativité de modeles, afin de disposer d'un modele le mieux adapté pour chaque sous-domaine de la structure.

L'objectif principal de la these est de répondre a des questions liées aux étapes clé d'un processus de l'adaptation de modeles de plaques. Comme l'adaptativité dépend des estimateurs d'erreurs fiables, une part importante du rapport est dédiée au développement des méthodes numériques pour les estimateurs d'erreurs aussi bien dues a la discrétisation qu'au choix du modele. Une comparaison des estimateurs d'erreurs de discrétisation d'un point de vue pratique est présentée. Une attention particuliere est pretée a la méthode de résiduels équilibrés (en anglais, "equilibrated residual method"), laquelle est potentiellement applicable aux estimations des deux types d'erreurs, de discrétisation et de modele. Il faut souligner que, contrairement aux estimateurs d'erreurs de discrétisation, les estimateurs d'erreur de modele sont plus difficiles a élaborer. Le concept de l'adaptativité de modeles pour les plaques est implémenté sur la base de la méthode de résiduels équilibrés et de la famille hiérararchique des éléments finis de plaques. Les éléments finis dérivés dans le cadre de la these, comprennent aussi bien les éléments de plaques minces et que les éléments de plaques épaisses. Ces derniers sont formulés en s'appuyant sur une théorie nouvelle de plaque, intégrant aussi les effets d'étirement le long de l'épaisseur. Les erreurs de modele sont estimées via des calculs élément par élément. Les erreurs de discrétisation et de modele sont estimées d'une maniere indépendante, ce qui rend l'approche tres robuste et facile a utiliser. Les méthodes développées sont appliquées sur plusieurs exemples numériques. Les travaux réalisés dans le cadre de la these représentent plusieurs contributions qui visent l'objectif final de la modélisation adaptative, ou une procédure completement automatique permettrait de faire un choix optimal du modele de plaques pour chaque élément de la structure.

ZAHVALA

Za nesebično pomoč in vso spodbudo se zahvaljujem mentorjema, prof. dr. Boštjanu Branku in prof. dr. Adnanu Ibrahimbegoviću. Na prehojeno pot se oziram z zadovoljstvom, da sem imel priložnost in čast delati z vama.

Zahvaljujem se izr. prof. dr. Andražu Legatu, ki me je podpiral ves čas študija, tudi takrat, ko to ni bilo lahko.

Vesel sem, da sem pri študiju vztrajal, saj sicer ne bi spoznal takih prijateljev, kot sta Jaka in Damijan. Čeprav se nisva spoznala med študijem, pa si prav takrat pokazal svojo srčnost in prijateljstvo. Vlado, hvala ti, ker si znal biti in ostati prijatelj do konca.

Brez svojih najbližjih, mojih staršev in staršev moje žene tega dela danes gotovo ne bi bilo. Ob dolgi in zaviti poti sem bil vedno deležen vaše nesebične podpore in pomoči, za kar sem vam iskreno hvaležen.

Moja družina, Polona, Blaž in Tine so sodelovali pri tem delu bolj, kot sem si upal predstavljati na začetku. Neskončno zaupanje in podporo, ki sem ju dobil od vas, lahko dobiš le od nekoga, ki te ima resnično rad.

To delo posvečam tebi, Klemen.

Contents

1 Introduction **1**

1.1 Motivation . . . 1

1.1.1 Verification and Validation . . . 2

1.1.2 Discretization . . . 2

1.1.3 Model error. Discretization error. The optimal model. . . . 3

1.1.4 Adaptive modeling. Error estimates and indicators . . . 5

1.2 Goals of the thesis . . . 6

1.3 Outline of the thesis . . . 7

2 Thin plates: theory and finite element formulations **9**

2.1 Introduction . . . 9

2.2 Theory . . . 9

2.2.1 Governing equations . . . 9

2.2.2 Further details of the Kirchhoff model . . . 19

2.3 Finite elements . . . 26

2.3.1 Preliminary considerations . . . 26

2.3.2 An overview of thin plate elements . . . 29

2.3.3 Natural coordinate systems . . . 30

2.3.4 Conforming triangular element . . . 37

2.3.5 Discrete Kirchhoff elements . . . 41

2.4 Examples . . . 50

2.4.1 Uniformly loaded simply supported square plate . . . 51

2.4.2 Uniformly loaded clamped square plate . . . 53

2.4.3 Uniformly loaded clamped circular plate . . . 54

2.4.4 Uniformly loaded hard simply supported skew plate . . . 70

2.5 Chapter summary and conclusions . . . 75

3 Moderately thick plates: theory and finite element formulations 77
3.1 Introduction . . . 77
3.2 Theory . . . 78
3.2.1 Governing equations . . . 78
3.2.2 Strong form . . . 82
3.2.3 Weak form . . . 85
3.2.4 Boundary layer and singularities . . . 86
3.3 Finite elements . . . 89
3.3.1 Elements with cubic interpolation of displacement . . . 92
3.3.2 Elements with incompatible modes . . . 95
3.4 Examples . . . 97
3.4.1 Uniformly loaded simply supported square plate . . . 97
3.4.2 Uniformly loaded simply supported free square plate . . . 98
3.4.3 Uniformly loaded simply supported skew plate . . . 100
3.4.4 Uniformly loaded soft simply supported L-shaped plate . . . 101
3.5 Chapter summary and conclusions . . . 119

4 Thick plates: theory and finite element formulations 121
4.1 Introduction . . . 121
4.2 Theory . . . 122
4.2.1 Governing equations . . . 122
4.2.2 Principle of virtual work . . . 124
4.3 Finite elements . . . 128
4.3.1 Higher-order plate elements . . . 128
4.4 Hierarchy of derived plate elements . . . 133
4.5 Examples . . . 136
4.5.1 Uniformly loaded simply supported square plate . . . 136
4.5.2 Uniformly loaded soft simply supported L-shaped plate . . . 137
4.5.3 Simply supported square plate with load variation . . . 138
4.6 Chapter summary and conclusions . . . 145

5 Discretization error estimates 147
5.1 Introduction. Classification of error estimates . . . 147
5.2 Definitions. Linear elasticity as a model problem . . . 149
5.3 Recovery based error estimates . . . 151

5.3.1 Lumped projection 153
5.3.2 Superconvergent patch recovery (SPR) 153
5.4 Residual based error estimates 155
5.4.1 Explicit 155
5.4.2 Implicit 158
5.5 Illustration of SPR and EqR methods on 1D problem 169
5.6 Chapter summary and conclusions 172

6 Discretization error for DK and RM elements 175
6.1 Introduction 175
6.2 Discretization error for DK elements 176
6.2.1 Discrete approximation for error estimates 176
6.2.2 Formulation of local boundary value problem 179
6.2.3 Enhanced approximation for the local computations 183
6.2.4 Numerical examples 185
6.2.5 An example of adaptive meshing 189
6.3 Discretization error for RM elements 201
6.4 Chapter summary and conclusions 201

7 Model error concept 203
7.1 Introduction 203
7.2 Model error indicator based on local EqR computations 205
7.2.1 Definition of model error indicator 205
7.2.2 Construction of equilibrated boundary tractions for local problems . 210
7.3 Chapter summary and conclusions 216

8 Model error indicator for DK elements 219
8.1 Introduction 219
8.2 Model error indicator 221
8.2.1 Regularization 223
8.2.2 The local problems with RM plate element 224
8.2.3 Computation of the model error indicator 226
8.2.4 Numerical examples 226
8.3 Chapter summary and conclusions 241

9 Conclusions 243

10 Razširjeni povzetek **247**
10.1 Motivacija . . . 247
10.1.1 Verifikacija in validacija . . . 248
10.1.2 Prilagodljivo modeliranje - optimalni model . . . 248
10.1.3 Napaka diskretizacije, modelska napaka . . . 250
10.2 Cilji . . . 251
10.3 Zgradba naloge . . . 252
10.4 Plošče . . . 253
10.4.1 Tanke plošče . . . 253
10.4.2 Srednje debele plošče . . . 261
10.4.3 Debele plošče . . . 268
10.5 Ocene napak . . . 273
10.5.1 Napaka diskretizacije . . . 273
10.5.2 Ocena modelske napake . . . 278
10.6 Zaključek . . . 281

List of Figures

2.2.1 Mathematical idealization of a plate, $\cdots$ 10
2.2.2 Stress resultants - shear forces and moments - on a midsurface differential element 13
2.2.3 Rotations at the boundary 14
2.2.4 Boundary coordinate system, moments and test rotations 17
2.2.5 Concentrated corner force at node I 19
2.2.6 To the definition of a corner force in (2.2.47) 19
2.2.7 Plate boundary traction loading $\cdots$ 20
2.2.8 Definition of a polar coordinate system (r, φ) at the corner 24
2.3.1 Problem domain Ω and its boundary Γ (left), finite element discretization Ω_h^e, Ω_h and patch of elements $\Omega_h^{\mathcal{P}_i}$ around node i (right) 28
2.3.2 Bi-unit element $\Omega^{\square}$ in coordinate system (ξ,η) 31
2.3.3 Quadrilateral element with the alternate shading between the coordinate lines of the quadrilateral natural coordinate system 33
2.3.4 Triangular (area) coordinates 33
2.3.5 Triangular element with the alternate shading between the coordinate lines $\zeta_i = const.$ of triangular coordinate system 35
2.3.6 To the definition of eccentricity parameter $\mu_{12} = 2e_1/l_{12}$ 37
2.3.7 Triangular Argyris plate element - ARGY 38
2.3.8 Hierarchical shape functions 42
2.3.9 Euler-Bernoulli beam element 42
2.3.10 Hermite shape functions 43
2.3.11 Node and side numbering in (2.3.64) 45
2.3.12 Triangular DK plate element - DK 46
2.3.13 Hierarchic shape functions of the triangular DK plate element 48
2.3.14 Hierarchic shape functions of the quadrilateral DK plate element 49
2.4.1 Designation of boundary conditions and loads 50
2.4.2 Problem definition and geometry for the uniformly loaded simply supported square plate (t/a=1/1000) 51

2.4.7 Problem definition and geometry for the uniformly loaded clamped square plate (t/a=1/1000) . . . 53
2.4.12 Clamped circular plate with uniform load (t/R=1/500) . . . 55
2.4.3 Reference solution of the uniformly loaded simply supported square plate ··· . . . 57
2.4.4 FE solution of the uniformly loaded simply supported square plate with Argyris plate element . . . 58
2.4.5 Finite element solution of the uniformly loaded simply supported square plate with DK plate elements . . . 59
2.4.6 Comparison of the convergence of FE solutions for the uniformly loaded simply supported square plate . . . 60
2.4.8 Reference solution of the uniformly loaded clamped square plate , ··· . . . 61
2.4.9 FE solution of the uniformly loaded clamped square plate with Argyris plate element . . . 62
2.4.10 FE solution of the uniformly loaded clamped square plate with DK plate elements . . . 63
2.4.11 Comparison of the convergence of FE solutions for the uniformly loaded clamped square plate . . . 64
2.4.13 Reference solution of the uniformly loaded clamped circular plate , ··· . . . 65
2.4.14 The sequence of meshes used for the finite element solution of uniformly loaded clamped circular plate . . . 66
2.4.15 FE solution of the uniformly loaded clamped circular plate with Argyris plate element . . . 67
2.4.16 FE solution of the uniformly loaded clamped circular plate with DK plate elements . . . 68
2.4.17 Comparison of the convergence of FE solutions for the uniformly loaded clamped circular plate . . . 69
2.4.18 Problem definition and geometry for the uniformly loaded simply supported skew plate (t/a=100) . . . 70
2.4.19 Reference solution of the uniformly loaded simply supported skew plate , ··· 71
2.4.20 FE solution of the uniformly loaded simply supported skew plate with ARGY element, ··· . . . 72
2.4.21 FE solution of the uniformly loaded simply supported skew plate with DK elements, ··· . . . 73
2.4.22 Comparison of the convergence of FE solutions for the uniformly loaded simply supported skew plate . . . 74

3.3.1 To the computation of the nodal shear $\hat{\gamma}_{h,I}$ from (3.3.18) . . . 94

3.3.2 Quadrilateral plate element P3Q with cubic displacement interpolation . . 96
3.4.1 Problem definition and geometry for the uniformly loaded hard-soft simply supported square plate (t/a=1/10) 97
3.4.6 Problem definition and geometry for the uniformly loaded hard simply supported-free square plate (t/a=10) 99
3.4.11 Problem definition and geometry for the uniformly loaded soft simply supported skew plate (t/a=10) 100
3.4.16 Problem definition and geometry for the uniformly loaded soft simply supported L-shaped plate (t/a=10) 101
3.4.2 Reference solution of the uniformly loaded hard-soft simply supported square plate with legend also valid for Figures 3.4.4 and 3.4.3 103
3.4.3 FE solution of the uniformly loaded hard-soft simply supported square plate with PI plate elements 104
3.4.4 FE solution of the uniformly loaded hard-soft simply supported square plate with P3 plate elements (mesh as in Figure 3.4.3) 105
3.4.5 Comparison of the convergence of FE solutions for the uniformly loaded hard-soft simply supported square plate 106
3.4.7 Reference solution of the uniformly loaded hard simply supported-free square plate with legend also valid for Figures 3.4.9 and 3.4.8 107
3.4.8 FE solutions of the uniformly loaded hard simply supported-free square plate with PI plate elements 108
3.4.9 FE solutions of the uniformly loaded hard simply supported-free square plate with P3 plate elements (mesh as in Figure 3.4.8) 109
3.4.10 Comparison of the convergence of FE solutions for the uniformly loaded hard simply supported-free square plate 110
3.4.12 Reference solution of the uniformly loaded soft simply supported skew plate with legend also valid for Figures 3.4.14 and 3.4.13 111
3.4.13 FE solution of the uniformly loaded soft simply supported skew plate with PI plate elements 112
3.4.14 FE solution of the uniformly loaded soft simply supported skew plate with P3 plate elements (mesh as in Figure 3.4.13) 113
3.4.15 Comparison of the convergence of FE solutions for the uniformly loaded soft simply supported skew plate 114
3.4.17 Reference solution of the uniformly loaded soft simply supported L-shaped plate with legend also valid for Figures 3.4.19 and 3.4.18 115
3.4.18 FE solution of the uniformly loaded soft simply supported L-shaped plate with PI plate elements 116

3.4.19 FE solution of the uniformly loaded soft simply supported L-shaped plate with P3 plate elements (mesh as in Figure 3.4.18) . . . 117
3.4.20 Comparison of the convergence of FE solutions for the uniformly loaded soft simply supported L-shaped plate . . . 118

4.2.1 Kinematics of through-the-thickness deformation in the thick plate model . 122
4.3.1 Designation of plate surfaces Ω^+, Ω^- and Γ . . . 132
4.5.1 Problem definition and geometry for the uniformly loaded hard-soft simply supported square plate (t/a=1/10) . . . 136
4.5.4 Problem definition and geometry for the uniformly loaded soft simply supported L shaped plate (t/a=1/10) . . . 137
4.5.7 Problem definition and geometry for the simply supported square plate with load variation (t/a=1/10 and t/b=1) . . . 138
4.5.2 FE solution of the uniformly loaded simply supported square plate with PZ plate elements . . . 139
4.5.3 Legend for Figures 4.5.2 . . . 140
4.5.5 FE solution of the uniformly loaded soft simply supported L shaped plate with PZ plate elements . . . 141
4.5.6 Legend for Figures 4.5.5 . . . 142
4.5.8 FE solution of the simply supported square plate with load variation with PZ plate elements . . . 143
4.5.9 Legend for Figures 4.5.8 . . . 144

5.1.1 Rough classification of a-posteriori error estimates/indicators . . . 149
5.3.1 SPR recovery of the enhanced stress $\boldsymbol{\sigma}_I^*$ at node I . . . 155
5.4.1 Notation . . . 159
5.4.2 Relation of tractions $\boldsymbol{t}_\Gamma^e$ to their projections $\boldsymbol{r}_{I,\Gamma}^e$ . . . 163
5.4.3 Element nodal residual $\boldsymbol{R}_I^e$ and boundary tractions projections $\boldsymbol{r}_{I,\Gamma_{1,2}}^e$ at node I of element e . . . 164
5.4.4 Continuity of boundary tractions projections $\boldsymbol{r}_{I,\Gamma}^e$ . . . 164
5.4.5 Patch $\mathcal{P}_I$ of four elements around node I . . . 165
5.4.6 Representation of element nodal residuals $\boldsymbol{R}_I^e$ by the projections $\boldsymbol{r}_{I,\Gamma}^e$ . . . 168
5.4.7 Boundary tractions $\boldsymbol{t}_\Gamma^e$ replace the action of element projections $\boldsymbol{r}_{I,\Gamma}^e$ . . . 168
5.5.1 One dimensional problem: hanging bar with variable cross section . . . 169
5.5.2 Solution of the model problem with linear elements . . . 171
5.5.3 Solution of the model problem with quadratic elements . . . 171
5.5.4 Computation of enhanced stress σ^*; comparison of SPR and EqR method . 172

6.2.1 Subdivision schemes for the DKT element . . . 184

6.2.2 Simply supported square plate under uniform loading - global energy error estimates . . . 186
6.2.3 Simply supported square plate under uniform loading - effectivity index of the global energy error estimates . . . 187
6.2.4 Simply supported square plate under uniform loading - comparison of relative local error estimates . . . 192
6.2.5 Clamped square plate under uniform loading - global energy error estimates 193
6.2.6 Clamped square plate under uniform loading - effectivity index of the global energy error estimates . . . 193
6.2.7 Clamped square plate under uniform loading - comparison of relative local error estimates . . . 194
6.2.8 Clamped circular plate under uniform loading - global energy error estimates 195
6.2.9 Clamped circular plate under uniform loading - effectivity index of the global energy error estimates . . . 195
6.2.10 Clamped circular plate under uniform loading - comparison of relative local error estimates . . . 196
6.2.11 Morley's skew plate under uniform loading - global energy error estimates . 197
6.2.12 Morley's skew plate under uniform loading - effectivity index of the global energy error estimates . . . 197
6.2.13 Morley's skew plate under uniform loading - comparison of relative local error estimates . . . 198
6.2.14 L-shaped plate under uniform loading - global energy error estimates . . . 199
6.2.15 L-shaped plate under uniform loading - effectivity index of the global energy error estimates . . . 199
6.2.16 L-shaped plate under uniform loading - comparison of relative local error estimates . . . 200

7.2.1 Local computation on a finite element domain Ω_h^e with Neumann boundary conditions $\boldsymbol{t}_{\Gamma^e}^e$ on Γ^e . . . 207

8.2.1 Model error indicator for thick SSSS problem for rectangular meshes . . . 228
8.2.2 Model error indicator for thin SSSS problem for distorted meshes . . . 229
8.2.3 Model error indicator for thin SSSS problem for rectangular meshes . . . 230
8.2.4 Model error indicator for thin SSSS problem for distorted meshes . . . 231
8.2.5 Model error indicator for thick SFSF problem for rectangular meshes . . . 232
8.2.6 Model error indicator for thick SFSF problem for distorted meshes . . . 233
8.2.7 Model error indicator for thin SFSF problem for rectangular meshes . . . 234
8.2.8 Model error indicator for thin SFSF problem for distorted meshes . . . 235
8.2.9 LSHP - model error indicator . . . 235

8.2.10 LSHP - stress resultant m_{xx} 236
8.2.11 LSHP - stress resultant m_{xy} 237
8.2.12 LSHP - stress resultant q_x 238
8.2.13 SKEW - model error indicator 238
8.2.14 SKEW - stress resultant m_{xx} 239
8.2.15 SKEW - stress resultant m_{xy} 239
8.2.16 SKEW - stress resultant q_x 240

List of Tables

2.1 Boundary conditions for thin plates. * $\theta_n = \frac{\partial w}{\partial s}$ is zero due to $w = 0$. 23
2.2 Critical opening angles for the Kirchhoff plate (* - the case reexamined in this section) 26
2.3 4 point triangular integration scheme for triangular finite elements (DKT) 47
2.4 4 point quadrilateral integration scheme for quadrilateral finite elements (DKQ) 48

3.1 Boundary conditions for moderately thick plates 80
3.2 Leading terms of thickness expansion in (3.2.38) 88
3.3 The singularity coefficients, λ_1 and λ_2 89

6.1 Comparison of errors of FE computation of the square clamped plate problem with various meshes adaptively constructed from discretization error estimate. 191

Chapter 1

Introduction

1.1 Motivation

Understanding the behavior of structures under various loads has always been of primary interest to man. Throughout the history the knowledge on the structural behavior was predominantly acquired by experiments. But due to the rising complexity of the man made structures it became obvious that it is not possible nor economical to perform the experimental validation of all possible loading situations. It was realized that mathematical models (i.e. equations) describing physical phenomena, which would be able to predict the structural behavior, were needed.

The models of physical phenomena have been build upon the experimental observations. The models are therefore only as accurate as the experiments are. The accuracy of the model predictions inherently depend on the accuracy of the experimental results. The accuracy is limited also by the computational ability of the solver, used to solve equations of the model, which affects the level of the detail attainable in the model.

In the early days the model equations were solved analytically. Only relatively small set of engineering problems with simple geometry and material laws were suitable to be solved that way. Some numerical approximations were attempted but were seriously limited by the computing power of the solver (usually human at that time). With the advent of the modern computers the numerical approximations of the solution became more elaborate and it became possible to numerically solve complex real life problems. Numerical computations have nowadays become an integral part of engineering design process. Critical design decisions are routinely made on the basis of numerical simulations. It is therefore vitally important to clearly define the reliability and accuracy (i.e. the error) of the computational predictions of the model.

A numerical simulation (i.e. the mathematical model plus the numerical methods) of a physical phenomena is accepted only when the predictions match the outcome of the controlled experiments. The model predictions are therefore always made in the form of measurable physical quantities. Since the engineering approach to modeling goes by the paradigm *as simple as possible and as complicated as necessary* the necessary level of complexity of a physical model is defined by the required accuracy of the model.

The difference between the controllably measured physical reality and the model predictions can be attributed to one of the two reasons: (i) the mathematical model is either based upon the wrong assumptions and/or (ii) the equations of the mathematical model can be solved only approximately for a given data. The error of a model prediction, which is caused by the wrong assumptions, is usually referred to as the *model error*. The approximative nature of the model results is related to the *discretization error*.

1.1.1 Verification and Validation

The total error of the prediction is thus always composed of a model error and a discretization error. The approximation of the exact model equations reflects itself in the model error, while the discretization error is a consequence of the approximation in the solution of the chosen model equations.

The concept of verification and validation (V&V) has been established to study the model performance in terms of accuracy. Comparison of the solution of the discretized model with the exact solution of the model is a subject of *verification*. The *validation* usually concerns the comparison of the model predictions with the results of the experiments.

1.1.2 Discretization

Mathematical model (or just model) is a mathematical idealization of a physical model which is build upon certain assumptions and simplifications. Certain degree of abstraction is used in the model derivation. It usually involves the concept of continuity, which assumes that the solution is known at every point of the problem domain. Such models cannot be solved numerically since the number of points in the problem domain is infinite. In order to obtain a numerically solvable system, the problem has to be discretized with a finite number of variables. A widespread method of the discretization of a given continuous mathematical model is the finite element method (FEM). The discretization introduces a

discretization error.

The finite element method was first conceived by engineers and mathematicians to solve the problems of linear elasticity. Nowadays, the prevalent use of the finite element method remains in the field of linear structural mechanics. The main focus of this work is the finite element analysis of bending of plate structures, which fits in that framework.

1.1.3 Model error. Discretization error. The optimal model.

In order to find the optimal model for the analysis of a structure behavior - in our case elastic plate bending - the criteria have to be set first. If the accuracy is the only criteria, the best possible model is the exact fully three-dimensional model of elastic plate bending. Such model is of course prohibitively complicated for usual plate bending problems. The plate model is therefore proclaimed as optimal in the engineering sense: besides the necessary (desired) accuracy, the model must be as simple as possible.

The plates are basic structural elements and several models of their bending behavior exist. Since the third dimension of the plate is significantly smaller than the other two, the plate models are subject to dimensional reduction. The computational advantage of using two-dimensional model instead of fully three-dimensional model is obvious. Although the three-dimensional model should asymptotically converge to two-dimensional plate model (for decreasing plate thickness), not many plate models are strictly build on the principles of asymptotic analysis. Various important plate models are rather based on a-priori assumptions coming from the engineering intuition. Nevertheless, a hierarchy of such plate models can still be established with respect to the convergence to the full three-dimensional model, [Babuška Li, 1990]. It is thus possible to form a family of hierarchically ordered plate models - a series of models, whose solutions converge to the exact three-dimensional solution of plate bending problem. The convergence to the exact three-dimensional solution manifests itself, for example, in the ability to describe the boundary layer effects, which are typical for the three-dimensional solution.

Model error

The a-priori assumptions of a plate model are usually related to its kinematics. The kinematics of the plate strongly depends on the boundary conditions, concentrated forces and abrupt changes in thickness or material properties. Since the kinematics changes over the plate problem domain, so does the validity of model assumptions. The model

is optimal only in the region, where its assumptions are valid. It is therefore clear that the optimal model is location dependant. There is no single model which is optimal for the whole plate domain. The plate domain should therefore be divided into regions, each being modeled with its own optimal model. The main goal of the model adaptivity is to identify the regions and determine the optimal model for each one of them.

The region dependent optimal model of the plate structure can be built iteratively. The engineering approach is to start from bottom up. Preferably, we start the analysis with the coarsest possible model over the whole problem domain. Through the postprocessing of the solution, the model error estimates are obtained. Based on the prescribed accuracy (i.e. the prescribed value of the model error), regions, where the starting model is to be enhanced, are identified. A new, mixed model, is built for the plate structure under consideration and a new solution is searched for. The model error is estimated again and the procedure is repeated iteratively until the desired accuracy is achieved in all the regions of the problem domain. The goal of this approach is an effective and accurate estimation of the model error. Ideally, the model error estimate should be effective and as accurate as possible. It is clear, that the above described procedure for choosing the most suitable plate model for each region of a plate structure is possible only when the equations of the chosen models are solved exactly.

The discretization error

Let us assume that a regional optimal model of a plate structure is somehow chosen. It has to be now discretized in order to obtain a numerically solvable problem. The finite element discretization divides the problem domain into the finite elements. On each of the elements the approximation of the solution is build based on the finite number of degrees of freedom. The quality of the approximation depends on the element size and the relative variation of the solution. The higher the variation of the solution, the smaller elements have to be used to properly describe it. The optimal discretization is the one, for which the discretization error is roughly the same for every element. In order to keep the discretization error uniformly distributed between the elements, the size of the element has to be adapted to the solution. The partition of the problem domain (the mesh) is therefore constructed iteratively. First, a relatively coarse mesh is constructed and an original solution is computed. A discretization error estimate is computed from the original solution. Since the dependance of the discretization on the element size is usually known a-priori and the predefined error tolerance is set, a new element size can be

computed. A new mesh is generated, which takes into account the computed element size distribution. The process is iterated until the discretization error is evenly distributed over the problem domain.

Total error

In the above paragraphs it has been assumed that the model error can be obtained with fixed (preferably zero) discretization error, and that discretization error can be obtained with fixed model error. In reality both errors are connected and can be separated only under certain assumptions.

Optimal model

The optimal model, in the sense of model and discretization error, has to be adapted to the problem studied. The main benefit of using the adapted model is probably not in the gain in the computational efficiency but rather in the control of the accuracy of the model predictions. The automated procedure for the selection of the optimal model should prevent a designer to oversimplify the model and potentially overlook the possible problematic issues. On the other hand, due to the ever increasing computational power, the temptation to use full three-dimensional models in the whole problem domain is increasing. Although the fine models do capture the physics of the phenomena, they are more difficult to interpret and they obscure the basic phenomena by unnecessary details.

1.1.4 Adaptive modeling. Error estimates and indicators

The adaptive modeling is an iterative process which crucially relies on the estimates of both model error and discretization error.

At this point, one should clearly distinguish between the error estimates and error indicators. The estimates define the boundaries of the error. They are usually quite conservative and they tend to overestimate the error by several orders of magnitude. Indicators on the other hand do not provide any guarantees on the error. In return they can give quite sharp indication of the error. Which type of model error to use depends on the purpose of the computation of the error. If the main goal is to control the adaptive construction of the optimal model, the indicators are the preferable choice.

The computation of reliable and efficient error indicators is a key step in the construction of the optimal model. Although the model error can be orders of magnitudes

higher than the discretization error, its evaluation is much harder. Therefore there are not many existing methods for the computation of model error indicator. Their development is mostly on the level of general treatment. In this work one of the existing concepts of model error indicators was applied to the subject of plate modeling. Its development is the main achievement of this thesis.

The effective procedure of computation of model error indicator is build upon the following idea. The model error, in principle, measures the difference of the solution of the applied (current) model and the solution of the exact (full three-dimensional) model. The global computation of the true solution - just to serve as the reference to model error computation - is obviously too expensive. An effective compromise is to repeat the computations with the exact model on smaller domains - preferably on elements. The local problems have to replicate the original problem. The interpretation is, that the elements are extracted from the continuum and its actions are replaced by boundary tractions. Therefore the boundary conditions for the local problems are of Neumann type.

The primary question of model error estimation now becomes: "How to estimate the boundary conditions for the local problems?". If the exact solution had been known, the boundary conditions for the elements would have been computed from the true stress state using the Cauchy principle. This is, however, not possible since the stresses are determined from the true solution, which is unknown and yet to be computed. An approximation of the boundary stresses must therefore be built based on the single information available: current finite element solution, an approximation to the true solution. The development of the method of the construction of the best possible estimates for the boundary conditions for local problems is thus the central topic of the model error computation.

The application of this general principle to the subject of modeling of plates is not very straightforward. The specific issues inherent to plate modeling have to be properly addressed. Additional complication presents the fact, that the formulations of plate elements are mostly incompatible.

1.2 Goals of the thesis

The main goal of the thesis is to develop a concept for adaptive modeling of plate structures. Therefore the first goal of the thesis is to derive a hierarchical family (in a model sense) of fine performing triangle and quadrilateral plate elements.

The concept of adaptive modeling depends on the reliable error estimates and error

indicators. In the following we will not always strictly distinguish in text between the error indicator and error estimate.

The second goal of the thesis is related to discretization error estimates. We derived, implemented and tested some of the most established a posteriori discretization error estimate methods. Two most prominent methods of discretization error estimation are *superconvergent patch recovery SPR* and *method of equilibrated residuals EqR* [Stein Ohnimus, 1999]. We implemented and compared the discretization error estimate methods for Discrete Kirchhoff (DK) and Reissner/Mindlin plate elements, which are very popular ana reliable finite elements for analysis of plate structures.

Currently, there exist several methods to obtain estimates of discretization error, while there are only a few methods available to obtain the model error estimates.

The third goal of the thesis is to explain the idea to use *equilibrated residual method (EqR)* to derive model error estimate.

The final goal of the thesis is to derive a procedure for adaptive modeling of plates. The procedure should go as follows: obtain an initial finite element solution of a chosen plate problem; estimate both model and discretisation error; build better (in terms of model and discretization errors) finite element model of the problem. This adaptive modeling procedure is planned to be build from bottom up: from the relatively coarse model and mesh to the model and mesh capable of capturing all the important phenomena and to control the overall error as well as the error distribution.

1.3 Outline of the thesis

The thesis consists of nine chapters. In the first chapter an overview of the subject and the state of the art is presented.

Chapters 2 to 4 present an overview of the theory of plates. The theories are presented in the bottom up fashion: from most basic one towards "quasi" three-dimensional theory. The theoretical treatment of plates reveals the phenomena typical for the plates: boundary layers and singularities. The plates theories which can be arranged in the hierarchical order are accompanied by the description of some possible discretizations: finite elements. Some of the most important and established finite elements are presented in these sections. The chapters conclude with the treatment of selected test cases each one illustrating different aspects of plate modeling.

Chapter 5 starts with an overview of the most important methods for the estimation

of discretization error. The general description of the methods is followed by the more detailed treatment of superconvergent patch recovery method and a method of equilibrated residuals. The implementation of the latter for the case of discrete Kirchhoff element is given a special focus in Chapter 6. The implementation of the method for the non-conforming plate elements is somewhat special and not treated before in the literature. Several numerical test illustrate the differences between the various error estimation methods.

Chapters 7 and 8 cover the question of model error. After the general treatment of the model error an approach to estimate the model error based on the method of equilibrated residuals is followed. The implementation of the method for the case of plate bending is covered in detail and tested by several numerical tests in Chapter 8. The tests are selected to exhibit the basic and most important phenomena specific to the plate models.

Concluding remarks of the thesis are given in Chapter 9.

Chapter 2

Thin plates: theory and finite element formulations

2.1 Introduction

In this chapter, the equations describing the linear elastic bending of thin plates - called Kirchhoff thin plate theory or Kirchhoff thin plate model - will be re-derived, and some conforming and nonconforming (discrete) triangular and quadrilateral Kirchhoff thin plate finite element formulations will be presented in detail - in forms suitable for immediate numerical implementation. For the sake of completeness, some specific details of the Kirchhoff thin plate model will be presented as well.

2.2 Theory

The first part of this section, related to the the basic equations of Kirchhoff thin plate theory, is organized in such a way that many equations are first derived for moderately thick plates (commonly called Reissner/Mindlin plates), and only further specialized for thin (i.e. Kirchhoff) plates. Moderately thick plates will be further addressed in the next chapter.

2.2.1 Governing equations

Kinematic equations

Let the position of an undeformed plate in the xyz coordinate system be given by $\Omega \times [-t/2, t/2]$, where t is plate thickness. The region Ω at xy plane (at $z = 0$) defines the midsurface of the plate. We denote the boundary of Ω by Γ. It is assumed that

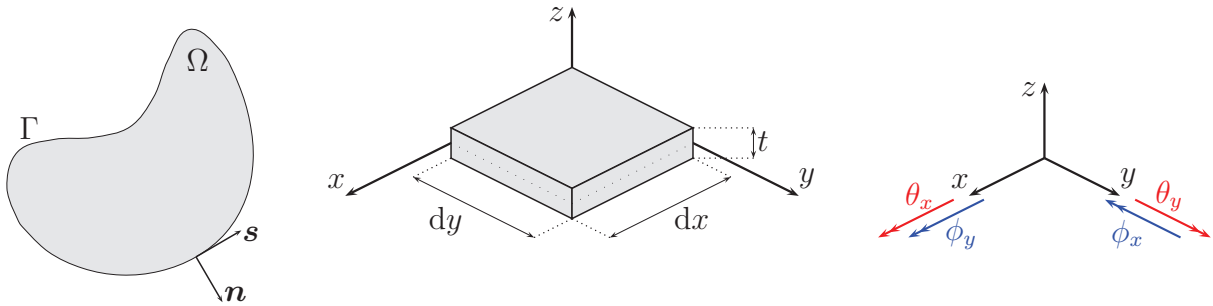

Figure 2.2.1: Mathematical idealization of a plate (left), a plate differential element (middle), directions of rotations (right)
Slika 2.2.1: Matematična idealizacija plošče (levo), diferencialni element (sredina), smer rotacij (desno)

when external loading is applied to the plate, any midsurface point can displace only in the direction of z coordinate; we will denote this displacement by w. It is further assumed that the deformation of the plate "fiber", which has initial orientation of the midsurface normal $\boldsymbol{n}_{\boldsymbol{\Omega}} = [0, 0, 1]^T$, can be described by a small rigid rotation, defined by a rotation vector $\boldsymbol{\theta} = [\theta_x, \theta_y]^T$, see Figure 2.2.1. In accordance with the above, the kinematic assumption, which defines small displacements of a point $P(x, y, z)$ of a plate is given as:

$$u_x = +z\theta_y; \quad u_y = -z\theta_x; \quad u_z = w \tag{2.2.1}$$

The displacements (2.2.1) yield the following strains:

$$\varepsilon_{xx} = \frac{\partial u_x}{\partial x} = +z\frac{\partial \theta_y}{\partial x}; \quad \varepsilon_{yy} = \frac{\partial u_y}{\partial y} = -z\frac{\partial \theta_x}{\partial y}; \quad \varepsilon_{xy} = +z\frac{1}{2}\left(\frac{\partial \theta_y}{\partial y} - \frac{\partial \theta_x}{\partial x}\right) \tag{2.2.2}$$

$$\varepsilon_{xz} = \frac{1}{2}\left(+\theta_y + \frac{\partial w}{\partial x}\right); \quad \varepsilon_{yz} = \frac{1}{2}\left(-\theta_x + \frac{\partial w}{\partial y}\right); \quad \varepsilon_{zz} = 0$$

and the engineering transverse shear strains, defined as

$$\boldsymbol{\gamma} = [\gamma_x, \gamma_y]^T = [2\varepsilon_{xz}, 2\varepsilon_{yz}]^T \tag{2.2.3}$$

The transverse strain ε_{zz} is for thin and moderately thick plate significantly smaller than the strains ε_{xx}, ε_{yy} and ε_{xy}, which makes the relation $\varepsilon_{zz} = 0$ justified. However, in plate regions near the supports, near the point loads, at sharp changes of thickness, etc., where $\varepsilon_{zz} = 0$ no longer holds true, the thin plate theory and the moderatelly thick plate theory are not adequate, and should be, if possible, replaced by a plate theory which better describes such local phenomena. We note, that the assumption $\varepsilon_{zz} = 0$ implies plane strain state in a plate. However, a closer approximation to the physics, according to the

experimental observations, is the plane stress state with $\sigma_{zz} = 0$, which implies nonzero ε_{zz}. As shown further below, the plane stress state is assumed in the thin plate theory and in the moderatelly thick plate theory rather than the plane strain state. The curvatures $\boldsymbol{\kappa} = [\kappa_{xx}, \kappa_{yy}, \kappa_{xy}]^T$ at the plate midsurface point are defined as

$$\kappa_{xx} = -\frac{\partial \theta_y}{\partial x}; \quad \kappa_{yy} = +\frac{\partial \theta_x}{\partial y}; \quad \kappa_{xy} = \frac{\partial \theta_x}{\partial x} - \frac{\partial \theta_y}{\partial y} \tag{2.2.4}$$

which leads to the following expressions for nonzero in-plane strains $\boldsymbol{\varepsilon} = [\varepsilon_{xx}, \varepsilon_{yy}, \varepsilon_{xy}]^T$

$$\varepsilon_{xx} = -z\kappa_{xx}; \quad \varepsilon_{yy} = -z\kappa_{yy}; \quad 2\varepsilon_{xy} = -z\kappa_{xy} \tag{2.2.5}$$

In the thin plate Kirchhoff model the transverse shear strains are negligible:

$$\gamma_x = \frac{\partial w}{\partial x} + \theta_y = 0; \qquad \gamma_y = \frac{\partial w}{\partial y} - \theta_x = 0 \tag{2.2.6}$$

which relates the midsurface deflection with the rotations

$$\theta_x = \frac{\partial w}{\partial y}; \quad \theta_y = -\frac{\partial w}{\partial x} \tag{2.2.7}$$

From (2.2.4) it thus follows that the curvatures for the Kirchhoff thin plate model are

$$\boldsymbol{\kappa} = [\frac{\partial^2 w}{\partial x^2}, \frac{\partial^2 w}{\partial y^2}, 2\frac{\partial^2 w}{\partial x \partial y}]^T \tag{2.2.8}$$

and, in more compact writing

$$\boldsymbol{\kappa} = \boldsymbol{\mathcal{L}} w; \quad \boldsymbol{\mathcal{L}} = [\frac{\partial^2}{\partial x^2}, \frac{\partial^2}{\partial y^2}, 2\frac{\partial^2}{\partial x \partial y}]^T \tag{2.2.9}$$

Constitutive equations

Let us assume that a plate under consideration is made of isotropic elastic material, characterized by elastic modulus E and Poisson's ratio ν. According to the accumulated engineering experience, the thin plate small strain elastic behavior is described well by the plane stress Hook's law:

$$\begin{bmatrix} \sigma_{xx} \\ \sigma_{yy} \\ \sigma_{xy} \end{bmatrix} = \frac{E}{1-\nu^2} \begin{bmatrix} 1 & \nu & 0 \\ \nu & 1 & 0 \\ 0 & 0 & \frac{1}{2}(1-\nu) \end{bmatrix} \begin{bmatrix} \varepsilon_{xx} \\ \varepsilon_{yy} \\ 2\varepsilon_{xy} \end{bmatrix} \tag{2.2.10}$$

Integration of (2.2.10) through the plate thickness leads to the plate in-plane forces, which are zero, and plate bending moments $\boldsymbol{m} = [m_{xx},\, m_{yy},\, m_{xy}]^T$ with dimension of moment per unit length (Figure 2.2.2).

$$m_{xx} = \int_{-t/2}^{+t/2} z\,\sigma_{xx}\,\mathrm{d}z; \quad m_{yy} = \int_{-t/2}^{+t/2} z\,\sigma_{yy}\,\mathrm{d}z; \quad m_{xy} = \int_{-t/2}^{+t/2} z\,\sigma_{xy}\,\mathrm{d}z \tag{2.2.11}$$

Positive moments yield tensile stresses at $z < 0$. Rotational equilibrium of a plate differential element around z axis implies $\sigma_{yx} = \sigma_{xy}$ and $m_{yx} = m_{xy}$. Using (2.2.5) and (2.2.10), we obtain the moment-curvature relationship

$$\boldsymbol{m} = \mathbf{C}_B \boldsymbol{\kappa} \tag{2.2.12}$$

where $\mathbf{C}_B$ is

$$\mathbf{C}_B = D \begin{bmatrix} 1 & \nu & 0 \\ \nu & 1 & 0 \\ 0 & 0 & \frac{1}{2}(1-\nu) \end{bmatrix} \tag{2.2.13}$$

and $D = \frac{1}{12}Et^3/(1-\nu^2)$ is isotropic plate rigidity constant. The transverse shear forces, with dimension of force per unit length, are defined as

$$q_x = \int_{-t/2}^{+t/2} \sigma_{xz}\,\mathrm{d}z; \quad q_y = \int_{-t/2}^{+t/2} \sigma_{yz}\,\mathrm{d}z \tag{2.2.14}$$

where

$$\begin{bmatrix} \sigma_{xz} \\ \sigma_{yz} \end{bmatrix} = \frac{Ec}{2(1+\nu)} \begin{bmatrix} 1 & 0 \\ 0 & 1 \end{bmatrix} \begin{bmatrix} \gamma_x \\ \gamma_y \end{bmatrix} \tag{2.2.15}$$

and c is transverse shear correction factor, which will be discussed in the next chapter. The relationship between the constitutive transverse shear forces and the engineering transverse shear strains can be given in compact form as $\boldsymbol{q} = \mathbf{C}_S \boldsymbol{\gamma}$, where $\boldsymbol{q} = [q_x, q_y]^T$ and structure of $\mathbf{C}_S$ can be seen from the above.

For the Kirchhoff thin plate theory the transverse shear forces q_x and q_y, when computed from the constitutive equations, are zero, see (2.2.6). Thus, in the Kirchhoff thin plate theory the shear forces need to be computed from the equilibrium equations, as shown below. We will not strictly use different notation for the "constitutive" and "equilibrium" shear forces to distinguish between them.

Equilibrium equations

The equilibrium of a midsurface differential element can be deduced by using Figure 2.2.2. The equilibrium of forces in z direction is

$$\nabla \cdot \boldsymbol{q} = \frac{\partial q_x}{\partial x} + \frac{\partial q_y}{\partial y} = -f \tag{2.2.16}$$

where f is the applied transverse force per unit area (in the direction of $+z$) and $\nabla = [\frac{\partial}{\partial x}, \frac{\partial}{\partial y}]^T$. Equilibrium of moments around x and y axes gives:

$$\frac{\partial m_{xx}}{\partial x} + \frac{\partial m_{xy}}{\partial y} = -q_x; \qquad \frac{\partial m_{yy}}{\partial y} + \frac{\partial m_{xy}}{\partial x} = -q_y \tag{2.2.17}$$

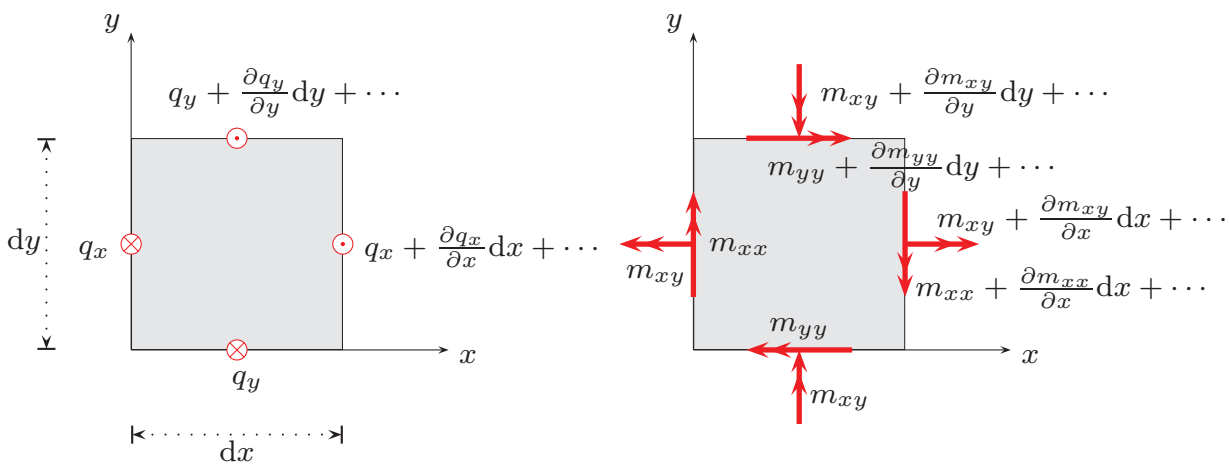

Figure 2.2.2: Stress resultants - shear forces and moments - on a midsurface differential element
Slika 2.2.2: Rezultante napetosti - strižne sile in momenti - na diferencialnem elementu nevtralne ploskve

or shortly

$$\nabla \cdot \mathbf{M} = \left[\ \nabla, \nabla\ \right]^T \mathbf{M} = -\boldsymbol{q}; \quad \mathbf{M} = \begin{bmatrix} m_{xx} & m_{xy} \\ m_{xy} & m_{yy} \end{bmatrix} \tag{2.2.18}$$

A single equilibrium equation is obtained by elimination of the shear forces from (2.2.17) and (2.2.18)

$$\frac{\partial^2 m_{xx}}{\partial x^2} + 2\frac{\partial^2 m_{xy}}{\partial x \partial y} + \frac{\partial^2 m_{yy}}{\partial y^2} = f \tag{2.2.19}$$

or in a more compact notation

$$\boldsymbol{\mathcal{L}} \cdot \boldsymbol{m} = f \tag{2.2.20}$$

Although the Kirchhoff model assumes constitutive transverse shear forces as zero, the equilibrium transverse shear forces should be non-zero also for the Kirchhoff model, if the equilibrium equations are to be satisfied.

Boundary conditions

Let us introduce at each boundary point an orthogonal basis $(\boldsymbol{n}, \boldsymbol{s})$, where $\boldsymbol{n}$ is the boundary normal and $\boldsymbol{s}$ is the boundary tangential vector, see Figure 2.2.1. We also define $\boldsymbol{\phi} = [\phi_x, \phi_y]^T = [-\theta_y, \theta_x]^T$. We further denote part of the boundary where w is prescribed $(w = \bar{w})$ as Γ_w. Similarly, part of the boundary where ϕ_n is prescribed $(\phi_n = \bar{\phi}_n)$ is denoted as Γ_{ϕ_n}, and part of the boundary where ϕ_s is prescribed $(\phi_s = \bar{\phi}_s)$ is denoted

as Γ_{ϕ_s}. We further define $\Gamma_w \cup \Gamma_{\phi_n} \cup \Gamma_{\phi_s} = \Gamma_D$. The transformation relations between ϕ_x, ϕ_y and ϕ_n, ϕ_s will be given further below. The boundary conditions on displacement and rotations are called *Dirichlet or essential boundary conditions*.

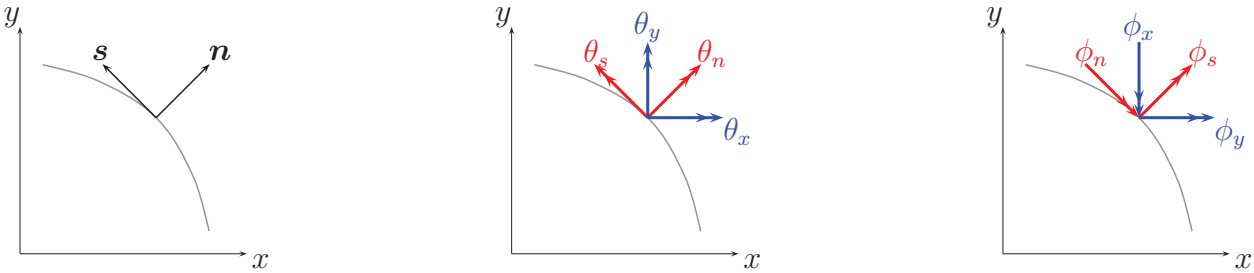

Figure 2.2.3: Rotations at the boundary
Slika 2.2.3: Rotacije na robu

In a similar fashion we define parts of the boundary where transverse force and bending moments are prescribed. Part of the boundary where transverse force is prescribed ($q = \bar{q}$) is Γ_q, part of the boundary where m_n is prescribed ($m_n = \bar{m}_n$) is Γ_{m_n} and part of the boundary where m_s is prescribed ($m_s = \bar{m}_s$) is Γ_{m_s}. We define $\Gamma_q \cup \Gamma_{m_n} \cup \Gamma_{m_s} = \Gamma_N$. The boundary transverse shear force is defined as $q = \boldsymbol{q} \cdot \boldsymbol{n}$. The transformation relations between m_{xx}, m_{yy}, m_{xy} and m_n, m_s will be given further below. The boundary conditions on transverse force and moments are called *Neumann or natural boundary conditions*. Note, that $\Gamma_w \cup \Gamma_q = \Gamma$, $\Gamma_{\phi_n} \cup \Gamma_{m_s} = \Gamma$ and $\Gamma_{\phi_s} \cup \Gamma_{m_n} = \Gamma$.

Strong form of the problem - biharmonic equation

A modified moment (or *Marcus moment* after [Marcus, 1932])

$$\underline{m} = D(\phi_{x,x} + \phi_{y,y}) = D\nabla \cdot \boldsymbol{\phi} = \frac{(m_{xx} + m_{yy})}{(1+\nu)} \tag{2.2.21}$$

can be introduced as an auxiliary variable when solving the above equations analytically. In (2.2.21) the notation $\boldsymbol{\phi} = [\phi_x, \phi_y]^T = [-\theta_y, \theta_x]^T$ has been used (see Figure 2.2.1). The equilibrium equation (2.2.20) then becomes (after some straightforward manipulations with (2.2.4) and (2.2.12))

$$\triangle \underline{m} = f \tag{2.2.22}$$

where $\triangle = \left(\frac{\partial^2}{\partial x^2} + \frac{\partial^2}{\partial y^2}\right)$.

For Kirchhoff model one has $\boldsymbol{\phi} = \nabla w$ (see (2.2.7)). Employing this in (2.2.21), one gets

$$\nabla \cdot \nabla w = \triangle w = \underline{m}/D \tag{2.2.23}$$

In passing we note also, that the equilibrium shear forces are related to the Marcus moment through the following relation

$$q_x = -\underline{m}_{,x}; \quad q_y = -\underline{m}_{,y} \tag{2.2.24}$$

By using (2.2.22) in (2.2.23), we arrive at the biharmonic equation

$$\triangle\triangle w = f/D \tag{2.2.25}$$

or

$$\frac{\partial^4 w}{\partial x^4} + 2\frac{\partial^4 w}{\partial x^2 \partial y^2} + \frac{\partial^4 w}{\partial x^4} = f/D \tag{2.2.26}$$

This equation can be solved analytically for some simple plate geometries (i.e. circular, rectangular), several types of boundary conditions and several types of loadings. We note, that the deflection of a plate, as computed by the Kirchhoff plate theory, is thickness independent up to the factor D (D itself is a function of thickness). The deflection w is thus thickness independent for surface loading $f = gt^3$, where $g(x, y)$ is a thickness independent function.

Weak form of the problem

The weak form of plate bending problem is needed if we want to solve the problem numerically by the finite element method. To arrive at the weak form, the equilibrium equations are first multiplied by arbitrary, yet kinematically admissible test functions. Then, an integral of the sum of those products over the plate midsurface is formed. Using the integration per partes, the integral is further transformed into a simpler form. Final form is obtained by using Neumann boundary conditions.

The above described procedure will be now presented in more detail. We introduce two independent test functions: a scalar function u and a vector function $\boldsymbol{\varphi} = [\varphi_x, \varphi_y]^T$. The function u is arbitrary, yet zero at the part of the boundary Γ_w where w is prescribed. Similarly, φ_x and φ_y are arbitrary, but zero at the parts of the boundary where rotations ϕ_x and ϕ_y are prescribed, respectively. Of course, φ_x and φ_y can be transformed to φ_n and φ_s in the same way as ϕ_x and ϕ_y into ϕ_n and ϕ_s. The difference between ∇u and $\boldsymbol{\varphi}$ is denoted as $\boldsymbol{\tau}$

$$\boldsymbol{\tau} = \nabla u - \boldsymbol{\varphi} \tag{2.2.27}$$

The equilibrium equations (2.2.16), (2.2.17) are multiplied by the corresponding test function, summed, and integrated over the plate midsurface Ω

$$\int_\Omega \left[\left(\frac{\partial m_{xx}}{\partial x} + \frac{\partial m_{xy}}{\partial y} \right) \varphi_x + \left(\frac{\partial m_{yy}}{\partial y} + \frac{\partial m_{xy}}{\partial x} \right) \varphi_y + \boldsymbol{q} \cdot \boldsymbol{\varphi} + (\nabla \cdot \boldsymbol{q} + f) u \right] \mathrm{d}\Omega = 0 \tag{2.2.28}$$

After reorganizing the first two terms in the above equation, we notice

$$\begin{aligned} &\left(\frac{\partial m_{xx}}{\partial x} \varphi_x + \frac{\partial m_{xy}}{\partial x} \varphi_y \right) + \left(\frac{\partial m_{yy}}{\partial y} \varphi_y + \frac{\partial m_{xy}}{\partial y} \varphi_x \right) = \\ &= + \left(\frac{\partial}{\partial x} \left(m_{xx} \varphi_x + m_{xy} \varphi_y \right) + \frac{\partial}{\partial y} \left(m_{yy} \varphi_y + m_{xy} \varphi_x \right) \right) \\ &\quad - \left(m_{xx} \frac{\partial \varphi_x}{\partial x} + m_{xy} \frac{\partial \varphi_y}{\partial x} + m_{yy} \frac{\partial \varphi_y}{\partial y} + m_{xy} \frac{\partial \varphi_x}{\partial y} \right) = \\ &= \nabla \cdot \begin{bmatrix} m_{xx} \varphi_x + m_{xy} \varphi_y \\ m_{yy} \varphi_y + m_{xy} \varphi_x \end{bmatrix} - \boldsymbol{m} \cdot \boldsymbol{\beta} \end{aligned} \tag{2.2.29}$$

where $\boldsymbol{\beta} = [\frac{\partial \varphi_x}{\partial x}, \frac{\partial \varphi_y}{\partial y}, (\frac{\partial \varphi_x}{\partial y} + \frac{\partial \varphi_y}{\partial x})]^T$. The reorganization makes possible integration per partes, since the Gauss statement $\int_\Omega \nabla \cdot \boldsymbol{v} \, \mathrm{d}\Omega = \int_\Gamma \boldsymbol{v} \cdot \boldsymbol{n} \, \mathrm{d}s$ for a vector field $\boldsymbol{v}$ can be used in (2.2.28) to obtain

$$\int_\Gamma \begin{bmatrix} m_{xx} \varphi_x + m_{xy} \varphi_y \\ m_{yy} \varphi_y + m_{xy} \varphi_x \end{bmatrix} \cdot \boldsymbol{n} \, \mathrm{d}s - \int_\Omega \boldsymbol{m} \cdot \boldsymbol{\beta} \, \mathrm{d}\Omega + \int_\Omega \boldsymbol{q} \cdot \boldsymbol{\varphi} \, \mathrm{d}\Omega + \int_\Omega (\nabla \cdot \boldsymbol{q} + f) \, \mathrm{d}\Omega \tag{2.2.30}$$

where Γ defines the boundary of Ω and $\boldsymbol{n} = [n_x, n_y]^T$ is its normal vector (see Figure 2.2.4). The first term of (2.2.30) deserves a special attention and can be further simplified. We may denote the bending moments at a boundary point that rotate around x and y axes as m_x and m_y, respectively

$$m_x = + \left(m_{yy} n_y + m_{xy} n_x \right); \quad m_y = - \left(m_{xx} n_x + m_{xy} n_y \right) \tag{2.2.31}$$

and rewrite the first term of (2.2.30) as

$$\int_\Gamma \begin{bmatrix} m_{xx} \varphi_x + m_{xy} \varphi_y \\ m_{yy} \varphi_y + m_{xy} \varphi_x \end{bmatrix} \cdot \boldsymbol{n} \, \mathrm{d}s = \int_\Gamma (m_x \varphi_y - m_y \varphi_x) \, \mathrm{d}s \tag{2.2.32}$$

def1.331 A vector test function $\boldsymbol{\vartheta} = [\vartheta_x, \vartheta_y]^T = [\varphi_y, -\varphi_x]^T$ with a more clear physical interpretation of test rotations (defined along the coordinates axes) may be now introduced, see Figure 2.2.4. Note, that the test rotation vector $\boldsymbol{\vartheta}$ can be expressed relative to the orthogonal basis $(\boldsymbol{n}, \boldsymbol{s})$, which is defined at the boundary Γ, as

$$\boldsymbol{\vartheta} = \begin{bmatrix} \vartheta_x \\ \vartheta_y \end{bmatrix} = \begin{bmatrix} \varphi_y \\ -\varphi_x \end{bmatrix} = \begin{bmatrix} n_x & -n_y \\ n_y & n_x \end{bmatrix} \begin{bmatrix} \vartheta_n \\ \vartheta_s \end{bmatrix} \tag{2.2.33}$$

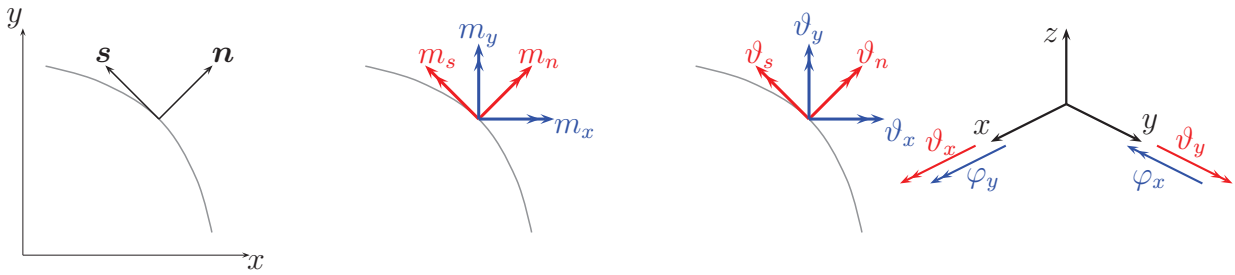

Figure 2.2.4: Boundary coordinate system, moments and test rotations

Slika 2.2.4: Koordinatni sistem na robu, momenti ter testne rotacije

and similarly

$$\begin{bmatrix} \theta_x \\ \theta_y \end{bmatrix} = \begin{bmatrix} \phi_y \\ -\phi_x \end{bmatrix} = \begin{bmatrix} n_x & -n_y \\ n_y & n_x \end{bmatrix} \begin{bmatrix} \theta_n \\ \theta_s \end{bmatrix} \tag{2.2.34}$$

Finally, with newly introduced notation, the expression (2.2.32) simplifies to

$$\int_\Gamma (m_x\vartheta_x + m_y\vartheta_y)\,\mathrm{d}s = \int_\Gamma (m_n\vartheta_n + m_s\vartheta_s)\,\mathrm{d}s \tag{2.2.35}$$

where

$$\begin{bmatrix} m_n \\ m_s \end{bmatrix} = \begin{bmatrix} n_x & n_y \\ -n_y & n_x \end{bmatrix} \begin{bmatrix} m_x \\ m_y \end{bmatrix} = \begin{bmatrix} (m_{yy} - m_{xx})n_x n_y + m_{xy}(n_x^2 - n_y^2) \\ -(m_{xx}n_x^2 + m_{yy}n_y^2 + 2m_{xy}n_x n_y) \end{bmatrix} \tag{2.2.36}$$

are the boundary moments in $(\boldsymbol{n}, \boldsymbol{s})$ basis (see Figure 2.2.4). The last two terms of (2.2.28) can also be partially integrated. Using the definition (2.2.27) we have

$$\int_\Omega (\boldsymbol{q}\cdot\boldsymbol{\varphi} + (\nabla\cdot\boldsymbol{q} + f)u)\,\mathrm{d}\Omega = \int_\Omega (\boldsymbol{q}\cdot\nabla u + u\nabla\cdot\boldsymbol{q})\mathrm{d}\Omega - \int_\Omega (\boldsymbol{q}\cdot\boldsymbol{\tau} - fu)\,\mathrm{d}\Omega \tag{2.2.37}$$

Due to $\nabla\cdot(u\boldsymbol{q}) = \boldsymbol{q}\cdot\nabla u + u\nabla\cdot\boldsymbol{q}$, the first part of (2.2.37) is integrated into

$$\int_\Omega (\boldsymbol{q}\cdot\nabla u + u\nabla\cdot\boldsymbol{q})\mathrm{d}\Omega = \int_\Omega \nabla\cdot(u\boldsymbol{q})\mathrm{d}\Omega = \int_\Gamma u\,\boldsymbol{q}\cdot\boldsymbol{n}\,\mathrm{d}s \tag{2.2.38}$$

Equation (2.2.37) can now be expressed as

$$\int_\Omega (\boldsymbol{q}\cdot\boldsymbol{\varphi} + u\nabla\cdot\boldsymbol{q} + fu)\,\mathrm{d}\Omega = \int_\Gamma u\,\boldsymbol{q}\cdot\boldsymbol{n}\,\mathrm{d}s - \int_\Omega \boldsymbol{q}\cdot\boldsymbol{\tau}\,\mathrm{d}\Omega + \int_\Omega fu\,\mathrm{d}\Omega \tag{2.2.39}$$

Finally, the expression (2.2.28) can be given as:

$$\int_\Omega (\boldsymbol{m}\cdot\boldsymbol{\beta} + \boldsymbol{q}\cdot\boldsymbol{\tau})\,\mathrm{d}\Omega = \int_\Omega f\,u\,\mathrm{d}\Omega + \int_\Gamma (q\,u + m_n\vartheta_n + m_s\vartheta_s)\,\mathrm{d}s \tag{2.2.40}$$

where the notation $q = \boldsymbol{q}\cdot\boldsymbol{n}$ was employed. The last terms in (2.2.40) vanish on parts of the boundary where u, ϑ_n and ϑ_s are zero. If one uses the Neumann boundary conditions in (2.2.40), the equation (2.2.40) becomes

$$\int_\Omega (\boldsymbol{m}\cdot\boldsymbol{\beta} + \boldsymbol{q}\cdot\boldsymbol{\tau})\,\mathrm{d}\Omega = \int_\Omega f\,u\,\mathrm{d}\Omega + \int_{\Gamma_q} \overline{q}\,u\mathrm{d}s + \int_{\Gamma_{m_n}} \overline{m}_n\vartheta_n\,\mathrm{d}s + \int_{\Gamma_{m_s}} \overline{m}_s\vartheta_s\,\mathrm{d}s \tag{2.2.41}$$

Up to this point, the Kirchhoff thin plate kinematic assumption has not been used in the derivation of the weak form. Therefore, (2.2.41) holds both for thin and moderately thick plates. We will now work towards specialization of the weak form for the thin plate Kirchhoff model. The test functions are in accordance with the Kirchhoff thin plate model only when $\boldsymbol{\tau} = 0$, which is equivalent to $\boldsymbol{\varphi} = \nabla u$. The test functions u and $\boldsymbol{\varphi}$ are no longer independent, since $\varphi_y = \vartheta_x = \frac{\partial u}{\partial y}$ and $-\varphi_x = \vartheta_y = -\frac{\partial u}{\partial x}$. From (2.2.33) we can also read

$$\begin{aligned} \vartheta_n &= \vartheta_x n_x + \vartheta_y n_y = +\frac{\partial u}{\partial y} n_x - \frac{\partial u}{\partial x} n_y = +\frac{\partial u}{\partial s} \\ \vartheta_s &= \vartheta_y n_x - \vartheta_x n_y = -\frac{\partial u}{\partial x} n_x - \frac{\partial u}{\partial y} n_y = -\frac{\partial u}{\partial n} \end{aligned} \tag{2.2.42}$$

It is common that the boundary of a plate is defined by a sequence of straight or curved edges. In that case the equation (2.2.40) has to be integrated for all the edges. Let us assume for simplicity that $\Gamma_q = \Gamma_{m_n} = \Gamma_{m_s} = \Gamma_N$ and consider the boundary $\Gamma_{N,AB}$ which extends from point A to point B. The integral over the boundary in (2.2.40) can be split into integral over the segments $\Gamma_{N,AB} = \bigcup \Gamma_{N,IJ}$:

$$\begin{aligned} &\int_{\Gamma_{N,IJ}} (q\,u + m_n \vartheta_n + m_s \vartheta_s)\,\mathrm{d}s = \int_{\Gamma_{N,IJ}} (q\,u + m_n \frac{\partial u}{\partial s} + m_s \vartheta_s)\,\mathrm{d}s = \\ &= [u\,m_n]_I^J + \int_{\Gamma_{N,IJ}} (u(q - \frac{\partial m_n}{\partial s}) + m_s \vartheta_s)\,\mathrm{d}s \\ &= [u\,m_n]_I^J + \int_{\Gamma_{N,IJ}} (u\,q_{ef} + m_s \vartheta_s)\,\mathrm{d}s \end{aligned} \tag{2.2.43}$$

where the *effective transverse shear* force was introduced:

$$q_{ef} = q - \frac{\partial m_n}{\partial s} \tag{2.2.44}$$

It can be seen from (2.2.43) that the boundary conditions for Kirchhoff plate differ from the boundary conditions already discussed above in previous section. Namely, the corresponding couples are w and q_{ef} and m_s and ϕ_n. Therefore, the Neumann boundary conditions are: $q_{ef} = \overline{q}_{ef}$ on Γ_q and $m_s = \overline{m}_s$ on Γ_{m_s}. The Dirichlet boundary conditions are: $w = \overline{w}$ on Γ_w and $\phi_n = \overline{\phi}_n$ on Γ_{ϕ_n}. One has $\Gamma_q \bigcup \Gamma_w = \Gamma$ and $\Gamma_{ms} \bigcup \Gamma_{\phi_n} = \Gamma$. The term in (2.2.44), $\frac{\partial m_n}{\partial s}$, can be graphically illustrated by representing the line twisting moment by a sequence of pairs of opposing forces, as done in many textbooks on plates.

By using boundary conditions in (2.2.43) one gets

$$\int_{\Gamma_{N,AB}} (q\,u + m_n\vartheta_n + m_s\vartheta_s)\,\mathrm{d}s = \tag{2.2.45}$$
$$\sum_I u_I(m_{n,I}|_B - m_{n,I}|_A) + \int_{\Gamma_{N,AB}} (u\,q_{ef} + m_s\vartheta_s)\,\mathrm{d}s$$

where the sum runs over the points I, which are located at intersections of edges on the part of the boundary $\Gamma_{N,AB}$. The $m_{n,I}|_A$ denotes the value of m_n at point I on its A side. The term in the sum corresponding to point I is nonzero only if the m_n is discontinuous at that point. The difference can be attributed to the *corner force* $F_{C,I} = [m_{n,I}]_A^B$, which is an internal force, see Figure 2.2.4.

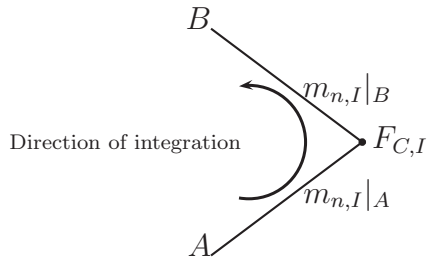

Figure 2.2.5: Concentrated corner force at node I
Slika 2.2.5: Koncentrirana sila v vozlišču I

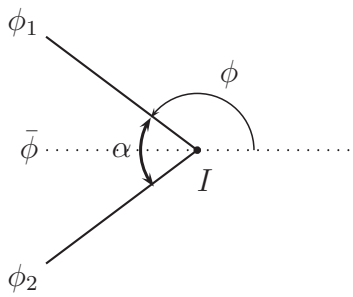

Figure 2.2.6: To the definition of a corner force in (2.2.47)
Slika 2.2.6: K definiciji vozliščne sile (2.2.47)

2.2.2 Further details of the Kirchhoff model

Effective transverse shear force

The biharmonic equation (2.2.26) is a partial differential equation of the fourth order. It can only have two boundary conditions at each boundary point. In the moderately

thick plate model three independent quantities appear naturally at a boundary point: the transverse displacement w, the normal rotation θ_n and the tangential rotation θ_s. The conjugate quantities are the transverse shear force q, twisting moment m_n and tangential (bending) moment m_s respectively. Integration per partes in (2.2.43), however, shows that only two pairs of conjugate quantities exist for the Kirchhoff model: (1) displacement w and effective shear q_{ef}, and (2) tangential rotation θ_s and tangential moment m_s. This is the direct consequence of the Kirchhoff assumption (2.2.6) which relates displacement to the rotations.

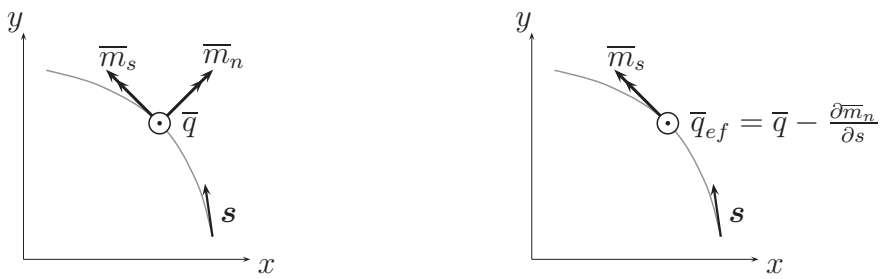

Figure 2.2.7: Boundary loading $\overline{m}_n$, $\overline{m}_s$ and $\overline{q}$ for moderately thick plate (left) and Kirchhoff plate (right)

Slika 2.2.7: Robna obtežba $\overline{m}_n$, $\overline{m}_s$ in $\overline{q}$ za srednje debele plošče (levo) in Kirchhoffove plošče (desno)

Reaction corner force

Let us consider the point lying at the corner of the plate, denoted by I. The corner with opening angle α extends between angles ϕ_1 and ϕ_2 ($\alpha = \phi_2 - \phi_1$), see Figure 2.2.6. ¡¡¿¿ If the moment stress resultants at the corner I are $[m_{xx}, m_{yy}, m_{xy}]^T$, the twisting moment at the side with angle ϕ is

$$m_n(\phi) = \frac{1}{2}(m_{yy} - m_{xx}) \sin 2\phi + m_{xy} \cos 2\phi \tag{2.2.46}$$

With this result and trigonometric identities $\sin a - \sin b = 2\sin((a-b)/2)\cos((a+b)/2)$ and $\cos a - \cos b = -2\sin((a-b)/2)\sin((a+b)/2)$, the corner force at I is expressed as

$$F_{C,I}(\bar{\phi}, \alpha) = m_n(\phi_2) - m_n(\phi_1) = 2m_n(\bar{\phi}) \sin \alpha; \quad \bar{\phi} = \frac{\phi_1 + \phi_2}{2} + \frac{\pi}{4} \tag{2.2.47}$$

For a given angle $\bar{\phi}$ the corner force depends only on the opening angle. The maximum corner force occurs at $\alpha = \pi/2$. For the obtuse corner, we have $F_{C,I}(\bar{\phi}, 2\pi - \alpha) = -F_{C,I}(\bar{\phi}, \alpha)$. If the vertical displacement at the corner boundary area of a plate is not restricted, the corner force tends to move the corner in the direction opposite to f. The

reaction corner force is present if the displacement at corner boundary area is fixed. The reaction corner force, however, does not appear if the edges meeting at the corner are free or clamped, because the twisting moment m_n on both sides of the corner point is zero.

Weak form of the problem

The weak form of the plate bending problem for the Kirchhoff model is

$$\int_\Omega \boldsymbol{m} \cdot \boldsymbol{\beta} \, \mathrm{d}\Omega = \int_\Omega u \, f \, \mathrm{d}\Omega + \int_\Gamma (\overline{q}_{ef} \, u - \overline{m}_s \frac{\partial u}{\partial n}) \, \mathrm{d}s \tag{2.2.48}$$

The corner forces are omitted from the expression (2.2.48). The constitutive equation and the kinematic equation are used point-wise. Therefore, the vector $\boldsymbol{\beta}$ is a function of u only, since $\boldsymbol{\beta} = \boldsymbol{\mathcal{L}} u$ and $\boldsymbol{m} = \mathbf{C}_B \boldsymbol{\kappa} = \mathbf{C}_B \boldsymbol{\mathcal{L}} w$, where $\boldsymbol{\kappa} = \boldsymbol{\mathcal{L}} w$. Left hand side of (2.2.48) becomes a bilinear form of w and u

$$a_K(w; u) = \int_\Omega u \boldsymbol{\mathcal{L}}^T \mathbf{C}_B \boldsymbol{\mathcal{L}} w \, \mathrm{d}\Omega \tag{2.2.49}$$

while the right hand side is a linear functional of u only:

$$l_K(u) = \int_\Omega u \, f \, \mathrm{d}\Omega + \int_\Gamma (\overline{q}_{ef} \, u - \overline{m}_s \frac{\partial u}{\partial n}) \, \mathrm{d}s + \sum_i \overline{F}_{Ci} u_i \tag{2.2.50}$$

The weak form of a thin plate Kirchhoff bending problem can be presented as

> For given geometry, Dirichlet and Neumann boundary conditions and area loads, find displacement $w \in \mathcal{V}$, such that
>
> $$a_K(w; u) = l_K(u) \quad \forall u \in \mathcal{V}_0 \tag{2.2.51}$$
>
> is satisfied for arbitrary test function u from the test space $\mathcal{V}_0$

The test space $\mathcal{V}$ consist of square integrable functions, which satisfy the boundary condition of the problem, while the test space $\mathcal{V}_0$ consists of square integrable functions which are zero at the part of the boundary where the Dirichlet boundary conditions are prescribed.

Virtual work

The principle of virtual work can be regarded as the weak form of the equilibrium equations. That becomes clear if the test functions are denoted as $u = \delta w$ and $\boldsymbol{\beta} = \delta \boldsymbol{\kappa}$ where δ stands for the variation. The variations δw and $\delta \frac{\partial w}{\partial n} = \frac{\partial \delta w}{\partial n}$ are zero at the boundary

where the displacement w or rotation $\frac{\partial w}{\partial n}$ are defined, respectively. The virtual work of internal forces for the thin plate is thus

$$\delta\Pi^{int} = \int_{\Omega} \delta\boldsymbol{\kappa}^T \boldsymbol{m} \, \mathrm{d}\Omega \tag{2.2.52}$$

and the virtual work of external forces:

$$\delta\Pi^{ext} = \int_{\Omega} \delta w \, f \, \mathrm{d}\Omega + \int_{\Gamma} (\overline{q}_{ef} \, \delta w - \overline{m}_s \frac{\partial \delta w}{\partial n}) \, \mathrm{d}s \tag{2.2.53}$$

By using constitutive and kinematic equations $\boldsymbol{m} = \mathbf{C}_B \boldsymbol{\kappa} = \mathbf{C}_B \boldsymbol{\mathcal{L}} w$ the virtual work equation transforms into the weak problem. The equilibrium displacement w is such that the virtual work of internal forces equals the virtual work of external forces for arbitrary admissible virtual displacement δw, which conforms to the boundary conditions

$$\delta\Pi^{int} = a_K(w; \delta w) = \delta\Pi^{ext} = l_K(\delta w) \qquad \forall \delta w \in \mathcal{V}_0 \tag{2.2.54}$$

Boundary conditions

The part of the boundary, where displacement and its normal derivative is prescribed, is called *fixed boundary* and the boundary conditions are expressed as

$$w = \overline{w}; \qquad \theta_s = -\frac{\partial w}{\partial n} = \overline{\theta}_s \tag{2.2.55}$$

Since the test function u and its normal derivative are zero, at that parts nonzero contribution to (2.2.50) is only from the region of boundary where stress resultants are prescribed (and displacements and its normal derivatives are not). The linear functional (2.2.50) suggests that there are two independent loads on the boundary Γ_N: moment $\overline{m}_s$ and shear force $\overline{q}_{ef}$. The boundary conditions for the *traction boundary* are:

$$q_{ef} = \overline{q}_{ef}; \qquad m_s = \overline{m}_s \tag{2.2.56}$$

From (2.2.43) we notice that at free edges the shear force q_{ef} and the tangential moment m_s vanish. However, (2.2.44) shows that vanishing shear force $q_{ef} = 0$ does not necessarily imply that the shear q at free edges also vanish. In fact the shear q and twisting moment m_n can both be nonzero at the free edges of the Kirchhoff plate. Another implication is that the support forces are not identical to shear forces if the twisting moment exists.

Some common boundary conditions for the thin plate problem are listed in Table 2.1. Notice, that the prescription of the displacement of the boundary implicitly defines also the normal rotation. Since the Kirchhoff constraint along the boundary is $\gamma_s = \frac{\partial w}{\partial s} - \theta_n = 0$

Table 2.1: Boundary conditions for thin plates. * $\theta_n = \frac{\partial w}{\partial s}$ is zero due to $w = 0$.
Tabela 2.1: Robni pogoji za tanke plošče. * $\theta_n = \frac{\partial w}{\partial s}$ je nič zaradi $w = 0$.

Clamped (fixed):	$w = 0$	$\theta_s = 0$	$\theta_n = 0^*$
Simply supported:	$w = 0$	$m_s = 0$	$\theta_n = 0^*$
Free:	$q_{ef} = 0$	$m_s = 0$	

the normal rotation is defined by $\theta_n = \frac{\partial w}{\partial s}$. In the case of simply supported or clamped boundary the constraint $w = 0$ implies also $\theta_n = 0$. Therefore, with the Kirchhoff model it is possible to model only hard simply supported boundary. The difference between the hard and the soft simple support will be presented in the next chapter.

Principal directions of the moments

The twisting moment m_n and the bending moment m_s in a given direction at a point $(x, y) \in \Omega$ are defined by (2.2.36). Let $\boldsymbol{n}$ in (2.2.36) be defined as $\boldsymbol{n} = [\cos\varphi, \sin\varphi]^T$. From the condition $m_n = 0$, one can compute angle φ at which the twisting moment vanishes:

$$\tan 2\varphi = \frac{2m_{xy}}{m_{xx} - m_{yy}} \tag{2.2.57}$$

The twisting moment has its extreme value at $\varphi \pm \pi/2$:

$$m_n^{max} = \sqrt{\left[\frac{m_{xx} - m_{yy}}{2}\right]^2 + m_{xy}^2} \tag{2.2.58}$$

The maximum and minimum bending moment are:

$$m_{I,II} = \frac{m_{xx} + m_{yy}}{2} \pm m_n^{max} \tag{2.2.59}$$

Singularities

An interesting implication of the Kirchhoff constraint occurs in the case of curved simply supported boundary, which is approximated by a polygonal boundary. The normal rotation at each corner point is defined twice - for each side a normal rotation $\theta_n = \frac{\partial w}{\partial s} = \nabla w \cdot \boldsymbol{s} = 0$ vanishes. Since the orientations of the sides meeting in corner point do not match, $\boldsymbol{s}_1 \neq \boldsymbol{s}_2$, this is only possible when $\nabla w = 0$ at the corner points

$$\nabla w \cdot \boldsymbol{s}_1 = 0; \quad \nabla w \cdot \boldsymbol{s}_2 = 0 \Rightarrow \nabla w = 0 \tag{2.2.60}$$

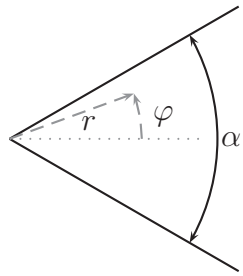

Figure 2.2.8: Definition of a polar coordinate system (r, φ) at the corner
Slika 2.2.8: Definicija polarnega koordinatnega sistema (r, φ) v vogalu

At corner points the plate is thus effectively clamped:

$$w = \frac{\partial w}{\partial x} = \frac{\partial w}{\partial y} = 0 \tag{2.2.61}$$

The corner clamping is the source of singularity at the corner points of simply supported polygonal boundary. The bending moments and shear forces may become singular.

The singular behavior of the solution in the vicinity of corner points has been studied in several works for simply supported and other boundary conditions. For the illustration of the approach we reexamine the case of a corner with opening angle α bounded by two simply supported edges of a plate. This problem was first presented in [Morley, 1963]. A polar coordinate (r, φ) system is introduced (see Figure 2.2.8). The origin of the coordinate system is in the corner point such that $\varphi \in [-\alpha/2, +\alpha/2]$. The biharmonic equation in polar coordinates reads [Timoshenko Vojnovski-Kriger, 1959]

$$\triangle\triangle w = f/D; \quad \triangle = \frac{\partial^2}{\partial r^2} + \frac{1}{r}\frac{\partial}{\partial r} + \frac{1}{r^2}\frac{\partial^2}{\partial \varphi^2} \tag{2.2.62}$$

with the stress resultants defined as:

$$\begin{aligned} m_r &= -D((1-\nu)\frac{\partial^2 w}{\partial r^2} + \nu\triangle w) \\ m_\varphi &= -D(\triangle w - (1-\nu)\frac{\partial^2 w}{\partial r^2}) \\ m_{r\varphi} &= (1-\nu)D(\frac{1}{r}\frac{\partial^2 w}{\partial r \partial \varphi} - \frac{1}{r^2}\frac{\partial w}{\partial \varphi}) \\ q_r &= -D\frac{\partial}{\partial r}\triangle w; \quad q_\varphi = -D\frac{1}{r}\frac{\partial}{\partial \varphi}\triangle w \end{aligned} \tag{2.2.63}$$

The boundary conditions for a simply supported edge are:

$$w = 0; \quad m_\varphi = 0 \tag{2.2.64}$$

Since the displacement along the radial edge is constant (e.g. zero), we have $\frac{\partial w}{\partial r} = \frac{\partial^2 w}{\partial r^2} = 0$ and the second condition $m_\varphi = 0$ is equivalent to $\triangle w = 0$. The general solution of (2.2.62), (2.2.64) can be presented as a sum $w = w_p + w_h$ of a particular solution w_p and a homogeneous solution w_h, which is biharmonic. A particular solution w_p, which satisfies (2.2.62) and (2.2.64) at $\varphi = \pm\alpha/2$ is

$$w_p = \frac{f\, r^4}{64D}\left(1 - \frac{4\cos(2\varphi)}{3\cos(\alpha)} + \frac{1}{3}\frac{\cos(4\varphi)}{\cos(2\alpha)}\right) \tag{2.2.65}$$

which can be checked by using it in (2.2.62) and (2.2.64). A special form of particular solution is required for angles α=$(\pi/4, \pi/2, 3\pi/4, 3\pi/2, 2\pi/2)$, when the cosine term in the denominator is zero. The homogeneous solution is chosen as an infinite series of eigenfunctions $w_{h,m}$, i.e. $w_h = \sum_{m=1}^{\infty} w_{h,m}$. Eigenfunctions which satisfy homogeneous biharmonic equation, as well as the boundary conditions $w = 0$, $\triangle w = 0$ along the radial edges at $\varphi = \pm\alpha/2$, are

$$w_{h,m} = (a_m + b_m r^2) r^\lambda \cos(\lambda\varphi) \tag{2.2.66}$$

where a_m and b_m are constants and λ is chosen so that

$$\cos(\pm\lambda\alpha/2) = 0 \Rightarrow \lambda = \pi/\alpha(1 + 2m); \quad m \geq 0 \tag{2.2.67}$$

For the displacement w and rotation $\frac{\partial w}{\partial r}$ to remain finite at $r = 0$ the condition $\lambda \geq 0$ has been taken into account. The leading term in the expression for the displacement w is of the form $r^\lambda \cos(\lambda\varphi)$. From (2.2.63), we see that the leading term for the moments m_r and m_φ is $r^{\lambda-2}$, while the leading term for the q_r, q_φ and $m_{r\varphi}$ is $r^{\lambda-3}$. The singularity occurs when the exponent is < 0. The singular behavior of (i) m_r and m_φ is expected when $\lambda < 2$ or $\alpha > \pi/2$. Correspondingly, the singularity in (ii) q_r, q_φ and $m_{r\varphi}$ can occur at angles $\alpha > \pi/3$. At a given angle the strongest singularity occurs for the stress components (ii) followed by one order weaker singularity in the components (i). The strength of the singularity $\lambda = \pi/\alpha$ is inversely proportional to the opening angle α. The angles $\alpha = \pi/4, \pi/2, 3\pi/4, 3\pi/2, 2\pi/2$ are exceptions. In general, the leading term r^λ in this case is replaced by $r^\lambda(\log r)^p$ where p is an integer. In the neighborhood of these exceptions the singular behavior is not continuous with respect to α. A list of critical angles for Kirchhoff plates for different boundary conditions of intersecting edges is shown in Table 2.2 (after [Melzer Rannacher, 1980]).

Table 2.2: Critical opening angles for the Kirchhoff plate (* - the case reexamined in this section)

Tabela 2.2: Kritični koti za Kirchhoffove plošče (* - primer je obravnavan v tem razdelku)

Support conditions	m_r, m_φ	q_r, q_φ, $m_{r\varphi}$
clamped - clamped	180°	126°
clamped - simply supp.	129°	90°
clamped - free	95°	52°
simply supp. - simply supp.*	90°	60°
simply supp. - free	90°	51°
free - free	180°	78°

2.3 Finite elements

2.3.1 Preliminary considerations

The departure point for the development of finite element method for the thin plate bending problem is the weak form (2.2.51).

Let us define the residuum as the difference between the bilinear and linear forms of the weak form (i.e. the difference between the virtual works of internal and external forces), by

$$\mathcal{R}(w;u) = a_K(w;u) - l_K(u) \tag{2.3.1}$$

The solution w satisfies $\mathcal{R}(w;u) = 0$ for arbitrary $u \in \mathcal{V}_0$. To solve the problem for an approximate solution, the problem domain Ω is discretized by the finite element mesh Ω_h consisting of finite elements Ω_h^e and nodes $i = 1, 2, \cdots, N_n$ (see Figure 2.3.1)

$$\Omega \approx \Omega_h = \bigcup_{\Omega_h^e \in \Omega_h} \Omega_h^e \tag{2.3.2}$$

Each finite element Ω_h^e is defined by a fixed number of nodes and the boundary Γ^e. The approximation of the solution of the problem is now limited to a search in a finite dimensional vector test space $\mathcal{V}_h \subset \mathcal{V}$[1]. It is defined by a finite set of parameters $\hat{w}_i$, associated to the nodes of the mesh, $i = 1, 2, \cdots, N_n$ and shape functions N_i (N_i equals

[1]Subscript h defines an approximation

1 at node i, and 0 at all other nodes)[2]

$$w_h = \sum_i^{N_n} N_i \hat{w}_i \tag{2.3.3}$$

After Bubnov and Galerkin, the optimal approximation of the solution is the one for which the residuum is zero only for the arbitrary test function u_h from the test space $\mathcal{V}_{0,h}$

$$\mathcal{R}(w_h; u_h) = 0 \qquad \forall u_h \in \mathcal{V}_{0,h} \tag{2.3.4}$$

The test space $\mathcal{V}_{0,h}$ is spanned over the shape functions N_i. An arbitrary test function u_h is a linear combination of shape functions: $u_h = \sum_i N_i \hat{u}_i$. The residuum for arbitrary test function u_h vanishes, if it vanishes for each shape function N_i

$$\mathcal{R}(w_h, N_i) = 0 \quad \text{or} \quad \sum_j a_K(N_j, N_i)\, \hat{w}_j = l_K(N_i) \quad \forall N_i \tag{2.3.5}$$

In the matrix form

$$\mathbf{K}\hat{\boldsymbol{u}} = \boldsymbol{f} \tag{2.3.6}$$

where $\mathbf{K} = [K_{ij}] = [a_K(N_i, N_j)]$, $\hat{\boldsymbol{u}} = [\hat{w}_1, \hat{w}_2, \cdots, \hat{w}_{N_n}]^T$ and $\boldsymbol{f} = [l_K(N_1), l_K(N_2), \cdots, l_K(N_{N_n})]^T$. The linear system (2.3.6) is finally solved for the unknown parameters $\hat{\boldsymbol{u}}$.

The approximate solution can be also searched from the spirit of the principle of virtual work. The solution $w_h = \sum_i N_i \hat{w}_i$ must be such that the virtual work of internal forces $\delta\Pi^{int}$ equals the virtual work of external forces $\delta\Pi^{ext}$ for arbitrary virtual displacement $\delta w_h = \sum_i N_i \delta\hat{w}_i$, member of the test space $\mathcal{V}_{0,h}$

$$\delta\Pi^{int} = \delta\Pi^{ext} \qquad \forall \delta w_h \in \mathcal{V}_{0,h} \tag{2.3.7}$$
$$\delta\Pi^{int} = a_K(w_h; \delta w_h); \quad \delta\Pi^{ext} = l_K(\delta w_h)$$

From $w_h = \sum_i N_i \hat{w}_i$ and $\delta w_h = \sum_i N_i \delta\hat{w}_i$ we have

$$\delta\Pi^{int} = a_K(w_h; \sum_i N_i \delta\hat{w}_i) = \sum_i a_K(w_h; N_i)\delta\hat{w}_i = \sum_i \sum_j \hat{w}_j a_K(N_j, N_i)\delta\hat{w}_i$$

where the linearity of bilinear form a_K was exploited. Using the matrix notation we have

$$\delta\Pi^{int} = \delta\hat{\boldsymbol{u}}^T \mathbf{K}\hat{\boldsymbol{u}}; \quad \mathbf{K} = [K_{ij}] = a_K(N_j, N_i); \quad \delta\hat{u} = [\delta\hat{w}_1, \delta\hat{w}_2, \cdots, \delta\hat{w}_n]^T \tag{2.3.8}$$

[2]For the sake of compactness the shape functions N_i are here defined over the whole domain Ω_h

$$\delta\Pi^{ext} = l_K(\delta w_h) = \sum_i \delta\hat{w}_i l_K(N_i) = \delta\hat{\boldsymbol{u}}^T \boldsymbol{f}; \quad \boldsymbol{f} = [f_i] = [l_K(N_i)] \tag{2.3.9}$$

Inserting the relations (2.3.8) and (2.3.9) into (2.3.7) we obtain

$$\delta\hat{\boldsymbol{u}}^T(\mathbf{K}\hat{\boldsymbol{u}} - \boldsymbol{f}) = 0 \tag{2.3.10}$$

Due to the fact that the variations $\delta\hat{w}_i$ are arbitrary and independent, the equation (2.3.10) is fulfilled only when $\mathbf{K}\hat{\boldsymbol{u}} - \boldsymbol{f} = \mathbf{0}$ holds. This is equivalent to (2.3.6).

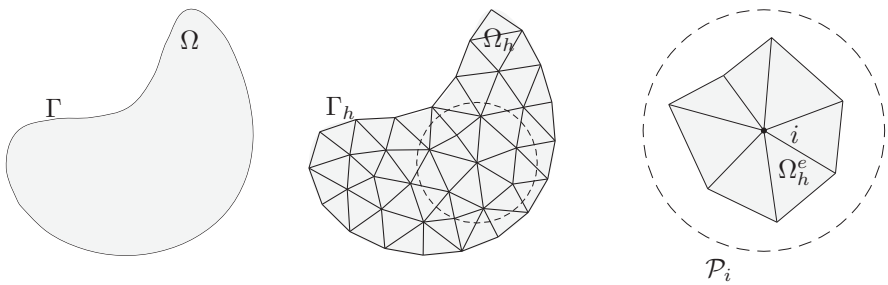

Figure 2.3.1: Problem domain Ω and its boundary Γ (left), finite element discretization Ω_h^e, Ω_h and patch of elements $\Omega_h^{\mathcal{P}_i}$ around node i (right)
Slika 2.3.1: Območje Ω in njegov rob Γ (levo), diskretizacija s končnimi elementi Ω_h^e, Ω_h in krpa elementov $\Omega_h^{\mathcal{P}_i}$ okoli vozlišča i (desno)

Shape functions

The shape function N_i takes unit value at node i and is zero at all other nodes of the finite element mesh. The shape function N_i is nonzero only on a finite domain $\Omega_h^{\mathcal{P}_i}$. Hence, the adjective ‘finite‘ in the name of the method.

Let m denote the variational index of the variational functional (the highest derivative present in the functional) that is to be solved by the finite element method. A basic requirement for the convergence of approximate solution is that the shape functions satisfy the completeness condition: the element shape functions must exactly represent all polynomial terms of order $\leq m$ in the Cartesian coordinates. In the case of (2.2.51), the variational index is $m = 2$, therefore the interpolation on Ω_h^e should be able to represent any field, which is a linear or quadratic polynomial in x and y; in particular, a constant value. Constant and linear polynomials represent rigid body motions, whereas quadratic polynomials represent constant curvature modes. The $\mathcal{C}^0$ continuity requires that the shape functions are continuous across the element edges. The shape functions

are continuous only if the displacement over any side of the element is defined only by DOFs on that side. The second derivatives in (2.2.51) indicate that the shape functions must satisfy not only $\mathcal{C}^0$ but also $\mathcal{C}^1$ continuity - continuity of the slopes of the shape functions. This can only be achieved if the shape functions are $\mathcal{C}^0$ continuous and the normal slope $\frac{\partial w}{\partial n}$ over any edge of the element is completely defined only by the DOFs on that edge. The elements based on $\mathcal{C}^1$ continuous shape functions are often referred to as *conforming* or *compatible*.

While obtaining $\mathcal{C}^0$ continuity is relatively simple, this is certainly not the case with $\mathcal{C}^1$ continuity. It was proven in ([Zienkiewicz Taylor, 2000], [Felippa, 2009]) that, when only w and its slopes are prescribed at the corner nodes, it is *impossible* to specify simple polynomial expressions for shape functions, which ensure the full compatibility.

2.3.2 An overview of thin plate elements

Among the first successful conforming plate elements was the rectangular element with 16 DOFs ($\hat{w}$, $\hat{w}_{,x}$,$\hat{w}_{,y}$ and $\hat{w}_{,xy}$ at each node) developed by [Bogner et al., 1966]. The element uses Hermitian interpolation functions with bi-cubic shape functions. The triangular elements offer more flexibility in the design of the conforming elements that the rectangular ones. It was shown in [Felippa, 2009] that a complete fifth order polynomial is the first which satisfy the $\mathcal{C}^1$ continuity requirements. From the Pascal's triangle it follows that the complete quintic polynomial contains 21 terms. Conforming triangular plate element with 21 DOFs was independently developed by several authors ([Argyris et al., 1968] et al., [Bell, 1969], [Bosshard, 1968], [Visser, 1968]). Conforming quadrilateral elements can be produced from the conforming triangular elements. If the combined element has an additional internal degrees of freedom they are eliminated by static condensation. A direct derivation of conforming quadrilateral element is also possible. The derivation was first proposed by [Sander, 1964] and [De Veubeke, 1968].

Although the conforming plate elements exhibit excellent accuracy and performance they have some important drawbacks. The $\mathcal{C}^1$ continuity presents a difficulty when discontinuous variation of material properties occurs. It is also difficult to impose the right boundary conditions since 'nodal forces' as energy conjugates to chosen degrees of freedom can no longer be interpreted intuitively.

It is relatively simple to obtain shape functions, which respect $\mathcal{C}^0$ continuity but violate the slope continuity between the elements. They can still be used to build plate elements. It is namely possible to found the convergence of such elements if only they pass the

"patch test" [Zienkiewicz Taylor, 2000]. They are referred to as *non-conforming* and can in many cases perform even better than the conforming ones. Additional conditions for the shape functions follow from the patch test. They are formulated for each straight side of the element Γ:

$$\int_\Gamma \Delta(\frac{\partial w}{\partial n})\mathrm{d}s = 0; \quad \int_\Gamma \Delta(\frac{\partial w}{\partial s})\mathrm{d}s = 0. \tag{2.3.11}$$

where Δ denotes the mismatch along the side of neighboring elements. Notice that, if the function w and its first derivatives are defined at the corner nodes, the satisfaction of the second condition in (2.3.11) is always ensured.

An early attempt to build a conforming rectangular element lead to the formulation of the first successful non-conforming quadrilateral plate bending element proposed by [Adini Clough, 1960]. The element has 12 DOFS and it satisfies completeness as well as transverse deflection continuity but normal slope continuity is maintained only at four corner points. One of the first successful non-conforming triangular plate elements is that presented by [Bazeley et al., 1965]. The element has nine DOFs. Since full cubic expansion contains 10 terms, one DOF is eliminated in such a way that the completeness is maintained. Although the element satisfies constant curvature criterion it does not pass the patch test for arbitrary mesh configurations. Despite the shortcomings the element became quite popular in practical applications.

A rather successful approach involves a direct interpolation of displacement w and rotation θ. Due to the independent interpolations the continuity requirement is only $\mathcal{C}^0$ for both unknowns w and θ. The interpolations are constructed such that the Kirchhoff constrain is satisfied only in certain discrete collocation points. Hence the name *discrete Kirchhoff - DK* elements. It is possible to impose the Kirchhoff constraint along the sides of the element resulting in superior performance. The most successful elements of this type are discrete Kirchhoff triangle (DKT) and discrete Kirchhoff quadrilateral (DKQ) ([Dhatt, 1970], [Batoz et al., 1980] and [Batoz, 1982]). Many finite element analyses of a plate bending problem are done with DK plate elements. They are widely accepted due to their efficiency and ease of use. One of the reasons for their popularity is also the fact that they employ only displacement and rotations as the nodal degrees of freedom.

2.3.3 Natural coordinate systems

We have thought of shape function N_i in section 2.3.1 as of a function defined over $\Omega_h^{\mathcal{P}_i}$. In practice, the shape functions are defined over a finite element Ω_h^e.

The description of the element shape functions in the Cartesian coordinates (x, y) is not very convenient. We therefore seek for coordinates ξ_i, $i = 1, 2$ such that the location of a point $P(x, y)$ inside an element defined by nodes $(x_i, y_i), i = (1, 2, 3)$(triangle) or $i = (1, 2, 3, 4)$(quadrilateral) would be described in a "natural" way; i.e. as $x = \sum_i N_i(\xi_k)x_i$ where N_i is now an element shape function, defined by ξ_i over Ω_h^e. The coordinate system which emerges naturally is therefore called a natural coordinate system.

Quadrilateral geometry

The natural coordinate system for the element with quadrilateral geometry is shown in Figure 2.3.2 ($\xi_1 = \xi, \xi_2 = \eta$). The location of a point $P(x, y)$ is given as

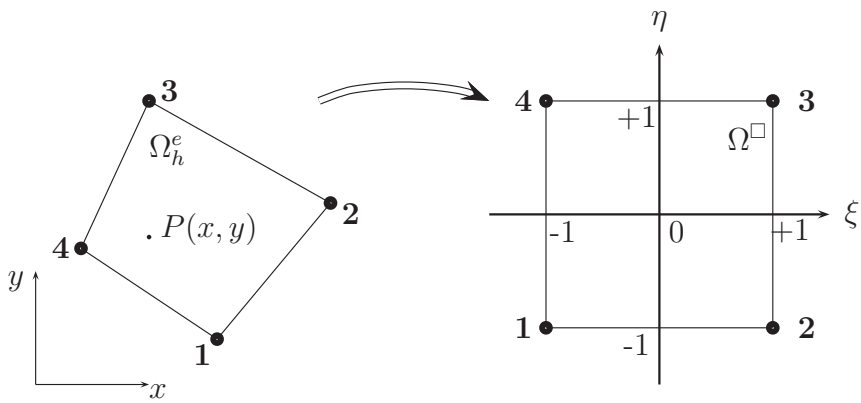

Figure 2.3.2: Bi-unit element $\Omega^\square$ in coordinate system (ξ,η)
Slika 2.3.2: Enotski element $\Omega^\square$ v koordinatnem sistemu (ξ,η)

$$x = N_1x_1 + N_2x_2 + N_3x_3 + N_4x_4; \quad y = N_1y_1 + N_2y_2 + N_3y_3 + N_4y_4 \tag{2.3.12}$$

or in matrix form

$$\begin{bmatrix} x \\ y \end{bmatrix} = \begin{bmatrix} x_1 & x_2 & x_3 & x_4 \\ y_1 & y_2 & y_3 & y_4 \end{bmatrix} \begin{bmatrix} N_1 \\ N_2 \\ N_3 \\ N_4 \end{bmatrix} \tag{2.3.13}$$

where N_i are bilinear Lagrangian functions; defined over $\Omega^\square$ as:

$$\begin{aligned} N_1 &= (1-\xi)(1-\eta)/4; & N_2 &= (1+\xi)(1-\eta)/4 \\ N_3 &= (1+\xi)(1+\eta)/4; & N_4 &= (1-\xi)(1+\eta)/4 \end{aligned} \tag{2.3.14}$$

The differentials of (x, y) are related to those of (ξ, η) and vice versa by:

$$\begin{bmatrix} \mathrm{d}x \\ \mathrm{d}y \end{bmatrix} = \underbrace{\begin{bmatrix} \frac{\partial x}{\partial \xi} & \frac{\partial x}{\partial \eta} \\ \frac{\partial y}{\partial \xi} & \frac{\partial y}{\partial \eta} \end{bmatrix}}_{\mathbf{J}} \begin{bmatrix} \mathrm{d}\xi \\ \mathrm{d}\eta \end{bmatrix}; \quad \begin{bmatrix} \mathrm{d}\xi \\ \mathrm{d}\eta \end{bmatrix} = \mathbf{J}^{-1} \begin{bmatrix} \mathrm{d}x \\ \mathrm{d}y \end{bmatrix} \tag{2.3.15}$$

The Jacobian of the transformation is denoted by $\mathbf{J}$ and is computed from (2.3.15), (2.3.12) and (2.3.14):

$$\mathbf{J} = \sum_i \begin{bmatrix} \frac{\partial N_i}{\partial \xi} x_i & \frac{\partial N_i}{\partial \eta} x_i \\ \frac{\partial N_i}{\partial \xi} y_i & \frac{\partial N_i}{\partial \eta} y_i \end{bmatrix} = \begin{bmatrix} x_1 & x_2 & x_3 & x_4 \\ y_1 & y_2 & y_3 & y_4 \end{bmatrix} \begin{bmatrix} \frac{\partial N_1}{\partial \xi} & \frac{\partial N_1}{\partial \eta} \\ \frac{\partial N_2}{\partial \xi} & \frac{\partial N_2}{\partial \eta} \\ \frac{\partial N_3}{\partial \xi} & \frac{\partial N_3}{\partial \eta} \\ \frac{\partial N_4}{\partial \xi} & \frac{\partial N_4}{\partial \eta} \end{bmatrix} \tag{2.3.16}$$

The derivatives of a function f with respect to the global coordinates (x, y) are related to the derivatives of f in the natural coordinate system by

$$\begin{bmatrix} \frac{\partial f}{\partial x} \\ \frac{\partial f}{\partial y} \end{bmatrix} = \begin{bmatrix} \frac{\partial \xi}{\partial x} & \frac{\partial \eta}{\partial x} \\ \frac{\partial \xi}{\partial y} & \frac{\partial \eta}{\partial y} \end{bmatrix} \begin{bmatrix} \frac{\partial f}{\partial \xi} \\ \frac{\partial f}{\partial \eta} \end{bmatrix} = \mathbf{J}^{-T} \begin{bmatrix} \frac{\partial f}{\partial \xi} \\ \frac{\partial f}{\partial \eta} \end{bmatrix} \tag{2.3.17}$$

The integration over the element domain is performed in the natural coordinates over the unit element $\Omega^{\square} = (\xi, \eta), \xi \in [-1, +1], \eta \in [-1, +1]$:

$$\int_{\Omega_h^e} f \mathrm{d}x\mathrm{d}y = \int_{\Omega^{\square}} f(\xi, \eta) \det \mathbf{J} \, \mathrm{d}\xi \mathrm{d}\eta \tag{2.3.18}$$

The expression for the determinant of Jacobian can be simplified into:

$$\begin{aligned} \det \mathbf{J} &= (A_{\Omega_h^e} + d_1 \xi + d_2 \eta)/4 \\ d_1 &= ((x_4 - x_3)(y_2 - y_1) - (x_2 - x_1)(y_4 - y_3))/2 \\ d_2 &= ((x_3 - x_2)(y_4 - y_1) - (x_4 - x_1)(y_3 - y_2))/2 \end{aligned} \tag{2.3.19}$$

The area of the element is denoted as $A_{\Omega_h^e}$ and the parameters d_1 and d_2 define the distortion of the quadrilateral element. Distortion vanishes if the quadrilateral element is parallelogram. In that case $\det \mathbf{J}$ is constant. Figure 2.3.3 shows the quadrilateral element with the coordinate lines of the natural coordinate system. Alternate shading between the coordinate lines is used to illustrate the variation of values of $\det \mathbf{J}$.

Triangular geometry

The coordinates used for the triangular elements are often called area, natural or even barycentric coordinates. The coordinates are denoted by $(\xi_1 = \zeta_1, \xi_2 = \zeta_2, \xi_3 = \zeta_3)$ with ζ_3

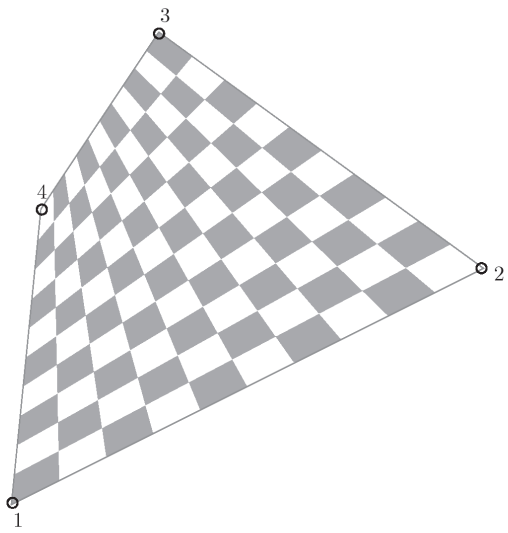

Figure 2.3.3: Quadrilateral element with the alternate shading between the coordinate lines of the quadrilateral natural coordinate system
Slika 2.3.3: Štirikotni element z izmeničnim senčenjem med koordinatnimi črtami naravnega koordinatnega sistema

being function of ζ_1 and ζ_2. The coordinate line $\zeta_i = const.$ is parallel to the side opposite to node i. The term area coordinates originates from the definition. Let us consider a point p inside the triangle defined by the nodes i, j, k. The triangle coordinate of the point is $\zeta_i = A_{pjk}/A_{ijk}$ (see Figure 2.3.4). Area of the triangle ijk is denoted by A_{ijk}, while A_{pjk} is the area of the triangle defined by the nodes p, j and k. Since $A_{ijk} = A_{pij} + A_{pjk} + A_{pki}$ the sum of the coordinates equals to unity

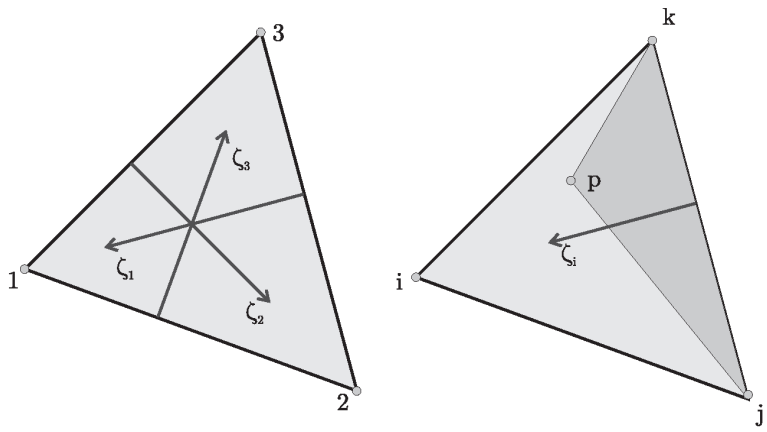

Figure 2.3.4: Triangular (area) coordinates
Slika 2.3.4: Trikotniške koordinate

$$1 = \zeta_1 + \zeta_2 + \zeta_3; \quad x = \zeta_1 x_1 + \zeta_2 x_2 + \zeta_3 x_3; \quad y = \zeta_1 y_1 + \zeta_2 y_2 + \zeta_3 y_3 \tag{2.3.20}$$

or in matrix form

$$\begin{bmatrix} 1 \\ x \\ y \end{bmatrix} = \begin{bmatrix} 1 & 1 & 1 \\ x_1 & x_2 & x_3 \\ y_1 & y_2 & y_3 \end{bmatrix} \begin{bmatrix} \zeta_1 \\ \zeta_2 \\ \zeta_3 \end{bmatrix} \tag{2.3.21}$$

By inverting this relation, we get:

$$\begin{bmatrix} \zeta_1 \\ \zeta_2 \\ \zeta_3 \end{bmatrix} = \frac{1}{2A_{\Omega_h^e}} \begin{bmatrix} x_2\, y_3 - x_3\, y_2 & +y_2 - y_3 & -x_2 + x_3 \\ x_3\, y_1 - x_1\, y_3 & +y_3 - y_1 & -x_3 + x_1 \\ x_1\, y_2 - x_2\, y_1 & +y_1 - y_2 & -x_1 + x_2 \end{bmatrix} \begin{bmatrix} 1 \\ x \\ y \end{bmatrix} \tag{2.3.22}$$

where (x_i, y_i) are the coordinates of the nodes of the triangle and $A_{\Omega_h^e}$ is its area. The Jacobian of the triangular coordinate transformation is

$$\mathbf{J} = \begin{bmatrix} 1 & 1 & 1 \\ x_1 & x_2 & x_3 \\ y_1 & y_2 & y_3 \end{bmatrix} \tag{2.3.23}$$

The $\det \mathbf{J}$ is twice the area of the triangle: $\det \mathbf{J} = 2A_{\Omega_h^e}$. The integral over the element domain is performed in the natural coordinates over the unit element $\Omega^{\triangle}$:

$$\int_{\Omega_h^e} f \mathrm{d}x\mathrm{d}y = \frac{1}{2} \int_{\Omega^{\triangle}} f(\zeta_1, \zeta_2, \zeta_3) \det \mathbf{J}\, \mathrm{d}\Omega^{\triangle} = A_{\Omega_h^e} \int_{\Omega^{\triangle}} f(\zeta_1, \zeta_2, \zeta_3)\, \mathrm{d}\Omega^{\triangle} \tag{2.3.24}$$

Since the unit element is a triangle, we have

$$\int_{\Omega^{\triangle}} f(\zeta_1, \zeta_2, \zeta_3)\, \mathrm{d}\Omega^{\triangle} = \int_0^1 \mathrm{d}\zeta_1 \int_0^{1-\zeta_1} f(\zeta_1, \zeta_2, 1 - \zeta_1 - \zeta_2)\, \mathrm{d}\zeta_2$$

Derivatives with respect to global coordinates (x, y) are related to the derivatives with respect to the triangular coordinates $(\zeta_1, \zeta_2, \zeta_3)$ via

$$\begin{bmatrix} \frac{\partial f}{\partial x} \\ \frac{\partial f}{\partial y} \end{bmatrix} = \begin{bmatrix} \frac{\partial \zeta_1}{\partial x} & \frac{\partial \zeta_2}{\partial x} & \frac{\partial \zeta_3}{\partial x} \\ \frac{\partial \zeta_1}{\partial y} & \frac{\partial \zeta_2}{\partial y} & \frac{\partial \zeta_3}{\partial y} \end{bmatrix} \begin{bmatrix} \frac{\partial f}{\partial \zeta_1} \\ \frac{\partial f}{\partial \zeta_2} \\ \frac{\partial f}{\partial \zeta_3} \end{bmatrix} \tag{2.3.25}$$

From (2.3.22) we have

$$\begin{bmatrix} \frac{\partial f}{\partial x} \\ \frac{\partial f}{\partial y} \end{bmatrix} = \frac{1}{2A_{\Omega_h^e}} \begin{bmatrix} y_2 - y_3 & y_3 - y_1 & y_1 - y_2 \\ x_3 - x_2 & x_1 - x_3 & x_2 - x_1 \end{bmatrix} \begin{bmatrix} \frac{\partial f}{\partial \zeta_1} \\ \frac{\partial f}{\partial \zeta_2} \\ \frac{\partial f}{\partial \zeta_3} \end{bmatrix} \tag{2.3.26}$$

and from (2.3.21)

$$\begin{bmatrix} \frac{\partial f}{\partial \zeta_1} \\ \frac{\partial f}{\partial \zeta_2} \\ \frac{\partial f}{\partial \zeta_3} \end{bmatrix} = \begin{bmatrix} x_1 & y_1 \\ x_2 & y_2 \\ x_3 & y_3 \end{bmatrix} \begin{bmatrix} \frac{\partial f}{\partial x} \\ \frac{\partial f}{\partial y} \end{bmatrix} \tag{2.3.27}$$

Figure 2.3.5 shows the triangular element with the coordinate lines of the natural coordinate system. Alternate shading provides the indication of $\det \mathbf{J}$. Since the factor $\det \mathbf{J}$ is constant over the element domain and equals $\det \mathbf{J} = A_{\Omega_h^e}/2$, the shaded areas are equal in size. Infinitesimal vector in the triangular coordinate system $\mathrm{d}\boldsymbol{\zeta} = [\mathrm{d}\zeta_1, \mathrm{d}\zeta_2, \mathrm{d}\zeta_3]^T$ is related to the infinitesimal vector $\mathrm{d}\boldsymbol{r} = [\mathrm{d}x, \mathrm{d}y]^T$ as

$$\begin{bmatrix} \mathrm{d}\zeta_1 \\ \mathrm{d}\zeta_2 \\ \mathrm{d}\zeta_3 \end{bmatrix} = \frac{1}{2A_{\Omega_h^e}} \begin{bmatrix} +y_2 - y_3 & -x_2 + x_3 \\ +y_3 - y_1 & -x_3 + x_1 \\ +y_1 - y_2 & -x_1 + x_2 \end{bmatrix} \begin{bmatrix} \mathrm{d}x \\ \mathrm{d}y \end{bmatrix} \tag{2.3.28}$$

For the triangular coordinate system the total differential is

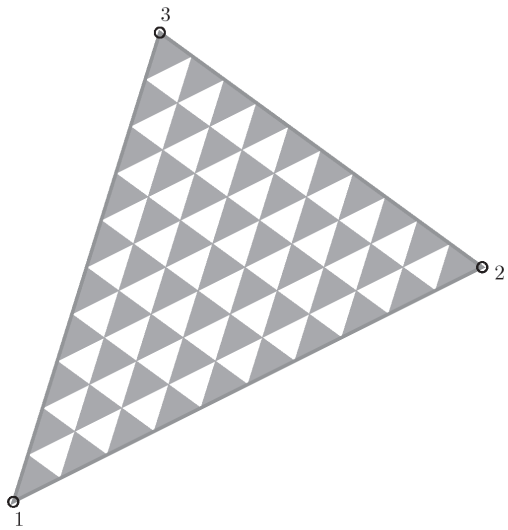

Figure 2.3.5: Triangular element with the alternate shading between the coordinate lines $\zeta_i = const.$ of triangular coordinate system
Slika 2.3.5: Trikotni element z izmeničnim senčenjem med koordinatnimi črtami trikotniškega koordinatnega sistema

$$\mathrm{d}f = \frac{\partial f}{\partial \zeta_1}\mathrm{d}\zeta_1 + \frac{\partial f}{\partial \zeta_2}\mathrm{d}\zeta_2 + \frac{\partial f}{\partial \zeta_3}\mathrm{d}\zeta_3 \tag{2.3.29}$$

To obtain the derivative along a defined direction, the directional vector $\mathrm{d}\boldsymbol{\zeta}$ has to be expressed in the triangular coordinate system.

Next, the derivative along the line will be defined. The position of the point lying on the line defined by the two points is:

$$\mathbf{r} = \mathbf{r}_1 + s\,\mathbf{r}_{12} \qquad s \in [0, 1]$$

where $\mathbf{r}_{12} = \mathbf{r}_2 - \mathbf{r}_1$. Inserting $\mathrm{d}\mathbf{r} = [\mathrm{d}x, \mathrm{d}y]^T = \mathrm{d}s[(x_2 - x_1), (y_2 - y_1)]^T$ into (2.3.28), we obtain

$$\mathrm{d}\boldsymbol{\zeta} = [\mathrm{d}\zeta_1, \mathrm{d}\zeta_2, \mathrm{d}\zeta_3]^T = \mathrm{d}s[-1, +1, 0].$$

The derivative along the direction $\mathbf{r}_{12}$ with respect to the parameter s is given by (2.3.29)

$$\frac{\partial f}{\partial s} = (\frac{\partial f}{\partial \zeta_2} - \frac{\partial f}{\partial \zeta_1}) \equiv f_{,12} \tag{2.3.30}$$

The definition of the second derivative along the line is straightforward

$$\frac{\partial^2 f}{\partial s^2} = \frac{\partial}{\partial s}(\frac{\partial f}{\partial \zeta_2} - \frac{\partial f}{\partial \zeta_1})) = (\frac{\partial^2 f}{\partial \zeta_2^2} - 2\frac{\partial f}{\partial \zeta_1}\frac{\partial f}{\partial \zeta_2} + \frac{\partial^2 f}{\partial \zeta_1^2}) \equiv f_{,12^2} \tag{2.3.31}$$

To determine the derivative with respect to the normal to the side of the triangle, one has to follow similar steps. First we parameterize the perpendicular line to a side (in this case side 1-2) going through the side middle point:

$$\boldsymbol{r} = \frac{1}{2}(\boldsymbol{r}_1 + \boldsymbol{r}_2) + 2\,\mathrm{d}s\, h_3\, \boldsymbol{n}_{12} = \bar{\boldsymbol{r}}_{12} + 2\,\mathrm{d}s\, h_3\, \boldsymbol{n}_{12} \tag{2.3.32}$$

where $\boldsymbol{n}_{12}$ is a normal vector to the side 1-2 with length l_{12}, h_3 is height of point 3 and $\bar{\boldsymbol{r}}_{12} = \frac{1}{2}(\boldsymbol{r}_1 + \boldsymbol{r}_2)$. The differential vector $\mathrm{d}\boldsymbol{r} = 2\mathrm{d}s\, h_3\, \boldsymbol{n}_{12}$ is in the global basis

$$\mathrm{d}\mathbf{r} = \begin{bmatrix} \mathrm{d}x \\ \mathrm{d}y \end{bmatrix} = 2\,\mathrm{d}s\, h_3 \begin{bmatrix} +y_2 - y_1 \\ -x_2 + x_1 \end{bmatrix} / l_{12} \tag{2.3.33}$$

and can be written in the triangular basis using (2.3.28):

$$\mathrm{d}\boldsymbol{\zeta} = \begin{bmatrix} \mathrm{d}\zeta_1 \\ \mathrm{d}\zeta_2 \\ \mathrm{d}\zeta_3 \end{bmatrix} = \frac{2h_3}{2A_{\Omega_h^e}} \begin{bmatrix} -(y_3 - y_2) & +(x_3 - x_2) \\ +(y_3 - y_1) & -(x_3 - x_1) \\ -(y_2 - y_1) & +(x_2 - x_1) \end{bmatrix} \begin{bmatrix} +y_2 - y_1 \\ -x_2 + x_1 \end{bmatrix} / \, l_{12}$$

We further notice that $A_{\Omega_h^e} = h_3\, l_{12}/2$, introduce the notation $x_{ij} = x_j - x_i$, and rewrite the upper expression as

$$\mathrm{d}\boldsymbol{\zeta} = \begin{bmatrix} \mathrm{d}\zeta_1 \\ \mathrm{d}\zeta_2 \\ \mathrm{d}\zeta_3 \end{bmatrix} = \frac{2}{l_{12}^2} \begin{bmatrix} -y_{23}\, y_{12} - x_{23}\, x_{12} \\ +y_{13}\, y_{12} + x_{13}\, x_{12} \\ -l_{12}^2 \end{bmatrix} = \begin{bmatrix} +1 - 2\,\boldsymbol{r}_{12} \cdot (\boldsymbol{r}_3 - \bar{\boldsymbol{r}}_{12})/l_{12}^2 \\ +1 + 2\,\boldsymbol{r}_{12} \cdot (\boldsymbol{r}_3 - \bar{\boldsymbol{r}}_{12})/l_{12}^2 \\ -2 \end{bmatrix} \tag{2.3.34}$$

We introduce the parameter $\mu_{12} = 2\boldsymbol{r}_{12} \cdot (\boldsymbol{r}_3 - \bar{\boldsymbol{r}}_{12})/l_{12}^2 = 2e_1/l_{12}$, which has a meaning of normalized eccentricity of node 3 with respect to the symmetry line of edge 1-2 (see Figure 2.3.6). Finally, we have

$$\mathrm{d}\zeta_1 = (1 - \mu_{12})\,\mathrm{d}s; \quad \mathrm{d}\zeta_2 = (1 + \mu_{12})\,\mathrm{d}s; \quad \mathrm{d}\zeta_3 = 2\,\mathrm{d}s \tag{2.3.35}$$

and the derivative normal to the edge 1-2

$$\frac{\partial f}{\partial n} = 2\frac{\partial f}{\partial \zeta_3} - (\frac{\partial f}{\partial \zeta_1} + \frac{\partial f}{\partial \zeta_2}) + \mu_{12}\,(\frac{\partial f}{\partial \zeta_2} - \frac{\partial f}{\partial \zeta_1}) = f_{,n} \tag{2.3.36}$$

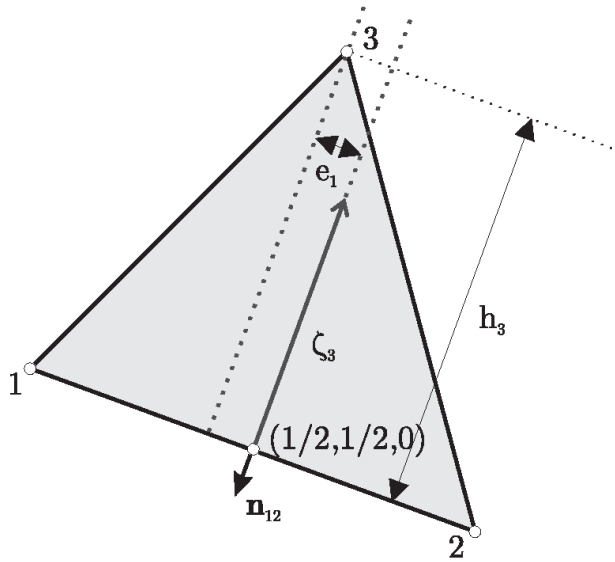

Figure 2.3.6: To the definition of eccentricity parameter $\mu_{12} = 2e_1/l_{12}$
Slika 2.3.6: K definiciji parametra ekscentričnosti $\mu_{12} = 2e_1/l_{12}$

2.3.4 Conforming triangular element

The derivation of the element presented below follows the work of [Argyris et al., 1968]. Here, only the outline of the derivation procedure will be presented. The element will be called TUBA6 or Argyris element in what follows.

The displacement field is interpolated with complete 5th order polynomial in natural (area) coordinates $(\zeta_1, \zeta_2, \zeta_3)$. Namely, the complete quintic polynomial, defined with 21 parameters, is the lowest discrete approximation, which satisfies $\mathcal{C}^1$ continuity across element boundaries [Zienkiewicz Taylor, 2000], [Argyris et al., 1968]. Hence, the discrete approximation of the displacement field can be written as:

$$w_h = \boldsymbol{\omega}^T \hat{\boldsymbol{p}} \tag{2.3.37}$$

where $\hat{\boldsymbol{p}} = [p_1, p_2, \cdots, p_{21}]^T$ denotes a vector of nodal interpolation parameters and $\boldsymbol{\omega}$ the set of shape functions. The latter contains 21 polynomials and can be written as:

$$\begin{aligned}\boldsymbol{\omega} = [&\zeta_1^5, \zeta_2^5, \zeta_3^5,\\ &\zeta_1\zeta_2^4, \zeta_2\zeta_3^4, \zeta_3\zeta_1^4, \zeta_2\zeta_1^4, \zeta_3\zeta_2^4, \zeta_1\zeta_3^4,\\ &\zeta_1^3\zeta_2^2, \zeta_2^3\zeta_3^2, \zeta_3^3\zeta_1^2, \zeta_2^3\zeta_1^2, \zeta_3^3\zeta_2^2, \zeta_1^3\zeta_3^2,\\ &\zeta_1^3\zeta_2\zeta_3, \zeta_1\zeta_2^3\zeta_3, \zeta_1\zeta_2\zeta_3^3, \zeta_1^2\zeta_2^2\zeta_3, \zeta_1^2\zeta_2\zeta_3^2, \zeta_1\zeta_2^2\zeta_3^2]^T\end{aligned}$$

The element nodal interpolation parameters pertain to 3 vertex nodes and 3 mid-side nodes. Each vertex node has 6 degrees of freedom: displacement, its first derivatives,

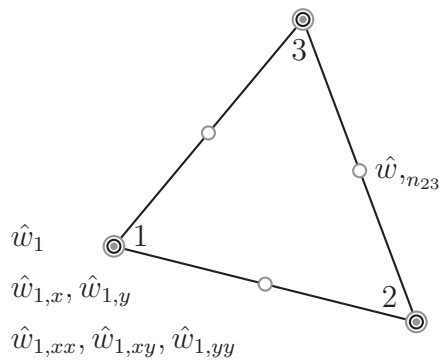

Figure 2.3.7: Triangular Argyris plate element - ARGY
Slika 2.3.7: Trikotni Argyrisov končni element za plošče - ARGY

and its second derivatives with respect to x and y. The mid-side nodes contain the first derivative in the direction of the exterior normal. The complete set of global degrees of freedom can be written as:

$$\begin{aligned}\hat{\boldsymbol{w}} = [&\hat{w}_1, \hat{w}_2, \hat{w}_3,\ \hat{w}_{1,x}, \hat{w}_{1,y},\ \hat{w}_{2,x}, \hat{w}_{2,y},\ \hat{w}_{3,x}, \hat{w}_{3,y},\\ &\hat{w}_{1,xx}, \hat{w}_{1,xy}, \hat{w}_{1,yy},\ \hat{w}_{2,xx}, \hat{w}_{2,xy}, \hat{w}_{2,yy},\ \hat{w}_{3,xx}, \hat{w}_{3,xy}, \hat{w}_{3,yy},\\ &\hat{w}_{,n_{12}}, \hat{w}_{,n_{23}}, \hat{w}_{,n_{31}}\ ]^T\end{aligned}$$

To establish the relation between $\hat{\boldsymbol{p}}$ and $\hat{\boldsymbol{w}}$, all the derivatives are computed at the nodes. As an intermediate step, we introduce an additional set of degrees of freedom $\hat{\boldsymbol{w}}_\rho$, where the derivatives are formed with respect to natural (area) coordinates:

$$\begin{aligned}\hat{\boldsymbol{w}}_\rho \ = [\ &\hat{w}_1, \hat{w}_2, \hat{w}_3,\ \hat{w}_{1,12}, \hat{w}_{1,31},\ \hat{w}_{2,23}, \hat{w}_{2,12},\ \hat{w}_{3,31}, \hat{w}_{3,23},\\ &\hat{w}_{1,12^2},\ \hat{w}_{1,31^2},\ \hat{w}_{1,23^2}, \hat{w}_{2,12^2},\ \hat{w}_{2,31^2},\ \hat{w}_{2,23^2}, \hat{w}_{3,12^2},\ \hat{w}_{3,31^2},\ \hat{w}_{3,23^2},\\ &\hat{w}_{,n_{12}}, \hat{w}_{,n_{23}}, \hat{w}_{,n_{31}}]^T\end{aligned}$$

The relation between $\hat{\boldsymbol{p}}$ and $\hat{\boldsymbol{w}}_\rho$ is defined by the system of equations which are obtained by using results in (2.3.30), (2.3.31) and (2.3.36) at the nodes of the element. At node 1

$(\zeta_1 = 1, \zeta_2 = 0, \zeta_3 = 0)$ we thus have:

$$\begin{aligned}
\hat{w}_1 &= p_1 \\
\hat{w}_{1,12} &= -5p_1 + p_4 \\
\hat{w}_{1,31} &= +5p_1 - p_5 \\
\hat{w}_{1,12^2} &= 20p_1 - 10p_1p_4 + 2p_{10} \\
\hat{w}_{1,31^2} &= 20p_1 - 10p_1p_5 + 2p_{11} \\
\hat{w}_{1,23^2} &= -2p_4p_5 + 2p_{10} + 2p_{11}
\end{aligned} \tag{2.3.38}$$

and at the midside node on edge $1-2$ $(\zeta_1 = 1/2, \zeta_2 = 1/2, \zeta_3 = 0)$ we have

$$\begin{aligned}
\hat{w}_{,n_{12}} =& (-5(1+\mu_{12})p_1 + 5(-1+\mu_{12})p_2 - (5+3\mu_{12})p_4 \\
&+ 2p_5 + 2p_6 - (5-3\mu_{12})p_7 - (5+\mu_{12})p_{10} \\
&- (5-\mu_{12})p_{13} + 2p_{16} + 2p_{17} + 2p_{19})/16
\end{aligned} \tag{2.3.39}$$

A linear system can be formed by writing down the equations (2.3.38) and (2.3.39) for all the nodes:

$$\hat{\boldsymbol{w}}_\rho = \mathbf{A}^{-1}\hat{\boldsymbol{p}} \tag{2.3.40}$$

where the matrix of the linear system is denoted as $\mathbf{A}^{-1}$.

From (2.3.30) we have:

$$\begin{bmatrix} w_{,12} \\ w_{,23} \\ w_{,31} \end{bmatrix} = \begin{bmatrix} x_{12} & y_{12} \\ x_{23} & y_{23} \\ x_{31} & y_{31} \end{bmatrix} \begin{bmatrix} w_{,x} \\ w_{,y} \end{bmatrix} \tag{2.3.41}$$

and from (2.3.31) we get

$$\begin{bmatrix} w_{,12^2} \\ w_{,31^2} \\ w_{,23^2} \end{bmatrix} = \underbrace{\begin{bmatrix} x_{12}^2 & y_{12}^2 & -x_{12}y_{12} \\ x_{31}^2 & y_{31}^2 & -x_{31}y_{31} \\ x_{23}^2 & y_{23}^2 & -x_{23}y_{23} \end{bmatrix}}_{\mathbf{T}^{-1}} \begin{bmatrix} w_{,xx} \\ w_{,yy} \\ 2w_{,xy} \end{bmatrix} \tag{2.3.42}$$

This relations enable to define the transformation between $\hat{\boldsymbol{w}}$ and $\hat{\boldsymbol{w}}_\rho$, which can be written in matrix notation as $\hat{\boldsymbol{w}}_\rho = \mathbf{X}_T\hat{\boldsymbol{w}}$, where $\mathbf{X}_T$ is matrix of the linear transformation. We insert this result in (2.3.40) and obtain

$$\hat{\boldsymbol{p}} = \mathbf{X}\hat{\boldsymbol{w}}; \qquad \mathbf{X} = \mathbf{A}\mathbf{X}_T \tag{2.3.43}$$

The discrete approximation of curvature vector $\boldsymbol{\kappa}_h$ is the second derivative of the displacement field $w_h = \boldsymbol{\omega}^T\mathbf{X}\hat{\boldsymbol{w}}$ according to (2.2.8):

$$\boldsymbol{\kappa}_h = \begin{bmatrix} w_{h,xx} \\ w_{h,yy} \\ 2w_{h,xy} \end{bmatrix} \tag{2.3.44}$$

Computing further the inverse of the relation (2.3.42), we obtain:

$$\boldsymbol{\kappa}_h = \mathbf{T}\boldsymbol{\kappa}_{h,\rho}; \quad \boldsymbol{\kappa}_{h,\rho} = [w_{h,12^2}\,, w_{h,23^2}\,, w_{h,31^2}\,]^T = \boldsymbol{\omega}_{,\rho}^T\hat{\boldsymbol{w}} \tag{2.3.45}$$

where $\boldsymbol{\omega}_{,\rho} = [\boldsymbol{\omega}_{,12^2}, \boldsymbol{\omega}_{,23^2}, \boldsymbol{\omega}_{,31^2}]^T$.

Stiffness matrix

The element stiffness matrix is obtained from the bilinear form defined for a single element

$$\begin{aligned} a_{K,e}(w_h; u_h) &= \int_{\Omega_h^e} \boldsymbol{\kappa}_h^T(u_h)\boldsymbol{m}_h(w_h)\,\mathrm{d}\Omega = \int_{\Omega_h^e} \boldsymbol{\kappa}_h^T(u_h)\,\mathbf{C}_B\,\boldsymbol{\kappa}_h(w_h)\,\mathrm{d}\Omega \\ &= \int_{\Omega_h^e} \boldsymbol{\kappa}_{h,\rho}^T(u_h)\mathbf{T}^T\,\mathbf{C}_B\,\mathbf{T}\,\boldsymbol{\kappa}_{h,\rho}(w_h)\,\mathrm{d}\Omega \end{aligned} \tag{2.3.46}$$

where the interpolation of the displacement is $w_h = \boldsymbol{\omega}^T\mathbf{X}\hat{\boldsymbol{w}}$ and of the test function $u_h = \boldsymbol{\omega}^T\mathbf{X}\hat{\boldsymbol{u}}$ where $\hat{\boldsymbol{u}}$ is vector of test function nodal parameters in cartesian coordinates. The product $\mathbf{G} = \mathbf{T}^T\,\mathbf{C}_B\,\mathbf{T}$ is constant in the case of homogeneous material. In that case it remains only to evaluate the integral

$$\int_{\Omega_h^e} \boldsymbol{\kappa}_{h,\rho}^T(u_h)\boldsymbol{\kappa}_{h,\rho}(w_h)\,\mathrm{d}\Omega = \hat{\boldsymbol{u}}^T\left(\int_{\Omega_h^e} \boldsymbol{\omega}_{,\rho}{}^T\boldsymbol{\omega}_{,\rho}\,\mathrm{d}\Omega\right)\hat{\boldsymbol{u}} = \hat{\boldsymbol{u}}^T\mathbf{S}\,\hat{\boldsymbol{w}} \tag{2.3.47}$$

where $\mathbf{S}$ is obtained by analytic integration with the use of:

$$\frac{1}{\Omega^{\triangle}}\int_{\Omega^{\triangle}} \zeta_1^p\zeta_2^q\zeta_3^r\,\mathrm{d}\Omega = \frac{2!\,p!\,q!\,r!}{(2+p+q+r)!} \tag{2.3.48}$$

The expression (2.3.46) can be put in a familiar matrix form

$$a_{K,e}(w_h; u_h) = \hat{\boldsymbol{u}}^T\left[\sum_{i,j}\mathbf{G}_{ij}\mathbf{S}_{ij}\right]\hat{\boldsymbol{w}} = \hat{\boldsymbol{u}}^T\mathbf{K}\hat{\boldsymbol{w}}. \tag{2.3.49}$$

where $\mathbf{K} = [K_{ij}] = [\sum_{i,j}\mathbf{G}_{ij}\mathbf{S}_{ij}]$ is the stiffness matrix of the element.

Load vector

The equivalent load vector is computed from the virtual work of external forces (pressure load f and boundary tractions $\overline{q}_{ef}$,$\overline{m}_s$)

$$\begin{aligned} l_{K,e}(u_h) &= \int_{\Omega_h^e} u_h\,f\,\mathrm{d}\Omega + \int_{\Gamma^e}(u_h\,\overline{q}_{ef} - \overline{m}_s\frac{\partial u_h}{\partial n})\,\mathrm{d}s \\ &= \hat{\boldsymbol{u}}^T\boldsymbol{X}^T\left(\int_{\Omega_h^e}\boldsymbol{\omega}\,f\,\mathrm{d}\Omega + \int_{\Gamma^e}(\boldsymbol{\omega}\,\overline{q}_{ef} - \overline{m}_s\frac{\partial\boldsymbol{\omega}}{\partial n})\,\mathrm{d}s\right) \end{aligned} \tag{2.3.50}$$

By using (2.3.43) the nodal load vector $\boldsymbol{f}$ is finally written as:

$$\boldsymbol{f} = \mathbf{X}^T \left(\int_{\Omega_h^e} \boldsymbol{\omega}\, f \, \mathrm{d}\Omega + \int_{\Gamma^e} (\boldsymbol{\omega}\, \overline{q}_{ef} - \overline{m}_s \frac{\partial \boldsymbol{\omega}}{\partial n}) \right) \tag{2.3.51}$$

The derivatives $\frac{\partial \boldsymbol{\omega}}{\partial n}$ are evaluated with the use of (2.3.36). The integrals in (2.3.51) can be obtained in a closed form with the aid of the formula (2.3.48).

2.3.5 Discrete Kirchhoff elements

The motivation for the Discrete Kirchhoff (DK) plate elements is based on the observation that it is quite challenging to construct a conforming approximation of the plate displacement field. Since the Kirchhoff constraint of zero shear strains is very difficult to satisfy at every point of the domain, a compromise is made: the constraint $\boldsymbol{\gamma} = \nabla w - \boldsymbol{\theta} = \mathbf{0}$ is relaxed and is satisfied only at chosen points and directions. Relaxation of the Kirchhoff constraint implies that the discretization of displacement w_h and rotations $\boldsymbol{\theta}_h$ are no longer tied together but are rather independent. They are related only along the sides of the element. Otherwise independent interpolations for displacement w_h and rotations $\boldsymbol{\theta}_h$ are constructed such that the shear strain $\boldsymbol{\gamma}_h$ along the element boundary (in the direction $\boldsymbol{s}$) vanishes

$$\boldsymbol{\gamma}_h \cdot \boldsymbol{s} = \frac{\partial w_h}{\partial s} - \boldsymbol{n} \cdot \boldsymbol{\theta}_h = 0 \tag{2.3.52}$$

Edge interpolation equals beam element interpolation

To illustrate the idea, let us consider a discretization of the Euler Bernoulli beam, see Figure 2.3.9. Two independent interpolations of displacement w_h and rotation θ_h are set:

$$w_h = \hat{w}_1 N_1 + \hat{w}_2 N_2 + \hat{w}_3 N_3 + \hat{w}_4 N_4 \tag{2.3.53}$$

$$\theta_h = \hat{\theta}_1 N_1 + \hat{\theta}_2 N_2 + \hat{\theta}_3 N_3 \tag{2.3.54}$$

where the hierarchic shape functions are (see Figure 2.3.8):

$$\begin{aligned} N_1 &= (1-\xi)/2; & N_2 &= (1+\xi)/2 & \xi &\in [-1,+1] \\ N_3 &= (1-\xi^2); & N_4 &= \xi(1-\xi^2) \end{aligned} \tag{2.3.55}$$

Due to the requirement for the $\mathcal{C}^1$ continuity of the displacement, the order of the interpolation is cubic. Only nodal displacements $\hat{w}_1, \hat{w}_2$ and rotations $\hat{\theta}_1, \hat{\theta}_2$ are acceptable

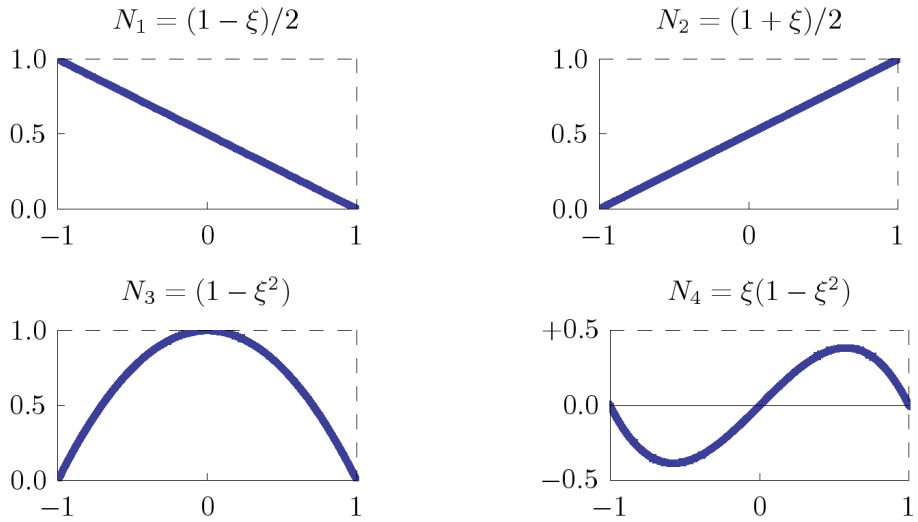

Figure 2.3.8: Hierarchical shape functions
Slika 2.3.8: Hierarhične interpolacijske funkcije

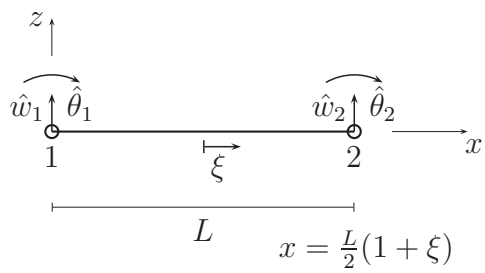

Figure 2.3.9: Euler-Bernoulli beam element
Slika 2.3.9: Končni element za nosilec po Euler-Bernoullijevi teoriji

nodal degrees of freedom. Other parameters $\hat{w}_3, \hat{w}_4, \hat{\theta}_3$ are thus eliminated by enforcing the constraint of vanishing transverse shear strain $\gamma_h = \frac{\partial w_h}{\partial x} - \theta_h = 0$. One gets from the latter equation and (2.3.53), (2.3.54)

$$\hat{w}_3 = +\frac{L}{8}(\hat{\theta}_1 - \hat{\theta}_2); \quad \hat{w}_4 = \frac{L}{4}(\frac{\hat{w}_2 - \hat{w}_1}{L} - \frac{1}{2}(\hat{\theta}_1 + \hat{\theta}_2)); \quad \hat{\theta}_3 = \frac{6}{L}\hat{w}_4 \tag{2.3.56}$$

Using (2.3.56), the interpolations (2.3.53) and (2.3.54) become:

$$\begin{aligned} w_h &= \hat{w}_1 H_1 + \hat{w}_2 H_2 + \hat{\theta}_1 H_3 + \hat{\theta}_2 H_4 \\ \theta_h &= \frac{1}{4}\hat{\theta}_1\left(3\xi^2 - 2\xi - 1\right) + \frac{1}{4}\hat{\theta}_2\left(3\xi^2 + 2\xi - 1\right) + \frac{3(\hat{w}_2 - \hat{w}_1)}{2L}(1-\xi^2) \end{aligned} \tag{2.3.57}$$

The functions H_i are the well known Hermitian cubic shape functions (see Figure 2.3.10):

$$H_1 = \frac{1}{4}(1-\xi)^2(2+\xi) \quad H_2 = \frac{1}{4}(1+\xi)^2(2-\xi) \tag{2.3.58}$$
$$H_3 = +\frac{L}{8}(1-\xi)^2(1+\xi) \quad H_4 = -\frac{L}{8}(1+\xi)^2(1-\xi)$$

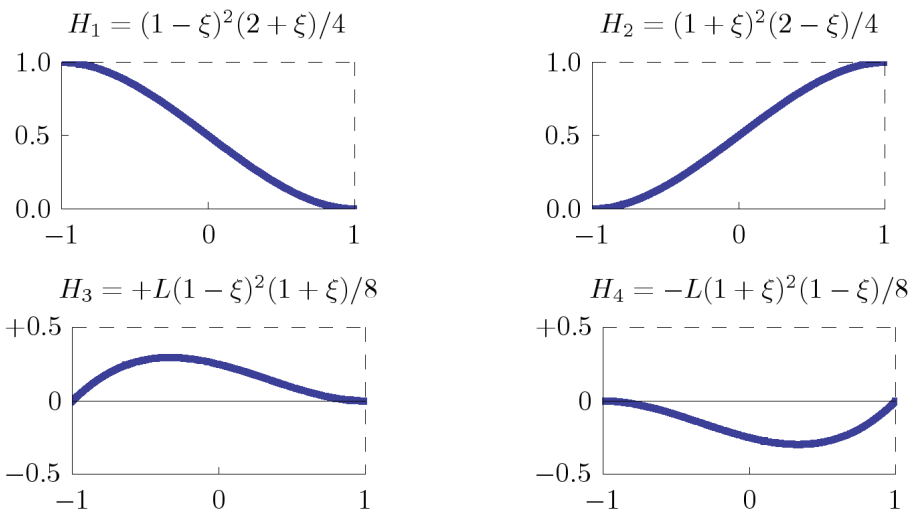

Figure 2.3.10: Hermite shape functions
Slika 2.3.10: Hermite-ove interpolacijske funkcije

Interpolation for Discrete Kirchhoff (DK) plate elements

Similar approach as for Euler-Bernoulli beam is taken also in the case of the Discrete Kirchhoff plate element: the side of the element is treated as Euler-Bernoulli beam. The interpolation on the boundary equals the interpolation (2.3.57). The rotation θ is now the normal rotation $\theta_n = \boldsymbol{\theta} \cdot \boldsymbol{n}$.

The interpolation of the displacement is defined as a sum of nodal (I) and side contributions (IJ):

$$w_h = \sum_I \hat{w}_I N_I + \sum_{IJ} (\hat{w}_{3,IJ} N_{IJ} + \hat{w}_{4,IJ} M_{IJ}) \tag{2.3.59}$$

where N_I are nodal shape functions while N_{IJ} and M_{IJ} are shape functions related to element side IJ. This nonconventional notation is beneficial since it holds generally. It enables that both triangular as well as quadrilateral DK element are treated in exactly the same way. The parameters $\hat{w}_{3,IJ}$ and $\hat{w}_{4,IJ}$ are eliminated from the interpolation by

enforcing zero transverse shear strain along the side IJ. It turns out that

$$\hat{w}_{3,IJ} = \frac{L_{IJ}}{8}\boldsymbol{n}_{IJ}\cdot(\hat{\boldsymbol{\theta}}_I - \hat{\boldsymbol{\theta}}_J); \tag{2.3.60}$$
$$\hat{w}_{4,IJ} = \frac{L_{IJ}}{4}\left(\frac{\hat{w}_J - \hat{w}_I}{L_{IJ}} - \frac{1}{2}\boldsymbol{n}_{IJ}\cdot(\hat{\boldsymbol{\theta}}_I + \hat{\boldsymbol{\theta}}_J)\right)$$

where $\hat{\boldsymbol{\theta}}_I = [\hat{\theta}_{xI}, \hat{\theta}_{yI}]$ and L_{IJ} is length of side between nodes I and J, and $\boldsymbol{n}_{IJ}$ is normal to the side between nodes I and J. Note the similarity between (2.3.60) and (2.3.56). The interpolation of the rotation is defined as

$$\boldsymbol{\theta}_h = \begin{bmatrix} \theta_{x,h} \\ \theta_{y,h} \end{bmatrix} = \sum_{I=1}^{3}\hat{\boldsymbol{\theta}}_I N_I + \sum_{IJ}\hat{\theta}_{3,IJ}\boldsymbol{n}_{IJ}N_{IJ} \tag{2.3.61}$$

where, due to zero transverse shear strain along the side IJ (2.3.56)

$$\hat{\theta}_{3,IJ} = \frac{6}{L}\hat{w}_{4,IJ} \tag{2.3.62}$$

The above interpolation leads to an element with only vertex nodes with degrees of freedom denoted by $\hat{\boldsymbol{w}}_I = [\hat{w}_I, \hat{\theta}_{xI}, \hat{\theta}_{yI}]^T$. The interpolations (2.3.59) and (2.3.61) can also be expressed as:

$$w_h = \mathbf{N}_w\hat{\boldsymbol{w}} = \sum_I \mathbf{N}_{w,I}\hat{\boldsymbol{w}}_I; \quad \boldsymbol{\theta}_h = \mathbf{N}_\theta\hat{\boldsymbol{w}} = \sum_I \mathbf{N}_{\theta,I}\hat{\boldsymbol{w}}_I; \tag{2.3.63}$$
$$\boldsymbol{\kappa}_h = \mathbf{B}_\kappa\hat{\boldsymbol{w}} = \sum_I \mathbf{B}_{\kappa,I}\hat{\boldsymbol{w}}_I$$

where $\hat{\boldsymbol{w}} = [\hat{\boldsymbol{w}}_1, \hat{\boldsymbol{w}}_2, \cdots, \hat{\boldsymbol{w}}_{nen}]$ and nen is the number of element nodes.

Explicit forms of $\mathbf{N}_{w,I}$ and $\mathbf{N}_{\theta,I} = [\mathbf{N}_{\theta_x,I}, \mathbf{N}_{\theta_y,I}]^T$ are obtained from (2.3.59)-(2.3.62):

$$\mathbf{N}_{w,I}^T = \begin{bmatrix} N_I \\ 0 \\ 0 \end{bmatrix} + \frac{1}{8}\begin{bmatrix} 2\,(M_{KI} - M_{IJ}) \\ L_{IJ}(N_{IJ} - M_{IJ})n_{IJ,x} - L_{KI}(N_{KI} + M_{KI})n_{KI,x} \\ L_{IJ}(N_{IJ} - M_{IJ})n_{IJ,y} - L_{KI}(N_{KI} + M_{KI})n_{KI,x} \end{bmatrix} \tag{2.3.64}$$

$$\mathbf{N}_{\theta_x,I}^T = \begin{bmatrix} 0 \\ N_I \\ 0 \end{bmatrix} + \frac{3}{4}\begin{bmatrix} 2\,(N_{KI}n_{KI,x}/L_{KI} - N_{IJ}n_{IJ,x}/L_{IJ}) \\ -(N_{KI}n_{KI,x}^2 + N_{IJ}n_{IJ,x}^2) \\ -(N_{KI}n_{KI,x}n_{KI,x} + N_{IJ}n_{IJ,x}n_{IJ,y}) \end{bmatrix} \tag{2.3.65}$$

$$\mathbf{N}_{\theta_y,I}^T = \begin{bmatrix} 0 \\ 0 \\ N_I \end{bmatrix} + \frac{3}{4}\begin{bmatrix} 2\,(N_{KI}n_{KI,y}/L_{KI} - N_{IJ}n_{IJ,y}/L_{IJ}) \\ -(N_{KI}n_{KI,x}n_{KI,y} + N_{IJ}n_{IJ,x}n_{IJ,y}) \\ -(N_{KI}n_{KI,y}^2 + N_{IJ}n_{IJ,y}^2) \end{bmatrix} \tag{2.3.66}$$

where the node ordering and side numbering is presented in Figure 2.3.11.

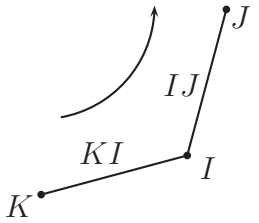

Figure 2.3.11: Node and side numbering in (2.3.64)

Slika 2.3.11: Označevanje vozlišč in stranic v (2.3.64)

The curvature vector $\boldsymbol{\kappa}_h$ is computed from (2.2.4):

$$\boldsymbol{\kappa}_h = [-\frac{\partial \theta_{y,h}}{\partial x}, \frac{\partial \theta_{x,h}}{\partial y}, \frac{\partial \theta_{x,h}}{\partial x} - \frac{\partial \theta_{y,h}}{\partial y}] \tag{2.3.67}$$

Since the shape functions are defined in the natural coordinate system ξ_i, $i = 1, 2$, their derivatives are related to those in the Cartesian coordinate system (x, y) by $\frac{\partial}{\partial x} = \sum_i \mathrm{J}^{-1}_{x\xi_i} \frac{\partial}{\partial \xi_i}$ where $\mathrm{J}_{x\xi_i} = \frac{\partial \xi_i}{\partial x}$ is the term of the Jacobian matrix of transformation. It depends on the geometry ((2.3.16), or (2.3.23)). The sum runs over the natural coordinates ξ_i: (which are $\xi_1 = \xi$ and $\xi_2 = \eta$ in case of quadrilateral geometry and $\xi_1 = \zeta_1$, $\xi_2 = \zeta_2$, $\xi_3 = 1 - \zeta_1 - \zeta 2$ for the triangles). Using these results and the results from (2.3.65), (2.3.66), we arrive at $\mathbf{B}_{\kappa,I} = [\mathbf{B}_{\kappa_{xx},I}, \mathbf{B}_{\kappa_{yy},I}, \mathbf{B}_{\kappa_{xy},I}]^T$:

$$\begin{aligned}
\mathbf{B}_{\kappa_{xx},I} &= -\frac{\partial \mathbf{N}_{\theta_y,I}}{\partial x} = -\sum_i (J^{-1}_{x\xi_i} \frac{\partial \mathbf{N}_{\theta_y,I}}{\partial \xi_i}) \\
\mathbf{B}_{\kappa_{yy},I} &= +\frac{\partial \mathbf{N}_{\theta_x,I}}{\partial y} = +\sum_i (J^{-1}_{y\xi_i} \frac{\partial \mathbf{N}_{\theta_x,I}}{\partial \xi_i}) \\
\mathbf{B}_{\kappa_{xy},I} &= +\frac{\partial \mathbf{N}_{\theta_x,I}}{\partial x} - \frac{\partial \mathbf{N}_{\theta_y,I}}{\partial y} = +\sum_i (J^{-1}_{x\xi_i} \frac{\partial \mathbf{N}_{\theta_x,I}}{\partial \xi_i} - J^{-1}_{y\xi_i} \frac{\partial \mathbf{N}_{\theta_y,I}}{\partial \xi_i})
\end{aligned} \tag{2.3.68}$$

Stiffness matrix

The stiffness matrix $\mathbf{K}$ of the element is obtained by the discretization of the weak form (2.2.51). It is written in a block matrix form with $\mathbf{K} = [\mathbf{K}_{IJ}]$

$$\begin{aligned}
a_{K,e}(w_h; u_h) &= \int_{\Omega^e_h} \boldsymbol{\kappa}^T(u_h) \boldsymbol{m}(w_h) \, \mathrm{d}\Omega = \\
&= \sum_{I,J} \hat{\boldsymbol{u}}^T_I \, \mathbf{K}_{IJ} \hat{\boldsymbol{w}}_J; \quad \mathbf{K}_{IJ} = \int_{\Omega^e_h} \mathbf{B}^T_{\kappa,I} \mathbf{C}_B \mathbf{B}_{\kappa,J} \, \mathrm{d}\Omega
\end{aligned} \tag{2.3.69}$$

The stiffness matrix depends entirely on the interpolation of rotations. Notice, that the interpolation of displacement w_h is needed only for the computation of the consistent load

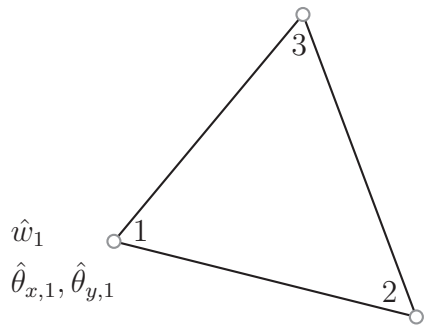

Figure 2.3.12: Triangular DK plate element - DK
Slika 2.3.12: Trikotni DK končni element za plošče - DK

vector $\boldsymbol{f}$. The explicit form of the displacement interpolation for the DK element was first obtained in [Ibrahimbegović, 1993].

Load vector

From (2.2.50) we have

$$l_{K,e}(u_h) = \sum_I \hat{\boldsymbol{u}}_I^T \boldsymbol{f}_I = \hat{\boldsymbol{u}}^T \boldsymbol{f} = \tag{2.3.70}$$

$$= \int_{\Omega_h^e} f\, u_h \mathrm{d}\Omega + \sum_{\Gamma_{IJ}^e} \left[\int_{\Gamma_{IJ}^e} (\bar{q}_{ef}\, u_h + \overline{m}_s\, \boldsymbol{\theta}_h(u_h) \cdot \boldsymbol{s})\, \mathrm{d}s + [\overline{m}_n u_{h,\Gamma}]_I^J \right]$$

$$\boldsymbol{f}_{f,I} = \int_{\Omega_h^e} f\, \mathbf{N}_{w,I} \mathrm{d}\Omega; \quad \boldsymbol{f}_{t,I} = \sum_{\Gamma_{e,IJ}} \int_{\Gamma_{e,IJ}} (\bar{q}_{ef} \mathbf{N}_{w,I} + \overline{m}_s\, \boldsymbol{s}^T \mathbf{N}_{\theta,I})\, \mathrm{d}s$$

The consistent nodal load vector is $\boldsymbol{f}_I = \boldsymbol{f}_{f,I} + \boldsymbol{f}_{t,I}$.

Triangular DK plate element - DKT

The DKT element has three vertex nodes with nodal degrees of freedom $\hat{\boldsymbol{u}}_I = [\hat{w}_I, \hat{\theta}_{xI}, \hat{\theta}_{yI}]$. The shape functions are formulated in the area coordinates:

$$N_I = \zeta_I; \quad N_{IJ} = 4\zeta_I\zeta_J; \quad M_{IJ} = 4\zeta_I\zeta_J(\zeta_J - \zeta_I) \tag{2.3.71}$$

The side between the nodes I and J is denoted by IJ. The shape functions (2.3.71) match the hierarchical shape functions (2.3.55) on the sides of the element. To show this, let us

Table 2.3: 4 point triangular integration scheme for triangular finite elements (DKT)
Tabela 2.3: 4 točkovna integracijska shema za trikotne končne elemente (DKT)

	ζ_1	ζ_1	ζ_1	w_i
1	1/3	1/3	1/3	-27/48
2	3/5	1/5	1/5	25/48
3	1/5	3/5	1/5	25/48
4	1/5	1/5	3/5	25/48

denote the coordinate along the side IJ by $\xi \in [-1, +1]$. On Γ_{IJ} we have

$$N_I = \zeta_I = (1-\xi)/2; \quad N_J = \zeta_J = (1+\xi)/2 \tag{2.3.72}$$

Inserting the expressions for N_I and N_J into (2.3.71), we recover

$$N_{IJ} = (1-\xi^2); \quad M_{IJ} = (1-\xi^2)\xi \tag{2.3.73}$$

A 4-point triangular scheme for the numerical integration is used in this work to compute stiffness matrix and load vector of DKT element (2.3.69), (2.3.70) (see [Zienkiewicz Taylor, 2000]). The coordinates of the integration points and the weights w_i are listed in Table 2.3.

The quadrilateral DK plate element - DKQ

The DKQ element has four vertex nodes with nodal degrees of freedom $\hat{\boldsymbol{u}}_I = [\hat{w}_I, \hat{\theta}_{xI}, \hat{\theta}_{yI}]$. The shape functions are constructed directly from the hierarchical shape functions (2.3.55). The compact definition of the shape functions is formulated in the natural coordinate system $(\xi, \eta) \in [-1, +1] \times [-1, +1]$:

I	1	2	3	4
IJ	12	23	34	41
r	ξ	η	ξ	η
s	η	ξ	η	ξ
p_r	+1	+1	-1	-1
p_s	+1	-1	-1	+1

$$\begin{aligned} N_I &= (1-p_r r)(1-p_s s)/4; \\ N_{IJ} &= (1-r^2)(1-p_s s)/2; \\ M_{IJ} &= p_r r(1-r^2)(1-p_s s)/2 \end{aligned} \tag{2.3.74}$$

The shape functions are depicted in Figure 2.3.14. A 2×2 Gauss scheme is used for the numerical integration to compute stiffness matrix and load vector of DKQ element (2.3.69), (2.3.70) (see [Zienkiewicz Taylor, 2000]). The coordinates of the integration points and the weights w_i are listed in Table 2.4.

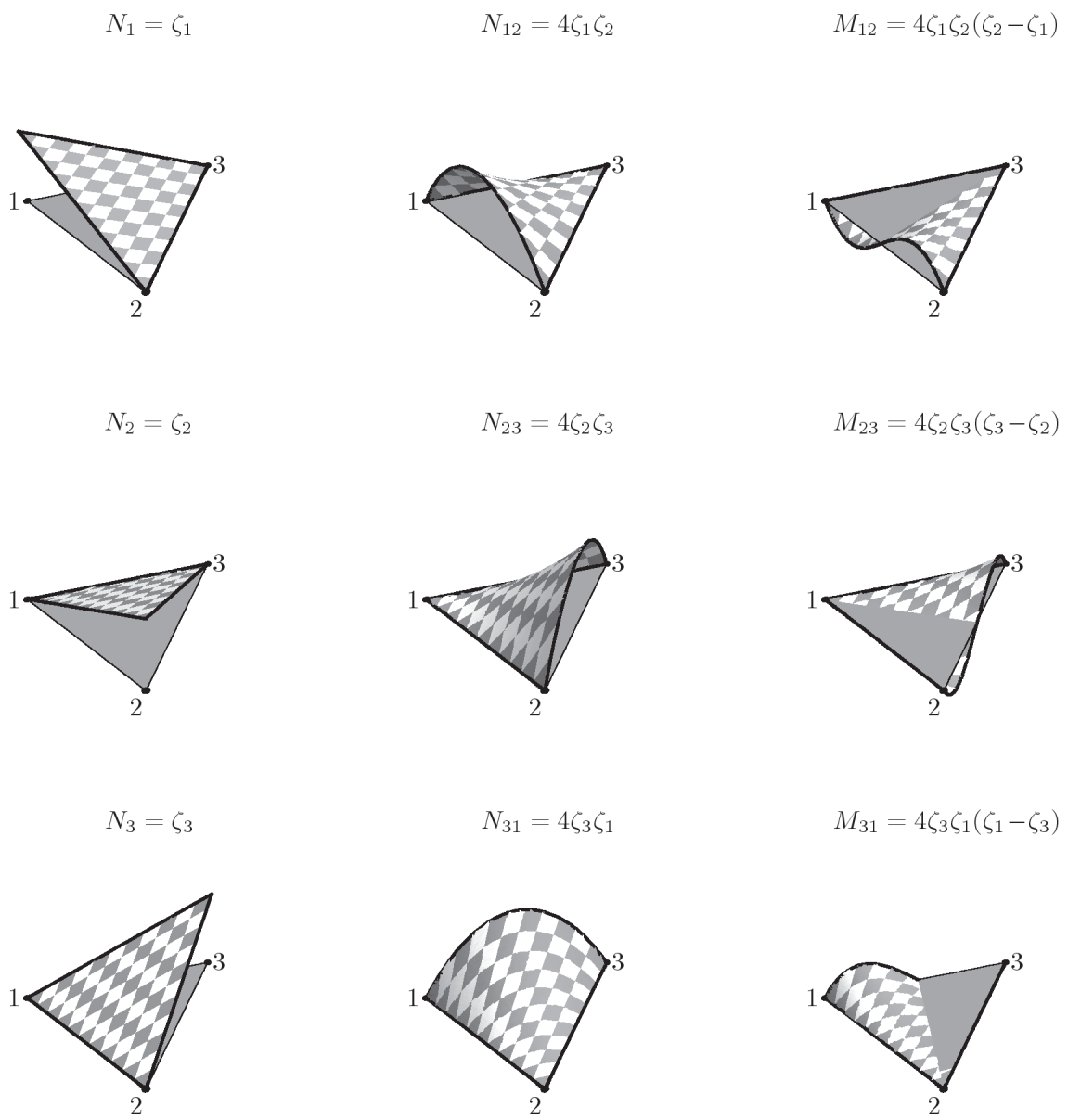

Figure 2.3.13: Hierarchic shape functions of the triangular DK plate element
Slika 2.3.13: Hierarhične interpolacijske funkcije trikotnega DK elementa

Table 2.4: 4 point quadrilateral integration scheme for quadrilateral finite elements (DKQ)

Tabela 2.4: 4 točkovna integracijska shema za štirikotne končne elemente (DKQ)

	ξ	η	w_i
1	$-1/\sqrt{3}$	$-1/\sqrt{3}$	1
2	$+1/\sqrt{3}$	$-1/\sqrt{3}$	1
3	$+1/\sqrt{3}$	$+1/\sqrt{3}$	1
4	$-1/\sqrt{3}$	$+1/\sqrt{3}$	1

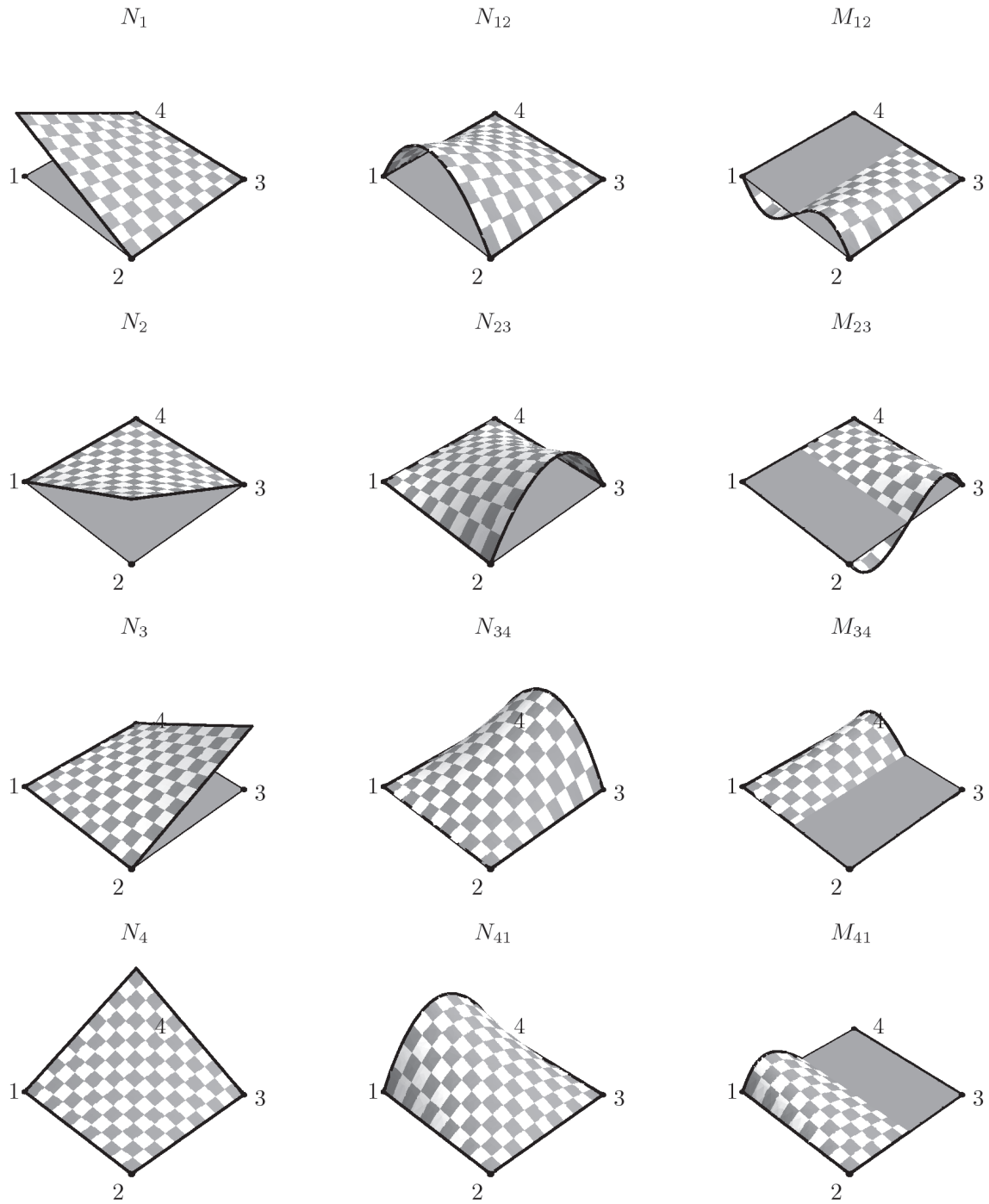

Figure 2.3.14: Hierarchic shape functions of the quadrilateral DK plate element
Slika 2.3.14: Hierarhične interpolacijske funkcije štirikotnega končnega elementa za plošče DKQ

2.4 Examples

The purpose of presented numerical examples is two-folds: (i) to illustrate specific issues involved in plate modeling and (ii) to compare the performance of finite elements that will be later used for discretization and model error estimation in different situations. The finite element solutions are compared to the reference ones. Where possible, the reference solutions are obtained analytically (in closed form or in the form of series expansion). In the cases where the analytical solution is not available, a finite element solution obtained with the most enhanced element on a very fine mesh presents the reference solution. In the figures, the nomenclature of Figure 2.4.1 is employed.

The presented finite elements were implemented in the Fortran based finite element program FEAP [Taylor, 2000], developed by R. Taylor. They were also implemented in the `C++` based finite element program AceFEM [Korelc, 2006], developed by J. Korelc. In the later implementation the symbolic manipulation code AceGEN [Korelc, 2006], developed by J. Korelc, was used. Additional routines, used for postprocessing were coded in Mathematica [Wolfram, 1988] and Matlab [Guide, 1998].

The computed FE stress resultants are not continuous across element boundaries, which makes the assessment of the results difficult. To produce readable plots of stress resultants, the nodal values are computed from the element integration point values using the standard averaging technique, see [Taylor], section 5.5. The shear forces are computed from the equilibrium equations (2.2.17). They depend on the derivatives of the moment resultants. To obtain the derivatives, the bilinear interpolation of moment resultants on Ω_h^e is first built from the integration point values. The equilibrium shear forces are indexed by $_{,e}$ in the FE plots to distinguish them from the constitutive shear forces.

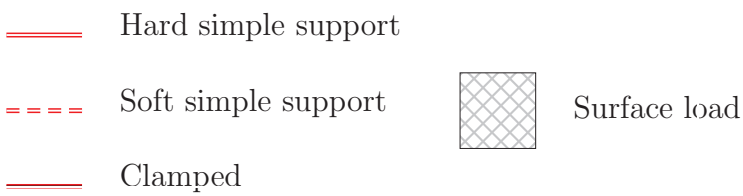

Figure 2.4.1: Designation of boundary conditions and loads
Slika 2.4.1: Oznake robnih pogojev in obtežb

2.4.1 Uniformly loaded simply supported square plate

A simply supported rectangular plate of side length $a = 10$ and thickness $t = 0.01$ under uniform loading $f = 1$ is considered. The material is linear elastic and isotropic, with Young's modulus $E = 10.92 \times 10^{10}$ and Poisson's ratio $\nu = 0.3$. The plate support is modeled as a hard simple support: the rotation θ_n at the sides of the plate is set to zero.

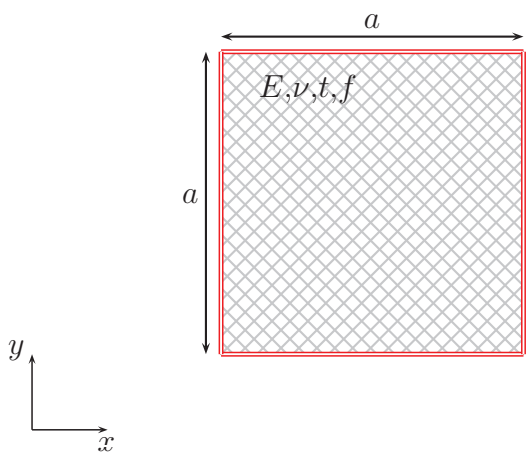

Figure 2.4.2: Problem definition and geometry for the uniformly loaded simply supported square plate (t/a=1/1000)
Slika 2.4.2: Definicija in geometrija problema enakomerno obremenjene prosto podprte kvadratne plošče (t/a=1/1000)

Reference solution

Since the plate is very thin (a/t=1000), the solution of the Kirchhoff theory is considered as the reference one. The bi-harmonic equation (2.2.26) is solved by the analytical function in the form of series expansion, see e.g. [Timoshenko Vojnovski-Kriger, 1959]:

$$w = \frac{f}{D}\frac{16}{\pi^6}\sum_{m=1}^{\infty}\sum_{n=1}^{\infty}\frac{\sin(n\pi\frac{x}{a})\sin(m\pi\frac{y}{b})}{m\,n\,((\frac{n}{a})^2+(\frac{m}{b})^2)^2}; \quad m = 1,3,5,\cdots \quad n = 1,3,5,\cdots$$

where a, b are the sides of the plate and $D = \frac{Et^3}{12(1-\nu^2)}$ is the plate bending stiffness. At the center of the square plate $b = a; x = y = a/2$, we have:

$$w = \frac{fa^4}{D}\overbrace{\frac{16}{\pi^6}\sum_{m=1}^{\infty}\sum_{n=1}^{\infty}\frac{\sin(\frac{n\pi}{2})\sin(\frac{m\pi}{2})}{mn(n^2+m^2)^2}}^{0.0040623532} \tag{2.4.1}$$
$$m = 1,3,5,\cdots \quad n = 1,3,5,\cdots$$

The curvatures are computed from $\boldsymbol{\kappa} = [\frac{\partial^2 w}{\partial x^2}, \frac{\partial^2 w}{\partial y^2}, 2\frac{\partial^2 w}{\partial x \partial y}]^T$ and moment resultants from $\boldsymbol{m} = \mathbf{C}_B \boldsymbol{\kappa}$, where $\mathbf{C}_B$ is the constitutive matrix. At the geometrical center of the rectangular plate, the moment resultants are

$$m_{xx} = -0.0368381\,(1-\nu)qa^2; \;\; m_{yy} = -0.0368381\,(1-\nu)qa^2; \;\; m_{xy} = 0$$

and at the corners of the plate

$$m_{xx} = 0; \;\; m_{yy} = 0; \;\; m_{xy} = \pm 0.0463741\,(1-\nu)qa^2$$

The reference solution is shown in Figure 2.4.3. It contains contour plots of the displacement w and the rotations θ_x, θ_y. In the second column, the moment resultants m_{xx}, m_{yy} and m_{xy} are shown. The third column contains the contour plots of equilibrium shear forces q_x and q_y. The solution is regular throughout the domain and does not exhibit any singularities.

Finite element solutions

The problem is solved with the conforming finite element ARGY and the nonconforming discrete Kirchhoff elements DKT and DKQ. All the solutions are obtained on a similar mesh. A rather coarse mesh is used in order to be able to clearly distinguish the differences between the solutions obtained with various finite elements. The hard-simple supports are modeled by constraining (setting to zero) the nodal displacements $\hat{w}_I$ and rotations $\hat{\theta}_{n,I}$. When using Argyris element, additionally the nodal curvatures $\hat{\kappa}_{xx,I}$ and $\hat{\kappa}_{yy,I}$ are set to zero. In the mid-side nodes lying at the supported edges the nodal normal slope $\hat{w}_{,n}|_I$ is left free.

Figures 2.4.4 and 2.4.5 show FE solutions. The comparison of FE solutions obtained with Argyris and DK elements shows good agreement with the reference solution. Since the range (and the color coding) in Figures 2.4.3, 2.4.4 and 2.4.5 is the same, it is possible to visually asses the differences of the FE solutions. In the current case, the differences between the solutions are, however, minor.

More quantitative comparison of element performance is shown in Figure (2.4.6), where a study of element performance versus mesh density is presented. The plots show the log-log plot of relative error of several selected quantities versus the total number of degrees of freedom (both constrained and unconstrained) which is inversely proportional to the average element size. The a-apriori estimate of the convergence rate is h^p, where h is the average size of the element and p the interpolation order. In the log-log plot, the

convergence lines are straight lines. The slope of the lines in the log-log plot indicates the rate of convergence. The comparison of Argyris and DK elements clearly shows the superior convergence rate of the Argyris element in all of the studied quantities: displacement w and moment m_{xx} at the center of the plate as well as the total deformation energy of the plate, defined as $W^{int} = \sum_e \int_{\Omega_h^e} \boldsymbol{\kappa}^T \mathbf{C}_B \boldsymbol{\kappa} \mathrm{d}\Omega$. The integrand is evaluated at integration points and numerically integrated. Convergence of W^{int} is not monotone for the case of ARGY element which explains a kink in the convergence plot. The effect can be attributed to the choice of the numerical integration scheme. The superconvergent points of the ARGY element are the element nodes, while the integration points of the triangular integration scheme (2.3) lie in the interior of the element domain.

The convergence rate for the ARGY element is roughly twice as higher as the convergence rate of DK elements.

2.4.2 Uniformly loaded clamped square plate

A rectangular plate of side length $a = 10$ and thickness $t = 0.01$ under uniform loading $f = 1$ is analyzed. All sides of the plates are clamped. The material is linear elastic and isotropic, with Young's modulus $E = 10.92 \times 10^{10}$ and Poisson's ratio $\nu = 0.3$.

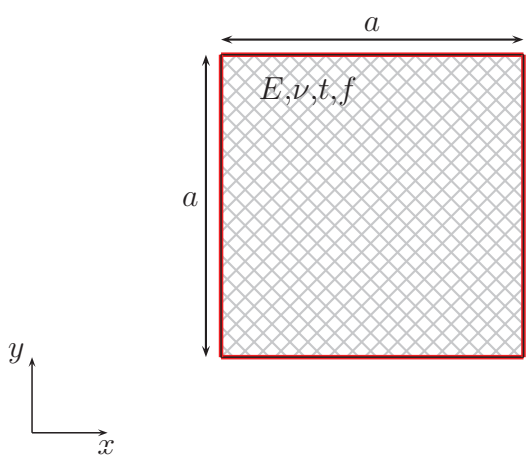

Figure 2.4.7: Problem definition and geometry for the uniformly loaded clamped square plate (t/a=1/1000)
Slika 2.4.7: Definicija in geometrija enakomerno obremenjene vpete kvadratne plošče (t/a=1/1000)

Reference solution

The reference solution is the analytical solution in the form of series expansion. Since the series converges quite slowly, a special treatment is necessary to be able to efficiently compute the reference result (see e.g. [Taylor Govindjee, 2002]). The main results are given at the center of the plate:

$$w = 1.26531908710^{-3}\frac{fa^4}{D}; \quad m_{xx} = -2.29050835210^{-2}fa^2 \tag{2.4.2}$$

The total deformation energy is $W^{int} = 3.89120077510^{-4}\frac{f^2a^4}{D}$. In this work we use the above results with the material and geometry data as given above.

Finite element solutions

FE solutions are shown in Figure 2.4.9 and Figure 2.4.10. The boundary conditions for DK elements were $\hat{w} = 0$, $\hat{\theta}_{x,I} = 0$ and $\hat{\theta}_{y,I} = 0$ at the clamped sides of the plate. The boundary conditions for the ARGY elements were $\hat{w} = 0, \hat{w}_{,x} = 0, \hat{w}_{,y} = 0$ at the vertex nodes and $\hat{w}_{,n} = 0$ at the midside nodes.

The qualitative comparison does not reveal any significant differences in the performance of the elements. However, the difference becomes clearly visible, when the convergence is observed (see Figure 2.4.11). The convergence of the ARGY element is one order higher that that of DK elements. Notice, however, that for the very coarse mesh, the results of both type of elements are quite comparable.

2.4.3 Uniformly loaded clamped circular plate

A clamped circular plate of radius $R = 5$ and thickness $t = 0.01$ under uniform loading $f = 1$ is considered. The material is linear elastic and isotropic, with Young's modulus $E = 6.825 \times 10^9$ and Poisson's ratio $\nu = 0.3$.

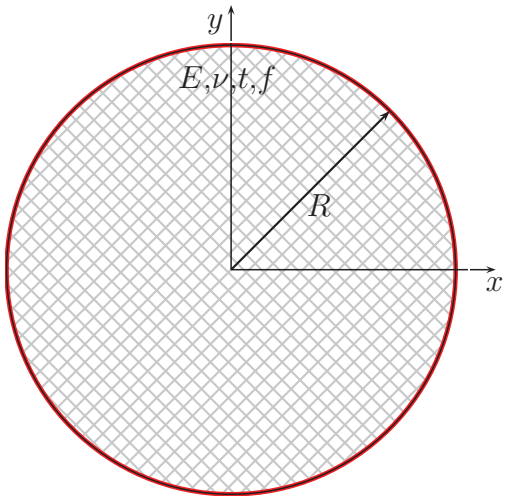

Figure 2.4.12: Clamped circular plate with uniform load (t/R=1/500)
Slika 2.4.12: Enakomerno obremenjena vpeta krožna plošča (t/R=1/500)

Reference solution

By taking into account the symmetry, it is possible to obtain the closed form solution of the problem (see [Timoshenko Vojnovski-Kriger, 1959]). The displacement of uniformly loaded clamped circular plate is defined by:

$$w = f(R^2 - r^2)^2/64/D \tag{2.4.3}$$

The moment resultants at the center of the plate are:

$$m_{xx} = -\frac{1}{16} f R^2/D(1+\nu); \quad m_{yy} = -\frac{1}{16} f R^2(1+\nu); \quad m_{xy} = 0 \tag{2.4.4}$$

In current case, where we have $D = R^4 = 625$, the displacement at the enter is $w = 1/64 = 0.015625$ and moment resultant $m_{xx} = -25/16 * 1.3 = -2.03125$.

Finite element solutions

A quarter of of the plate is modeled in FE analyses. The symmetry boundary conditions are taken into account at $x = 0$ and $y = 0$. The boundary conditions are listed in (2.4.5).

DK	$\hat{w}_I$	$\hat{\theta}_{x,I}$	$\hat{\theta}_{y,I}$
$x = 0$	-	-	0
$y = 0$	-	0	-
$r = R$	0	0	0

ARGY	$\hat{w}_I$	$\hat{w}_{I,x}$	$\hat{w}_{I,y}$	$\hat{w}_{I,xx}$	$\hat{w}_{I,yy}$	$\hat{w}_{I,xy}$	$\hat{w}_{I-J,n}$
$x = 0$	-	-	0	-	-	0	0
$y = 0$	-	0	-	-	-	0	0
$r = R$	0	0	0	-	-	-	0

(2.4.5)

The meshes were constructed so, that the distortion of the elements was minimized. In the case of quadrilateral elements, the distortion of the elements is, however, still significant. The sequence of meshes used in the convergence analysis is shown in Figure 2.4.14.

Notice that the area of the FE problem domain Ω_h converges to the area Ω as the mesh is refined. As shown in Figure 2.4.15, the FE solution with ARGY element shows very good qualitative agreement with the reference solution. Results of the DK elements are being influenced by the mesh distortion (quadrilaterals) and mesh orientation (triangles). The influence is, however, noticeable only when the comparison of the equilibrium shear forces with the reference solution is made. One can thus conclude that the mesh distortion (quadrilaterals) and mesh orientation (triangles) has the greatest influence on the computation of the transverse shear forces.

The comparison of the convergence, shown in Figure 2.4.17, reveals an interesting fact. The convergence of the ARGY element is no longer superior to that of DK elements, but is rather of the same order. This can be attributed to the fact, that the error made in the approximation of the curved domain boundary dominates the overall error.

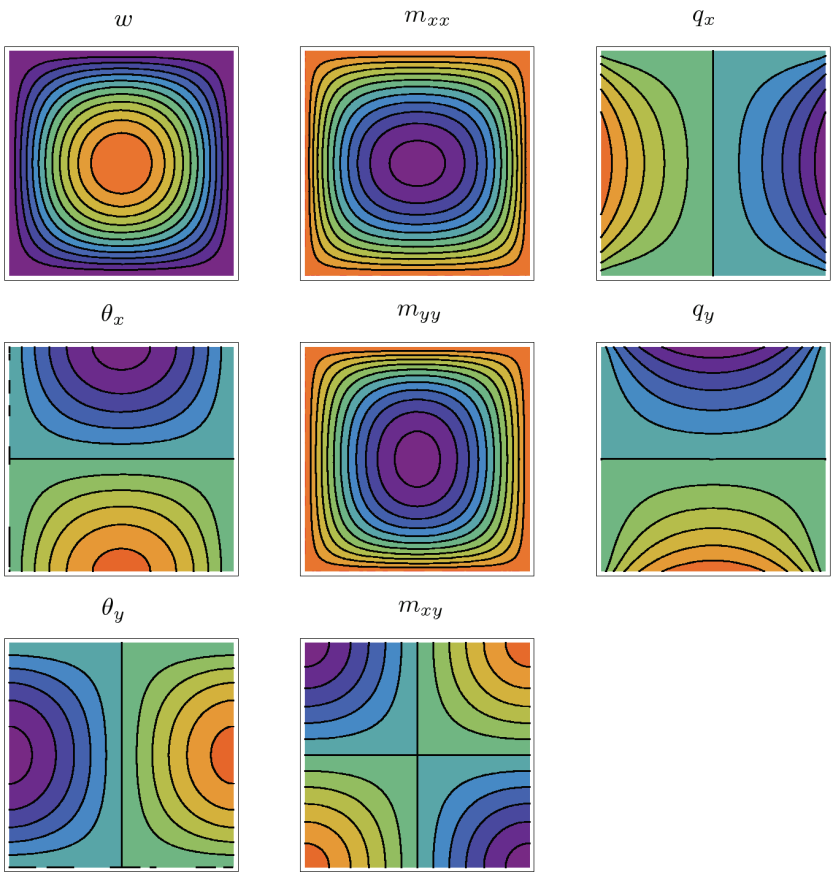

	w	θ_x	θ_y	m_{xx}	m_{yy}	m_{xy}	q_x	q_y
	0.	−0.0015	−0.0015	−5.	−5.	−3.5	−3.5	−3.5
	≃	≃	≃	≃	≃	≃	≃	≃
	0.000338	−0.00125	−0.00125	−4.58	−4.58	−2.92	−2.92	−2.92
	0.000338	−0.00125	−0.00125	−4.58	−4.58	−2.92	−2.92	−2.92
	≃	≃	≃	≃	≃	≃	≃	≃
	0.000677	−0.001	−0.001	−4.17	−4.17	−2.33	−2.33	−2.33
	0.000677	−0.001	−0.001	−4.17	−4.17	−2.33	−2.33	−2.33
	≃	≃	≃	≃	≃	≃	≃	≃
	0.00102	−0.00075	−0.00075	−3.75	−3.75	−1.75	−1.75	−1.75
	0.00102	−0.00075	−0.00075	−3.75	−3.75	−1.75	−1.75	−1.75
	≃	≃	≃	≃	≃	≃	≃	≃
	0.00135	−0.0005	−0.0005	−3.33	−3.33	−1.17	−1.17	−1.17
	0.00135	−0.0005	−0.0005	−3.33	−3.33	−1.17	−1.17	−1.17
	≃	≃	≃	≃	≃	≃	≃	≃
	0.00169	−0.00025	−0.00025	−2.92	−2.92	−0.583	−0.583	−0.583
	0.00169	−0.00025	−0.00025	−2.92	−2.92	−0.583	−0.583	−0.583
	≃	≃	≃	≃	≃	≃	≃	≃
	0.00203	0.	0.	−2.5	−2.5	0.	0.	0.
	0.00203	0.	0.	−2.5	−2.5	0.	0.	0.
	≃	≃	≃	≃	≃	≃	≃	≃
	0.00237	0.00025	0.00025	−2.08	−2.08	0.583	0.583	0.583
	0.00237	0.00025	0.00025	−2.08	−2.08	0.583	0.583	0.583
	≃	≃	≃	≃	≃	≃	≃	≃
	0.00271	0.0005	0.0005	−1.67	−1.67	1.17	1.17	1.17
	0.00271	0.0005	0.0005	−1.67	−1.67	1.17	1.17	1.17
	≃	≃	≃	≃	≃	≃	≃	≃
	0.00305	0.00075	0.00075	−1.25	−1.25	1.75	1.75	1.75
	0.00305	0.00075	0.00075	−1.25	−1.25	1.75	1.75	1.75
	≃	≃	≃	≃	≃	≃	≃	≃
	0.00338	0.001	0.001	−0.833	−0.833	2.33	2.33	2.33
	0.00338	0.001	0.001	−0.833	−0.833	2.33	2.33	2.33
	≃	≃	≃	≃	≃	≃	≃	≃
	0.00372	0.00125	0.00125	−0.417	−0.417	2.92	2.92	2.92
	0.00372	0.00125	0.00125	−0.417	−0.417	2.92	2.92	2.92
	≃	≃	≃	≃	≃	≃	≃	≃
	0.00406	0.0015	0.0015	0.	0.	3.5	3.5	3.5

Figure 2.4.3: Reference solution of the uniformly loaded simply supported square plate with legend also valid for Figures 2.4.4 and 2.4.5

Slika 2.4.3: Referenčna rešitev enakomerno obremenjene prosto podprte kvadratne plošče z legendo, ki velja tudi za Sliki 2.4.4 in 2.4.5

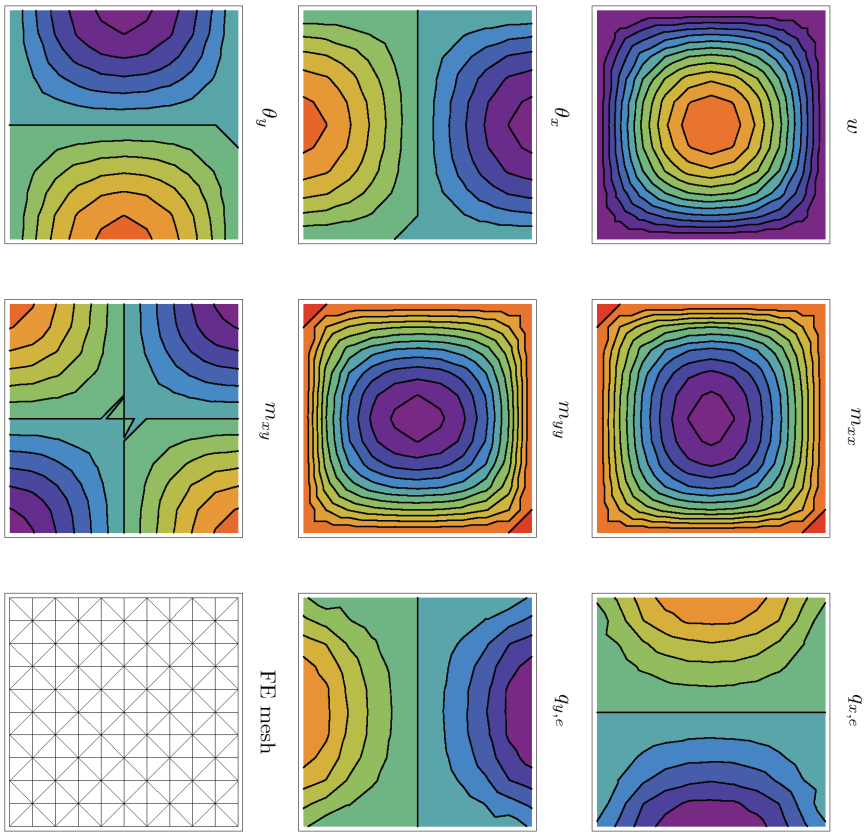

(ARGY element)

Figure 2.4.4: FE solution of the uniformly loaded simply supported square plate with Argyris plate element
Slika 2.4.4: Računska rešitev enakomerno obremenjene prosto podprte kvadratne plošče z Argyrisovim končnim elementom

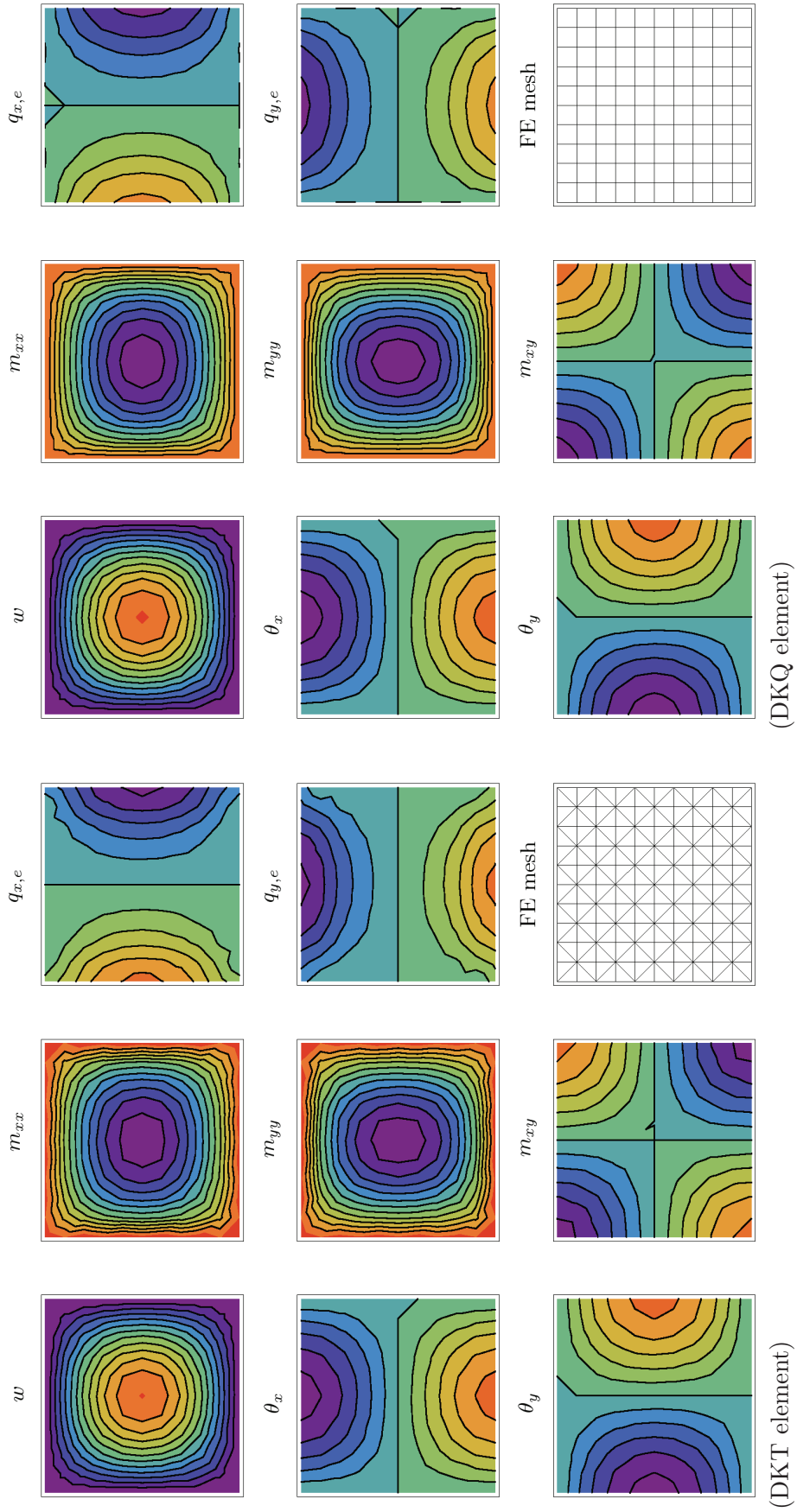

Figure 2.4.5: Finite element solution of the uniformly loaded simply supported square plate with DK plate elements
Slika 2.4.5: Računska rešitev enakomerno obremenjene prosto podprte kvadratne plošče z DK končnimi elementi

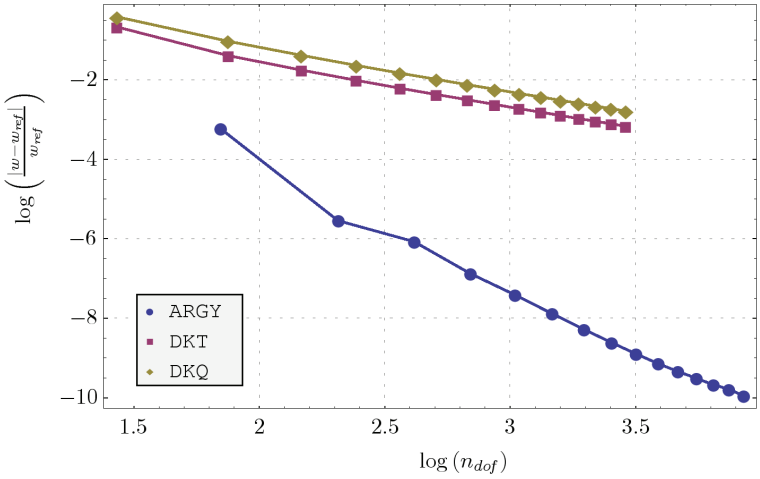

(Displacement w at center)

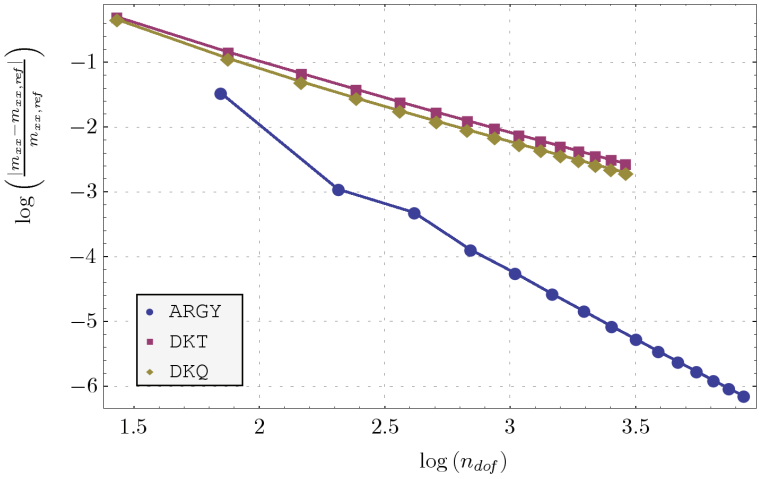

(Moment resultant m_{xx} at center)

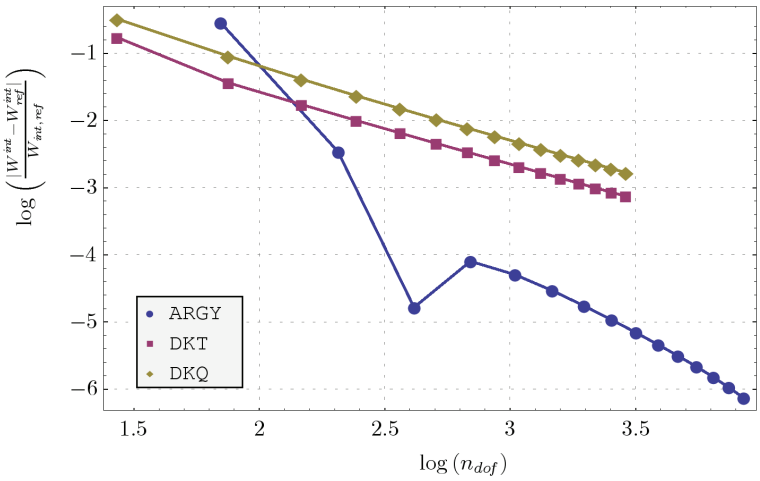

(Energy norm)

Figure 2.4.6: Comparison of the convergence of FE solutions for the uniformly loaded simply supported square plate
Slika 2.4.6: Primerjava konvergence računske rešitve problema enakomerno obremenjene prosto podprte kvadratne plošče

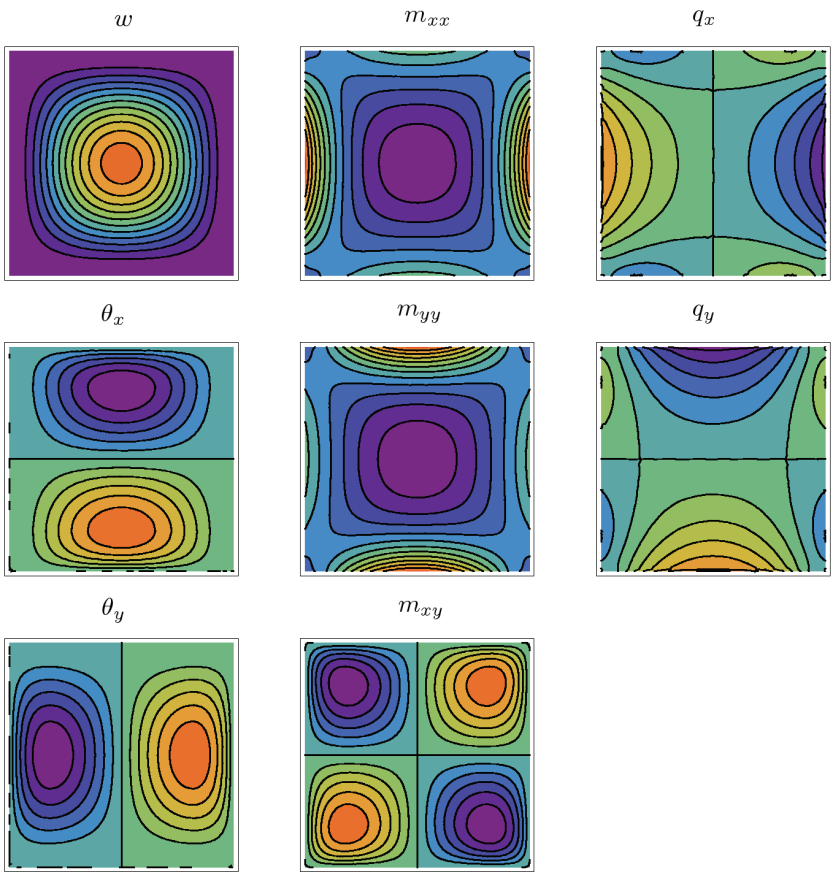

	w	θ_x	θ_y	m_{xx}	m_{yy}	m_{xy}	q_x	q_y
	0.	−0.0004	−0.0004	−2.4	−2.4	−0.88	−5.1	−5.1
	≃	≃	≃	≃	≃	≃	≃	≃
	0.000108	−0.000333	−0.000333	−1.78	−1.78	−0.733	−4.25	−4.25
	0.000108	−0.000333	−0.000333	−1.78	−1.78	−0.733	−4.25	−4.25
	≃	≃	≃	≃	≃	≃	≃	≃
	0.000217	−0.000267	−0.000267	−1.15	−1.15	−0.587	−3.4	−3.4
	0.000217	−0.000267	−0.000267	−1.15	−1.15	−0.587	−3.4	−3.4
	≃	≃	≃	≃	≃	≃	≃	≃
	0.000325	−0.0002	−0.0002	−0.525	−0.525	−0.44	−2.55	−2.55
	0.000325	−0.0002	−0.0002	−0.525	−0.525	−0.44	−2.55	−2.55
	≃	≃	≃	≃	≃	≃	≃	≃
	0.000433	−0.000133	−0.000133	0.1	0.1	−0.293	−1.7	−1.7
	0.000433	−0.000133	−0.000133	0.1	0.1	−0.293	−1.7	−1.7
	≃	≃	≃	≃	≃	≃	≃	≃
	0.000542	−0.0000667	−0.0000667	0.725	0.725	−0.147	−0.85	−0.85
	0.000542	−0.0000667	−0.0000667	0.725	0.725	−0.147	−0.85	−0.85
	≃	≃	≃	≃	≃	≃	≃	≃
	0.00065	0.	0.	1.35	1.35	0.	0.	0.
	0.00065	0.	0.	1.35	1.35	0.	0.	0.
	≃	≃	≃	≃	≃	≃	≃	≃
	0.000758	0.0000667	0.0000667	1.98	1.98	0.147	0.85	0.85
	0.000758	0.0000667	0.0000667	1.98	1.98	0.147	0.85	0.85
	≃	≃	≃	≃	≃	≃	≃	≃
	0.000867	0.000133	0.000133	2.6	2.6	0.293	1.7	1.7
	0.000867	0.000133	0.000133	2.6	2.6	0.293	1.7	1.7
	≃	≃	≃	≃	≃	≃	≃	≃
	0.000975	0.0002	0.0002	3.23	3.23	0.44	2.55	2.55
	0.000975	0.0002	0.0002	3.23	3.23	0.44	2.55	2.55
	≃	≃	≃	≃	≃	≃	≃	≃
	0.00108	0.000267	0.000267	3.85	3.85	0.587	3.4	3.4
	0.00108	0.000267	0.000267	3.85	3.85	0.587	3.4	3.4
	≃	≃	≃	≃	≃	≃	≃	≃
	0.00119	0.000333	0.000333	4.48	4.48	0.733	4.25	4.25
	0.00119	0.000333	0.000333	4.48	4.48	0.733	4.25	4.25
	≃	≃	≃	≃	≃	≃	≃	≃
	0.0013	0.0004	0.0004	5.1	5.1	0.88	5.1	5.1

Figure 2.4.8: Reference solution of the uniformly loaded clamped square plate with legend also valid for Figures 2.4.9 and 2.4.10

Slika 2.4.8: Referenčna rešitev enakomerno obremenjene vpete kvadratne plošče z legendo, ki velja tudi za Sliki 2.4.9 in 2.4.10

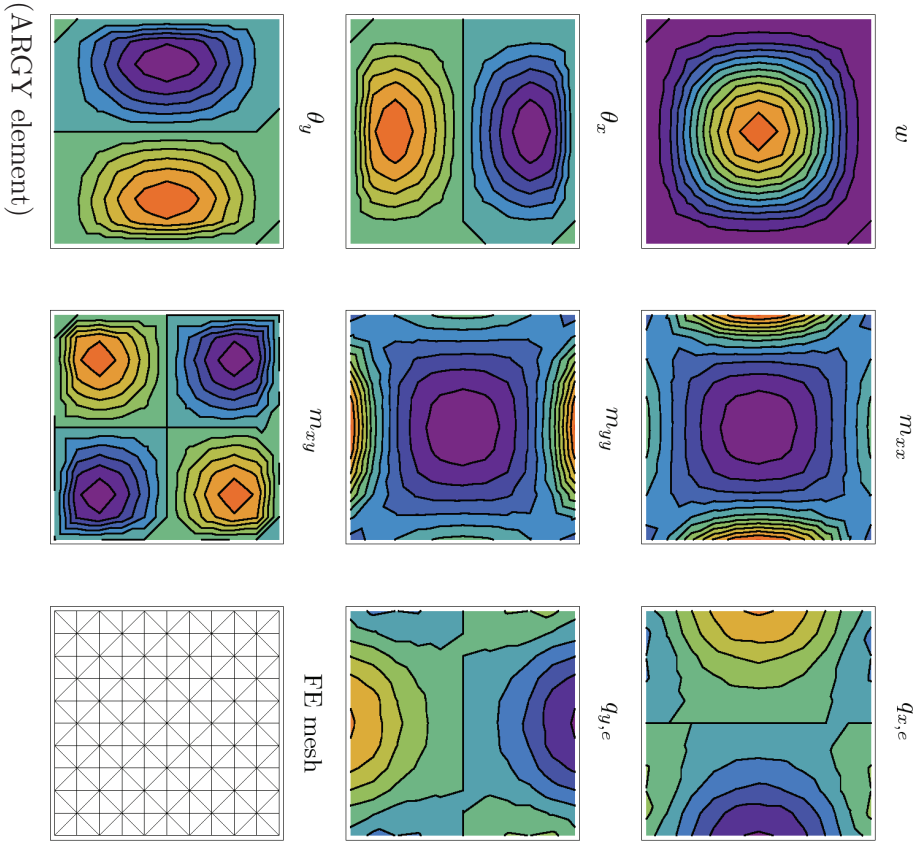

(ARGY element)

Figure 2.4.9: FE solution of the uniformly loaded clamped square plate with Argyris plate element
Slika 2.4.9: Računska rešitev enakomerno obremenjene vpete kvadratne plošče z Argyrisovim končnim elementom

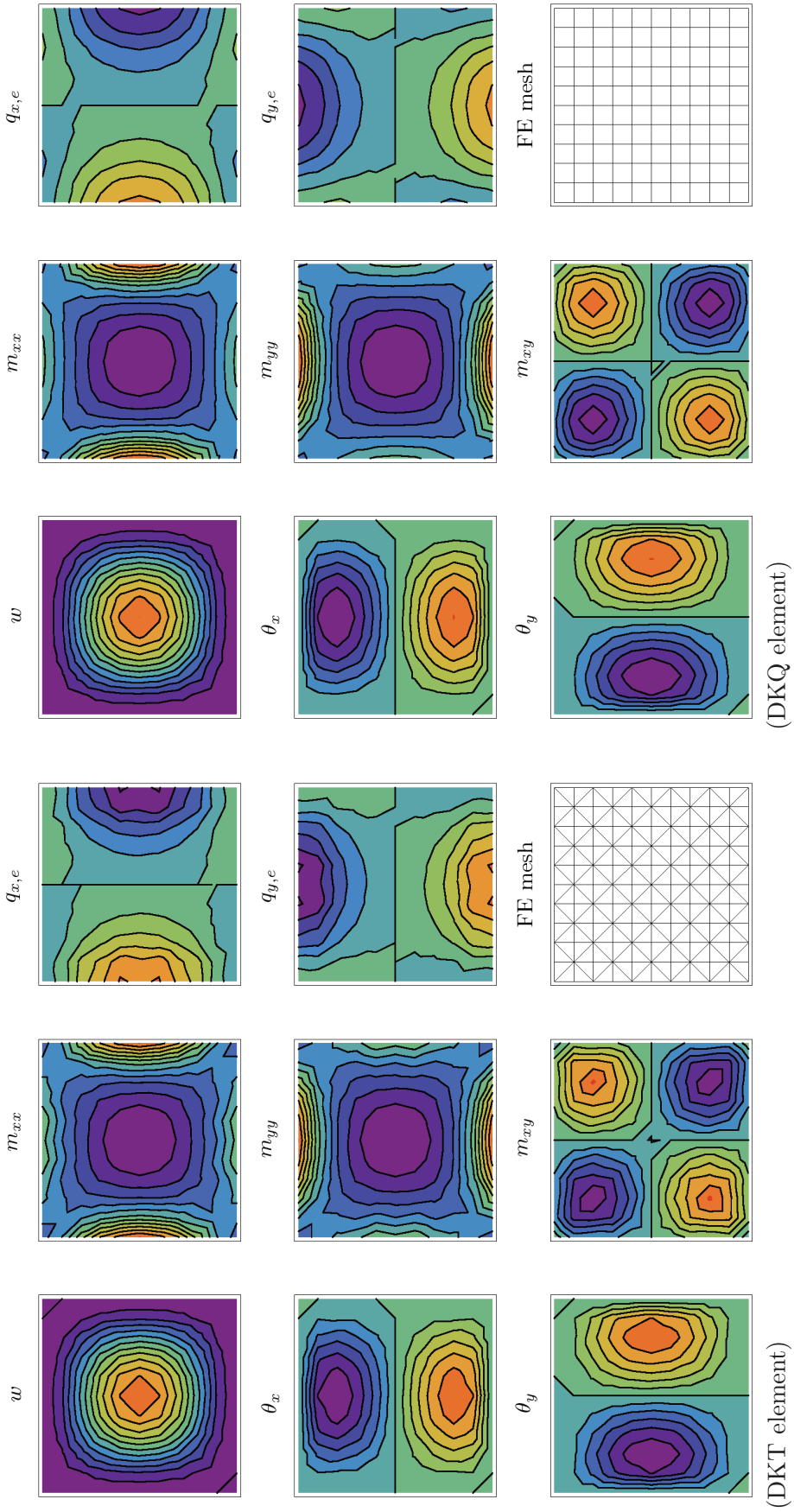

Figure 2.4.10: FE solution of the uniformly loaded clamped square plate with DK plate elements
Slika 2.4.10: Računska rešitev enakomerno obremenjene vpete kvadratne plošče z DK končnimi elementi

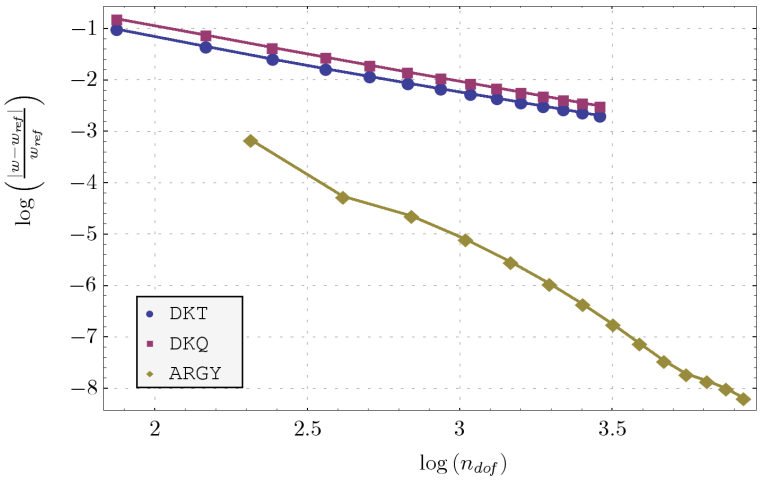

(Displacement w at center)

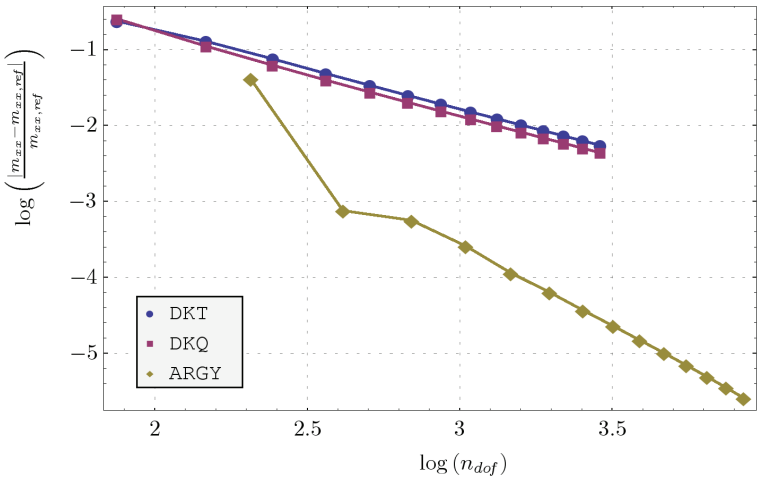

(Moment resultant m_{xx} at center)

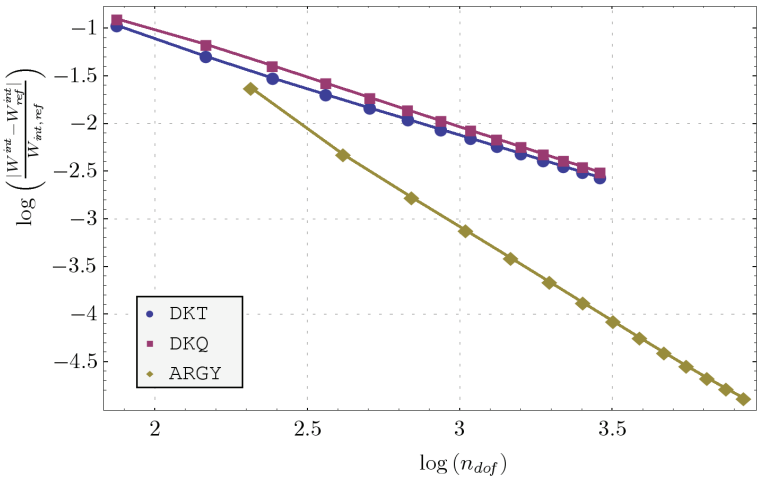

(Energy norm)

Figure 2.4.11: Comparison of the convergence of FE solutions for the uniformly loaded clamped square plate

Slika 2.4.11: Primerjava konvergence računske rešitve problema enakomerno obremenjene vpete kvadratne plošče

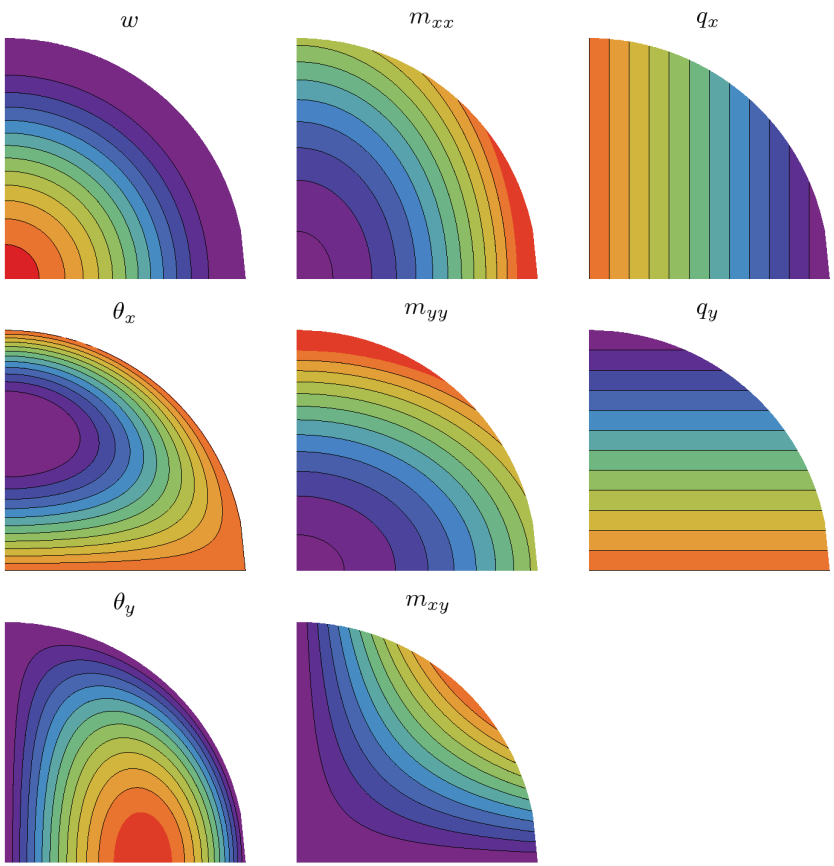

	w	θ_x	θ_y	m_{xx}	m_{yy}	m_{xy}	q_x	q_y
	0. ~ 0.00125	−0.0045 ~ −0.00413	0. ~ 0.000375	−2.3 ~ −1.92	−2.3 ~ −1.92	0. ~ 0.0917	−2.5 ~ −2.29	−2.5 ~ −2.29
	0.00125 ~ 0.0025	−0.00413 ~ −0.00375	0.000375 ~ 0.00075	−1.92 ~ −1.53	−1.92 ~ −1.53	0.0917 ~ 0.183	−2.29 ~ −2.08	−2.29 ~ −2.08
	0.0025 ~ 0.00375	−0.00375 ~ −0.00338	0.00075 ~ 0.00113	−1.53 ~ −1.15	−1.53 ~ −1.15	0.183 ~ 0.275	−2.08 ~ −1.88	−2.08 ~ −1.88
	0.00375 ~ 0.005	−0.00338 ~ −0.003	0.00113 ~ 0.0015	−1.15 ~ −0.767	−1.15 ~ −0.767	0.275 ~ 0.367	−1.88 ~ −1.67	−1.88 ~ −1.67
	0.005 ~ 0.00625	−0.003 ~ −0.00263	0.0015 ~ 0.00188	−0.767 ~ −0.383	−0.767 ~ −0.383	0.367 ~ 0.458	−1.67 ~ −1.46	−1.67 ~ −1.46
	0.00625 ~ 0.0075	−0.00263 ~ −0.00225	0.00188 ~ 0.00225	−0.383 ~ 0.	−0.383 ~ 0.	0.458 ~ 0.55	−1.46 ~ −1.25	−1.46 ~ −1.25
	0.0075 ~ 0.00875	−0.00225 ~ −0.00188	0.00225 ~ 0.00263	0. ~ 0.383	0. ~ 0.383	0.55 ~ 0.642	−1.25 ~ −1.04	−1.25 ~ −1.04
	0.00875 ~ 0.01	−0.00188 ~ −0.0015	0.00263 ~ 0.003	0.383 ~ 0.767	0.383 ~ 0.767	0.642 ~ 0.733	−1.04 ~ −0.833	−1.04 ~ −0.833
	0.01 ~ 0.0113	−0.0015 ~ −0.00113	0.003 ~ 0.00338	0.767 ~ 1.15	0.767 ~ 1.15	0.733 ~ 0.825	−0.833 ~ −0.625	−0.833 ~ −0.625
	0.0113 ~ 0.0125	−0.00113 ~ −0.00075	0.00338 ~ 0.00375	1.15 ~ 1.53	1.15 ~ 1.53	0.825 ~ 0.917	−0.625 ~ −0.417	−0.625 ~ −0.417
	0.0125 ~ 0.0138	−0.00075 ~ −0.000375	0.00375 ~ 0.00413	1.53 ~ 1.92	1.53 ~ 1.92	0.917 ~ 1.01	−0.417 ~ −0.208	−0.417 ~ −0.208
	0.0138 ~ 0.015	−0.000375 ~ 0.	0.00413 ~ 0.0045	1.92 ~ 2.3	1.92 ~ 2.3	1.01 ~ 1.1	−0.208 ~ 0.	−0.208 ~ 0.

Figure 2.4.13: Reference solution of the uniformly loaded clamped circular plate with legend also valid for Figures 2.4.15 and 2.4.16

Slika 2.4.13: Referenčna rešitev enakomerno obremenjene vpete krožne plošče z legendo, ki velja tudi za Sliki 2.4.15 in 2.4.16

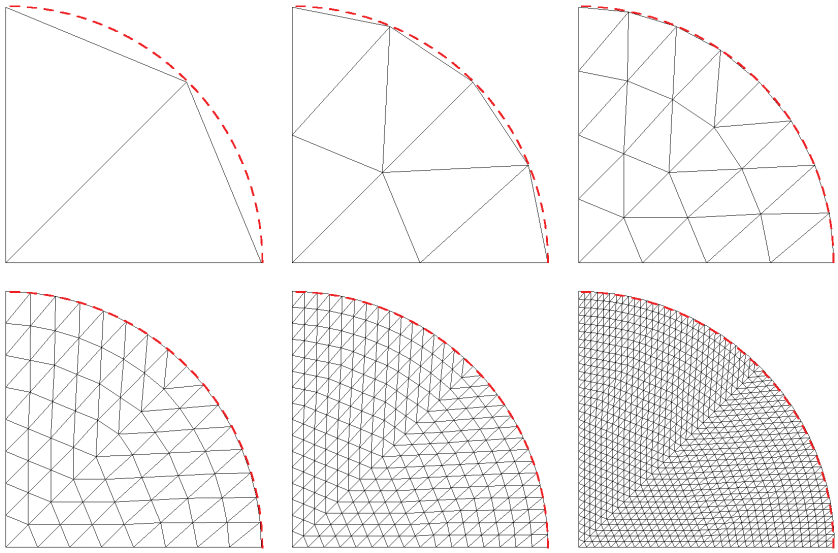

(Sequence of meshes of triangular elements)

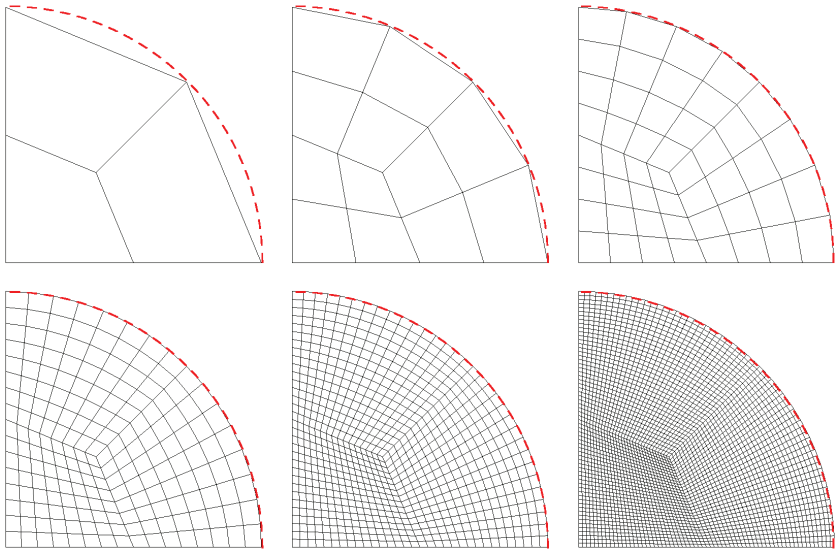

(Sequence of meshes of quadrilateral elements)

Figure 2.4.14: The sequence of meshes used for the finite element solution of uniformly loaded clamped circular plate
Slika 2.4.14: Zaporedje mrež uporabljenih pri rešitvi enakomerno obremenjene vpete krožne plošče

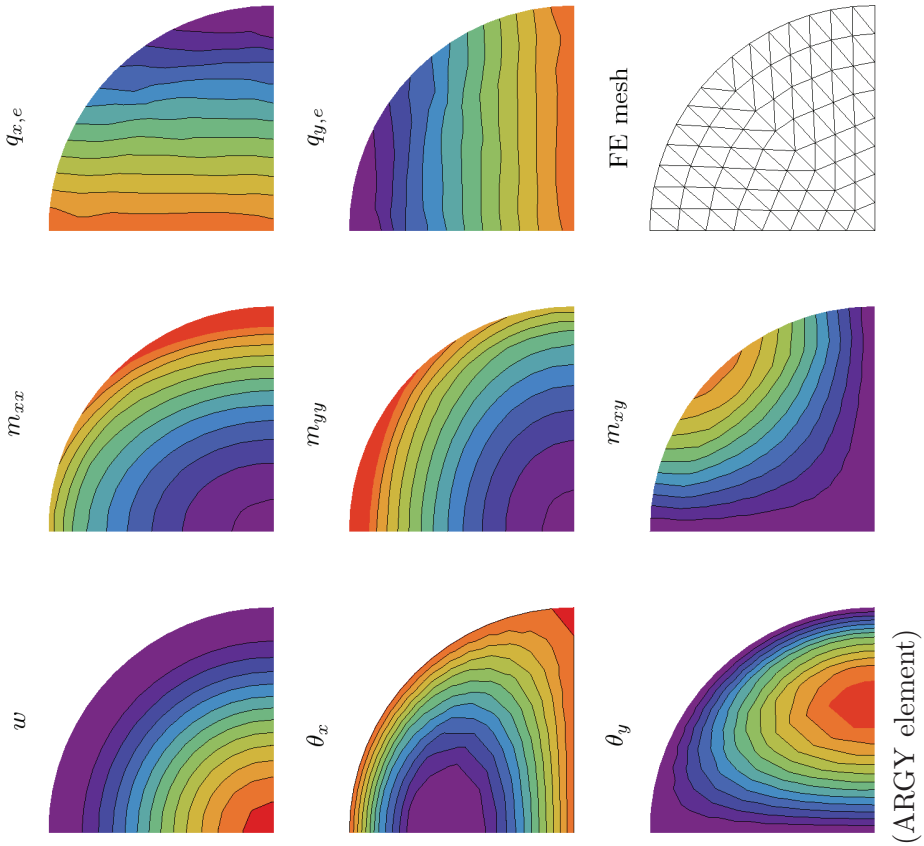

(ARGY element)

Figure 2.4.15: FE solution of the uniformly loaded clamped circular plate with Argyris plate element
Slika 2.4.15: Računska rešitev enakomerno obremenjene vpete krožne plošče z Argyrisovim končnim elementom

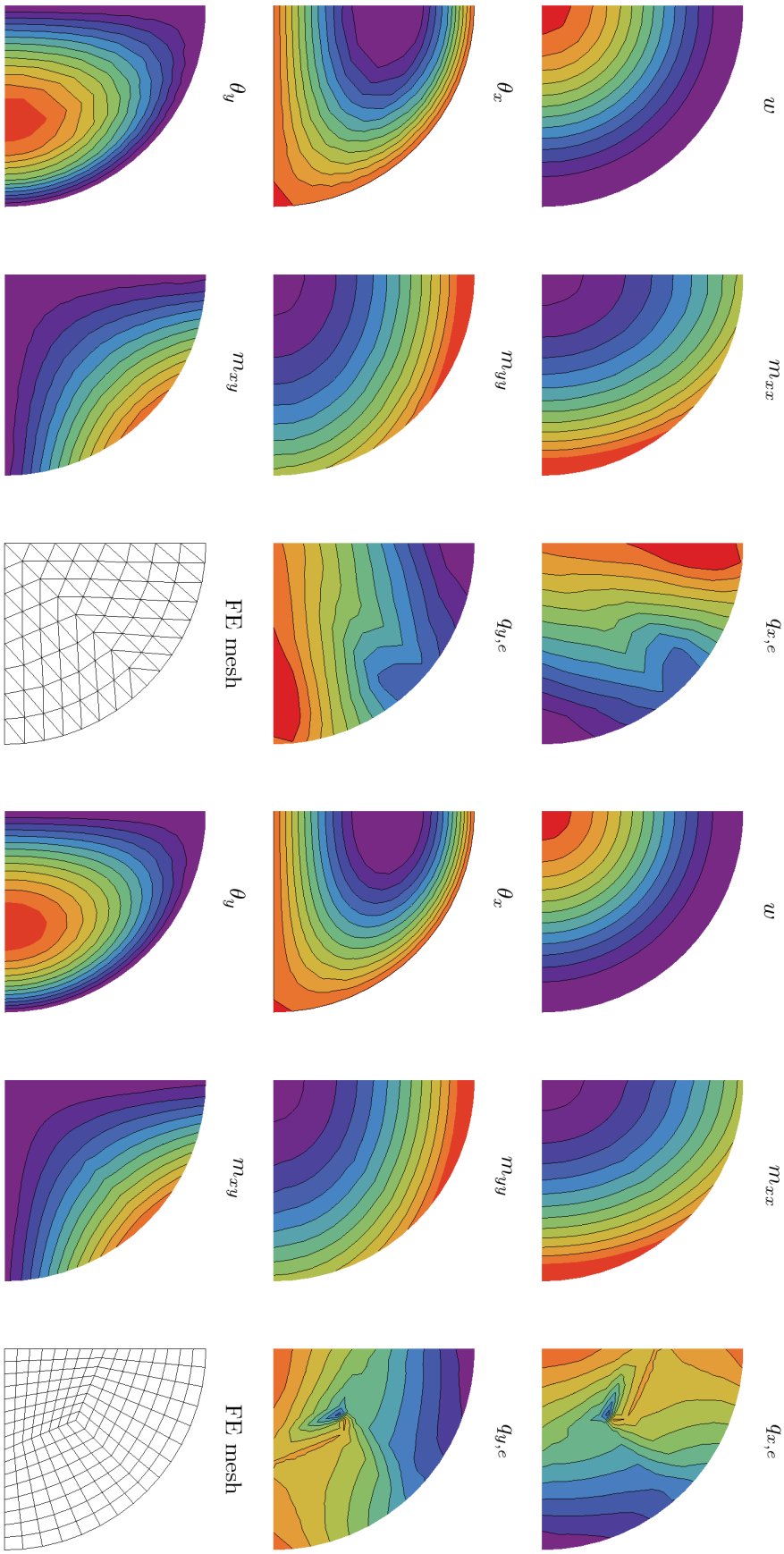

Figure 2.4.16: FE solution of the uniformly loaded clamped circular plate with DK plate elements
Slika 2.4.16: Računska rešitev enakomerno obremenjene vpete krožne plošče z DK končnimi elementi

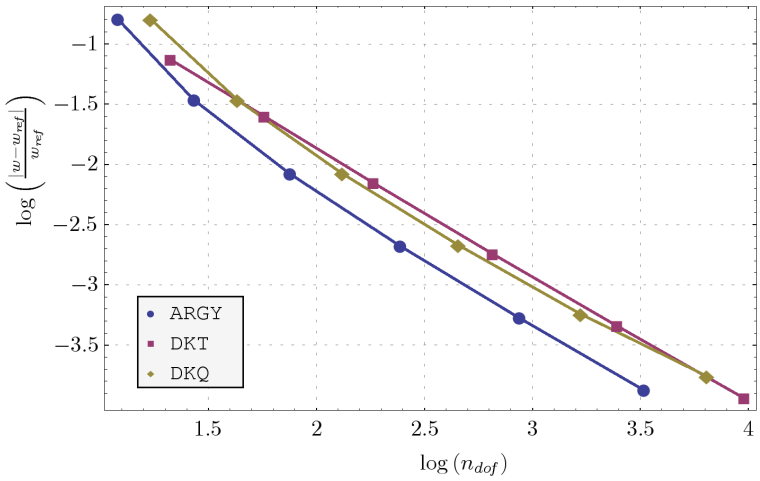

(Displacement w at center)

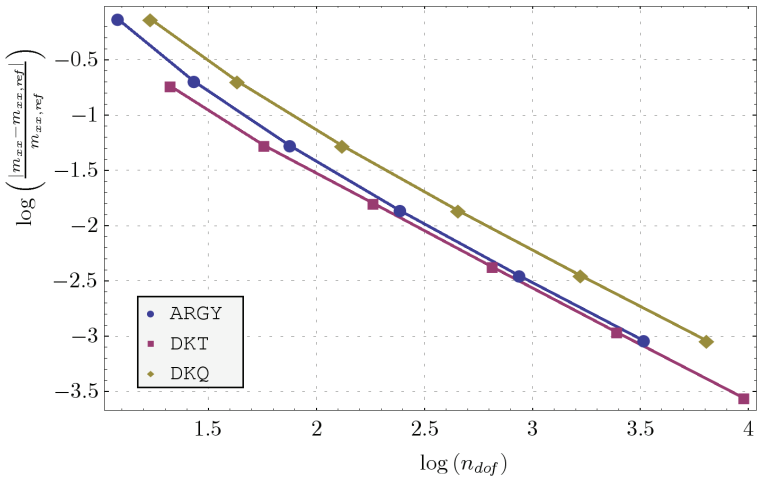

(Moment resultant m_{xx} at center)

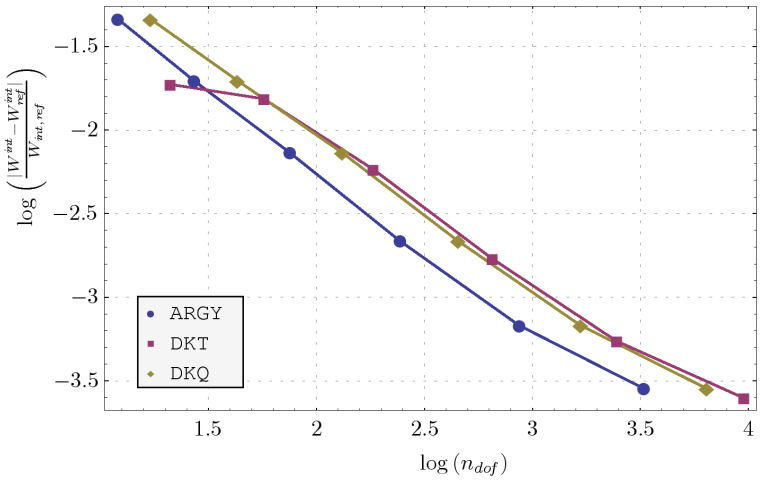

(Energy norm)

Figure 2.4.17: Comparison of the convergence of FE solutions for the uniformly loaded clamped circular plate

Slika 2.4.17: Primerjava konvergence računske rešitve problema enakomerno obremenjene vpete krožne plošče

2.4.4 Uniformly loaded hard simply supported skew plate

The analysis of Morley's $\alpha = 30°$ skew plate under uniform loading $f = 1$ with thickness $t = 0.1$ and side length $a = 10$ is considered. The plate is hard simply supported on all sides. The Young's modulus is $E = 10.92 \times 10^7$ and Poisson's ratio is $\nu = 0.3$.

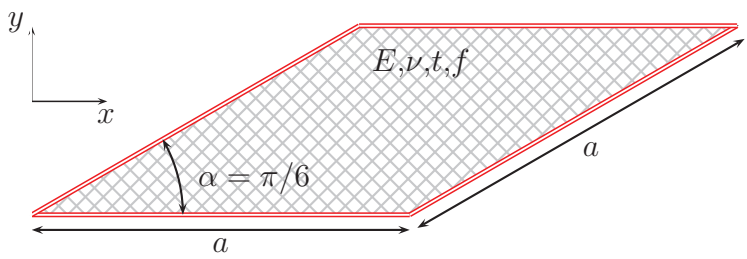

Figure 2.4.18: Problem definition and geometry for the uniformly loaded simply supported skew plate (t/a=100)
Slika 2.4.18: Definicija in geometrija problema enakomerno obremenjene prosto podprte romboidne plošče (t/a=1/100)

Reference solution

The most interesting feature of the solution concerns two singular points at the two obtuse corners of the plate, which strongly influence the quality of the computed results (e.g. see [Morley, 1963]). The strength of the singularity is $\lambda = 6/5 = 1.2$ see (2.2.66). In the vicinity of the corner, the moment resultants m_{xx}, m_{yy} vary as $r^{\lambda-2}$, while the moments resultant m_{xy} and shear forces q_x and q_y vary as $r^{\lambda-3}$, where r is the distance from the corner. As the analytic solution is not available, a finite element computation with Argyris element on a fine mesh (the elements with side $h = 0.1$) is taken as the reference solution. The reference solution confirms the existence of the singularity in the obtuse corners.

Finite element solutions

The boundary conditions used for the hard simply supported edge at $y = const.$ are: $\hat{w}_I = 0$, $\hat{\theta}_{x,I} = 0$ for DK elements and $\hat{w}_I = 0$, $\hat{w}_{I,x} = 0$ for the ARGY element. At the hard simply supported sloped edge $y/x = \tan\alpha$ the rotation $\hat{\theta}_n$ is set to zero, which results in the boundary condition: $\hat{\theta}_{x,I} - \tan\alpha\,\hat{\theta}_{y,I} = 0$ for DK elements and $\hat{w}_{I,y} + \tan\alpha\,\hat{w}_{I,x} = 0$.

The finite element solutions with ARGY element is shown in Figure 2.4.20. A serious deterioration of the accuracy is observed at the obtuse corners. In order to capture the

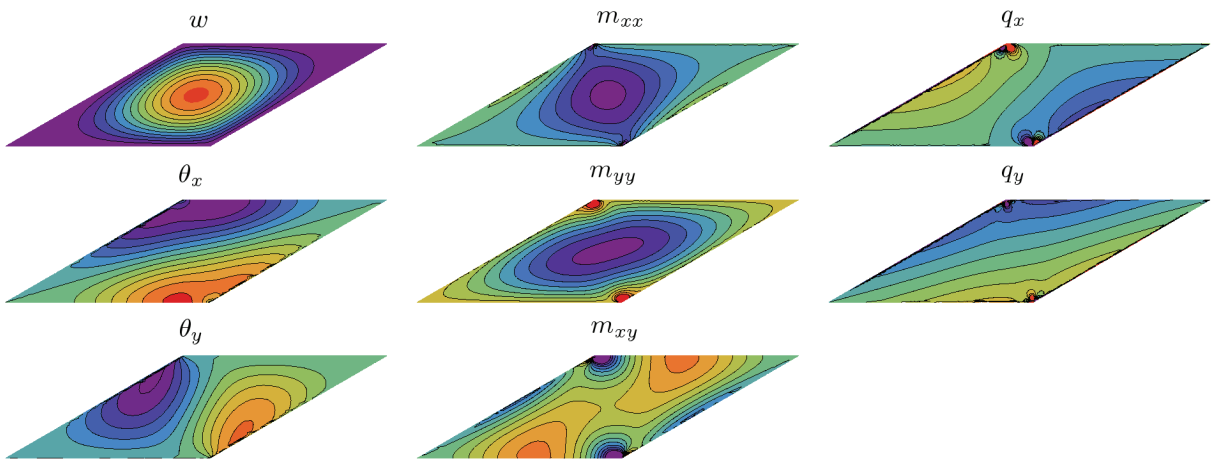

	w	θ_x	θ_y	m_{xx}	m_{yy}	m_{xy}	q_x	q_y	Ω
	0. ~ 0.00005	−0.0003 ~ −0.00025	−0.000145 ~ −0.000121	−1.5 ~ −1.38	−2.2 ~ −1.98	−0.5 ~ −0.417	−1.5 ~ −1.25	−3. ~ −2.5	~
	0.00005 ~ 0.0001	−0.00025 ~ −0.0002	−0.000121 ~ −0.0000967	−1.38 ~ −1.25	−1.98 ~ −1.75	−0.417 ~ −0.333	−1.25 ~ −1.	−2.5 ~ −2.	~
	0.0001 ~ 0.00015	−0.0002 ~ −0.00015	−0.0000967 ~ −0.0000725	−1.25 ~ −1.13	−1.75 ~ −1.53	−0.333 ~ −0.25	−1. ~ −0.75	−2. ~ −1.5	~
	0.00015 ~ 0.0002	−0.00015 ~ −0.0001	−0.0000725 ~ −0.0000483	−1.13 ~ −1.	−1.53 ~ −1.3	−0.25 ~ −0.167	−0.75 ~ −0.5	−1.5 ~ −1.	~
	0.0002 ~ 0.00025	−0.0001 ~ −0.00005	−0.0000483 ~ −0.0000242	−1. ~ −0.875	−1.3 ~ −1.08	−0.167 ~ −0.0833	−0.5 ~ −0.25	−1. ~ −0.5	~
	0.00025 ~ 0.0003	−0.00005 ~ 0.	−0.0000242 ~ 0.	−0.875 ~ −0.75	−1.08 ~ −0.85	−0.0833 ~ 0.	−0.25 ~ 0.	−0.5 ~ 0.	~
	0.0003 ~ 0.00035	0. ~ 0.00005	0. ~ 0.0000242	−0.75 ~ −0.625	−0.85 ~ −0.625	0. ~ 0.0833	0. ~ 0.25	0. ~ 0.5	~
	0.00035 ~ 0.0004	0.00005 ~ 0.0001	0.0000242 ~ 0.0000483	−0.625 ~ −0.5	−0.625 ~ −0.4	0.0833 ~ 0.167	0.25 ~ 0.5	0.5 ~ 1.	~
	0.0004 ~ 0.00045	0.0001 ~ 0.00015	0.0000483 ~ 0.0000725	−0.5 ~ −0.375	−0.4 ~ −0.175	0.167 ~ 0.25	0.5 ~ 0.75	1. ~ 1.5	~
	0.00045 ~ 0.0005	0.00015 ~ 0.0002	0.0000725 ~ 0.0000967	−0.375 ~ −0.25	−0.175 ~ 0.05	0.25 ~ 0.333	0.75 ~ 1.	1.5 ~ 2.	~
	0.0005 ~ 0.00055	0.0002 ~ 0.00025	0.0000967 ~ 0.000121	−0.25 ~ −0.125	0.05 ~ 0.275	0.333 ~ 0.417	1. ~ 1.25	2. ~ 2.5	~
	0.00055 ~ 0.0006	0.00025 ~ 0.0003	0.000121 ~ 0.000145	−0.125 ~ 0.	0.275 ~ 0.5	0.417 ~ 0.5	1.25 ~ 1.5	2.5 ~ 3.	~

Figure 2.4.19: Reference solution of the uniformly loaded simply supported skew plate with legend also valid for Figures 2.4.20 and 2.4.21
Slika 2.4.19: Referenčna rešitev enakomerno obremenjene prosto podprte romboidne plošče z legendo, ki velja tudi za Sliki 2.4.20 in 2.4.21

singularity better, the density of the mesh has to be increased at the obtuse corners. The finite element solution with DK elements qualitatively matches the reference solution in problem domain except at the obtuse corners. The quality of the finite element solution is influenced by the mesh distortion (see Figure 2.4.22). The performance of triangular element DKT does not the reach the performance of the quadrilateral element DKQ. The comparison of the converge rates shows, surprisingly, that the superior accuracy of the ARGY element, which was observed in the previous tests, is now lost.

In Figures 2.4.20 and 2.4.21, the singularity can be observed at the obtuse corners in moments m_{xx}, m_{yy} and m_{xy} and in equilibrium shear forces q_x and q_y. The contour plots are, however, not very suitable to study the singularities due to the fixed finite values of contour lines. At the obtuse corners (singularities) the gradients of the solution are infinite and in the limit, the optimal size of the elements is zero. With the decreasing mesh size, the singularity is captured increasingly better. The singularity thus manifests itself the most in the convergence rates (see Figure 2.4.22). The DK elements and ARGY element exhibit similar convergence rates. The monotonic convergence is observed at DK elements, while the convergence of the ARGY element is not monotone. Additionally the difference between the convergence of the triangular and quadrilateral elements is observed: the later converge slightly faster. This fact can be contributed to the singularity and the effect of distortion on the element performance.

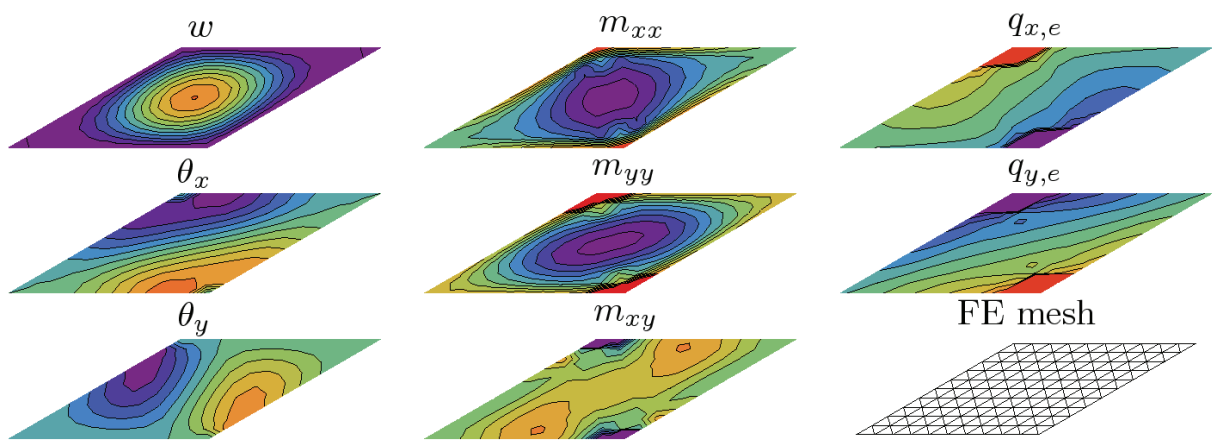

(ARGY element)

Figure 2.4.20: FE solution of the uniformly loaded simply supported skew plate with Argyris plate element
Slika 2.4.20: Računska rešitev enakomerno obremenjene prosto podprte romboidne plošče z Argyrisovim končnim elementom

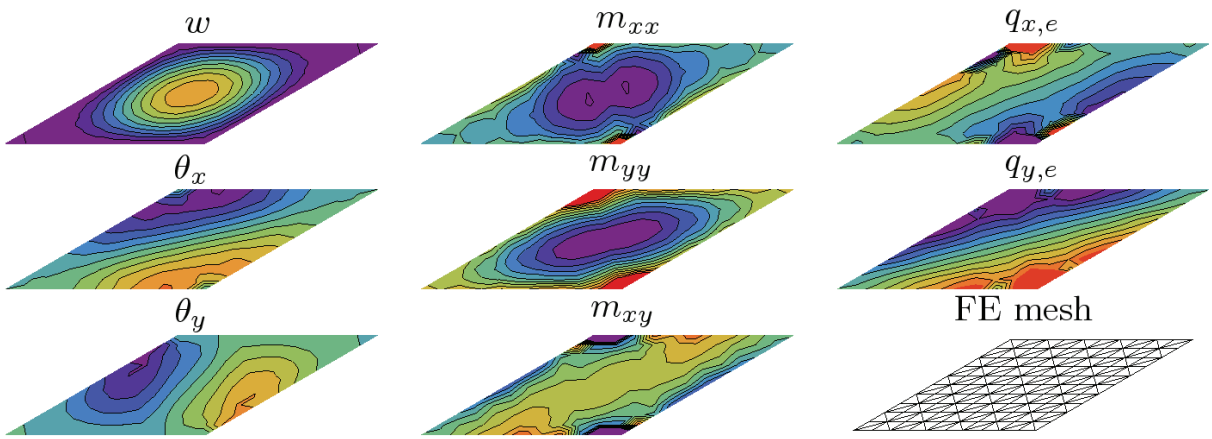

(DKT element)

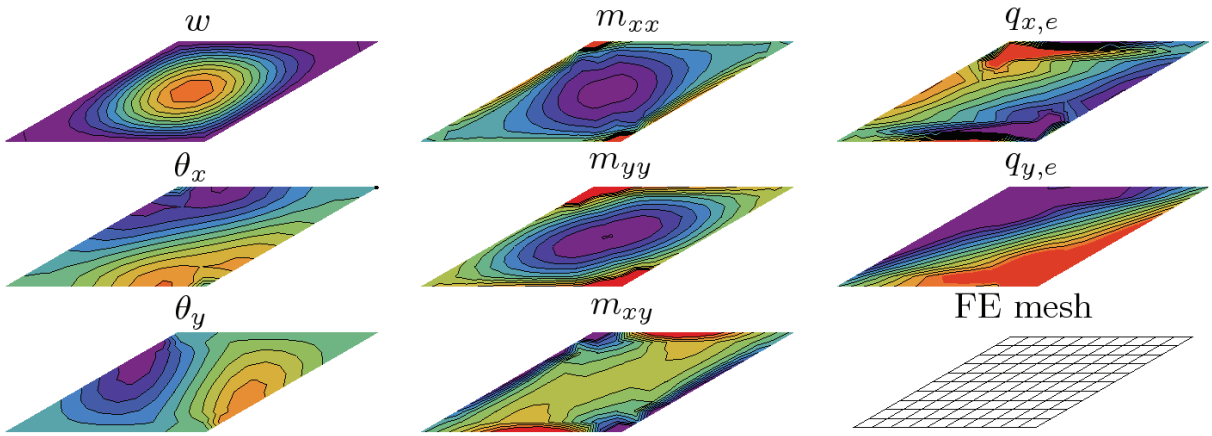

(DKQ element)

Figure 2.4.21: FE solution of the uniformly loaded simply supported skew plate with DK plate elements
Slika 2.4.21: Računska rešitev enakomerno obremenjene prosto podprte romboidne plošče z DK končnimi elementi

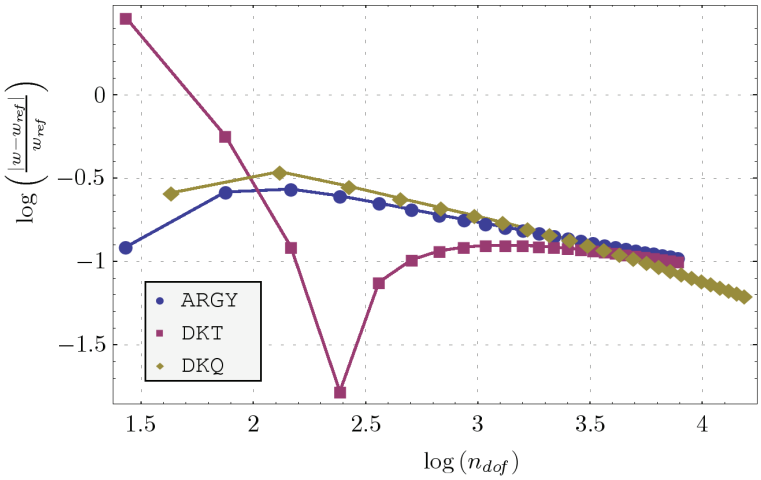

(Displacement w at center)

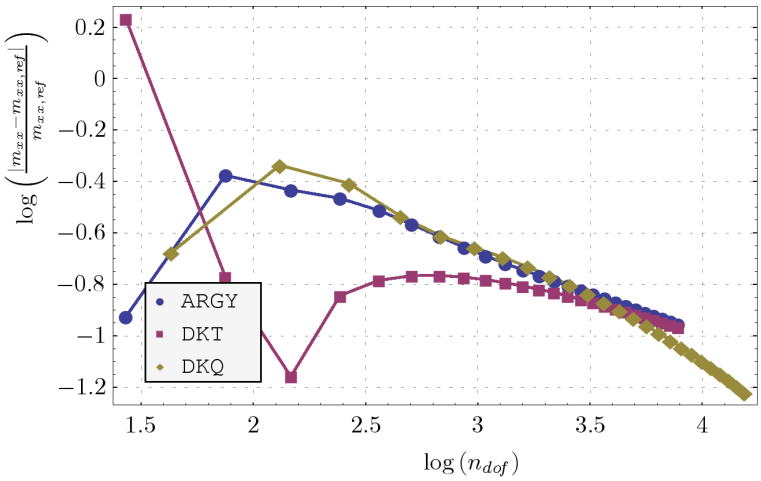

(Moment m_{xx} at center)

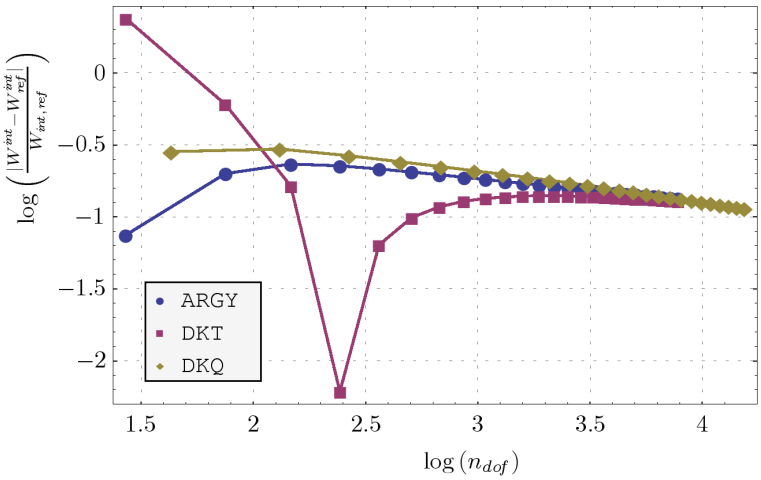

(Energy norm)

Figure 2.4.22: Comparison of the convergence of FE solutions for the uniformly loaded simply supported skew plate

Slika 2.4.22: Primerjava konvergence računske rešitve problema enakomerno obremenjene prosto podprte romboidne plošče

2.5 Chapter summary and conclusions

In this chapter, we studied and revisited the theory of the (thin) Kirchhoff plate model and derived several finite element formulations based on that model. The motivation to dedicate some effort to study in more detail the well known topic - the Kirchhoff plate theory - is strongly connected to the main goals of this thesis. The main goals of the thesis are namely related to the derivation of procedures for discretization error estimation and model error estimation in the process of the finite element computation of plate-like structure.

As it will be explained in the following chapters, both discretization error estimation and model error estimation can be performed by a comparison of numerical results that are obtained by using two different level of complexities in the computations. In the model error estimation, the complexity is associated with the type of the used hierarchical plate model (i.e. thin, moderately thick, thick). Those models are covered in the first three chapters. On the other hand, in the discretization error estimation, the complexity is associated with the type of finite element formulation (less rigorous, more rigorous) within the framework of a single plate model.

Due to the above reasons, the thin plate model (theory) was studied in some detail in the first part of this chapter. The topis, like strong form of the boundary value problem, and singularities of solution, which may not be very familiar to those dealing with finite element computations of plates, were considered in order to prepare ourselves for better understanding of problems that might pop-up when dealing with discretization and model error of plates.

In the second part of this chapter, several finite elements were derived. First, a conforming triangular element with 21 dofs was presented in detail. This element has not been used by the engineers, although, due to its completeness, it is relatively popular by mathematicians dealing with the plate problems (e.g. [Bernadou, 1996]). This element is very rigorous with respect of taking into account assumptions of Kirchhoff plate model. Next, triangular and quadrilateral discrete Kirchhoff plate elements were rederived. Those elements are more relaxed with respect to the Kirchhoff plate theory assumptions than the conforming one. The elements perform very well in general and may be found in many commercial finite element codes (e.g. [Wilson, 1997]).

The chapter concludes with the numerical examples, where the results obtained by the three above mentioned elements are compared by each other and by reference analytical

solutions. As expected, the conforming element shows superiority to the DK elements.

In summary, this chapter deals with the thin plate theory and some corresponding finite element formulations that are of our interest for the later purpose. The main novelty of this chapter can be related to the nonconventional notation in the derivation of the DK elements, which is such, that both triangular and quadrilateral element formulations can be covered by using a single notation.

Chapter 3

Moderately thick plates: theory and finite element formulations

3.1 Introduction

The theory of moderately thick plates, in contrast to the Kirchhoff plate theory, takes into account transverse shear deformations. The Kirchhoff constraint is relaxed. Therefore, an additional freedom exists for the modes of deformation. A relaxation of the assumptions of the Kirchhoff theory was first made by [Reissner, 1945] and later, in a slightly different manner, by [Mindlin, 1951]. Since Reissner and Mindlin theories are not very different, it is common to denote a theory for plates with moderate thickness as a theory of Reissner/Mindlin type. An analogy exists between the Euler-Bernoulli and the Timoshenko beam theories and Kirchhoff and Reissner/Mindlin plate theories, respectively.

In the Kirchhoff theory, the rotation of the plate normal is completely defined by the displacement of the midsurface, whereas in the Reissner/Mindlin plate theory it is independent of displacement. The independence of rotations and transverse displacement has several consequences. The continuity of the rotations is no longer required and Reissner/Mindlin plate loaded with a line load, can have kinks with abrupt change of slope. On the other hand, a point load, which produces in Kirchhoff plate finite displacement exhibits singularity in the Reissner/Mindlin plate. Perhaps the most interesting manifestation of the additional freedom, gained by the relaxation of Kirchhoff constraint, is the existence of a boundary layers - a region of a plate close to the boundary, where quick and significant changes in twisting moment and shear forces occur. The boundary effect, however, is not only a consequence of the assumptions of the Reissner/Mindlin plate theory, but rather a real physical phenomenon.

In Reissner/Mindlin treatment of plate bending the basic assumptions are: (i) the

material normal to the original reference surface remains straight, although no longer normal to the deformed reference surface, (ii) the thickness of the plate does not change during deformation and (iii) transverse normal stresses are negligible. The latter two assumptions are contradictory, which can easily be verified. Reissner and Mindlin plate theories differ from each other in a way how they solve this problem. While Reissner assumed a cubic variation in thickness direction of transverse normal stress, Mindlin manipulated the material law in order to comply with both assumptions [Reissner, 1945], [Mindlin, 1951]. Although conceptionally different, both plate theories deliver practically the same results for transverse displacements, shear forces and bending moments in actual structural problems. The basic consequence of the above assumptions is that the deformation of the moderately thick plate can no longer be defined by the transverse displacement w and its derivatives only. The rotation of material normal $\boldsymbol{\theta}$ is introduced as an independent variable.

3.2 Theory

3.2.1 Governing equations

Kinematics

In the following, the rotation $\boldsymbol{\phi}$ will be employed instead of the conventional rotation $\boldsymbol{\theta}$, see Figure 2.2.1. Recall that the rotations are related as $\boldsymbol{\phi} = [\phi_x, \phi_y]^T = [-\theta_y, \theta_x]^T$. According to (2.2.3) and (2.2.4), the kinematic relations, which relate the displacement w and rotation $\boldsymbol{\phi}$ to the curvatures $\boldsymbol{\kappa} = [\kappa_{xx}, \kappa_{yy}, \kappa_{xy}]^T$ and transverse shear strains $\boldsymbol{\gamma} = [\gamma_x, \gamma_y]^T$, are

$$\boldsymbol{\kappa} = [\frac{\partial \phi_x}{\partial x}, \frac{\partial \phi_y}{\partial y}, (\frac{\partial \phi_y}{\partial x} + \frac{\partial \phi_x}{\partial y})]^T; \quad \boldsymbol{\gamma} = [\frac{\partial w}{\partial x} - \phi_x, \frac{\partial w}{\partial y} - \phi_y]^T \tag{3.2.1}$$

In a compact notation we have

$$\boldsymbol{\gamma} = \nabla w - \boldsymbol{\phi}; \quad \boldsymbol{\kappa} = \mathcal{D}\boldsymbol{\phi} \tag{3.2.2}$$

where the differential operator $\mathcal{D}$ is

$$\mathcal{D} = \begin{bmatrix} \frac{\partial}{\partial x} & 0 \\ 0 & \frac{\partial}{\partial y} \\ \frac{\partial}{\partial y} & \frac{\partial}{\partial x} \end{bmatrix} \tag{3.2.3}$$

Equilibrium equations

The equilibrium equations were derived already in the previous chapter. We recall the main result:

$$\nabla \cdot \boldsymbol{q}_{eq} = -f \tag{3.2.4}$$

where the shear forces obtained from the equilibrium equations are denoted in this chapter as $\boldsymbol{q}_{eq} = [q_{x,eq}, q_{y,eq}]^T$. We also recall from (2.2.18):

$$\nabla \cdot \mathbf{M} = -\boldsymbol{q}_{eq}; \quad \mathbf{M} = \begin{bmatrix} m_{xx} & m_{xy} \\ m_{xy} & m_{yy} \end{bmatrix} \tag{3.2.5}$$

Constitutive relations

To obtain the moment-curvature relationship, we recall from (2.2.12) and (2.2.13): the moments are related to curvatures as

$$\boldsymbol{m} = \mathbf{C}_B \boldsymbol{\kappa} \tag{3.2.6}$$

The kinematic shear strains $\boldsymbol{\gamma}$ computed from the kinematic assumptions (3.2.1) are constant through the thickness, which is approximation to the actual variation, even for a homogeneous cross-section. The equilibrium equations show, that the variation of the shear stresses through the thickness must exist. For the homogeneous cross-sections, the shear strain distribution is commonly accepted to be a parabolic function of z.

Strains following from the kinematic assumptions are in contrast with the equilibrium of differential plate element. To overcome this difficulty, two theories were presented ([Reissner, 1945] and [Mindlin, 1951]), both resulting in the introduction of the *shear correction factor* c which enables the definition of the following simplified constitutive relation, where the *constitutive shear forces* are denoted by $\boldsymbol{q}_c$:

$$\boldsymbol{q}_c = \mathbf{C}_S \boldsymbol{\gamma}; \quad \mathbf{C}_S = cGt\mathbb{1} = \frac{cEt}{2(1+\nu)}\mathbb{1} = \tilde{c}/t^2 D\mathbb{1}; \quad \mathbb{1} = \begin{bmatrix} 1 & 0 \\ 0 & 1 \end{bmatrix} \tag{3.2.7}$$

where $G = E/2(1+\nu)$ is shear modulus and $\tilde{c} = 6c(1-\nu)$. The shear correction factor c is usually set to 5/6, although also different values can be taken.

Boundary conditions

The Reissner/Mindlin plate theory provides a wider range of possibilities for the boundary conditions than the Kirchhoff theory. Some of them are listed in the Table 3.1. Notice

Table 3.1: Boundary conditions for moderately thick plates
Tabela 3.1: Robni pogoji za srednje debele plošče

Clamped - hard:	$w = 0;$	$\theta_s = 0$	$\theta_n = 0$
Clamped - soft:	$w = 0;$	$\theta_s = 0$	$m_n = 0$
Simply supported - hard:	$w = 0;$	$\theta_n = 0$	$\overline{m}_s = 0$
Simply supported - soft:	$w = 0;$	$\overline{m}_s = 0$	$\overline{m}_n = 0$
Free:	$q = 0;$	$\overline{m}_s = 0$	$\overline{m}_n = 0$

the difference between hard and soft simply supported plate. In many cases more realistic is soft simple support with both twisting and normal moments set to zero. In the case of thin plates, however, (Table 2.1) it is possible to model only hard simple support.

Shear correction factor

The shear correction factor approximates, on an average basis, the transverse shear strain energy. The transverse shear strain deformation energy density w_s^0 equals

$$w_s^{(0)} = \gamma_{xz}\sigma_{xz} + \gamma_{yz}\sigma_{yz} = (\sigma_{xz}^2 + \sigma_{yz}^2)/G \tag{3.2.8}$$

where $\gamma_x = \gamma_{xz} = \sigma_{xz}/G$ and $\gamma_y = \gamma_{yz} = \sigma_{yz}/G$, was employed. The superscript (0) denotes that the the stress level constitutive relations were used. Integration of $w_s^{(0)}$ through the thickness gives the transverse shear strain deformation energy per unit area of a plate:

$$\frac{\mathrm{d}W_S^{(0)}}{\mathrm{d}\Omega} = \int_{-t/2}^{t/2} w_s^{(0)}\mathrm{d}z = \int_{-t/2}^{t/2} (\sigma_{xz}^2 + \sigma_{yz}^2)/G\,\mathrm{d}z \tag{3.2.9}$$

The transverse shear deformation energy per unit area can, on the other hand, be computed also with the shear strains $\boldsymbol{\gamma}$ and the constitutive shear forces $\boldsymbol{q}_c = [q_{x,c}, q_{y,c}]^T$ as

$$\frac{\mathrm{d}W_S^{(1)}}{\mathrm{d}\Omega} = \gamma_x q_{x,c} + \gamma_y q_{y,c} = (q_{x,c}^2 + q_{y,c})^2/(cGt) \tag{3.2.10}$$

where the (3.2.7) was employed. The superscript (1) denotes that the stress resultant level of constitutive relations was used. The shear correction factor c can be computed from the requirement that the shear deformation energies (3.2.10) and (3.2.9) are equal.

Let us now write the expression (3.2.9) with equilibrium stress resultants. We start with the two stress equilibrium equations, which are related to the transverse shear

stresses:

$$\frac{\partial \sigma_{xz}}{\partial z} + \frac{\partial \sigma_{xy}}{\partial y} + \frac{\partial \sigma_{xx}}{\partial x} = 0; \quad \frac{\partial \sigma_{yz}}{\partial z} + \frac{\partial \sigma_{yy}}{\partial y} + \frac{\partial \sigma_{xy}}{\partial x} = 0 \tag{3.2.11}$$

The distribution of transverse shear stresses across the thickness at fixed (x, y) can be computed by integration of (3.2.11):

$$\sigma_{xz}(z) = -\int_{-t/2}^{z} (\sigma_{xx,x} + \sigma_{xy,y})\mathrm{d}z; \quad \sigma_{yz}(z) = -\int_{-t/2}^{z} (\sigma_{yy,y} + \sigma_{xy,x})\mathrm{d}z \tag{3.2.12}$$

We know, that the stresses σ_{xx}, σ_{yy} and σ_{xy} share the same (i.e. linear) through the thickness dependence, which we denote by $g(z)$. These stresses can be written as:

$$\sigma_{xx}(x, y, z) = \sigma_{xx0}(x, y)\, g(z); \quad \sigma_{yy}(x, y, z) = \sigma_{yy0}(x, y)\, g(z); \quad \sigma_{xy}(x, y, z) = \sigma_{xy0}(x, y)\, g(z) \tag{3.2.13}$$

After inserting (3.2.13) into (3.2.12) and integrating through the thickness we can write (3.2.9) as

$$\frac{\mathrm{d}W_S^{(0)}}{\mathrm{d}\Omega} = \frac{1}{G}[(\sigma_{xx0,x} + \sigma_{xy0,y})^2 + (\sigma_{yy0,y} + \sigma_{xy0,x})^2] \int_{-t/2}^{+t/2} \left(\int_{-t/2}^{z} g(z)\, \mathrm{d}z \right)^2 \mathrm{d}z \tag{3.2.14}$$

Next, we write the equilibrium shear forces (2.2.14) in terms of:

$$q_{x,eq} = \frac{\partial m_{xx}}{\partial x} + \frac{\partial m_{xy}}{\partial y} = \sigma_{xx0,x} \int_{-t/2}^{t/2} zg(z)\mathrm{d}z + \sigma_{xy0,y} \int_{-t/2}^{t/2} zg(z)\mathrm{d}z \tag{3.2.15}$$

$$q_{x,eq} = (\sigma_{xx0,x} + \sigma_{xy0,y}) \int_{-t/2}^{t/2} zg(z)\mathrm{d}z$$

$$q_{y,eq} = \frac{\partial m_{yy}}{\partial y} + \frac{\partial m_{xy}}{\partial x} = \sigma_{yy0,y} \int_{-t/2}^{t/2} zg(z)\mathrm{d}z + \sigma_{xy0,x} \int_{-t/2}^{t/2} zg(z)\mathrm{d}z$$

$$q_{y,eq} = (\sigma_{yy0,y} + \sigma_{xy0,x}) \int_{-t/2}^{t/2} zg(z)\mathrm{d}z$$

Using (3.2.15) in (3.2.14), we finally have (3.2.9) written in terms of equilibrium stress resultants

$$\frac{\mathrm{d}W_S^{(1)}}{\mathrm{d}\Omega} = (q_{x,eq}^2 + q_{y,eq}^2)/G \left(\int_{-t/2}^{+t/2} P^2(z)\, \mathrm{d}z \right) / R^2 \tag{3.2.16}$$

where the following definition was used:

$$R = \int_{-t/2}^{+t/2} zg(z)\, \mathrm{d}z; \quad P(z) = \int_{-t/2}^{z} g(z)\, \mathrm{d}z \tag{3.2.17}$$

The demand that the transverse shear energies defined in (3.2.16) and (3.2.10) must match, leads to the expression for the shear correction factor:

$$c = \frac{R^2}{t \int_{-t/2}^{t/2} P^2(z)\,\mathrm{d}z} \tag{3.2.18}$$

For the case of homogeneous isotropic plate, where $g(z) = 2z/t$, we have $R = t^2/6$ and $P(z) = (t/4)((2z/t)^2 - 1)$. Since $\int_{-t/2}^{t/2} P^2(z)\,\mathrm{d}z = t^3/30$, we thus obtain $c = 5/6$.

3.2.2 Strong form

From the constitutive relations (3.2.7) and kinematic relations (3.2.2), we have

$$\boldsymbol{\gamma} = \nabla w - \boldsymbol{\phi} = \frac{t^2}{D\tilde{c}}\boldsymbol{q} \tag{3.2.19}$$

Taking a divergence of (3.2.19) and using the definitions (2.2.21) $\nabla\cdot\boldsymbol{\phi} = \underline{m}/D$ and (2.2.16) $\nabla\cdot\boldsymbol{q} = -f$, we arrive at

$$\triangle w = \frac{\underline{m}}{D} - \frac{f}{D}\frac{t^2}{\tilde{c}} \tag{3.2.20}$$

By applying the $\triangle$ operator to both sides and using (2.2.22) $\triangle\underline{m} = f$, the modified biharmonic equation for the displacement of the thick plate is obtained:

$$\triangle\triangle w = +\frac{f}{D}\left(1 - \frac{t^2}{\tilde{c}}\frac{\triangle f}{f}\right) \tag{3.2.21}$$

Notice, that in the limit as $t \to 0$, the standard biharmonic equation (2.2.26) is recovered. This is also the case, when $\triangle f = 0$.

From the definition $\gamma_x = \frac{\partial w}{\partial x} - \phi_x$, $\gamma_y = \frac{\partial w}{\partial y} - \phi_y$ and by noticing that $\frac{\partial}{\partial y}\frac{\partial w}{\partial x} = \frac{\partial}{\partial x}\frac{\partial w}{\partial y}$, we have

$$\frac{\partial\gamma_x}{\partial y} - \frac{\partial\gamma_y}{\partial x} = \frac{\partial\phi_y}{\partial x} - \frac{\partial\phi_x}{\partial y} = -\Omega(\boldsymbol{\phi}), \tag{3.2.22}$$

where we introduced the function

$$\Omega(\boldsymbol{\phi}) = \phi_{x,y} - \phi_{y,x} \tag{3.2.23}$$

which can be interpreted as the local transverse twist. Notice that, in the thin plate limit $\Omega = 0$ or $\phi_{x,y} = \phi_{y,x}$. The vector field $\boldsymbol{\phi}$ is in that case *potential*, which implies, that there exists such a scalar field (displacement w in this case) whose gradient equals the vector field $\boldsymbol{\phi}$ ($\boldsymbol{\phi} = \nabla w$ or $\boldsymbol{\gamma} = \nabla w - \boldsymbol{\phi} = 0$).

A useful relation is obtained if we express transverse shear strain $\boldsymbol{\gamma}$ with the rotations $\boldsymbol{\phi}$. We start with (3.2.7), where we take into account the equilibrium equations (3.2.5). The constitutive relation (3.2.6) relates moments to curvatures which are defined by the rotations through (3.2.2). Finally we have

$$\gamma_x = \frac{t^2}{2\tilde{c}}((-1+\nu)\frac{\partial^2\phi_x}{\partial y^2} - (1+\nu)\frac{\partial^2\phi_y}{\partial x\partial y} - 2\frac{\partial^2\phi_x}{\partial x^2})$$
$$\gamma_y = \frac{t^2}{2\tilde{c}}((-1+\nu)\frac{\partial^2\phi_y}{\partial x^2} - (1+\nu)\frac{\partial^2\phi_x}{\partial x\partial y} - 2\frac{\partial^2\phi_y}{\partial y^2})$$

From the results above, we now compute $\Omega = \frac{\partial\gamma_y}{\partial x} - \frac{\partial\gamma_x}{\partial y}$:

$$\Omega = \frac{t^2}{12c}(\frac{\partial^3\phi_x}{\partial y^3} + \frac{\partial^3\phi_x}{\partial y\partial x^2} - \frac{\partial^3\phi_y}{\partial x\partial y^2} - \frac{\partial^3\phi_y}{\partial x^3}) \tag{3.2.24}$$

By taking $\triangle\Omega = \frac{\partial^2\Omega}{\partial x^2} + \frac{\partial^2\Omega}{\partial y^2}$ and using the definition (3.2.23), we observe that the following relation holds:

$$\Omega = \frac{t^2}{12c}\triangle\Omega \tag{3.2.25}$$

Additional result relates shear forces to the Marcus moment (see (2.2.21) for the definition of $\underline{m}$):

$$q_x = -\underline{m}_{,x} + \frac{1}{2}D(1-\nu)\Omega_{,y} \tag{3.2.26}$$
$$q_y = -\underline{m}_{,y} - \frac{1}{2}D(1-\nu)\Omega_{,x}$$

Note the similarity to (2.2.24), which relates Marcus moment to the equilibrium shear forces for the Kirchhoff theory.

The behavior of the plate according to Reissner/Mindlin theory is governed by the system of differential equations for displacement w and transverse twist Ω:

$$\triangle\triangle w = f/D - \frac{t^2}{D\tilde{c}}\triangle f; \quad \Omega - \frac{t^2}{12c}\triangle\Omega = 0 \tag{3.2.27}$$

with the appropriate boundary conditions specified for the transverse displacement, rotations or stress resultants (expressed in terms of w and Ω). The two equations in (3.2.27) are coupled through the boundary conditions. With the decreasing thickness, the transverse twist plays an increasingly smaller role in the interior part of the plate. In thin plate situations Ω is substantially different from zero only near the boundary. An alternative formulation of the Reissner/Mindlin theory, which uses the displacement w and

rotations $\boldsymbol{\phi}$ is also possible. Differentiating (3.2.25) and again using $\triangle \underline{m} = f$, we obtain the relations

$$\begin{aligned} \triangle\triangle\phi_x - (\triangle\Omega)_{,y} &= f_{,x}/D \\ \triangle\triangle\phi_y + (\triangle\Omega)_{,x} &= f_{,y}/D \end{aligned} \tag{3.2.28}$$

Inserting $\triangle\Omega = \frac{12c}{t^2}\Omega$ into (3.2.28), we obtain together with (3.2.21) the following system of fourth-order differential equations for the displacement w and rotations $\boldsymbol{\phi}$

$$\begin{aligned} \triangle\triangle w &= f/D - \frac{t^2}{D\tilde{c}}\triangle f \\ +\frac{t^2}{12c}\triangle\triangle\phi_x - (\phi_{x,y} - \phi_{y,x})_{,y} &= f_{,x}/D \\ +\frac{t^2}{12c}\triangle\triangle\phi_y + (\phi_{x,y} - \phi_{y,x})_{,x} &= f_{,y}/D \end{aligned} \tag{3.2.29}$$

Strong form of the Reissner/Mindlin problem can now be formulated as: by knowing f, D, t and c, find the solution of (3.2.29) for transverse displacement w and rotations $\boldsymbol{\phi}$ that satisfies the corresponding boundary conditions.

Kirchhoff versus Reissner/Mindlin solutions

The Reissner/Mindlin plate theory is a hierarchic extension of the Kirchhoff theory. It is thus possible to express the solutions $w^M, \boldsymbol{\phi}^M$ (the superscript M refers to the Reissner/Mindlin theory) of the equations (3.2.21) and (3.2.29) as the hierarchic extension of the Kirchhoff solution w^K (the superscript K refers to the Kirchhoff theory) (see [Lee et al., 2002]).

To that end, we introduce the scalar functions Φ and Ψ with the following properties:

$$\begin{aligned} &\triangle\triangle\Phi = 0; \quad \triangle\Psi = 0 \\ &\triangle\underline{m}^K = \triangle\underline{m}^M = f; \quad \underline{m}^M = \underline{m}^K + D\triangle\Phi; \underline{m}^K = D\triangle w^K \end{aligned} \tag{3.2.30}$$

From (3.2.30), (3.2.20) and (3.2.26), the relations between Reissner/Mindlin and Kirchhoff solutions are obtained as

$$\begin{aligned} w^M &= w^K - \frac{t^2}{D\tilde{c}}\underline{m}^K + \Psi + \Phi = w^K - \frac{t^2}{\tilde{c}}\triangle w^K + \Psi + \Phi \\ \phi_x^M &= w_{,x}^K + \frac{\partial}{\partial x}\left(\frac{t^2}{\tilde{c}}\triangle\Phi + \Psi + \Phi\right) + \frac{t^2}{12c}\Omega_{,y} = \phi_{,x}^K + \Lambda_2 \\ \phi_y^M &= w_{,y}^K + \frac{\partial}{\partial y}\left(\frac{t^2}{\tilde{c}}\triangle\Phi + \Psi + \Phi\right) - \frac{t^2}{12c}\Omega_{,x} = \phi_{,y}^K + \Lambda_1 \end{aligned} \tag{3.2.31}$$

To obtain the rotations $\boldsymbol{\phi}^M$, in addition to the Kirchhoff solution the functions Ψ, Ω and Φ have to be computed from the equations

$$\triangle\triangle\Phi = 0; \quad \triangle\Psi = 0; \quad \Omega = \frac{t^2}{12c}\triangle\Omega \tag{3.2.32}$$

The equations above are solved with some given boundary conditions (note, that Φ, Ψ and Ω depend both on displacement/rotation boundary conditions and loading).

All the Mindlin stress resultants can be computed from (3.2.31) and are related to the Kirchhoff stress resultants. The Kirchhoff shear forces are computed from the equilibrium, using (2.2.24). This relations are: (3.2.33):

$$\begin{aligned} m_{xx}^M &= m_{xx}^K + D\triangle\Phi - D(1-\nu)\Lambda_{1,y} \\ m_{yy}^M &= m_{xx}^K + D\triangle\Phi - D(1-\nu)\Lambda_{2,x} \\ m_{xy}^M &= m_{xy}^K + D(1-\nu)/2\,(\Lambda_{1,x} + \Lambda_{2,y}) \\ \\ q_x^M &= q_x^K - D(\triangle\Phi)_{,x} + D(1-\nu)/2\,\Omega_{,y} \\ q_y^M &= q_y^K - D(\triangle\Phi)_{,y} - D(1-\nu)/2\,\Omega_{,x} \end{aligned} \tag{3.2.33}$$

where

$$\begin{aligned} \Lambda_1 &= (\frac{t^2}{\tilde{c}}\triangle\Phi + \Phi + \Psi)_{,y} - \frac{t^2}{12c}\Omega_{,x} \\ \Lambda_2 &= (\frac{t^2}{\tilde{c}}\triangle\Phi + \Phi + \Psi)_{,x} + \frac{t^2}{12c}\Omega_{,y} \\ \Lambda_{1,x} + \Lambda_{2,y} &= 2(\frac{t^2}{\tilde{c}}\triangle\Phi + \Phi + \Psi)_{,xy} + \frac{t^2}{12c}(\Omega_{,yy} - \Omega_{,xx}) \end{aligned} \tag{3.2.34}$$

The equations (3.2.30)-(3.2.34) have not been derived but rather presented in this work. For the derivation details we refer to [Wang et al., 2001] and [Brank et al., 2008].

3.2.3 Weak form

Taking into account that the weak form of the equilibrium equation (2.2.41) is valid for both thick and thin plates, we start from (2.2.41) and rewrite it by using the variational notation $u = \delta w$, $\boldsymbol{\vartheta} = \delta\boldsymbol{\theta}$, $\boldsymbol{\beta} = \delta\boldsymbol{\kappa}$ and $\boldsymbol{\tau} = \delta\boldsymbol{\gamma}$:

$$\int_\Omega \left(\delta\boldsymbol{\kappa}^T\boldsymbol{m} + \delta\boldsymbol{\gamma}^T\boldsymbol{q}\right)\,\mathrm{d}\Omega = \int_\Omega f\,\delta w\,\mathrm{d}\Omega + \int_{\Gamma_q} \overline{q}\,\delta w \mathrm{d}s + \int_{\Gamma_{m_n}} \overline{m}_n\delta\theta_n\,\mathrm{d}s + \int_{\Gamma_{m_s}} \overline{m}_s\delta\theta_s\,\mathrm{d}s \tag{3.2.35}$$

The virtual work of internal forces of the thick plate is

$$\delta\Pi^{int}\left(w, \boldsymbol{\theta}; \delta w, \delta\boldsymbol{\theta}\right) = \int_\Omega \left(\delta\boldsymbol{\kappa}^T\boldsymbol{m} + \delta\boldsymbol{\gamma}^T\boldsymbol{q}\right)\,\mathrm{d}\Omega \tag{3.2.36}$$

and the virtual work of external forces is

$$\delta\Pi^{ext}\left(\delta w, \delta\boldsymbol{\theta}\right) = \int_{\Omega} f\,\delta w\,\mathrm{d}\Omega + \int_{\Gamma_q} \overline{q}\,\delta w \mathrm{d}s + \int_{\Gamma_{mn}} \overline{m}_n \delta\theta_n\,\mathrm{d}s + \int_{\Gamma_{ms}} \overline{m}_s \delta\theta_s\,\mathrm{d}s \tag{3.2.37}$$

The variational formulation (3.2.35) reveals that the highest derivatives of the unknowns are now of first order. The approximations w and $\boldsymbol{\theta}$ need to be therefore no more than $\mathcal{C}^0$ continuous. This is the key simplification compared to the Kirchhoff theory.

3.2.4 Boundary layer and singularities

Rotations and stress resultants in the Reissner/Mindlin model can exhibit sharp changes in the behavior near the plate edge. To understand this phenomena extensive mathematical and numerical studies on boundary effects in plate models have been performed by many researchers ([Babuška Li, 1990], [Selman et al., 1990], [Arnold Falk, 1989] among others). The most important difference between the Kirchhoff and the Reissner/Mindlin plate models is that the solution of the Kirchhoff plate theory is thickness independent (up to the scaling factor), while the solution of the Reissner/Mindlin plate theory depends on thickness in a complicated way (see (3.2.31)). The Reissner/Mindlin solution can be regarded as the perturbed Kirchhoff solution (see Section 3.2.2). From (3.2.31), which relates the Reissner/Mindlin solution to the Kirchhoff solution, we realize, that the source of the sharp changes in the Reissner/Mindlin solution can only be the function Ω. The functions Φ and Ψ respect the biharmonic and Laplace equations, respectively, and are therefore inherently smooth. The function $\Omega = \phi_{x,y} - \phi_{y,x}$ can be interpreted as the local transverse twist. From inspection of $\Omega = \frac{t^2}{12c}\triangle\Omega$, we conclude that the term on the right decreases as $t \to 0$ and in the limit the Kirchhoff assumption is met: $\phi_{x,y} = \phi_{y,x}$. The inspection shows also that for small t the functions Ω exhibits a strong boundary layer within a distance of the order $t/\sqrt{12c}$ from the boundary. According to the relation (3.2.21), the transverse displacement w has no boundary layer. Transverse twist Ω alone governs the edge-zone behavior of rotations and stress resultants.

For that reason [Häggblad Bathe, 1990], see also [Arnold Falk, 1989], assumed that in the neighborhood of the domain boundary it is possible to make an asymptotic expansion of displacement w and rotation $\boldsymbol{\phi}$ in powers of the plate thickness t:

$$w \approx \sum_{i=0}^{\infty} t^i w_i; \quad \boldsymbol{\phi} = \sum_{i=0}^{\infty} t^i \boldsymbol{\phi}_i + \Xi\left(\sum_{i=0}^{\infty} t^i \boldsymbol{\Phi}_i\right) \tag{3.2.38}$$

The terms w_i and $\boldsymbol{\phi}_i$ are smooth functions independent of thickness. The first two terms in (3.2.38) also satisfy $\nabla w_0 = \boldsymbol{\phi}_0$ and $\nabla w_1 = \boldsymbol{\phi}_1$. Function Ξ is a cut-off function, which

equals unity when the point in question is close to boundary and is zero otherwise. The functions $\boldsymbol{\Phi}_i$ are exponential decay functions of the form

$$\boldsymbol{\Phi}_i = e^{-\sqrt{12c}\,\rho/t}\boldsymbol{F}_i(\rho/t, \varphi) \tag{3.2.39}$$

where c is the shear correction factor and $\boldsymbol{F}_i$ are smooth functions independent of t. The boundary fitted coordinate system (ρ, φ) defines the position of the point relative to the boundary: the coordinate φ is the coordinate along the boundary curve and ρ is the distance from the point under consideration to the nearest point on the boundary. Due to the presence of the decay function and the cut-off function Ξ, all the boundary effects die out quickly and are negligibly small outside a layer of width of order t adjacent to the boundary. In [Arnold Falk, 1989] it is shown that depending on type of support condition certain terms in the expansion of w and $\boldsymbol{\phi}$ vanish. Since the boundary effects are determined by the existence of these terms, the boundary layer strength is defined by the power of t corresponding to first non-vanishing term of the boundary layer expansion.

In the finite element analysis of the plates the stress resultants are of primary importance. The boundary effect is more pronounced for the shear forces since they are derived both from rotations $\boldsymbol{\phi}$ and displacement w. The bending moment for instance depends on the first derivatives of $\boldsymbol{\phi}$ and it has a boundary layer one order higher than that of $\boldsymbol{\phi}$. The shear force vector is defined by $\boldsymbol{q} = \lambda D/t^2(\nabla w - \boldsymbol{\phi})$ and can be expanded as

$$\boldsymbol{q} = \lambda D[(\nabla w_2 - \boldsymbol{\phi}_2) + t(\nabla w_3 - \boldsymbol{\phi}_3) + \cdots] - \Xi(t^{-1}\boldsymbol{\Phi}_1 + \boldsymbol{\Phi}_2) \tag{3.2.40}$$

According to Table 3.2 ([Selman et al., 1990]) a strong boundary layer effect is expected in the case of soft simply supported or free boundary. The boundary layer dominates the shear force vector. The strength of the effect is inversely proportional to thickness. Since the boundary layer is limited to distances of order t from the boundary, the shear force as well as the twisting moment have very steep gradients. Notice, however, that despite the steep gradients the shear force and twisting moment will always be bounded for any thickness of the plate. Since all the terms in the expansion (3.2.38) are differentiable with respect to ρ and t, the shear forces and moments are continuous everywhere along the edges. The boundary layer does not introduce any singular point into the problem domain.

The boundary layer effect of order one is expected for the shear force vector in the case of hard simply supported or clamped (fixed) edge. The soft clamped edge experiences the weakest boundary layer. On the other hand, the soft simply supported plate and

Table 3.2: Leading terms of thickness expansion in (3.2.38)
Tabela 3.2: Vodilni členi v izrazu (3.2.38)

	θ_n	θ_s	m_n	m_s	m_{ns}	q_n	q_s
Clamped - soft:	t^4	t^3	t^3	t^3	t^2	t^2	t
Clamped - fixed:	t^3	t^2	t^2	t^2	t	t	1
Simply supported - hard:	t^3	t^2	t^2	t^2	t	t	1
Simply supported - soft:	t^2	t	t	t	1	1	$1/t$
Free:	t^2	t	t	t	1	1	$1/t$

free plate have the strongest boundary layers. It is interesting to notice (see [Arnold Falk, 1989], [Brank Bohinc, 2006], [Brank et al., 2008]) that the boundary layer effect disappears altogether in the case of hard simply supported or soft clamped edge if the boundary is straight.

Singularities

The response of the Reissner/Mindlin plate to the point load is singular - the displacement under load is infinite. Although the finite element approximation predicts finite displacement at point load application, the magnitude of the displacement increases without limit as mesh is refined near the loads.

As already discussed in the case of Kirchhoff plate theory certain configurations of the boundary conditions can cause the singularities in the stress resultants. Such singular effects are most commonly induced at a corner of the plate when the internal angle is greater than the right angle. In the vicinity of the plate corners the stress resultants can be expressed in polar coordinates (r, φ) as (see [Babuška Li, 1992])

$$\begin{aligned} m_{ns} &= C_1\, r^{\lambda_1 - 1} \psi_{ns}(\varphi) + \text{smoother terms} \\ q_s &= C_2\, r^{\lambda_2 - 1} \psi_s(\varphi) + \text{smoother terms} \\ \lambda &= \min(\lambda_1, \lambda_2) \end{aligned} \tag{3.2.41}$$

where the functions ψ_{ns} and ψ_s are analytical functions of φ. The $C_1(z)$, $C_2(z)$ are smooth functions of z . The powers λ_1, λ_2 define the strength of the singularity. If $\lambda < 1$ the moments and shear forces will become unbounded at the corner point. Furthermore, if λ is not an integer and $1 < \lambda < 2$ the moments and the shear forces will be discontinuous at the singular points. The parameter λ depends on the opening angle of the plate α as well

Table 3.3: The coefficients λ_1 and λ_2 for the hard $(\lambda_1^H, \lambda_2^H)$ and soft $(\lambda_1^S, \lambda_2^S)$ simple support
Tabela 3.3: Koeficienta λ_1 in λ_2 za togo $(\lambda_1^H, \lambda_2^H)$ in mehko $(\lambda_1^S, \lambda_2^S)$ prosto podporo

α	λ_1^H	λ_2^H	λ_1^S	λ_2^S
30°	3.4846	6	8.0630+i4.2028	6
45°	2.4129	4	5.3905+i2.7204	4
90°	1.4208	2	2.7396+i1.1190	2
120°	1.2048	3/2	2.0941+i0.6046	3/2
135°	1.1368	4/3	1.8853+i0.3606	4/3
150°	1.0832	6/5	1.5339	6/5
225°	0.7263	4/5	0.6736	4/5
270°	0.5951	2/3	0.5445	2/3
315°	0.5330	4/7	0.5050	4/7
360°	0.500	1/2	1/2	1/2

as on the support conditions in the neighborhood of the corner point but is independent of plate thickness t and Poisson's ratio ν. Moments and shear force will be unbounded or discontinuous only at the singular point. The singular behavior is confined to the immediate neighborhood of the point in question.

The Table (3.3) lists the parameters λ_1, λ_2 for the hard (H) and soft (S) simply supported boundary conditions ([Babuška Li, 1990]) with respect to the opening angle of the corner α. It can be seen, that the strength of singularity for the shear forces is the same for both support condition. This is, however, not the case for the moments. Coefficients λ can also be complex. It such a case, there is always a pair of conjugate coefficients, since the quantities in (3.2.41) have to be real.

3.3 Finite elements

Reissner/Mindlin plate theory allows greater flexibility in the element design than the Kirchhoff theory. The Kirchhoff constraint is no longer required nor is the need to build the $\mathcal{C}^1$ continuous approximation of the displacement. Since in the Reissner/Mindlin model the shear deformation is allowed, the rotation $\boldsymbol{\theta}$ is no longer defined by the displacement w. Independent approximations are built for the displacement w and the rotations $\boldsymbol{\theta} = [\theta_x, \theta_y]^T$.

Principle of virtual work

The displacement based finite element discretization is built upon the weak form of the equilibrium (3.2.4), which has already been presented in (2.2.41) and is repeated here for the convenience in the form of principle of virtual work $\delta\Pi^{int} = \delta\Pi^{ext}$:

$$\delta\Pi^{int}(w, \boldsymbol{\theta}; \delta w, \delta\boldsymbol{\theta}) = \int_\Omega (\boldsymbol{m}(\boldsymbol{\theta}) \cdot \delta\boldsymbol{\kappa}(\delta\boldsymbol{\theta}) + \boldsymbol{q}(w, \boldsymbol{\theta}) \cdot \delta\boldsymbol{\gamma}(\delta w, \delta\boldsymbol{\theta}))\, \mathrm{d}\Omega \tag{3.3.1}$$
$$\delta\Pi^{ext}(\delta w, \delta\boldsymbol{\theta}) = \int_\Omega f\, \delta w\, \mathrm{d}\Omega + \int_{\Gamma_q} \overline{q}_n\, \delta w\, \mathrm{d}s + \int_{\Gamma_m} \delta\boldsymbol{\theta} \cdot \overline{\boldsymbol{m}}\, \mathrm{d}s$$

where f is the surface loading. The boundary is a union of Dirichlet and Neumann boundary. The tractions prescribed at Neumann boundary have three independent components; shear force line load $\overline{q}$ and two components of moment line load $\overline{\boldsymbol{m}} = [\overline{m}_x, \overline{m}_y]^T$.

Interpolation

The displacement w and the rotation $\boldsymbol{\theta}$ are independent and can be interpolated over a single element in a usual fashion as

$$w_h = \mathbf{N}_w \hat{\boldsymbol{u}}; \quad \boldsymbol{\theta}_h = \mathbf{N}_\theta \hat{\boldsymbol{u}} \tag{3.3.2}$$

where the element degrees of freedom are collected in $\hat{\boldsymbol{u}}$ and $\mathbf{N}_w$ and $\mathbf{N}_\theta$ are matrices of interpolation functions. When w_h depends on both $\hat{w}_I$ and $\hat{\boldsymbol{\theta}}_I$, and $\hat{\theta}_h$ depend on both $\hat{w}_I$ and $\hat{\boldsymbol{\theta}}_I$ we talk about linked interpolation. The matrices $\mathbf{N}_w$ and $\mathbf{N}_\theta$ are specified for the considered elements. The discretized curvatures and shear strains are:

$$\boldsymbol{\kappa}_h = \mathbf{B}_\kappa \hat{\boldsymbol{u}}; \quad \boldsymbol{\gamma}_h = \mathbf{B}_\gamma \hat{\boldsymbol{u}} \tag{3.3.3}$$

where $\mathbf{B}_\kappa$, $\mathbf{B}_\gamma$ are matrices of derivatives of interpolation functions.

Stiffness matrix

The stiffness matrix $\mathbf{K}$ of the element is revealed by the discretization of the weak form (3.3.1) $\Omega \approx \bigcup_e \Omega_h^e$ and by using the interpolation (3.3.3):

$$a_e(\boldsymbol{u}_h; \delta\boldsymbol{u}_h) = \delta\Pi_e^{int}(\boldsymbol{u}_h; \delta\boldsymbol{u}_h) = \tag{3.3.4}$$
$$\int_{\Omega^e} \delta\boldsymbol{\kappa}^T(\delta\boldsymbol{\theta}_h)\boldsymbol{m}(\boldsymbol{\theta}_h)\, \mathrm{d}\Omega + \int_{\Omega^e} \delta\boldsymbol{\gamma}^T(\delta w_h, \delta\boldsymbol{\theta}_h)\boldsymbol{q}(w_h; \boldsymbol{\theta}_h)\, \mathrm{d}\Omega = \delta\hat{\boldsymbol{u}}^T \mathbf{K} \hat{\boldsymbol{u}}$$

where $u_h = (w_h; \boldsymbol{\theta}_h$ and $\delta u_h = (\delta w_h, \delta\theta_h)$. The stiffness matrix of the element $\mathbf{K}$ has two parts: bending stiffness and shear stiffness

$$\mathbf{K} = \mathbf{K}^B + \mathbf{K}^S \tag{3.3.5}$$

where

$$\mathbf{K}^B = \int_{\Omega^e} \mathbf{B}_\kappa^T \boldsymbol{C}_B \mathbf{B}_\kappa \mathrm{d}\Omega; \quad \mathbf{K}^S = \int_{\Omega^e} \mathbf{B}_\gamma^T \boldsymbol{C}_S \mathbf{B}_\gamma \mathrm{d}\Omega \tag{3.3.6}$$

The matrices $\mathbf{B}_\kappa$ and $\mathbf{B}_\gamma$ are specified for considered elements, by using $\mathbf{N}_w$ and $\mathbf{N}_\theta$.

Load vector

Following from the discretization of the (3.3.1) we have

$$l_e(\delta \boldsymbol{u}_h) = \delta \Pi_e^{ext}(\delta \boldsymbol{u}_h) = \sum_I \delta \hat{\boldsymbol{u}}_I^T \boldsymbol{f}_I = \tag{3.3.7}$$

$$\int_{\Omega^e} \delta \hat{\boldsymbol{u}}^T f \mathbf{N}_w \, \mathrm{d}\Omega + \int_{\Gamma_{Ne}} \delta \hat{\boldsymbol{u}}^T \left(\bar{q} \mathbf{N}_w + \overline{\boldsymbol{m}}^T \mathbf{N}_\theta \right) \mathrm{d}s = \delta \hat{\boldsymbol{u}}^T \boldsymbol{f}$$

where the consistent nodal load vector is $\boldsymbol{f} = \boldsymbol{f}_f + \boldsymbol{f}_{\bar{t}}$

$$\boldsymbol{f}_f = \int_{\Omega^e} f \, \mathbf{N}_w \mathrm{d}\Omega; \quad \boldsymbol{f}_{\bar{t}} = \int_{\Gamma_{Ne}} (\bar{q} \mathbf{N}_w + \overline{\boldsymbol{m}}^T \mathbf{N}_\theta) \, \mathrm{d}s$$

Shear locking

The leading term of the bending stiffness is t^3 while the leading term of the shear stiffness is t. In the limit as $t \to 0$, the shear strain, due to the high shear stiffness, vanishes and the bending prevails. Bending is most favorable deformation mode in the thin plate limit. The problem occurs if the discretization is unable to describe accurately pure bending of thin plates. To do so, the discretization must be able to satisfy the Kirchhoff constraint $\nabla w_h = \boldsymbol{\phi}_h$, where $\boldsymbol{\phi}_h = [-\theta_{y,h}, \theta_{x,h}]^T$. If the discretization fails to eliminate shear strains in the thin plate limit, the total deformation energy is dominated by the shear and the minimization of total potential energy de facto equals the minimization of the shear deformation energy. In the thin plate limit, the shear stiffness becomes very large relative to bending stiffness. Unless the finite element is able to describe pure bending, and thus completely avoid the shear deformation, the displacements of the plate vanish. The finite element solution "locks". The phenomena is known by the name *shear locking*. In order to build a successful Reissner/Mindlin element which avoids shear locking the discretization of displacement w_h and rotation $\boldsymbol{\theta}_h$ must be carefully balanced.

3.3.1 Elements with cubic interpolation of displacement

In the following, a family of Reissner/Mindlin plate elements will be presented. The derived elements follow the work of [Ibrahimbegović, 1992] and [Ibrahimbegović, 1993]. They are extensions of DK elements presented in previous chapter, therefore linked interpolation is used.

Edge interpolation equals Timoshenko beam interpolation

Again, the basis of the element construction is an analogy with beams. Recall that in the development of DK elements the shear free interpolation of the Euler Bernoulli beam, (2.3.53)-(2.3.56) and Figure 2.3.9, was employed. We modify that interpolation so that the constraint of zero shear $\gamma_h = \frac{\partial w_h}{\partial x} - \theta_h = 0$ is replaced by the constraint of constant shear $\gamma_h = \frac{\partial w_h}{\partial x} - \theta_h = \hat{\gamma}_0 = const$. In that case the Euler-Bernoulli parameters (2.3.56) transform into the Timoshenko beam parameters

$$\hat{w}_3 = +\frac{L}{8}(\hat{\theta}_1 - \hat{\theta}_2); \quad \hat{w}_4 = \frac{L}{4}(\frac{\hat{w}_2 - \hat{w}_1}{L} - \frac{1}{2}(\hat{\theta}_1 + \hat{\theta}_2)) - \frac{L}{4}\hat{\gamma}_0; \quad \hat{\theta}_3 = \frac{6}{L}\hat{w}_4 \tag{3.3.8}$$

The Timoshenko (TM) beam interpolation can be presented as the hierarchical extension of the Euler Bernoulli (EB) interpolation

$$w_h^{TM} = w_h^{EB} - \frac{L}{4}\hat{\gamma}_0 N_4; \qquad \theta_h^{TM} = \theta_h^{EB} + \frac{3}{2}\hat{\gamma}_0 N_3 \tag{3.3.9}$$

where EB interpolation is given in (2.3.57)-(2.3.58).

P3T and P3Q elements

Let us express the interpolation of considered plate elements as a hierarchic extension of the DK interpolation (2.3.63):

$$\begin{aligned} w_h &= w_h^{DK} - \sum_{IJ} \frac{1}{4} L_{IJ}\hat{\gamma}_{IJ} M_{IJ}; \\ \boldsymbol{\theta}_h &= \boldsymbol{\theta}_h^{DK} + \sum_{IJ} \frac{3}{2} \boldsymbol{n}_{IJ}\hat{\gamma}_{IJ} N_{IJ} \end{aligned} \tag{3.3.10}$$

The shear along the side IJ is denoted by $\hat{\gamma}_{IJ}$, L_{IJ} is length of the side IJ, and $\boldsymbol{n}_{IJ}$ is normal to the side IJ, see Figure 2.3.11. Note the similarities between (3.3.9) and (3.3.10).

The P3Q/P3T elements have the same vertex degrees of freedoms $\hat{\boldsymbol{u}}_I = [\hat{w}_I, \hat{\theta}_{x,I}, \hat{\theta}_{y,I}]^T$ as DK elements. However, they have additional midside degrees of freedom $\hat{\boldsymbol{u}}_{IJ} = [\hat{\gamma}_{IJ}]$.

The displacement and rotation of an element point is designated by $\boldsymbol{u}_h = [w_h, \theta_{x,h}, \theta_{y,h}]^T$. The elements have nen vertex nodes and nen midside nodes (nen=4 for the quadrilateral, and $nen = 3$ for triangular elements). The vertex nodes are numbered as $I = 1, \ldots, nen$, the midside nodes as $IJ = (nen+1), \ldots, 2\,nen$. Element degrees of freedom are arranged into $\hat{\boldsymbol{u}} = [\hat{\boldsymbol{u}}_1^T, \cdots, \hat{\boldsymbol{u}}_{nen}^T, \hat{\boldsymbol{u}}_{nen+1}^T, \cdots, \hat{\boldsymbol{u}}_{2\,nen}]^T$.

In the matrix notation, the interpolations can be written as

$$w_h = \mathbf{N}_w \hat{\boldsymbol{u}} = \sum_I \mathbf{N}_{w,I} \hat{\boldsymbol{u}}_I + \sum_{IJ} \mathbf{N}_{w,IJ} \hat{\boldsymbol{u}}_{IJ}; \qquad \mathbf{N}_{w,IJ} = -\frac{L_{IJ}}{4} M_{IJ} \tag{3.3.11}$$

$$\boldsymbol{\theta}_h = \mathbf{N}_\theta \hat{\boldsymbol{u}} = \sum_I \mathbf{N}_{\theta,I} \hat{\boldsymbol{u}}_I + \sum_{IJ} \mathbf{N}_{\theta,IJ} \hat{\boldsymbol{u}}_{IJ}; \qquad \mathbf{N}_{\theta,IJ} = +\frac{3}{2} \boldsymbol{n}_{IJ} N_{IJ}$$

where the $\mathbf{N}_{w,I} = \mathbf{N}_{w,I}^{DK}$, $\mathbf{N}_{\theta,I} = \mathbf{N}_{\theta,I}^{DK}$ are the matrices introduced in DK elements, see (2.3.63)-(2.3.66). Notice, that the additional terms in the interpolations (3.3.11) and (3.3.12) depend only on midside degrees of freedom collected in $\hat{\boldsymbol{u}}_{IJ}$. The curvature $\boldsymbol{\kappa}_h$ is computed directly from the rotations $\boldsymbol{\theta}_h$ and is expressed as

$$\boldsymbol{\kappa}_h = \mathbf{B}_\kappa \hat{\boldsymbol{u}} = \sum_I \mathbf{B}_{\kappa,I} \hat{\boldsymbol{u}}_I + \sum_{IJ} \mathbf{B}_{\kappa,IJ} \hat{\boldsymbol{u}}_{IJ} \tag{3.3.12}$$

The matrix $\mathbf{B}_{\kappa,I}$ equals to the matrix of the DK element defined in (2.3.68): $\mathbf{B}_{\kappa,I} = \mathbf{B}_{\kappa,I}^{DK}$. The curvature interpolation can therefore be written as: $\boldsymbol{\kappa}_h = \boldsymbol{\kappa}_h^{DK} + \tilde{\boldsymbol{\kappa}}_h$, where $\tilde{\boldsymbol{\kappa}}_h$ is the part of the curvature, depending entirely on $\hat{\boldsymbol{u}}_{IJ}$:

$$\tilde{\boldsymbol{\kappa}}_h = \sum_{IJ} \mathbf{B}_{\kappa,IJ} \hat{\boldsymbol{u}}_{IJ}; \tag{3.3.13}$$

$$\mathbf{B}_{\kappa,IJ} = \frac{3}{2} \left[-n_{IJ,y} N_{IJ,x}, +n_{IJ,x} N_{IJ,y}, n_{IJ,x} N_{IJ,x} - n_{IJ,y} N_{IJ,y} \right]^T \tag{3.3.14}$$

The P3T/P3Q element stiffness matrix is a sum of bending stiffness matrix $\mathbf{K}^B$ and shear stiffness matrix $\mathbf{K}^S$. The stiffness matrix is expressed as a block matrix $\mathbf{K} = [\mathbf{K}_{ij}]$, where blocks $\mathbf{K}_{ij}$ correspond to the interaction of degrees of freedom of nodes i and j. The indexes referring to the vertex node are denoted by I and J. The indexes IJ and KL are used to denote the midside nodes. The stiffness matrix is then organized as:

$$\mathbf{K} = \begin{bmatrix} [\mathbf{K}_{I,J}] & [\mathbf{K}_{I,KL}] \\ [\mathbf{K}_{IJ,J}] & [\mathbf{K}_{IJ,KL}] \end{bmatrix} \tag{3.3.15}$$

Bending stiffness

The bending stiffness matrix is obtained as

$$\mathbf{K}^B = [\mathbf{K}_{ij}^B] = \int_{\Omega^e} \mathbf{B}_\kappa^T \mathbf{C}_B \mathbf{B}_\kappa \mathrm{d}\Omega; \quad \mathbf{K}_{ij}^B = \int_{\Omega^e} \mathbf{B}_{\kappa,i}^T \mathbf{C}_B \mathbf{B}_{\kappa,j} \mathrm{d}\Omega \tag{3.3.16}$$

where $\mathbf{B}_\kappa = [\mathbf{B}_{\kappa,1}, \cdots, \mathbf{B}_{\kappa,nen}, \mathbf{B}_{\kappa,nen+1}, \cdots, \mathbf{B}_{\kappa,2nen}]^T$ with $\mathbf{B}_{\kappa,I}$ defined in (2.3.68) and $\mathbf{B}_{\kappa,IJ}$ defined in (3.3.14) and $\mathbf{C}_B$ defined in (2.2.12). Notice, that the block matrix $\left[\mathbf{K}^B_{I,J}\right]$ equals the stiffness matrix of the corresponding DK element $\mathbf{K}^{B,DK}$, defined in (2.3.69).

Shear stiffness

Although the interpolations w_h and $\boldsymbol{\theta}_h$ were constructed such that the shear strain is constant along the sides of the element, i.e. equals $\hat{\gamma}_{IJ}$ along side IJ, these interpolations still fail to describe the pure bending deformation without the spurious shear strains. Therefore, the shear locking is still present. A robust and efficient remedy for the shear locking is the use of the assumed shear strain approach. The shear strains may be interpolated in the form of bilinear distribution

$$\boldsymbol{\gamma}_h = \sum_I N_I \hat{\boldsymbol{\gamma}}_{h,I} = \sum_{IJ} \mathbf{B}_{\gamma,IJ} \hat{\boldsymbol{u}}_{IJ} = \mathbf{B}_\gamma \hat{\boldsymbol{u}} \tag{3.3.17}$$

where $\hat{\boldsymbol{\gamma}}_{h,I}$ are transverse shear nodal parameters at vertex nodes and N_I are standard Lagrangian function. The $\hat{\boldsymbol{\gamma}}_{h,I}$ are chosen to be consistent with the values of $\hat{\gamma}_{IJ}$, which define the constant shear along the side IJ. For the node I, where the sides IJ and IK meet, the nodal parameters $\hat{\boldsymbol{\gamma}}_{h,I}$ are chosen so, that the projections of $\hat{\boldsymbol{\gamma}}_{h,I}$ to the sides IJ and IK match the values $\hat{\gamma}_{IJ}$ and $\hat{\gamma}_{IK}$ respectively (see Figure 3.3.1):

$$\hat{\boldsymbol{\gamma}}_{h,I} \cdot \boldsymbol{s}_{IJ} = \hat{\gamma}_{IJ}; \quad \hat{\boldsymbol{\gamma}}_{h,I} \cdot \boldsymbol{s}_{IK} = \hat{\gamma}_{IK} \tag{3.3.18}$$

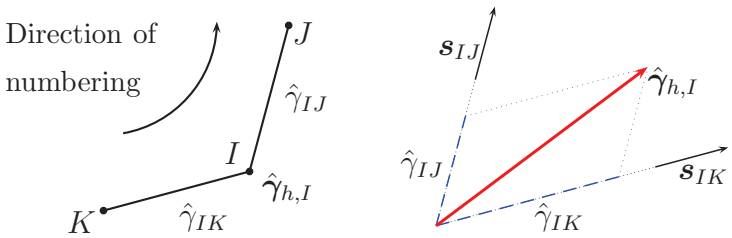

Figure 3.3.1: To the computation of the nodal shear $\hat{\boldsymbol{\gamma}}_{h,I}$ from (3.3.18)
Slika 3.3.1: K izračunu vozliščnega vektorja strižne sile $\hat{\boldsymbol{\gamma}}_{h,I}$ iz izraza (3.3.18)

The solution of the linear system is:

$$\hat{\boldsymbol{\gamma}}_{h,I} = \frac{\hat{\gamma}_{IK}\boldsymbol{n}_{IJ} - \hat{\gamma}_{IJ}\boldsymbol{n}_{IK}}{\boldsymbol{n}_{IJ} \cdot \boldsymbol{s}_{IK}} \tag{3.3.19}$$

Notice, that the nodal shear strains $\hat{\boldsymbol{\gamma}}_{h,I}$ depend only on the parameters $\hat{\gamma}_{IJ}$. Consequently the discretization $\boldsymbol{\gamma}_h$ depends only on $\hat{\boldsymbol{u}}_{IJ}$:

$$\boldsymbol{\gamma}_h = \sum_{IJ} \mathbf{B}_{\gamma,IJ} \hat{\boldsymbol{u}}_{IJ} \tag{3.3.20}$$

The element shear stiffness matrix $\mathbf{K}^S$ is

$$\mathbf{K}^S = \begin{bmatrix} \left[\mathbf{K}^S_{I,J}\right] & \left[\mathbf{K}^S_{I,KL}\right] \\ \left[\mathbf{K}^S_{IJ,J}\right] & \left[\mathbf{K}^S_{IJ,KL}\right] \end{bmatrix} \tag{3.3.21}$$

where

$$\mathbf{K}^S_{I,J} = \mathbf{0}_{3\times3}; \quad \mathbf{K}^S_{I,KL} = \mathbf{0}_{3\times1}; \quad \mathbf{K}^S_{IJ,J} = \mathbf{0}_{1\times3} \tag{3.3.22}$$

and

$$\mathbf{K}^S_{IJ,KL} = \int_{\Omega^e} \mathbf{B}^T_{\gamma,IJ} \mathbf{C}_S \mathbf{B}_{\gamma,KL} \mathrm{d}\Omega \tag{3.3.23}$$

The explicit form of matrix $\mathbf{B}_{\gamma,IJ}$, related to the side IJ, is:

$$\mathbf{B}_{\gamma,IJ} = \left(N_J \frac{\boldsymbol{n}_{JK}}{\boldsymbol{n}_{JK} \cdot \boldsymbol{s}_{IJ}} - N_I \frac{\boldsymbol{n}_{HI}}{\boldsymbol{n}_{IJ} \cdot \boldsymbol{s}_{HI}} \right) \tag{3.3.24}$$

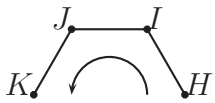

The above developments apply for both quadrilateral and triangular elements. We named such elements as P3Q and P3T, respectively. Since the P3Q/P3T elements are hierarchical extensions of DKQ/DKT elements, they share the same shape functions, given in (2.3.71) and (2.3.74).

3.3.2 Elements with incompatible modes

The midside parameters $\hat{\gamma}_{IJ}$ complicate the practical usage of the P3Q/P3T element. It is possible to reduce that midside degrees of freedom collected $\hat{\boldsymbol{u}}_{IJ}$ by elimination made by means of static condensation. To do that we follow the steps of method of incompatible modes presented in [Ibrahimbegović, 1992]. Not only that the parameters $\hat{\gamma}_{IJ}$ define the $\boldsymbol{\gamma}_h$ but they also affect $\boldsymbol{\kappa}_h$, since

$$\boldsymbol{\kappa}_h = \mathbf{B}_\kappa \hat{\boldsymbol{u}} = \sum_I \mathbf{B}_{\kappa,I} \hat{\boldsymbol{u}}_I + \sum_{IJ} \mathbf{B}_{\kappa,IJ} \boldsymbol{n}_{IJ} \hat{\boldsymbol{\gamma}}_{IJ}; \tag{3.3.25}$$

The $\mathbf{B}_{\kappa,IJ}\boldsymbol{n}_{IJ}$ can be seen as additional deformation modes. The parameters $\hat{\boldsymbol{\gamma}}_{IJ}$ can thus be interpreted as the amplitudes of the additional deformation modes. These modes are

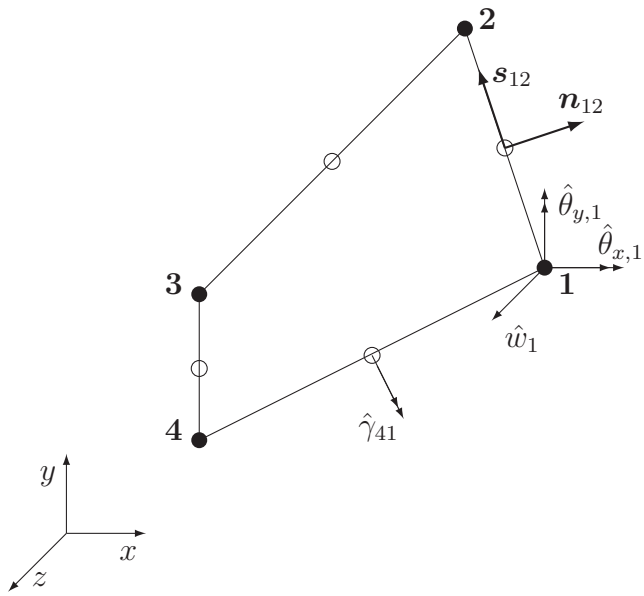

Figure 3.3.2: Quadrilateral plate element P3Q with cubic displacement interpolation
Slika 3.3.2: Štirikotni končni element za plošče P3Q s kubično interpolacijo pomika

treated as incompatible modes and are subject to static condensation. To ensure that the element passes the patch test (see [Ibrahimbegović, 1992]), the matrix $\mathbf{B}_{\kappa,IJ}$ must be modified in the following way

$$\mathbf{B}_{\kappa,IJ} \mapsto \mathbf{B}_{\kappa,IJ} - \frac{1}{\Omega^e} \int_{\Omega^e} \mathbf{B}_{\kappa,IJ} \mathrm{d}\Omega \tag{3.3.26}$$

The stiffness matrix of the element is reduced by standard static condensation procedure ([Zienkiewicz Taylor, 2000]). The resulting elements will be denoted as PIT and PIQ.

3.4 Examples

3.4.1 Uniformly loaded simply supported square plate

The square plate of side length $a = 10$ and thickness $t = 1$ under uniform loading $f = 1$ is analyzed. The sides of the plate at $x = 0, a$ are hard simply supported, while the sides at $y = 0, a$ are soft simply supported. The difference between soft and hard simply supported boundary condition is defined in Table 3.1. The material is linear elastic and isotropic, with Young's modulus $E = 10.92 \times 10^4$ and Poisson's ratio $\nu = 0.3$.

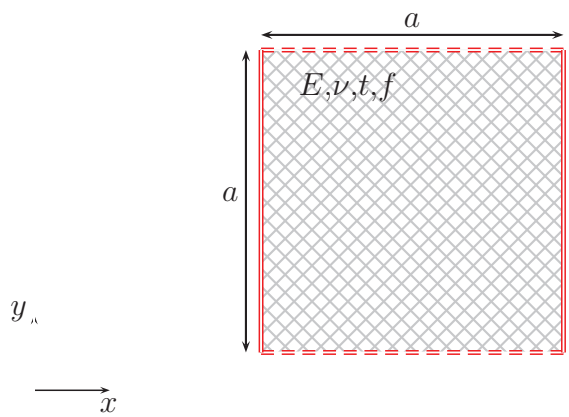

Figure 3.4.1: Problem definition and geometry for the uniformly loaded hard-soft simply supported square plate (t/a=1/10)
Slika 3.4.1: Definicija in geometrija problema enakomerno obremenjene togo-mehko podprte kvadratne plošče (t/a=1/10)

Reference solution

The reference solution is an analytical solution in the form of series expansion (see Section 3.2.2). Using the approach suggested in [Lee et al., 2002], it is possible to express the solution of the Reissner/Mindlin model as a hierarchic extension of the Kirchhoff solution (see [Brank, 2008]). While the differences between the solutions are small in the interior of the plate, they are significant along the boundary. The characteristic width of the boundary layer is proportional to the plate thickness. The local transverse twist $\Omega = \phi_{x,y} - \phi_{y,x} = -(\theta_{y,y} + \theta_{x,x})$ is directly related to the boundary layer (see (3.2.25)). Its inspection can provide a valuable insight into the mechanism of the boundary layer phenomena. The Figure 3.4.2 shows the contour plots of reference solution. Comparison with Figure 2.4.3 reveals, that the boundary layer develops at the soft simply supported sides. The contour plots confirm that the thickness of boundary layer is proportional and

approximately equal to the plate thickness. The boundary layer is much stronger at soft simply supported sides as predicted by Table 3.2. The manifestation of boundary layer is stronger for the stress resultants components m_{xy}, q_x and q_y. At the soft simply supported side the twisting moment vanishes. Reference equilibrium transverse shear forces are equal to the reference constitutive transverse shear forces.

Finite element solutions

The problem is solved with plate elements with cubic interpolation of displacement (P3) and its version with the incompatible modes (PI). The P3 elements have an additional degree of freedom at the midsides, which is directly related to the shear deformation. The vertex DOFs are: displacement $\hat{w}_I$ and the two rotations $\hat{\theta}_{x,I}$ and $\hat{\theta}_{y,I}$. The PI elements are derived from the P3 formulation, where the shear deformation is treated as the incompatible deformation mode. The boundary conditions for the P3 and PI elements are: $\hat{w}_I = 0$ at soft simply supported sides at $y = 0, a$ and $\hat{w}_I = 0, \hat{\theta}_y = 0$ at hard simply supported sides at $x = 0, a$. All other degrees of freedom are unconstrained.

The FE solution on a regular mesh is shown in Figure 3.4.3 and Figure 3.4.4. One immediately notices that the PI elements completely fail to capture the boundary layer. In the interior of the domain the PI solution is close to the reference solution. The P3 elements on the other hand successfully capture the boundary layer effect and show otherwise satisfactory performance. The performance of the elements is further studied in the convergence plots, see Figure 3.4.5. The PI solutions apparently do not converge to the reference solution. Additionally one notices the differences in the performance of the triangular and quadrilateral P3/PI elements. Slower convergence of triangular elements compared to the convergence of quadrilateral elements is partly due to the fact that the quadrilateral elements are not distorted in the regular mesh.

3.4.2 Uniformly loaded simply supported free square plate

The problem of uniformly loaded ($f = 1$) square plate of side length $a = 10$ and thickness $t = 1$ is considered. The sides of the plate at $x = 0, a$ are hard simply supported, while the sides at $y = 0, a$ are free. The material is linear elastic and isotropic, with Young's modulus $E = 10.92 \times 10^4$ and Poisson's ratio $\nu = 0.3$.

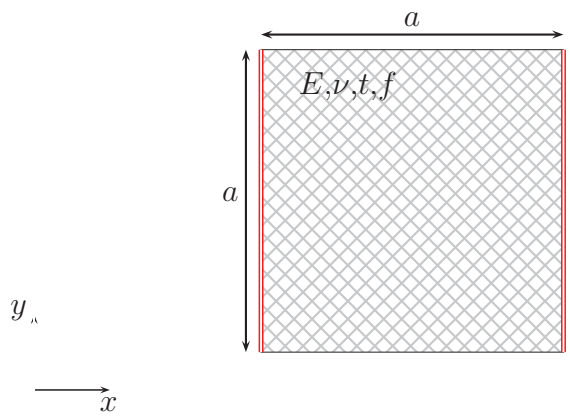

Figure 3.4.6: Problem definition and geometry for the uniformly loaded hard simply supported-free square plate (t/a=10)
Slika 3.4.6: Definicija in geometrija problema enakomerno togo prosto podprte - proste kvadratne plošče (t/a=1/10)

Reference solution

The reference solution is the analytical Mindlin model solution in the form of series expansion, expressed as the hierarchic expansion of Kirchhoff model according to [Lee et al., 2002]. The problem is solved with 40 terms as shown in [Brank, 2008]. The solution, contrary to intuition, but according to Table 3.2, exhibits a strong boundary layer along the free sides. The boundary layer is again most pronounced for the stress components m_{xy} and q_x, q_y. The local transverse twist shows strong resemblance with that in Figure 3.4.2. Reference equilibrium transverse shear forces are equal to the reference constitutive transverse shear forces.

Finite element solutions

The comparison of the P3 and PI finite element solutions shows that the PI elements are incapable of detecting the boundary layers. Qualitative comparison of P3 solution with reference solution does not reveal any significant discrepancies. The convergence plots shown in Figure 3.4.10 confirm that the PI elements do not converge to the reference solution. The P3 finite element solution converges to the reference solution. The relative error (in total deformation energy, center displacement and center moment resultant m_{xx}) is inversely proportional to the number of global degrees of freedom (convergence rate is 1).

3.4.3 Uniformly loaded simply supported skew plate

Uniformly loaded ($f = 1$) skew plate ($\alpha = 30°$) with side length $a = 10$ and thickness $t = 1$ is analyzed. The sides of the plate are soft simply supported. The material is linear elastic and isotropic, with Young's modulus $E = 10.92 \times 10^4$ and Poisson's ratio $\nu = 0.3$.

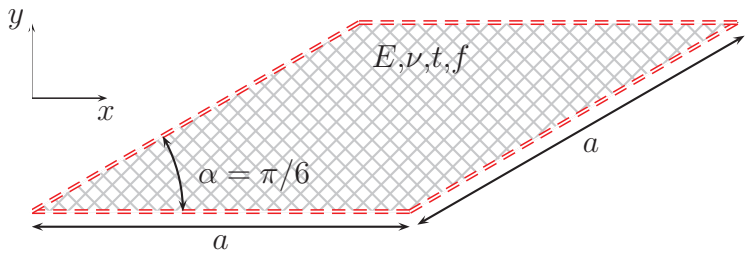

Figure 3.4.11: Problem definition and geometry for the uniformly loaded soft simply supported skew plate (t/a=10)
Slika 3.4.11: Definicija in geometrija enakomerno obremenjene mehko podprte romboidne plošče (t/a=10)

Reference solution

As the analytical solution of the problem is unavailable, a finite element computation with P3T elements on a dense mesh (the elements with side $h = 0.1$) is taken as the reference solution. The Figure 3.4.12 shows that a boundary layer develops at the sides of the plate. The width of the boundary layer is of the order of plate thickness. Notice, that, compared to the Kirchhoff solution of the hard simply supported skew plate (see Figure 2.4.19), the singularity vanishes at the obtuse corners (see Table 3.3).

Finite element solutions

At the soft simply supported sides of the plate only displacement is constrained $\hat{w}_I = 0$. The boundary condition is the same for both P3 and PI elements. The additional degree of freedom $\hat{\gamma}_{IJ}$ is unconstrained at the supports. Since the reference solution is dominated by the boundary layer effect, the performance of P3 elements is clearly superior to that of PI elements. The comparison of the convergence rates in Figure 3.4.15 confirms that the PI elements do not converge to the reference solution. From Figure 3.4.13 it is also clear, that the PI elements are not able to distinguish between soft simple and hard simple support.

3.4.4 Uniformly loaded soft simply supported L-shaped plate

Uniformly loaded soft simply supported L-shaped plate with the geometry shown in Figure 3.4.16 is analyzed. The side length is $a = 10$ and thickness of the plate is $t = 1$. The material is linear elastic and isotropic, with Young's modulus $E = 10.92 \times 10^4$ and Poisson's ratio $\nu = 0.3$.

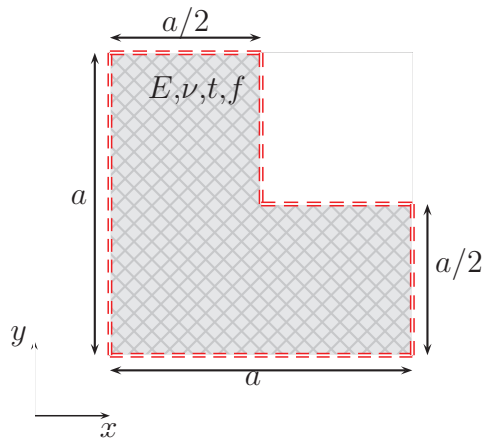

Figure 3.4.16: Problem definition and geometry for the uniformly loaded soft simply supported L-shaped plate (t/a=10)
Slika 3.4.16: Definicija in geometrija problema enakomerno obremenjene mehko podprte L plošče (t/a=1/10)

Reference solution

The reference solution is taken to be the finite element solution with the P3Q elements on a dense mesh (the elements with side $h = 0.1$). The solution shown in Figure 3.4.17 exhibits a singularity at the reentrant corner as well as the boundary layers along all the sides of the problem domain. According to the Table 3.3, the strength of the singularity is $\lambda_1 = 0.5445$ for the moment resultants m_{xx}, m_{yy} and $\lambda_2 = 2/3$ for the moment resultant m_{xy} and shear forces q_x, q_y.

Finite element solutions

At the soft simply supported sides of the plate only displacement is constrained $\hat{w}_I = 0$. The comparison of finite element solutions (see Figures 3.4.19 and 3.4.18) shows that both P3 and PI elements qualitatively capture the reference solution. The boundary layer is, however, captured only by the P3 elements. The finite element solution with PI elements does not converge to the reference solution. Additionally, the Figure 3.4.20 shows that

due to the boundary layers, the convergence rate of P3 elements is deteriorated. The singularity at the re-entrant corner exists for the moments m_{xx}, m_{yy}, m_{xy} and shear forces q_x, q_y.

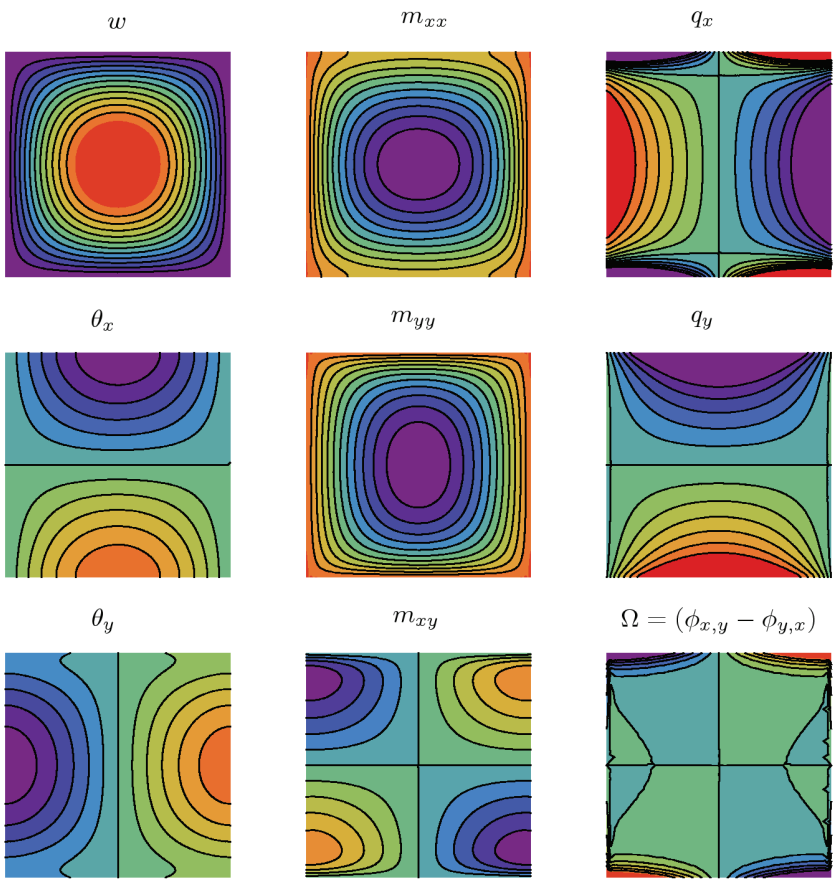

	w	θ_x	θ_y	m_{xx}	m_{yy}	m_{xy}	q_x	q_y	Ω
	0. $\sim$ 0.000338	−0.0015 $\sim$ −0.00125	−0.0015 $\sim$ −0.00125	−5. $\sim$ −4.58	−5. $\sim$ −4.58	−3.5 $\sim$ −2.92	−3.5 $\sim$ −2.92	−3.5 $\sim$ −2.92	−0.0006 $\sim$ −0.0005
	0.000338 $\sim$ 0.000677	−0.00125 $\sim$ −0.001	−0.00125 $\sim$ −0.001	−4.58 $\sim$ −4.17	−4.58 $\sim$ −4.17	−2.92 $\sim$ −2.33	−2.92 $\sim$ −2.33	−2.92 $\sim$ −2.33	−0.0005 $\sim$ −0.0004
	0.000677 $\sim$ 0.00102	−0.001 $\sim$ −0.00075	−0.001 $\sim$ −0.00075	−4.17 $\sim$ −3.75	−4.17 $\sim$ −3.75	−2.33 $\sim$ −1.75	−2.33 $\sim$ −1.75	−2.33 $\sim$ −1.75	−0.0004 $\sim$ −0.0003
	0.00102 $\sim$ 0.00135	−0.00075 $\sim$ −0.0005	−0.00075 $\sim$ −0.0005	−3.75 $\sim$ −3.33	−3.75 $\sim$ −3.33	−1.75 $\sim$ −1.17	−1.75 $\sim$ −1.17	−1.75 $\sim$ −1.17	−0.0003 $\sim$ −0.0002
	0.00135 $\sim$ 0.00169	−0.0005 $\sim$ −0.00025	−0.0005 $\sim$ −0.00025	−3.33 $\sim$ −2.92	−3.33 $\sim$ −2.92	−1.17 $\sim$ −0.583	−1.17 $\sim$ −0.583	−1.17 $\sim$ −0.583	−0.0002 $\sim$ −0.0001
	0.00169 $\sim$ 0.00203	−0.00025 $\sim$ 0.	−0.00025 $\sim$ 0.	−2.92 $\sim$ −2.5	−2.92 $\sim$ −2.5	−0.583 $\sim$ 0.	−0.583 $\sim$ 0.	−0.583 $\sim$ 0.	−0.0001 $\sim$ 0.
	0.00203 $\sim$ 0.00237	0. $\sim$ 0.00025	0. $\sim$ 0.00025	−2.5 $\sim$ −2.08	−2.5 $\sim$ −2.08	0. $\sim$ 0.583	0. $\sim$ 0.583	0. $\sim$ 0.583	0. $\sim$ 0.0001
	0.00237 $\sim$ 0.00271	0.00025 $\sim$ 0.0005	0.00025 $\sim$ 0.0005	−2.08 $\sim$ −1.67	−2.08 $\sim$ −1.67	0.583 $\sim$ 1.17	0.583 $\sim$ 1.17	0.583 $\sim$ 1.17	0.0001 $\sim$ 0.0002
	0.00271 $\sim$ 0.00305	0.0005 $\sim$ 0.00075	0.0005 $\sim$ 0.00075	−1.67 $\sim$ −1.25	−1.67 $\sim$ −1.25	1.17 $\sim$ 1.75	1.17 $\sim$ 1.75	1.17 $\sim$ 1.75	0.0002 $\sim$ 0.0003
	0.00305 $\sim$ 0.00338	0.00075 $\sim$ 0.001	0.00075 $\sim$ 0.001	−1.25 $\sim$ −0.833	−1.25 $\sim$ −0.833	1.75 $\sim$ 2.33	1.75 $\sim$ 2.33	1.75 $\sim$ 2.33	0.0003 $\sim$ 0.0004
	0.00338 $\sim$ 0.00372	0.001 $\sim$ 0.00125	0.001 $\sim$ 0.00125	−0.833 $\sim$ −0.417	−0.833 $\sim$ −0.417	2.33 $\sim$ 2.92	2.33 $\sim$ 2.92	2.33 $\sim$ 2.92	0.0004 $\sim$ 0.0005
	0.00372 $\sim$ 0.00406	0.00125 $\sim$ 0.0015	0.00125 $\sim$ 0.0015	−0.417 $\sim$ 0.	−0.417 $\sim$ 0.	2.92 $\sim$ 3.5	2.92 $\sim$ 3.5	2.92 $\sim$ 3.5	0.0005 $\sim$ 0.0006

Figure 3.4.2: Reference solution of the uniformly loaded hard-soft simply supported square plate with legend also valid for Figures 3.4.4 and 3.4.3

Slika 3.4.2: Referenčna rešitev enakomerno obremenjene togo-mehko podprte kvadratne plošče z legendo, ki velja tudi za Sliki 3.4.4 in 3.4.3

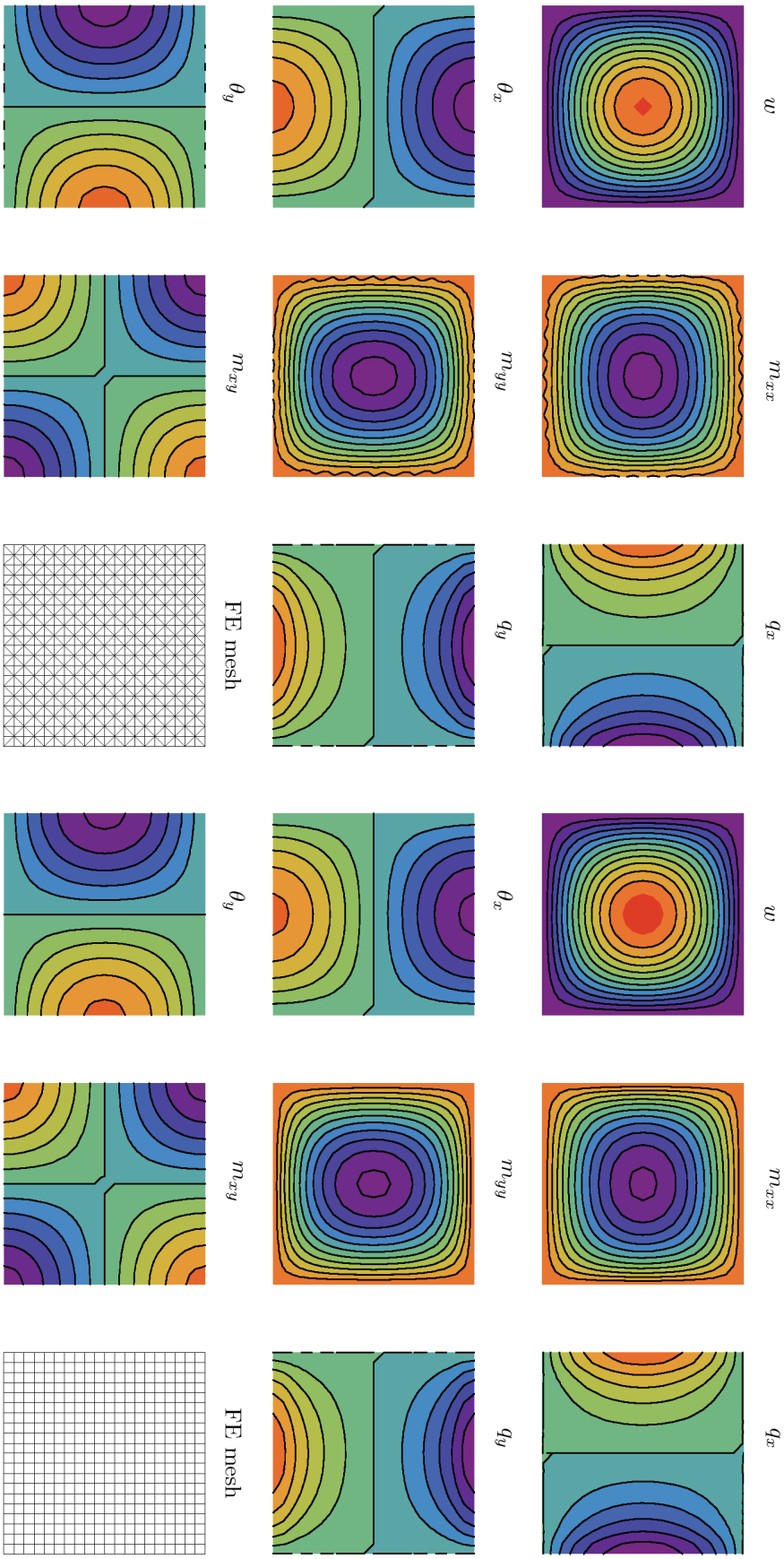

Figure 3.4.3: FE solution of the uniformly loaded hard-soft simply supported square plate with PI plate elements
Slika 3.4.3: Računska rešitev enakomerno obremenjene togo-mehko podprte kvadratne plošče s PI končnimi elementi

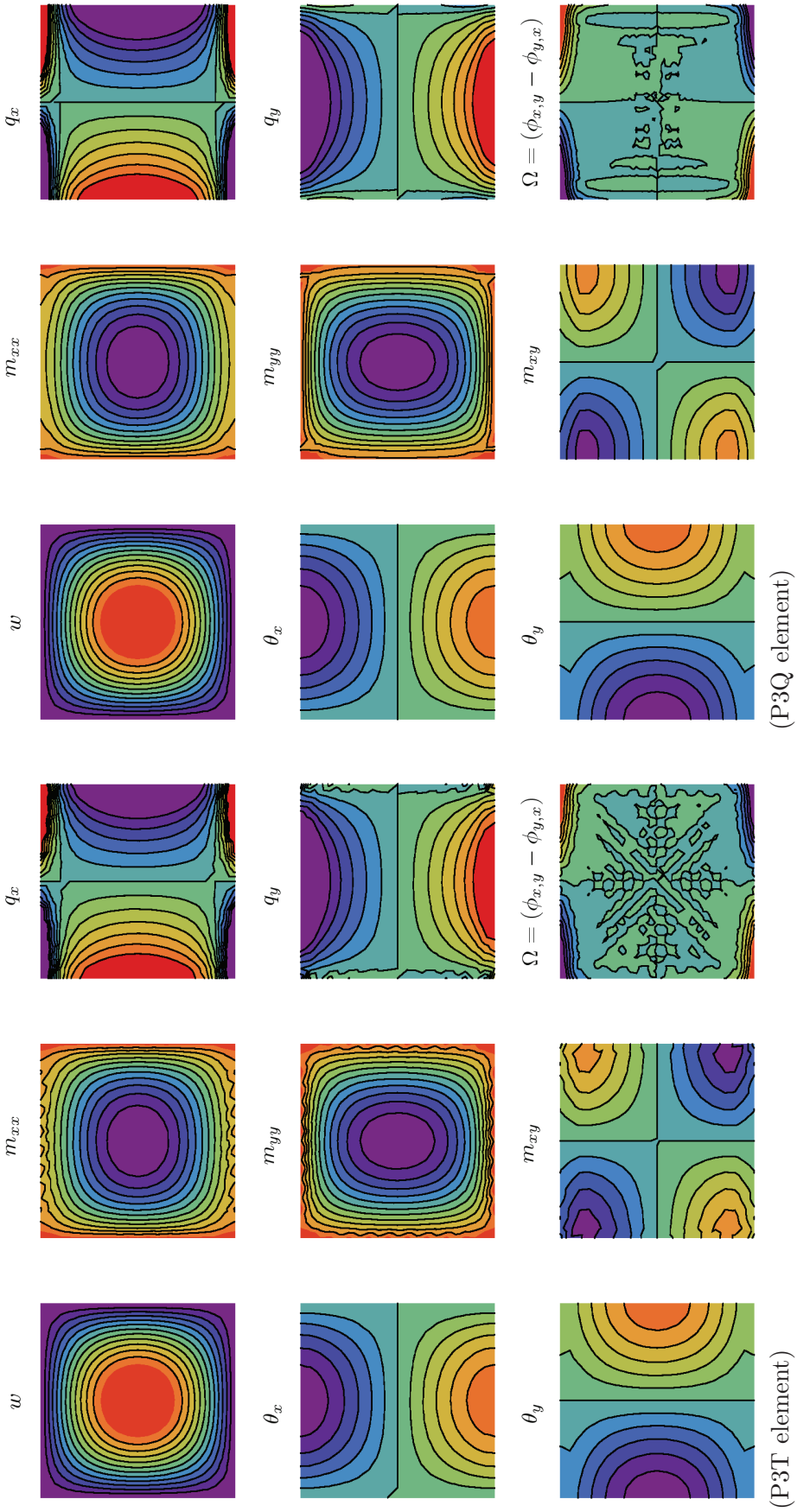

Figure 3.4.4: FE solution of the uniformly loaded hard-soft simply supported square plate with P3 plate elements (mesh as in Figure 3.4.3)

Slika 3.4.4: Računska rešitev enakomerno obremenjene togo-mehko podprte kvadratne plošče s P3 končnimi elementi (mreža, kot je prikazana na Sliki 3.4.3)

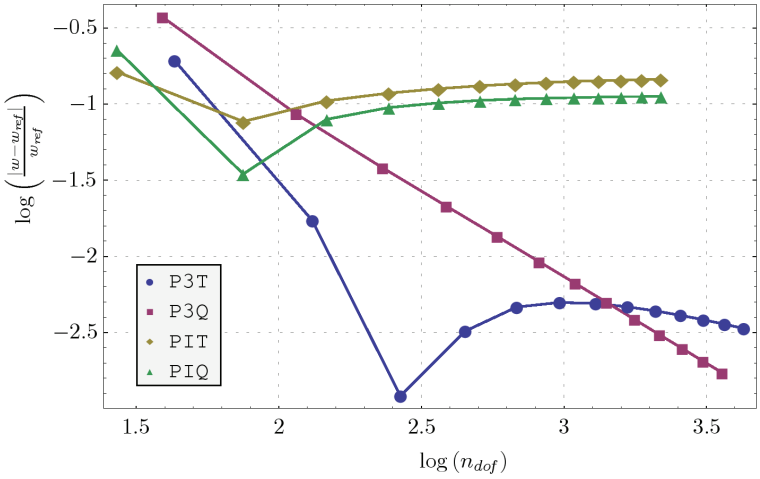

(Displacement w at center)

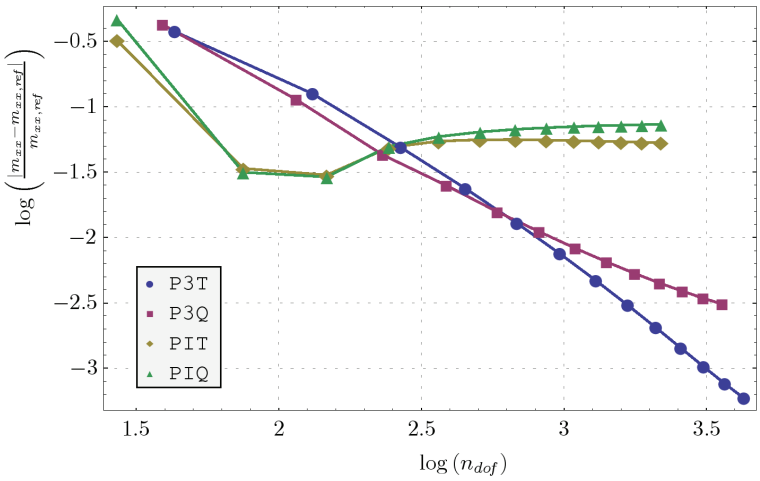

(Moment resultant m_{xx} at center)

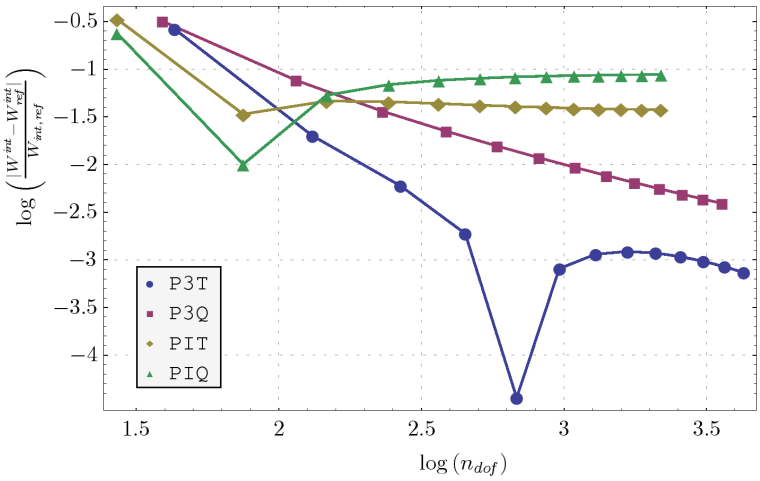

(Energy norm)

Figure 3.4.5: Comparison of the convergence of FE solutions for the uniformly loaded hard-soft simply supported square plate
Slika 3.4.5: Primerjava konvergence računske rešitve problema enakomerno obremenjene togo-mehko podprte kvadratne plošče

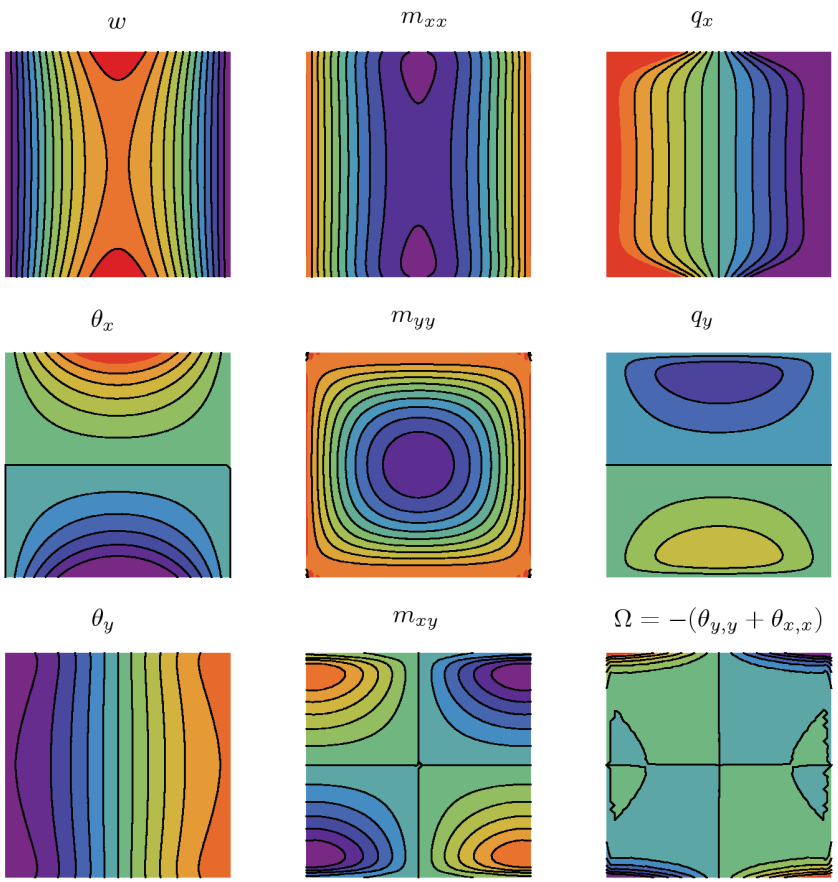

	w	θ_x	θ_y	m_{xx}	m_{yy}	m_{xy}	q_x	q_y
	0. ~ 0.00125	−0.001 ~ −0.000833	−0.005 ~ −0.00417	−15. ~ −13.8	−3. ~ −2.75	−1.5 ~ −1.25	−6. ~ −5.	−1.5 ~ −1.25
	0.00125 ~ 0.0025	−0.000833 ~ −0.000667	−0.00417 ~ −0.00333	−13.8 ~ −12.5	−2.75 ~ −2.5	−1.25 ~ −1.	−5. ~ −4.	−1.25 ~ −1.
	0.0025 ~ 0.00375	−0.000667 ~ −0.0005	−0.00333 ~ −0.0025	−12.5 ~ −11.3	−2.5 ~ −2.25	−1. ~ −0.75	−4. ~ −3.	−1. ~ −0.75
	0.00375 ~ 0.005	−0.0005 ~ −0.000333	−0.0025 ~ −0.00167	−11.3 ~ −10.	−2.25 ~ −2.	−0.75 ~ −0.5	−3. ~ −2.	−0.75 ~ −0.5
	0.005 ~ 0.00625	−0.000333 ~ −0.000167	−0.00167 ~ −0.000833	−10. ~ −8.75	−2. ~ −1.75	−0.5 ~ −0.25	−2. ~ −1.	−0.5 ~ −0.25
	0.00625 ~ 0.0075	−0.000167 ~ 0.	−0.000833 ~ 0.	−8.75 ~ −7.5	−1.75 ~ −1.5	−0.25 ~ 0.	−1. ~ 0.	−0.25 ~ 0.
	0.0075 ~ 0.00875	0. ~ 0.000167	0. ~ 0.000833	−7.5 ~ −6.25	−1.5 ~ −1.25	0. ~ 0.25	0. ~ 1.	0. ~ 0.25
	0.00875 ~ 0.01	0.000167 ~ 0.000333	0.000833 ~ 0.00167	−6.25 ~ −5.	−1.25 ~ −1.	0.25 ~ 0.5	1. ~ 2.	0.25 ~ 0.5
	0.01 ~ 0.0113	0.000333 ~ 0.0005	0.00167 ~ 0.0025	−5. ~ −3.75	−1. ~ −0.75	0.5 ~ 0.75	2. ~ 3.	0.5 ~ 0.75
	0.0113 ~ 0.0125	0.0005 ~ 0.000667	0.0025 ~ 0.00333	−3.75 ~ −2.5	−0.75 ~ −0.5	0.75 ~ 1.	3. ~ 4.	0.75 ~ 1.
	0.0125 ~ 0.0138	0.000667 ~ 0.000833	0.00333 ~ 0.00417	−2.5 ~ −1.25	−0.5 ~ −0.25	1. ~ 1.25	4. ~ 5.	1. ~ 1.25
	0.0138 ~ 0.015	0.000833 ~ 0.001	0.00417 ~ 0.005	−1.25 ~ 0.	−0.25 ~ 0.	1.25 ~ 1.5	5. ~ 6.	1.25 ~ 1.5

Figure 3.4.7: Reference solution of the uniformly loaded hard simply supported-free square plate with legend also valid for Figures 3.4.9 and 3.4.8

Slika 3.4.7: Referenčna rešitev enakomerno togo prosto podprte - proste kvadratne plošče z legendo, ki velja tudi za Sliki 3.4.9 in 3.4.8

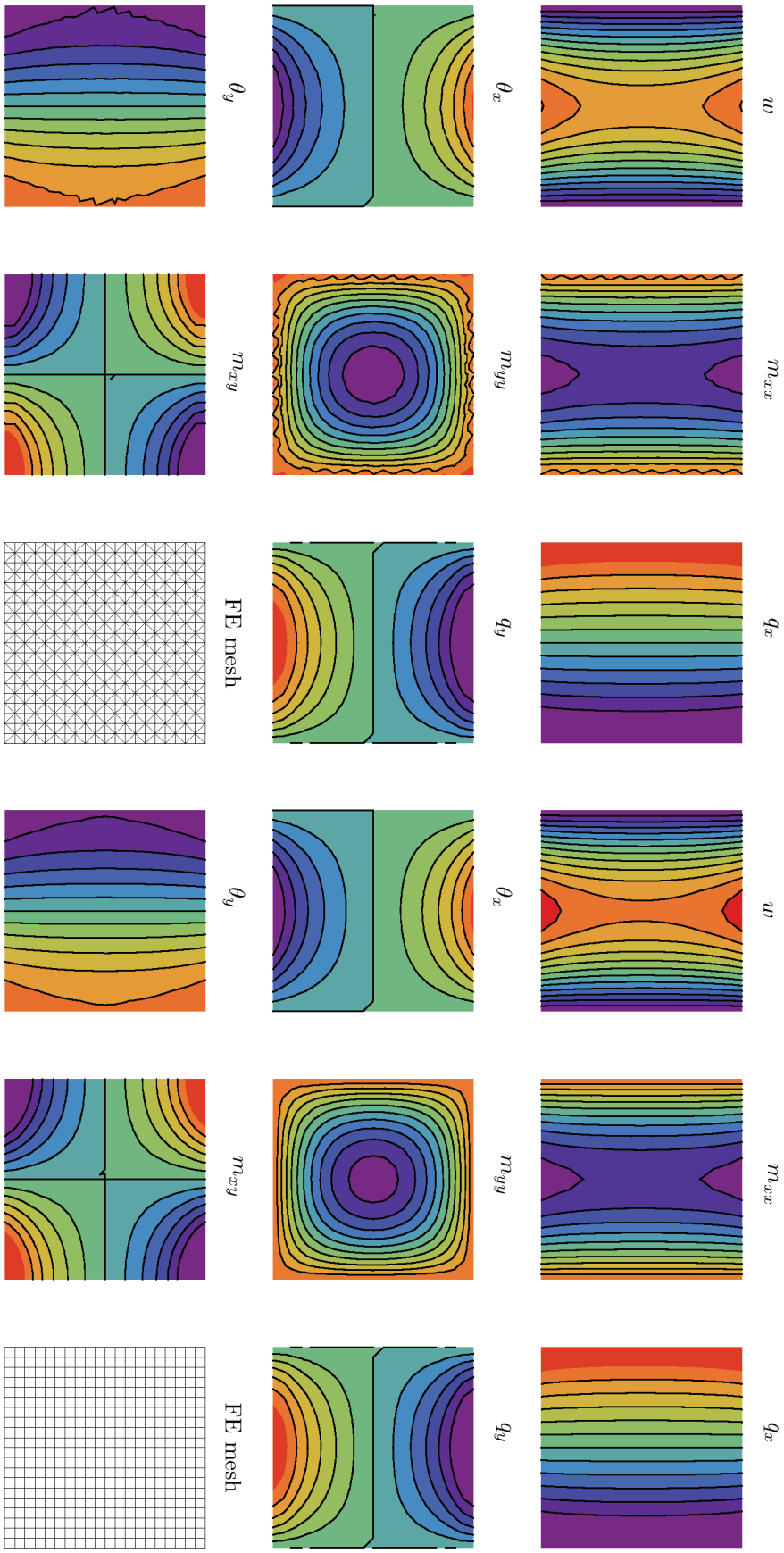

Figure 3.4.8: FE solutions of the uniformly loaded hard simply supported-free square plate with PI plate elements

Slika 3.4.8: Računska rešitev enakomerno togo prosto podprte - proste kvadratne plošče s PI končnimi elementi

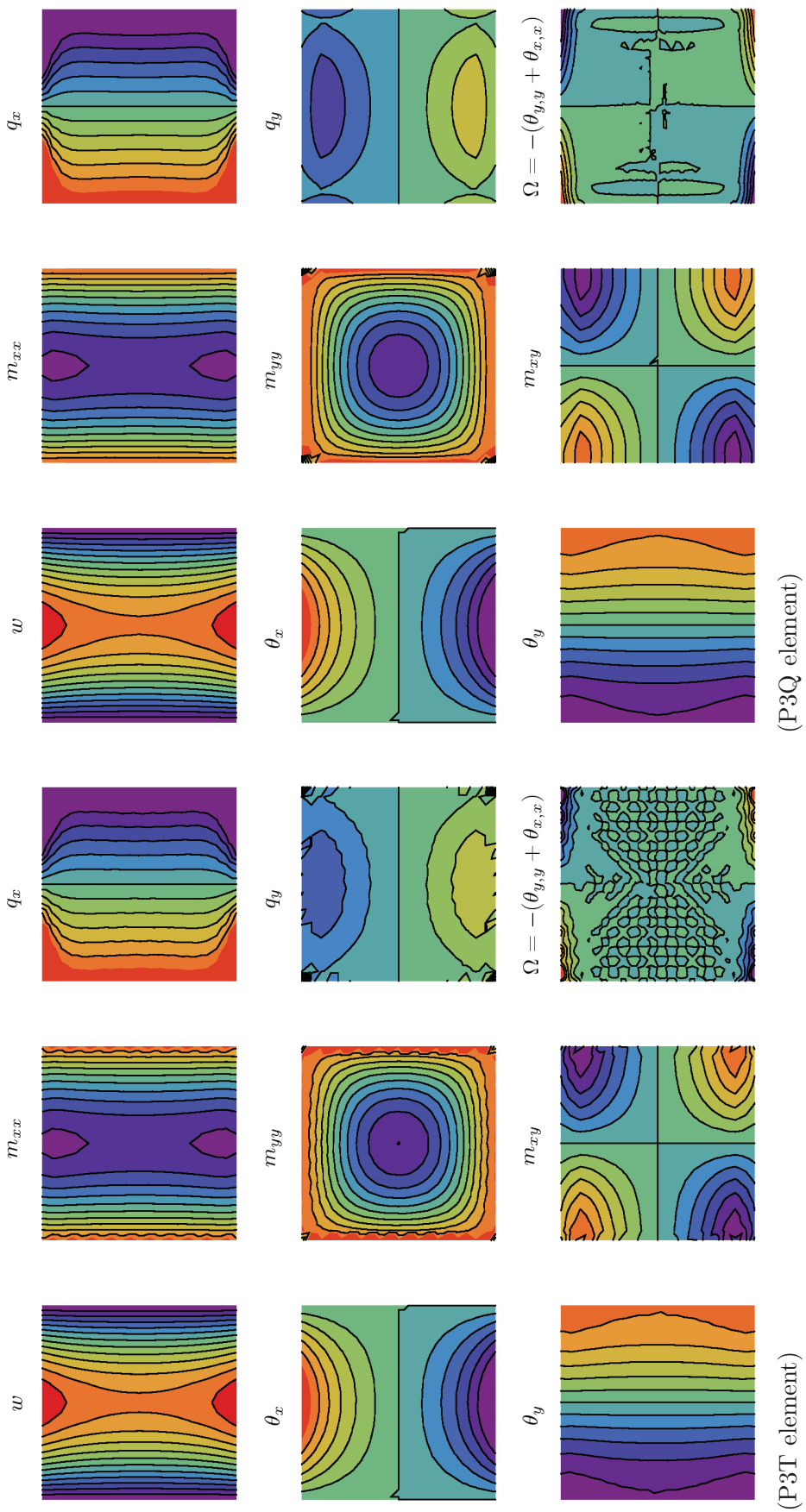

Figure 3.4.9: FE solutions of the uniformly loaded hard simply supported-free square plate with P3 plate elements (mesh as in Figure 3.4.8)

Slika 3.4.9: Računska rešitev enakomerno togo prosto podprte - proste kvadratne plošče s P3 končnimi elementi (mreža, kot je prikazana na Sliki 3.4.8)

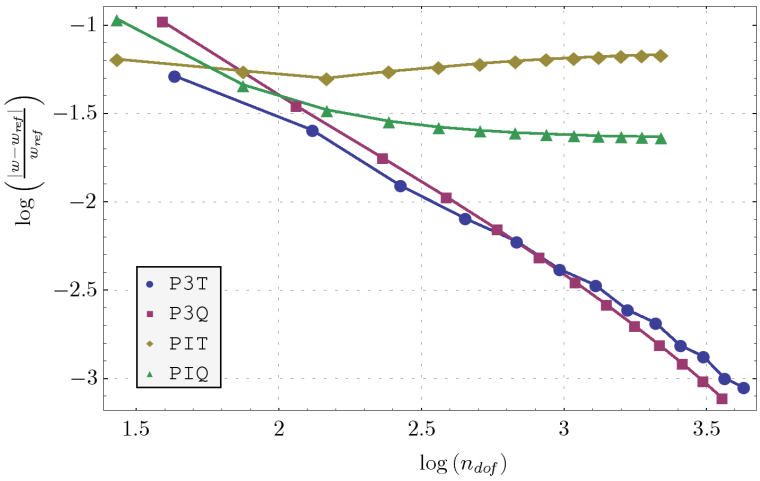

(Displacement w at center)

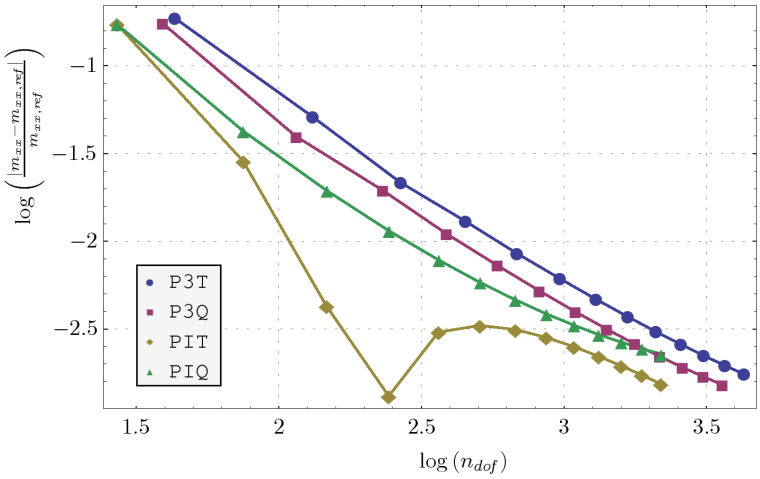

(Moment resultant m_{xx} at center)

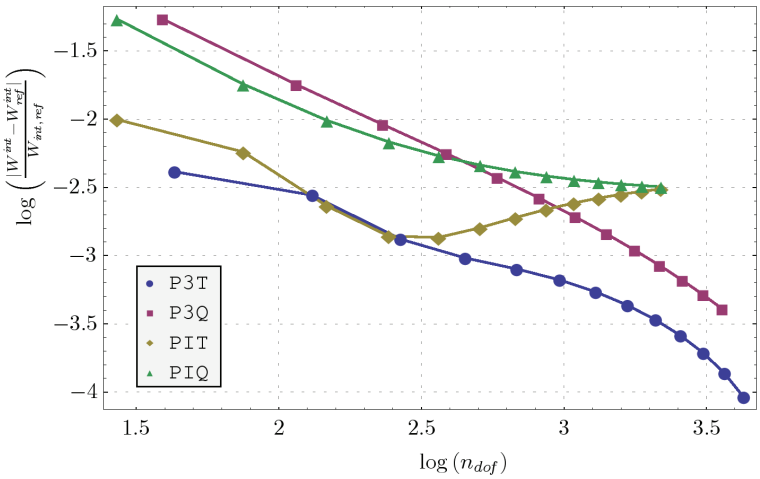

(Energy norm)

Figure 3.4.10: Comparison of the convergence of FE solutions for the uniformly loaded hard simply supported-free square plate

Slika 3.4.10: Primerjava konvergence računske rešitve problema enakomerno togo prosto podprte - proste kvadratne plošče

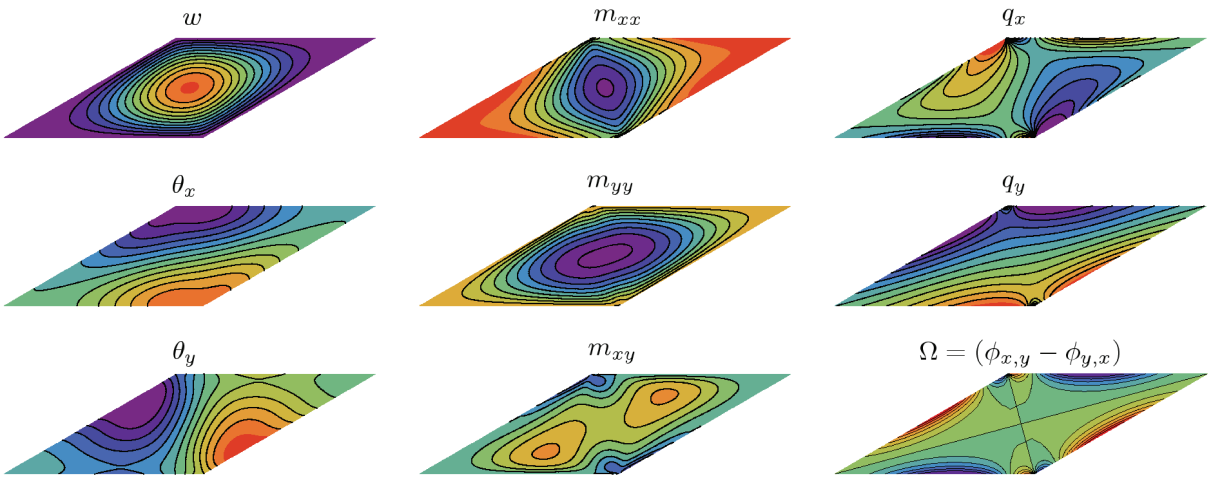

	w	θ_x	θ_y	m_{xx}	m_{yy}	m_{xy}	q_x	q_y	Ω
	0.	−0.0003	−0.000145	−1.5	−2.2	−0.5	−1.5	−3.	−0.00011
	∼	∼	∼	∼	∼	∼	∼	∼	∼
	0.00005	−0.00025	−0.000121	−1.38	−1.98	−0.417	−1.25	−2.5	−0.0000917
	0.00005	−0.00025	−0.000121	−1.38	−1.98	−0.417	−1.25	−2.5	−0.0000917
	∼	∼	∼	∼	∼	∼	∼	∼	∼
	0.0001	−0.0002	−0.0000967	−1.25	−1.75	−0.333	−1.	−2.	−0.0000733
	0.0001	−0.0002	−0.0000967	−1.25	−1.75	−0.333	−1.	−2.	−0.0000733
	∼	∼	∼	∼	∼	∼	∼	∼	∼
	0.00015	−0.00015	−0.0000725	−1.13	−1.53	−0.25	−0.75	−1.5	−0.000055
	0.00015	−0.00015	−0.0000725	−1.13	−1.53	−0.25	−0.75	−1.5	−0.000055
	∼	∼	∼	∼	∼	∼	∼	∼	∼
	0.0002	−0.0001	−0.0000483	−1.	−1.3	−0.167	−0.5	−1.	−0.0000367
	0.0002	−0.0001	−0.0000483	−1.	−1.3	−0.167	−0.5	−1.	−0.0000367
	∼	∼	∼	∼	∼	∼	∼	∼	∼
	0.00025	−0.00005	−0.0000242	−0.875	−1.08	−0.0833	−0.25	−0.5	−0.0000183
	0.00025	−0.00005	−0.0000242	−0.875	−1.08	−0.0833	−0.25	−0.5	−0.0000183
	∼	∼	∼	∼	∼	∼	∼	∼	∼
	0.0003	0.	0.	−0.75	−0.85	0.	0.	0.	0.
	0.0003	0.	0.	−0.75	−0.85	0.	0.	0.	0.
	∼	∼	∼	∼	∼	∼	∼	∼	∼
	0.00035	0.00005	0.0000242	−0.625	−0.625	0.0833	0.25	0.5	0.0000183
	0.00035	0.00005	0.0000242	−0.625	−0.625	0.0833	0.25	0.5	0.0000183
	∼	∼	∼	∼	∼	∼	∼	∼	∼
	0.0004	0.0001	0.0000483	−0.5	−0.4	0.167	0.5	1.	0.0000367
	0.0004	0.0001	0.0000483	−0.5	−0.4	0.167	0.5	1.	0.0000367
	∼	∼	∼	∼	∼	∼	∼	∼	∼
	0.00045	0.00015	0.0000725	−0.375	−0.175	0.25	0.75	1.5	0.000055
	0.00045	0.00015	0.0000725	−0.375	−0.175	0.25	0.75	1.5	0.000055
	∼	∼	∼	∼	∼	∼	∼	∼	∼
	0.0005	0.0002	0.0000967	−0.25	0.05	0.333	1.	2.	0.0000733
	0.0005	0.0002	0.0000967	−0.25	0.05	0.333	1.	2.	0.0000733
	∼	∼	∼	∼	∼	∼	∼	∼	∼
	0.00055	0.00025	0.000121	−0.125	0.275	0.417	1.25	2.5	0.0000917
	0.00055	0.00025	0.000121	−0.125	0.275	0.417	1.25	2.5	0.0000917
	∼	∼	∼	∼	∼	∼	∼	∼	∼
	0.0006	0.0003	0.000145	0.	0.5	0.5	1.5	3.	0.00011

Figure 3.4.12: Reference solution of the uniformly loaded soft simply supported skew plate with legend also valid for Figures 3.4.14 and 3.4.13

Slika 3.4.12: Referenčna rešitev enakomerno obremenjene mehko podprte romboidne plošče z legendo, ki velja tudi za Sliki 3.4.14 in 3.4.13

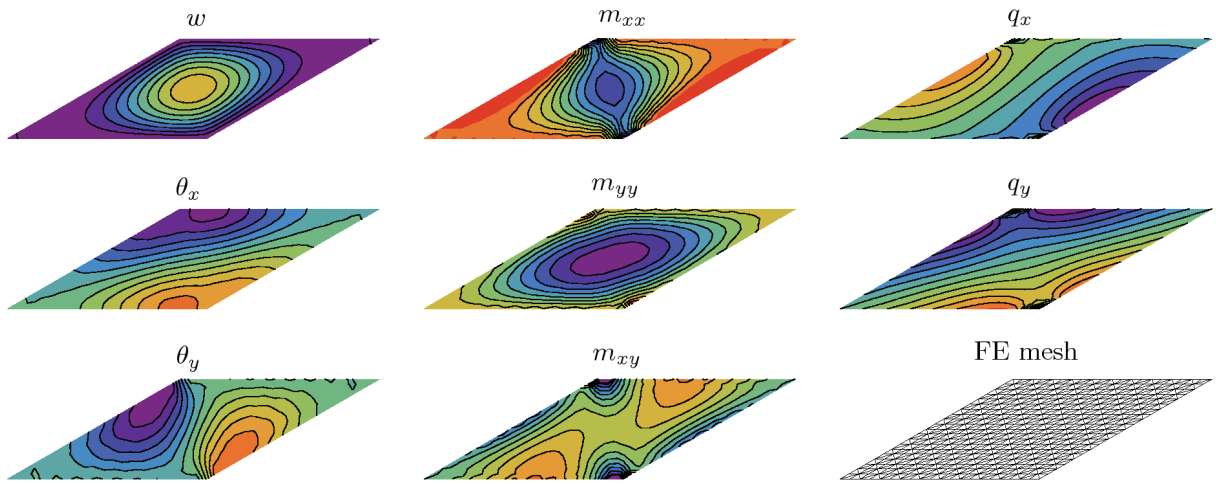

(PIT element)

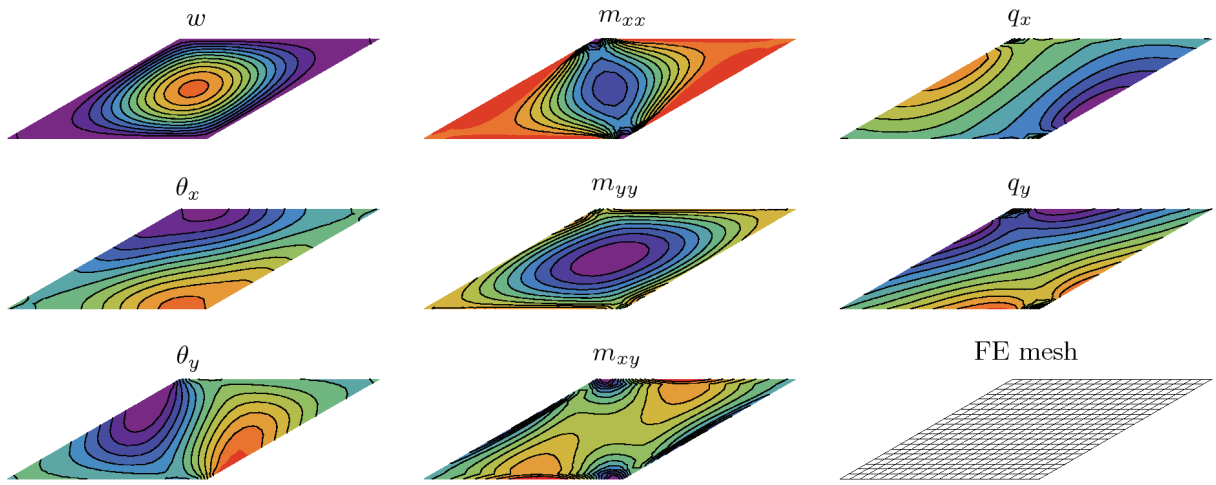

(PIQ element)

Figure 3.4.13: FE solution of the uniformly loaded soft simply supported skew plate with PI plate elements

Slika 3.4.13: Računska rešitev enakomerno obremenjene togo podprte romboidne plošče s PI končnimi elementi

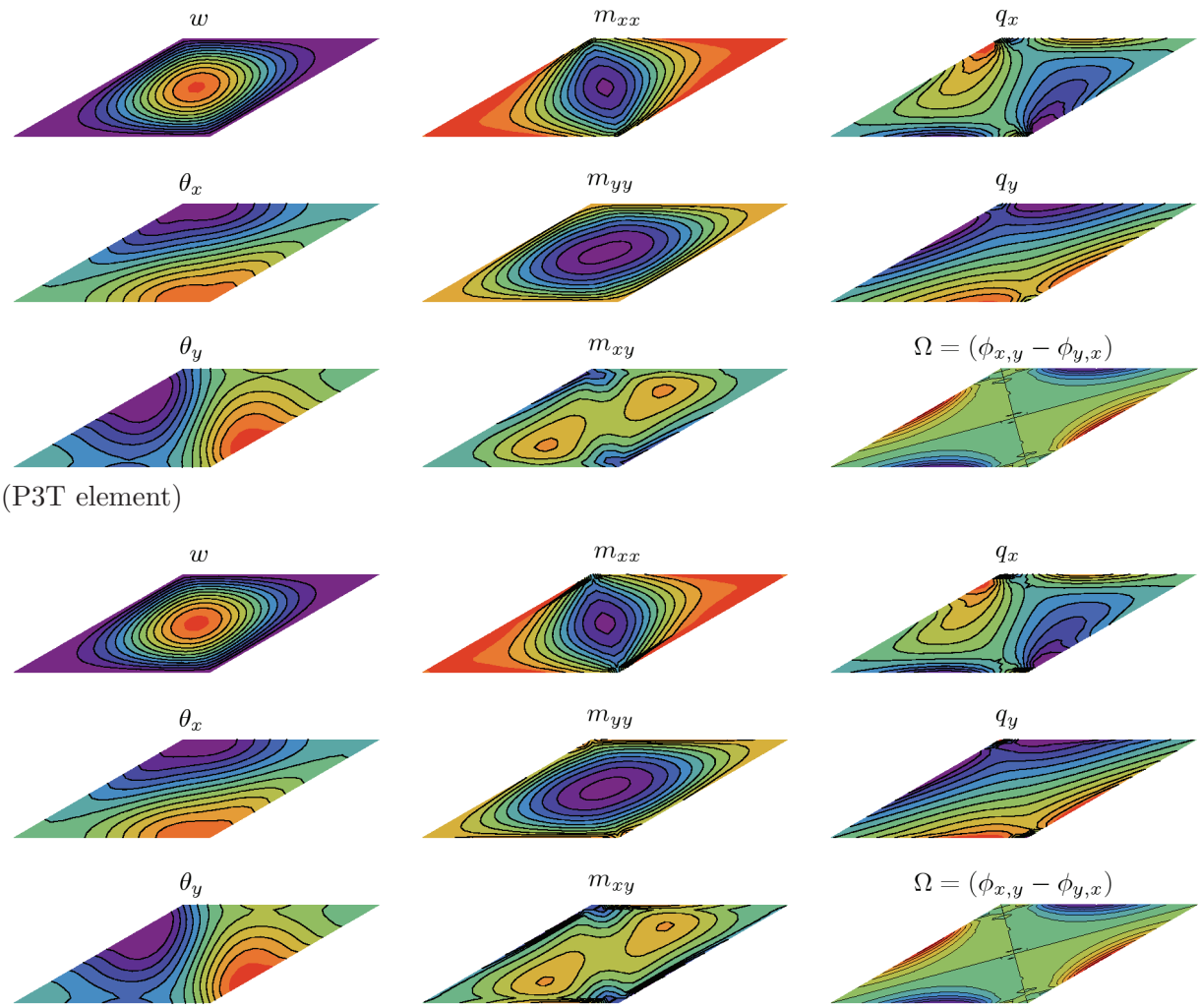

Figure 3.4.14: FE solution of the uniformly loaded soft simply supported skew plate with P3 plate elements (mesh as in Figure 3.4.13)
Slika 3.4.14: Računska rešitev enakomerno obremenjene togo podprte romboidne plošče s P3 končnimi elementi (mreža, kot je prikazana na Sliki 3.4.13)

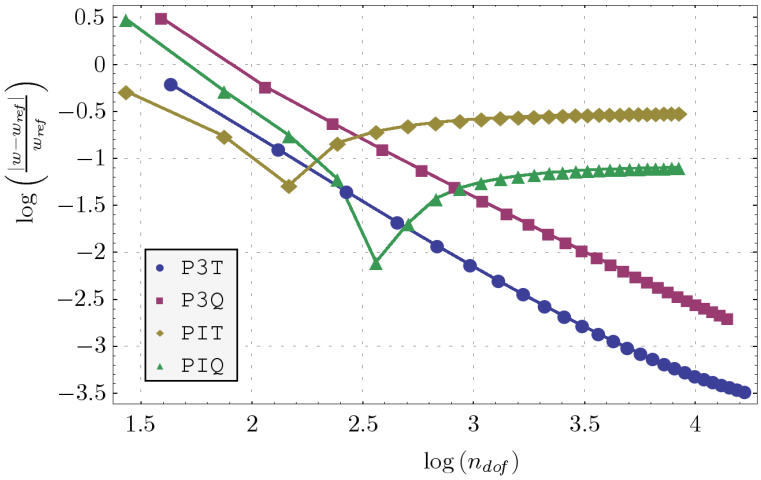

(Displacement w at center)

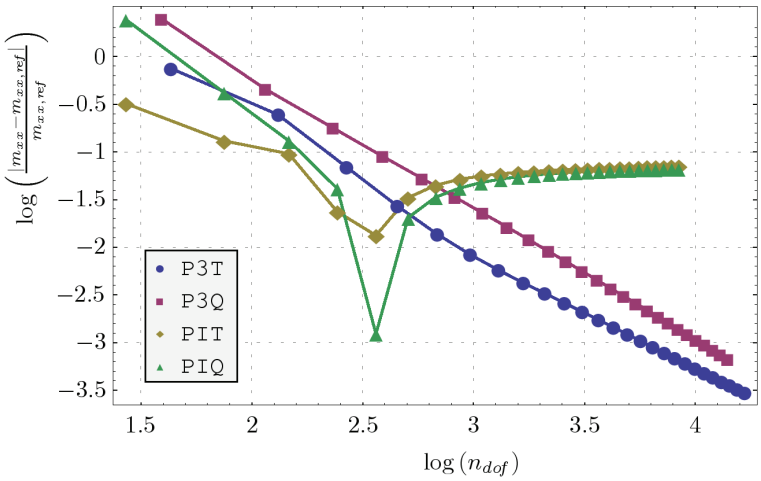

(Moment resultant m_{xx} at center)

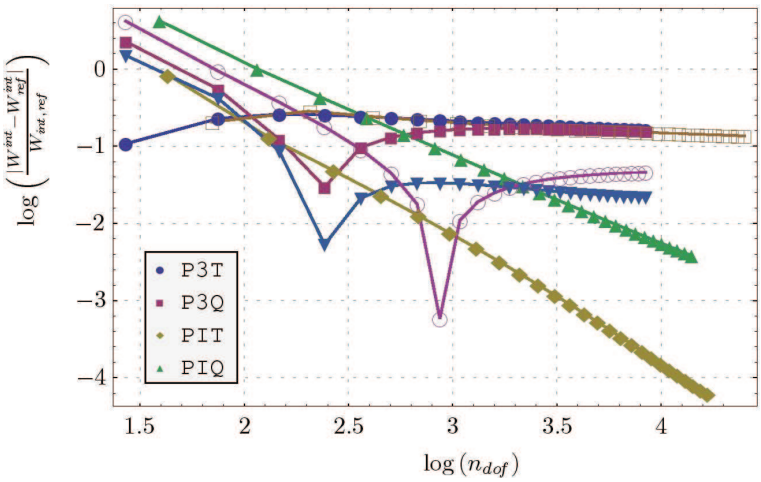

(Energy norm)

Figure 3.4.15: Comparison of the convergence of FE solutions for the uniformly loaded soft simply supported skew plate

Slika 3.4.15: Primerjava konvergence računske rešitve problema enakomerno obremenjene mehko podprte romboidne plošče

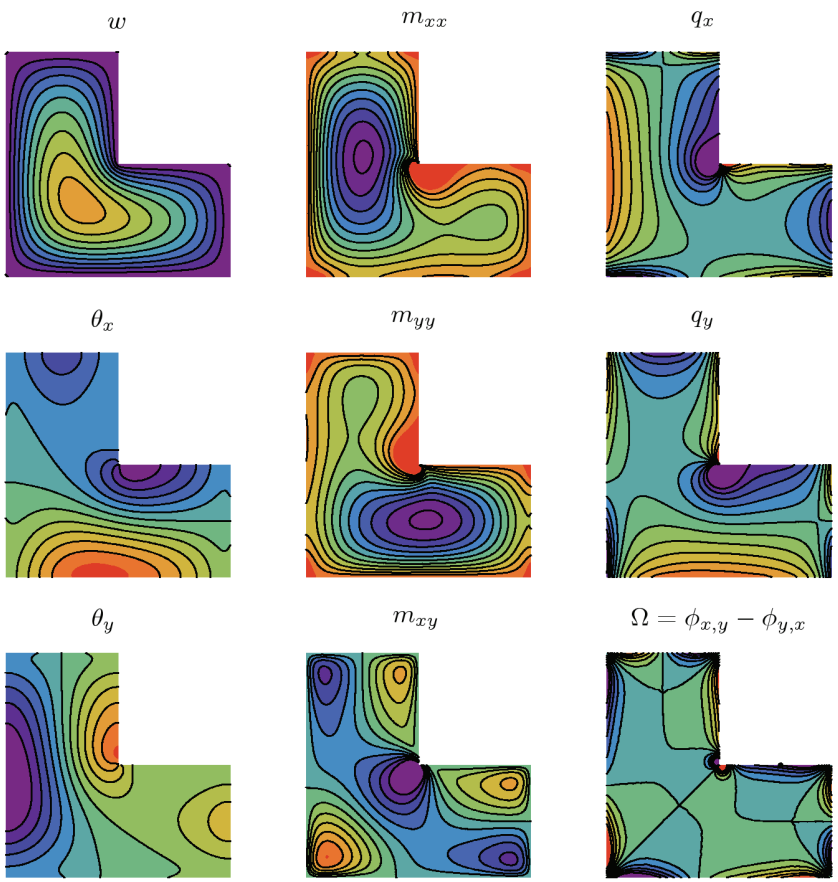

w	θ_x	θ_y	m_{xx}	m_{yy}	m_{xy}	q_x	q_y	Ω
0.	−0.0005	−0.0005	−3.	−3.	−1.	−4.	−4.	−0.00025
≈ 0.000125	≈ −0.000417	≈ −0.000417	≈ −2.75	≈ −2.75	≈ −0.833	≈ −3.33	≈ −3.33	≈ −0.000208
0.000125	−0.000417	−0.000417	−2.75	−2.75	−0.833	−3.33	−3.33	−0.000208
≈ 0.00025	≈ −0.000333	≈ −0.000333	≈ −2.5	≈ −2.5	≈ −0.667	≈ −2.67	≈ −2.67	≈ −0.000167
0.00025	−0.000333	−0.000333	−2.5	−2.5	−0.667	−2.67	−2.67	−0.000167
≈ 0.000375	≈ −0.00025	≈ −0.00025	≈ −2.25	≈ −2.25	≈ −0.5	≈ −2.	≈ −2.	≈ −0.000125
0.000375	−0.00025	−0.00025	−2.25	−2.25	−0.5	−2.	−2.	−0.000125
≈ 0.0005	≈ −0.000167	≈ −0.000167	≈ −2.	≈ −2.	≈ −0.333	≈ −1.33	≈ −1.33	≈ −0.0000833
0.0005	−0.000167	−0.000167	−2.	−2.	−0.333	−1.33	−1.33	−0.0000833
≈ 0.000625	≈ −0.0000833	≈ −0.0000833	≈ −1.75	≈ −1.75	≈ −0.167	≈ −0.667	≈ −0.667	≈ −0.0000417
0.000625	−0.0000833	−0.0000833	−1.75	−1.75	−0.167	−0.667	−0.667	−0.0000417
≈ 0.00075	≈ 0.	≈ 0.	≈ −1.5	≈ −1.5	≈ 0.	≈ 0.	≈ 0.	≈ 0.
0.00075	0.	0.	−1.5	−1.5	0.	0.	0.	0.
≈ 0.000875	≈ 0.0000833	≈ 0.0000833	≈ −1.25	≈ −1.25	≈ 0.167	≈ 0.667	≈ 0.667	≈ 0.0000417
0.000875	0.0000833	0.0000833	−1.25	−1.25	0.167	0.667	0.667	0.0000417
≈ 0.001	≈ 0.000167	≈ 0.000167	≈ −1.	≈ −1.	≈ 0.333	≈ 1.33	≈ 1.33	≈ 0.0000833
0.001	0.000167	0.000167	−1.	−1.	0.333	1.33	1.33	0.0000833
≈ 0.00113	≈ 0.00025	≈ 0.00025	≈ −0.75	≈ −0.75	≈ 0.5	≈ 2.	≈ 2.	≈ 0.000125
0.00113	0.00025	0.00025	−0.75	−0.75	0.5	2.	2.	0.000125
≈ 0.00125	≈ 0.000333	≈ 0.000333	≈ −0.5	≈ −0.5	≈ 0.667	≈ 2.67	≈ 2.67	≈ 0.000167
0.00125	0.000333	0.000333	−0.5	−0.5	0.667	2.67	2.67	0.000167
≈ 0.00138	≈ 0.000417	≈ 0.000417	≈ −0.25	≈ −0.25	≈ 0.833	≈ 3.33	≈ 3.33	≈ 0.000208
0.00138	0.000417	0.000417	−0.25	−0.25	0.833	3.33	3.33	0.000208
≈ 0.0015	≈ 0.0005	≈ 0.0005	≈ 0.	≈ 0.	≈ 1.	≈ 4.	≈ 4.	≈ 0.00025

Figure 3.4.17: Reference solution of the uniformly loaded soft simply supported L-shaped plate with legend also valid for Figures 3.4.19 and 3.4.18

Slika 3.4.17: Referenčna rešitev enakomerno obremenjene mehko podprte L plošče z legendo, ki velja tudi za Sliki 3.4.19 in 3.4.18

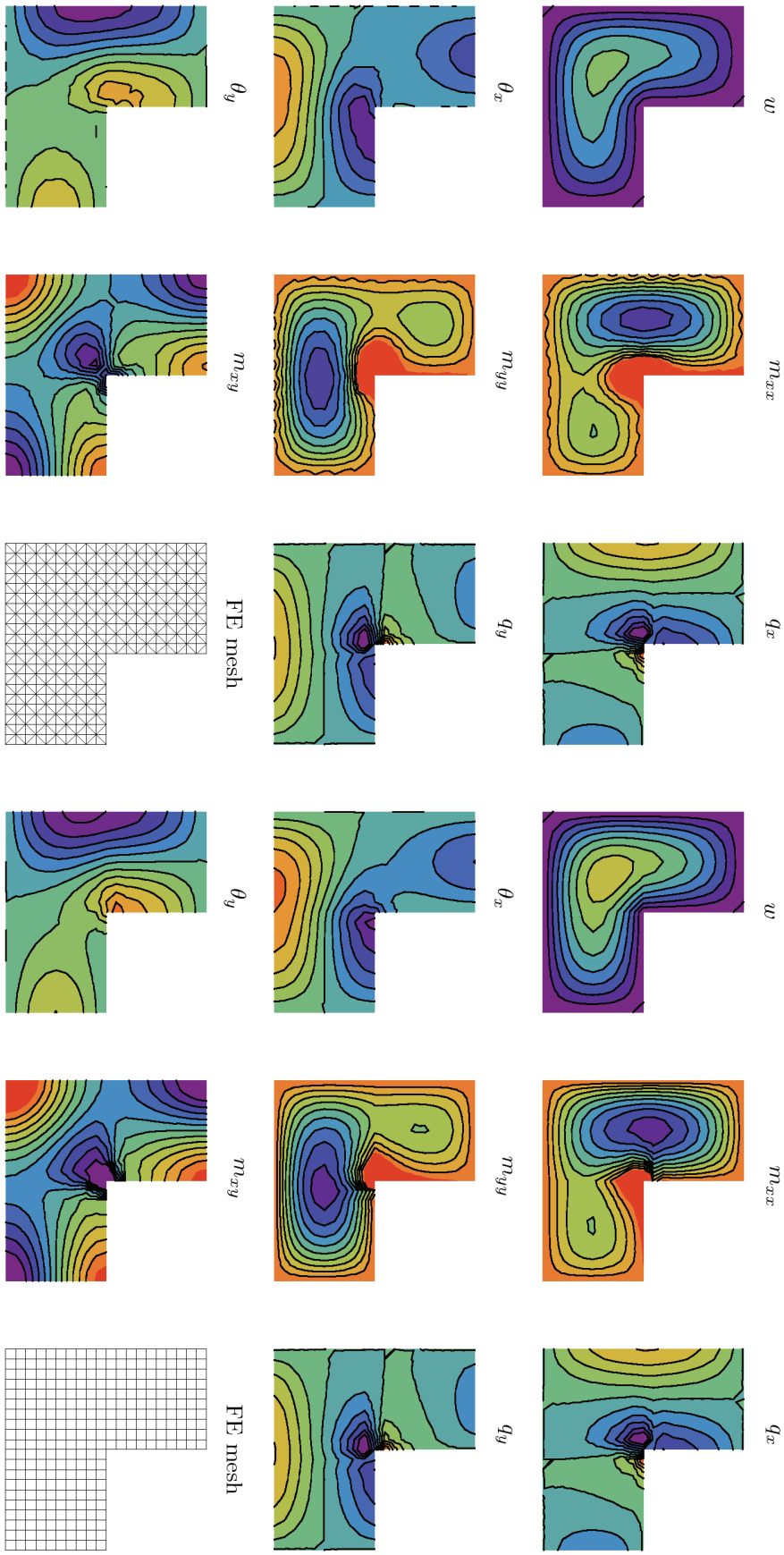

Figure 3.4.18: FE solution of the uniformly loaded soft simply supported L-shaped plate with PI plate elements
Slika 3.4.18: Računska rešitev enakomerno obremenjene mehko podprte L plošče s PI končnimi elementi

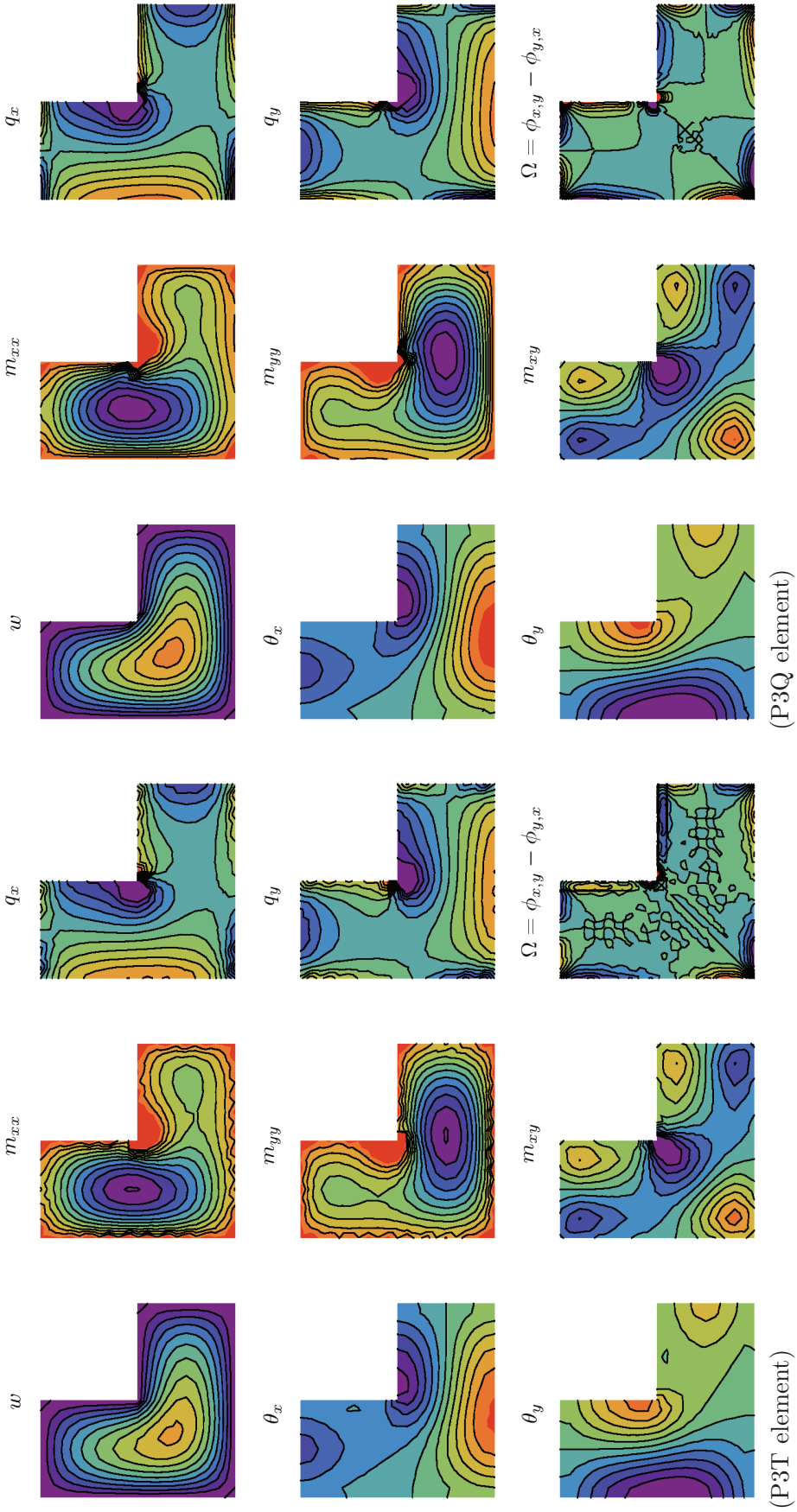

Figure 3.4.19: FE solution of the uniformly loaded soft simply supported L-shaped plate with P3 plate elements (mesh as in Figure 3.4.18)

Slika 3.4.19: Računska rešitev enakomerno obremenjene mehko podprte L plošče s P3 končnimi elementi (mreža, kot je prikazana na Sliki 3.4.18)

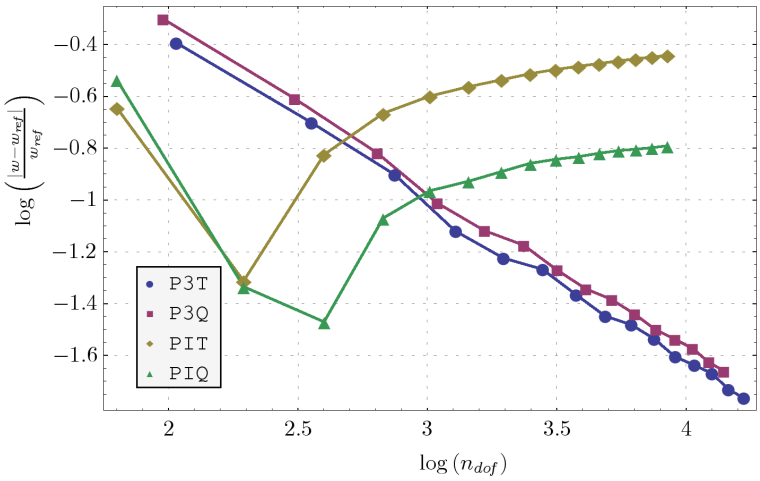

(Displacement w at center)

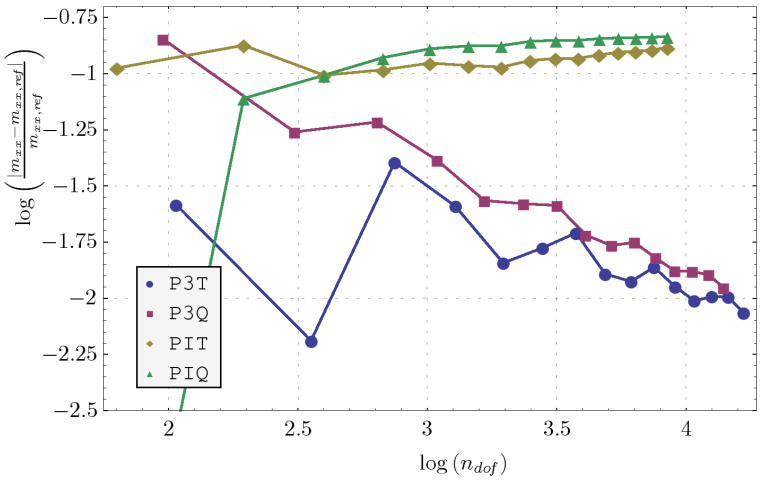

(Moment resultant m_{xx} at center)

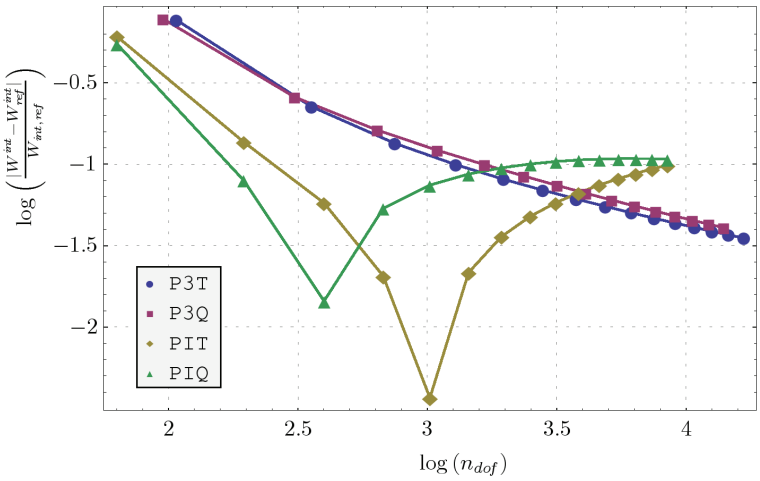

(Energy norm)

Figure 3.4.20: Comparison of the convergence of FE solutions for the uniformly loaded soft simply supported L-shaped plate

Slika 3.4.20: Primerjava konvergence računske rešitve problema enakomerno obremenjene mehko podprte L plošče

3.5 Chapter summary and conclusions

A Reissner/Mindlin plate theory, which covers the behavior of moderately thick plates is presented. The Kirchhoff assumption is abandoned as the theory takes into account the transverse shear: the midsurface deflection of the plate is independent of rotation of normal fibers.

In the first section the basic equations are derived. The shear correction factor is treated alongside for the sake of completeness. There are three coupled differential equations of sixth order for midsurface deflection w and two components of rotation ϕ_x, ϕ_y which govern the deformation of the moderately thick plates. Since the hierarchic relation of the Reissner/Mindlin theory to the Kirchhoff theory is followed throughout the derivation, one of the equations can be presented as the modified biharmonic equation. This hierarchical treatment is advantageous since it enables us to clearly identify the novelties.

The Reissner/Mindlin theory is able to describe a larger set of boundary conditions. There are three independent components of boundary traction loading: normal shear, twisting and bending moment. However, being closer to the full three-dimensional theory, and thus able to describe more flexible plate structures, the Reissner/Mindlin plates do not handle concentrated loads - contrary to the Kirchhoff plates.

The introduction of transverse shear triggers some interesting phenomena. Most notable is *the boundary layer effect*, which concern the areas near the plate boundary, where steep gradients of stress resultants exist. The influence of boundary layer effects is limited to the distance of the order of plate thickness into the plate interior. The existence and strength of boundary layers is related to the type of boundary conditions imposed. Maybe the most counter-intuitive fact concerning the boundary layers is, that it is the most prominent along the free boundary of the plate. The singularities, already encountered in the Kirchhoff theory of thin plates, exist also in the Reissner/Mindlin theory.

The second section deals with the development of the finite element based on Reissner/Mindlin theory. An alternative notation enables the presentation of the finite elements as the hierarchical extension of the DK thin plate elements. Additional degrees of freedom at the element mid-sides are directly related to the projection of the transverse shear on the direction of the element side. An analysis of the stiffness matrix of the element shows that the part related to the shear strain depends only on the mid-side degrees of freedom. Equivalent formulation of triangular and quadrilateral elements is possible due to the alternative element notation. A variation of the elements is also presented. Here

the additional degrees of freedom are related to incompatible deformation modes, and are thus subject to elimination by means of static condensation.

The chapter concludes with several typical plate problems, which illustrate the specific issues of moderately thick plate modeling including singularities and boundary layers. The performance of the presented finite elements is assessed in terms of the convergence rates of various selected quantities. The functionality of element implementation is tested through the comparison to the reference solutions. An interesting observation is made, regarding the performance of the elements with the incompatible modes. Although the elements are able to capture the transverse shear, they fail to detect the boundary layers.

Chapter 4

Thick plates: theory and finite element formulations

4.1 Introduction

A logical successor of the Reissner/Mindlin model in the hierarchy of the models for bending of elastic isotropic plates is a higher-order plate model which includes through the thickness stretching. The higher-order plate model, considered in this chapter is a special case of a shell model presented in [Brank, 2005] and [Brank et al., 2008]. It treats a plate as a 2d surface in a full 3d stress state. This is advantageous, since the usual modification of 3d constitutive equations due to the plane stress assumption (see chapters 2 and 3) is omitted, resulting in a simpler implementation of complex material models for example hiperelasticity or elasto-plasticity. Also the boundary layer effect, which is full 3d effect, is much better represented by the higher-order plate models as shown below. The considered higher-order plate model fits between the Reisnner/Mindlin model and the 3d solid model, which makes it an ideal choice for the model adaptivity of plates. In this chapter we will thus present a new higher-order plate theory and a new higher-order plate elements based on that theory. The elements will be a direct refinement of the Reissner/Mindlin finite elements with cubic interpolation of displacement and linked interpolation of displacement and rotations, denoted in previous chapter as P3T and P3Q.

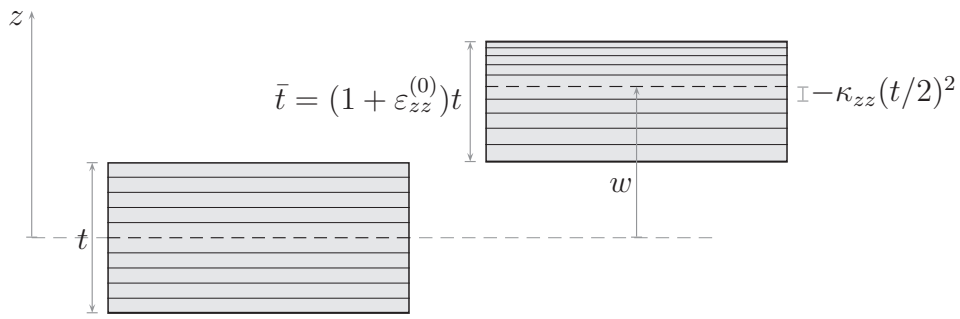

Figure 4.2.1: Kinematics of through-the-thickness deformation in the thick plate model
Slika 4.2.1: Kinematika deformacije vzdolž debeline plošče v modelu debelih plošč

4.2 Theory

We start by abandoning the assumption of zero through the thickness stress: $\sigma_{zz} \neq 0$. In the case of 3d linear elasticity we thus have:

$$\sigma_{zz} = (\lambda + 2\mu)\varepsilon_{zz} + \lambda(\varepsilon_{xx} + \varepsilon_{yy}) \neq 0 \tag{4.2.1}$$

with $\lambda = \frac{\nu E}{(1+\nu)(1-2\nu)}$, $\mu = \frac{E}{2(1+\nu)}$ as Lamé coefficients. Nevertheless in the limit $t \to 0$ the plane stress assumption $\sigma_{zz} = 0$ must be satisfied resulting in the thickness stretching ε_{zz}:

$$\varepsilon_{zz} = -\frac{\lambda}{\lambda + 2\mu}(\varepsilon_{xx} + \varepsilon_{yy})$$

This kind of limit behavior can be achieved only if the strains ε_{xx}, ε_{yy}, ε_{zz} are of the same order with respect to z coordinate. In such a case they can cancel each other in (4.2.1). If for instance ε_{xx}, ε_{yy} are linear with respect to z coordinate, so must be ε_{zz}. The linear variation of ε_{zz} with z also implies that the transverse displacement u_z should be at least quadratic function of z since $\varepsilon_{zz} = \frac{\partial u_z}{\partial z}$.

4.2.1 Governing equations

Kinematic equations

The following kinematics of plate displacement is therefore assumed:

$$\boldsymbol{u} = \boldsymbol{u}^{RM} + \boldsymbol{u}^{S}$$

where $\boldsymbol{u}^{RM}$ denotes kinematics of Reissner/Mindlin model

$$\boldsymbol{u}^{RM} = w\boldsymbol{n}_\Omega - z\boldsymbol{\phi}; \quad \boldsymbol{n}_\Omega = [0,0,1]^T$$

and $\boldsymbol{u}^S$ defines the displacements that produce the through-the-thickness stretch (see Figure 4.2.1)

$$\boldsymbol{u}^S = \left((\bar{t}/t - 1)z - \kappa_{zz}z^2/2\right)\boldsymbol{n}_\Omega = \left(\varepsilon_{zz}^{(0)}z - \varepsilon_{zz}^{(1)}z^2/t\right)\boldsymbol{n}_\Omega \tag{4.2.2}$$

The $\boldsymbol{u}^S$ is a quadratic function of z coordinate; $\bar{t}$ is the thickness of the deformed plate, t is the thickness of the plate prior to deformation, $\kappa_{zz} = \varepsilon_{zz}^{(1)}2/t$ is the parameter of the stretch and $\boldsymbol{n}_\Omega$ the normal to the midsurface of the undeformed plate. The $\boldsymbol{u}^S$ direction is limited to the direction of $\boldsymbol{n}_\Omega$. We denote the relative thickness change by $\varepsilon_{zz}^{(0)} = \bar{t}/t - 1$.

The components of displacement $w = [u_x, u_y, u_z]^T$ are:

$$u_x = -z\phi_x; \quad u_y = -z\phi_y; \quad u_z = w + \varepsilon_{zz}^{(0)}z - \varepsilon_{zz}^{(1)}z^2/t \tag{4.2.3}$$

and the resulting strains are

$$\begin{aligned} \varepsilon_{xx} &= -z\kappa_{xx}; & 2\varepsilon_{xy} &= -z\kappa_{xy} \\ \varepsilon_{yy} &= -z\kappa_{yy}; & 2\varepsilon_{xz} &= \gamma_x + \varepsilon_{zz,x}^{(0)}z - \varepsilon_{zz,x}^{(1)}z^2/t \\ \varepsilon_{zz} &= \varepsilon_{zz}^{(0)} - 2z\varepsilon_{zz}^{(1)}/t = \varepsilon_{zz}^{(0)} - z\kappa_{zz}; & 2\varepsilon_{yz} &= \gamma_y + \varepsilon_{zz,y}^{(0)}z - \varepsilon_{zz,y}^{(1)}z^2/t \end{aligned} \tag{4.2.4}$$

where the definitions from chapters 2 and 3 were employed

$$\begin{aligned} \kappa_{xx} &= \phi_{x,x}; & \gamma_x &= w_{,x} - \phi_x \\ \kappa_{yy} &= \phi_{y,y}; & \gamma_y &= w_{,y} - \phi_y \\ \kappa_{xy} &= \phi_{x,y} + \phi_{y,x} \end{aligned} \tag{4.2.5}$$

Additionally, using the analogy with the deformation terms due to bending, which vary with z, the curvature κ_{zz} was introduced in (4.2.4):

$$\kappa_{zz} = \varepsilon_{zz}^{(1)}/(t/2) \tag{4.2.6}$$

Constitutive equations

The Hooke's relations for the 3d linear elastic material are:

$$\begin{aligned} \sigma_{xx} &= (\lambda + 2\mu)\varepsilon_{xx} + \lambda\varepsilon_{yy} + \lambda\varepsilon_{zz}; & \sigma_{xy} &= 2\mu\varepsilon_{xy} \\ \sigma_{yy} &= (\lambda + 2\mu)\varepsilon_{yy} + \lambda\varepsilon_{xx} + \lambda\varepsilon_{zz}; & \sigma_{xz} &= 2\mu\varepsilon_{xz} \\ \sigma_{zz} &= (\lambda + 2\mu)\varepsilon_{zz} + \lambda\varepsilon_{xx} + \lambda\varepsilon_{yy}; & \sigma_{yz} &= 2\mu\varepsilon_{yz} \end{aligned} \tag{4.2.7}$$

Equilibrium equations

Equilibrium equations will be presented in the next section in their weak form.

4.2.2 Principle of virtual work

Virtual work of internal forces

The virtual work of internal forces that takes into account also kinematic and constitutive equations, is defined by

$$\delta\Pi^{int}(w, \boldsymbol{\phi}, \varepsilon_{zz}^{(0)}, \kappa_{zz}; \delta w, \delta\boldsymbol{\phi}, \delta\varepsilon_{zz}^{(0)}, \delta\kappa_{zz}) = \int_V \delta\boldsymbol{\varepsilon}^T \boldsymbol{\sigma} \mathrm{d}\Omega = \tag{4.2.8}$$
$$\int_\Omega \int_{-t/2}^{t/2} (\sigma_{xx}\delta\varepsilon_{xx} + \sigma_{yy}\delta\varepsilon_{yy} + \sigma_{zz}\delta\varepsilon_{zz} + \sigma_{xy}2\delta\varepsilon_{xy} + \sigma_{xz}2\delta\varepsilon_{xz} + \sigma_{yz}2\delta\varepsilon_{yz})\, \mathrm{d}z\mathrm{d}\Omega$$

where $\boldsymbol{\sigma} = [\sigma_{xx}, \sigma_{yy}, \sigma_{zz}, \sigma_{xy}, \sigma_{xz}, \sigma_{yz}]^T$ are defined through (4.2.4), (4.2.5) and (4.2.7) in terms of kinematic quantities and $\delta\boldsymbol{\varepsilon} = [\delta\varepsilon_{xx}, \delta\varepsilon_{yy}, \delta\varepsilon_{zz}, 2\delta\varepsilon_{xy}, 2\delta\varepsilon_{xz}, 2\delta\varepsilon_{yz}]^T$ are virtual strains defined in terms of virtual kinematic quantities $\delta w, \delta\boldsymbol{\phi}, \delta\varepsilon_{zz}^{(0)}, \delta\kappa_{zz}$ in the same manner as real strains are defined in terms of real kinematic quantities (4.2.4), (4.2.7).

$$\begin{aligned} m_{xx} &= \int_{-t/2}^{t/2} z\sigma_{xx}\mathrm{d}z; & m_{yy} &= \int_{-t/2}^{t/2} z\sigma_{yy}\mathrm{d}z; & m_{xy} &= \int_{-t/2}^{t/2} z\sigma_{xy}\mathrm{d}z \\ q_x &= \int_{-t/2}^{t/2} \sigma_{xz}\mathrm{d}z; & q_y &= \int_{-t/2}^{t/2} \sigma_{yz}\mathrm{d}z \end{aligned} \tag{4.2.9}$$

$$m_{zz} = \int_{-t/2}^{t/2} z\sigma_{zz}\mathrm{d}z; \quad n_{zz} = \int_{-t/2}^{t/2} \sigma_{zz}\mathrm{d}z \tag{4.2.10}$$

After through the thickness integration of (4.2.8) and use of some algebraic manipulations, we arrive at the following expression for the virtual work of internal forces:

$$\delta\Pi^{int} = \int_\Omega \left(\delta\tilde{\boldsymbol{\kappa}}^T\tilde{\boldsymbol{m}} + \delta\tilde{\boldsymbol{\gamma}}^T\tilde{\boldsymbol{q}} + \delta\varepsilon_{zz}^{(0)}n_{zz}\right)\mathrm{d}\Omega \tag{4.2.11}$$

$$\delta\Pi^{int} = \delta\Pi_\kappa^{int} + \delta\Pi_\gamma^{int} + \delta\Pi_{zz}^{int}$$

$$\delta\Pi_\kappa^{int} = \int_\Omega \delta\tilde{\boldsymbol{\kappa}}^T\tilde{\boldsymbol{m}}\,\mathrm{d}\Omega; \quad \delta\Pi_\gamma^{int} = \int_\Omega \delta\tilde{\boldsymbol{\gamma}}^T\tilde{\boldsymbol{q}}\,\mathrm{d}\Omega; \quad \delta\Pi_{zz}^{int} = \int_\Omega \delta\varepsilon_{zz}^{(0)}n_{zz}\,\mathrm{d}\Omega$$

where $\tilde{\boldsymbol{m}} = [m_{xx}, m_{yy}, m_{xy}, m_{zz}]^T$ and $\delta\tilde{\boldsymbol{\kappa}} = [\delta\kappa_{xx}, \delta\kappa_{yy}, \delta\kappa_{xy}, \delta\kappa_{zz}]^T$. The vectors $\delta\tilde{\boldsymbol{\gamma}}$ and $\delta\tilde{\boldsymbol{q}}$ represent virtual strains and shear forces respectively. Their definition will be given below.

The components of $\tilde{\boldsymbol{m}}$ are related to the curvatures $\tilde{\boldsymbol{\kappa}} = [\kappa_{xx}, \kappa_{yy}, \kappa_{xy}, \kappa_{zz}]^T$ through (constitutive (4.2.14) and kinematic (4.2.4) equations are used in (4.2.9), (4.2.10))

$$\begin{aligned} m_{xx} &= \frac{t^3}{12}\left((\lambda+2\mu)\kappa_{xx} + \lambda\kappa_{yy} + \lambda\kappa_{zz}\right) \\ m_{yy} &= \frac{t^3}{12}\left((\lambda+2\mu)\kappa_{yy} + \lambda\kappa_{xx} + \lambda\kappa_{zz}\right) \\ m_{zz} &= \frac{t^3}{12}\left((\lambda+2\mu)\kappa_{zz} + \lambda\kappa_{xx} + \lambda\kappa_{yy}\right) \\ m_{xy} &= \frac{t^3}{12}\mu\kappa_{xy} \end{aligned} \tag{4.2.12}$$

and the stress resultant n_{zz} is related to $\varepsilon_{zz}^{(0)}$ through

$$n_{zz} = t(\lambda+2\mu)\varepsilon_{zz}^{(0)} = \mathrm{C}_Z\varepsilon_{zz}^{(0)}; \quad \mathrm{C}_Z = t(\lambda+2\mu) \tag{4.2.13}$$

In matrix notation the constitutive matrix is

$$\tilde{\mathbf{C}}_B = \frac{t^3}{12}\begin{bmatrix} (\lambda+2\mu) & \lambda & 0 & \lambda \\ \lambda & (\lambda+2\mu) & 0 & \lambda \\ 0 & 0 & \mu & 0 \\ \lambda & \lambda & 0 & (\lambda+2\mu) \end{bmatrix} \tag{4.2.14}$$

which allows for the relations (4.2.12) to be expressed in a compact form:

$$\tilde{\boldsymbol{m}} = \tilde{\mathbf{C}}_B\tilde{\boldsymbol{\kappa}} \tag{4.2.15}$$

In order to make the the theory more comparable to the Reissner/Mindlin one, we decide to make the following decomposition of κ_{zz}:

$$\kappa_{zz} = \kappa_{zz}^{(0)} + \kappa_{zz}^{(1)}; \quad \kappa_{zz}^{(0)} = -\frac{\lambda}{\lambda+2\mu}(\kappa_{xx}+\kappa_{yy}) = \frac{-\nu}{1-\nu}(\kappa_{xx}+\kappa_{yy}) \tag{4.2.16}$$

Since we have

$$\begin{aligned}\varepsilon_{zz} &= \varepsilon_{zz}^{(0)} - z\kappa_{zz} = \varepsilon_{zz}^{(0)} \overbrace{-\frac{\lambda}{\lambda+2\mu}(\varepsilon_{xx}+\varepsilon_{yy})}^{-z\kappa_{zz}^{(0)}} - z\kappa_{zz}^{(1)} \\ \varepsilon_{zz}^{(1)} &= (t/2)\kappa_{zz} = (t/2)(\kappa_{zz}^{(0)} + \kappa_{zz}^{(1)})\end{aligned} \tag{4.2.17}$$

the decomposition leads to plane stress assumption $\sigma_{zz} = 0$, if $\varepsilon_{zz}^{(0)} = 0$ and $\kappa_{zz}^{(1)} = 0$. According to (4.2.3), the kinematics of stretch becomes:

$$u_z = w + \varepsilon_{zz}^{(0)} z + \frac{1}{2}\frac{\nu}{1-\nu}(\kappa_{xx}+\kappa_{yy})z^2 - \frac{1}{2}\kappa_{zz}^{(1)} z^2 \tag{4.2.18}$$

By using (4.2.18), eq. (4.2.11) can be simplified to:

$$\delta\Pi_\kappa^{int} = \int_\Omega \delta\tilde{\boldsymbol{\kappa}}^T \tilde{\boldsymbol{m}} \mathrm{d}\Omega = \int_\Omega \delta\tilde{\boldsymbol{\kappa}}^T \tilde{\mathbf{C}}_B \tilde{\boldsymbol{\kappa}}\, \mathrm{d}\Omega = \delta\Pi_\kappa^{int,RM} + \delta\Pi_\kappa^{int,\Delta} \tag{4.2.19}$$

$$\delta\Pi_\kappa^{int,RM} = \int_\Omega \delta\boldsymbol{\kappa}\mathbf{C}_B\boldsymbol{\kappa}\, \mathrm{d}\Omega; \quad \delta\Pi_\kappa^{int,\Delta} = \int_\Omega \delta\kappa_{zz}^{(1)} \mathrm{C}_{B,zz} \kappa_{zz}^{(1)} \mathrm{d}\Omega$$

where $\boldsymbol{\kappa} = [\kappa_{xx}, \kappa_{yy}, \kappa_{xy}]^T$ and $\mathbf{C}_B$ is the constitutive matrix as defined in (2.2.13). Additionally, we have $\mathrm{C}_{B,zz} = \frac{Et^3(1-\nu)}{12(1+\nu)(1-2\nu)} = D\frac{(1-\nu)^2}{(1-2\nu)}$, where $D = \frac{Et^3}{12(1-\nu^2)}$.

Next, the expanded shear strain vector is introduced, see (4.2.4)

$$\tilde{\boldsymbol{\gamma}} = [\gamma_x, \gamma_y, \gamma_x^{(1)}, \gamma_y^{(1)}, \gamma_x^{(2)}, \gamma_y^{(2)}]^T \tag{4.2.20}$$

where

$$[2\varepsilon_{xz}, 2\varepsilon_{yz}]^T = \boldsymbol{\gamma} + \bar{z}\boldsymbol{\gamma}^{(1)} + \frac{\bar{z}^2}{2}\boldsymbol{\gamma}^{(2)}; \quad \bar{z} = z/(t/2) \tag{4.2.21}$$

$$\begin{aligned}[\gamma_x, \gamma_y]^T &= \boldsymbol{\gamma} = \nabla w - \boldsymbol{\phi} \\ [\gamma_x^{(1)}, \gamma_y^{(1)}]^T &= \boldsymbol{\gamma}^{(1)} = (t/2)\nabla\varepsilon_{zz}^{(0)} \\ [\gamma_x^{(2)}, \gamma_y^{(2)}]^T &= \boldsymbol{\gamma}^{(2)} = -\,(t/2)\,\nabla\varepsilon_{zz}^{(1)}\end{aligned}$$

The components of the shear force vector $\tilde{\boldsymbol{q}} = [q_x, q_y, q_x^{(1)}, q_y^{(1)}, q_x^{(2)}, q_y^{(2)}]^T$ are obtained from (4.2.9) as:

$$\boldsymbol{q} = c\mu t\left(\boldsymbol{\gamma} + \boldsymbol{\gamma}^{(2)}/6\right); \quad \boldsymbol{q}^{(1)} = c\mu t\left(\boldsymbol{\gamma}^{(1)}/3\right); \quad \boldsymbol{q}^{(2)} = c\mu t\left(\boldsymbol{\gamma}/6 + \boldsymbol{\gamma}^{(2)}/20\right) \tag{4.2.22}$$

where

$$\sigma_{xz} = c\,\mu\,2\varepsilon_{xz}; \quad \sigma_{yz} = c\,\mu\,2\varepsilon_{yz} \tag{4.2.23}$$

was used and the shear correction factor is denoted by c (which should have different value than 5/6, derived in chapter 3). They can also be expressed in a compact form:

$$\tilde{\boldsymbol{q}} = \tilde{\mathbf{C}}_S \tilde{\boldsymbol{\gamma}} \tag{4.2.24}$$

where the block matrix $\tilde{\mathbf{C}}_S$ is defined as

$$\tilde{\mathbf{C}}_S = c\mu t \begin{bmatrix} \mathbb{1}_{2\times 2} & \mathbf{0} & \frac{1}{6}\mathbb{1}_{2\times 2} \\ \mathbf{0} & \frac{1}{3}\mathbb{1}_{2\times 2} & \mathbf{0} \\ \frac{1}{6}\mathbb{1}_{2\times 2} & \mathbf{0} & \frac{1}{20}\mathbb{1}_{2\times 2} \end{bmatrix} \tag{4.2.25}$$

and $\mathbb{1}_{2\times 2}$ denotes the 2×2 identity matrix. The term contributing to the virtual work (second term on the rhs of (4.2.11)) is thus:

$$\delta\Pi_\gamma^{int} = \int_\Omega \tilde{\boldsymbol{\gamma}} \delta \tilde{\boldsymbol{q}}^T \mathrm{d}\Omega = \delta\Pi_\gamma^{int,RM} + \delta\Pi_\gamma^{int,\Delta} \tag{4.2.26}$$

where

$$\delta\Pi_\gamma^{int,RM} = \int_\Omega \delta\boldsymbol{\gamma}^T \mathbf{C}_S \boldsymbol{\gamma}\, \mathrm{d}\Omega; \quad \delta\Pi_\gamma^{int,\Delta} = \int_\Omega \delta\tilde{\boldsymbol{\gamma}}^T \bar{\mathbf{C}}_S \tilde{\boldsymbol{\gamma}}\, \mathrm{d}\Omega \tag{4.2.27}$$

and

$$\delta\gamma = [\delta\gamma_x, \delta\gamma_y]^T; \tag{4.2.28}$$

$$\delta\tilde{\gamma} = [\delta\gamma_x, \delta\gamma_y, \delta\gamma_x^{(1)}, \delta\gamma_y^{(1)}, \delta\gamma_x^{(2)}, \delta\gamma_y^{(2)}]^T \tag{4.2.29}$$

$$\bar{\mathbf{C}}_S = c\mu t \begin{bmatrix} \mathbf{0} & \mathbf{0} & \frac{1}{6}\mathbb{1}_{2\times 2} \\ \mathbf{0} & \frac{1}{3}\mathbb{1}_{2\times 2} & \mathbf{0} \\ \frac{1}{6}\mathbb{1}_{2\times 2} & \mathbf{0} & \frac{1}{20}\mathbb{1}_{2\times 2} \end{bmatrix} \tag{4.2.30}$$

With the notation introduced above, the virtual work of internal forces (4.2.11) is expressed hierarchically as:

$$\delta\Pi^{int} = \delta\Pi_\kappa^{int} + \delta\Pi_\gamma^{int} + \delta\Pi_{zz}^{int} = \delta\Pi^{int,RM} + \delta\Pi_\kappa^{int,\Delta} + \delta\Pi_\gamma^{int,\Delta} + \delta\Pi_{zz}^{int} \tag{4.2.31}$$

where

$$\delta\Pi^{int,RM} = \int_\Omega \left(\delta\boldsymbol{\kappa}^T \mathbf{C}_B \boldsymbol{\kappa} + \delta\boldsymbol{\gamma}^T \mathbf{C}_S \boldsymbol{\gamma}\right) \mathrm{d}\Omega = \delta\Pi_\kappa^{int,RM} + \delta\Pi_\gamma^{int,RM} \tag{4.2.32}$$

and $\delta\Pi_\gamma^{int,\Delta}$ is given in (4.2.28), $\delta\Pi_\kappa^{int,\Delta}$ is given in (4.2.8) and $\delta\Pi_{zz}^{int}$ is given in (4.2.11).

Virtual work of external forces

The external forces (boundary tractions) act on the boundary surface(s) of the plate: the upper and bottom surfaces of the plate (commonly indicated by Ω^+ and Ω^-) and the side surface of the plate (indicated by Γ):

$$\delta\Pi^{ext} = \delta\Pi^{ext,\Omega} + \delta\Pi^{ext,\Gamma} \tag{4.2.33}$$

The tractions acting on the side of the plate $\overline{\boldsymbol{t}}$ are assumed to be constant over the plate thickness, therefore the traction load can be integrated through the thickness and presented in form of normal moment $\overline{m}_n$, twisting moment $\overline{m}_s$ and shear force $\overline{q}_n$:

$$\delta\Pi^{ext,\Gamma}(\delta w, \delta\boldsymbol{\phi}) = \int_\Gamma \int_{-t/2}^{t/2} \delta\boldsymbol{u}^T \overline{\boldsymbol{t}}\, \mathrm{d}z\, \mathrm{d}s = \tag{4.2.34}$$
$$\int_\Gamma (\delta w \overline{q}_n + \delta\theta_n \overline{m}_n + \delta\theta_s \overline{m}_s)\mathrm{d}s = \int_\Gamma (\delta w \bar{q}_n + \delta\boldsymbol{\theta}\, \overline{\boldsymbol{m}})\, \mathrm{d}s$$

Since the top (+) and bottom (-) of the plate are distinguished in the higher-order model, the distributed surface load can in general act on one or both surfaces (note that $u_z = w + \varepsilon_{zz}^{(0)} z - \frac{1}{2}\kappa_{zz} z^2$)

$$\delta\Pi^{ext,\Omega}(\delta w, \delta\varepsilon_{zz}^{(0)}, \delta\kappa_{zz}) = \int_{\Omega^+} f^+ \delta u_z^+\, \mathrm{d}\Omega + \int_{\Omega^-} f^- \delta u_z^-\, \mathrm{d}\Omega + = \tag{4.2.35}$$
$$\int_{\Omega^+} f^+ (\delta w + \frac{t}{2}\delta\varepsilon_{zz}^{(0)} - \frac{t^2}{8}\delta\kappa_{zz})\mathrm{d}\Omega + \int_{\Omega^-} f^- (\delta w - \frac{t}{2}\delta\varepsilon_{zz}^{(0)} - \frac{t^2}{8}\delta\kappa_{zz})\mathrm{d}\Omega$$

4.3 Finite elements

4.3.1 Higher-order plate elements

Since our aim is to build a hierarchic family of plate finite elements (in the model sense), the higher-order finite elements are built on the basis of P3 elements derived in chapter 3. They are designated by PZ.

Discretization

The transverse displacement w and the rotations $\boldsymbol{\phi}$ are interpolated using the same discretization as in the case of P3 elements. Additionally, the fields $\varepsilon_{zz}^{(0)}$ and $\kappa_{zz}^{(1)}$ are to be

discretized. A bilinear discretization of both fields is assumed:

$$\varepsilon^{(0)}_{zz,h} = \sum_I N_I \hat{\varepsilon}^{(0)}_{zz,I}; \quad \kappa^{(1)}_{zz,h} = \sum_I N_I \hat{\kappa}^{(1)}_{zz,I} \tag{4.3.1}$$

where $\hat{\varepsilon}^{(0)}_{zz,I}$ and $\hat{\kappa}^{(1)}_{zz,I}$ are the additional nodal degrees of freedom. The vertex degrees of freedom of the PZ element are thus $\hat{\boldsymbol{u}}_I = [w_I, \theta_{x,I}, \theta_{y,I}, \varepsilon^{(0)}_{zz,I}, \kappa^{(1)}_{zz,I}]^T$ and the midside degrees of freedom are $\hat{\boldsymbol{u}}_{IJ} = [\gamma_{IJ}]$. The elements have nen vertex nodes and nen midside nodes (nen=4 for the quadrilateral, and $nen = 3$ for triangular elements). The vertex nodes are numbered as $I = 1, \ldots, nen$, the midside nodes as $IJ = (nen + 1), \ldots, 2\,nen$. Element degrees of freedom are arranged into $\hat{\boldsymbol{u}} = [\hat{\boldsymbol{u}}^T_1, \cdots, \hat{\boldsymbol{u}}^T_{nen}, \hat{\boldsymbol{u}}^T_{nen+1}, \cdots, \hat{\boldsymbol{u}}^T_{2\,nen}]^T$.

The interpolations can be expressed as:

$$\begin{aligned}
\boldsymbol{\kappa}_h &= \sum_I \mathbf{B}_{\kappa,I}\hat{\boldsymbol{u}}_I + \sum_{IJ} \mathbf{B}_{\kappa,IJ}\hat{\boldsymbol{u}}_{IJ}; & \boldsymbol{\gamma}_h &= \sum_{IJ} \mathbf{B}_{\gamma,IJ}\hat{\boldsymbol{u}}_{IJ}; \\
\varepsilon^{(0)}_{zz,h} &= \sum_I \mathbf{B}_{\varepsilon^{(0)}_{zz},I}\hat{\boldsymbol{u}}_I; & \boldsymbol{\gamma}^{(1)}_h &= \sum_I \mathbf{B}_{\gamma^{(1)},I}\hat{\boldsymbol{u}}_I; \\
\kappa^{(1)}_{zz,h} &= \sum_I \mathbf{B}_{\kappa^{(1)}_{zz},I}\hat{\boldsymbol{u}}_I; & \boldsymbol{\gamma}^{(2)}_h &= \sum_I \mathbf{B}_{\gamma^{(2)},I}\hat{\boldsymbol{u}}_I + \sum_{IJ} \mathbf{B}_{\gamma^{(2)},IJ}\hat{\boldsymbol{u}}_{IJ}
\end{aligned} \tag{4.3.2}$$

where

$$\begin{aligned}
\boldsymbol{\kappa}_h &= [\kappa_{xx,h}, \kappa_{yy,h}, \kappa_{xy,h}]^T; \quad \boldsymbol{\gamma}_h = [\gamma_{x,h}, \gamma_{y,h}]^T \\
\boldsymbol{\gamma}^{(1)}_h &= \frac{t}{2}\left[\frac{\partial \varepsilon^{(0)}_{zz,h}}{\partial x}, \frac{\partial \varepsilon^{(0)}_{zz,h}}{\partial y}\right]^T; \quad \boldsymbol{\gamma}^{(2)}_h = \frac{t}{2}\left[\frac{\partial \varepsilon^{(1)}_{zz,h}}{\partial x}, \frac{\partial \varepsilon^{(1)}_{zz,h}}{\partial y}\right]^T
\end{aligned} \tag{4.3.3}$$

The following definitions apply:

$$\mathbf{B}_{\kappa,I} = [\mathbf{B}_{\kappa_{xx},I}, \mathbf{B}_{\kappa_{yy},I}, \mathbf{B}_{\kappa_{xy},I}]^T = [\mathbf{B}^{P3}_{\kappa,I}, \mathbf{0}_{3\times 2}]; \tag{4.3.4}$$

$$\mathbf{B}_{\kappa,IJ} = \mathbf{B}^{P3}_{\kappa,IJ}; \quad \mathbf{B}_{\gamma,IJ} = \mathbf{B}^{P3}_{\gamma,IJ}$$

$$\mathbf{B}_{\kappa^{(1)}_{zz},I} = [0,0,0,0,N_I]; \quad \mathbf{B}_{\varepsilon^{(0)}_{zz},I} = [0,0,0,N_I,0]$$

$$\mathbf{B}_{\gamma^{(1)},I} = (t/2)\begin{bmatrix} 0 & 0 & 0 & N_{I,x} & 0 \\ 0 & 0 & 0 & N_{I,y} & 0 \end{bmatrix}$$

$$\mathbf{B}_{\gamma^{(2)},I} = \mathbf{B}^{(0)}_{\gamma^{(2)},I} + \mathbf{B}^{(1)}_{\gamma^{(2)},I}$$

$$\mathbf{B}^{(0)}_{\gamma^{(2)},I} = -\frac{\nu}{1-\nu}(t/2)^2 \begin{bmatrix} \frac{\partial}{\partial x}(\mathbf{B}_{\kappa_{xx},I} + \mathbf{B}_{\kappa_{yy},I}) \\ \frac{\partial}{\partial y}(\mathbf{B}_{\kappa_{xx},I} + \mathbf{B}_{\kappa_{yy},I}) \end{bmatrix}$$

$$\mathbf{B}^{(1)}_{\gamma^{(2)},I} = -(t/2)^2 \begin{bmatrix} 0 & 0 & 0 & 0 & N_{I,x} \\ 0 & 0 & 0 & 0 & N_{I,y} \end{bmatrix}$$

$$\mathbf{B}_{\gamma^{(2)},IJ} = -\frac{\nu}{1-\nu}(t/2)^2 \begin{bmatrix} \frac{\partial}{\partial x}(\mathbf{B}_{\kappa_{xx},IJ} + \mathbf{B}_{\kappa_{yy},IJ}) \\ \frac{\partial}{\partial y}(\mathbf{B}_{\kappa_{xx},IJ} + \mathbf{B}_{\kappa_{yy},IJ}) \end{bmatrix}$$

Stiffness matrix

The stiffness matrix $\mathbf{K}$ of PZ element is obtained by inserting the discretization (4.3.2) into (4.2.11) and taking into account the constitutive relations (4.2.13), (4.2.15) and (4.2.24). It consists of three parts, which correspond to bending stiffness, shear stiffness and the through-the-thickness stretching stiffness:

$$\mathbf{K} = \mathbf{K}^B + \mathbf{K}^S + \mathbf{K}^Z \tag{4.3.5}$$

The stiffness matrix is expressed as a block matrix $\mathbf{K} = [\mathbf{K}_{ij}]$, where blocks $\mathbf{K}_{ij}$ correspond to the interaction of degrees of freedom of nodes i and j. The stiffness matrix is expressed as a block matrix $\mathbf{K} = [\mathbf{K}_{ij}]$, where blocks $\mathbf{K}_{ij}$ correspond to the interaction of degrees of freedom of nodes i and j. The indexes referring to the vertex node are denoted by I and J. The indexes IJ and KL are used to denote the midside nodes. The stiffness matrix is then organized as:

$$\mathbf{K} = \begin{bmatrix} [\mathbf{K}_{I,J}] & [\mathbf{K}_{I,KL}] \\ [\mathbf{K}_{IJ,J}] & [\mathbf{K}_{IJ,KL}] \end{bmatrix} \tag{4.3.6}$$

According to the (4.2.19), the bending stiffness $\mathbf{K}^B_{ij}$ is a sum of two components

$$\mathbf{K}^B_{ij} = \mathbf{K}^{B,0}_{ij} + \mathbf{K}^{B,\Delta}_{ij}$$

where

$$\mathbf{K}^{B,0}_{ij} = \int_\Omega \mathbf{B}^T_{\kappa,i}\mathbf{C}_B\mathbf{B}_{\kappa,j}\,\mathrm{d}\Omega; \qquad \mathbf{K}^{B,\Delta}_{ij} = \int_\Omega \mathbf{B}^T_{\kappa^{(1)}_{zz},i}\mathrm{C}_{B,zz}\mathbf{B}_{\kappa^{(1)}_{zz},j}\,\mathrm{d}\Omega \tag{4.3.7}$$

Notice that, since $\mathbf{B}_{\kappa,I} = [\mathbf{B}^{P3}_{\kappa,I}, \mathbf{0}_{3\times 2}]$, the matrix $\mathbf{K}^{B,0}_{I,J}$ corresponds to the bending stiffness matrix of P3 elements.

$$\mathbf{K}^{B,0}_{I,J} = \int_{\Omega^e} \mathbf{B}^T_{\kappa,I}\mathbf{C}_B\mathbf{B}_{\kappa,J}\mathrm{d}\Omega = \begin{bmatrix} \mathbf{K}^{B,P3}_{I,J} & \mathbf{0}_{3\times 2} \\ \mathbf{0}_{2\times 3} & \mathbf{0}_{2\times 2} \end{bmatrix} \tag{4.3.8}$$

Since the interpolation of $\kappa^{(1)}_{zz}$ is independent of all degrees of freedom other than $\kappa^{(1)}_{zz,i}$, the deformation mode $\kappa^{(1)}_{zz}$ is independent of bending. The block matrix $\mathbf{K}^{B,\Delta}_{I,J}$ is thus:

$$\mathbf{K}^{B,\Delta}_{I,J} = \begin{bmatrix} \mathbf{0}_{4\times 4} & \mathbf{0}_{4\times 1} \\ \mathbf{0}_{1\times 4} & \mathrm{K}_{\kappa^{(1)}_{zz},I,J} \end{bmatrix} \tag{4.3.9}$$

where

$$\mathrm{K}_{\kappa^{(1)}_{zz},I,J} = \int_\Omega \mathbf{B}^T_{\kappa^{(1)}_{zz},I}\mathrm{C}_{B,zz}\mathbf{B}_{\kappa^{(1)}_{zz},J}\,\mathrm{d}\Omega = \int_\Omega \mathrm{C}_{B,zz}N_I N_J\mathrm{d}\Omega \tag{4.3.10}$$

Similarly, from (4.2.26), (4.2.27), we can decompose the shear part of the stiffness matrix into

$$\mathbf{K}^S = \mathbf{K}^{S,0} + \mathbf{K}^{S,\Delta}$$

where (according to (4.2.26), (4.3.2))

$$\mathbf{K}^{S,0}_{ij} = \int_\Omega \mathbf{B}^T_{\gamma,i}\mathbf{C}_S\mathbf{B}_{\gamma,j}\,\mathrm{d}\Omega \tag{4.3.11}$$

and

$$\begin{aligned}\mathbf{K}^{S,\Delta}_{ij} =& \frac{1}{3}\int_\Omega \mathbf{B}^T_{\gamma^{(1)},i}\mathbf{C}_S\mathbf{B}_{\gamma^{(1)},j}\,\mathrm{d}\Omega + \frac{1}{20}\int_\Omega \mathbf{B}^T_{\gamma^{(2)},i}\mathbf{C}_S\mathbf{B}_{\gamma^{(2)},j}\,\mathrm{d}\Omega + \\ & \frac{1}{6}\int_\Omega \mathbf{B}^T_{\gamma,i}\mathbf{C}_S\mathbf{B}_{\gamma^{(2)},j}\,\mathrm{d}\Omega + \frac{1}{6}\int_\Omega \mathbf{B}^T_{\gamma^{(2)},i}\mathbf{C}_S\mathbf{B}_{\gamma,j}\,\mathrm{d}\Omega\end{aligned}$$

The part $\mathbf{K}^{S,\Delta}_{ij}$ corresponds to the contribution of the through the thickness stretching to the shear deformation.

Notice, that the block matrix $\mathbf{K}^{S,0}_{IJ,KL}$ corresponds to the shear stiffness matrix of P3 elements (4.3.2)

$$\mathbf{K}^{S,0}_{IJ,KL} = \int_{\Omega^e} \mathbf{B}^T_{\gamma,IJ}\mathbf{C}_S\mathbf{B}_{\gamma,KL}\mathrm{d}\Omega = \int_{\Omega^e} \mathbf{B}^{P3,T}_{\gamma,IJ}\mathbf{C}_S\mathbf{B}^{P3}_{\gamma,KL}\mathrm{d}\Omega = \mathbf{K}^{S,P3}_{IJ,KL} \tag{4.3.12}$$

and

$$\mathbf{K}^{S,0}_{I,J} = \mathbf{0}_{5\times5}; \quad \mathbf{K}^{S,0}_{I,KL} = \mathbf{0}_{5\times1}; \quad \mathbf{K}^{S,0}_{IJ,J} = \mathbf{0}_{1\times5}$$

The part of the stiffness matrix, which directly corresponds to the through the thickness stretching $\mathbf{K}^Z$ is a block matrix

$$\mathbf{K}^Z_{I,J} = \int_{\Omega} \mathbf{B}^T_{\varepsilon^{(0)}_{zz},I}\mathbf{C}_Z\mathbf{B}_{\varepsilon^{(0)}_{zz},J}\,\mathrm{d}\Omega; \quad \mathbf{K}^Z_{IJ,J} = \mathbf{0}_{1\times5}; \quad \mathbf{K}^Z_{I,KL} = \mathbf{0}_{5\times1}; \quad \mathbf{K}^Z_{IJ,KL} = \mathbf{0}_{1\times1}$$

Load vector

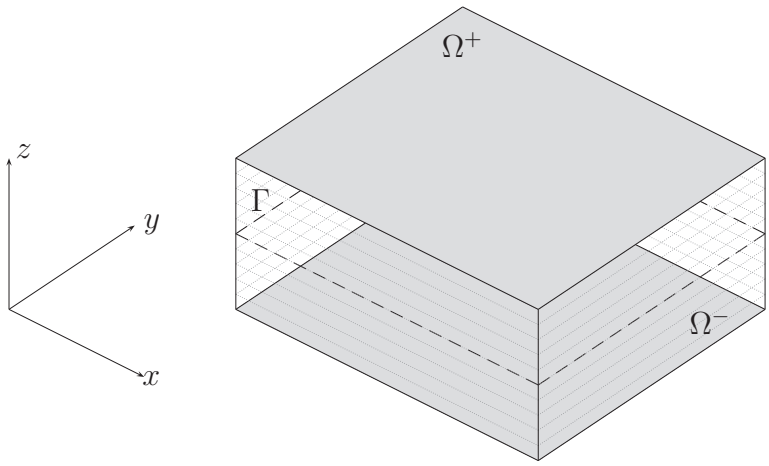

Figure 4.3.1: Designation of plate surfaces Ω^+, Ω^- and Γ
Slika 4.3.1: Oznaka površin Ω^+, Ω^- in Γ

The load vector $\boldsymbol{f}$ is revealed by inserting the discretization (4.3.2) into (4.2.34) and (4.2.35). Since we distinguish between the top and bottom surface (see Figure 4.3.1) Ω^+ and Ω^-, the load vector consists of three parts $\boldsymbol{f} = \boldsymbol{f}_{f^+} + \boldsymbol{f}_{f^-} + \boldsymbol{f}_{\bar{t}}$, where

$$\boldsymbol{f}_{f^\pm} = \int_{\Omega^e} f^\pm\left(\mathbf{B}_w \pm \frac{t}{2}\mathbf{B}_{\varepsilon^{(0)}_{zz}} + \frac{t^2}{8}\mathbf{B}_{\kappa_{zz}}\right)\mathrm{d}\Omega; \tag{4.3.13}$$
$$\boldsymbol{f}_{\bar{t}} = \int_{\Gamma_{Ne}} \left(\bar{q}\mathbf{B}_w + \overline{\boldsymbol{m}}^T\mathbf{B}_\theta\right)\mathrm{d}s$$

4.4 Hierarchy of derived plate elements

The hierarchy (in the model sense) can be observed through the comparison of the kinematics of the elements derived in chapters 2, 3 and 4. All the interpolations make use of the same shape functions defined in (2.3.74) and (2.3.71) (shown in Figure 2.3.13 and Figure 2.3.14).

DK plate element

The element has *nen* vertex nodes with the degrees of freedom $\hat{\boldsymbol{u}}_I = [\hat{w}_I, \hat{\theta}_{x,I}, \hat{\theta}_{y,I}]^T$. The interpolations of the displacement and rotation are:

$$w_h^{DK} = \sum_I \hat{w}_I N_I + \sum_{IJ} (\hat{w}_{3,IJ} N_{IJ} + \hat{w}_{4,IJ} M_{IJ}) \tag{4.4.1}$$

$$\boldsymbol{\theta}_h^{DK} = \sum_{I=1}^{3} \hat{\boldsymbol{\theta}}_I N_I + \sum_{IJ} \hat{\boldsymbol{\theta}}_{3,IJ} \boldsymbol{n}_{IJ} N_{IJ}$$

$$\hat{\boldsymbol{\theta}}_{3,IJ} = \frac{6}{L} \hat{w}_{4,IJ}; \quad \hat{w}_{3,IJ} = \frac{L_{IJ}}{8} \boldsymbol{n}_{IJ} \cdot (\hat{\boldsymbol{\theta}}_I - \hat{\boldsymbol{\theta}}_J);$$
$$\hat{w}_{4,IJ} = \frac{L_{IJ}}{4} (\frac{\hat{w}_J - \hat{w}_I}{L_{IJ}} - \frac{1}{2} \boldsymbol{n}_{IJ} \cdot (\hat{\boldsymbol{\theta}}_I + \hat{\boldsymbol{\theta}}_J))$$

Using the given kinematic assumptions, the interpolation of curvature is computed directly through

$$\boldsymbol{\kappa}_h = [-\frac{\partial \theta_{y,h}}{\partial x}, \frac{\partial \theta_{x,h}}{\partial y}, \frac{\partial \theta_{x,h}}{\partial x} - \frac{\partial \theta_{y,h}}{\partial y}] \tag{4.4.2}$$

From the interpolation of rotation $\boldsymbol{\theta}_h^{DK}$, we have

$$\boldsymbol{\kappa}_h^{DK} = \sum_I \mathbf{B}_{\kappa,I}^{DK} \boldsymbol{u}_I; \quad \mathbf{B}_{\kappa,I}^{DK} \tag{4.4.3}$$

The transverse shear is neglected; bending is the only deformation mode.

P3 plate element

In addition to the *nen* vertex nodes with the degrees of freedom $\hat{\boldsymbol{u}}_I = [\hat{w}_I, \hat{\theta}_{x,I}, \hat{\theta}_{y,I}]^T$, the element has *nen* midside nodes with the degrees of freedom $\hat{\boldsymbol{u}}_{IJ} = [\hat{\gamma}_{IJ}]^T$. The

interpolations are

$$w_h^{P3} = w_h^{DK} - \sum_{IJ} \frac{1}{4} L_{IJ} \hat{\gamma}_{IJ} M_{IJ}; \tag{4.4.4}$$
$$\boldsymbol{\theta}_h^{P3} = \boldsymbol{\theta}_h^{DK} + \sum_{IJ} \frac{3}{2} \boldsymbol{n}_{IJ} \hat{\gamma}_{IJ} N_{IJ}$$

The curvature interpolation $\boldsymbol{\kappa}_h^{P3}$ is defined by the rotation $\boldsymbol{\theta}_h^{P3}$

$$\boldsymbol{\kappa}_h^{P3} = \boldsymbol{\kappa}_h^{DK} + \tilde{\boldsymbol{\kappa}}_h; \quad \tilde{\boldsymbol{\kappa}}_h = \sum_{IJ} \tilde{\mathbf{B}}_{\kappa,IJ} \boldsymbol{u}_{IJ}; \quad \tilde{\mathbf{B}}_{\kappa,IJ} \tag{4.4.5}$$

The interpolation of the transverse shear is:

$$\boldsymbol{\gamma}_h^{P3} = \sum_{I} N_I \hat{\boldsymbol{\gamma}}_{h,I} \tag{4.4.6}$$

where the nodal values $\hat{\boldsymbol{\gamma}}_{h,I}$ depend on the midside degrees of freedom $\hat{\gamma}_{IJ}$ according to

$$\hat{\boldsymbol{\gamma}}_{h,I} = \frac{\hat{\gamma}_{IK} \boldsymbol{n}_{IJ} - \hat{\gamma}_{IJ} \boldsymbol{n}_{IK}}{\boldsymbol{n}_{IJ} \cdot \boldsymbol{s}_{IK}} \tag{4.4.7}$$

Note, that the interpolation of the transverse shear conform to the assumed kinematics only along the sides of the element. At the element interior, an assumption of the variation of the transverse shear strain is made.

PZ plate element

Element has *nen* vertex nodes with the degrees of freedom $\hat{\boldsymbol{u}}_I = [\hat{w}_I, \hat{\theta}_{x,I}, \hat{\theta}_{y,I}, \hat{\varepsilon}_{zz,I}^{(0)}, \hat{\kappa}_{zz,I}^{(1)}]^T$, and *nen* midside nodes with the degrees of freedom $\hat{\boldsymbol{u}}_{IJ} = [\hat{\gamma}_{IJ}]^T$. The kinematics of the material point is interpolated as

$$\boldsymbol{u}_h^{PZ} = \boldsymbol{u}_h^{P3} + \boldsymbol{u}_h^{S} \tag{4.4.8}$$

$$\boldsymbol{u}_h^{P3} = w_h^{P3} \boldsymbol{n}_\Omega - z \boldsymbol{\phi}_h^{P3}; \quad \boldsymbol{u}_h^{S} = \left(\varepsilon_{zz}^{(0)} z - \varepsilon_{zz}^{(1)} z^2/t\right) \boldsymbol{n}_\Omega$$

$$\boldsymbol{n}_\Omega = [0, 0, 1]^T; \quad \boldsymbol{\phi}_h^{P3} = [\phi_{x,h}^{P3}, \phi_{y,h}^{P3}]^T = [-\theta_{y,h}^{P3}, +\theta_{x,h}^{P3}]^T$$

The curvature interpolation corresponds to the curvature interpolation of $P3$ element:

$$\boldsymbol{\kappa}_h^{PZ} = \boldsymbol{\kappa}_h^{P3} \tag{4.4.9}$$

The transverse shear is interpolated as

$$\boldsymbol{\gamma}_h^{PZ} = \boldsymbol{\gamma}_h^{P3} + \overline{z}\boldsymbol{\gamma}_h^{(1)} + \frac{\overline{z}^2}{2}\boldsymbol{\gamma}_h^{(2)}; \quad \overline{z} = \frac{z}{t/2} \tag{4.4.10}$$

$$\boldsymbol{\gamma}_h^{(1)} = \sum_I \mathbf{B}_{\boldsymbol{\gamma}^{(1)},I}\hat{u}_I;$$
$$\boldsymbol{\gamma}_h^{(2)} = \sum_I \mathbf{B}_{\boldsymbol{\gamma}^{(2)},I}\hat{u}_I + \sum_{IJ} \mathbf{B}_{\boldsymbol{\gamma}^{(2)},IJ}\hat{u}_{IJ}$$

The matrices $\mathbf{B}_{\boldsymbol{\gamma}^{(1)},I}$, $\mathbf{B}_{\boldsymbol{\gamma}^{(2)},I}$ and $\mathbf{B}_{\boldsymbol{\gamma}^{(2)},IJ}$ are defined in (4.3.4).

The discretizations of hrough the thickness deformation $\varepsilon_{zz,h}^{(0)}$ and $\kappa_{zz,h}^{(1)}$ are defined by (4.3.1):

$$\varepsilon_{zz,h}^{(0)} = \sum_I N_I\hat{\varepsilon}_{zz,I}^{(0)}; \quad \kappa_{zz,h}^{(1)} = \sum_I N_I\hat{\kappa}_{zz,I}^{(1)} \tag{4.4.11}$$

4.5 Examples

The selected problems are solved with the PZQ and PZT finite elements. Due to its hierarchical construction, the basic novelty of the solution, compared to those obtained with P3Q or P3T elements, can be described with fields $\varepsilon_{zz}^{(0)}$ and κ_{zz}. Both components have the strongest impact on the stress component σ_{zz} which varies through the thickness as

$$\sigma_{zz}(z) = (\lambda + 2\mu)(\varepsilon_{zz}^{(0)} - z\kappa_{zz}) + \lambda\varepsilon_{xx} + \lambda\varepsilon_{yy}$$

In the following, the quantities $\sigma_{zz}^{+} = \sigma_{zz}(t/2)$ and $\Delta\sigma_{zz} = (\lambda + 2\mu)\kappa_{zz}$ will be presented. Since in the following problems, the loading is applied on the top surface Ω^{+}, the value of σ_{zz}^{+} corresponds to the loading f. The quantity $\Delta\sigma_{zz}$ can be interpreted as the shift of midsurface relative to the surfaces Ω^{+} and Ω^{-} (see Figure 4.2.1).

4.5.1 Uniformly loaded simply supported square plate

The square plate of side length $a = 10$ and thickness $t = 1$ under uniform loading $f = 1$ is analyzed. The sides of the plate at $x = 0, a$ are hard simply supported, while the sides at $y = 0, a$ are soft simply supported. The material is linear elastic and isotropic, with Young's modulus $E = 10.92 \times 10^4$ and Poisson's ratio $\nu = 0.3$. The problem is identical to that analyzed already in section 3.4.1.

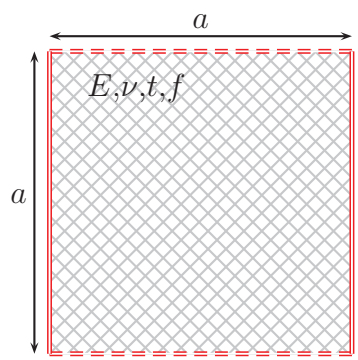

Figure 4.5.1: Problem definition and geometry for the uniformly loaded hard-soft simply supported square plate (t/a=1/10)
Slika 4.5.1: Definicija in geometrija problema enakomerno obremenjene togor-mehko prosto podprte plošče (t/a=1/10)

Finite element solutions on a regular mesh are shown in Figure 4.5.2. When compared to the solutions obtained with PQ3 and PT3 elements (see Figure 3.4.4) one notices, that the basic features of the PZQ/PZT solutions are captured qualitatively at the same level. The major difference is in the stress component σ_{zz}. The interpolation field $\Delta\sigma_{zz}$ indicates the shift of the position the midsurface relative to the plate surfaces.

4.5.2 Uniformly loaded soft simply supported L-shaped plate

Uniformly loaded soft simply supported L-shaped plate with the geometry shown in Figure 4.5.4 is analyzed. The side length is $a = 10$ and thickness of the plate $t = 1$. The material is linear elastic and isotropic, with Young's modulus $E = 10.92 \times 10^4$ and Poisson's ratio $\nu = 0.3$. The problem is identical to that presented in section 3.4.4.

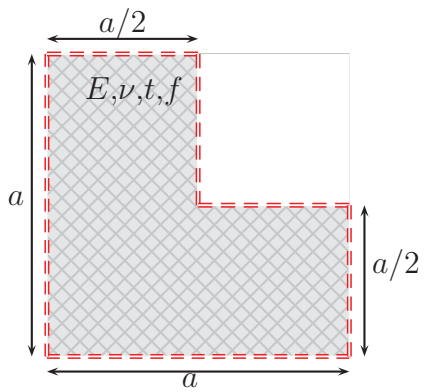

Figure 4.5.4: Problem definition and geometry for the uniformly loaded soft simply supported L shaped plate (t/a=1/10)
Slika 4.5.4: Definicija in geometrija problema enakomerno obremenjene mehko podprte L plošče (t/a=1/10)

The finite element solution on a regular mesh is shown in Figure 4.5.5. The solution captures both the singularity at the re-entrant corner as well as the boundary layers along the supports. In that sense, the solution is close to the solution obtained with the P3 elements (see Figure 3.4.19). However, the ability of PZ elements to take into account also the through-the-thickness stretching is manifested in the nonzero values of $\Delta\sigma_{zz}$. Notice, that the singularity at the re-entrant corner, while it significantly affects the moments and shear forces, it does not have a significant effect on $\Delta\sigma_{zz}$. In the interior of the plate,

the stress σ_{zz}^{+} follows the distribution of the area load f. At supports it is dominated by the reactions, as expected.

4.5.3 Simply supported square plate with load variation

The square plate of side length $a = 10$ and thickness $t = 1$ under uniform loading $f = 1$ is analyzed. The uniform loading on central square area of the plate ($b = 1$) is $f = 50$ (see Figure 4.5.7). The sides of the plate at $x = 0, a$ are hard simply supported, while the sides at $y = 0, a$ are soft simply supported. The material is linear elastic and isotropic, with Young's modulus $E = 10.92 \times 10^4$ and Poisson's ratio $\nu = 0.3$.

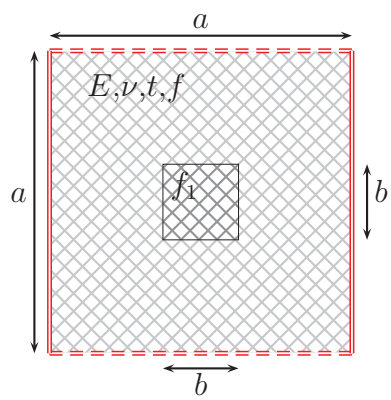

Figure 4.5.7: Problem definition and geometry for the simply supported square plate with load variation (t/a=1/10 and t/b=1)
Slika 4.5.7: Definicija in geometrija problema prosto podprte kvadratne plošče y neenakomerno obtežbo (t/a=1/10 in t/b=1)

The finite element solution on a regular mesh is shown in Figure 4.5.8. It is to be compared with Figure 4.5.2, where the area load is constant throughout the plate. In the interior of the plate, the stress σ_{zz}^{+} closely follows the distribution of the area load f and at the supports support it matches the reactions. Near the supports the stress σ_{zz}^{+} exhibit the oscillations. This effect, however, has not been yet further confirmed by the comparison with the three-dimensional solution. The shift of the midsurface, related to $\Delta\sigma_{zz}$ varies relatively smoothly and does not exhibit any quick changes.

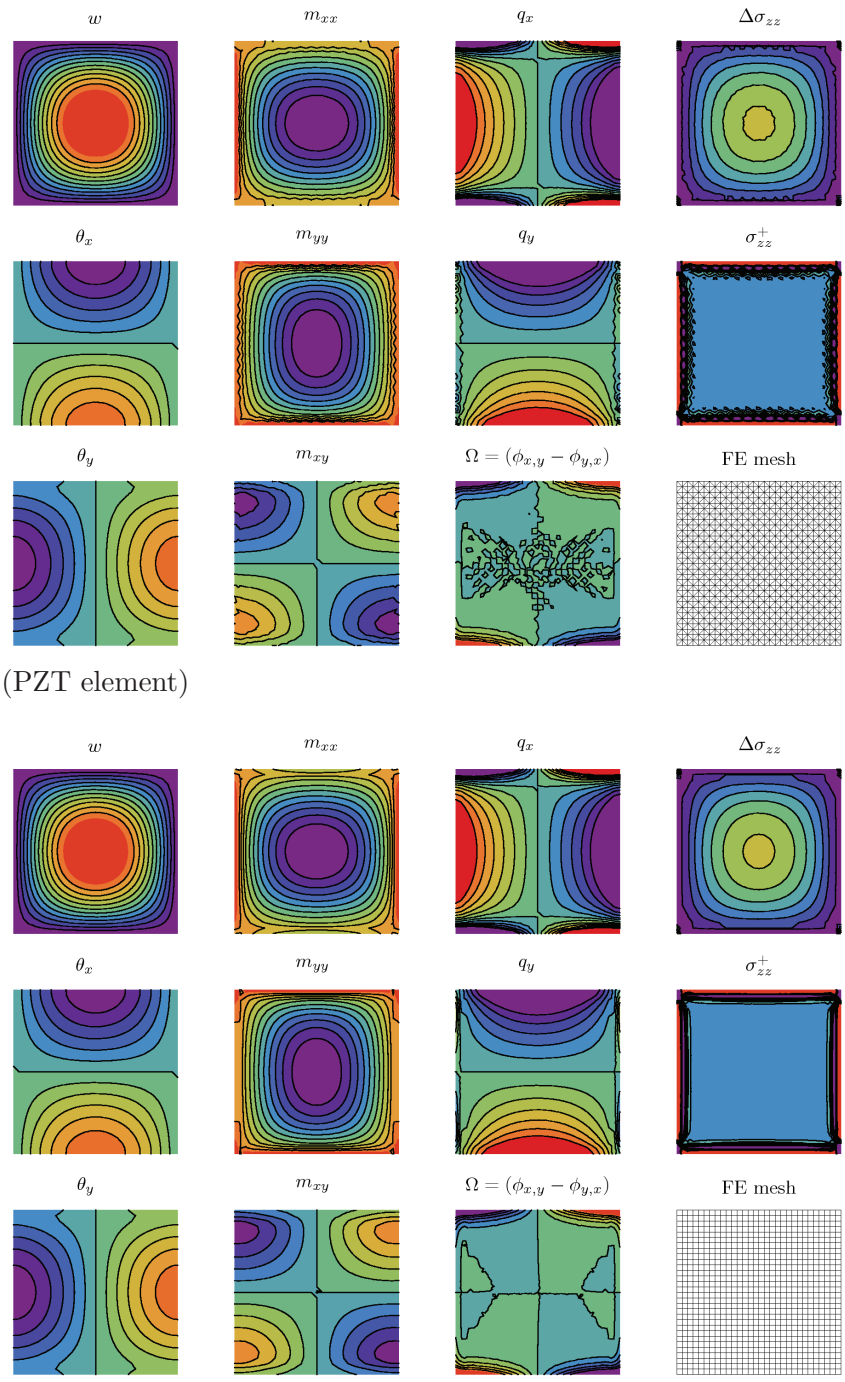

Figure 4.5.2: FE solution of the uniformly loaded simply supported square plate with PZ plate elements

Slika 4.5.2: Računska rešitev enakomerno obremenjene prosto podprte kvadratne plošče s PZ končnimi elementi

	w	θ_x	θ_y	m_{xx}	m_{yy}	m_{xy}	q_x	q_y	Ω	σ_{zz}^{+}	$\Delta\sigma_{zz}$
	$0. \sim 0.000338$	$-0.0015 \sim -0.00125$	$-0.0015 \sim -0.00125$	$-5. \sim -4.58$	$-5. \sim -4.58$	$-3.5 \sim -2.92$	$-3.5 \sim -2.92$	$-3.5 \sim -2.92$	$-0.0006 \sim -0.0005$	$0. \sim 0.208$	$-40. \sim -33.3$
	$0.000338 \sim 0.000677$	$-0.00125 \sim -0.001$	$-0.00125 \sim -0.001$	$-4.58 \sim -4.17$	$-4.58 \sim -4.17$	$-2.92 \sim -2.33$	$-2.92 \sim -2.33$	$-2.92 \sim -2.33$	$-0.0005 \sim -0.0004$	$0.208 \sim 0.417$	$-33.3 \sim -26.7$
	$0.000677 \sim 0.00102$	$-0.001 \sim -0.00075$	$-0.001 \sim -0.00075$	$-4.17 \sim -3.75$	$-4.17 \sim -3.75$	$-2.33 \sim -1.75$	$-2.33 \sim -1.75$	$-2.33 \sim -1.75$	$-0.0004 \sim -0.0003$	$0.417 \sim 0.625$	$-26.7 \sim -20.$
	$0.00102 \sim 0.00135$	$-0.00075 \sim -0.0005$	$-0.00075 \sim -0.0005$	$-3.75 \sim -3.33$	$-3.75 \sim -3.33$	$-1.75 \sim -1.17$	$-1.75 \sim -1.17$	$-1.75 \sim -1.17$	$-0.0003 \sim -0.0002$	$0.625 \sim 0.833$	$-20. \sim -13.3$
	$0.00135 \sim 0.00169$	$-0.0005 \sim -0.00025$	$-0.0005 \sim -0.00025$	$-3.33 \sim -2.92$	$-3.33 \sim -2.92$	$-1.17 \sim -0.583$	$-1.17 \sim -0.583$	$-1.17 \sim -0.583$	$-0.0002 \sim -0.0001$	$0.833 \sim 1.04$	$-13.3 \sim -6.67$
	$0.00169 \sim 0.00203$	$-0.00025 \sim 0.$	$-0.00025 \sim 0.$	$-2.92 \sim -2.5$	$-2.92 \sim -2.5$	$-0.583 \sim 0.$	$-0.583 \sim 0.$	$-0.583 \sim 0.$	$-0.0001 \sim 0.$	$1.04 \sim 1.25$	$-6.67 \sim 0.$
	$0.00203 \sim 0.00237$	$0. \sim 0.00025$	$0. \sim 0.00025$	$-2.5 \sim -2.08$	$-2.5 \sim -2.08$	$0. \sim 0.583$	$0. \sim 0.583$	$0. \sim 0.583$	$0. \sim 0.0001$	$1.25 \sim 1.46$	$0. \sim 6.67$
	$0.00237 \sim 0.00271$	$0.00025 \sim 0.0005$	$0.00025 \sim 0.0005$	$-2.08 \sim -1.67$	$-2.08 \sim -1.67$	$0.583 \sim 1.17$	$0.583 \sim 1.17$	$0.583 \sim 1.17$	$0.0001 \sim 0.0002$	$1.46 \sim 1.67$	$6.67 \sim 13.3$
	$0.00271 \sim 0.00305$	$0.0005 \sim 0.00075$	$0.0005 \sim 0.00075$	$-1.67 \sim -1.25$	$-1.67 \sim -1.25$	$1.17 \sim 1.75$	$1.17 \sim 1.75$	$1.17 \sim 1.75$	$0.0002 \sim 0.0003$	$1.67 \sim 1.88$	$13.3 \sim 20.$
	$0.00305 \sim 0.00338$	$0.00075 \sim 0.001$	$0.00075 \sim 0.001$	$-1.25 \sim -0.833$	$-1.25 \sim -0.833$	$1.75 \sim 2.33$	$1.75 \sim 2.33$	$1.75 \sim 2.33$	$0.0003 \sim 0.0004$	$1.88 \sim 2.08$	$20. \sim 26.7$
	$0.00338 \sim 0.00372$	$0.001 \sim 0.00125$	$0.001 \sim 0.00125$	$-0.833 \sim -0.417$	$-0.833 \sim -0.417$	$2.33 \sim 2.92$	$2.33 \sim 2.92$	$2.33 \sim 2.92$	$0.0004 \sim 0.0005$	$2.08 \sim 2.29$	$26.7 \sim 33.3$
	$0.00372 \sim 0.00406$	$0.00125 \sim 0.0015$	$0.00125 \sim 0.0015$	$-0.417 \sim 0.$	$-0.417 \sim 0.$	$2.92 \sim 3.5$	$2.92 \sim 3.5$	$2.92 \sim 3.5$	$0.0005 \sim 0.0006$	$2.29 \sim 2.5$	$33.3 \sim 40.$

Figure 4.5.3: Legend for Figures 4.5.2
Slika 4.5.3: Legenda za Slike 4.5.2

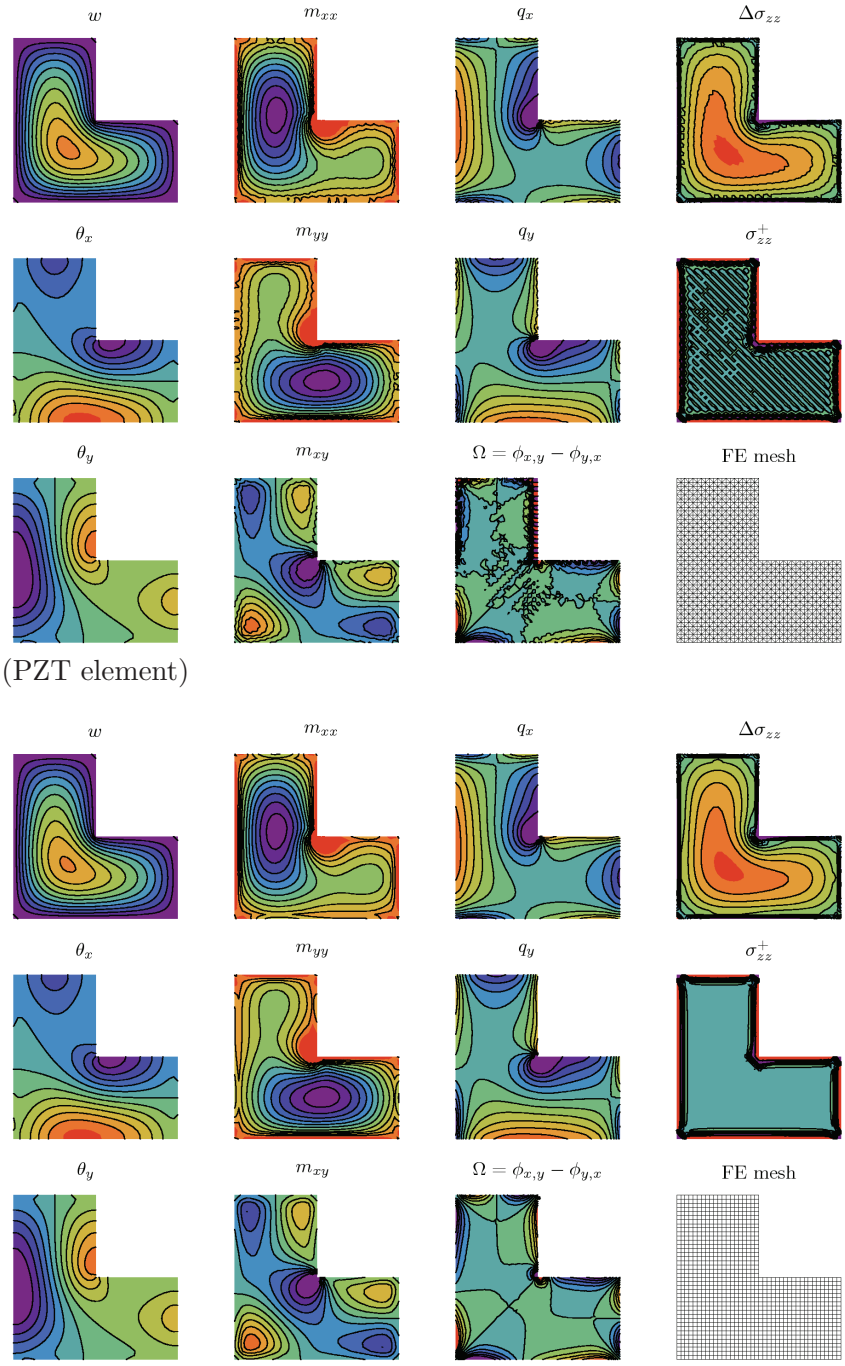

Figure 4.5.5: FE solution of the uniformly loaded soft simply supported L shaped plate with PZ plate elements

Slika 4.5.5: Računska rešitev enakomerno obremenjene mehko podprte L plošče s PZ končnimi elementi

	w	θ_x	θ_y	m_{xx}	m_{yy}	m_{xy}	q_x	q_y	Ω	σ_{zz}^{+}	$\Delta\sigma_{zz}$
	$0. \sim 0.000125$	$-0.0005 \sim -0.000417$	$-0.0005 \sim -0.000417$	$-3. \sim -2.75$	$-3. \sim -2.75$	$-1. \sim -0.833$	$-4. \sim -3.33$	$-4. \sim -3.33$	$-0.00025 \sim -0.000208$	$0. \sim 0.167$	$-10. \sim -8.33$
	$0.000125 \sim 0.00025$	$-0.000417 \sim -0.000333$	$-0.000417 \sim -0.000333$	$-2.75 \sim -2.5$	$-2.75 \sim -2.5$	$-0.833 \sim -0.667$	$-3.33 \sim -2.67$	$-3.33 \sim -2.67$	$-0.000208 \sim -0.000167$	$0.167 \sim 0.333$	$-8.33 \sim -6.67$
	$0.00025 \sim 0.000375$	$-0.000333 \sim -0.00025$	$-0.000333 \sim -0.00025$	$-2.5 \sim -2.25$	$-2.5 \sim -2.25$	$-0.667 \sim -0.5$	$-2.67 \sim -2.$	$-2.67 \sim -2.$	$-0.000167 \sim -0.000125$	$0.333 \sim 0.5$	$-6.67 \sim -5.$
	$0.000375 \sim 0.0005$	$-0.00025 \sim -0.000167$	$-0.00025 \sim -0.000167$	$-2.25 \sim -2.$	$-2.25 \sim -2.$	$-0.5 \sim -0.333$	$-2. \sim -1.33$	$-2. \sim -1.33$	$-0.000125 \sim -0.0000833$	$0.5 \sim 0.667$	$-5. \sim -3.33$
	$0.0005 \sim 0.000625$	$-0.000167 \sim -0.0000833$	$-0.000167 \sim -0.0000833$	$-2. \sim -1.75$	$-2. \sim -1.75$	$-0.333 \sim -0.167$	$-1.33 \sim -0.667$	$-1.33 \sim -0.667$	$-0.0000833 \sim -0.0000417$	$0.667 \sim 0.833$	$-3.33 \sim -1.67$
	$0.000625 \sim 0.00075$	$-0.0000833 \sim 0.$	$-0.0000833 \sim 0.$	$-1.75 \sim -1.5$	$-1.75 \sim -1.5$	$-0.167 \sim 0.$	$-0.667 \sim 0.$	$-0.667 \sim 0.$	$-0.0000417 \sim 0.$	$0.833 \sim 1.$	$-1.67 \sim 0.$
	$0.00075 \sim 0.000875$	$0. \sim 0.0000833$	$0. \sim 0.0000833$	$-1.5 \sim -1.25$	$-1.5 \sim -1.25$	$0. \sim 0.167$	$0. \sim 0.667$	$0. \sim 0.667$	$0. \sim 0.0000417$	$1. \sim 1.17$	$0. \sim 1.67$
	$0.000875 \sim 0.001$	$0.0000833 \sim 0.000167$	$0.0000833 \sim 0.000167$	$-1.25 \sim -1.$	$-1.25 \sim -1.$	$0.167 \sim 0.333$	$0.667 \sim 1.33$	$0.667 \sim 1.33$	$0.0000417 \sim 0.0000833$	$1.17 \sim 1.33$	$1.67 \sim 3.33$
	$0.001 \sim 0.00113$	$0.000167 \sim 0.00025$	$0.000167 \sim 0.00025$	$-1. \sim -0.75$	$-1. \sim -0.75$	$0.333 \sim 0.5$	$1.33 \sim 2.$	$1.33 \sim 2.$	$0.0000833 \sim 0.000125$	$1.33 \sim 1.5$	$3.33 \sim 5.$
	$0.00113 \sim 0.00125$	$0.00025 \sim 0.000333$	$0.00025 \sim 0.000333$	$-0.75 \sim -0.5$	$-0.75 \sim -0.5$	$0.5 \sim 0.667$	$2. \sim 2.67$	$2. \sim 2.67$	$0.000125 \sim 0.000167$	$1.5 \sim 1.67$	$5. \sim 6.67$
	$0.00125 \sim 0.00138$	$0.000333 \sim 0.000417$	$0.000333 \sim 0.000417$	$-0.5 \sim -0.25$	$-0.5 \sim -0.25$	$0.667 \sim 0.833$	$2.67 \sim 3.33$	$2.67 \sim 3.33$	$0.000167 \sim 0.000208$	$1.67 \sim 1.83$	$6.67 \sim 8.33$
	$0.00138 \sim 0.0015$	$0.000417 \sim 0.0005$	$0.000417 \sim 0.0005$	$-0.25 \sim 0.$	$-0.25 \sim 0.$	$0.833 \sim 1.$	$3.33 \sim 4.$	$3.33 \sim 4.$	$0.000208 \sim 0.00025$	$1.83 \sim 2.$	$8.33 \sim 10.$

Figure 4.5.6: Legend for Figures 4.5.5
Slika 4.5.6: Legenda za Slike 4.5.5

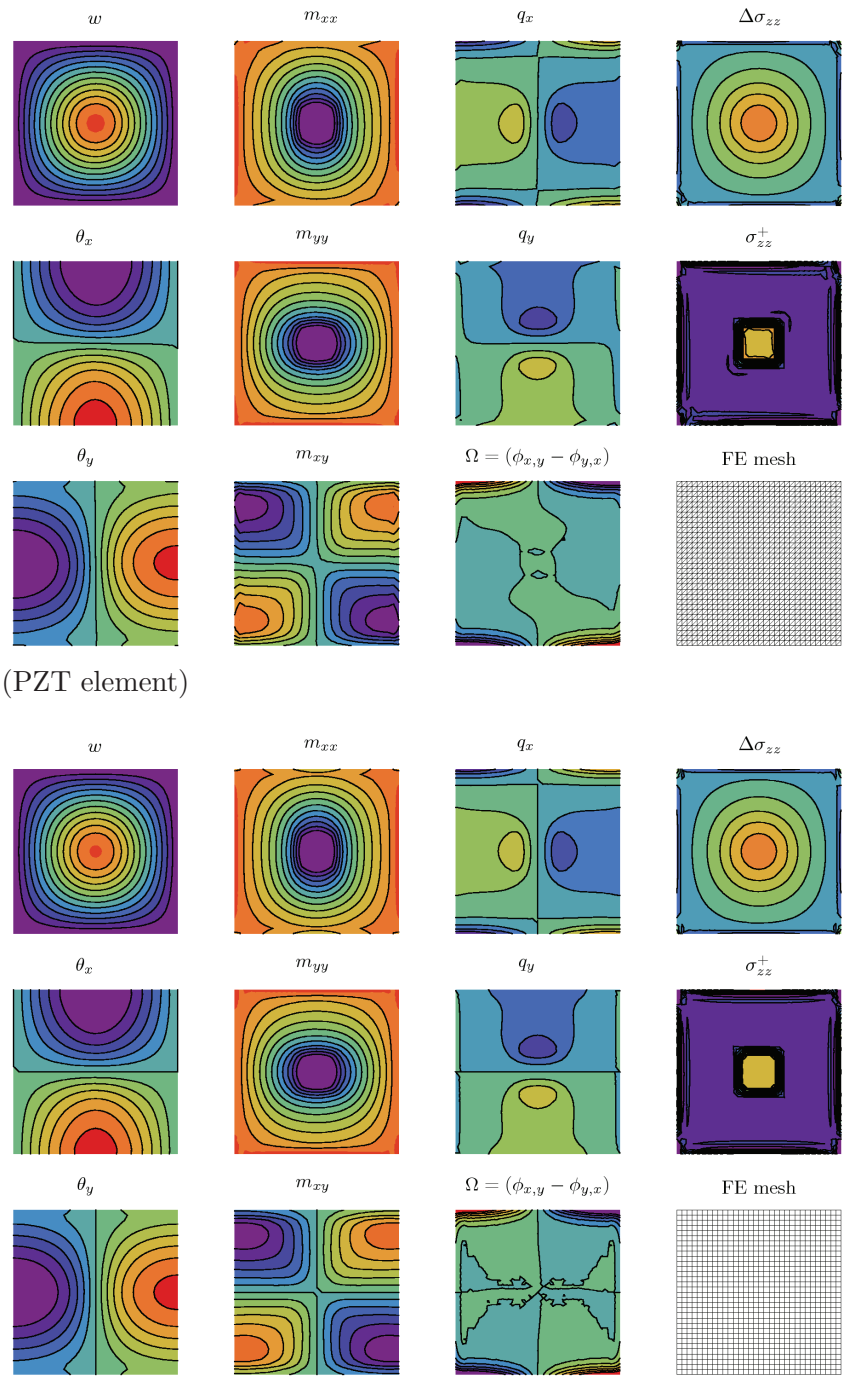

Figure 4.5.8: FE solution of the simply supported square plate with load variation with PZ plate elements

Slika 4.5.8: Računska rešitev prosto podprte kvadratne plošče y neenakomerno obtežbo s PZ končnimi elementi

	w	θ_x	θ_y	m_{xx}	m_{yy}	m_{xy}	q_x	q_y	Ω	σ_{zz}^{+}	$\Delta\sigma_{zz}$
	$0. \sim 0.00375$	$-0.01 \sim -0.00833$	$-0.01 \sim -0.00833$	$-60. \sim -55.$	$-60. \sim -55.$	$-20. \sim -16.7$	$-100. \sim -83.3$	$-100. \sim -83.3$	$-0.005 \sim -0.00417$	$-10. \sim -4.17$	$-300. \sim -250.$
	$0.00375 \sim 0.0075$	$-0.00833 \sim -0.00667$	$-0.00833 \sim -0.00667$	$-55. \sim -50.$	$-55. \sim -50.$	$-16.7 \sim -13.3$	$-83.3 \sim -66.7$	$-83.3 \sim -66.7$	$-0.00417 \sim -0.00333$	$-4.17 \sim 1.67$	$-250. \sim -200.$
	$0.0075 \sim 0.0113$	$-0.00667 \sim -0.005$	$-0.00667 \sim -0.005$	$-50. \sim -45.$	$-50. \sim -45.$	$-13.3 \sim -10.$	$-66.7 \sim -50.$	$-66.7 \sim -50.$	$-0.00333 \sim -0.0025$	$1.67 \sim 7.5$	$-200. \sim -150.$
	$0.0113 \sim 0.015$	$-0.005 \sim -0.00333$	$-0.005 \sim -0.00333$	$-45. \sim -40.$	$-45. \sim -40.$	$-10. \sim -6.67$	$-50. \sim -33.3$	$-50. \sim -33.3$	$-0.0025 \sim -0.00167$	$7.5 \sim 13.3$	$-150. \sim -100.$
	$0.015 \sim 0.0188$	$-0.00333 \sim -0.00167$	$-0.00333 \sim -0.00167$	$-40. \sim -35.$	$-40. \sim -35.$	$-6.67 \sim -3.33$	$-33.3 \sim -16.7$	$-33.3 \sim -16.7$	$-0.00167 \sim -0.000833$	$13.3 \sim 19.2$	$-100. \sim -50.$
	$0.0188 \sim 0.0225$	$-0.00167 \sim 0.$	$-0.00167 \sim 0.$	$-35. \sim -30.$	$-35. \sim -30.$	$-3.33 \sim 0.$	$-16.7 \sim 0.$	$-16.7 \sim 0.$	$-0.000833 \sim 0.$	$19.2 \sim 25.$	$-50. \sim 0.$
	$0.0225 \sim 0.0263$	$0. \sim 0.00167$	$0. \sim 0.00167$	$-30. \sim -25.$	$-30. \sim -25.$	$0. \sim 3.33$	$0. \sim 16.7$	$0. \sim 16.7$	$0. \sim 0.000833$	$25. \sim 30.8$	$0. \sim 50.$
	$0.0263 \sim 0.03$	$0.00167 \sim 0.00333$	$0.00167 \sim 0.00333$	$-25. \sim -20.$	$-25. \sim -20.$	$3.33 \sim 6.67$	$16.7 \sim 33.3$	$16.7 \sim 33.3$	$0.000833 \sim 0.00167$	$30.8 \sim 36.7$	$50. \sim 100.$
	$0.03 \sim 0.0338$	$0.00333 \sim 0.005$	$0.00333 \sim 0.005$	$-20. \sim -15.$	$-20. \sim -15.$	$6.67 \sim 10.$	$33.3 \sim 50.$	$33.3 \sim 50.$	$0.00167 \sim 0.0025$	$36.7 \sim 42.5$	$100. \sim 150.$
	$0.0338 \sim 0.0375$	$0.005 \sim 0.00667$	$0.005 \sim 0.00667$	$-15. \sim -10.$	$-15. \sim -10.$	$10. \sim 13.3$	$50. \sim 66.7$	$50. \sim 66.7$	$0.0025 \sim 0.00333$	$42.5 \sim 48.3$	$150. \sim 200.$
	$0.0375 \sim 0.0413$	$0.00667 \sim 0.00833$	$0.00667 \sim 0.00833$	$-10. \sim -5.$	$-10. \sim -5.$	$13.3 \sim 16.7$	$66.7 \sim 83.3$	$66.7 \sim 83.3$	$0.00333 \sim 0.00417$	$48.3 \sim 54.2$	$200. \sim 250.$
	$0.0413 \sim 0.045$	$0.00833 \sim 0.01$	$0.00833 \sim 0.01$	$-5. \sim 0.$	$-5. \sim 0.$	$16.7 \sim 20.$	$83.3 \sim 100.$	$83.3 \sim 100.$	$0.00417 \sim 0.005$	$54.2 \sim 60.$	$250. \sim 300.$

Figure 4.5.9: Legend for Figures 4.5.8
Slika 4.5.9: Legenda za Slike 4.5.8

4.6 Chapter summary and conclusions

Both Kirchhoff and Reissner/Mindlin theories neglect the normal stress σ_{zz}. The normal stress is significant in the regions near the supports, point loads and at sharp changes of plate thickness. In this chapter a higher-order plate theory is presented, which takes explicitly into account also the through the thickness stretching and consequently σ_{zz} is not neglected. No assumptions are made regarding the stress state which enables the use of full three dimensional constitutive relations.

Assumed kinematics of the plate deformation allows for the linear variation of the normal strain through the thickness of the plate. Consistent derivation of the two-dimensional principle of virtual work is presented in the following. Owing to the chosen interpolation of the normal strain it is possible to follow hierarchical relations to the Reissner/Mindlin model and the differences of both theories are clearly visible. A concise treatment of the computation of terms involved in principle of virtual work is given.

Based on the proposed theory, a novel finite element is developed. Since the theory is formulated as the hierarchical extension of the Reissner/Mindlin theory, so is the formulation of the proposed finite element based on the P3 elements. Two additional nodal degrees of freedom are introduced. They can be directly related to the constant and linear variation of normal stress σ_{zz}. The loading on top and bottom of the plate is treated separately.

The chapter concludes with several numerical tests. Since the full three-dimensional solution is unavailable and due to the hierarchical nature of the elements, the solution is rather compared to solution obtained with P3 elements. The results of the computations confirm the functionality of the finite element implementation. Numerical tests show that the significant normal strain is limited to the relative narrow area close to the supports. Additionally, small oscillations of the normal strain are observed near the supports.

Chapter 5

Discretization error estimates

5.1 Introduction. Classification of error estimates

Finite element method is a numerical method, which gives only an approximate solution to a given boundary value problem ([Zienkiewicz Taylor, 2000], [Ibrahimbegović, 2009]). It is therefore natural to try to evaluate the error of the approximate solution with respect to the (unknown) exact solution. The main reason to deal with a measure of how close the finite element approximation $\boldsymbol{u}_h$ is to the exact solution $\boldsymbol{u}$ is the quality control of the approximate solution and the adaptivity of the finite element mesh related to adaptive modeling of disretization problem (e.g. see [Ainsworth Oden, 2000], [Ladevèze Pelle, 2006], [Stein Ramm, 2003]). Quality control is needed in order to meet a predefined limit of error of approximation, which will guarantee a desired quality of the approximate solution. If the guarantee that the error remains inside the error bounds has to be provided, we will seek for *error estimates*, which can be obtained by a rigorous mathematical analysis. Although the true error bounds can be very attractive, they are often compromised by the fact that these estimates are very pessimistic and can overestimate the error by several orders of magnitude.

A pretty good idea of overall quality of approximation can also be obtained by *error indicators* ([Babuška Rheinboldt, 1978]), which do not provide error bounds. However, error indicators are not only easier to handle but also represent the actual error better than the error estimates do. Error indicators can thus provide efficient and also reliable basis for adaptive modeling of the finite element mesh. In other words, they can be effectively used to steer the adaptive algorithms in order to get optimal accuracy of a finite element analysis with a minimum number of degrees of freedom. In what follows, we will refer mainly to error indicators. Moreover, we will not strictly distinguish between

error estimates and error indicators. In what follows, the word estimate will denote either estimate or indicator.

Yet another classification of error estimates concerns a priori versus a posteriori error estimates. The *a priori error estimates* consider the asymptotic behavior of the error with respect to the element size h and the order p of the polynomial approximation. They do not provide the information on the actual error of the finite element approximation $\boldsymbol{u}_h$. The *a posteriori error estimates* rely on postprocessing of the finite element approximation $\boldsymbol{u}_h$ to obtain the error estimates of the finite element approximation $\boldsymbol{u}_h$. There are basically two distinct types of a posteriori error estimates: *recovery based error estimates* and *residual based error estimates*.

Recovery based error estimates are much more popular than the residual based error estimates, since they provide easier way for the assessment of the finite element approximation error. The Superconvergent patch recovery (SPR) rely on the existence of the superconvergent points, where the rate of the convergence of gradient of the finite element solution is higher than elsewhere in the element. The recovered (i.e. smoother) gradient of the solution can be constructed over the whole domain based on the values at superconvergent points. The recovered gradient of this kind can serve as an approximation of the gradient of the exact solution. The error is usually estimated by evaluating the energy norm of the difference between the finite element solution and the recovered approximation of the exact solution.

Residual based error estimates make use of the residuals of the finite element approximation, either explicitly or implicitly ([Ainsworth Oden, 2000], [Ladevèze Pelle, 2006], [Ladevèze Leguillon, 1983], [Stein Ramm, 2003], [Becher Rannacher, 2001]). Explicit residual based error estimates rely on a direct computation of the interior element residuals and the jumps at the element boundaries to find an estimate for the error ([Babuška Rheinboldt, 1978], [Babuška Miller, 1987]). Implicit residual based error estimates involve construction of auxiliary boundary value problems, whose solution yields an approximation of the actual error. The auxiliary boundary value problems that need to be solved are local in a sense that they are posed on either patch of elements (*subdomain residual method*) or on single element (*element residual method* (EqR), e.g. see [Stein Ramm, 2003]). We note that the element residual method needs to approximate the prescribed Neumann boundary conditions on each single element.

The above mentioned error estimate methods are all concerned with the global energy norm of the error. In the finite element analysis it is, however, frequently the case that

a specific output data (i.e. a stress at the selected point) is of special interest. The goal-oriented error estimates were developed for such cases. They estimate the error in individual quantity of interest by using duality techniques [Ainsworth Oden, 2000]. The key for estimating the error in such quantity is the formulation of an auxiliary problem, which is the dual problem to the primal actually considered. The dual problem filters out the necessary information for an accurate estimate of the error in the quantity of interest. The estimates of this kind, however, will not be considered in this work.

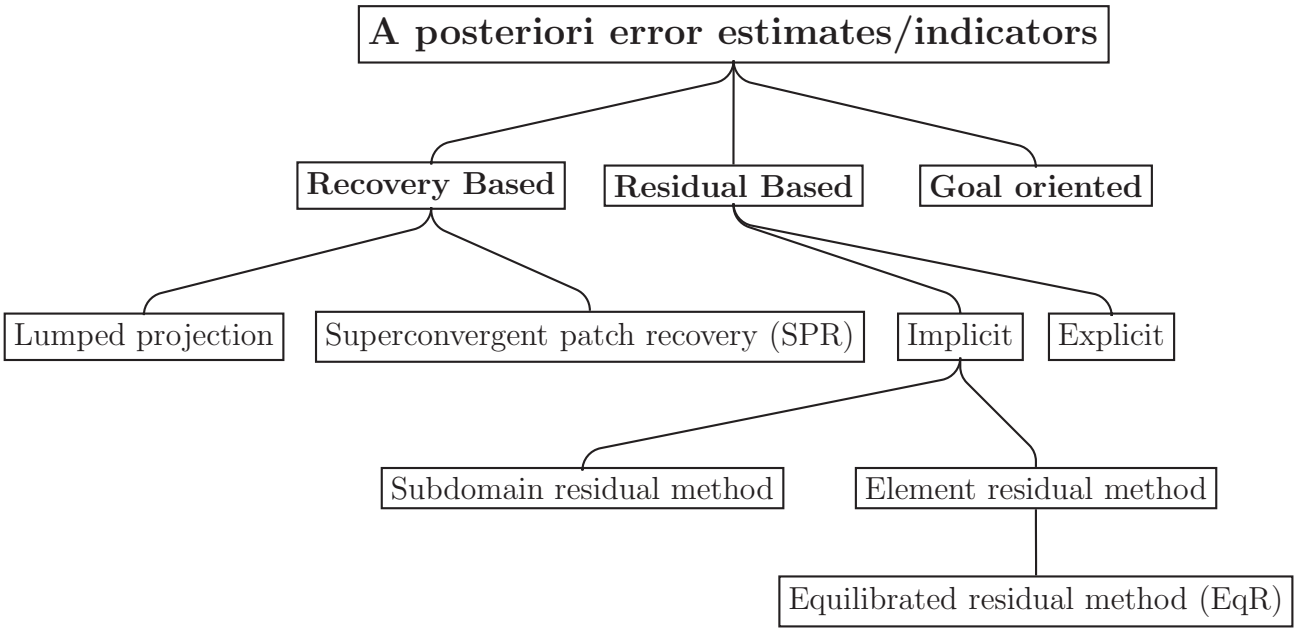

Figure 5.1.1: Rough classification of a-posteriori error estimates/indicators
Slika 5.1.1: Groba klasifikacija a-posteriori ocen napake

The above introduced classification of error estimates/indicators is presented in Figure 5.1.1. For more refined classification see e.g. [Ainsworth Oden, 2000].

5.2 Definitions. Linear elasticity as a model problem

In order to clarify the notation, we further study a model problem of linear elasticity. The weak formulation of the problem is written as:

Given $\boldsymbol{f} : \Omega \mapsto \mathbb{R}$, $\bar{\boldsymbol{t}} : \Gamma_N \mapsto \mathbb{R}$ and $\overline{\boldsymbol{u}} : \Gamma_D \mapsto \mathbb{R}, \Gamma = \Gamma_D \bigcup \Gamma_N$
find $\boldsymbol{u} \in \mathcal{V}$ such that

$$a(\boldsymbol{u}, \boldsymbol{v}) = l(\boldsymbol{v}) \qquad \forall \boldsymbol{v} \in \mathcal{V}_0 \tag{5.2.1}$$

Bilinear and linear form of linear elasticity (e.g. see [Ibrahimbegović, 2009]) are:

$$a(\boldsymbol{u}, \boldsymbol{v}) := \int_\Omega [\boldsymbol{\sigma}(\boldsymbol{u})] : [\boldsymbol{\varepsilon}(\boldsymbol{v})] \, \mathrm{d}\Omega = \int_\Omega \boldsymbol{\sigma} \cdot \boldsymbol{\varepsilon} \, \mathrm{d}\Omega \tag{5.2.2}$$

$$l(\boldsymbol{v}) := \int_\Gamma \boldsymbol{v} \cdot \bar{\boldsymbol{t}} \, \mathrm{d}\Gamma + \int_\Omega \boldsymbol{f} \cdot \boldsymbol{v} \, \mathrm{d}\Omega \tag{5.2.3}$$

where $[\boldsymbol{\varepsilon}] = \left[\nabla^S \boldsymbol{v}\right] = \frac{1}{2}(\nabla \boldsymbol{v} + (\nabla \boldsymbol{v})^T)$ denotes the infinitesimal strain tensor and $[\boldsymbol{\sigma}]$ the stress tensor. The corresponding vector representation of these tensors is denoted by $\boldsymbol{\varepsilon}$ and $\boldsymbol{\sigma}$, respectively. Body forces are denoted by $\boldsymbol{f}$ and surface (boundary) tractions by $\bar{\boldsymbol{t}}$. Solution $\boldsymbol{u}$ is sought in the test space $\mathcal{V}$, which respects the Dirichlet boundary conditions ($\boldsymbol{u} = \bar{\boldsymbol{u}}|_{\Gamma_D}$), while the test space $\mathcal{V}_0$ consists of functions which are equal to zero on Γ_D ($\boldsymbol{v} = 0|_{\Gamma_D}$). A finite element approximation $\boldsymbol{u}_h$ to the solution $\boldsymbol{u}$ of the problem formulated in (5.2.1) is sought in the subspace $\mathcal{V}_h \subset \mathcal{V}$. Subspace $\mathcal{V}_h$ consists of element-wise polynomial functions of order p over the finite element partition Ω_h which satisfy Dirichlet (displacement) boundary conditions (e.g. see [Zienkiewicz Taylor, 2000], [Ibrahimbegović, 2009]).

According to the Bubnov-Galerkin method, the optimal approximation from the given subspace is the one for which

$$a(\boldsymbol{u}_h, \boldsymbol{v}_h) = l(\boldsymbol{v}_h) \tag{5.2.4}$$

holds for all test functions $\boldsymbol{v}_h \in \mathcal{V}_{0,h} \subset \mathcal{V}_0$. Test space $\mathcal{V}_{0,h}$ shares the same properties with $\mathcal{V}_h$ except that functions $\boldsymbol{v}_h \in \mathcal{V}_{0,h}$ satisfy homogeneous Dirichlet boundary conditions. Finite element solution $\boldsymbol{u}_h$ is found by solving the system of equations defined by (5.2.4). Since the $\mathcal{V}_{0,h} \subset \mathcal{V}_0$, it follows from (5.2.1) that the exact solution $\boldsymbol{u}$ also satisfies

$$a(\boldsymbol{u}, \boldsymbol{v}_h) = l(\boldsymbol{v}_h); \qquad \forall \boldsymbol{v}_h \in \mathcal{V}_{0,h} \subset \mathcal{V}_0 \tag{5.2.5}$$

By subtracting equation (5.2.5) from (5.2.4), and accounting for linearity of each functional, the *Galerkin orthogonality* condition is obtained:

$$a(\boldsymbol{u} - \boldsymbol{u}_h, \boldsymbol{v}_h) = 0 \tag{5.2.6}$$

The discretization error is defined as the difference between the exact solution $\boldsymbol{u}$ and its finite element approximation $\boldsymbol{u}_h$:

$$\boldsymbol{e}_h = \boldsymbol{u} - \boldsymbol{u}_h \tag{5.2.7}$$

Thus, the Galerkin orthogonality (5.2.6) reads

$$a(\boldsymbol{e}_h, \boldsymbol{v}_h) = 0 \tag{5.2.8}$$

The error of the finite element solution $\boldsymbol{e}_h$ is energy-orthogonal to the space of test functions $\mathcal{V}_{0,h}$. In other words, the error $\boldsymbol{e}_h$ does not contribute to the total energy of the solution. In that sense, the finite element solution is an orthogonal projection of the exact solution onto the approximation space. Since the bilinear form $a(\cdot,\cdot)$ is symmetric and positive-definite, the Galerkin orthogonality implies that the finite element approximation $\boldsymbol{u}_h$ is optimal among all possible approximations from $\mathcal{V}_h$.

The definition (5.2.7) of the error is local in a sense, that it refers to the specific point of the problem domain. It is possible in case of singularities that the error will locally be infinite, while the overall solution may well be acceptable. Therefore, the energy norm of the error is introduced which measures the error globally:

$$\|\boldsymbol{e}_h\|_E^2 = a(\boldsymbol{e}_h, \boldsymbol{e}_h) \tag{5.2.9}$$

The integral over the domain Ω_h is computed as the sum of integrals over the elements Ω_h^e. Therefore, the total error $\|\boldsymbol{e}_h\|_E$ can be decomposed into element contributions $\|\boldsymbol{e}_{e,h}\|_E$

$$\|\boldsymbol{e}_h\|_E^2 = \sum_e \|\boldsymbol{e}_{e,h}\|_E^2 \tag{5.2.10}$$

5.3 Recovery based error estimates

The recovery based error estimates are based on a rather heuristic basis. The main idea originates from the fact, that the stresses of the finite element solution are in general discontinuous across the interelement boundaries. The stresses of the exact solution are, however, continuous. By constructing smooth stress fields from the original finite element solution (by post-processing) a better estimate of the true stresses can be obtained. An estimate for the true error is obtained by comparing the post-processed stresses and the non post-processed stresses of the approximation.

Let us denote the stresses obtained from the original finite element solution as $\boldsymbol{\sigma}_h$ and the exact stresses as $\boldsymbol{\sigma}$. The error (5.2.9) can then be expressed in terms of stresses only

$$\|\boldsymbol{e}_h\|_E^2 = \int_{\Omega_h} (\boldsymbol{\sigma} - \boldsymbol{\sigma}_h)^T \mathbf{C}^{-1} (\boldsymbol{\sigma} - \boldsymbol{\sigma}_h)\, \mathrm{d}\Omega \tag{5.3.1}$$

where the relations $\boldsymbol{\sigma}(\boldsymbol{u} - \boldsymbol{u}_h) = \boldsymbol{\sigma}(\boldsymbol{u}) - \boldsymbol{\sigma}(\boldsymbol{u}_h)$, $\boldsymbol{\sigma} = \mathbf{C}\boldsymbol{\varepsilon}$ and $\boldsymbol{\sigma}_h = \mathbf{C}\boldsymbol{\varepsilon}_h$ are taken into account, with $\mathbf{C}$ being the constitutive matrix.

The exact stresses $\boldsymbol{\sigma}$ are not known. Their approximation is tried to be reconstructed from $\boldsymbol{\sigma}_h$ by a postprocessing procedure. The recovered values, denoted by $\boldsymbol{\sigma}^*$, are continuous stresses over the element

$$\boldsymbol{\sigma}^* = \sum_i \boldsymbol{\sigma}_i^* \, N_i \tag{5.3.2}$$

where i runs over the nodes of the element and, N_i are shape functions defined on the patch pertaining to node i, denoted by $\mathcal{P}_i$. Nodal stresses are denoted as $\boldsymbol{\sigma}_i^*$. The recovery based approximation of the error can thus be written as

$$\|\boldsymbol{e}^*\|_E^2 = \int_{\Omega_h} (\boldsymbol{\sigma}^* - \boldsymbol{\sigma}_h)^T \mathbf{C}^{-1} (\boldsymbol{\sigma}^* - \boldsymbol{\sigma}_h) \, \mathrm{d}\Omega \tag{5.3.3}$$

The integral in (5.3.3) can be decomposed into element contributions as

$$\|\boldsymbol{e}^*\|_E^2 = \sum_e \eta_e^2; \quad \eta_e^2 = \int_{\Omega_h^e} (\boldsymbol{\sigma}^* - \boldsymbol{\sigma}_h)^T \mathbf{C}^{-1} (\boldsymbol{\sigma}^* - \boldsymbol{\sigma}_h) \, \mathrm{d}\Omega \tag{5.3.4}$$

where the indicator of the global error $\|\boldsymbol{e}^*\|_E^2$ is expressed as the sum of the local error indicators η_e^2.

The primary goal of the recovery based error estimates becomes the determination of the enhanced stresses $\boldsymbol{\sigma}^*$ or rather their nodal values $\boldsymbol{\sigma}_i^*$. They can be determined by using the following argumentation: continuous approximation of the stress field $\boldsymbol{\sigma}^*$ should be as close as possible to the finite element approximation $\boldsymbol{\sigma}_h$, therefore we seek for the function $\boldsymbol{\sigma}^*$ which minimize the functional

$$\frac{1}{2} \int_{\Omega} (\boldsymbol{\sigma}^* - \boldsymbol{\sigma}_h)^2 \mathrm{d}\Omega \to min \tag{5.3.5}$$

The minimization of (5.3.5) with respect to $\boldsymbol{\sigma}_i^*$ leads to

$$\int_{\Omega_{\mathcal{P}_i}} (\boldsymbol{\sigma}^* - \boldsymbol{\sigma}_h) N_i \mathrm{d}\Omega = 0 \tag{5.3.6}$$

Finally, we obtain a system of equations for the $\boldsymbol{\sigma}_i^*$ in the form:

$$\sum_j \left(\int_{\Omega_{\mathcal{P}_i}} N_i N_j \mathrm{d}\Omega \right) \boldsymbol{\sigma}_j^* = \int_{\Omega_{\mathcal{P}_i}} \boldsymbol{\sigma}_h N_i \mathrm{d}\Omega \tag{5.3.7}$$

This problem is global, therefore the solution is as computationally expensive as the solution of the original problem. This is of course not a desired feature of the effective error estimation.

5.3.1 Lumped projection

A more effective procedure for the computation of nodal values $\boldsymbol{\sigma}_i^*$ can be obtained by the diagonalization of (5.3.5). The left hand side of (5.3.7) is simplified to

$$\boldsymbol{\sigma}_i^* \left(\int_{\Omega_{\mathcal{P}_i}} N_i (\sum_j N_j) \mathrm{d}\Omega \right) = \int_{\Omega_{\mathcal{P}_i}} \boldsymbol{\sigma}_h N_i \mathrm{d}\Omega \tag{5.3.8}$$

by assuming $\boldsymbol{\sigma}_j^* = \boldsymbol{\sigma}_i^*$. Note, that the shape functions N_i are complete, therefore we have $\sum_i N_i = 1$ and the nodal value $\boldsymbol{\sigma}_i^*$ can be explicitly computed from

$$\boldsymbol{\sigma}_i^* = \frac{1}{m_i} \int_{\Omega_{\mathcal{P}_i}} \boldsymbol{\sigma}_h N_i \mathrm{d}\Omega \tag{5.3.9}$$

where $m_i = \int_{\Omega_{\mathcal{P}_i}} N_i \mathrm{d}\Omega$. Due to its simplicity, this procedure is implemented in various finite element codes to smooth the stress field prior to plotting.

The procedure (5.3.8)-(5.3.9) is denoted as "lumped projection" in Figure 5.1.1.

5.3.2 Superconvergent patch recovery (SPR)

The SPR procedure takes advantage of the superconvergence property of the finite element solution (e.g. see [Zienkiewicz Taylor, 2000], [Ibrahimbegović, 2009]). Namely, the solution error in displacements is locally the smallest at the nodes of the element, whereas the error in displacement gradients (or stresses) is smallest not at nodes but at the points inside the element usually coinciding with the Gauss points. At such points the order of convergence of the gradients is at least one order higher than the one that would be anticipated from the approximation polynomial. This is known as the *superconvergence* property.

The values of stresses sampled in Gauss points $\boldsymbol{\xi}_{gp}$ (or other optimal sampling points) are denoted by $\boldsymbol{\sigma}_h(\boldsymbol{\xi}_{gp})$. These values serve as the basis for the reconstruction of the recovered stress field $\boldsymbol{\sigma}^*$, which will, due to the superconvergent property of sampling points, provide the best approximation of exact solution $\boldsymbol{\sigma}$.

In the neighborhood of a particular node i each component of $\boldsymbol{\sigma}^*$ is interpolated by

$$\bar{\sigma}_k^* = \boldsymbol{a}_k \boldsymbol{p} \tag{5.3.10}$$

where, for example for a 2D problem

$$\boldsymbol{p} = \boldsymbol{p}(x, y) = [1, \bar{x}, \bar{y}, \cdots, \bar{y}^p]^T \tag{5.3.11}$$
$$\boldsymbol{a}_k = [a_{k1}, a_{k2}, \cdots, a_{km}]$$

and $\bar{x} = x - x_i, \bar{y} = y - y_i$ with $\boldsymbol{x}_i = (x_i, y_i)$ denoting the coordinates of node i. The nodal parameters $\boldsymbol{\sigma}_i^*$ are taken simply as the value of $\bar{\boldsymbol{\sigma}}^*$ at the node i

$$\boldsymbol{\sigma}_i^* = \bar{\boldsymbol{\sigma}}^*(\boldsymbol{x}_i) \tag{5.3.12}$$

The parameters $\boldsymbol{a}_k$ are determined using the least square fit of $\bar{\boldsymbol{\sigma}}^*$ to the values $\boldsymbol{\sigma}_h(\boldsymbol{x}_{gp})$ sampled in the n_{gp} superconvergent points $\boldsymbol{x}_{gp} = (x_{gp}, y_{gp})$ over the patch of elements surrounding node i. For each stress component k we have

$$\frac{1}{2}\sum_{gp=1}^{ngp} \left(\sigma_{h,k}(\boldsymbol{x}_{gp}) - \bar{\sigma}_k^*(\boldsymbol{x}_{gp})\right)^2 \longmapsto min. \tag{5.3.13}$$

This leads to a small set of linear algebraic equations for the coefficients $\boldsymbol{a}_k$

$$\begin{aligned} &\boldsymbol{M}\boldsymbol{a}_k = \boldsymbol{b}; \quad \boldsymbol{M} = [M_{ij}]; \quad \boldsymbol{b} = [b_i] \\ &M_{ij} = \sum_{gp} p_i(\boldsymbol{x}_{gp})\, p_j(\boldsymbol{x}_{gp}); \quad b_i = \sum_{gp} \sigma_{h,k}(\boldsymbol{x}_{gp}) p_i(\boldsymbol{x}_{gp}) \end{aligned} \tag{5.3.14}$$

The approximation $\boldsymbol{\sigma}^*$ is superconvergent in each Gauss integration point in a case of regular mesh with rectangular elements. For the elements with distorted geometry the superconvergence is no longer exactly satisfied at the Gauss points. However, the procedure gives reasonably good approximation even in such cases. An overview of the SPR procedure is given in Box 1.

Box 1 : The superconvergent patch recovery - SPR
Algoritem 1: SPR metoda

1. Obtain original finite element solution $\boldsymbol{u}_h$ of the problem (5.2.4) and obtain $\boldsymbol{\sigma}_h(\boldsymbol{x}_{gp})$
2. Chose interpolation (5.3.10) of each $\bar{\sigma}_k^*$ in the neighborhood of node i
3. Evaluate $[M_{ij}]$ and $[b_i]$ from (5.3.14)
4. Solve (5.3.14) for $\boldsymbol{a}_k$
5. Define $\boldsymbol{\sigma}_i^*$ from (5.3.12)
6. Use the interpolation (5.3.2) to get $\boldsymbol{\sigma}^*$

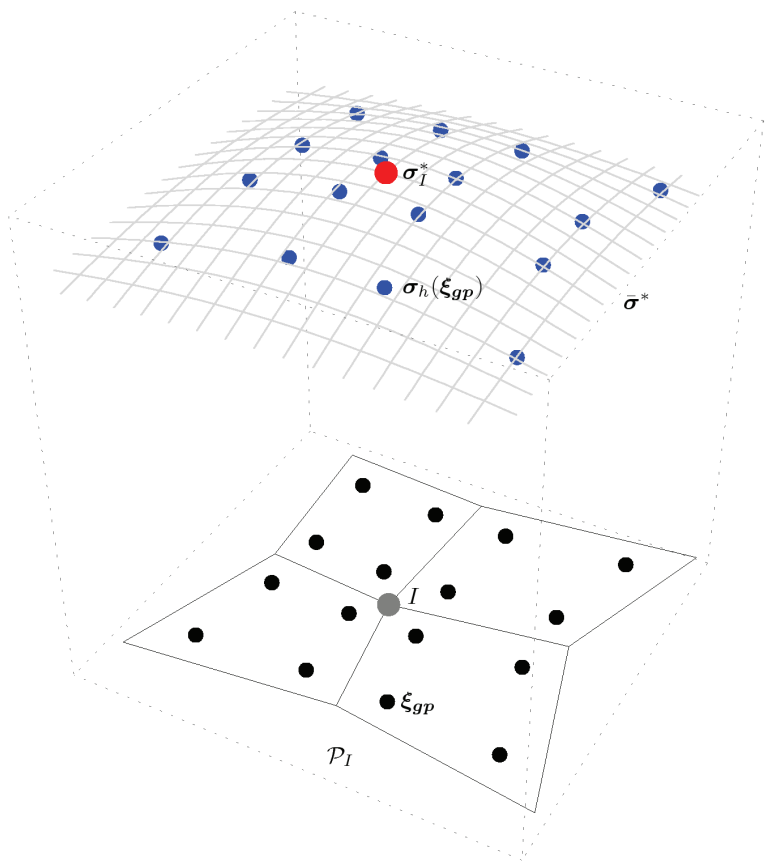

Figure 5.3.1: SPR recovery of the enhanced stress $\boldsymbol{\sigma}_I^*$ at node I
Slika 5.3.1: Izračun izboljšanih napetosti $\boldsymbol{\sigma}_I^*$ v vozliščih I po metodi SPR

5.4 Residual based error estimates

5.4.1 Explicit

One can find an estimate for the global error in the energy norm (5.2.9) by *explicit residual based* error estimates. They are based on the the direct computation of the interior element residuals and the jumps at the element boundaries. The basic idea of residual based error estimates comes from the observation that the residual $\mathcal{R}(\boldsymbol{u}_h, \boldsymbol{v}) = a(\boldsymbol{u}_h, \boldsymbol{v}) - l(\boldsymbol{v})$ is directly related to the error $\boldsymbol{e}_h$. From (5.2.1) and (5.2.7) if follows that the error satisfies the equation

$$a(\boldsymbol{e}_h, \boldsymbol{v}) = l(\boldsymbol{v}) - a(\boldsymbol{u}_h, \boldsymbol{v}); \quad \forall \boldsymbol{v} \in \mathcal{V}_0 \tag{5.4.1}$$

where $\boldsymbol{v}$ belongs to the test space and it holds true for an arbitrarily chosen test function $\boldsymbol{v} \in \mathcal{V}_0$. The integrals in (5.4.1) are split into element contributions:

$$a(\boldsymbol{e}_h, \boldsymbol{v}) = \sum_e \{l_e(\boldsymbol{v}) - a_e(\boldsymbol{u}_h, \boldsymbol{v})\}; \quad \forall \boldsymbol{v} \in \mathcal{V}_0 \tag{5.4.2}$$

The forms l_e and a_e are:

$$\begin{aligned} a_e(\boldsymbol{u}_h, \boldsymbol{v}) &= \int_{\Omega^e} [\boldsymbol{\sigma}(\boldsymbol{u}_h)] : [\boldsymbol{\varepsilon}(\boldsymbol{v})] \, \mathrm{d}\Omega \qquad (5.4.3) \\ &= \int_{\Gamma^e} ([\boldsymbol{\sigma}(\boldsymbol{u}_h)]\boldsymbol{n}) \cdot \boldsymbol{v} \, \mathrm{d}\Gamma - \int_{\Omega^e} (\nabla \cdot [\boldsymbol{\sigma}(\boldsymbol{u}_h)]) \cdot \boldsymbol{v} \, \mathrm{d}\Omega \\ l_e(\boldsymbol{v}) &= \int_{\Gamma_N^e} \boldsymbol{v} \cdot \bar{\boldsymbol{t}} \, \mathrm{d}\Gamma + \int_{\Omega^e} \boldsymbol{f} \cdot \boldsymbol{v} \, \mathrm{d}\Omega \qquad (5.4.4) \end{aligned}$$

where the Gauss statement was used to perform integration per partes in (5.4.3). The divergence of stress tensor $[\boldsymbol{\sigma}]$ is denoted by $\nabla \cdot [\boldsymbol{\sigma}]$ and the normal to the element side is denoted by $\boldsymbol{n}$. The sides with Neumann boundary conditions are denoted by Γ_N^e ($\Gamma^e = \Gamma_N^e \bigcup \Gamma_D^e$).

Using the definitions (5.4.3) and (5.4.4), the expression (5.4.2) transforms to

$$\begin{aligned} a(\boldsymbol{e}_h, \boldsymbol{v}) = &\sum_e \int_{\Omega^e} (\boldsymbol{f} + \nabla \cdot [\boldsymbol{\sigma}(\boldsymbol{u}_h)]) \mathrm{d}\Omega \qquad (5.4.5) \\ &+ \sum_e \int_{\Gamma_N^e} (\bar{\boldsymbol{t}} - [\boldsymbol{\sigma}(\boldsymbol{u}_h)]\boldsymbol{n}) \cdot \boldsymbol{v} \, \mathrm{d}\Omega \\ &+ \sum_e \int_{\Gamma_D^e} ([\boldsymbol{\sigma}(\boldsymbol{u}_h)]\boldsymbol{n}) \cdot \boldsymbol{v} \, \mathrm{d}\Gamma \end{aligned}$$

With the rearrangement of the summation it is possible to split the residual (5.4.5) into element and side contributions:

$$a(\boldsymbol{e}_h, \boldsymbol{v}) = \sum_{\Omega^e} \int_{\Omega^e} \mathcal{R}_{\Omega^e}(\boldsymbol{u}_h) \cdot \boldsymbol{v} \, \mathrm{d}\Omega + \sum_{\Gamma} \int_{\Gamma} \mathcal{R}_{\Gamma}(\boldsymbol{u}_h) \cdot \boldsymbol{v} \, \mathrm{d}\Gamma \tag{5.4.6}$$

$$\mathcal{R}_{\Omega^e} = \boldsymbol{f} + \nabla \cdot [\boldsymbol{\sigma}(\boldsymbol{u}_h)]; \quad \mathcal{R}_{\Gamma} = \begin{cases} [\![[\boldsymbol{\sigma}(\boldsymbol{u}_h)]\boldsymbol{n}]\!] & \forall \Gamma \in \Gamma^e \\ \bar{\boldsymbol{t}} - [\boldsymbol{\sigma}(\boldsymbol{u}_h)]\boldsymbol{n} & \forall \Gamma \in \Gamma_N^e \\ 0 & \forall \Gamma \in \Gamma_D^e \end{cases} \tag{5.4.7}$$

The jump term, denoted by $[\![\cdot]\!]$, is related to the edge Γ, adjacent to elements e_i and e_j, and is defined as

$$[\![\boldsymbol{\sigma}(\boldsymbol{u}_h) \cdot \boldsymbol{n}]\!]_{\Gamma} = [\boldsymbol{\sigma}_{e_i}(\boldsymbol{u}_h)] \cdot \boldsymbol{n}_{e_i} + [\boldsymbol{\sigma}_{e_j}(\boldsymbol{u}_h)] \cdot \boldsymbol{n}_{e_j} \tag{5.4.8}$$

Note that $\boldsymbol{n}_{e_i} = -\boldsymbol{n}_{e_j} = \boldsymbol{n}$, therefore the jump term equals to

$$[\![\boldsymbol{\sigma}(\boldsymbol{u}_h)]\!] = ([\boldsymbol{\sigma}_{e_i}(\boldsymbol{u}_h)] - [\boldsymbol{\sigma}_{e_j}(\boldsymbol{u}_h)]) \cdot \boldsymbol{n}$$

The Clément operator Π_h maps the test functions $\boldsymbol{v}$ from $\mathcal{V}$ to $\mathcal{V}_h$ and builds all possible test functions from $\mathcal{V}_h$:

$$\Pi_h = \mathcal{V} \to \mathcal{V}_h \quad \text{with} \quad \Pi_h \boldsymbol{v} \in \mathcal{V}_h \quad \text{and} \quad \boldsymbol{v}_h = \Pi_h \boldsymbol{v} \tag{5.4.9}$$

Due to Galerkin orthogonality (5.2.8), we may write (5.4.6)

$$a(\boldsymbol{e}_h, \boldsymbol{v}) = \sum_{\Omega^e} \int_{\Omega^e} \mathcal{R}_{\Omega^e}(\boldsymbol{u}_h) \cdot (\boldsymbol{v} - \Pi_h \boldsymbol{v}) \, \mathrm{d}\Omega + \sum_{\Gamma} \int_{\Gamma} \mathcal{R}_{\Gamma}(\boldsymbol{u}_h) \cdot (\boldsymbol{v} - \Pi_h \boldsymbol{v}) \, \mathrm{d}\Gamma \tag{5.4.10}$$

After applying the Cauchy-Schwartz inequality element-wise for the integrals in (5.4.10), the residual is bounded by

$$\begin{aligned} a(\boldsymbol{e}_h, \boldsymbol{v}) \leq & \sum_{\Omega^e} \|\mathcal{R}_{\Omega^e}(\boldsymbol{u}_h)\|_{L^2(\Omega^e)} \|\boldsymbol{v} - \Pi_h \boldsymbol{v}\|_{L^2(\Omega^e)} \\ & + \sum_{\Gamma} \|\mathcal{R}_{\Gamma}(\boldsymbol{u}_h)\|_{L^2(\Gamma)} \|\boldsymbol{v} - \Pi_h \boldsymbol{v}\|_{L^2(\Gamma)} \end{aligned} \tag{5.4.11}$$

According to the results of the interpolation theory ([Clément, 1975],[Ciarlet, 1991]), we further have

$$\|\boldsymbol{v} - \Pi_h \boldsymbol{v}\|_{L^2(\Omega^e)} \leq C_1 h_e \|\nabla \boldsymbol{v}\|_{L^2(\bar{\Omega}^e)} = C_1 h_e |\boldsymbol{v}|_{\mathcal{H}_1(\bar{\Omega}^e)} \tag{5.4.12}$$

$$\|\boldsymbol{v} - \Pi_h \boldsymbol{v}\|_{L^2(\Gamma)} \leq C_2 \sqrt{h_e} \|\nabla \boldsymbol{v}\|_{L^2(\bar{\Gamma})} = C_2 \sqrt{h_e} |\boldsymbol{v}|_{\mathcal{H}_1(\bar{\Gamma})} \tag{5.4.13}$$

where h_e is the diameter of the element e. The symbols $\bar{\Omega}^e$, $\bar{\Gamma}$ denote the subdomain of the elements sharing a common edge with element e (adjacent to edge Γ) (see [Verfürth, 1994] for details). The L^2 norm is denoted by $\|\cdot\|_{L^2}$ and the $\mathcal{H}_1$ semi-norm by $\|\cdot\|_{\mathcal{H}_1}$.

The constants C_1 and C_2 are unknown interpolation constants, which depend on the model problem and on the shape of the elements. From (5.4.11)-(5.4.13) we have

$$\begin{aligned} a(\boldsymbol{e}_h, \boldsymbol{v}) \leq & \sum_{\Omega^e} C_1 h_e \|\mathcal{R}_{\Omega^e}(\boldsymbol{u}_h)\|_{L^2(\Omega^e)} |\boldsymbol{v}|_{\mathcal{H}_1(\bar{\Omega}^e)} \, \mathrm{d}\Omega \\ & + \sum_{\Gamma} C_2 h_e^{1/2} \|\mathcal{R}_{\Gamma}(\boldsymbol{u}_h)\|_{L^2(\Gamma)} |\boldsymbol{v}|_{\mathcal{H}_1(\bar{\Gamma})} \, \mathrm{d}\Gamma \\ & \leq \left\{ \sum_{\Omega^e} C_1^2 h_e^2 \|\mathcal{R}_{\Omega^e}(\boldsymbol{u}_h)\|^2 + \sum_{\Omega^e} \sum_{\Gamma^e} \frac{1}{2} C_2^2 h_e \|\mathcal{R}_{\Gamma^e}(\boldsymbol{u}_h)\|^2 \right\}^{1/2} \\ & \cdot \underbrace{\left\{ \sum_{\Omega^e} |\boldsymbol{v}|^2_{\mathcal{H}_1(\bar{\boldsymbol{\Omega}}^e)} + \sum_{\Omega^e} \sum_{\Gamma^e} \frac{1}{2} |\boldsymbol{v}|^2_{\mathcal{H}_1(\bar{\Gamma})} \right\}^{1/2}}_{\leq C_R |\boldsymbol{v}|_{\mathcal{H}_1(\bar{\Omega}^e)}} \end{aligned} \tag{5.4.14}$$

The $\mathcal{H}_1$ semi-norm can be estimated with the energy norm by $\|\boldsymbol{v}\|_{\mathcal{H}_1} \leq C_S \|\boldsymbol{v}\|_E$, where C_S is the stability constant and the energy norm $\|\boldsymbol{v}\|_E = \sqrt{a(\boldsymbol{v}, \boldsymbol{v})}$. If the model problem does not involve any singularities or boundary layers, usually the value $C_S = 1$ is taken. The constant C_R depends on the maximum number of elements in $\bar{\Gamma}^e$ and $\bar{\Omega}^e$. The global energy norm of the error follows:

$$\|\boldsymbol{e}_h\|_E^2 \leq C_R C_S \{\sum_{\Omega^e} C_1 h_e^2 \|\mathcal{R}_{\Omega^e}\|_{L^2(\Omega^e)} + \sum_{\Omega^e} \sum_{\Gamma^e} C_2 h_e \|\mathcal{R}_{\Gamma^e}\|_{L^2(\Gamma^e)}^2\} \tag{5.4.15}$$

Finally the explicit residual based error estimate is:

$$\|\boldsymbol{e}_h\|_E^2 \leq \sum_e \eta_e^2; \quad \eta_e^2 = c_1 h_e^2 \|\mathcal{R}_{\Omega^e}\|_{L^2(\Omega^e)} + \sum_{\Gamma^e} c_2 h_e \|\mathcal{R}_{\Gamma^e}(\boldsymbol{u}_h)\|_{L^2(\Gamma^e)}^2 \tag{5.4.16}$$

where the local error indicator is denoted by η_e.

The constants C_1 and C_2 are in general unknown. For general linear elastic analysis, the constants cannot be calculated with a reasonable computational effort. It has to be pointed that the introduction of the Cauchy-Schwarz inequality severely affects the accuracy of the error estimate. Therefore, the best possible constants C_1 and C_2 do not considerably improve the overall accuracy.

5.4.2 Implicit

The element residual method follows from the work of [Bank Weiser, 1985], [Stein Ohnimus, 1997], [Stein Ohnimus, 1999], [Stein et al., 2004]. The interest in implicit schemes stems from the fact that in explicit schemes the whole information for the total error is obtained only from the given solution $\boldsymbol{u}_h$. It is possible to obtain more accurate information on the error by solving additional auxiliary problems. Implicit error estimates thus involve the construction of the auxiliary boundary value problems, whose solution yields an approximation to the actual error.

The boundary problems to be solved are local, which means that they are posed either on a small patch of elements (subdomain residual method) or even on a single element (element residual method). In general, a drawback of the subdomain residual method can be that solving the local problems is rather expensive, since each element is considered several times. Moreover, the element residual method needs to approximate the prescribed Neumann boundary conditions on each single element ([Grätsch Bathe, 2005]). In the following, a variant of the element residual method will be presented; so-called *the equilibrated residual method (EqR)* (closely related to PEM method introduced in [Stein Ohnimus, 1997]).

The equilibrated residual method (EqR)

From (5.2.1) and (5.2.7) it follows that the error satisfies the equation

$$a(\boldsymbol{e}_h, \boldsymbol{v}) = l(\boldsymbol{v}) - a(\boldsymbol{u}_h, \boldsymbol{v}); \quad \forall \boldsymbol{v} \in \mathcal{V}_0 \tag{5.4.17}$$

This problem can be solved approximately for $\boldsymbol{e}_h$ by replacing $\boldsymbol{v}$ with a suitable candidate and thus furnish an approximation $\tilde{\boldsymbol{e}}$ to the actual error $\boldsymbol{e}_h$. According to (5.2.8), reusing the finite element subspace $\mathcal{V}_h$ to produce such an approximation will result in trivial solution $\tilde{\boldsymbol{e}} = 0$. It thus follows, that in order to get non trivial estimate of the error, the test space should be enhanced with respect to the finite element space.

Solving of global problem (5.4.17) to obtain error estimate is as computationally demanding as solving the original problem. Clearly, this is not an optimal choice. For any practically acceptable procedure, the computation of error estimate should be more efficient than computation of the global problem. One way to increase the efficiency, is to replace the global problem with a sequence of uncoupled boundary value problems, with each one posed over a single element. Doing so, so-called element residual method is obtained.

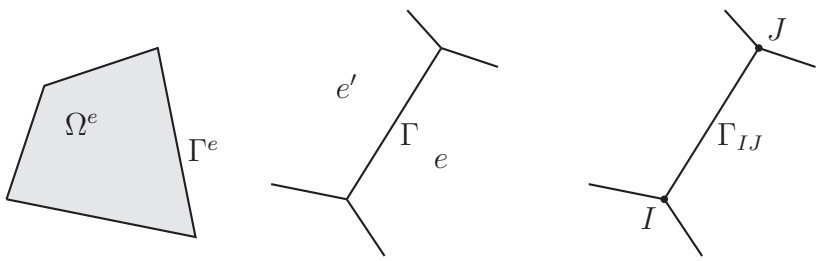

Figure 5.4.1: Notation
Slika 5.4.1: Oznake

The error equation (5.4.17) can be decomposed into element contributions:

$$a(\boldsymbol{e}_h, \boldsymbol{v}) = \sum_e \{l_e(\boldsymbol{v}) - a_e(\boldsymbol{u}_h, \boldsymbol{v})\} + \sum_e \int_{\Gamma^e} \boldsymbol{t}_\Gamma^e \cdot \boldsymbol{v} \, \mathrm{d}\Gamma; \quad \forall \boldsymbol{v} \in \mathcal{V}_0 \tag{5.4.18}$$

where we indicated that such decomposition is introducing additional boundary tractions $\boldsymbol{t}_\Gamma^e$ which act on the edges Γ^e of all the elements (see Figure 5.4.1). Let two neighboring elements e and e' share the edge Γ (Figure 5.4.1). The comparison between (5.4.17) and (5.4.18) implies

$$\sum_e \int_{\Gamma^e} \boldsymbol{t}_\Gamma^e \cdot \boldsymbol{v} \, \mathrm{d}s = 0. \tag{5.4.19}$$

The equation (5.4.19) requires that the work of boundary tractions from both elements, adjacent to the edge Γ, cancels out. Considering that the same displacement interpolation along the edge Γ is shared by adjacent elements, denoted by e and e', we can further conclude:

$$\boldsymbol{t}_\Gamma^e + \boldsymbol{t}_\Gamma^{e'} = 0. \tag{5.4.20}$$

With these results, the expression in (5.4.18) can then be replaced by local, element-wise ones. To that end, let $\boldsymbol{\vartheta}_{e,h}$ denote the solution of the weak form of the local boundary value problem for the error computation over the element e:

$$a_e(\boldsymbol{\vartheta}_{e,h}, \boldsymbol{v}) = l_e(\boldsymbol{v}) - a_e(\boldsymbol{u}_h, \boldsymbol{v}) + \int_{\Gamma^e} \boldsymbol{t}_\Gamma^e \cdot \boldsymbol{v} \, \mathrm{d}s; \quad \forall \boldsymbol{v} \in \mathcal{V}_0 \tag{5.4.21}$$

Note, that the local element problems (5.4.21) for unknown $\boldsymbol{\vartheta}_{e,h}$ are of Neumann type, since only tractions $\boldsymbol{t}_\Gamma^e$ are prescribed on element edges.

Moreover, the boundary tractions $\boldsymbol{t}_\Gamma^e$ are unknown and are yet to be constructed from the finite element solution $\boldsymbol{u}_h$, and in agreement with (5.4.20). In this manner, the global error computation (5.4.1) has been split into element contributions

$$a(\boldsymbol{e}_h, \boldsymbol{v}) = \sum_e a_e(\boldsymbol{\vartheta}_{e,h}, \boldsymbol{v}) \tag{5.4.22}$$

With the use of the Cauchy-Schwartz inequality, the relation between global error $\boldsymbol{e}_h$ and local solutions $\boldsymbol{\vartheta}_{e,h}$, the upper bound of a global error can be estimated

$$\|\boldsymbol{e}_h\|_E^2 \leq \sum_e \|\boldsymbol{\vartheta}_{e,h}\|_E^2 = \sum_e \eta_e^2 \tag{5.4.23}$$

where the *local error indicator* η_e is defined as

$$\eta_e^2 = \|\boldsymbol{\vartheta}_{e,h}\|_E^2 \tag{5.4.24}$$

In the case when element boundary tractions $\boldsymbol{t}_\Gamma^e$ coincide with the boundary tractions obtained from the exact solution for the right choice of $\boldsymbol{v} \in \mathcal{V}_0$, the estimated error is exact, since the exact solution to (5.4.18) can be recovered. It is thus obvious that the quality of approximation of element boundary tractions is critical for the effective error estimate. In the following, an efficient method for building the approximation of true boundary tractions will be presented.

We first see that the Galerkin orthogonality property (5.2.8) of the finite element solution $\boldsymbol{u}_h$ through the use of (5.4.22) implies $a_e(\boldsymbol{\vartheta}_{e,h}, \boldsymbol{v}_h) = 0$. Then, by using (5.4.21), an additional constraint for the unknown boundary tractions $\boldsymbol{t}_\Gamma^e$ can be constructed:

$$\int_{\Gamma^e} \boldsymbol{t}_\Gamma^e \cdot \boldsymbol{v}_h \, \mathrm{d}s = a_e(\boldsymbol{u}_h, \boldsymbol{v}_h) - l_e(\boldsymbol{v}_h) \tag{5.4.25}$$

The meaning of the equation (5.4.21) becomes more evident if $\boldsymbol{\vartheta}_{e,h}$ is defined as the difference between element approximation to the exact solution $\tilde{\boldsymbol{u}}_{e,h}$, and the FE solution $\boldsymbol{u}_{e,h}$

$$\boldsymbol{\vartheta}_{e,h} = \tilde{\boldsymbol{u}}_{e,h} - \boldsymbol{u}_{e,h}$$

Due to linearity of bilinear form a, the local problem (5.4.21) for $\tilde{\boldsymbol{u}}_e$ then becomes

$$a_e(\tilde{\boldsymbol{u}}_{e,h}, \boldsymbol{v}) = l_e(\boldsymbol{v}) + \int_{\Gamma^e} \boldsymbol{t}_\Gamma^e \cdot \boldsymbol{v} \, \mathrm{d}s; \quad \forall \boldsymbol{v} \in \mathcal{V} \tag{5.4.26}$$

The result $a_e(\boldsymbol{\vartheta}_{e,h}, \boldsymbol{v}_h) = 0$ implies $a_e(\tilde{\boldsymbol{u}}_{e,h}, \boldsymbol{v}_h) = a_e(\boldsymbol{u}_{e,h}, \boldsymbol{v}_h)$. It is thus clear that $\tilde{\boldsymbol{u}}_{e,h} = \boldsymbol{u}_{e,h}$, when the subspace used to obtain a local solution of (5.4.26) is identical to the original subspace $\mathcal{V}_h$, which was used to obtain the global finite element solution. Therefore, to be able to get an error estimate from (5.4.26), an enhanced test space should be used with $\boldsymbol{v}_{h^+} \in \mathcal{V}$.

The enhanced space deformation modes should also include rigid body modes $\boldsymbol{v}_\Lambda$, for which it holds $a_e(\boldsymbol{u}_h, \boldsymbol{v}_\Lambda) = 0$. In this case, the result in (5.4.25) will reduce to

$$\int_{\Gamma^e} \boldsymbol{t}_\Gamma^e \cdot \boldsymbol{v}_\Lambda \, \mathrm{d}s + l_e(\boldsymbol{v}_\Lambda) = 0 \tag{5.4.27}$$

By closer inspection of the expression (5.4.27), the equilibrium of the boundary tractions with the external loading can be deduced in the sense of virtual work principle.

An estimate of the discretization error can then be obtained through the solution of local problems (5.4.26) of Neumann type where $\mathcal{V}$ is replaced by its best possible approximation $\mathcal{V}_{h^+}$ that must be sufficiently enhanced with respect to $\mathcal{V}_h$

$$a_e(\tilde{\boldsymbol{u}}_{e,h^+}, \boldsymbol{v}_{h^+}) = l_e(\boldsymbol{v}_{h^+}) + \int_{\Gamma^e} \boldsymbol{t}_\Gamma^e \cdot \boldsymbol{v}_{h^+} \, \mathrm{d}s; \qquad \boldsymbol{v}_{h^+} \in \mathcal{V}_{h^+} \tag{5.4.28}$$

The loading of element problems consists of the sum of the external loading and the boundary tractions $\boldsymbol{t}_\Gamma^e$. They are referred to as *equilibrated boundary tractions*, due to the property (5.4.27) which implies that they are in equilibrium with the external loading. In a sense, the equilibrated boundary tractions are introduced to represent the action of surrounding elements on the selected element. Introduced boundary tractions are continuous across element edges. In summary, the main steps involved in the error estimation procedure are given in Box 2.

Computation of equilibrated boundary tractions for EqR

The performance of element residual method depends crucially on the estimation of equilibrated boundary tractions (see Box 2). In the following, a general procedure for the computation will be presented, which follows the work of [Ladevèze Leguillon, 1983].

Box 2 : The equilibrated residual method - EqR
Algoritem 2: EqR metoda

1. Obtain original finite element solution $\boldsymbol{u}_h$ of the problem (5.2.4)
2. Compute equilibrated boundary tractions $\boldsymbol{t}^e_\Gamma$ for each edge $\Gamma \subset \Gamma^e$ of each element e (see Box 3)
3. Approximately solve (5.4.28) for $\tilde{\boldsymbol{u}}_{e,h^+}$ by using test space $\mathcal{V}_{h^+}$ as enhanced approximation to $\mathcal{V}_h$
4. Compute local error estimates η_e^2 from (5.4.24) and $\boldsymbol{\vartheta}_{e,h} = \tilde{\boldsymbol{u}}_{e,h^+} - \boldsymbol{u}_{e,h}$

Recall that j-th component of the test function $\boldsymbol{v}_h$ is a linear combination of shape functions $N_{j,k}$ and nodal degrees of freedom $\hat{v}_k$. The interpolation of j-th component of $\boldsymbol{v}_h$ along an edge Γ is thus

$$(\boldsymbol{v}_{h|\Gamma})_j = \sum_k N_{j,k} v_k = \sum_K \boldsymbol{N}_j^K \cdot \hat{\boldsymbol{v}}_K \tag{5.4.29}$$

The alternative notation $(\boldsymbol{N}_j^K; \hat{\boldsymbol{v}}_K)$ refers to a set of the shape functions and interpolation parameters which pertain in any manner to node K. Specifically, we have $\hat{\boldsymbol{v}}_K = [\hat{v}_{i,K}]^T$ and $\boldsymbol{N}_j^K = [N_{j,i}^K]^T$ with $i = 1 \dots n_{ndof_K}$, where n_{ndof_K} is number of degrees of freedom at node K.

The virtual work of boundary tractions on edge Γ, spanning between nodes I and J, can then be reduced to[1] :

$$\int_\Gamma \boldsymbol{t}^e_\Gamma \cdot \boldsymbol{v}_h \, \mathrm{d}s = \boldsymbol{r}^e_{I,\Gamma} \cdot \hat{\boldsymbol{v}}_I + \boldsymbol{r}^e_{J,\Gamma} \cdot \hat{\boldsymbol{v}}_J, \tag{5.4.30}$$

where $\boldsymbol{r}^e_{I,\Gamma}$ denotes the "projection" (in a virtual work sense) of boundary traction $\boldsymbol{t}^e_\Gamma$ to node I. The components of $\boldsymbol{r}^e_{I,\Gamma}$ are directly related to the components of $\hat{\boldsymbol{v}}_I$. Thus, the number of components in $\boldsymbol{r}^e_{I,\Gamma}$ matches the number of nodal degrees of freedom at node I.

Let us assume that the boundary tractions $\boldsymbol{t}^e_\Gamma$ variations are described with some chosen interpolation. Regarding edge Γ, boundary tractions $\boldsymbol{t}^e_\Gamma$, can thus always be recovered from the projections $\boldsymbol{r}^e_{I,\Gamma}$, $\boldsymbol{r}^e_{J,\Gamma}$:

$$\boldsymbol{r}^e_{I,\Gamma}, \boldsymbol{r}^e_{J,\Gamma} \Rightarrow \boldsymbol{t}^e_\Gamma \tag{5.4.31}$$

[1] We reduce attention to the edge with two vertex nodes, although the edge with more nodes could be treated in the same manner

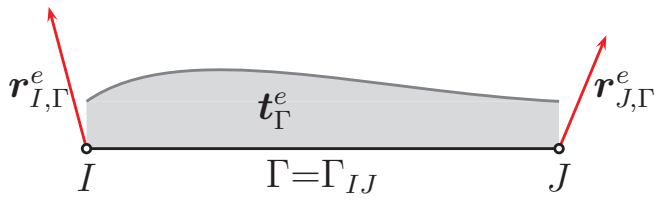

Figure 5.4.2: Relation between the tractions $\boldsymbol{t}^e_\Gamma$ and their projections $\boldsymbol{r}^e_{I,\Gamma}$
Slika 5.4.2: Relacija med robno obtežbo $\boldsymbol{t}^e_\Gamma$ in projekcijami $\boldsymbol{r}_{I,\Gamma}$

We therefore decide to replace in what follows the unknown tractions $\boldsymbol{t}^e_\Gamma$ with their projections $\boldsymbol{r}^e_{I,\Gamma}$. This will enable the patch-wise computation of boundary tractions $\boldsymbol{t}^e_\Gamma$.

By using $\boldsymbol{R}^e_I$ to denote the element nodal residuals[2], the right hand side of (5.4.25) can be rewritten as

$$a_e(\boldsymbol{u}_h, \boldsymbol{v}_h) - l_e(\boldsymbol{v}_h) = \boldsymbol{R}^e_I \cdot \hat{\boldsymbol{v}}_I \tag{5.4.32}$$

Moreover, the continuity condition for boundary tractions (5.4.20) can be rewritten as, see Figure 5.4.3:

$$\boldsymbol{r}^e_{I,\Gamma} + \boldsymbol{r}^{e'}_{I,\Gamma} = 0 \tag{5.4.33}$$

From (5.4.25), (5.4.30) and (5.4.32) we have (with a slight change in notation[3]), see Figure 5.4.4

$$\boldsymbol{r}^e_{I,\Gamma_1} + \boldsymbol{r}^e_{I,\Gamma_2} = \boldsymbol{R}^e_I \tag{5.4.34}$$

where Γ_1 and Γ_2 are edges of the same element e meeting at node I. Gathering (5.4.33) and (5.4.34), we obtain a linear system of algebraic equations with the projections $\boldsymbol{r}^e_{I,\Gamma}$ as unknowns. These systems are formed patchwise for the projections $\boldsymbol{r}^e_{I,\Gamma}$ of the node I.

To illustrate the patchwise formation of a local system of this kind we inspect an example with a patch of four 2D elements surrounding node I of the FE mesh (see Figure 5.4.5). Equations (5.4.34) and (5.4.33) for this case read (with a slight abuse of notation):

$$\begin{aligned}
\boldsymbol{R}^{e1}_I &= \boldsymbol{r}^{e1}_{I,\Gamma_4} + \boldsymbol{r}^{e1}_{I,\Gamma_1} & \boldsymbol{r}^{e1}_{I,\Gamma_1} + \boldsymbol{r}^{e2}_{I,\Gamma_1} &= 0 \\
\boldsymbol{R}^{e2}_I &= \boldsymbol{r}^{e2}_{I,\Gamma_1} + \boldsymbol{r}^{e2}_{I,\Gamma_2} & \boldsymbol{r}^{e2}_{I,\Gamma_2} + \boldsymbol{r}^{e3}_{I,\Gamma_2} &= 0 \\
\boldsymbol{R}^{e3}_I &= \boldsymbol{r}^{e3}_{I,\Gamma_2} + \boldsymbol{r}^{e3}_{I,\Gamma_3} & \boldsymbol{r}^{e3}_{I,\Gamma_3} + \boldsymbol{r}^{e4}_{I,\Gamma_3} &= 0 \\
\boldsymbol{R}^{e4}_I &= \boldsymbol{r}^{e4}_{I,\Gamma_3} + \boldsymbol{r}^{e4}_{I,\Gamma_4} & \boldsymbol{r}^{e4}_{I,\Gamma_4} + \boldsymbol{r}^{e1}_{I,\Gamma_4} &= 0
\end{aligned} \tag{5.4.35}$$

[2]Element nodal residuals can also be interpreted as the element nodal reactions i.e. the forces acting on the nodes of the element.

[3]The edge Γ has sometimes subscript related to the index of the edge; e.g. Γ_1, Γ_2, $\cdots$

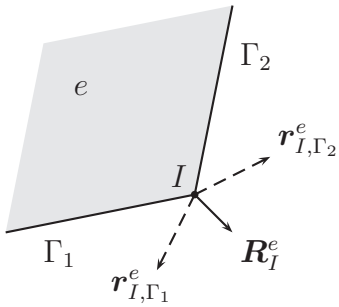

Figure 5.4.3: Element nodal residual $\boldsymbol{R}^e_I$ and boundary tractions projections $\boldsymbol{r}^e_{I,\Gamma_{1,2}}$ at node I of element e

Slika 5.4.3: Vozliščne reakcije $\boldsymbol{R}^e_I$ elementa in projekcije robnih obtežb $\boldsymbol{r}^e_{I,\Gamma_{1,2}}$ v vozlišču I elementa e

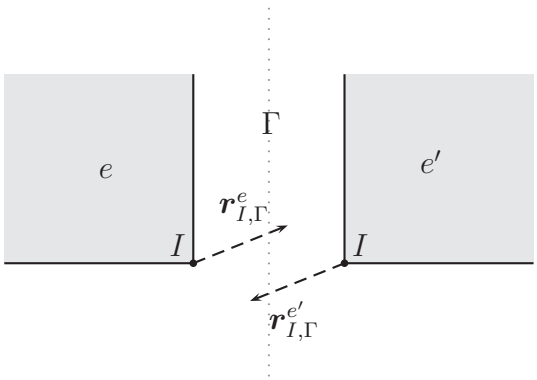

Figure 5.4.4: Continuity of boundary tractions projections $\boldsymbol{r}^e_{I,\Gamma}$

Slika 5.4.4: Zveznost projekcij robnih obtežb $\boldsymbol{r}^e_{I,\Gamma}$

Note, that the equations (5.4.35) also imply the node equilibrium $\sum_{e_i} \boldsymbol{R}^{e_i}_I = 0$. Combining the last set of equations, we obtain the following system of equations with the only remaining unknowns $\boldsymbol{r}^{e_k}_{I,\Gamma_k}$

$$\begin{bmatrix} \boldsymbol{R}^{e_1}_I \\ \boldsymbol{R}^{e_2}_I \\ \boldsymbol{R}^{e_3}_I \\ \boldsymbol{R}^{e_4}_I \end{bmatrix} = \begin{bmatrix} +1 & 0 & 0 & -1 \\ -1 & +1 & 0 & 0 \\ 0 & -1 & +1 & 0 \\ 0 & 0 & -1 & +1 \end{bmatrix} \begin{bmatrix} \boldsymbol{r}^{e_1}_{I,\Gamma_1} \\ \boldsymbol{r}^{e_2}_{I,\Gamma_2} \\ \boldsymbol{r}^{e_3}_{I,\Gamma_3} \\ \boldsymbol{r}^{e_4}_{I,\Gamma_4} \end{bmatrix} \tag{5.4.36}$$

Unfortunately, the local system in (5.4.36) is singular and its solution is not unique. To obtain the unique solution, a regularization has to be used. In the following, the regularization introduced in ([Stein Ohnimus, 1999], [Ainsworth Oden, 2000]) will be used.

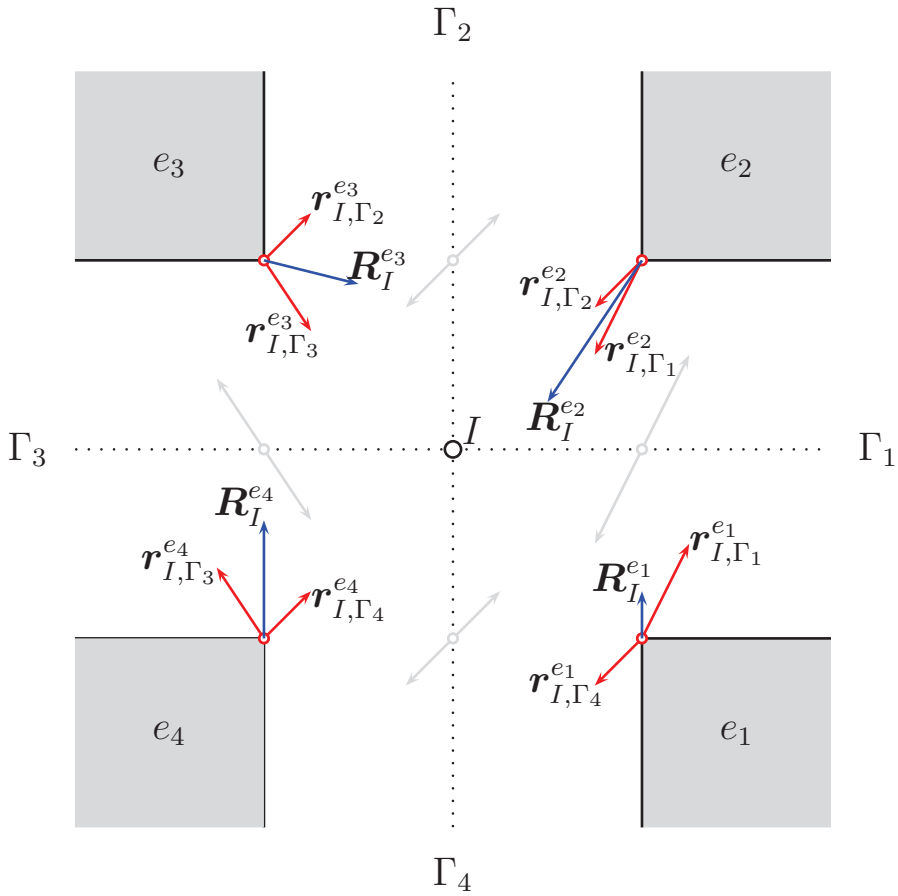

Figure 5.4.5: Patch $\mathcal{P}_I$ of four elements around node I

Slika 5.4.5: Krpa $\mathcal{P}_I$ štirih elementov okoli vozlišča I

Regularization of (5.4.33), (5.4.34)

First, an alternative estimate for the boundary tractions which will be denoted as $\tilde{\boldsymbol{t}}^e_\Gamma$ has to be constructed. Next, we use (5.4.30) to compute the projections $\tilde{\boldsymbol{r}}^e_{I,\Gamma}$:

$$\int_\Gamma \tilde{\boldsymbol{t}}^e_\Gamma \cdot \boldsymbol{v}_h \, \mathrm{d}s = \tilde{\boldsymbol{r}}^e_{I,\Gamma} \cdot \hat{\boldsymbol{v}}_I + \tilde{\boldsymbol{r}}^e_{J,\Gamma} \cdot \hat{\boldsymbol{v}}_J, \tag{5.4.37}$$

The basic idea of the regularization is to seek for the projections $\boldsymbol{r}^e_{I,\Gamma}$ which are as close as possible, in a least squares sense, to the projections $\tilde{\boldsymbol{r}}^e_{I,\Gamma}$. Hence, beside imposing the constraints (5.4.33) and (5.4.34), we will seek for the projections $\boldsymbol{r}^e_{I,\Gamma}$ that minimize the objective function over a patch $\mathcal{P}_I$ around node I (a slight change in notation is

introduced[4])

$$\frac{1}{2}\sum_{e\in\mathcal{P}_I}\sum_{\Gamma_{IK}}\left(\boldsymbol{r}^e_{I,\Gamma_{IK}}-\tilde{\boldsymbol{r}}^e_{I,\Gamma_{IK}}\right)^2 \longmapsto min. \tag{5.4.38}$$

The alternative boundary tractions $\tilde{\boldsymbol{t}}^e_\Gamma$ are usually computed from the stresses $\boldsymbol{\sigma}_h(\boldsymbol{u}_h)$. Since the finite element stresses $\boldsymbol{\sigma}_h$ are discontinuous over the edges of the elements their continuity is first enforced. Simple averaging can be performed

$$\tilde{\boldsymbol{\sigma}}|_\Gamma = (\boldsymbol{\sigma}^e_h|_\Gamma + \boldsymbol{\sigma}^{e'}_h|_\Gamma)/2 \tag{5.4.39}$$

The alternative boundary tractions are then

$$\tilde{\boldsymbol{t}}^e_\Gamma = [\tilde{\boldsymbol{\sigma}}|_\Gamma]\boldsymbol{n}^e_\Gamma \tag{5.4.40}$$

The procedure for the determination of the equilibrated boundary tractions is summarized in Box 3:

Box 3 : Computation of equilibrated boundary tractions
Algoritem 3: Uravnoteženje robnih obtežb

1. Compute element nodal residuals $\boldsymbol{R}^e_I$ from $\boldsymbol{u}_h$ using (5.4.32)
2. Construct $\tilde{\boldsymbol{t}}^e_\Gamma$ from (5.4.40) and (5.4.39)
3. Compute alternative projections $\tilde{\boldsymbol{r}}^e_{I,\Gamma}$ from (5.4.37)
4. Form patchwise systems of equations (5.4.35) and solve them for $\boldsymbol{r}^e_{I,\Gamma}$ by (5.4.38)
5. Choose the interpolation ψ^I_k, ψ^J_k for boundary tractions $\boldsymbol{t}^e_\Gamma$ and solve for nodal values of boundary tractions $\boldsymbol{p}^e_{\Gamma,I}$ from (5.4.43)
6. Compute boundary tractions by (5.4.40)

Let us now elaborate on Step 5 in Box 2 and introduce parametrization of k-th component of the boundary traction $\boldsymbol{t}^e_\Gamma$ (let Γ be element edge between element nodes I and J) as

$$(\boldsymbol{t}^e_\Gamma)_k = \psi^I_k p_{k,I} + \psi^J_k p_{k,J} \tag{5.4.41}$$

where ψ^I_k are interpolation functions (yet to be chosen) and $p_{k,I}$ are the nodal values of $(\boldsymbol{t}^e_\Gamma)_k$. The variation of virtual displacements along the edge Γ can be written as

$$(\boldsymbol{v}_{h,\Gamma})_k = \sum_{i=1}^{n_{ndof_I}} N^I_{k,i}\hat{v}_{i,I} + \sum_{i=1}^{n_{ndof_J}} N^J_{k,i}\hat{v}_{i,J} \tag{5.4.42}$$

[4]The edge Γ (see Figure 5.4.2) has sometimes subscript related to the indices of vertex nodes of the edge: e.g. Γ_{IJ}, Γ_{IK}, $\cdots$

where $\hat{v}_{j,I}$ is related to the j-th degree of freedom at node I, and $N^I_{k,i}$ are the corresponding shape functions. In other words, the shape function $N^I_{k,i}$ interpolates the k-th component of virtual displacements $\boldsymbol{v}_{h,\Gamma}$ and is weighted by nodal degree of freedom $\hat{v}_{i,I}$ in the linear interpolation (5.4.42). We can now insert the above parameterizations into (5.4.30) and express residuals at nodes I and J with respect to the boundary traction on edge Γ (that spans between I and J). The result can be written in a compact form as:

$$\begin{bmatrix} \boldsymbol{r}^e_{I,\Gamma} \\ \boldsymbol{r}^e_{J,\Gamma} \end{bmatrix} = \begin{bmatrix} \mathbf{M}^{II}_\Gamma & \mathbf{M}^{IJ}_\Gamma \\ \mathbf{M}^{JI}_\Gamma & \mathbf{M}^{JJ}_\Gamma \end{bmatrix} \begin{bmatrix} \boldsymbol{p}_{\Gamma,I} \\ \boldsymbol{p}_{\Gamma,J} \end{bmatrix}; \tag{5.4.43}$$

$$\mathbf{M}^{IJ}_\Gamma = [\mathbf{M}^{I,J}_\Gamma]; \quad \mathbf{M}^{I,J}_\Gamma = [M^{I,J}_{\Gamma,nm}]$$

where $\boldsymbol{p}_{\Gamma,I} = [p_{k,I}]^T$, $k = 1, \ldots n_{\text{dim}}$, and n_{dim} is a dimension of $\boldsymbol{t}^e_\Gamma$. The block matrices $\mathbf{M}^{I,J}_\Gamma$ have n_{ndof_I} rows and n_{dim} columns with the elements

$$M^{I,J}_{\Gamma,nm} = \int_\Gamma N^I_{\bar{m},n} \psi^J_m ds \tag{5.4.44}$$

The index $\bar{m}$ is denotes the virtual displacement component which is conjugated (in the sense of the virtual work principle) to the traction component m.

By solving (5.4.43) for every element edge Γ, we obtain parameters $\boldsymbol{p}_{\Gamma,I}$ and $\boldsymbol{p}_{\Gamma,J}$, which completely define element boundary traction $\boldsymbol{t}^e_{\Gamma_{IJ}}$ through (5.4.41). The choice of the shape functions ψ^I_k, which describe the variation of the boundary tractions along the edge, is somewhat arbitrary. It is suggested in the literature (e.g. [Ainsworth Oden, 2000], [Oden Cho, 1997]) that shape functions ψ^J_k and ψ^I_k should be orthogonal to the shape functions describing the variation of the test function $\boldsymbol{v}_h$. In this case the terms $\mathbf{M}^{IJ}_\Gamma$ and $\mathbf{M}^{JI}_\Gamma$ vanish and the matrix $\mathbf{M}$ becomes block diagonal. The relation (5.4.43) simplifies to

$$\boldsymbol{r}^e_{I,\Gamma} = \mathbf{M}^{II}_\Gamma \boldsymbol{p}^I_\Gamma \tag{5.4.45}$$

which significantly reduces the computation cost. Note, however, that the specific choice of parametrization (5.4.45) does not affect the local patch-wise computation of boundary tractions.

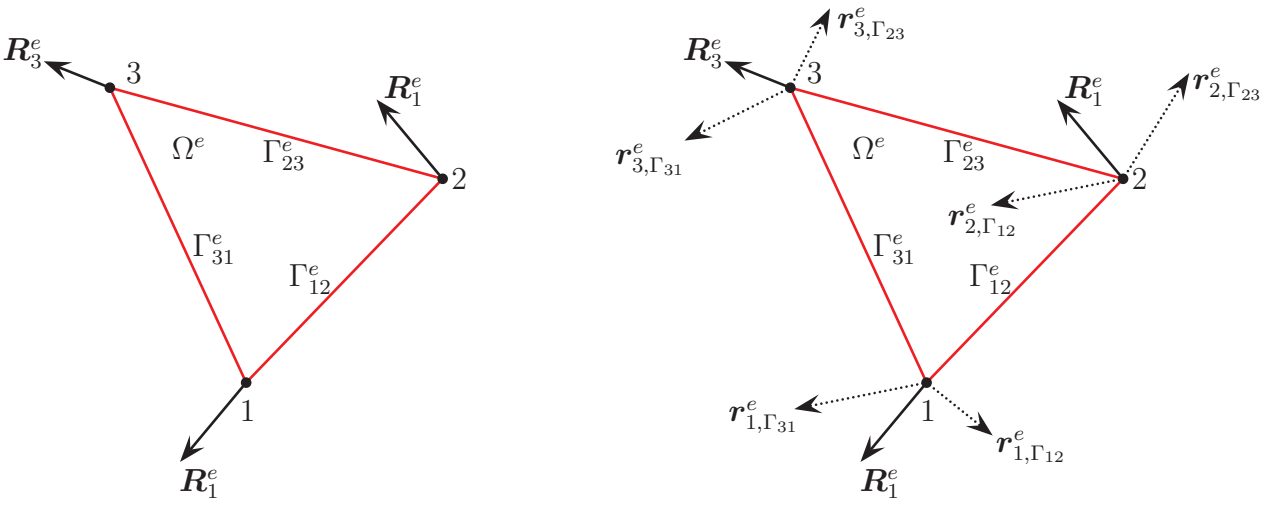

Figure 5.4.6: Representation of element nodal residuals $\boldsymbol{R}_I^e$ by the projections $\boldsymbol{r}_{I,\Gamma}^e$

Slika 5.4.6: Vozliščne reakcije elementa $\boldsymbol{R}_I^e$ in projekcije $\boldsymbol{r}_{I,\Gamma}^e$ robne obtežbe $\boldsymbol{t}_\Gamma^e$

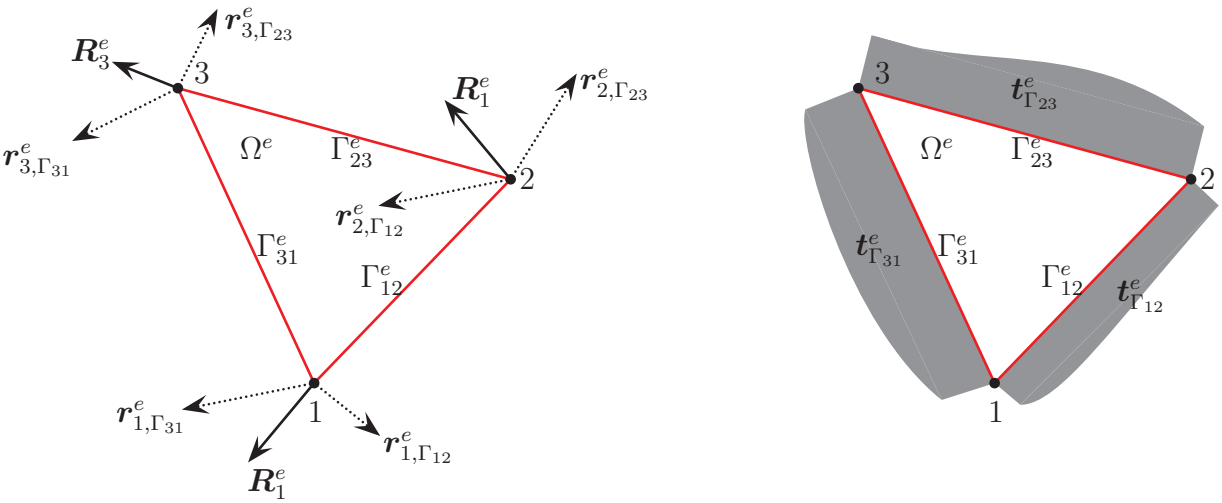

Figure 5.4.7: Boundary tractions $\boldsymbol{t}_\Gamma^e$ replace the action of element projections $\boldsymbol{r}_{I,\Gamma}^e$

Slika 5.4.7: Robna obtežba $\boldsymbol{t}_\Gamma^e$ je po principu virtualnega dela ekvivalentna delovanju projekcij $\boldsymbol{r}_{I,\Gamma}^e$ (in s tem tudi $\boldsymbol{R}_I^e$)

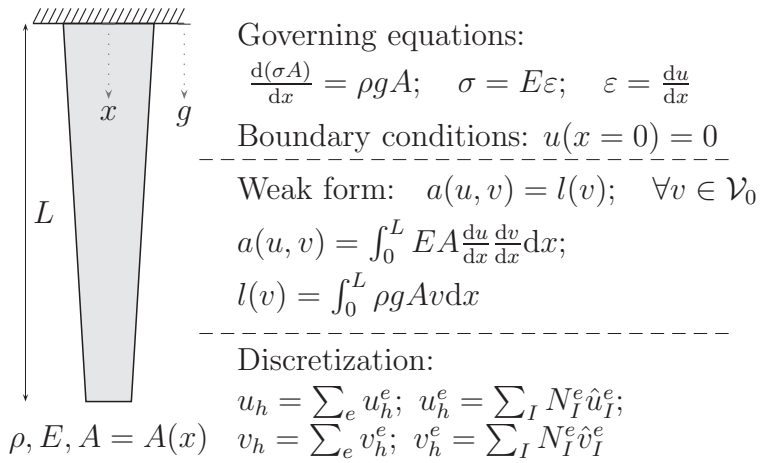

Figure 5.5.1: One dimensional problem: hanging bar with variable cross section
Slika 5.5.1: Enodimenzionalni problem: viseča palica s spremenljivim presekom

5.5 Illustration of SPR and EqR methods on 1D problem

In the following, the basic principles of EqR and SPR error estimates will be illustrated on a simple one-dimensional problem. The illustration of the error estimation methods on a simple problem reveals the fundamental differences in the concepts. The one-dimensional problem also clearly identifies the key steps of the computation procedures.

The subject of a model problem is a hanging bar with a variable cross section A. The bar of length L is made of linear elastic material with the modulus of elasticity E and density ρ (see Figure 5.5.1).

The displacement of the bar along the x axis is denoted by u. The deformation is $\varepsilon = \frac{\mathrm{d}u}{\mathrm{d}x}$. Hooke's law gives the stress $\sigma = E\varepsilon$. The line force $A\rho g$ (g is earth acceleration) is equilibrated by the axial force σA:

$$\frac{\mathrm{d}(\sigma A)}{\mathrm{d}x} = \rho g A$$

The summary of governing equations is given in Figure 5.5.1.

The displacement of the bar u is discretized by the function $u_h = \sum_e u_h^e$. We introduce linear and quadratic finite elements. The linear element has two degrees of freedom $\hat{u}_1^e$ and $\hat{u}_2^e$ at vertex nodes 1 and 2. The nodal coordinates are denoted by x_1^e and x_2^e. The displacement of linear element is approximated by $u_h^e = u_{h,L}^e = N_1^e \hat{u}_1^e + N_2^e \hat{u}_2^e$, where N_1^e

and N_2^e are defined as:

$$N_1^e(x) = \frac{x_2^e - x}{L_e}; \quad N_2^e(x) = \frac{x - x_1^e}{L_e}; \quad N_3^e(x) = 4N_1^e(x)N_2^e(x) \tag{5.5.1}$$

where L_e denotes the length of the element. The quadratic element has an additional degree of freedom $\hat{u}_3^e$ at the middle point of the element $x_3^e = (x_1^e + x_2^e)/2$. The approximation of displacement of a quadratic element is a hierarchic extension of that of the linear element $u_h^e = u_{h,Q}^e = u_{h,L}^e + N_3^e \hat{u}_3^e$.

The finite element solution u_h satisfies

$$a(u_h, v_h) = l(v_h); \quad \forall v_h \in \mathcal{V}_h \tag{5.5.2}$$

The test functions v_h are interpolated as $v_h = \sum_e v_h^e$, where $v_h^e = \sum_I N_I^e \hat{v}_I^e$ the sum runs over all the degrees of freedom. The shape function N_k is related to the degree of freedom k and is defined as the sum of element shape functions $N_k = \sum_e N_I^e$ pertaining to the chosen degree of freedom. The set of equations defining the solution , which follows from (5.5.2), is:

$$a(u_h, N_k) = \sum_e a_e(u_h^e, N_k) = l(N_k); \quad \forall N_k \tag{5.5.3}$$

The element stiffness matrix and the load vector are introduced to enable the matrix notation of (5.5.3). They are defined as:

$$K_{IJ}^e = a_e(N_J^e, N_I^e) = \int_{x_1^e}^{x_2^e} EA \frac{\mathrm{d}N_J^e}{\mathrm{d}x} \frac{\mathrm{d}N_I^e}{\mathrm{d}x} \mathrm{d}x; \tag{5.5.4}$$

$$F_I^e = l(N_I^e) = \int_{x_1^e}^{x_2^e} \rho g A N_I^e \mathrm{d}x \tag{5.5.5}$$

In the example below we are solving for the displacement of the tapered hanging bar of the cross section $A = A_0(1 + p - 12p(1 - x/L)^2 x/L)$, where p is the taper parameter. The linear and quadratic solutions for the case $p = 1$ are shown in Figure 5.5.2 and Figure 5.5.3 ($u_0 = \rho g L^2/(2E)$ and $\sigma_0 = \rho g L$ are values of maximum displacement and stress for the case $p = 0$ - rod with constant cross section). The significant variation of cross section is reflected in rich stress variation. Relatively small number of elements (5), which are used to obtain the finite element solution, enable to visually asses the quality of the solution in terms of displacement as well as in terms of the stress. As expected, significant stress jumps occur in the case of linear elements, whereas quadratic elements capture the variation of stress much better. The stress jumps between the elements are in this case smaller, although they do not vanish completely.

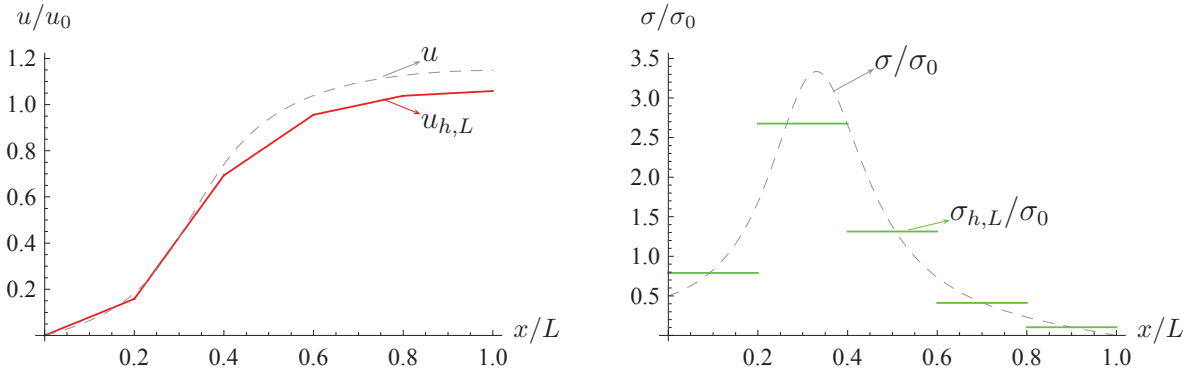

Figure 5.5.2: Solution of the model problem with linear elements
Slika 5.5.2: Rešitev modelnega problema z linearnimi elementi

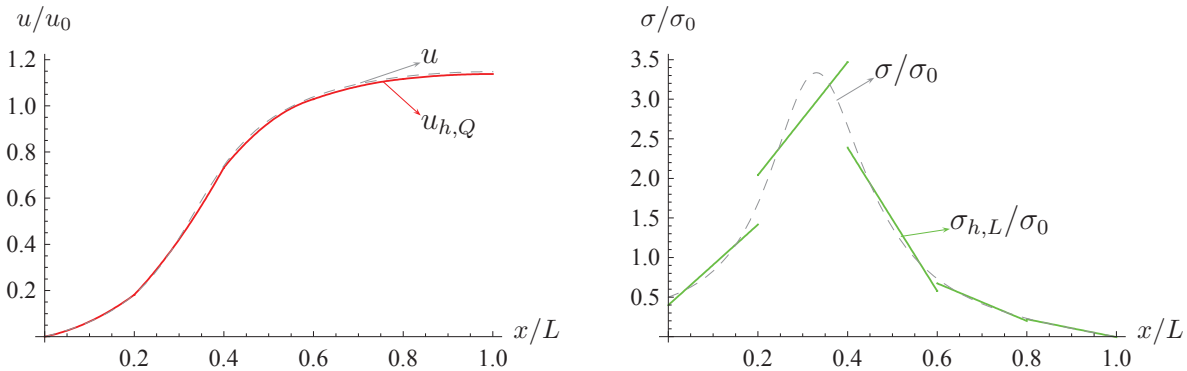

Figure 5.5.3: Solution of the model problem with quadratic elements
Slika 5.5.3: Rešitev modelnega problema s kvadratičnimi elementi

First, we compute the error of linear elements by the SPR procedure. Enhanced stress σ^* is computed from the original finite element solution. Since the problem is one-dimensional, the nodal values of enhanced stress σ^* are effectively computed as the average of the integration point values of stress of two neighboring elements. The integration point (with superconvergent properties) is taken at the midside of the element. In Figure 5.5.4 the enhanced stress is depicted as solid blue line and the nodal values of enhanced stress are shown as red points. Note, that the SPR method, although better than the original finite element stress estimate, is unable to fully capture the variation of the exact (analytic) stress (shown as gray dashed line). The key feature of the method - averaging of discontinuous stress field - can clearly be recognized.

Next, we compute the error of linear elements by the EqR procedure. The EqR computation of the enhanced stress σ^* is based on local element computations with enhanced

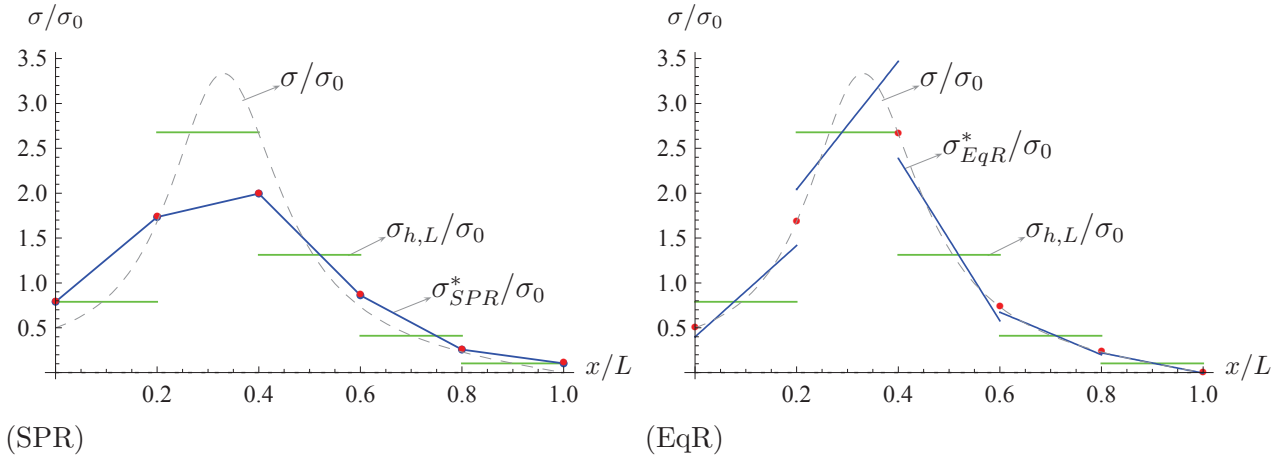

Figure 5.5.4: Computation of enhanced stress σ^*; comparison of SPR and EqR method
Slika 5.5.4: Izračun izboljšanih napetosti σ^*; primerjava med SPR in EqR metodo

model. The boundary conditions for the element problems are of Neumman type and are computed from the current finite element solution. The nodal element residuals are computed from $\boldsymbol{R}^e = [R_1^e, R_2^e]^T = \mathbf{K}_L^e \boldsymbol{u}^e - \boldsymbol{F}_L^e$, where L denotes the linear element. In the simple one-dimensional model no additional equilibration is needed and the reactions R_1^e and R_2^e are already the nodal forces used in the local element computation. Since we are using the quadratic element as the enhanced model, the load vector is $\tilde{\boldsymbol{R}}^e = [R_1^e, R_2^e, 0]^T$. Enhanced element stresses σ^* are finally computed from the solutions $\tilde{u}^e$ of the local element problems:

$$\mathbf{K}_Q^e \tilde{\boldsymbol{u}}^e = \tilde{\boldsymbol{R}}^e + \boldsymbol{F}_Q^e$$

Figure 5.5.4-(EqR) depicts the enhanced stress σ^* computed from $\tilde{u}^e$. The red points show the values $|R^e|/A$, which can be interpreted as the nodal stress values σ_I^*. Note that they coincide with true nodal stress values σ_I. Also the enhanced stresses σ^* show very good overall agreement of the true ones computed from analytical solution.

5.6 Chapter summary and conclusions

The chapter is concerned with the computation of discretization error in general. An overview of existing a-posteriori methods is given. Among them, two are covered in detail: the superconvergent patch recovery method (SPR) and the equilibrated residual method (EqR). Both methods are treated to the level ready for the implementation. The treatment

of SPR and EqR method is accompanied with a small illustrative numerical example. The detailed, independent and systematic treatment of the EqR method revealed some important results relevant for the application of the method to the modeling of plate structures. The main step in the EqR method is the computation of the admissible boundary tractions for the local problem. Perhaps the key finding of this chapter is, that the interpolation of the boundary tractions does not enter the equilibration procedure directly. The equilibration procedure is computed independently on the level of boundary traction projections. The specific form of the interpolation of boundary tractions enters the computation only through the regularization.

Chapter 6

Discretization error for DK and RM elements

6.1 Introduction

There exist a very large number of applications from aerospace, civil and mechanical engineering, which call for the plate finite element (FE) models. Among plate finite elements, perhaps the most frequently used, are the discrete-Kirchhoff (DK) finite elements for thin plates (e.g. see [Batoz et al., 1980], [Batoz, 1982] or [Bernadou, 1996]). These elements deliver near optimal performance for thin plate element with the smallest possible number of nodes. Thus they are used in practically any commercial code, either as 3-node triangle (DKT) or as 4-node quadrilateral (DKQ). Hence, the main question addressed in this chapter, pertaining to discretization error and choice of the FE mesh size when a plate is discretized by DK elements, is of great practical importance.

The DK plate element, delivering optimal performance, is the result of the long line of developments on Kirchhoff-Love plate FE models (such as [Clough Tocher, 1965] or [Felippa Clough, 1965]) that also benefited from more recent works on Reissner/Mindlin thick plate FE models (e.q. see [Zienkiewicz Taylor, 2000] and references herein). However, as opposed to shear locking phenomena of Reissner/Mindlin FE plate models (e.q. see [Zienkiewicz Taylor, 2000] or [Hughes, 2000], Taylor et al [Zienkiewicz Taylor, 2000]), the DK plate model completely removes the shear deformation and thus eliminates the locking. This results with non-conventional FE interpolations with $\mathcal{C}^1$ continuity (e.q. see [Ibrahimbegović, 1993]). Therefore, most of the previous results on error estimates, coming from solid mechanics FE models with $\mathcal{C}^0$-interpolations (e.g. see [Ainsworth Oden, 2000], [Ladevèze Pelle, 2006] or [Stein Ramm, 2003]), do not directly apply to this case. Moreover, the non-conventional FE interpolations of DK plate elements are the result of

enforcing the Kirchhoff constraint selectively, and they are not based on the minimum energy principles. For all these reasons, it is not easy to provide the error estimates for DK plate elements with rigorous upper and lower bounds, but rather the most useful error indicators.

In this chapter we present the error estimates and indicators for DK plate elements based upon two main families, the superconvergent patch recovery (e.g. see [Zienkiewicz Zhu, 1992], [Babuška Pitkaranta, 1990]) and the equilibrated residual method (e.g. see [Becher Rannacher, 2001], [Johnson Hansbo, 1992] or [Ladevèze Leguillon, 1983]). In what follows, we will not, strictly distinguish between error estimates and error indicators.

It turns out that the superconvergent patch recovery procedure is easy to apply to discrete-Kirchhoff plate elements, by constructing the enhanced approximation through superconvergence property of Gauss point values (e.g. see [Zienkiewicz Taylor, 2000], [Flajs et al., 2010]). On the contrary, the equilibrated residual method needs somewhat more ingenious procedure. Namely, it was found out, that the best estimate of the exact solution is constructed by using the plate elements suggested by Argyris and co-workers (see [Argyris et al., 1968]) that have been used by mathematicians (see [Bernadou, 1996]) but never reached the wide acceptance by engineers.

At the end of the chapter we show that the error estimates and indicators for Reissner/Mindlin (RM) plate elements can be obtained in a very similar way as it is presented here for DK elements.

6.2 Discretization error for DK elements

The local error indicator for the DK elements is computed from

$$\eta_{e,DK}^2 = \sum_e \int_{\Omega_h^e} (\boldsymbol{m}^* - \boldsymbol{m}_h)^T \mathbf{C}_B^{-1} (\boldsymbol{m}^* - \boldsymbol{m}_h) \, \mathrm{d}\Omega \tag{6.2.1}$$

where $\boldsymbol{m}^*$ are the enhanced moments. They are computed using either SPR method or the EqR method. In the case of EqR method, the enhanced moments are computed from the solution of the local problems $\tilde{\boldsymbol{u}}_{e,h}$: $\boldsymbol{m}^* = \boldsymbol{m}^*(\tilde{\boldsymbol{u}}_{e,h})$.[1]

6.2.1 Discrete approximation for error estimates

The computation of the equilibrated boundary tractions, which represent the input data for the element problems in EqR method, is defined in Box 3. Steps 1 and 3 do not,

[1] The definition of the local error indicator (6.2.1) follows from (5.4.24) and is equivalent to (5.3.4).

besides the topology, change with respect to the element used. The steps 2 and 4 depend on the interpolation. The main issue becomes the relation between boundary tractions $\boldsymbol{t}^e_\Gamma$ and their projections $\boldsymbol{r}^e_{I,\Gamma}$.

Let us recall the interpolation of displacement and rotations over the edges of the element. The variation of displacement along the element boundary Γ_{IJ}, spanned between the element nodes I and J, is defined (according to (2.3.59)) by:

$$w_{h,\Gamma_{IJ}} = \hat{w}_I\,\varphi_1 + \hat{w}_J\,\varphi_2 + \frac{L_{IJ}}{4}\mathbf{n}_{IJ}\cdot(\hat{\boldsymbol{\theta}}_I - \hat{\boldsymbol{\theta}}_J)\,\varphi_3 + \frac{L_{IJ}}{3}\Delta\theta_{IJ}\,\varphi_4 \tag{6.2.2}$$

where $\Delta\theta_{IJ} = \frac{3}{2\,L_{IJ}}(\hat{w}_J - \hat{w}_I) - \frac{3}{4}\mathbf{n}_{IJ}\cdot(\hat{\boldsymbol{\theta}}_I + \hat{\boldsymbol{\theta}}_J)$, L_{IJ} is the length of the edge Γ_{IJ} and $\boldsymbol{n}_{IJ} = [n_{x,IJ}, n_{y,IJ}]^T$ is the unit exterior normal and $\phi_1, \cdots, \phi_4$ are shape functions. Similarly, variation of rotation vector along the same edge can be written as

$$\boldsymbol{\theta}_{h,\Gamma_{IJ}} = \hat{\boldsymbol{\theta}}_I\,\varphi_1 + \hat{\boldsymbol{\theta}}_J\,\varphi_2 + \mathbf{n}_{IJ}\Delta\theta_{IJ}\,\varphi_3 \tag{6.2.3}$$

The shape functions φ_i in (6.2.2) and (6.2.3) are defined as, see (2.3.55)

$$\begin{aligned} \varphi_1 &= (1-\xi)/2 & \varphi_2 &= (1+\xi)/2 \\ \varphi_3 &= (1-\xi^2)/2 & \varphi_4 &= \xi(1-\xi^2)/2, \end{aligned} \tag{6.2.4}$$

where $\xi \in [-1, 1]$.

We compute the boundary traction projections $\boldsymbol{r}^e_{I,\Gamma_{IJ}}$, which pertain to the boundary tractions $\boldsymbol{t}^e_{\Gamma_{IJ}} = [\overline{q}_{ef}, \overline{m}_s, \overline{m}_n]$ through (5.4.30).

In order to evaluate the traction projections, the following integral has to be evaluated:

$$\int_{\Gamma_{IJ}} \left(\overline{q}_{ef,\Gamma_{IJ}} w_{h,\Gamma_{IJ}} + \overline{m}_{s,\Gamma_{IJ}}(\boldsymbol{s}\cdot\boldsymbol{\theta}_{h,\Gamma_{IJ}})\right)\,\mathrm{d}s + [\overline{m}_n w_{h,\Gamma_{IJ}}]_I^J = \boldsymbol{r}^e_{I,\Gamma_{IJ}}\cdot\hat{\boldsymbol{u}}_I + \boldsymbol{r}^e_{J,\Gamma_{IJ}}\cdot\hat{\boldsymbol{u}}_J \tag{6.2.5}$$

Comparison of the corresponding terms on both sides of the equation (6.2.5) will provide the components of the projections $\boldsymbol{r}^e_{I,\Gamma} = [r^{\hat{w}}_{I,\Gamma}, r^{\hat{\theta}_x}_{I,\Gamma}, r^{\hat{\theta}_y}_{I,\Gamma}]^T$, where the notation $\Gamma = \Gamma_{IJ}$ is employed. These components are energy conjugated to the plate element degrees of freedom and the chosen discretization.

The boundary traction $\boldsymbol{t}^e_\Gamma$ consists of three components: shear $\overline{q}_\Gamma$ and moments $\overline{m}_{s,\Gamma}$, $\overline{m}_{n,\Gamma}$. For the given interpolation for $\boldsymbol{t}^e_\Gamma$, the components can be reconstructed from the projections $\boldsymbol{r}^e_{I,\Gamma}$ from (7.2.25). We chose to interpolate each of the components of $\boldsymbol{t}^e_\Gamma$ with the same interpolation: a linear combination of the shape functions ψ_I and ψ_J:

$$\begin{aligned} \overline{q}_\Gamma &= \overline{q}^I_\Gamma\psi_I + \overline{q}^J_\Gamma\psi_J \\ \overline{m}_{s,\Gamma} &= \overline{m}^I_{s,\Gamma}\psi_I + \overline{m}^J_{s,\Gamma}\psi_J \\ \overline{m}_{n,\Gamma} &= \overline{m}^I_{n,\Gamma}\psi_I + \overline{m}^J_{n,\Gamma}\psi_J \end{aligned} \tag{6.2.6}$$

Note, that $\bar{q}_{ef,\Gamma}$ in (6.2.5) is defined as $\overline{q}_\Gamma - \frac{\partial \overline{m}_{n,\Gamma}}{\partial s}$, where s is a boundary coordinate, see Figure (2.2.7), with normal $[n_x, n_y]^T$. The shape functions ψ_I are not yet specified here, except that $\psi_{k,I} = \psi_I$ for $k \in [q, m_s, m_n]$. The relation between the projections of $\boldsymbol{r}^e_{I,\Gamma}$ and the parameters $[\bar{q}^I_\Gamma, \overline{m}^I_{s,\Gamma}, \overline{m}^I_{n,\Gamma}]$ can then be obtained according to (compare to more general formulation (5.4.43)):

$$\begin{bmatrix} \boldsymbol{r}^e_{I,\Gamma} \\ \boldsymbol{r}^e_{J,\Gamma} \end{bmatrix} = \boldsymbol{A}^q \begin{bmatrix} \bar{q}^I_\Gamma \\ \bar{q}^J_\Gamma \end{bmatrix} + \boldsymbol{A}^{m_s} \begin{bmatrix} \overline{m}^I_{s,\Gamma} \\ \overline{m}^J_{s,\Gamma} \end{bmatrix} + \boldsymbol{A}^{m_n} \begin{bmatrix} \overline{m}^I_{n,\Gamma} \\ \overline{m}^J_{n,\Gamma} \end{bmatrix}, \tag{6.2.7}$$

where

$$\boldsymbol{A}^{m_s} = (-n_y \boldsymbol{A}^{m_x} + n_x \boldsymbol{A}^{m_y}); \quad \boldsymbol{A}^{m_n} = \begin{bmatrix} 1 & 0 & 0 & 0 & 0 & 0 \\ 0 & 0 & 0 & 1 & 0 & 0 \end{bmatrix}^T; \tag{6.2.8}$$

$$\boldsymbol{A}^k = \begin{bmatrix} \boldsymbol{A}^k_{II} & \boldsymbol{A}^k_{IJ} \\ \boldsymbol{A}^k_{JI} & \boldsymbol{A}^k_{JJ} \end{bmatrix}; \qquad \boldsymbol{A}^k_{IJ} = \int_{\Gamma_{IJ}} \begin{bmatrix} N^I_{\bar{k},\hat{w}} \\ N^I_{\bar{k},\hat{\theta}_x} \\ N^I_{\bar{k},\hat{\theta}_y} \end{bmatrix} \psi_J \, \mathrm{d}s \, ; \quad k \in [q, m_x, m_y]; \;\; \bar{k} \in [w, \theta_x, \theta_y]$$

The shape functions employed in (6.2.8) can be written explicitly as:

$$\begin{aligned}
N^I_{w,\hat{w}} &= \varphi_1 - \varphi_4/2 & N^J_{w,\hat{w}} &= \varphi_2 + \varphi_4/2 \\
N^I_{w,\hat{\theta}_x} &= -L\, n_x(-\varphi_3 + \varphi_4)/2 & N^J_{w,\hat{\theta}_x} &= -L\, n_x(+\varphi_3 + \varphi_4)/2 \\
N^I_{w,\hat{\theta}_y} &= -L\, n_y(-\varphi_3 + \varphi_4)/2 & N^J_{w,\hat{\theta}_y} &= -L\, n_y(+\varphi_3 + \varphi_4)/2 \\
\\
N^I_{\theta_x,\hat{w}} &= +(3n_x/L)\, \varphi_3 & N^J_{\theta_x,\hat{w}} &= -(3n_x/L)\, \varphi_3 \\
N^I_{\theta_x,\hat{\theta}_x} &= \varphi_1 + 3n_x^2\varphi_3/2 & N^J_{\theta_x,\hat{\theta}_x} &= \varphi_2 + 3n_x^2\varphi_3/2 \\
N^I_{m_x\theta_y} &= +3n_x n_y \varphi_3/2 & N^J_{\theta_x,\hat{\theta}_y} &= +3n_x n_y \varphi_3/2 \\
\\
N^I_{\theta_y,\hat{w}} &= +(3n_y/L)\, \varphi_3 & N^J_{\theta_y,\hat{w}} &= -(3n_y/L)\, \varphi_3 \\
N^I_{\theta_y,\hat{\theta}_x} &= +3n_x n_y \varphi_3/2 & N^J_{\theta_y,\hat{\theta}_x} &= +3n_x n_y \varphi_3/2 \\
N^I_{\theta_y,\hat{\theta}_y} &= \varphi_1 + 3n_y^2\varphi_3/2 & N^J_{\theta_y,\hat{\theta}_y} &= \varphi_2 + 3n_y^2\varphi_3/2
\end{aligned} \tag{6.2.9}$$

where L is the length of the edge Γ_{IJ} and n_x, n_y are components of the normal to that edge. They are obtained from (6.2.2) and (6.2.3) according to (5.4.42). According to (5.4.41) the following notation is used for edge Γ:

$$p_{q,I} = \overline{q}^I_\Gamma; \quad p_{m_s,I} = \overline{m}^I_{s,\Gamma}; \quad p_{m_n,I} = \overline{m}^I_{n,\Gamma} \tag{6.2.10}$$

By choosing linear interpolations in (6.2.6) with

$$\psi_I = \varphi_1; \qquad \psi_J = \varphi_2 \tag{6.2.11}$$

we can explicitly compute the inverse of the system (6.2.7) and obtain the final result for the traction components:

$$
\begin{aligned}
\bar{q}_{\Gamma}^{I} &= -\frac{12}{L^2}\left(n_x(2r_{I,\Gamma}^{\theta_x}+3r_{J,\Gamma}^{\theta_x})+n_y(2r_{I,\Gamma}^{\theta_y}+3r_{J,\Gamma}^{\theta_y})\right) \\
\overline{m}_{s,\Gamma}^{I} &= +\frac{2}{L}(n_y(-2r_{I,\Gamma}^{\theta_x}+r_{J,\Gamma}^{\theta_x})+n_x(+2r_{I,\Gamma}^{\theta_y}-r_{J,\Gamma}^{\theta_y})) \\
\overline{m}_{n,\Gamma}^{I} &= +\frac{1}{L}(n_x(r_{I,\Gamma}^{\theta_x}+7r_{J,\Gamma}^{\theta_x})+n_y(r_{I,\Gamma}^{\theta_y}+7r_{J,\Gamma}^{\theta_y}))-r_{I,\Gamma}^{w} \\
\\
\bar{q}_{\Gamma}^{J} &= +\frac{12}{L^2}\left(n_x(2r_{J,\Gamma}^{\theta_x}+3r_{I,\Gamma}^{\theta_x})+n_y(2r_{J,\Gamma}^{\theta_y}+3r_{I,\Gamma}^{\theta_y})\right) \\
\overline{m}_{s,\Gamma}^{J} &= +\frac{2}{L}(n_y(-2r_{J,\Gamma}^{\theta_x}+r_{I,\Gamma}^{\theta_x})+n_x(+2r_{J,\Gamma}^{\theta_y}-r_{I,\Gamma}^{\theta_y})) \\
\overline{m}_{n,\Gamma}^{J} &= -\frac{1}{L}(n_x(r_{J,\Gamma}^{\theta_x}+7r_{I,\Gamma}^{\theta_x})+n_y(r_{J,\Gamma}^{\theta_y}+7r_{I,\Gamma}^{\theta_y}))+r_{J,\Gamma}^{w}
\end{aligned}
\tag{6.2.12}
$$

By inserting (6.2.12) into (6.2.6) the boundary tractions $\boldsymbol{t}_{\Gamma_{IJ}}^{e}=[\overline{q}_{\Gamma},\overline{m}_{s,\Gamma},\overline{m}_{n,\Gamma}]^T$ at the element edge Γ_{IJ} can be obtained. Thus, the procedure, described in this section, represents step 4 of Box 3 for DKT plate element for the case of interpolation (6.2.6) and (6.2.11).

6.2.2 Formulation of local boundary value problem

The discretization error is estimated by solving local problems (5.4.28). In the case of thin plates, the weak formulation of local problem is defined as: find the displacement w_{e,h^+}, which satisfies

$$
\begin{aligned}
&\int_{\Omega^e}\boldsymbol{m}(w_{e,h^+})\cdot\boldsymbol{\kappa}(v_{h^+})\,\mathrm{d}\Omega=\int_{\Omega^e}f\,v_{h^+}\,\mathrm{d}\Omega \\
&+\sum_{\Gamma_{IJ}}\{\int_{\Gamma_{IJ}}[\bar{q}_{ef,\Gamma_{IJ}}\,v_{h^+}+\overline{m}_{s,\Gamma_{IJ}}\theta_s(v_{h^+})]\,\mathrm{d}s+[\overline{m}_{n,\Gamma_{IJ}}v_{h^+}]_I^J\};\quad \forall v_{h^+}\in\mathcal{V}_{0,h^+}
\end{aligned}
\tag{6.2.13}
$$

where $\mathcal{V}_{h^+}$ is the best possible approximation of the solution space $\mathcal{V}$ that must be sufficiently enhanced with respect to the finite element space $\mathcal{V}_h$ constructed by DK plate element. The equilibrated boundary tractions $\boldsymbol{t}_{\Gamma_{IJ}}^{e}=[\bar{q}_{ef,\Gamma_{IJ}},\overline{m}_{s,\Gamma_{IJ}},\overline{m}_{n,\Gamma_{IJ}}]^T$ are those obtained from the original finite element solution using the equilibration procedure (see Box 3).

On the other hand, the finite element solution $w_{e,h}$ satisfies the following weak form

defined on the element domain:

$$\int_{\Omega^e} \boldsymbol{m}(w_{e,h}) \cdot \boldsymbol{\kappa}(v_h)\, \mathrm{d}\Omega = \int_{\Omega^e} f\, v_h\, \mathrm{d}\Omega$$
$$+ \sum_{\Gamma_{IJ}} \left[\int_{\Gamma_{IJ}} [\bar{q}_{ef,\Gamma_{IJ}}\, v_h + \overline{m}_{s,\Gamma_{IJ}}\, \theta_s(v_h)]\, \mathrm{d}s + [\overline{m}_{n,\Gamma_{IJ}} v_h]_I^J \right]; \quad \forall v_h \in \mathcal{V}_{0,h} \tag{6.2.14}$$

The equivalent matrix form of (6.2.14) can be written as

$$\mathbf{K}^e \hat{\boldsymbol{u}}^e = \mathbf{f}_f^e + \sum_{\Gamma_{IJ}} \left[\boldsymbol{r}^e_{I,\Gamma_{IJ}} + \boldsymbol{r}^e_{J,\Gamma_{IJ}} \right] \tag{6.2.15}$$

where $\boldsymbol{r}_{I,\Gamma_{IJ}}$ are the projections defined by (6.2.5). Isolating the equations regarding the node I we arrive at (compare to (5.4.34)):

$$\boldsymbol{R}_I^e = \sum_J \mathbf{K}^e_{IJ} \hat{\boldsymbol{u}}^e_J - \mathbf{f}^e_{f,I} = \boldsymbol{r}^e_{I,\Gamma_{IJ}} + \boldsymbol{r}^e_{I,\Gamma_{IK}} \tag{6.2.16}$$

Local patchwise systems with the unknowns $\boldsymbol{r}^e_{I,\Gamma_{IJ}}$ are formed using the equilibration procedure described in Box 3.

Solution of the local system gives projections $\boldsymbol{r}^e_{I,\Gamma_{IJ}}$ for all nodes I and edges Γ_{IJ}. The boundary traction $\boldsymbol{t}^e_{\Gamma_{IJ}}$ at the edge Γ_{IJ} is recovered from projections $\boldsymbol{r}^e_{I,\Gamma_{IJ}}$ and $\boldsymbol{r}^e_{J,\Gamma_{IJ}}$ using (6.2.12).

Regularization

To form the optimization function (5.4.38), the projections $\tilde{\boldsymbol{r}}^e_{I,\Gamma}$ are required which are computed from the improved approximation of the boundary traction $\tilde{\boldsymbol{t}}^e_\Gamma = [\tilde{q}_{ef}, \widetilde{m}_s, \widetilde{m}_n]$ using the inverse of (6.2.12).

The boundary traction approximation is computed from the current finite element solution using the following simple technique: edge boundary traction $\tilde{\boldsymbol{t}}^e_\Gamma$ is taken as an average of the boundary tractions $\tilde{\boldsymbol{t}}^e_\Gamma$ and $\tilde{\boldsymbol{t}}^{e'}_\Gamma$ computed from the stress resultants of the two elements e and e' adjacent to the edge Γ:

$$\tilde{\boldsymbol{t}}_\Gamma = (\tilde{\boldsymbol{t}}^e_\Gamma - \tilde{\boldsymbol{t}}^{e'}_\Gamma)/2 \tag{6.2.17}$$

Boundary tractions $\tilde{\boldsymbol{t}}^e_\Gamma$ are evaluated at side Γ from element stress resultants from the Cauchy principle. First, the stress resultants are evaluated at the integration points and are denoted as $\boldsymbol{m}_h(\boldsymbol{\xi}_{gp}) = \mathbf{C}_B \boldsymbol{\kappa}_h(\boldsymbol{\xi}_{gp})$. A linear interpolation of the stress resultants over the element

$$\widetilde{\boldsymbol{m}} = \sum_I \widetilde{\boldsymbol{m}}_I N_I \tag{6.2.18}$$

is constructed using the least squares fit to $\boldsymbol{m}_h(\boldsymbol{\xi}_{gp})$

$$\sum_{gp} \frac{1}{2}(\widetilde{\boldsymbol{m}}(\boldsymbol{\xi}_{gp}) - \boldsymbol{m}_h(\boldsymbol{\xi}_{gp})) \to \min.$$

At the element side Γ defined by unit exterior normal $\boldsymbol{n} = [n_x, n_y]^T$ we thus have:

$$\begin{aligned} \widetilde{m}_n &= (\widetilde{m}_{yy} - \widetilde{m}_{xx})\, n_x n_y + \widetilde{m}_{xy}(n_x^2 - n_y^2) \\ \widetilde{m}_s &= (\widetilde{m}_{xx} n_x^2 + \widetilde{m}_{yy} n_y^2 + 2\widetilde{m}_{xy} n_x n_y) \end{aligned} \tag{6.2.19}$$

The shear component normal to the edge is obtained from

$$\tilde{q} = \tilde{q}_x n_x + \tilde{q}_y n_y$$

where the components $\tilde{q}_x, \tilde{q}_y$ are computed from equilibrium equations:

$$\tilde{q}_x = -(\frac{\partial \widetilde{m}_{xx}}{\partial x} + \frac{\partial \widetilde{m}_{xy}}{\partial y}); \quad \tilde{q}_y = -(\frac{\partial \widetilde{m}_{yy}}{\partial y} + \frac{\partial \widetilde{m}_{xy}}{\partial x}) \tag{6.2.20}$$

The effective shear $\tilde{q}_{ef}$ however is computed from $\tilde{q}_{ef} = \tilde{q} - \frac{\partial \widetilde{m}_n}{\partial s}$ and the derivative $\frac{\partial \widetilde{m}_n}{\partial s}$ is evaluated from (6.2.19) using the interpolation (6.2.18).

Remark 6.1. *Instead of computing the element nodal stresses $\widetilde{\boldsymbol{m}}_I$ by the procedure described above, the nodal stresses can be approximated from the integration points stresses by a simple lumping procedure presented in 5.3.1. Such procedure is namely standardly employed in finite element softwares to produce nodal stresses for plotting purposes.*

Remark 6.2. *The equilibration procedure does not depend on the number of nodes of the element and therefore remains the same for both DKT and DKQ elements. Further, the equilibration procedure is independent of element geometry or eventual distortion, since the only input data are the element nodal reactions $\boldsymbol{R}_I^e$ and the projections $\tilde{\boldsymbol{r}}_{I,\Gamma_{IJ}}^e$.*

Remark 6.3. *The equilibration procedure is not influenced by the particular choice of the boundary traction parametrization since it only concerns the projections $\tilde{\boldsymbol{r}}_{I,\Gamma_{IJ}}^e$. The choice of parametrization is therefore arbitrary. Yet, the specific form of parametrization of boundary tractions affects the computation of the external load vector and is therefore relevant in the computation of the error estimates.*

Remark 6.4. *There exists a particular choice of the parametrization presented in detail in [Ladevèze Leguillon, 1983], [Ladevèze Pelle, 2006] and [Ainsworth Oden, 2000], which significantly simplifies the system (6.2.7). However, the parametrization involves use of specific orthogonal shape functions which may introduce spurious loads in the enhanced model. Therefore this approach was not followed here.*

The linear system corresponding to (6.2.13) is

$$\mathbf{K}^e_{h+}\boldsymbol{w}^e_{h+} = \boldsymbol{f}^e_{h+} \tag{6.2.21}$$

The element stiffness matrix $\mathbf{K}^e_{h+}$ is singular due to the rigid body motion modes, and the system (6.2.21) does not have a unique solution.

Solution of local (element) Neumann boundary value problem

Let us consider a system $\mathbf{K}^e\hat{\boldsymbol{w}}^e = \boldsymbol{f}^e$ to explain how (6.2.21) is solved. The rigid body modes of an element can be written in matrix $\mathbf{D}$ where every column represents one mode. This allows to write plate displacement field due to rigid body motion as $\hat{\boldsymbol{w}}^e_R = \mathbf{D}\hat{\boldsymbol{\alpha}}$ where $\hat{\boldsymbol{\alpha}}$ is vector of amplitudes of the modes. Note, that it holds: $\mathbf{K}^e\hat{\boldsymbol{w}}^e_R = \mathbf{K}^e\mathbf{D}\hat{\boldsymbol{\alpha}} = \mathbf{0}$. Obviously, the solution $\hat{\boldsymbol{w}}^e$ remains unknown up to arbitrary rigid body motion $\hat{\boldsymbol{w}}^e_R$. The values of generalized strains or stress resultants are, however, not affected by the rigid body motion modes. In order to be able to obtain a solution to the singular system (6.2.21) thus a simple procedure is used. It is based on the fact that the range of a linear operator $\mathbf{D}\mathbf{D}^T$ is complementary to the range of the stiffness matrix $\mathbf{K}^e$. Therefore the sum $\mathbf{K}^e + \mathbf{D}\mathbf{D}^T$ is not singular and the solution to the system

$$(\mathbf{K}^e + \mathbf{D}\mathbf{D}^T)\hat{\hat{\boldsymbol{w}}}^e = \boldsymbol{f}^e$$

exists and is unique. Moreover, the solution satisfies $\mathbf{K}^e\hat{\hat{\boldsymbol{w}}}^e = \boldsymbol{f}^e$. If needed, the rigid body modes can be purged by $\hat{\boldsymbol{w}}^e = \hat{\hat{\boldsymbol{w}}}^e - \mathbf{D}\mathbf{D}^T\hat{\hat{\boldsymbol{w}}}^e$.

To illustrate the formation of $\mathbf{D}$, let us consider the case of DKT element. It has nine nodal degrees of freedom, arranged in a vector

$$\hat{\boldsymbol{w}}^{DKT} = [\hat{w}_1, \hat{\theta}_{x,1}, \hat{\theta}_{y,1}, \hat{w}_2, \hat{\theta}_{x,2}, \hat{\theta}_{y,2}, \hat{w}_3, \hat{\theta}_{x,3}, \hat{\theta}_{y,3}]^T$$

The three rigid body modes of the DKT finite element are the translation along z and two rotations: along the x and y axis. The matrix $\mathbf{D}^{DKT}$ corresponding to the rigid body modes is

$$\mathbf{D}^{DKT} = \begin{bmatrix} 1 & 0 & 0 & 1 & 0 & 0 & 1 & 0 & 0 \\ +(y_1 - y_0) & 1 & 0 & +(y_1 - y_0) & 1 & 0 & +(y_1 - y_0) & 1 & 0 \\ -(x_1 - x_0) & 0 & 1 & -(x_1 - x_0) & 0 & 1 & -(x_1 - x_0) & 0 & 1 \end{bmatrix}^T \tag{6.2.22}$$

where (x_0, y_0) is the coordinate of the finite element center point $x_0 = (x_1 + x_2 + x_3)/3$, $y_0 = (y_1 + y_2 + y_3)/3$.

6.2.3 Enhanced approximation for the local computations

It is important to note that the solution space $\mathcal{V}_{h+}$ has to be enhanced with respect to the finite element approximation space $\mathcal{V}_h$ constructed by the chosen mesh of DKT element. If the solution space is left unchanged ($\mathcal{V}_{h+} = \mathcal{V}_h$), we have from (6.2.13) and (6.2.14)

$$\int_{\Omega^e} [\boldsymbol{m}(w_{e,h+}) - \boldsymbol{m}(w_{e,h})] \cdot \boldsymbol{\kappa}(v_h) \, \mathrm{d}\Omega = 0, \qquad \forall v_h \in \mathcal{V}_{0,h}$$

implying that $w_{e,h+} = w_h$. In other words: if the original DK element is employed to solve the local problem (6.2.13), the finite element solution is exactly recovered[2].

Numerous possibilities exist for constructing enhanced approximations with some of them further tested in this work:

(i) Subdivision of the DKT plate element into 3 elements

The most straightforward approach is to subdivide the given DKT element into a number of smaller elements. The simplest choice is obviously a subdivision of the element into 3 triangular subelements as shown in Figure 6.2.1. The subdivision scheme, further referred to as SDKT, has an additional node in the center of the triangle, compared to the original element. Original test space is enhanced by additional three degrees of freedom.

Any field interpolation along the edge Γ depends only on nodal degrees of freedom that belong to that edge. Besides the center node, the SDKT shares all the nodes with DKT. Therefore the SDKT interpolation will exactly match the DKT interpolation on the edge ($v_{h+} = v_h$ on Γ). From (6.2.13) and (6.2.14) it follows $\boldsymbol{R}_I^+ = \boldsymbol{R}_I$ which renders the equilibration procedure unnecessary. The SDKT model can be considered as the simplest nontrivial enhancement of the test space DKT.

(ii) Subdivision of the DKT plate element into 6 elements

Another subdivision scheme of this kind, called CDKT, uses SDKT as a starting point and further subdivides each element into two using the symmetry line between the center node and the midside node (see Figure 6.2.1). This element has 7 nodes in total and 21 degrees of freedom.

[2]This fact has been exploited for debugging purposes to check the validity of the code performing the equilibration of boundary tractions.

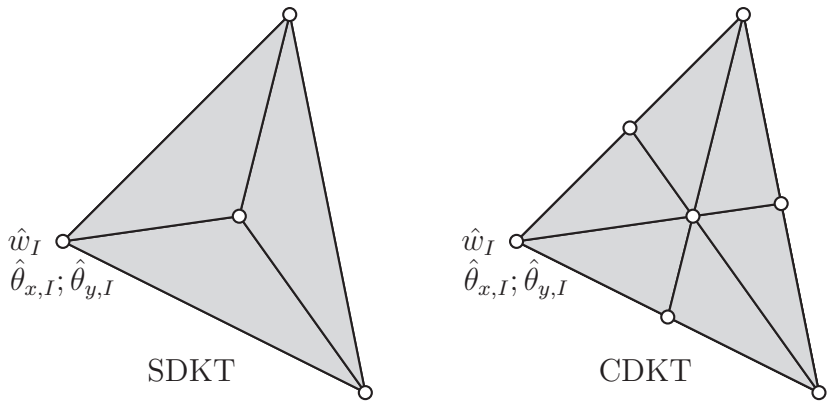

Figure 6.2.1: Subdivision schemes for the DKT element
Slika 6.2.1: Delitvene sheme za DKT element

(iii) Conforming plate element ARGY

A more involved approach uses a conforming plate element as the enhanced discretization. In our case a plate element presented in section 2.3.4 is used. The plate element has 21 degrees of freedom: 6 at each vertex node and one at each midside node. The load vector for the local problem is computed from (2.3.51) using the equilibrated boundary tractions $\boldsymbol{t}^e_\Gamma = [\bar{q}_{ef,\Gamma}, \bar{m}_{s,\Gamma}, \bar{m}_{n,\Gamma}]^T$ given in (6.2.6).

6.2.4 Numerical examples

The selected numerical examples are presented in this section in order to illustrate different aspects of the two error estimates: the *SPR* and the *EqR* methods.

The error estimate for the plate problems is computed according to (5.3.3):

$$\|e_h\|_E^{*\,2} = \sum_e \eta_e^{*2} = \sum_e \underbrace{\int_{\Omega^e} (\boldsymbol{m}^* - \boldsymbol{m}_h)^T \mathbf{C}_B^{-1} (\boldsymbol{m}^* - \boldsymbol{m}_h)\, \mathrm{d}\Omega}_{\|e_h\|_{E,e}^*} \tag{6.2.23}$$

The energy norm of the true error of the FE solution, denoted by $\|e_h\|_E$, was also computed by using the reference "exact" solution. For a number of simple plate structures, the reference Kirchhoff solution can be obtained analytically. In the case where analytical solution is not available, the reference solution is computed using the FE approximation with very fine mesh of Argyris TUBA6 (ARGY) element. The effectivity index of the error estimate is defined as the ratio between estimated and the true error:

$$\Theta = \frac{\|e_h\|_E^*}{\|e_h\|_E} \tag{6.2.24}$$

In the process of adaptive meshing, the new mesh is generated using the distribution of the error as the input. In order to asses the performance of the error estimate in the context of adaptivity, the local error estimate is introduced. The local error estimate is

$$\eta_e^* = \|e_h\|_{E,e}^*$$

and the global error estimate

$$\eta^{*2} = \sum_e \eta_e^{*2}$$

The relative local error estimate $\eta_{e,r}^*$ is defined as

$$\eta_{e,r}^* = \frac{\|e_h\|_{E,e}^*}{\|u_h\|_{E,e}} \tag{6.2.25}$$

where the energy norm of the solution $\|u_h\|_E$ is defined as

$$\|u_h\|_E^2 = \sum_e \|u_h\|_{E,e}^2; \quad \|u_h\|_{E,e}^2 = \int_{\Omega^e} \boldsymbol{m}_h^T \mathbf{C}_B^{-1} \boldsymbol{m}_h \, \mathrm{d}s \tag{6.2.26}$$

The relative local error estimate is normally expressed in percents. The relative global error estimate is defined as:

$$\eta_r^* = \frac{\|e_h\|_E^*}{\|u_h\|_E} \tag{6.2.27}$$

Simply supported square plate under uniform loading

In the first problem we consider simply supported square plate of side length $a = 10$ and thickness $t = 0.01$ under uniform loading $f = 1$. The material behavior is linear elastic and isotropic, with Young's modulus $E = 10.92 \times 10^{10}$ and Poisson's ratio $\nu = 0.3$. The reference solution is the analytic solution in the form of series expansion; see [Timoshenko Vojnovski-Kriger, 1959]. The solution is regular over the whole domain and does not exhibit any singularities. In Figure 6.2.2 we give the results for energy norm computations showing the convergence of the FE solution with respect to the number of elements expressed as $1/h$, with h indicating the typical element size. The typical element size is computed from the average area of the element $h^2 = \Omega/nelem$.

The global error estimates are compared to the true global error. The comparison shows that the "EqR-SDKT" estimate is lower than the true error, while other error estimation techniques overestimate the error. The error estimation procedure EqR-ARGY performs best. The effectivity index converges towards 1 as the number of elements is increased (see Figure 6.2.3). The Figure 6.2.4 shows the comparison of the relative local error estimates $\eta^*_{e,r}$. The overall distribution of the error is captured quite well by all the error estimation procedures, with only minor differences between them. The error estimates based upon "EqR-ARGY" again performs best.

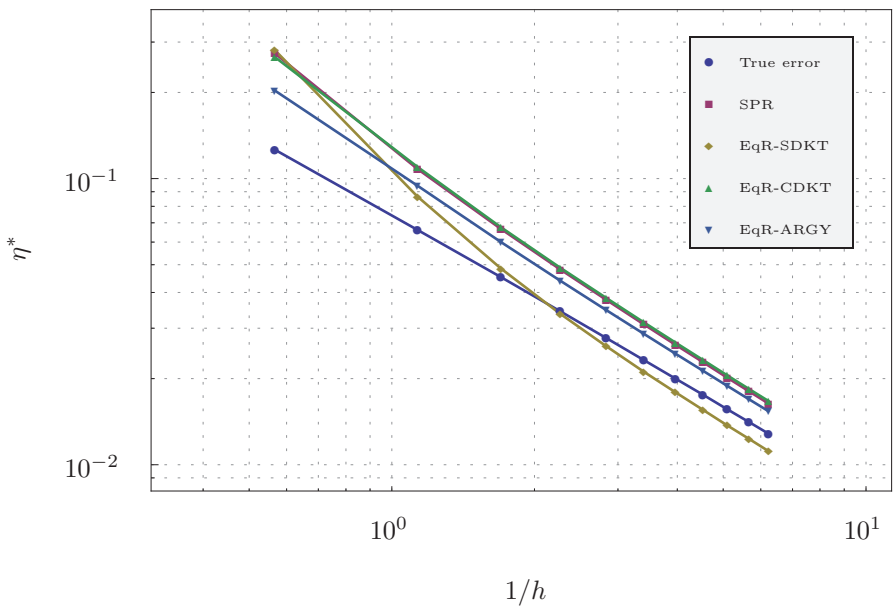

Figure 6.2.2: Simply supported square plate under uniform loading - global energy error estimates
Slika 6.2.2: Enakomerno obremenjena prosto podprta kvadratna plošča - globalna ocena napake

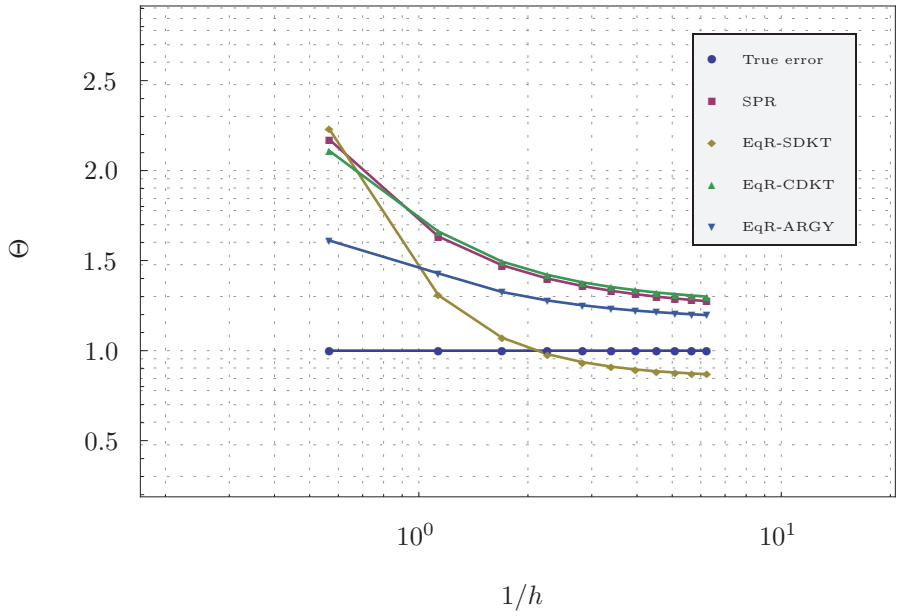

Figure 6.2.3: Simply supported square plate under uniform loading - effectivity index of the global energy error estimates
Slika 6.2.3: Enakomerno obremenjena prosto podprta kvadratna plošča - indeks učinkovitosti ocene

Clamped square plate under uniform loading

The second example is a clamped square plate of side length $a = 10$ and thickness $t = 0.01$ under uniform loading $f = 1$. The material behavior is linear elastic and isotropic, with Young's modulus $E = 10.92 \times 10^{10}$ and Poisson's ratio $\nu = 0.3$. The reference solution is the analytical solution in the form of series expansion; see [Taylor Govindjee, 2002]. The solution is regular over the whole domain and does not exhibit any singularities. In Figure 6.2.5 we show the convergence of the FE solution in the energy norm with respect to the number of elements. The comparison of the global error estimates shows that the "EqR-SDKT" estimate is again lower than the true error, while other error estimation techniques overestimate the error. The effectivity index (see Figure 6.2.6) is close to 1 for the SPR procedure. The effectivity index of the EqR-CDKT and EqR-ARGY procedures remains close to 1. However, it increases as the mesh density is increased. The performance of both procedures is comparable. Comparison of the relative local error estimates $\eta^*_{e,r}$, shown in Figure 6.2.7, reveals an interesting detail. While the overall distribution of the error is estimated quite similarly by all the error estimation procedures, the error in the corners is severely underestimated by both SPR and EqR-SDKT procedures. The local error estimates is again favorable to EqR-ARGY procedure.

Clamped circular plate under uniform loading

The clamped circular plate of radius $a = 1$ and thickness $t = 0.001$ under uniform loading $f = 1$ is considered in this example. The material is linear elastic and isotropic, with Young's modulus $E = 1.70625 \times 10^8$ and Poisson's ratio $\nu = 0.3$. A quarter of the plate is modeled only, with symmetry enforcing boundary conditions. The reference solution is the analytic solution; see [Timoshenko Vojnovski-Kriger, 1959]. In the convergence study the mesh was refined in each step by factor 2. The mesh refinement was done carefully to minimize the effects of Babuška paradox [Babuška Pitkaranta, 1990]. Namely, since the curved boundary cannot be captured exactly, the discretization of the domain introduces spurious singularities in the obtuse corners. With the mesh refinement, the curved boundary is better represented, but on the other hand the number of obtuse corners, where the singularities are expected, also increases.

The convergence of the FE solution is shown in Figure 6.2.8 in terms of the energy norm for increasing number of elements. All the error estimates overestimate the error in this particular case, due to high solution regularity (see Figure 6.2.9). The comparison of the relative local error estimates $\eta^*_{e,r}$ shown in Figure 6.2.10 again reveals some interesting discrepancies. The error is overestimated in the corner elements of the discretized domain for the EqR error estimates, while this is not the case for the SPR error estimate. Main reason seems to be deficiency of the equilibration procedure in the local patch systems for corner nodes, which are overly constrained.

Enakomerno obremenjena vpeta krožna plošča - globalna ocena napake

Morley's skew plate under uniform loading

The analysis of Morley's 30° skew plate (see [Morley, 1963]) with thickness $t = 1$, side length $a = 10$, simply supported on all sides, and loaded with unit uniform pressure is examined. The plate material is linear elastic and isotropic, with Young's modulus $E = 10.92$ and Poisson's ratio $\nu = 0.3$. The most interesting feature of the solution to this problem concerns two singular points at the two obtuse corners of the plate, which strongly influence the quality of the computed results (e.g. see [Ibrahimbegović, 1993]).

In Figure 6.2.11, the convergence of the solution is shown along with the error estimates. Both SPR and EqR-SDKT procedure underestimate the error, while EqR-ARGY and EqR-CDKT procedures overestimate the error by approximately the same amount. It is interesting to note that the convergence of the solution is not monotonic. The effectivity

index of all the error estimates is relatively close to 1 despite the singularities (see Figure 6.2.12). The comparison of the relative local error estimates given in Figure 6.2.13 clearly shows that EqR-SDKT is completely incapable of capturing the singularities. The SPR procedure performs better but it clearly underestimates the error at the obtuse corners. The EqR-CDKT and EqR-ARGY both capture the singularities.

L-shaped plate under uniform loading

The analysis of L-shaped plate with thickness $t = 0.01$, side length $a = 10$, simply supported on all sides, and loaded with unit uniform pressure is considered in this example. The plate is of linear elastic isotropic material, with Young's modulus $E = 10.92 \times 10^9$ and Poisson's ratio $\nu = 0.3$. The solution exhibits a singularity in stress resultant components at the re-entrant corner. The singularity for the components m_{xx} and m_{yy} is defined by the leading term $r^{\lambda-2}$ and for the component m_{xy} by $r^{\lambda-3}$, where r is the distance from the singular point and λ the exponent which depends on the opening angle α: $\lambda = \pi/\alpha$. In the case of the opening angle $\alpha = 3\pi/2$, we have $\lambda = 2/3$. The problem is solved with a non-uniform mesh which is denser around the singular point. The distortion of the element (measured by the eccentricity) is significant.

The Figure 6.2.14 shows the non-monotonic convergence of the true error of the solution although all the error estimates indicate otherwise. The effectivity index of SPR and EqR error estimates is close to 1.0 which indicates that the mesh distortion does not deteriorate the effectivity of error estimates significantly.

6.2.5 An example of adaptive meshing

The discretization error estimate is usually employed to control the adaptive mesh generation. The main goal of the adaptive meshing is to generate a mesh where the local element error η_e will be approximately constant over the domain i.e. equal for every element $\eta_e \approx \bar{\eta}_e$.

By knowing the desired local element error $\bar{\eta}_e$ and the local error estimate η_e^* it is possible to deduce the element size from the a-priori estimate of the local element error

$$\tilde{\eta}_e = Ch^p \tag{6.2.28}$$

where the element size is denoted by h, C is a constant and p the polynomial order of finite element interpolation. The estimated element size $\bar{h}$ is deduced from

$$\eta_e^* = Ch^p; \quad \bar{\eta}_e = C\bar{h}^p \quad \Rightarrow \quad \bar{h} = h(\bar{\eta}_e/\eta_e^*)^{1/p} \tag{6.2.29}$$

The software `gmsh` [Geuzaine Remacle, 2009] was employed to generate the mesh. It enables the generation of the mesh according the input scalar field ('background mesh') which defines the element size over the domain.

In the following numerical test the comparison of different error estimation procedures with respect to the adaptive meshing is presented. A problem of uniformly loaded clamped square plate is chosen as the model problem.

The analysis was performed as follows: after the first FE solution was obtained on a uniform mesh, a model problem was recomputed on several meshes, which were generated according to different error estimates. The true error of each solution was computed using the reference solution. Finally a comparison of local element errors η_e was made. The number of the elements in the generated meshes was controlled to approximately match the number of the elements in the original mesh. A value $p = 1.1$, determined from Figure 6.2.5, was used in (6.2.29).

The results of the computation are summarized in Table 6.1. Along the meshes, it contains also the distributions of the local element error η_e and their histograms. In the first row of the table, the errors of original solution made with a uniform mesh, are presented. The histogram of the local element error is relatively coarse, as expected. In the second row the results of the solution computed on the mesh, based on the true local element errors of the original solution, are presented. The histogram is noticeably narrower but it is not just a single peak. This can be accounted to the limited capability of the mesh generation algorithm and the lack of ability of the a-priori error estimate to predict the effect of element distortion.

Other rows depict the results of error computation on the FE solutions obtained on several other meshes which were based on different error estimates. The results (local element errors) are quite comparable and do not expose any specific method. The difference of the generated meshes is however apparent. The visual assessment of the overall distribution of the local element errors clearly reveals the difference between the original solution and the solution obtained on the 'adapted' meshes.

Table 6.1: Comparison of errors of FE computation of the square clamped plate problem with various meshes adaptively constructed from discretization error estimate.
Tabela 6.1: Primerjava napak rešitev s KE za problem enakomerno obremenjene vpete plošče za različne mreže, konstruirane na osnovi ocene napake diskretizacije.

	Mesh	Local element error η_e 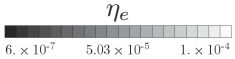	Histogram of local element error η_e
Original mesh 1156 elements, η_r: 6.2%	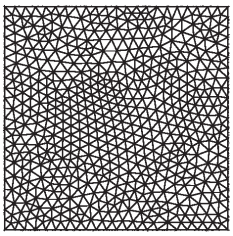	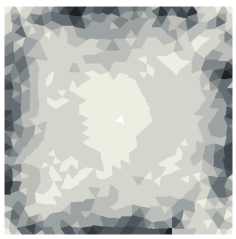	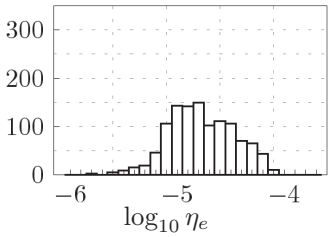
Mesh based on true error 1171 elements, η_r: 5.4%	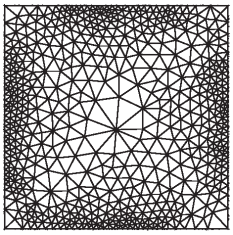	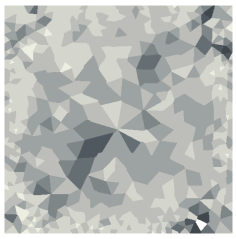	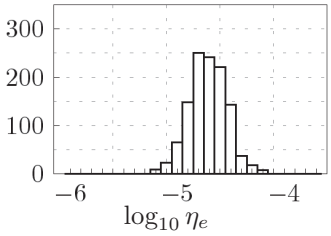
Mesh based on SPR error estimate 1170 elements, η_r: 5.7%	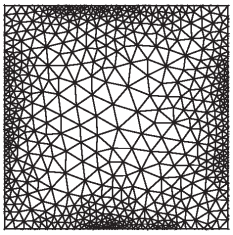	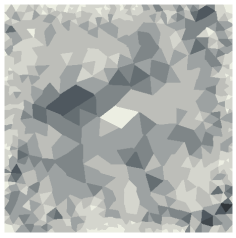	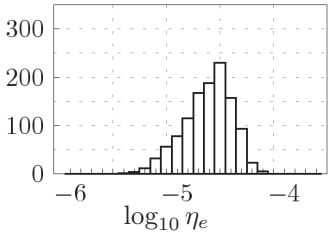
Mesh based on EqR-SDKT error estimate 1168 elements, η_r: 5.5%	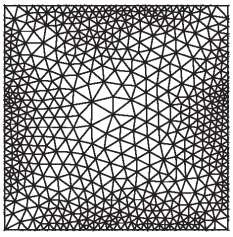	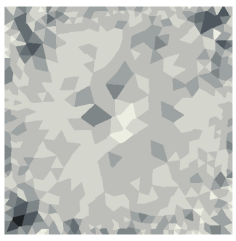	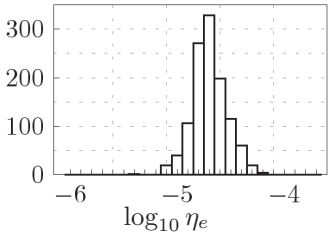
Mesh based on EqR-CDKT error estimate 1158 elements, η_r: 5.4%	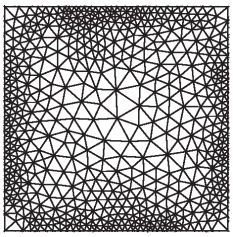	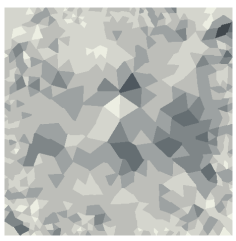	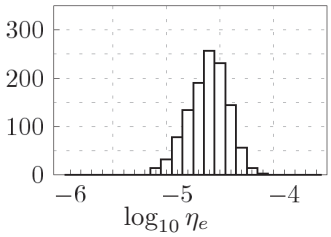
Mesh based on EqR-Argyris error estimate 1261 elements, η_r: 5.4%	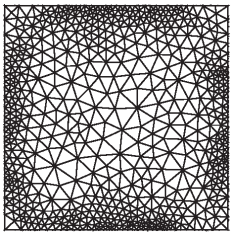	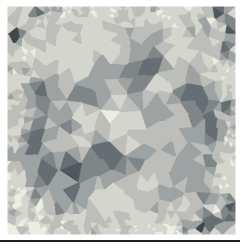	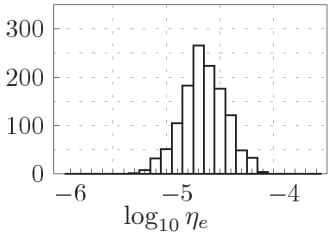

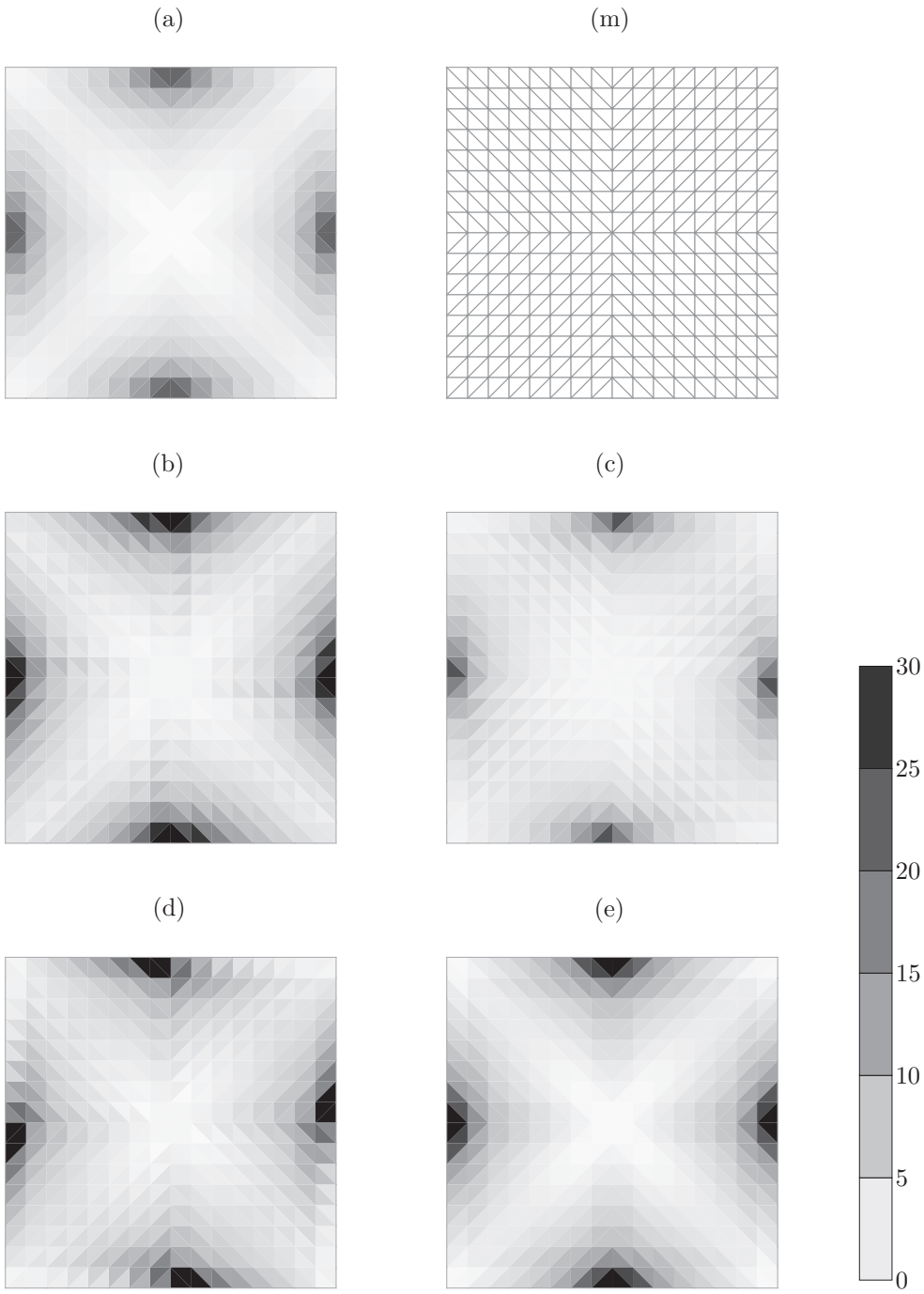

Figure 6.2.4: Simply supported square plate under uniform loading
Comparison of relative local error estimates $\eta^*_{e,r}$ in [%] on the mesh (m):
(a) True error, (b) SPR, (c) EqR-SDKT, (d) EqR-CDKT, (e) EqR-ARGY
Slika 6.2.4: Enakomerno obremenjena prosto podprta kvadratna plošča
Primerjava relativnih lokalnih ocen napake $\eta^*_{e,r}$ v [%] na mreži (m):
(a) Dejanska napaka, (b) SPR, (c) EqR-SDKT, (d) EqR-CDKT, (e) EqR-ARGY

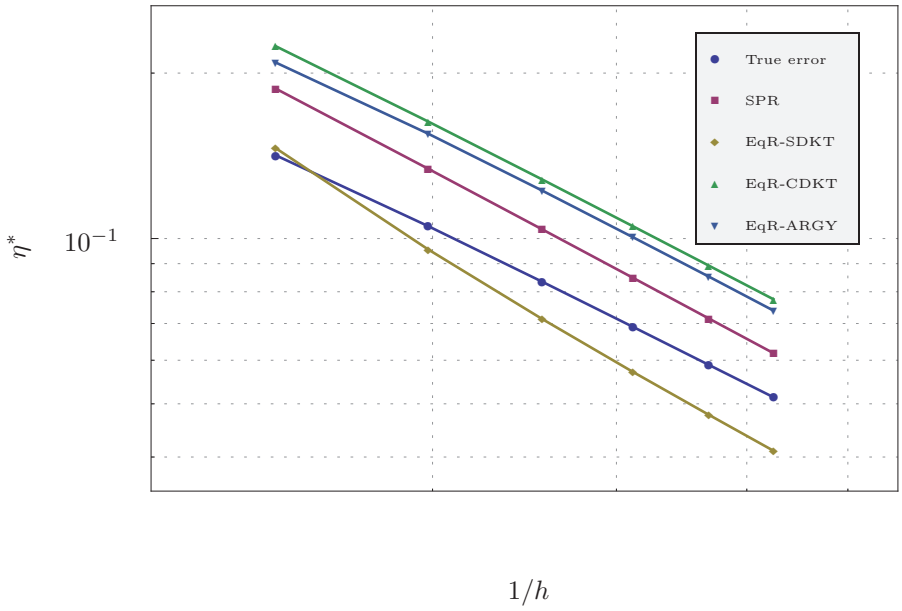

Figure 6.2.5: Clamped square plate under uniform loading - global energy error estimates
Slika 6.2.5: Enakomerno obremenjena vpeta kvadratna plošča - globalna ocena napake

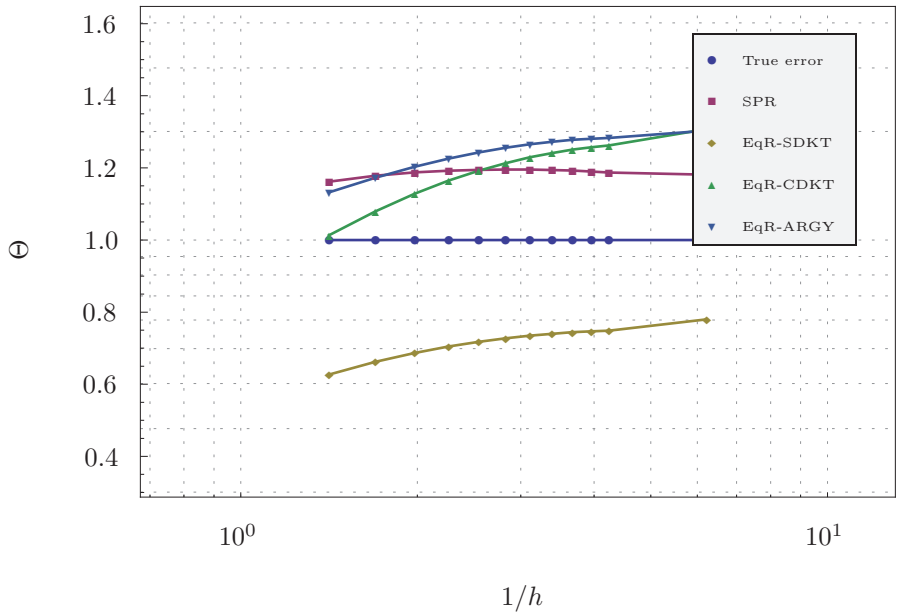

Figure 6.2.6: Clamped square plate under uniform loading - effectivity index of the global energy error estimates
Slika 6.2.6: Enakomerno obremenjena vpeta kvadratna plošča - indeks učinkovitosti ocene

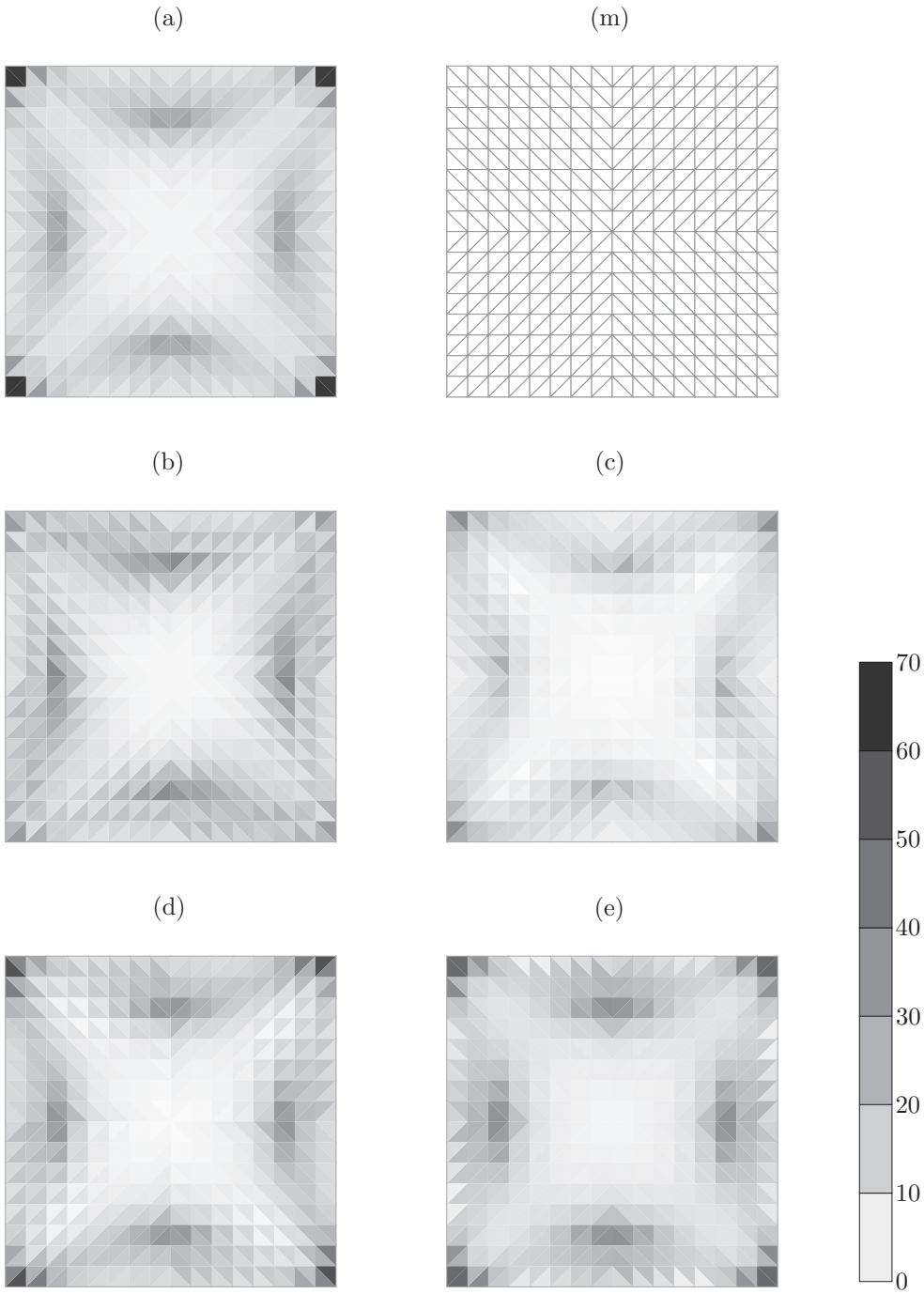

Figure 6.2.7: Clamped square plate under uniform loading
Comparison of relative local error estimates $\eta^*_{e,r}$ in [%] on the mesh (m):
(a) True error, (b) SPR, (c) EqR-SDKT, (d) EqR-CDKT, (e) EqR-ARGY
Slika 6.2.7: Enakomerno obremenjena vpeta kvadratna plošča
Primerjava relativnih lokalnih ocen napake $\eta^*_{e,r}$ v [%] na mreži (m):
(a) Dejanska napaka, (b) SPR, (c) EqR-SDKT, (d) EqR-CDKT, (e) EqR-ARGY

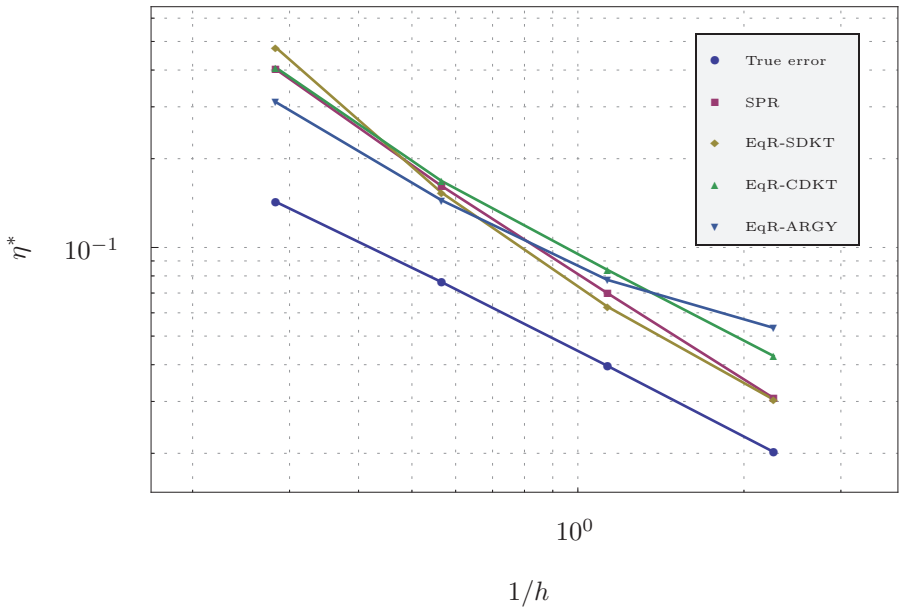

Figure 6.2.8: Clamped circular plate under uniform loading - global energy error estimates
Slika 6.2.8: Enakomerno obremenjena vpeta krožna plošča - globalna ocena napake

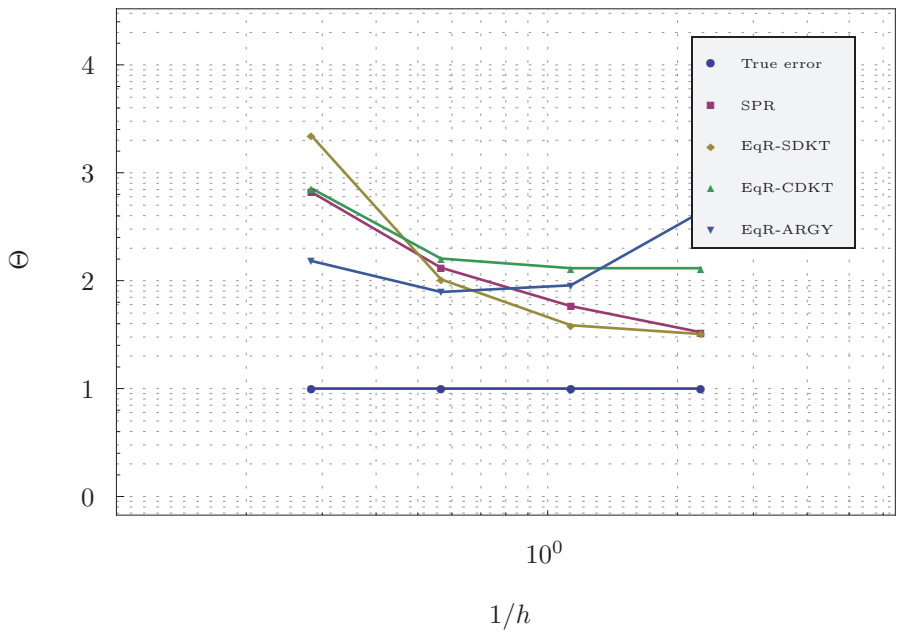

Figure 6.2.9: Clamped circular plate under uniform loading - effectivity index of the global energy error estimates
Slika 6.2.9: Enakomerno obremenjena vpeta krožna plošča - indeks učinkovitosti ocene

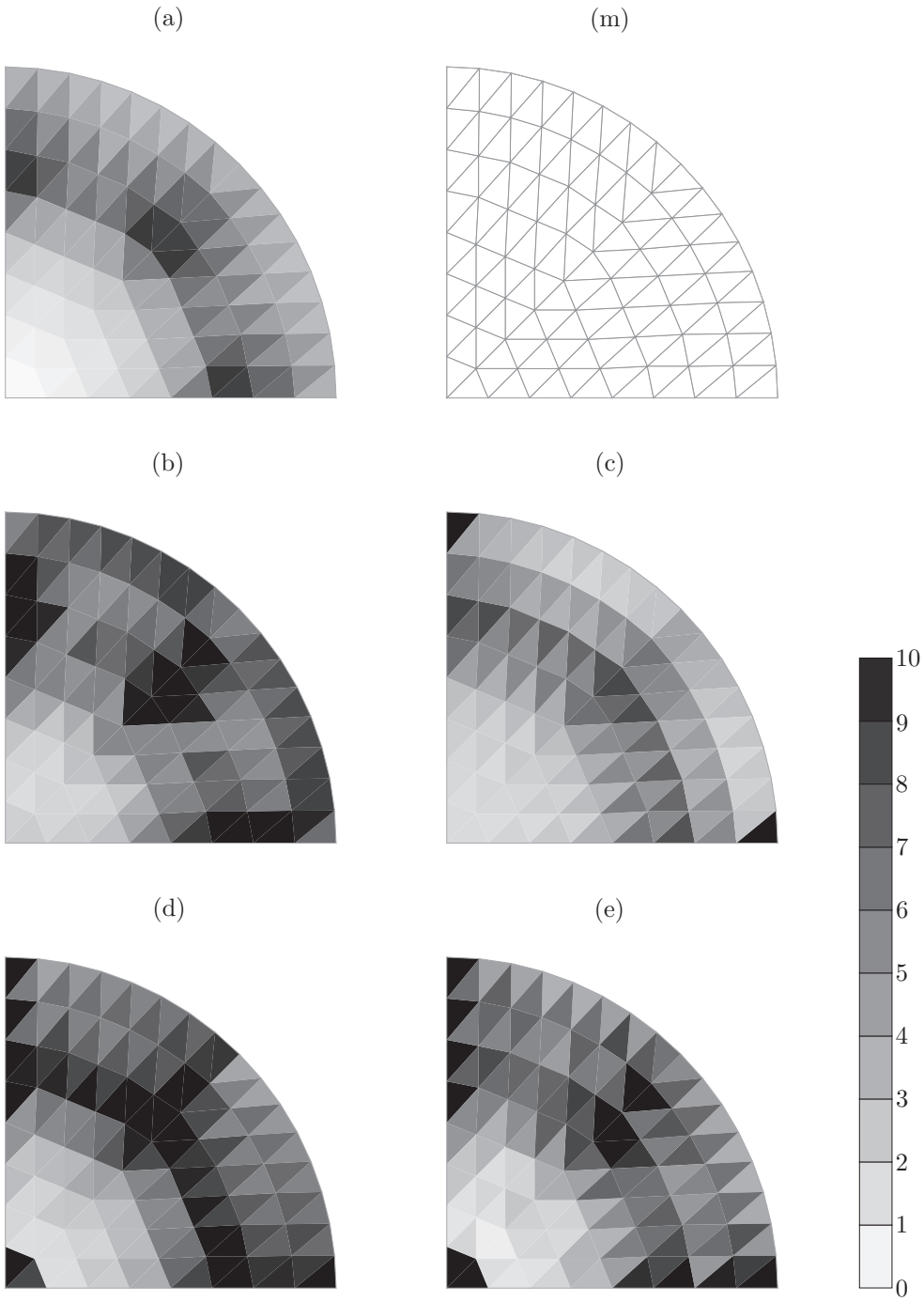

Figure 6.2.10: Clamped circular plate under uniform loading
Comparison of relative local error estimates $\eta^*_{e,r}$ in [%] on the mesh (m):
(a) True error, (b) SPR, (c) EqR-SDKT, (d) EqR-CDKT, (e) EqR-ARGY
Slika 6.2.10: Enakomerno obremenjena vpeta krožna plošča
Primerjava relativnih lokalnih ocen napake $\eta^*_{e,r}$ v [%] na mreži (m):
(a) Dejanska napaka, (b) SPR, (c) EqR-SDKT, (d) EqR-CDKT, (e) EqR-ARGY

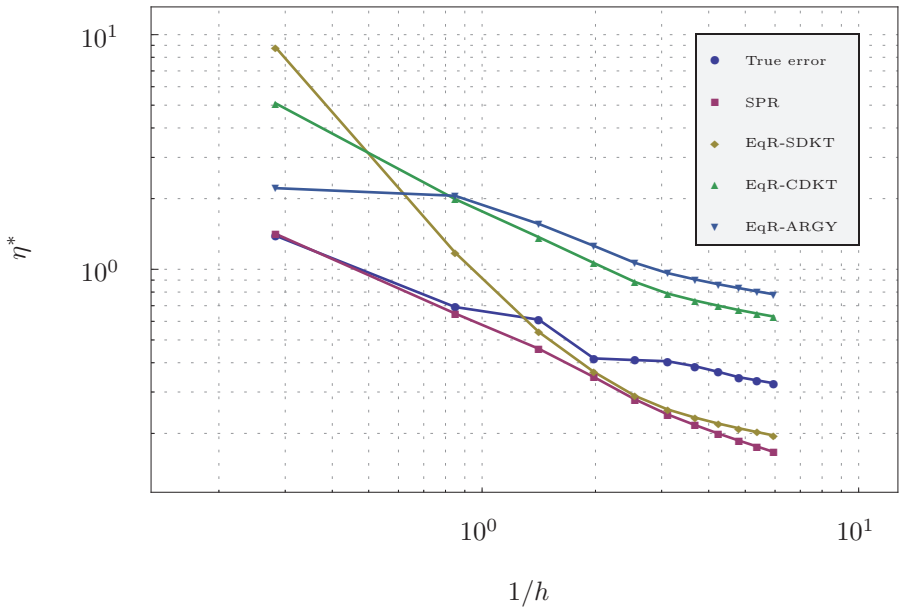

Figure 6.2.11: Morley's skew plate under uniform loading - global energy error estimates
Slika 6.2.11: Enakomerno obremenjena prosto podprta romboidna plošča - globalna ocena napake

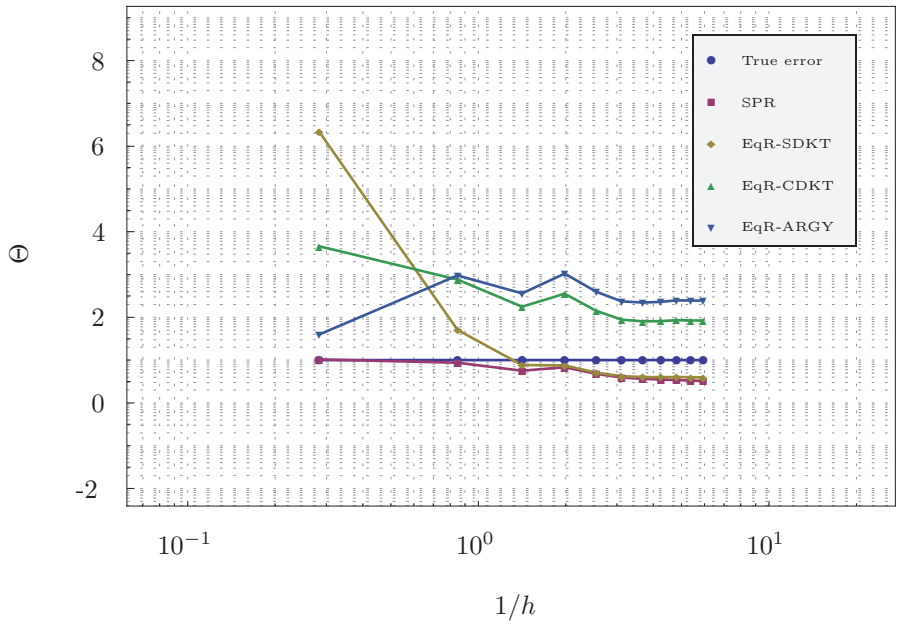

Figure 6.2.12: Morley's skew plate under uniform loading - effectivity index of the global energy error estimates
Slika 6.2.12: Enakomerno obremenjena prosto podprta romboidna plošča - indeks učinkovitosti napake

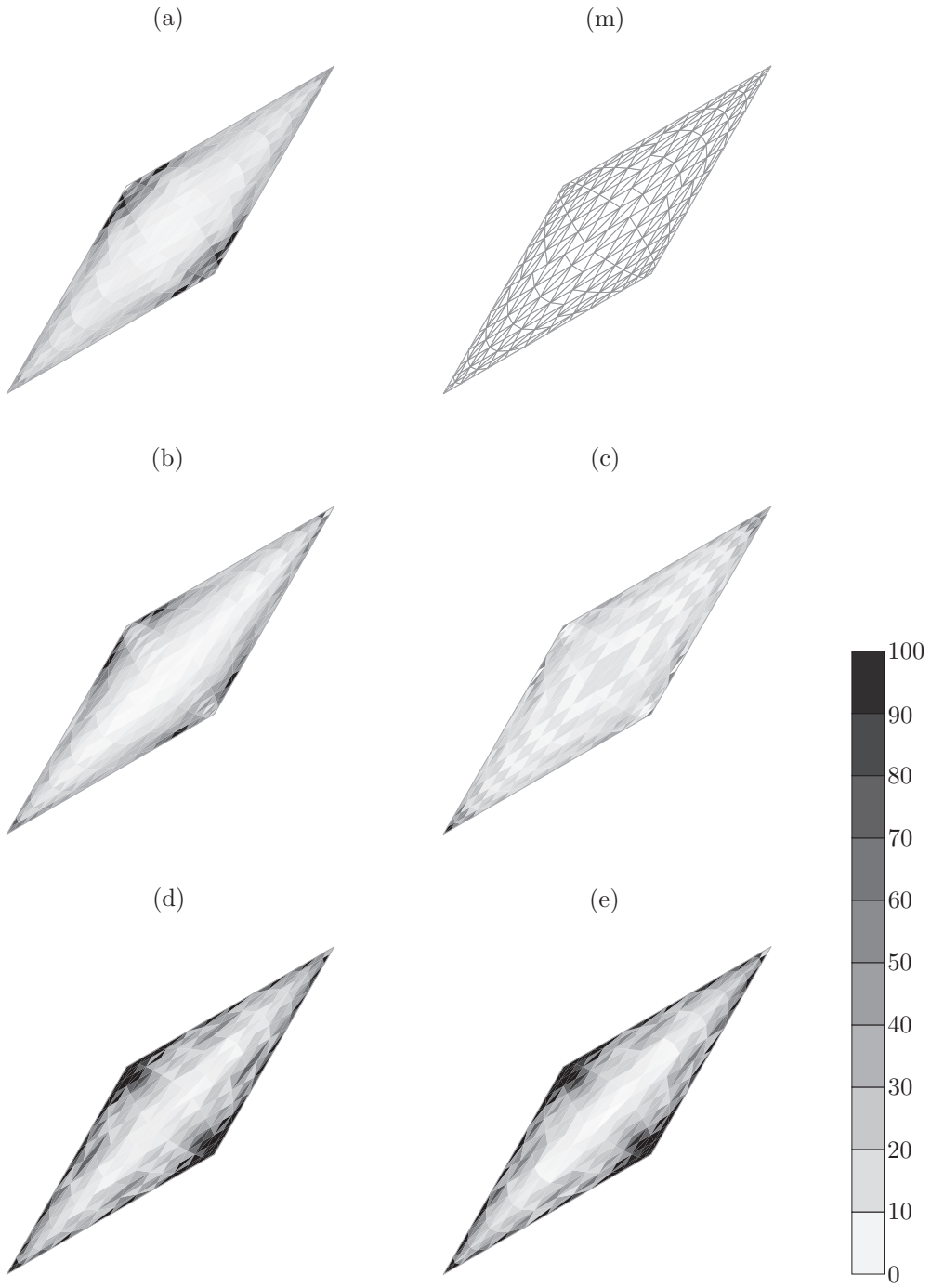

Figure 6.2.13: Morley's skew plate under uniform loading
Comparison of relative local error estimates $\eta^*_{e,r}$ in [%] on the mesh (m):
(a) True error, (b) SPR, (c) EqR-SDKT, (d) EqR-CDKT, (e) EqR-ARGY
Slika 6.2.13: Enakomerno obremenjena prosto podprta romboidna plošča
Primerjava relativnih lokalnih ocen napake $\eta^*_{e,r}$ v [%] na mreži (m):
(a) Dejanska napaka, (b) SPR, (c) EqR-SDKT, (d) EqR-CDKT, (e) EqR-ARGY

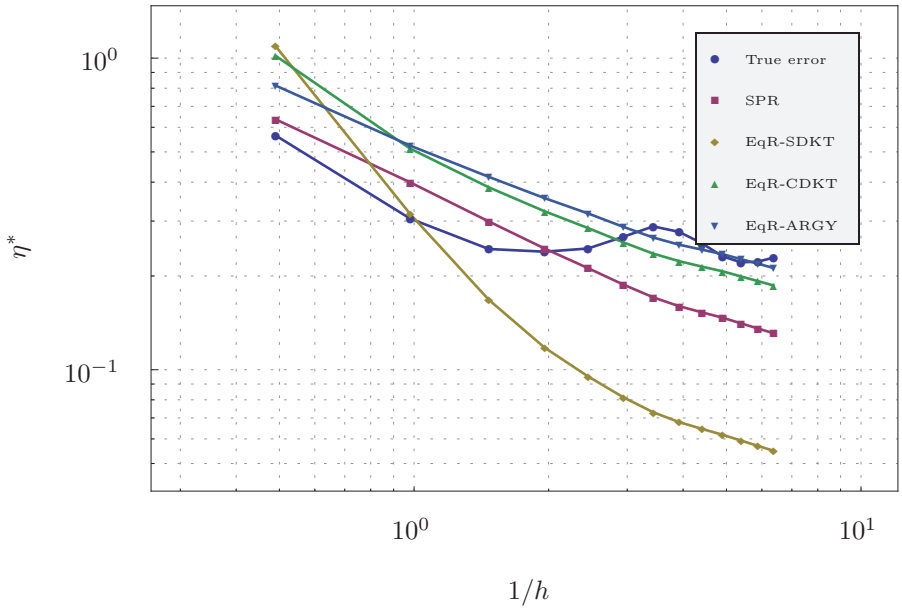

Figure 6.2.14: L-shaped plate under uniform loading - global energy error estimates
Slika 6.2.14: Enakomerno obremenjena prosto podprta L plošča - globalna ocena napake

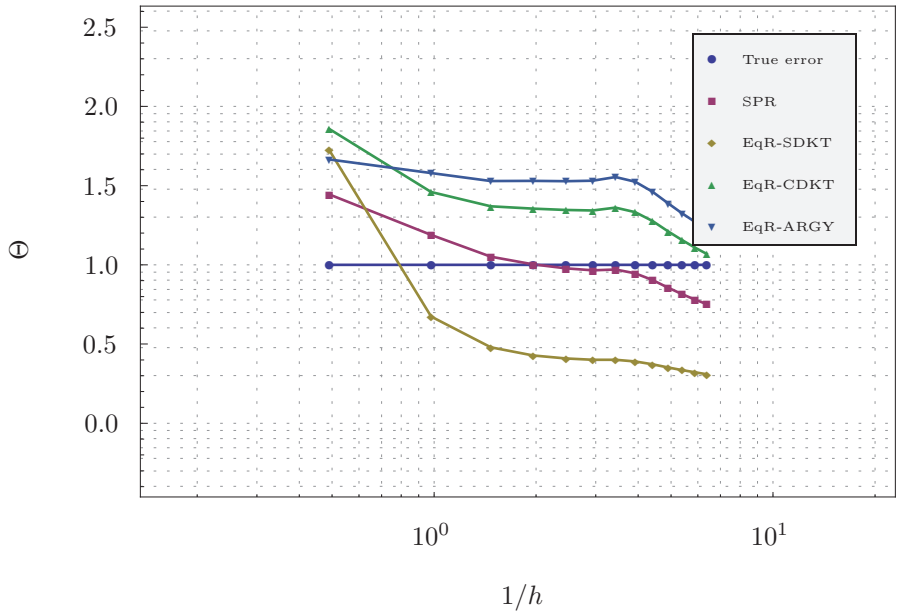

Figure 6.2.15: L-shaped plate under uniform loading - effectivity index of the global energy error estimates
Slika 6.2.15: Enakomerno obremenjena prosto podprta L plošča - indeks učinkovitosti ocene

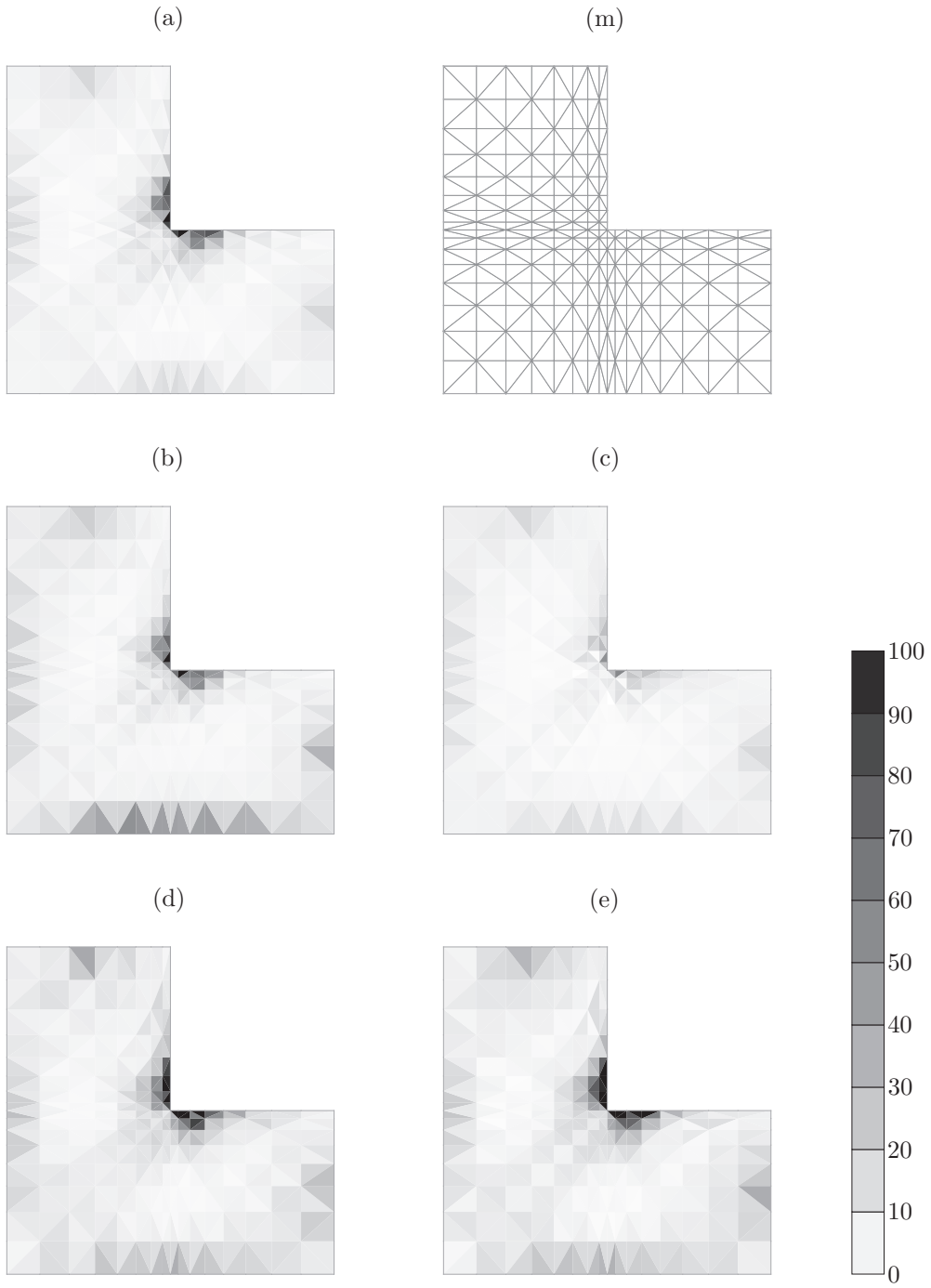

Figure 6.2.16: L-shaped plate under uniform loading
Comparison of relative local error estimates $\eta^*_{e,r}$ in [%] on the mesh (m):
(a) True error, (b) SPR, (c) EqR-SDKT, (d) EqR-CDKT, (e) EqR-ARGY
Slika 6.2.16: Enakomerno obremenjena prosto podprta L plošča
Primerjava relativnih lokalnih ocen napake $\eta^*_{e,r}$ v [%] na mreži (m):
(a) Dejanska napaka, (b) SPR, (c) EqR-SDKT, (d) EqR-CDKT, (e) EqR-ARGY

6.3 Discretization error for RM elements

RM plate elements, specifically the P3 elements introduced in Chapter 3, conform to the same principles given above for the DK elements. The definition (5.3.4) of the local error indicator is modified so, that it includes, besides the bending, also the shear deformation energy:

$$\eta_{e,RM}^2 = \sum_e \int_{\Omega_h^e} (\boldsymbol{m}^* - \boldsymbol{m}_h)^T \mathbf{C}_B^{-1} (\boldsymbol{m}^* - \boldsymbol{m}_h)\, \mathrm{d}\Omega + \sum_e \int_{\Omega_h^e} (\boldsymbol{q}^* - \boldsymbol{q}_h)^T \mathbf{C}_S^{-1} (\boldsymbol{q}^* - \boldsymbol{q}_h)\, \mathrm{d}\Omega \quad (6.3.1)$$

SPR is method is applied in exactly the same manner as for the DK elements (practial issues are discussed in [Lee Hobbs, 1998] and [Kettil Wiberg, 1999]). The application of the EqR method to the P3 elements follows the same same steps as for the DK elements. The reason for the similar treatment lies in the close similarity of the interpolations since they are build on a hierarchic basis. Conceptually, the only novelty is the treatment of the residuals to the midside degrees of freedom in P3 elements in the equilibration procedure. It is apparent, that due to the simple topology, equilibration of the midside DOF is not needed. Thus the equilibration procedures for DK and P3 elements are effectively equal. The enhanced interpolations for the local computations are, however, limited to the subdivision schemes, since there does not exist an enhanced P3 element (equivalent to the ARGY element in the case of DK elements).

6.4 Chapter summary and conclusions

The focus of the chapter is the discretization error for the case of finite element Discrete Kirchhoff plate model, which is widely accepted as finite element for the analysis of bending of thin plates. Of particular challenge are the non-conventional finite element interpolations for Discrete Kirchhoff plate bending elements. Hence, we can only provide the error indicators (rather that rigorous error bounds), and even those require quite ingenious procedures for constructing enhanced finite element space for error estimates.

The SPR method is nowadays widely accepted and found its way in many finite element codes. The implementation for the Discrete Kirchhoff plate elements follows the general principles of the method and it does not take into account the specific nature of the problem. The EqR method, however, is significantly more difficult to implement, but it has the potential of capturing specific issues related to modeling of plate bending. In this work a special attention was given to the development of EqR method for this case.

In particular, we have tested the equilibrated residual method with enhanced space constructed by either subdividing the original element into 6 smaller elements (subdivision into 3 smaller elements proved to be of no interest) or by using the Argyris plate element. Although each of these enhanced elements possesses 21 degrees of freedom, they differ in terms of providing the enhanced space. The former uses the patch like construction with third order polynomials, whereas the latter uses the complete fifth order polynomial. Thus, although both enhanced elements provide useful estimates, the latter, or the Argyris element, furnishes superior results quality.

Chapter 7

Model error concept

7.1 Introduction

For the case of linear elasticity, which is the subject of this work, a complete and validated three-dimensional theory exists, which captures all the physics of the deformation. In the practical work in solid and structural mechanics, however, the theory is rarely applied. The reason is, that for a given accuracy, the computational effort to obtain a solution is exceptionally high. Simplified models were therefore developed which are valid only under certain assumptions. The accuracy of this models is satisfactory for the most engineering computations as long as the assumptions are satisfied.

Similar situation exists also in other areas. The motion of free falling body in the air, for instance, is effectively computed using a Newton theory, rather than using quantum theory, which is known to be more accurate. If the result of the computation is simply a trajectory of the ball with a given accuracy, the Newton theory is obviously quite adequate. For the practical use, the model must be computationally efficient while the accuracy must match the prescribed one.

Engineering approach to modeling requires that the models are only as complex as necessary. In the structural mechanics the need to develop the computationally effective models is of particular importance. Several models of the typical structural members were developed and tested which give accurate measurable predictions. They are based on certain assumptions, which are typically satisfied in regular regions of a structure. In the disturbed regions such as boundary layers, thickness jumps, stiffeners and regions with concentrated loads enhanced models have to be used. Ultimately in the regions where none of the assumptions apply a full three-dimensional theory of elasticity have to be employed. Adaptive modeling in structural analysis has the goal to produce the most suitable (i.e.

optimal) model of a structure. In order to construct a mixed - regionally adapted - model, a sequence of hierarchically reduced, i.e. simplified, mathematical models derived from an appropriate master model is required. The choice of particular model depends on estimate of the model error. This information is the key to successful control of the adaptive construction of the optimal model. The model error is related to the suitability of model itself.

One should clearly distinguish between the model error estimates and model error indicators. The estimates define the boundaries of the error. They are usually quite conservative and they tend to overestimate the error by several orders of magnitude. Indicators on the other hand do not provide any guarantees on the error. In return they can give quite sharp indication of the error. Which type of model error to use depends on the purpose of the computation of the model error. If the goal is to control the adaptive construction of the optimal regional dependent model, the model indicators are the preferable choice.

To locate regions of the domain where the chosen mathematical model (usually the simplest one in a set of available hierarchic models) no longer performs well, one has to provide an estimate of model performance. Ideally, such an estimate for the chosen model should follow from the comparison with the best possible mathematical model (which is often the 2D/3D solid model). However, the best model estimate is in general not feasible, since it remains prohibitively expensive or simply inaccessible. Thus, for the practical model error estimation, it is sufficient to compare the chosen model with the one which is known to perform better; the latter will be called the enhanced model.

In principle, two global computations would be required to compare two different mathematical models: the chosen against the enhanced one. However, the computations with the enhanced model is usually simplified in trying to estimate the true stress state. This is made possible by using the EqR method originaly developed for discretization error estimation (see section 5.4.2). The procedure starts by extracting a portion of the domain, reducing the computation to a single finite element based on the enhanced model, applying the loading on its edges according to the true stress state estimate, computing the local enhanced solution and comparing it to the original solution obtained by the chosen model. This is of course possible only in principle, since the true stress state is unknown. However, its approximation can be obtained by improving the FE solution obtained with the chosen model to be best-possible approximation of the true stress state. This is done as follows: the FE solution for any stress component (which is discontinuous

between the elements) is improved to be continuous in order to approximate the true stress state, which is continuous (unless there is thickness, loading or material discontinuity). In accordance with the best-possible approximation of the true stress state, the edge loading (so-called boundary traction) for each finite element of the mesh is computed. That loading is further used in computation of local (element-wise) Neumann problems based on the enhanced model. Comparison of two mathematical models can be thus achieved by one global and a set of local computations.

The effective procedure of computation od model error indicator is build upon the following idea. The model error, in principle, measures the difference of the solutions of the current and full three-dimensional model. Based on the assumption that the family of models is hierarchically ordered, the model solution does not need to be compared to the solution of the exact model. Due to the hierarchy, it suffices to compare the current solution with the solution of the next model from the hierarchic family of models.

The global computation of the enhanced solution - just to serve as the reference to model error computation - is too expensive. An effective compromise is to repeat the computations with the enhanced model on smaller domains - preferably on elements. The local problems have to replicate the original problem. The interpretation is, that the elements are extracted from the continuum and its actions are replaced by boundary tractions. The boundary conditions for the local problems are therefore of Neumann type.

7.2 Model error indicator based on local EqR computations

7.2.1 Definition of model error indicator

The primary question of model error computation based on EqR method becomes: "How to estimate the boundary conditions for the local problems?". If the enhanced solution is known, the boundary conditions for the elements are computed from the stress state using the Cauchy principle. This is, however, not possible since the stresses are computed from the enhanced solution, which is unknown and yet to be computed. An approximation of the boundary stresses must therefore be built based on the single information available: current finite element solution. The development of the method of the construction of the best possible estimates for the boundary conditions for local problems is thus the central topic of the model error computation based on EqR method.

The enhanced solution, to which the original solution is compared to, is thus ap-

proximated twice: (i) the boundary conditions for the local problems are computed only approximately and (ii) the local problems are not solved exactly but rather in the weak sense (finite element method) with the enhanced model. Such double approximation is however still acceptable since the goal of the model error indicator is not to provide the error bounds but to drive the model adaptivity procedure.

The starting point for the computation of the model error indicator is the finite element solution of the problem using the coarse model - model 1. The finite element solution is $\boldsymbol{u}_{1,h}$.

Let us suppose that the finite element solution $\boldsymbol{u}_{2,h}$ using the enhanced model - model 2 - is available. Since the model error is of primary interest, let us assume also that the discretization error is negligible or at least much smaller than the model error. In this case the difference between the solutions can be entirely contributed to the model error. Since the difference $\boldsymbol{u}_{2,h} - \boldsymbol{u}_{1,h}$ is mathematically inconsistent, the difference of the solutions is computed as:

$$\boldsymbol{e}_{u,mod} = \boldsymbol{u}_{2,h} - \mathscr{P}_{u,1\to 2}\boldsymbol{u}_{1,h}$$

where $\mathscr{P}_{u,1\to 2}\boldsymbol{u}_{h,1}$ denotes the kinematic transformation of the solution $\boldsymbol{u}_{h,1}$ to the solution space of model 2.

Several measures of the difference of the solutions $\boldsymbol{u}_{2,h}$,$\boldsymbol{u}_{h,1}$ exist for the definition of the model error indicator. The most straightforward is probably to use the energy norm of $\boldsymbol{e}_{u,mod}$ as the model error indicator

$$\eta_{u,mod} = \|\boldsymbol{e}_{u,mod}\|_E = \|\boldsymbol{u}_{2,h} - \mathscr{P}_{u,1\to 2}\boldsymbol{u}_{h,1}\|_E$$

This definition of model error indicator is, however, prone to strong overestimation. Another option is to measure the model error in terms of the energy difference

$$\eta_{u,mod} = \|\boldsymbol{u}_{2,h}\|_E - \|\boldsymbol{u}_{h,1}\|_E$$

In most cases investigated this estimate is not sensitive enough, since the global energies of the models 1 and 2 usually do not differ enough. In order to avoid the problems mentioned, a model error is rather measured in terms of the stresses, i.e.:

$$\boldsymbol{e}_{\sigma,mod} = \boldsymbol{\sigma}_{2,h} - \mathscr{P}_{\sigma,1\to 2}\boldsymbol{\sigma}_{h,1}$$

The transformation $\mathscr{P}_{\sigma,1\to 2}\boldsymbol{\sigma}_{h,1}$ transforms the stresses from model 1 to model 2 using the constitutive relation of model 2. Note, that $\boldsymbol{e}_{u,mod}$ and $\boldsymbol{e}_{\sigma,mod}$ are in different solution spaces. The model error indicator is computed as the energy norm of $\boldsymbol{e}_{\sigma,mod}$:

$$\eta_{\sigma,mod} = \|\boldsymbol{e}_{\sigma,mod}\|_E = \|\boldsymbol{\sigma}_{2,h} - \mathscr{P}_{\sigma,1\to 2}\boldsymbol{\sigma}_{h,1}\|_E$$

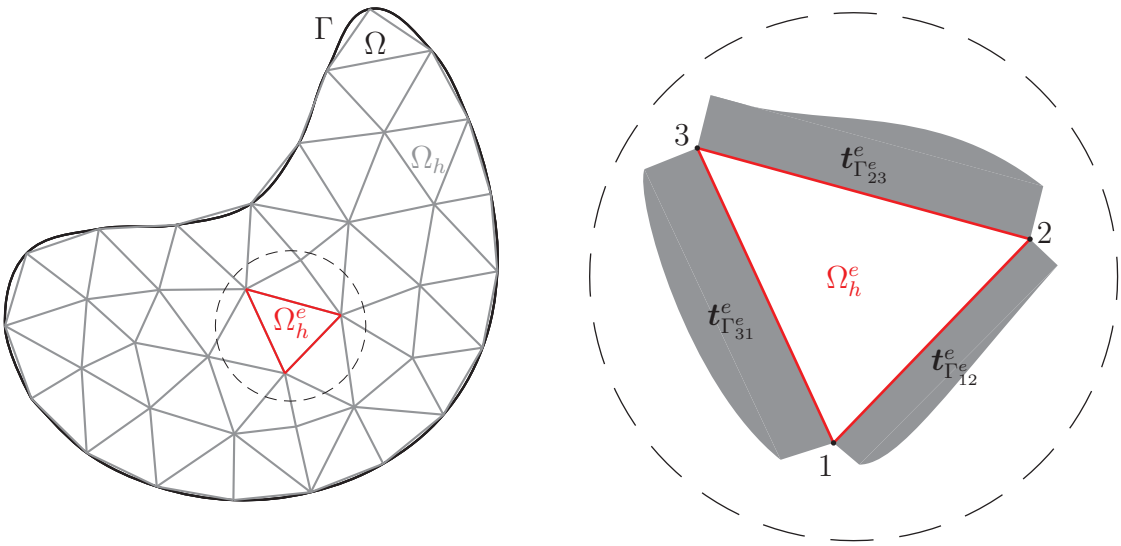

Figure 7.2.1: Local computation on a finite element domain Ω_h^e with Neumann boundary conditions $\boldsymbol{t}^e_{\Gamma^e}$ on Γ^e
Slika 7.2.1: Lokalni izračun s končnimi elementi na območju Ω_h^e z Neumannovimi robnimi pogoji $\boldsymbol{t}^e_{\Gamma^e}$ on Γ^e

The complementary energy norm $\|\cdot\|_E$ is related to the model 2:

$$\|\boldsymbol{\sigma}_2\|_E^2 = \int_\Omega \boldsymbol{\sigma}_2 : \mathbb{C}_2^{-2} : \boldsymbol{\sigma}_2 d\Omega$$

Construction of local problems

The model error can be estimated only via the comparison of the current solution with the solution of the enhanced model. The global computation of the enhanced solution $\boldsymbol{u}_{2,h}$ is, however, not feasible. An alternative is the decomposition of the global problem into smaller local problems. The local computations - preferably on elements - should ideally give the same results as the global one. By a suitable choice of boundary conditions it is possible in principle to define local problems with this property.

The finite element solution of the enhanced model 2[1], denoted by $\boldsymbol{u}_{2,h}$, satisfies the weak form:

$$a_2(\boldsymbol{u}_{2,h}, \boldsymbol{v}_{2,h}) = l_2(\boldsymbol{v}_{2,h}); \quad \forall \boldsymbol{v}_{2,h} \in \mathcal{V}_{2,h} \tag{7.2.1}$$

The linear forms a_2 and l_2 refer to the model 2. The finite element solution space is denoted by $\mathcal{V}_{2,h}$. The global problem can be replaced by a set of local problems, formed

[1]The subscript 2 will be related to the enhanced model.

as:

$$a_{2,e}(\tilde{\boldsymbol{u}}_{2,e,h}, \boldsymbol{v}_{2,h}) = l_{2,e}(\boldsymbol{v}_{2,h}) + \int_{\Gamma^e} \boldsymbol{t}^e_{2,\Gamma^e} \cdot \boldsymbol{v}_{2,h} \mathrm{d}s; \quad \forall \boldsymbol{v}_{2,h} \in \mathcal{V}_{2,h} \tag{7.2.2}$$

where the boundary conditions are of Neumann type. Along the boundary of the element, denoted by $\Gamma^e \equiv \partial\Omega^e$, the element is loaded by boundary tractions $\boldsymbol{t}^e_{2,\Gamma^e}$. Boundary tractions $\boldsymbol{t}^e_{2,\Gamma_{IJ}}$ are undefined and are yet to be determined.

Additional condition for their construction comes from the observation, that the solution of the local problems should match the global finite element solution:

$$\tilde{\boldsymbol{u}}_{2,e,h} = \boldsymbol{u}_{2,e,h} \tag{7.2.3}$$

The element solution $\boldsymbol{u}_{2,e,h} = \boldsymbol{u}_{2,h}|_{\Omega^e}$ is the restriction of the global finite element solution to the element domain Ω^e. Assuming that the global finite element solution $\boldsymbol{u}_{2,h}$ is known, the additional condition for the boundary tractions is:

$$\int_{\Gamma^e} \boldsymbol{t}^e_{2,\Gamma^e} \cdot \boldsymbol{v}_{2,h} \mathrm{d}s = a_{2,e}(\boldsymbol{u}_{2,e,h}, \boldsymbol{v}_{2,h}) - l_{2,e}(\boldsymbol{v}_{2,h}); \quad \forall \boldsymbol{v}_{2,h} \in \mathcal{V}_{2,h} \tag{7.2.4}$$

The symbolic form of the discretization of the j-th component of the test function $\boldsymbol{v}_{2,h}$ is $(v_{2,h})_j = \sum_I N^I_{2,j} \hat{\boldsymbol{v}}_{2,I}$, where $N^I_{2,j}$ are the shape functions. Employing this notation, we have for the integral over side Γ_{IJ}:

$$\int_{\Gamma_{IJ}} \boldsymbol{t}^e_{2,\Gamma_{IJ}} \cdot \boldsymbol{v}_{2,h} \, \mathrm{d}u = \boldsymbol{r}^e_{2,I,\Gamma_{IJ}} \cdot \hat{\boldsymbol{v}}_{2,I} + \boldsymbol{r}^e_{2,J,\Gamma_{IJ}} \cdot \hat{\boldsymbol{v}}_{2,J} \tag{7.2.5}$$

where the $\boldsymbol{r}^e_{2,I,\Gamma_{IJ}}$ is the 'projection' of the boundary traction $\boldsymbol{t}^e_{2,\Gamma_{IJ}}$ to the node I in the finite element test space $\mathcal{V}_{2,h}$. We can interpret $\boldsymbol{r}^e_{2,I,\Gamma_{IJ}}$ as residual forces at node I of element e due to the boundary traction applied on edge Γ_{IJ}, i.e.

$$\boldsymbol{r}^e_{2,I,\Gamma_{IJ}} = \frac{\partial W^e_{\Gamma_{IJ}}(\boldsymbol{t}^e_{2,\Gamma_{IJ}})}{\partial \hat{\boldsymbol{v}}_{2,I}}; \qquad W^e_{\Gamma_{IJ}}(\boldsymbol{t}^e_{2,\Gamma_{IJ}}) = \int_{\Gamma_{IJ}} \boldsymbol{t}^e_{2,\Gamma_{IJ}} \cdot \boldsymbol{v}_{2,h} ds \tag{7.2.6}$$

From (7.2.4) the finite element equilibrium equation for a single element (7.2.4) can be written also as

$$\boldsymbol{R}^e_2 = \mathbf{F}^{int,e}_2 - \mathbf{F}^{ext,e}_2 \tag{7.2.7}$$

where $\mathbf{F}^{ext,e}_2$, $\boldsymbol{R}^e_2$ and $\mathbf{F}^{int,e}_2$ are nodal values of external, residual and internal forces, respectively. The later are proportional to the stiffness matrix $\mathbf{K}^e_2$ and the nodal displacements $\hat{\boldsymbol{u}}^e_2$, so that (7.2.7) becomes:

$$\mathbf{K}^e_2 \hat{\boldsymbol{u}}^e_2 = \mathbf{F}^{ext,e}_2 + \boldsymbol{R}^e_2$$

Residual forces $\boldsymbol{R}^e_2$ represent the action of the surrounding elements.

The goal is to find such boundary traction forces that exactly replace the residual forces and are continuous across element boundaries. We thus seek for boundary traction $\boldsymbol{t}^e_{\Gamma^e}$ acting on an edge Γ^e, which will replace (in an energy manner) the action of residual nodal forces and reflect the continuity of the stress field. We can write

$$\sum_I \boldsymbol{R}^e_{2,I} \cdot \hat{\boldsymbol{v}}_{2,I} = \int_{\Gamma^e} \boldsymbol{t}^e_{\Gamma^e} \cdot \boldsymbol{v}_{2,\Gamma^e,h} \, \mathrm{d}s = \sum_{\Gamma_{IJ}} \int_{\Gamma_{IJ}} \boldsymbol{t}^e_{\Gamma_{IJ}} \cdot \boldsymbol{v}_{2,\Gamma_{IJ},h} \mathrm{d}s \tag{7.2.8}$$

where $\boldsymbol{v}_{2,\Gamma^e} = \boldsymbol{v}_2|_{\Gamma^e}$ are edge virtual displacements, and $\hat{\boldsymbol{v}}_{2,I}$ are nodal virtual displacements. The relation follows directly from (7.2.4):

$$a_{2,e}(\boldsymbol{u}_{2,e,h}, \boldsymbol{v}_{2,h}) - l_{2,e}(\boldsymbol{v}_{2,h}) = \sum_I \boldsymbol{R}^e_{2,I} \cdot \hat{\boldsymbol{v}}_{2,I} \tag{7.2.9}$$

where $\boldsymbol{R}^e_{2,I}$ is the nodal residual on node I of the element e. The vector of degrees of freedom pertaining to the node I is denoted by $\hat{\boldsymbol{v}}_{2,I}$.

From (7.2.5) we further express the nodal value of the element residual force $\boldsymbol{R}^e_{2,I}$ in (7.2.8) as the sum (with slight abuse of the notation)

$$\boldsymbol{R}^e_{2,I} = \boldsymbol{r}^e_{2,I,\Gamma_1} + \boldsymbol{r}^e_{2,I,\Gamma_2} \tag{7.2.10}$$

where Γ_1 and Γ_2 are two edges of element e that both include node I, see Figure 5.4.4.

Since the boundary tractions reflect the continuity of stress field, they conform to, see Figure 5.4.3:

$$\boldsymbol{t}^e_{2,\Gamma_{IJ}} + \boldsymbol{t}^{e'}_{2,\Gamma_{IJ}} = 0 \tag{7.2.11}$$

Here the Γ_{IJ} denotes the edge between the vertices I and J, adjacent to elements e and e', sharing the same edge Γ_{IJ}. We note that the condition in (7.2.11) follows from $\boldsymbol{t}^e_{2,\Gamma} = \boldsymbol{\sigma}\boldsymbol{n}^e$ and $\boldsymbol{n}^{e'} = -\boldsymbol{n}^e$, where $\boldsymbol{n}$ is normal to the edge Γ and $\boldsymbol{\sigma}$ is continuous stress tensor. The equation (7.2.11) is required to hold in the weak sense only:

$$\int_{\Gamma_{IJ}} (\boldsymbol{t}^e_{2,\Gamma_{IJ}} + \boldsymbol{t}^{e'}_{2,\Gamma_{IJ}}) \cdot \boldsymbol{v}_{2,h} \, \mathrm{d}s = 0 \tag{7.2.12}$$

$$\boldsymbol{r}^e_{2,I,\Gamma_{IJ}} + \boldsymbol{r}^{e'}_{2,I,\Gamma_{IJ}} = 0$$

By collecting equations (7.2.10) and (7.2.11) for all elements in the mesh ($e = 1, \ldots, n_{el}$), all element edges ($\Gamma_{IJ} = 1, \ldots n_\Gamma$) and all element nodes ($I = 1, \ldots n_{en}$), we could get a global system of equations for the unknowns $\boldsymbol{r}^e_{2,I,\Gamma_{IJ}}$ (the number of unknowns in such a system is reduced if there are regions of the discretized domain where boundary traction forces are prescribed). Moreover, introduction of the projections $\boldsymbol{r}^e_{2,I,\Gamma_{IJ}}$ as the unknowns,

enables the formation of patchwise linear systems. For the patch of elements around node I, we have (with sligh abuse of the notation):

$$\begin{aligned} \boldsymbol{r}^e_{2,I,\Gamma_{IJ}} + \boldsymbol{r}^e_{2,I,\Gamma_{IK}} &= \boldsymbol{R}^e_{2,I} \\ \boldsymbol{r}^e_{2,I,\Gamma_{IJ}} + \boldsymbol{r}^{e'}_{2,I,\Gamma_{IJ}} &= 0 \end{aligned} \tag{7.2.13}$$

where the only input (known) data are the element nodal reactions $\boldsymbol{R}^e_{2,I}$. With a suitable discretization, the boundary tractions are recovered from (7.2.5).

7.2.2 Construction of equilibrated boundary tractions for local problems

The decomposition of the global problem as described above is possible only if the global finite element solution $\boldsymbol{u}_{2,h}$ is known in advance. In our case, the solution is yet to be found and therefore the element nodal reactions $\boldsymbol{R}^e_{2,I}$ are unavailable for the computation. The boundary tractions $\boldsymbol{t}^e_{2,\Gamma_{IJ}}$, which satisfy (7.2.13), cannot be computed and an approximation have to be used. Note, however, that if the approximation for the boundary tractions $\boldsymbol{t}^e_{2,\Gamma_{IJ}}$ is used in the local problems (7.2.4), the solution $\tilde{\boldsymbol{u}}_{2,e,h}$ of (7.2.2) no longer matches the finite element solution $\boldsymbol{u}_{2,e,h}$.

The approximation of the boundary tractions $\tilde{\boldsymbol{t}}^e_{2,\Gamma_{IJ}}$ must meet some basic conditions. First, the boundary tractions must maintain the element equilibrium. The element is in equilibrium if the virtual work of the external forces vanishes at rigid body motion. Using $\boldsymbol{v}_\Lambda$ to denote rigid body motion, the condition for $\tilde{\boldsymbol{t}}^e_{2,\Gamma^e}$ reads:

$$\int_{\Gamma^e} \tilde{\boldsymbol{t}}^e_{2,\Gamma^e} \cdot \boldsymbol{v}_\Lambda = l_{2,e}(\boldsymbol{v}_\Lambda); \quad \forall \boldsymbol{v}_\Lambda \in \mathcal{V}_\Lambda \subset \mathcal{V}_{2,h} \tag{7.2.14}$$

The boundary tractions satisfying (7.2.14) guarantee the element is in equilibrium. Second, the global equilibrium of the assembly of elements is achieved if the boundary tractions satisfy

$$\int_{\Gamma_{IJ}} (\tilde{\boldsymbol{t}}^e_{2,\Gamma_{IJ}} + \tilde{\boldsymbol{t}}^{e'}_{2,\Gamma_{IJ}}) \cdot \boldsymbol{v}_\Lambda = 0; \quad \forall \boldsymbol{v}_\Lambda \in \mathcal{V}_\Lambda \subset \mathcal{V}_{2,h} \tag{7.2.15}$$

Although the two conditions (7.2.14) and (7.2.15) are necessary, they are quite general and do not contribute to the any meaningful information about the problem in question. Therefore, the third additional condition is set by specifying that the boundary traction approximation should be chosen so, that the following holds:

$$\int_{\Gamma^e} \tilde{\boldsymbol{t}}^e_{2,\Gamma^e} \cdot \boldsymbol{v}_{1,h} \mathrm{d}s = a_{1,e}(\boldsymbol{u}_{1,e,h}, \boldsymbol{v}_{1,h}) - l_{1,e}(\boldsymbol{v}_{1,h}); \quad \forall \boldsymbol{v}_{1,h} \in \mathcal{V}_{1,h} \tag{7.2.16}$$

In that case the solution of local problems $\boldsymbol{u}_{1,e,h}$

$$a_{1,e}(\tilde{\boldsymbol{u}}_{1,e,h}, \boldsymbol{v}_{1,h}) = l_{1,e}(\boldsymbol{v}_{1,h}) + \int_{\Gamma^e} \tilde{\boldsymbol{t}}^e_{2,\Gamma^e} \cdot \boldsymbol{v}_{1,h} \mathrm{d}s; \quad \forall \boldsymbol{v}_{1,h} \in \mathcal{V}_{1,h} \tag{7.2.17}$$

match the original finite element solution $\tilde{\boldsymbol{u}}_{1,e,h} = \boldsymbol{u}_{1,e,h}$ (obtained with the model 1). Note, that, since $\mathcal{V}_\Lambda \subset \mathcal{V}_{1,h}$, the condition (7.2.14) is automatically satisfied.

The discretization of j-th component of $\boldsymbol{v}_{1,h}$ is defined as $(v_{1,h})_j = \sum_I N^I_{1,j} \hat{v}^I_{1,j}$, which gives:

$$\int_{\Gamma_{IJ}} \tilde{\boldsymbol{t}}^e_{2,\Gamma_{IJ}} \cdot \boldsymbol{v}_{1,h} \, \mathrm{d}u = \boldsymbol{r}^e_{2_1,I,\Gamma_{IJ}} \cdot \hat{\boldsymbol{v}}_{1,I} + \boldsymbol{r}^e_{2_1,J,\Gamma_{IJ}} \cdot \hat{\boldsymbol{v}}_{1,J} \tag{7.2.18}$$

$$a_{1,e}(\boldsymbol{u}_{1,e,h}, \boldsymbol{v}_{1,h}) - l_{1,e}(\boldsymbol{v}_{1,h}) = \sum_I \boldsymbol{R}^e_{1,I} \cdot \hat{\boldsymbol{v}}_{1,I} \tag{7.2.19}$$

where the $\boldsymbol{r}^e_{2_1,I,\Gamma_{IJ}}$ is the projection of the boundary traction $\tilde{\boldsymbol{t}}^e_{2,\Gamma_{IJ}}$ to the node I in the finite element test space $\mathcal{V}_{1,h}$. The element nodal reaction on node I on the element e (model 1) is denoted as $\boldsymbol{R}^e_{1,I}$.

The projections $\boldsymbol{r}^e_{2_1,I,\Gamma_{IJ}}$ are the unknowns of the local patchwise systems - similar to (7.2.13). For the patch of elements around node I we thus have

$$\begin{aligned} \boldsymbol{r}^e_{2_1,I,\Gamma_{IJ}} + \boldsymbol{r}^e_{2_1,I,\Gamma_{IK}} &= \boldsymbol{R}^e_{1,I} \\ \boldsymbol{r}^e_{2_1,I,\Gamma_{IJ}} + \boldsymbol{r}^{e'}_{2_1,I,\Gamma_{IJ}} &= 0 \end{aligned} \tag{7.2.20}$$

Example

In order to get further insight into the procedure of computation of boundary traction projections, we inspect a patch of four 2D elements surrounding node I of the FE mesh (see Figure 7.2.2). In this example the notation will be simplified so that the index denoting the model will be dropped: $\boldsymbol{R}^e_{1,I} \to \boldsymbol{R}^e_I$, $\boldsymbol{r}^e_{2_1,I,\Gamma} \to \boldsymbol{r}^e_{I,\Gamma}$. Edges and elements are numbered in counter-clockwise manner. Application of equation (7.2.10) for this case gives

$$
\begin{aligned}
\boldsymbol{R}_I^{e_1} &= \boldsymbol{r}_{I,\Gamma_4}^{e_1} + \boldsymbol{r}_{I,\Gamma_1}^{e_1} \\
\boldsymbol{R}_I^{e_2} &= \boldsymbol{r}_{I,\Gamma_1}^{e_2} + \boldsymbol{r}_{I,\Gamma_2}^{e_2} \\
\boldsymbol{R}_I^{e_3} &= \boldsymbol{r}_{I,\Gamma_2}^{e_3} + \boldsymbol{r}_{I,\Gamma_3}^{e_3} \\
\boldsymbol{R}_I^{e_4} &= \boldsymbol{r}_{I,\Gamma_3}^{e_4} + \boldsymbol{r}_{I,\Gamma_4}^{e_4}
\end{aligned}
$$

The demand for continuity further leads to

$$
\begin{aligned}
\boldsymbol{r}_{I,\Gamma_1}^{e_1} + \boldsymbol{r}_{I,\Gamma_1}^{e_2} &= 0 \\
\boldsymbol{r}_{I,\Gamma_2}^{e_2} + \boldsymbol{r}_{I,\Gamma_2}^{e_3} &= 0 \\
\boldsymbol{r}_{I,\Gamma_3}^{e_3} + \boldsymbol{r}_{I,\Gamma_3}^{e_4} &= 0 \\
\boldsymbol{r}_{I,\Gamma_4}^{e_4} + \boldsymbol{r}_{I,\Gamma_4}^{e_1} &= 0
\end{aligned}
$$

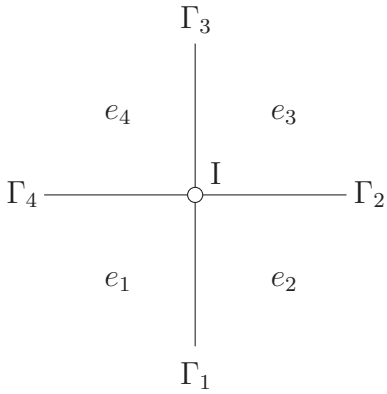

Figure 7.2.2: A patch of four elements surrounding node I

Combination of the last two sets of equations leads to the following system

$$
\begin{bmatrix} \boldsymbol{R}_I^{e_1} \\ \boldsymbol{R}_I^{e_2} \\ \boldsymbol{R}_I^{e_3} \\ \boldsymbol{R}_I^{e_4} \end{bmatrix} = \begin{bmatrix} +1 & 0 & 0 & -1 \\ -1 & +1 & 0 & 0 \\ 0 & -1 & +1 & 0 \\ 0 & 0 & -1 & +1 \end{bmatrix} \begin{bmatrix} \boldsymbol{r}_{I,\Gamma_1}^{e_1} \\ \boldsymbol{r}_{I,\Gamma_2}^{e_2} \\ \boldsymbol{r}_{I,\Gamma_3}^{e_3} \\ \boldsymbol{r}_{I,\Gamma_4}^{e_4} \end{bmatrix} \tag{7.2.21}
$$

for the unknowns $\boldsymbol{r}_{I,\Gamma_k}^{e_k}$. Since all the unknowns refer only to node I of the FE mesh, the system is independent from other nodes. One thus obtains a local (patch-wise) problem; a global system is actually a composition of independent patch-wise systems. If local system (7.2.21) is solved for each node of the FE mesh, we obtain $\boldsymbol{r}_{I,\Gamma}^{e_k}$, for all elements of the mesh ($e_k = e = 1, \ldots, n_{el}$), all element edges ($\Gamma = 1, \ldots n_\Gamma$) and all element nodes ($I = 1, \ldots n_{en}$).

Recovery of boundary tractions from the projections

Result of the local patchwise computations are the projections $\boldsymbol{r}_{2_1,I,\Gamma_{IJ}}^{e}$ for all nodes and edges Γ_{IJ}. Two projections exist for every edge Γ_{IJ}: $\boldsymbol{r}_{2_1,I,\Gamma_{IJ}}^{e}$ and $\boldsymbol{r}_{2_1,J,\Gamma_{IJ}}^{e}$. After a suitable discretization of $\tilde{\boldsymbol{t}}_{2,\Gamma_{IJ}}^{e}$ is chosen, the boundary tractions are reconstructed using the relation (7.2.18). The boundary tractions $\tilde{\boldsymbol{t}}_{2,\Gamma_{IJ}}^{e}$ are consistent with model 2 and caution should be taken when solving for $\tilde{\boldsymbol{t}}_{2,\Gamma_{IJ}}^{e}$. The relation (7.2.18) namely assumes that the boundary tractions conform to the kinematics of model 1.

Evaluation of boundary traction parameters from (7.2.18)

If $\boldsymbol{r}^e_{I,\Gamma}$ are known[2], the boundary traction can be computed for each element as follows. We introduce parametrization of k-th component of the boundary traction $\boldsymbol{t}^e_\Gamma$ (let Γ be element edge between element nodes I and J) as

$$(t^e_\Gamma)_k = p^I_k \psi^I_k + p^J_k \psi^J_k + p^K_k \psi^K_k \tag{7.2.22}$$

where ψ^I_k are shape functions (yet to be chosen) and p^I_k are nodal values of $(t^e_\Gamma)_k$. Here we assumed, the edge has vertex nodes I and J and a midside node K. The variation of virtual displacements along the same edge Γ can then be written as

$$(v_{\Gamma,h})_k = N^I_{k,m}\hat{v}^I_m + N^J_{k,m}\hat{v}^J_m + N^K_{k,m}\hat{v}^K_m \tag{7.2.23}$$

where $\hat{v}^I_m$ is the m-th degree of freedom at node I, and $N^I_{k,m}$ are the corresponding shape functions. In other words, the shape function $N^I_{k,i}$ interpolates the k-th component of virtual displacements $\boldsymbol{v}_{h,\Gamma}$ and is weighted by nodal degree of freedom $\hat{v}_{i,I}$ in the linear interpolation (7.2.23). We can now insert the above parameterizations into (7.2.18) and express residuals at nodes I and J with respect to the boundary traction on edge Γ (that spans between I and J). The result can be written in a compact form as:

$$\begin{bmatrix} \boldsymbol{r}^e_{I,\Gamma} \\ \boldsymbol{r}^e_{J,\Gamma} \end{bmatrix} = \begin{bmatrix} \mathbf{M}^{II}_\Gamma & \mathbf{M}^{IJ}_\Gamma & \mathbf{M}^{IK}_\Gamma \\ \mathbf{M}^{JI}_\Gamma & \mathbf{M}^{JJ}_\Gamma & \mathbf{M}^{JK}_\Gamma \end{bmatrix} \begin{bmatrix} \mathbf{p}^I_\Gamma \\ \mathbf{p}^J_\Gamma \\ \mathbf{p}^K_\Gamma \end{bmatrix}; \tag{7.2.24}$$

$$\mathbf{M}^{IJ}_\Gamma = [\mathbf{M}^{I,J}_\Gamma]; \quad \mathbf{M}^{I,J}_\Gamma = [M^{I,J}_{\Gamma,nm}]$$

where $\mathbf{p}^I_\Gamma = \left[p^I_k, k = 1, \ldots n_{\text{dim}}\right]^T$, and n_{dim} is vector dimension. The block matrices $\mathbf{M}^{I,J}_\Gamma$ have n_{ndof_I} rows and n_{dim} columns with the elements

$$M^{I,J}_{\Gamma,nm} = \int_\Gamma N^I_{\bar{m},n}\psi^J_m ds \tag{7.2.25}$$

The index $\bar{m}$ is denotes the virtual displacement component which is conjugated (in the sense of the virtual work principle) to the traction component m.

By solving (7.2.25) for every element edge Γ, we obtain parameters $\mathbf{p}^I_\Gamma$, which define element boundary traction $\boldsymbol{t}^e_\Gamma$ through (7.2.22).

It is suggested in the literature (e.g. [Ainsworth Oden, 2000], [Oden Cho, 1997]) that shape functions ψ^J_k and ψ^I_k should be such that $\mathbf{M}^{IJ}_\Gamma$ and $\mathbf{M}^{JI}_\Gamma$ vanish and the matrix $\mathbf{M}$

[2]The subscript related to the model is dropped.

becomes block diagonal. In such a case (7.2.25) simplifies to

$$\boldsymbol{r}^e_{I,\Gamma} = \mathbf{M}^{II}_{\Gamma}\mathbf{p}^I_{\Gamma} \tag{7.2.26}$$

This makes the bookkeeping for the computations much easier. However, our experience is that the form of boundary traction obtained in this way is very specific and it does not represent well the stress field. We also note that the specific choice of parametrization (7.2.26) is not necessary, since local patch-wise computation can be performed, see (7.2.21).

Regularization of local system (7.2.21)

The solution of local system of equations, e.g. (7.2.21) for 2D problem, is not unique, unless we impose an adequate additional regularization. The latter can be derived in accordance with the estimate of the true stress state with the continuous boundary traction across the element interfaces. However, the true stress state is not known, but only its (discontinuous) element-wise approximations $\boldsymbol{\sigma}^e_{FE}$ obtained by model 1. Continuous stresses at the edge Γ, denoted as $\boldsymbol{\sigma}_0|_\Gamma$, follow from the smooth stress recovery which may be coupled with previous mesh adaptivity procedure. Boundary traction forces resulting from a such stresses $\boldsymbol{\sigma}_0|_\Gamma$ are obtained by the use of the Cauchy principle $\boldsymbol{t}^{e,0}_\Gamma = \boldsymbol{\sigma}_0|_\Gamma \boldsymbol{n}^e$. It is now possible to calculate the effect of this edge loading on neighboring nodes by using[3] (7.2.6)

$$\boldsymbol{r}^{e,0}_{I,\Gamma} = \frac{\partial W^e_\Gamma(\boldsymbol{t}^{e,0}_\Gamma)}{\partial \hat{\boldsymbol{v}}_I} \tag{7.2.27}$$

We want $\boldsymbol{r}^e_{I,\Gamma}$ to be as close as possible to this result in the least square sense. We construct the following constrained patch-wise minimization problem:

$$\begin{aligned}\mathcal{L}\{\boldsymbol{r}^e_{I,\Gamma};\lambda^\Gamma;\sigma^e\} &= \frac{1}{2}\sum_{e\in\mathcal{P}_I}\sum_\Gamma\left(\boldsymbol{r}^{e,0}_{I,\Gamma}-\boldsymbol{r}^e_{I,\Gamma}\right)^2 \\ &+ \sum_{e\in\mathcal{P}_I}\sigma^e_I(\boldsymbol{R}^e_I-\sum_\Gamma \boldsymbol{r}^e_{I,\Gamma}) \\ &+ \sum_\Gamma \lambda^\Gamma_I(\boldsymbol{r}^e_{I,\Gamma}+\boldsymbol{r}^{e'}_{I,\Gamma})\end{aligned} \tag{7.2.28}$$

where the constraints (7.2.11) and (7.2.10) are also introduced by means of the corresponding Lagrange multipliers σ^e_I and λ^Γ_I, and $\mathcal{P}_I$ is patch of elements around node I of the FE mesh.

[3]The subscript related to the model is dropped again.

The Kuhn-Tucker optimality conditions for stationary point are then given by differentiating the Lagrangian with respect to unknowns $\boldsymbol{r}^e_{I,\Gamma}$:

$$\boldsymbol{r}^e_{I,\Gamma} - \boldsymbol{r}^{e,0}_{I,\Gamma} - \sigma^e_I + \lambda^\Gamma_I = 0$$

The same equation also holds for the residual force on the neighboring element $\boldsymbol{r}^{e'}_{I,\Gamma}$:

$$\boldsymbol{r}^{e'}_{I,\Gamma} - \boldsymbol{r}^{e',0}_{I,\Gamma} - \sigma^{e'}_I + \lambda^\Gamma_I = 0$$

If we sum up the last two equations and take into account the continuity condition $\boldsymbol{r}^e_{I,\Gamma} + \boldsymbol{r}^{e'}_{I,\Gamma} = 0$, we can express the Lagrange multiplier λ^Γ_I as

$$\lambda^\Gamma_I = \frac{1}{2}(\sigma^e_I + \sigma^{e'}_I + \boldsymbol{r}^{e,0}_{I,\Gamma} + \boldsymbol{r}^{e',0}_{I,\Gamma})$$

The unknowns $\boldsymbol{r}^e_{I,\Gamma}$ can then be expressed in terms of the multiplier σ^e_I

$$\boldsymbol{r}^e_{I,\Gamma} = \frac{1}{2}(\sigma^e_I - \sigma^{e'}_I + \boldsymbol{r}^{e,0}_{I,\Gamma} - \boldsymbol{r}^{e',0}_{I,\Gamma}) \tag{7.2.29}$$

The condition $\boldsymbol{r}^e_I = \boldsymbol{r}^e_{I,\Gamma_1} + \boldsymbol{r}^e_{I,\Gamma_2}$ is rewritten as

$$\boldsymbol{r}^e_I = \frac{1}{2}(\boldsymbol{r}^{e,0}_{I,\Gamma_1} - \boldsymbol{r}^{e_1,0}_{I,\Gamma_1}) + \frac{1}{2}(\boldsymbol{r}^{e,0}_{I,\Gamma_2} - \boldsymbol{r}^{e_2,0}_{I,\Gamma_2}) + \frac{1}{2}(\sigma^e_I - \sigma^{e_1}_I + \sigma^e_I - \sigma^{e_2}_I)$$

By exploiting the above results, the local system for the patch of four elements can be rewritten as

$$\begin{bmatrix} \tilde{\boldsymbol{R}}^{e_1}_I \\ \tilde{\boldsymbol{R}}^{e_2}_I \\ \tilde{\boldsymbol{R}}^{e_3}_I \\ \tilde{\boldsymbol{R}}^{e_4}_I \end{bmatrix} = \frac{1}{2} \begin{bmatrix} 2 & -1 & 0 & -1 \\ -1 & 2 & -1 & 0 \\ 0 & -1 & 2 & -1 \\ -1 & 0 & -1 & 2 \end{bmatrix} \begin{bmatrix} \sigma^{e1}_I \\ \sigma^{e2}_I \\ \sigma^{e3}_I \\ \sigma^{e4}_I \end{bmatrix} \tag{7.2.30}$$

where we introduced notation

$$\tilde{\boldsymbol{R}}^e_I = \boldsymbol{R}^e_I - \sum_{\Gamma \in \partial\Omega e,I} < \boldsymbol{r}^{e,0}_{I,\Gamma} >; \qquad < \boldsymbol{r}^{e,0}_{I,\Gamma} >= \frac{1}{2}(\boldsymbol{r}^{e,0}_{I,\Gamma} - \boldsymbol{r}^{e',0}_{I,\Gamma})$$

The notation $< \cdot >$ implies averaging. The $< \boldsymbol{r}^{e,0}_{I,\Gamma} >$ thus represent averaged boundary traction on Γ (evaluated from FE solution) 'projected' to node I.

To summarize, the element-wise boundary traction are computed from FE solution (based on chosen mathematical model) in two steps: (i) by solutions of patch-wise problems in (7.2.30) to obtain $\boldsymbol{r}^e_{I,\Gamma}$; (ii) by solutions of element-wise problems (7.2.25) to compute nodal values p^I_k of boundary tractions (7.2.22).

Local problems as floating structures

The local problems (7.2.2) are of Neumann type. An element with only Neumman boundary conditions is essentially a floating structure, and one thus ought to eliminate the rigid body modes to get a unique result. This can be done simply by using the element geometry, as shown in [Park Felippa, 1998]. A rigid body displacement $\boldsymbol{d}_R^e$ of an element is a linear combination of all its rigid body modes

$$\boldsymbol{d}_R^e = \mathbf{D}^e \boldsymbol{\alpha} \tag{7.2.31}$$

where $\boldsymbol{\alpha}$ is a vector of amplitudes that correspond to rigid body modes, and $\mathbf{D}^e$ is a matrix containing the rigid body modes of the element (arranged column-wise). Since the element stiffness matrix $\mathbf{K}^e$ is singular due to the rigid body modes contribution, one can form a modified nonsingular stiffness matrix $\mathbf{K}^e$ by adding a product $\mathbf{D}^e\mathbf{D}^{eT}$ to $\mathbf{K}^e$

$$\bar{\mathbf{K}}^e = \mathbf{K}^e + \mathbf{D}^e\mathbf{D}^{eT}$$

The inversion of $\bar{\mathbf{K}}$ is possible and solution $\bar{\mathbf{d}}$ ('rigid-body-polluted' element nodal displacements/rotations) can be obtained. Since the matrix $\mathbf{D}^e\mathbf{D}^{eT}$ projects onto the space spanned by rigid body modes, we have

$$\bar{\boldsymbol{d}} = \boldsymbol{d}^e + \boldsymbol{d}_R^e$$

where $\boldsymbol{d}^e$ are real nodal displacements/rotations. As we are interested only in stress resultants, such a 'pollution' is not critical due to the following property $\mathbf{K}^e\boldsymbol{d}_R^e = \mathbf{0}$.

7.3 Chapter summary and conclusions

A general discussion of the model error estimation is given and a concept of hierarchically ordered models is introduced. Hierarchy of models enables computation of a model estimate on the basis of the comparison of the results of two model computations: original (model 1) and the enhanced one (model 2). Comparison of the results of two global computations is clearly not rational. It is therefore desirable if the computation with the enhanced model is done only locally - preferably on finite elements.

The local problems are of Neumann type - the boundaries are loaded with boundary tractions representing the action of the surrounding continua. The central question of model error estimation is: *how to make an educated guess of the boundary tractions for the local problems?* The boundary tractions of the local problems are optimally computed

from the true stress state using the Cauchy principle. However, since the true stress state is unknown, we seek for an alternative method for the computation of boundary tractions. The alternative identified as useful is the method of equilibrated residuals (EqR). The EqR method produces the boundary tractions, which exactly represent (in the sense of principle of virtual work) the action of the element residual forces of the original model (model 1). The basic principle of EqR method therefore coincides with the concept of model error estimation. The second part of the chapter is thus devoted to a general discussion of the computational aspects of EqR method related to the model error computation.

Chapter 8

Model error indicator for DK elements

8.1 Introduction

Analysis of plate structure with complex shape, loading and boundary conditions is one of the most frequently encountered problems in structural engineering practice. A problem of selecting the most suitable model for a particular plate structure, which is the topic of this chapter, has therefore interesting practical aspects. If successfully solved, it can lead to an efficient and accurate plate analysis, which is of great practical interest. Since plate structures are often combined with frame and other skeletal structures, for which one can develop by far the most efficient finite element analysis by exploiting one dimensional form of the governing model and the superconvergence properties of the corresponding finite element method, the solution of the above mentioned problem would clearly have a very practical value.

Plates are basic structural elements and historically much attention has been given to the derivation of different models. The derivation of the models has often been based on various mechanical considerations and principles with no rigorous proof of the relationship between the three-dimensional solution and the plate model. This kind of derivation has also been used in this work (see chapters 2-4).

A sequence of plate models can be derived in an hierarchical way from three-dimensional model. Using a model reduction a hierarchical sequence of elastic 2D plate models can be be produced from 3D theory ([Babuška et al., 1983], [Szabó Sahrmann, 1988]). The models are controlled by two parameters p and q (p denotes the polynomial degree in terms of standard plate coordinates, and q the polynomial degree in normal direction to the mid-surface). Computable upper-bound error estimates are given by [Babuška Schwab, 1993],

presuming that the resulting 2D PDEs (by reduction) are solved with prescribed error tolerances. The plate modeling naturally can thus fit into the framework of hierarchic modeling.

The hierarchic sequence of plate models can also be constructed with plate models, based on the engineering insight as those presented in Chapters 2-4. Those models are widely accepted in the practical computations since they are computationaly robust and fast. In our work, we choose three plate models, which form a hierarchic family: the Kirchhoff plate model (chapter 2), the Reissner/Mindlin plate model (chapter 3) and the (1,1,2) plate model with through the thickness stretching (chapter 4).

An adaptive structural analysis of a plate structure as organized in our work starts with a simplest possible plate model (Kirchhoff model). The model error with respect to Reisnner/Mindlin model is computed and the regions where more refined model should be used can be identified. The procedure can be iterated until the prescribed accuracy is achieved throughout the problem domain by using the available models. An effective computation of the model error is thus the key of the concept of adaptive modeling. The above described procedure implies the need for a hierarchic family of plate models.

The model error indicator procedure described in chapter 7 will be specialized for plates in this chapter. To construct the boundary stress resultants (which are plate counterparts of solid boundary traction) we follow the procedure outlined e.g in [Ladevèze Leguillon, 1983], [Ladevèze Maunder, 1996], [Stein Ohnimus, 1997], [Oden Cho, 1997] for 3D elasticity and briefly presented in chapter 7. The local problem that needs to be solved (to get a model error indicator/estimate) deals with single plate element, which is floating structure, loaded on the surface and along its edges in such a way that the loads are self-equilibrated. We can thus speak about the model adaptivity procedure for plates that is based on equilibrated boundary stress resultants[1].

Due to the hybrid construction of the DK plate elements, the standard computation of equilibrated boundary tractions is modified. The detailed procedure for the computation of the boundary tractions of the local problems will be given in the following (see also [Bohinc et al., 2006], [Bohinc et al., 2009]).

[1]We will not distinguish between boundary stress resultants and boundary tractions in what follows

8.2 Model error indicator

In order to find equilibrated stress resultants for the DK plate elements, we start with interpolations for displacement and rotations. The displacement along the element boundary Γ_{IJ}, spanned between the element nodes I and J, is defined (according to (2.3.59)) by:

$$w_{h,\Gamma_{IJ}} = \hat{w}_I\,\varphi_1 + \hat{w}_J\,\varphi_2 + \frac{L_{IJ}}{4}\mathbf{n}_{IJ}\cdot(\hat{\boldsymbol{\theta}}_I - \hat{\boldsymbol{\theta}}_J)\,\varphi_3 + \frac{L_{IJ}}{3}\Delta\theta_{IJ}\,\varphi_4 \tag{8.2.1}$$

where $\Delta\theta_{IJ} = \frac{3}{2\,L_{IJ}}(\hat{w}_J - \hat{w}_I) - \frac{3}{4}\mathbf{n}_{IJ}\cdot(\hat{\boldsymbol{\theta}}_I + \hat{\boldsymbol{\theta}}_J)$, L_{IJ} is the length of the edge Γ_{IJ} and $\boldsymbol{n}_{IJ} = [n_{x,IJ}, n_{y,IJ}]^T$ is the unit exterior normal. Similarly, rotation vector along the same edge is defined as

$$\boldsymbol{\theta}_{h,\Gamma_{IJ}} = \hat{\boldsymbol{\theta}}_I\,\varphi_1 + \hat{\boldsymbol{\theta}}_J\,\varphi_2 + \mathbf{n}_{IJ}\Delta\theta_{IJ}\,\varphi_3 \tag{8.2.2}$$

The shape functions φ_i in (6.2.2) and (6.2.3) are:

$$\begin{aligned} \varphi_1 &= (1-\xi)/2 & \varphi_2 &= (1+\xi)/2 \\ \varphi_3 &= (1-\xi^2)/2 & \varphi_4 &= \xi(1-\xi^2)/2, \end{aligned} \tag{8.2.3}$$

where $\xi \in [-1, 1]$. In accordance with (8.2.1), (8.2.2) and notation used in (7.2.23), one can write the interpolation functions. For displacement or rotations on the edge Γ (between vertex nodes I and J) as

$$\begin{aligned} N^I_{w,\hat{w}} &= \varphi_1 - \varphi_4/2 & N^J_{w,\hat{w}} &= \varphi_2 + \varphi_4/2 \\ N^I_{w,\hat{\theta}_x} &= -L\,n_x(-\varphi_3 + \varphi_4)/2 & N^J_{w,\hat{\theta}_x} &= -L\,n_x(+\varphi_3 + \varphi_4)/2 \\ N^I_{w,\hat{\theta}_y} &= -L\,n_y(-\varphi_3 + \varphi_4)/2 & N^J_{w,\hat{\theta}_y} &= -L\,n_y(+\varphi_3 + \varphi_4)/2 \\ \\ N^I_{\theta_x,\hat{w}} &= +(3n_x/L)\,\varphi_3 & N^J_{\theta_x,\hat{w}} &= -(3n_x/L)\,\varphi_3 \\ N^I_{\theta_x,\hat{\theta}_x} &= \varphi_1 + 3n_x^2\varphi_3/2 & N^J_{\theta_x,\hat{\theta}_x} &= \varphi_2 + 3n_x^2\varphi_3/2 \\ N^I_{m_x\theta_y} &= +3n_xn_y\varphi_3/2 & N^J_{\theta_x,\hat{\theta}_y} &= +3n_xn_y\varphi_3/2 \\ \\ N^I_{\theta_y,\hat{w}} &= +(3n_y/L)\,\varphi_3 & N^J_{\theta_y,\hat{w}} &= -(3n_y/L)\,\varphi_3 \\ N^I_{\theta_y,\hat{\theta}_x} &= +3n_xn_y\varphi_3/2 & N^J_{\theta_y,\hat{\theta}_x} &= +3n_xn_y\varphi_3/2 \\ N^I_{\theta_y,\hat{\theta}_y} &= \varphi_1 + 3n_y^2\varphi_3/2 & N^J_{\theta_y,\hat{\theta}_y} &= \varphi_2 + 3n_y^2\varphi_3/2 \end{aligned} \tag{8.2.4}$$

where $L = L_{IJ}$, $\mathbf{n}_{IJ} = [n_x, n_y]$, $\theta_x = \theta_1$ and $\theta_y = \theta_2$. Note, that with respect to (7.2.23) and notation in previous chapter one has: $k \in [w, \theta_x, \theta_y], m \in [\hat{w}, \hat{\theta}_x, \hat{\theta}_y]$ and

$$(v_{\Gamma,h})_w = w_{h,\Gamma}, \quad (v_{\Gamma,h})_{\theta_x} = \theta_{xh,\Gamma}, \quad (v_{\Gamma,h})_{\theta_y} = \theta_{y_{h,\Gamma}}$$

The boundary stress resultant vector for the DK plate element at the edge Γ has three components

$$\boldsymbol{t}^e_\Gamma = [\overline{q}, \overline{m}_s, \overline{m}_n] \tag{8.2.5}$$

where q is the shear force along the edge defined in direction of z-axis, and m_n, m_s are the moments defined in the direction normal to the element side and along the element side, respectively. We choose to parameterize[2] them as

$$\begin{aligned} \overline{q}_\Gamma &= \overline{q}_{K,\Gamma} \\ \overline{m}_{s,\Gamma} &= \overline{m}_{sI,\Gamma}\varphi_1 + \overline{m}_{sJ,\Gamma}\varphi_2 \\ \overline{m}_{n,\Gamma} &= \overline{m}_{nI,\Gamma}\varphi_1 + \overline{m}_{nJ,\Gamma}\varphi_2 + \overline{m}_{nK,\Gamma}\varphi_3 \end{aligned} \tag{8.2.6}$$

With respect to the notation introduced in (5.4.41), we note that

$$\psi^I_k = \varphi_1 \quad \psi^J_k = \varphi_2 \quad \psi^K_k = \varphi_3 \tag{8.2.7}$$

and

$$p^I_q = 0 \qquad p^J_q = 0 \qquad p^K_q = \overline{q}_{K,\Gamma} \tag{8.2.8}$$

$$p^I_{m_s} = \overline{m}_{sI,\Gamma} \qquad p^J_{m_s} = \overline{m}_{sJ,\Gamma} \qquad p^K_{m_s} = 0 \tag{8.2.9}$$

$$p^I_{m_n} = \overline{m}_{nI,\Gamma} \qquad p^J_{m_n} = \overline{m}_{nJ,\Gamma} \qquad p^K_{m_n} = \overline{m}_{nK,\Gamma} \tag{8.2.10}$$

$$\tag{8.2.11}$$

To get the nodal parameters of (8.2.6) from (7.2.25) we have to evaluate integrals $M^{IJ}_{\Gamma,nm} = \int_\Gamma N^I_{m,n}\psi^J_m ds$, elements of block matrix $\mathbf{M}^{IJ}_\Gamma$

$$\mathbf{M}^{IJ}_\Gamma = \frac{L}{2}\int_{-1}^{+1} \begin{pmatrix} N^I_{w,\hat{w}}\psi^J_q & N^I_{\theta_s,\hat{w}}\psi^J_{m_s} & N^I_{\theta_n,\hat{w}}\psi^J_{m_n} \\ N^I_{w,\hat{\theta}_x}\psi^J_q & N^I_{\theta_s,\hat{\theta}_x}\psi^J_{m_s} & N^I_{\theta_n,\hat{\theta}_x}\psi^J_{m_n} \\ N^I_{w,\hat{\theta}_y}\psi^J_q & N^I_{\theta_s,\hat{\theta}_y}\psi^J_{m_s} & N^I_{\theta_n,\hat{\theta}_y}\psi^J_{m_n} \end{pmatrix} d\xi \tag{8.2.12}$$

where the following transformation was used:

$$\begin{aligned} N_{\theta_s,\cdot} &= -n_y N_{\theta_x,\cdot} + n_x N_{\theta_y,\cdot} \\ N_{\theta_n,\cdot} &= +n_x N_{\theta_x,\cdot} + n_y N_{\theta_y,\cdot} \end{aligned} \tag{8.2.13}$$

with $(\cdot)$ standing for $\hat{w}$, $\hat{\theta}_x$ and $\hat{\theta}_y$.

[2]The parametrization is arbitrary, however, the total number of free parameters must not exceed the number of components of input data $\boldsymbol{r}^e_{I,\Gamma}$

The boundary tractions projections $\mathbf{r}^e_{I,\Gamma} = [r^{\hat{w}}_{I,\Gamma}, r^{\hat{\theta}_x}_{I,\Gamma}, r^{\hat{\theta}_y}_{I,\Gamma}]$ are computed from the patch-wise local systems of equations (7.2.30). The parameters for (8.2.6) are computed form the inverse of the system (7.2.25). We obtain:

$$
\begin{aligned}
\overline{q}^K_\Gamma &= \frac{r^{\hat{w}}_{I,\Gamma} + r^{\hat{w}}_{J,\Gamma}}{L} \\
\overline{m}^I_{s,\Gamma} &= \frac{2n_y(+r^{\hat{\theta}_x}_{J,\Gamma} - 2r^{\hat{\theta}_x}_{I,\Gamma}) + 2n_x(+2r^{\hat{\theta}_y}_{I,\Gamma} - r^{\hat{\theta}_y}_{J,\Gamma})}{L} \\
\overline{m}^J_{s,\Gamma} &= \frac{2n_y(+r^{\hat{\theta}_x}_{I,\Gamma} - 2r^{\hat{\theta}_x}_{J,\Gamma}) + 2n_x(+2r^{\hat{\theta}_y}_{J,\Gamma} - r^{\hat{\theta}_y}_{I,\Gamma})}{L} \\
\overline{m}^I_{n,\Gamma} &= \frac{n_y(+33r^{\hat{\theta}_y}_{I,\Gamma} + 21r^{\hat{\theta}_y}_{J,\Gamma}) + n_x(+33r^{\hat{\theta}_x}_{I,\Gamma} + 21r^{\hat{\theta}_y}_{J,\Gamma})}{2L} - r^{\hat{w}}_{I,\Gamma} \\
\overline{m}^J_{n,\Gamma} &= \frac{n_y(+33r^{\hat{\theta}_y}_{J,\Gamma} + 21r^{\hat{\theta}_y}_{I,\Gamma}) + n_x(+33r^{\hat{\theta}_x}_{J,\Gamma} + 21r^{\hat{\theta}_y}_{I,\Gamma})}{2L} + r^{\hat{w}}_{I,\Gamma} \\
\overline{m}^K_{n,\Gamma} &= \frac{15(n_x(r^{\hat{\theta}_x}_{I,\Gamma} + r^{\hat{\theta}_x}_{J,\Gamma}) + n_y(r^{\hat{\theta}_y}_{I,\Gamma} + r^{\hat{\theta}_y}_{J,\Gamma}))}{L}
\end{aligned}
\tag{8.2.14}
$$

8.2.1 Regularization

To form the minimization function (7.2.28), the projections $\boldsymbol{r}^{e,0}_{I,\Gamma}$ are required. They are computed from the improved approximation of the boundary traction $\boldsymbol{t}^{e,0}_\Gamma = [\overline{q}^0, \overline{m}^0_s, \overline{m}^0_n]$. If the improved boundary tractions are expressed in the form (7.2.22), the projections are computed using the equation (7.2.25).

The boundary traction approximation $\boldsymbol{t}^{e,0}_\Gamma$ is computed from the current finite element solution using the following technique: edge boundary traction $\boldsymbol{t}^0_\Gamma$ is taken as an average of the boundary tractions $\boldsymbol{t}^{e,0}_\Gamma$ and $\boldsymbol{t}^{e',0}_\Gamma$ computed from the stress resultants of the two elements e and e' adjacent to the edge Γ:

$$
\boldsymbol{t}^0_\Gamma = (\boldsymbol{t}^{e,0}_\Gamma - \boldsymbol{t}^{e',0}_\Gamma)/2 \tag{8.2.15}
$$

Boundary tractions $\boldsymbol{t}^{e,0}_\Gamma$ are evaluated at side Γ from element stress resultants from the Cauchy principle. First, the stress resultants at the integration points $\boldsymbol{m}_h(\boldsymbol{\xi}_{gp}) = \mathbf{C}_B\boldsymbol{\kappa}_h(\boldsymbol{\xi}_{gp})$ are evaluated. A linear interpolation of the stress resultants

$$
\boldsymbol{m}^0 = \sum_I \boldsymbol{m}^0_I N_I \tag{8.2.16}
$$

is constructed using the least squares fit to $\boldsymbol{m}_h(\boldsymbol{\xi}_{gp})$. At the element side Γ, defined by

unit exterior normal $\boldsymbol{n} = [n_x, n_y]^T$, we thus have:

$$m_n^0 = (m_{yy}^0 - m_{xx}^0)\, n_x n_y + m_{xy}^0 (n_x^2 - n_y^2) \qquad (8.2.17)$$
$$m_s^0 = (m_{xx}^0 n_x^2 + m_{yy}^0 n_y^2 + 2 m_{xy}^0 n_x n_y)$$

The shear component normal to the edge is obtained from

$$q^0 = q_x^0 n_x + q_y^0 n_y$$

where the components q_x^0, q_y^0 are computed from equilibrium equations:

$$q_x^0 = -(\frac{\partial m_{xx}^0}{\partial x} + \frac{\partial m_{xy}^0}{\partial y}); \quad q_y^0 = -(\frac{\partial m_{yy}^0}{\partial y} + \frac{\partial m_{xy}^0}{\partial x}) \qquad (8.2.18)$$

The effective shear q_{ef}^0 however is computed from $q_{ef}^0 = q^0 - \frac{\partial m_n^0}{\partial s}$ and the derivative $\frac{\partial m_n^0}{\partial s}$ is evaluated from (8.2.17) using the interpolation (8.2.16).

Model error indicator for the DK plate elements is obtained by comparing its results with the ones obtained by an element based on more refined plate model RM. As shown above, the later results can be obtained by element-wise computation with the DK boundary stress resultants applied as external edge loading. Thus, a Neumann-type problem has to be solved for each element of the mesh.

8.2.2 The local problems with RM plate element

The local problems are written as

$$\mathbf{K}_2^e \hat{\boldsymbol{u}}_2^e = \mathbf{F}_2^{ext,e} + \boldsymbol{R}_2^e \qquad (8.2.19)$$

where $\mathbf{K}_2^e$ is the RM element stiffness matrix, $\mathbf{F}_2^{ext,e}$ is the external load vector contributed to surface load and $\boldsymbol{R}_2^e$ are the element nodal residuals due to external edge load. The external load vector $\boldsymbol{R}_2^e = [\boldsymbol{R}_{2,I}^e, \cdots, \boldsymbol{R}_{2,IJ}^e, \cdots]^T$ corresponding to the external edge loading is computed from

$$\sum_I \boldsymbol{R}_{2,I}^e \cdot \hat{\boldsymbol{v}}_{2,I}^e + \sum_{IJ} \boldsymbol{R}_{2,IJ}^e \cdot \hat{\boldsymbol{v}}_{2,IJ}^e = \int_{\Gamma^e} \boldsymbol{t}_{\Gamma^e}^e \cdot \boldsymbol{v}_{2,\Gamma^e,h}\, \mathrm{d}s = \sum_{\Gamma_{IJ}} \int_{\Gamma_{IJ}} \boldsymbol{t}_{\Gamma_{IJ}}^e \cdot \boldsymbol{v}_{2,\Gamma_{IJ},h} \mathrm{d}s \qquad (8.2.20)$$

where $\hat{\boldsymbol{v}}_2^e = [\hat{\boldsymbol{v}}_{2,I}^e, \cdots, \hat{\boldsymbol{v}}_{2,IJ}^e, \cdots]^T$. The element edge load $\boldsymbol{t}_{2,\Gamma_{IJ}}^e = [\overline{q}_{\Gamma_{IJ}}, \overline{m}_{s,\Gamma_{IJ}}, \overline{m}_{n,\Gamma_{IJ}}]^T$ is defined by (8.2.14) and (8.2.6). We have

$$\int_{\Gamma^e} \boldsymbol{t}_{2,\Gamma_{IJ}}^e \cdot \boldsymbol{v}_{2,\Gamma_{IJ},h}^e\, \mathrm{d}s = \int_{\Gamma^e} (q v_h^{RM} + m_s \vartheta_{s,h}^{RM} + m_n \vartheta_{n,h}^{RM})\, \mathrm{d}s \qquad (8.2.21)$$

where the virtual displacements $\boldsymbol{v}^e_{2,h} = [v^{RM}_h, \vartheta^{RM}_{s,h}, \vartheta^{RM}_{n,h}]^T$ are those of RM element.

The interpolation of the RM plate elements is an hierarchic extension of the interpolation of the DK element:

$$v^{RM}_h = v^{DK}_h - \sum_{IJ} \frac{L}{4}\hat{\gamma}_{IJ} M_{IJ}$$
$$\boldsymbol{\vartheta}^{RM}_h = \boldsymbol{\vartheta}^{DK}_h + \sum_{IJ} \frac{3}{2}\boldsymbol{n}_{IJ}\hat{\gamma}_{IJ} N_{IJ}$$

With respect to the DK plate elements, RM plate elements have an additional degree of freedom $\hat{\boldsymbol{v}}^e_{2,IJ} = [\hat{\gamma}_{IJ}]$ on the midside of the element edges ($\boldsymbol{R}^e_{2,IJ} = [R^e_{2,IJ}]$). The nodal degrees of freedom are the same for both elements $\hat{\boldsymbol{v}}^e_{2,I} = \hat{\boldsymbol{v}}^e_{1,I}$.

On the edge Γ_{IJ} we have:

$$v^{RM}_{\Gamma_{IJ},h} = v^{DK}_{\Gamma_{IJ},h} - \frac{1}{2}L_{IJ}\hat{\gamma}_{IJ}\varphi_4; \quad \vartheta^{RM}_{s,\Gamma_{IJ},h} = \vartheta^{DK}_{s,\Gamma_{IJ},h}; \quad \vartheta^{RM}_{n,\Gamma_{IJ},h} = \vartheta^{DK}_{n,\Gamma_{IJ},h} - 3\hat{\gamma}_{IJ}\varphi_3$$

which leads to:

$$\sum_{\Gamma_{IJ}} \int_{\Gamma_{IJ}} (\overline{q} v^{RM}_h + \overline{m}_s \vartheta^{RM}_{s,h} + \overline{m}_n \vartheta^{RM}_{n,h}) \mathrm{d}s = \tag{8.2.22}$$
$$\sum_{\Gamma_{IJ}} \int_{\Gamma_{IJ}} (\overline{q} v^{DK}_h + \overline{m}_s \vartheta^{DK}_{s,h} + \overline{m}_n \vartheta^{DK}_{n,h}) \mathrm{d}s - \sum_{\Gamma_{IJ}} \hat{\gamma}_{IJ} \int_{\Gamma_{IJ}} \left(\frac{L_{IJ}}{2}\overline{q}\,\varphi_4 + 3\overline{m}_n\,\varphi_3 \right) \mathrm{d}s$$

Since

$$\sum_{\Gamma_{IJ}} \int_{\Gamma_{IJ}} (\overline{q} v^{DK}_h + \overline{m}_s \vartheta^{DK}_{s,h} + \overline{m}_n \vartheta^{DK}_{n,h}) \mathrm{d}s = \sum_I \boldsymbol{R}^e_{1,I} \hat{\boldsymbol{v}}^e_{1,I} \tag{8.2.23}$$

we realize from (8.2.22), that the following holds:

$$\boldsymbol{R}^e_{2,I} = \boldsymbol{R}^e_{1,I}; \tag{8.2.24}$$
$$R^e_{2,IJ} = \int_{\Gamma^e} \left(\frac{L_{IJ}}{2} q\,\varphi_4 + 3 m_n\,\varphi_3 \right) \mathrm{d}s$$

The element nodal residuals of the RM element are the same as those of DK element, except for the element residuals corresponding to the midside degrees of freedom. The equilibration procedure does not influence the element nodal residuals $\boldsymbol{R}^e_{2,I}$. However, the equilibration is still necessary, since it determines the edge loading q and m_n, which define the load vector $R^e_{2,IJ}$ through (8.2.24). By taking the values for q and m_n from (8.2.14) and (8.2.6) we have

$$R^e_{2,IJ} = \frac{L_{IJ}}{2}(r^q_{J,\Gamma_{IJ}} - r^q_{I,\Gamma_{IJ}}) \tag{8.2.25}$$

8.2.3 Computation of the model error indicator

Having defined the stress resultants for the RM, the RM deformation energy can be calculated, by taking into account the corresponding bending and shear deformations

$$\begin{aligned} E^{RM,e} &= \int_{\Omega}^{e} \boldsymbol{m}^{RM,T}\, \mathbf{C}_B{}^{-1} \boldsymbol{m}^{RM}\, d\Omega + \int_{\Omega}^{e} \boldsymbol{q}^{RM,T}\, \mathbf{C}_S{}^{-1} \boldsymbol{q}^{RM}\, d\Omega \\ &= E_B^{RM,e} + E_S^{RM,e} \end{aligned} \tag{8.2.26}$$

where $\boldsymbol{m}^{RM} = [m_{xx}, m_{yy}, m_{xy}]^T$ and $\boldsymbol{q}^{RM} = [q_x, q_y]^T$.

Since DK and RM plate elements predict very similar values for moments and the DK assumes zero shear strains, the shear deformation energy $E_S^{RM,e}$ of RM can be used to determine how well the DK plate model performs in a given situation. If shear strain contribution is low enough, the DK could be considered as a sufficiently good model, otherwise it should be replaced by a more suitable element based on Reissner/Mindlin model (i.e. by the RM plate element). A fairly reasonable choice for a model error indicator η_e^M we use herein is therefore the ratio of the energy norm of the shear difference between the RM and the DK element to the total energy of the RM element. Due to the zero shear strain assumption in the DK, and similar prediction for moments of both elements, one can define the model error indicator as

$$\eta_e^M = E_S^{RM,e} / E^{RM,e} \tag{8.2.27}$$

This indicator is used below in all numerical examples.

8.2.4 Numerical examples

We present in this section results of numerical examples, which were chosen to illustrate performance of the proposed approach to adaptive modeling of plates. The departure point for the present model adaptivity procedure should be an optimally adapted FE mesh, with the discretization error uniformly distributed and placed within a predefined limit. We note that the plate elements in such an automatically generated mesh of quadrilaterals, which takes into account predefined element size distribution, can be quite distorted. For this reason we also present examples where the influence of mesh distortion on the chosen model error indicator is studied.

Simply supported square plate

Problem of simply supported (SSSS) square plate under uniform loading is used to test the sensitivity of model error indicator on mesh distortion; as well as to compare those

effects for thin and thick plate situations. The material is linear elastic and isotropic, with Young's modulus $E = 10.92$ and Poisson's ratio $\nu = 0.3$. The side length is $a = 10$. Two values for the plate thickness $t = 0.1$ (thin) and $t = 1$ (thick) are selected. Due to the symmetry, only one quarter of the plate (the lower left one) is chosen for the numerical analysis.

The model error indicator (8.2.27) is computed for each DKQ element of the mesh. This value is then compared with the corresponding analytical (reference) value, which can be for this simple problem obtained by using analytical (series) solution for Mindlin plates, see e.g. [Lee et al., 2002], [Brank, 2008]. In Figure 8.2.1, we show the comparison of two structured (regular) meshes with the same number of elements for the case of thick plate. The meshes differ in discretization error, which is lower for the second mesh that is more refined towards the outer edges. It can be observed that the computed model error indicator is very close to the reference one, except for the corner element. This is due to the fact that the equilibration is not possible to carry out at the corner node. We thus obtain as a consequence that the estimated boundary stress resultants for the corner element are not as good as for the inner elements.

To estimate the effect of mesh distortion, the model error indicator (8.2.27) is computed (for the case of thick plate) with two distorted meshes. The first mesh is obtained by adaptive mesh refinement with 5% tolerance in discretization error. The second one is derived from the mesh shown in Figure 8.2.1 by a parametrical displacement of the nodes. The results are presented in Figure 8.2.2. Again, comparison is made with the analytical (reference) solution. We note that the performance of model error indicator is slightly better for parametrical distortion of the mesh. One may conclude from the results shown in Figure 8.2.2 that the model error indicator is slightly (but not severely) influenced by mesh distortion.

We repeat the above mentioned comparison also for the case of thin plate. The result are shown in Figure 8.2.3 and 8.2.4 (notice the change of scale). The model error indicator shows that the DKQ is sufficiently good (almost) for the whole mesh. Comparison with the analytical solution shows that the sensitivity of model error indicator is of the same range as in the case of thick plate.

Square plate with two simply supported and two free edges

The second problem we study is a square plate with two opposite edges simply supported and two other edges free (SFSF). It has been chosen to test the ability of the proposed

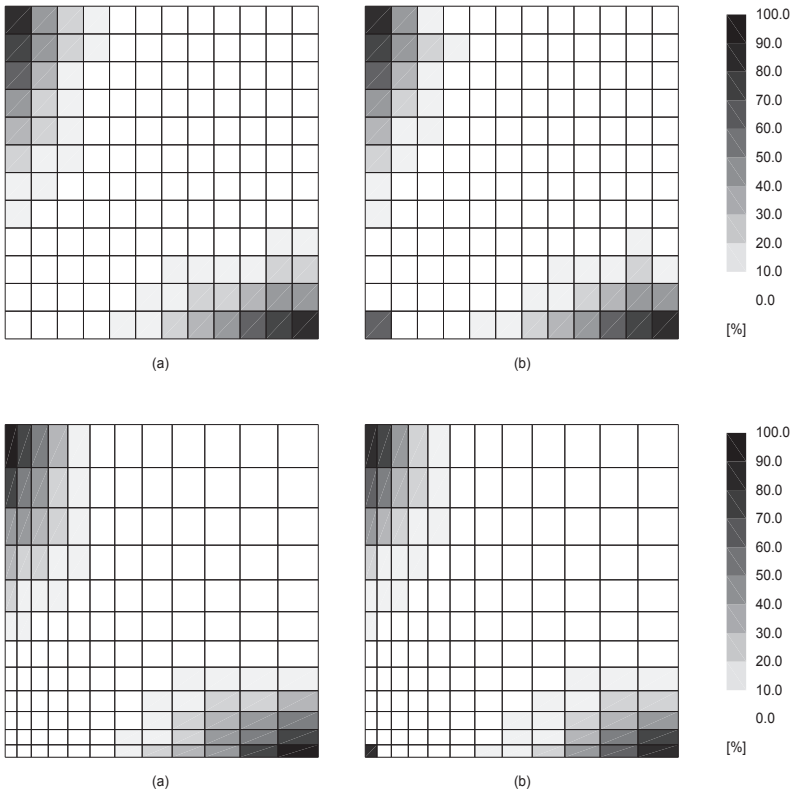

Figure 8.2.1: Reference value of model error indicator (a) and its estimated value (b) for thick SSSS plate for rectangular meshes
Slika 8.2.1: Referenčna vrednost modelske napake (a) ter njena ocena (b) za srednje debelo SSSS ploščo s pravokotno mrežo

procedure to detect boundary layer effect, which is most prominent along the free edges, see [Arnold Falk, 1989]. The width of the boundary layer is proportional to the thickness of the plate, and it is most pronounced for the transverse shear component, which varies as $1/t$. The geometry and material parameters are the same as in the first example. Due to the symmetry, only one quarter of the plate (the lower left one) is used in the analysis; the boundary conditions are imposed as follows: the left edge in simply supported, the lower one is free, and the right and the upper ones take into account symmetry.

Since the boundary layer effect is intrinsic to the Reissner/Mindlin theory, the DKQ can not detect it. In the present procedure the equilibrated boundary stress resultants are derived from the DKQ solution and subsequently applied to the P3Q in order to evaluate model error indicator. It is therefore interesting to see weather this procedure can effectively detect the boundary layer. The result shown in Figure 8.2.5 indicates that the procedure is able to detect a region with increased shear deformation energy (along

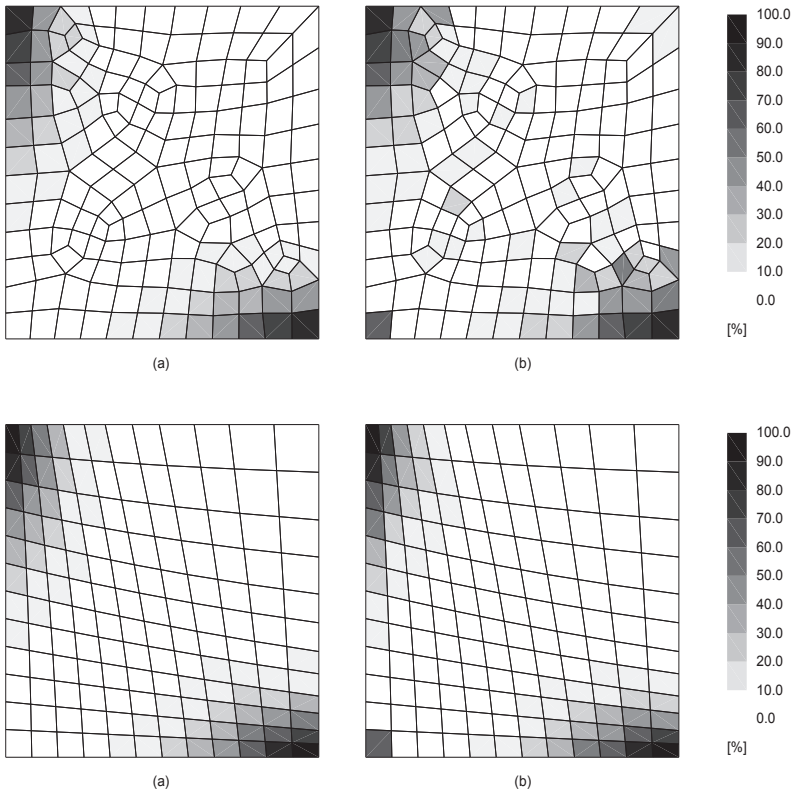

Figure 8.2.2: Reference value of model error indicator (a) and its estimated value (b) for thick SSSS plate for distorted meshes
Slika 8.2.2: Referenčna vrednost modelske napake (a) ter njena ocena (b) za srednje debelo SSSS ploščo z deformirano mrežo

the left edge) but is not very successful to detect the boundary layer (along the lower free edge), which is clearly observable in the reference (analytical) solution. Comparison with the analytical solution shows (see Figures 8.2.5, 8.2.6, 8.2.7 and 8.2.8) that the sensitivity of model error indicator is of the same range as in the case of SSSS plate.

Adaptive analysis of L-shaped plate

Adaptive model analysis of an L-shaped plate under uniform unit pressure is considered in this example. Long sides ($a = 10$) of the plate are clamped, all other sides ($b = 5$) are free. The plate is made of linear elastic isotropic material, with Young's modulus $E = 10.92$ and Poisson's ratio $\nu = 0.3$. Thickness of the plate is equal to 1. Non distorted mesh was chosen for this example in order to avoid effect of element distortion on model error indicator.

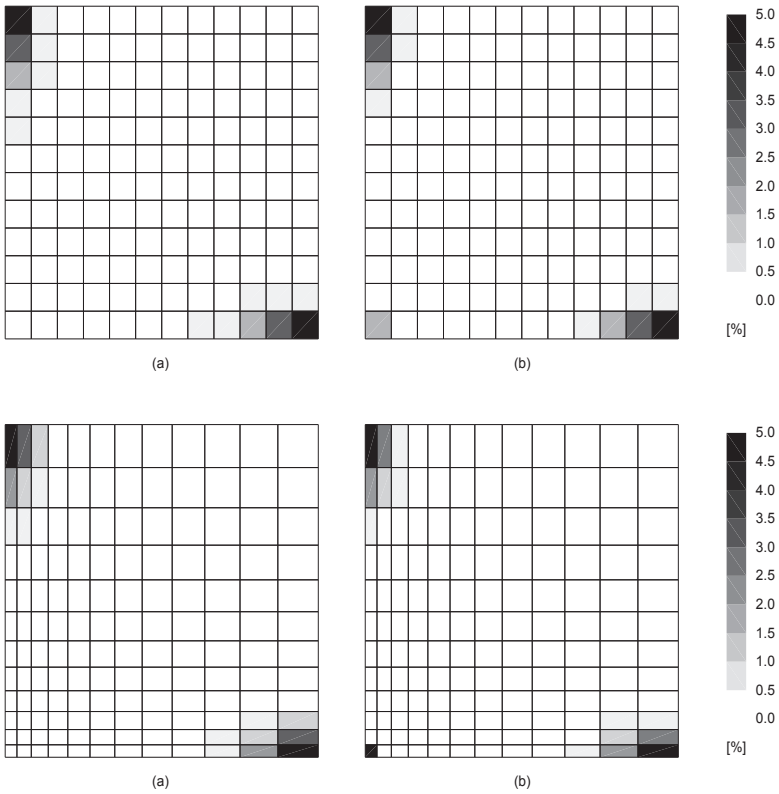

Figure 8.2.3: Reference value of model error indicator (a) and its estimated value (b) for thin SSSS plate for rectangular meshes
Slika 8.2.3: Referenčna vrednost modelske napake (a) ter njena ocena (b) za tanko SSSS ploščo s pravokotno mrežo

The computation started with the analysis of the plate by using DKQ elements. The model error indicator (8.2.27) was further computed and the result is shown in Figure 8.2.9. The indicator identified several regions where the model error was high. The limit of 15% model error was chosen to determine the elements of the mesh, where the P3Q should be used instead of the DKQ. Those elements are colored dark grey in Figures 8.2.10-8.2.12 (b). Finally, the computation with both the DKQ (light grey in Figures 8.2.10-8.2.12 (b)) and the P3Q elements (dark grey in Figures 8.2.10-8.2.12 (b)), used at different regions of the plate, was performed. Kinematic coupling of elements based on different models was considered, i.e. the hierarchic rotation $\Delta\theta$ of the P3Q was restrained on edges where the P3Q elements were adjacent to the DKQ elements in order to account for zero transverse shear modelling along those edges.

The comparison of stress resultants evaluated with the DKQ elements (Figures 8.2.10-8.2.12 (a)), with the P3Q elements (Figures 8.2.10-8.2.12 (c)) and with both the DKQ

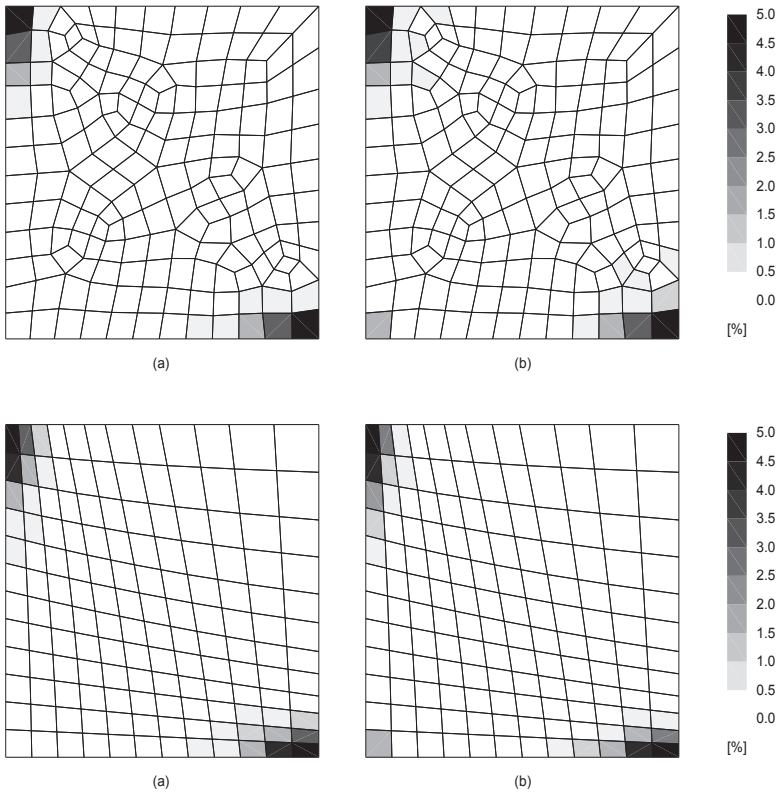

Figure 8.2.4: Reference value of model error indicator (a) and its estimated value (b) for thin SSSS plate for distorted meshes
Slika 8.2.4: Referenčna vrednost modelske napake (a) ter njena ocena (b) za tanko SSSS ploščo z deformirano mrežo

and the P3Q elements (Figures 8.2.10-8.2.12 (d)) is shown. It can be seen that the P3Q based computation and the mixed DKQ-P3Q based computation produce almost identical results; on the other hand, the results are not equal to those obtained by using only DKQ elements. Therefore, the comparison of these different results (and especially close agreement between the DKQ-P3Q and the P3Q computations), clearly indicates that the adaptive procedure of this kind performs successfully. One can hope for the same trend when applying the same procedure to higher order plate models, where a significant computational savings could also be obtained in the process.

Adaptive analysis of Morley's skew plate

Adaptive model analysis of Morley's 30° skew plate (see [Morley, 1963]) with thickness $t = 1$, side length $a = 10$, simple supports on all sides, and unit uniform pressure is performed

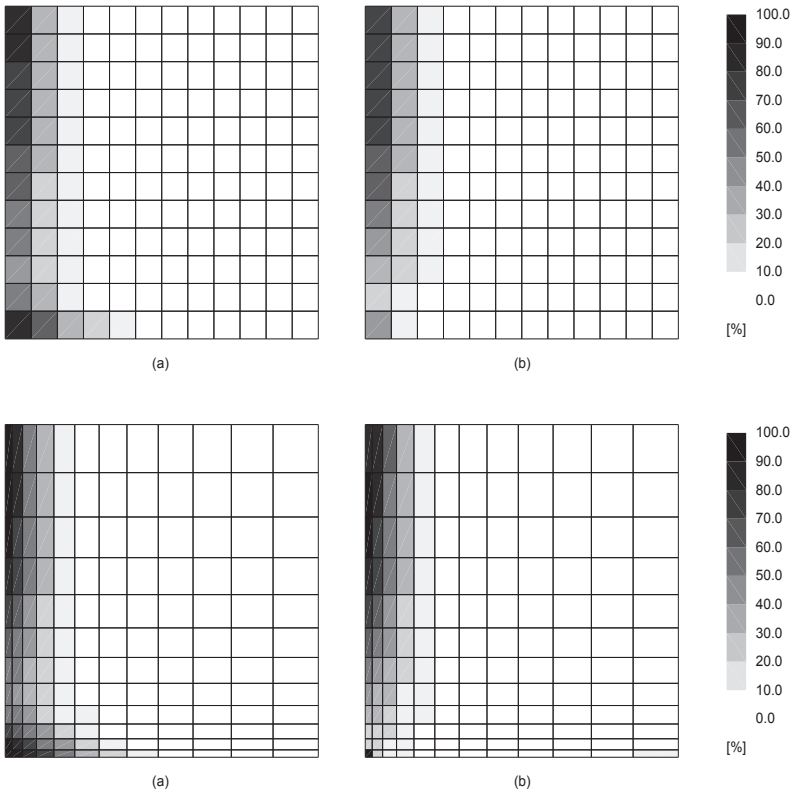

Figure 8.2.5: Reference value of model error indicator (a) and its estimated value (b) for thick SFSF plate for rectangular meshes
Slika 8.2.5: Referenčna vrednost modelske napake (a) ter njena ocena (b) za debelo SFSF ploščo s pravokotno mrežo

in this example. The plate is built of linear elastic isotropic material, with Young's modulus $E = 10.92$ and Poisson's ratio $\nu = 0.3$. The most interesting feature of the solution to this problem concerns two singular points at the two obtuse corners of the plate, which strongly influence the quality of the computed results (e.g. see [Ibrahimbegović, 1993]). The chosen FE mesh is made more dense near the sides of the plate where singularities are expected.

The computation started with the analysis by using DKQ elements. The model error indicator (8.2.27) was further computed, see Figure 8.2.13. It can be seen from Figure 8.2.13 that the error was increased near the sides and in the vicinity of the obtuse corners. Again, the limit of 15% model error was chosen to determine the elements of the mesh, where the P3Q should be used instead of the DKQ; all such elements are colored dark grey in (b) part of Figures 8.2.14 and 8.2.15. Finally, the computation with both the DKQ (light grey in Figures 8.2.14(b) and 8.2.15(b)) and the P3Q elements (dark grey

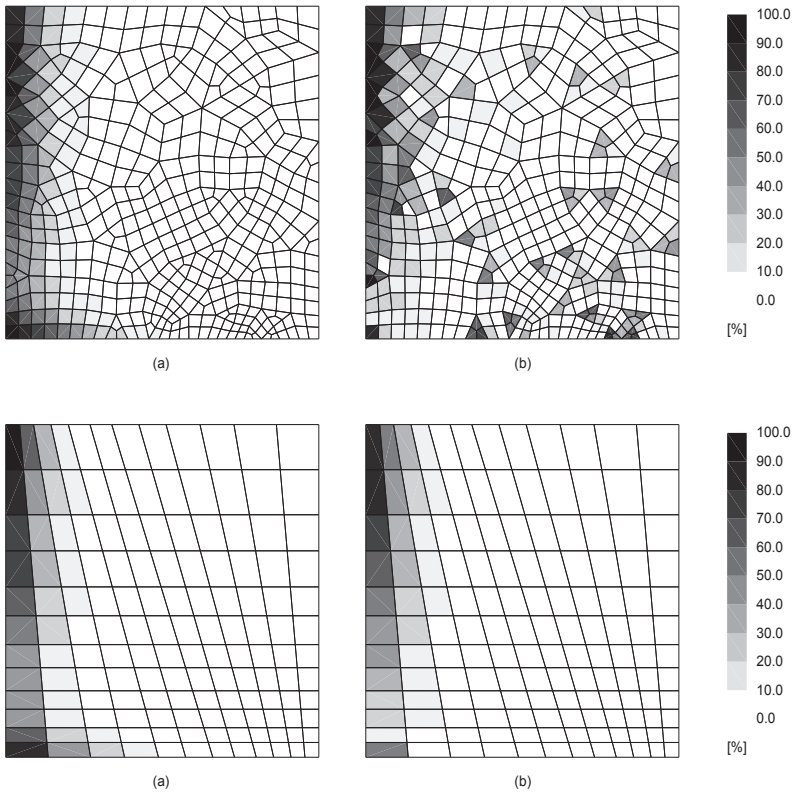

Figure 8.2.6: Reference value of model error indicator (a) and its estimated value (b) for thick SFSF plate for distorted meshes
Slika 8.2.6: Referenčna vrednost modelske napake (a) ter njena ocena (b) za debelo SFSF ploščo z deformirano mrežo

in Figures 8.2.14-8.2.15 (b)), used at different regions of the plate, was performed.

It can be seen in Figure 8.2.14 that in this case the difference in results for moments between all three computational models is negligible. The difference however still shows in the results for the shear force, which are presented in Figure 8.2.16.

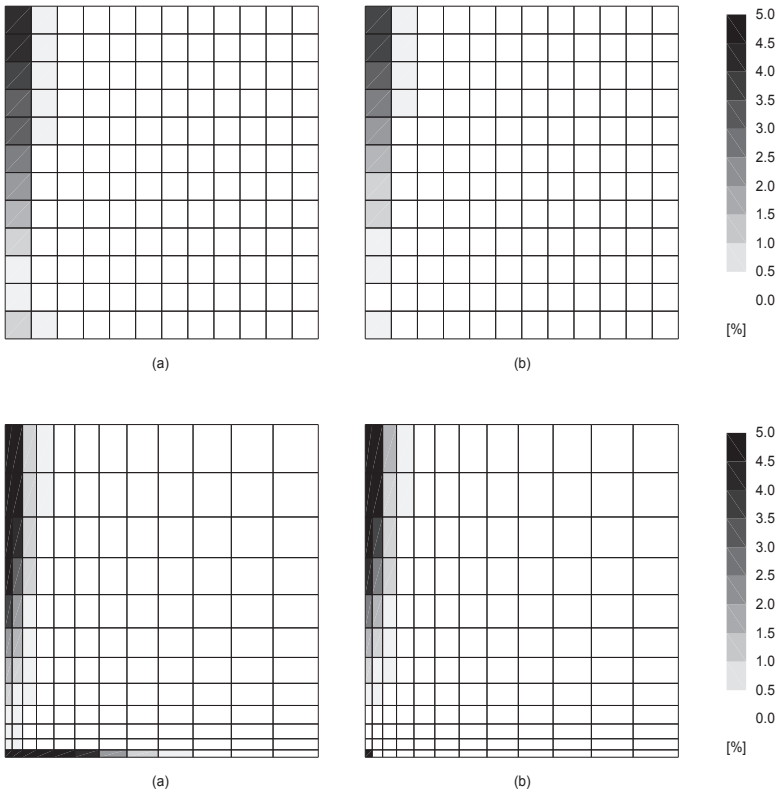

Figure 8.2.7: Reference value of model error indicator (a) and its estimated value (b) for thin SFSF plate for rectangular meshes
Slika 8.2.7: Referenčna vrednost modelske napake (a) ter njena ocena (b) za tanko SFSF ploščo s pravokotno mrežo

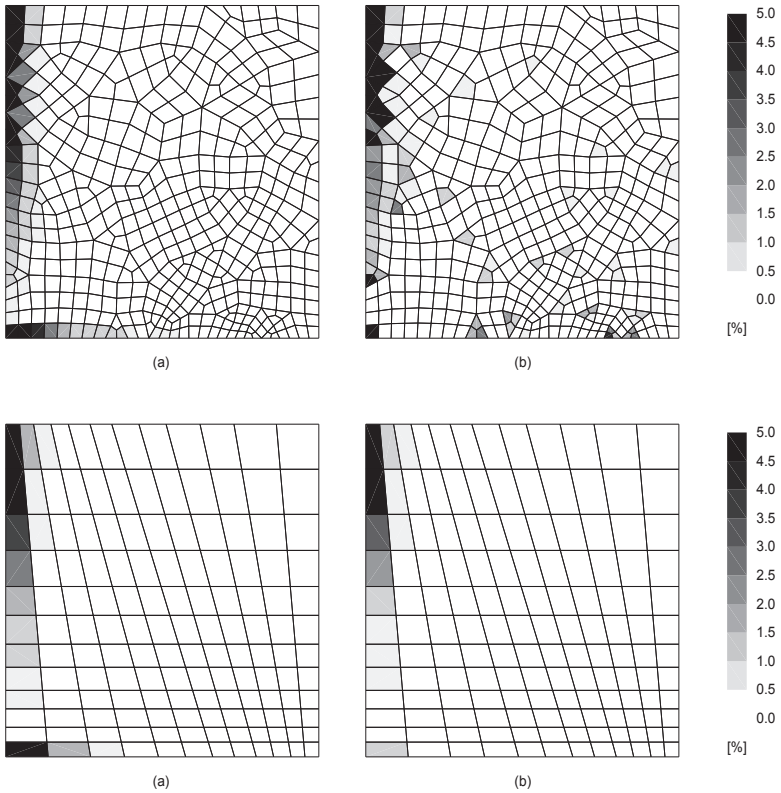

Figure 8.2.8: Reference value of model error indicator (a) and its estimated value (b) for thin SFSF plate for distorted meshes
Slika 8.2.8: Referenčna vrednost modelske napake (a) ter njena ocena (b) za tanko SFSF ploščo z deformirano mrežo

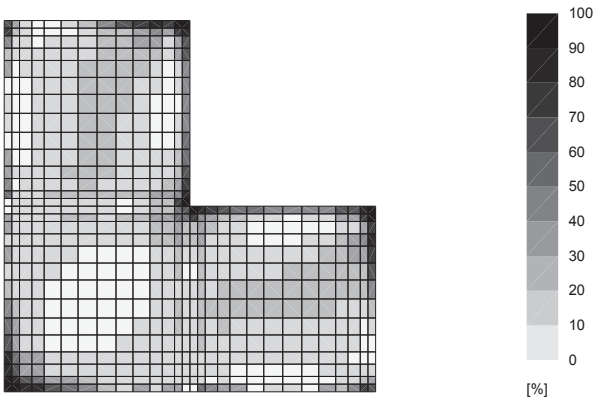

Figure 8.2.9: Model error indicator for LSHP problem
Slika 8.2.9: Ocena modelske napake za primer LSHP

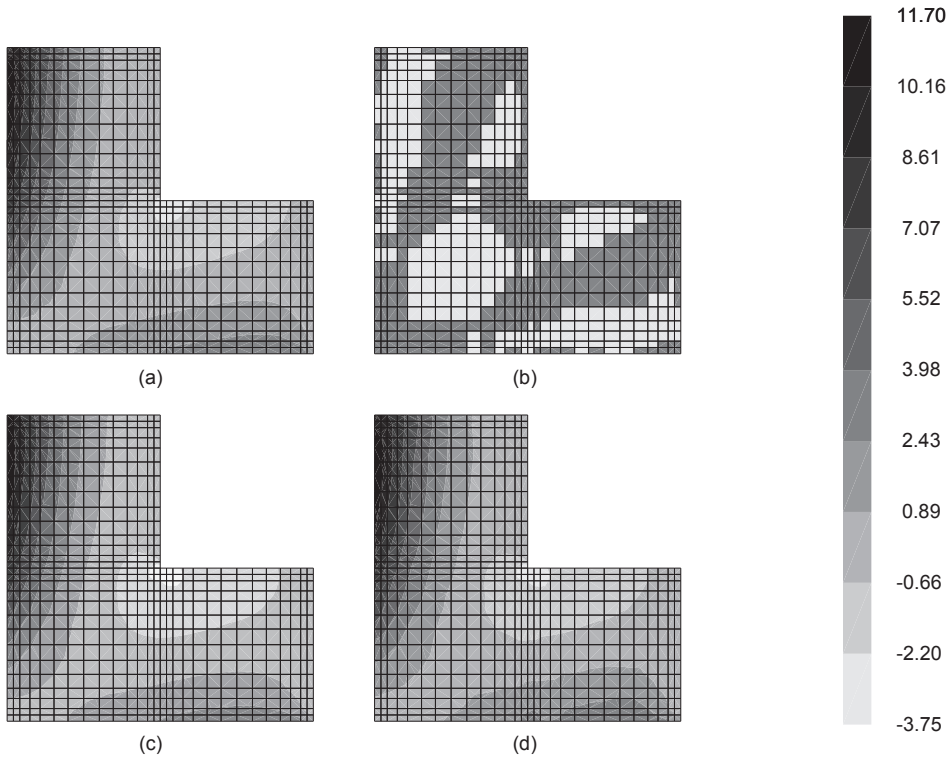

Figure 8.2.10: Stress resultant m_{xx} (a) DKQ, (c) P3Q and (d) DKQ-P3Q model. The modelisation of (d) is presented in (b), where dark areas represent P3Q and light ones DKQ model.
Slika 8.2.10: Rezultante napetosti m_{xx} (a) DKQ, (c) P3Q in (d) DKQ-P3Q model. Mešan model (d) je predstavljen v (b), kjer temnejša področja prikazujejo P3Q in svetlejša DKQ model.

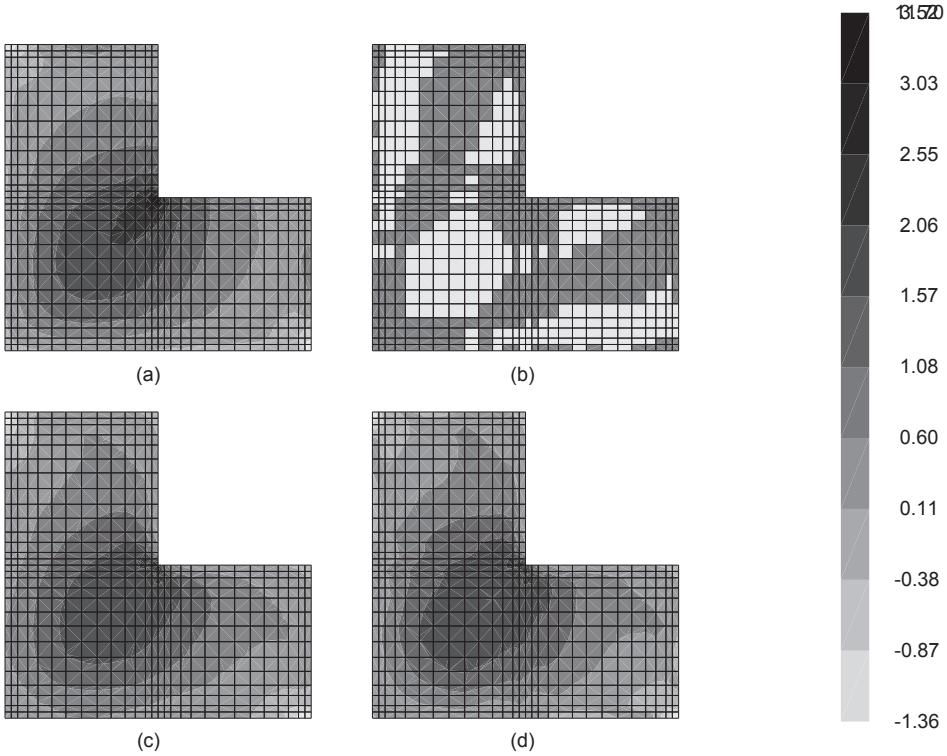

Figure 8.2.11: Stress resultant m_{xy} (a) DKQ, (c) P3Q and (d) DKQ-P3Q model. The modelisation of (d) is presented in (b), where dark areas represent P3Q and light ones DKQ model.
Slika 8.2.11: Rezultante napetosti m_{xy} (a) DKQ, (c) P3Q in (d) DKQ-P3Q model. Mešan model (d) je predstavljen v (b), kjer temnejša področja prikazujejo P3Q in svetlejša DKQ model.

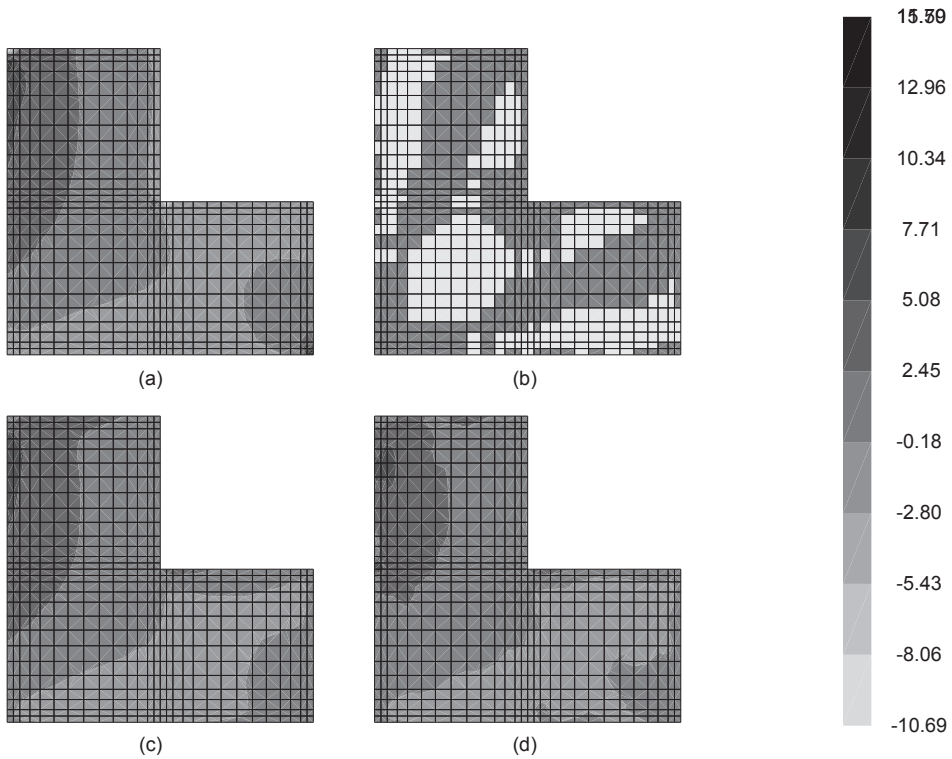

Figure 8.2.12: Stress resultant q_x (a) DKQ, (c) P3Q and (d) DKQ-P3Q model. The modelisation of (d) is presented in (b), where dark areas represent P3Q and light ones DKQ model.
Slika 8.2.12: Rezultante napetosti q_x (a) DKQ, (c) P3Q in (d) DKQ-P3Q model. Mešan model (d) je predstavljen v (b), kjer temnejša področja prikazujejo P3Q in svetlejša DKQ model.

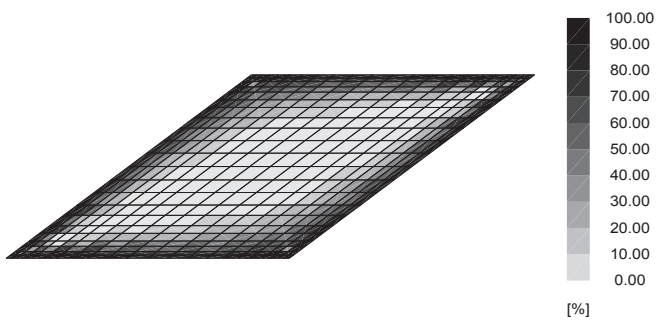

Figure 8.2.13: Model error indicator for SKEW problem
Slika 8.2.13: Ocena modelske napake za primer SKEW

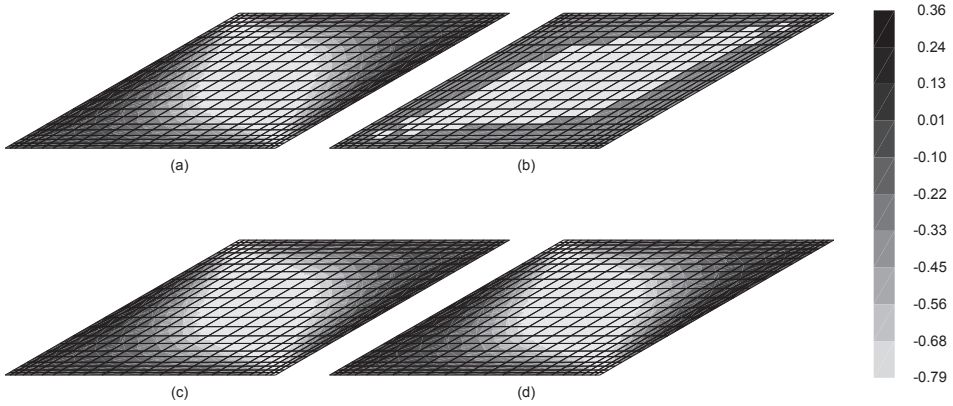

Figure 8.2.14: Stress resultant m_{xx} computed with: (a) DKQ, (c) P3Q and (d) DKQ-P3Q model. The modelisation of (d) is presented in (b), where dark areas represent P3Q and light ones DKQ model.
Slika 8.2.14: Rezultante napetosti m_{xx} (a) DKQ, (c) P3Q in (d) DKQ-P3Q model. Mešan model (d) je predstavljen v (b), kjer temnejša področja prikazujejo P3Q in svetlejša DKQ model.

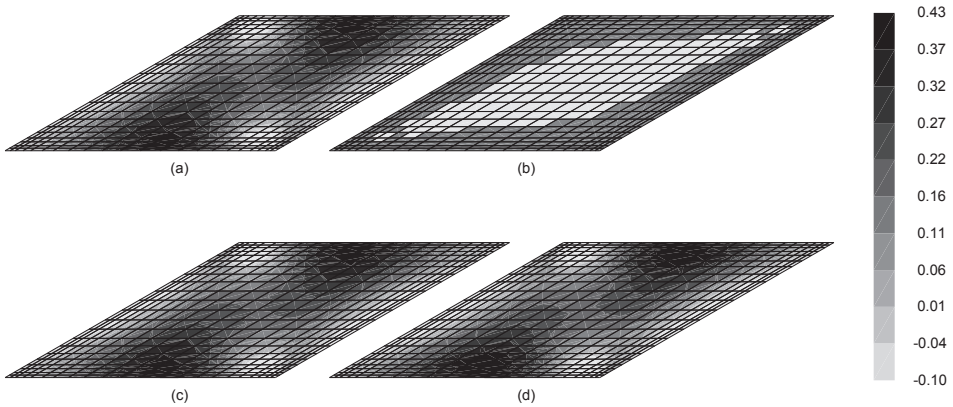

Figure 8.2.15: Stress resultant m_{xy} computed with: (a) DKQ, (c) P3Q and (d) DKQ-P3Q model. The modelisation of (d) is presented in (b), where dark areas represent P3Q and light ones DKQ model.
Slika 8.2.15: Rezultante napetosti m_{xy} (a) DKQ, (c) P3Q in (d) DKQ-P3Q model. Mešan model (d) je predstavljen v (b), kjer temnejša področja prikazujejo P3Q in svetlejša DKQ model.

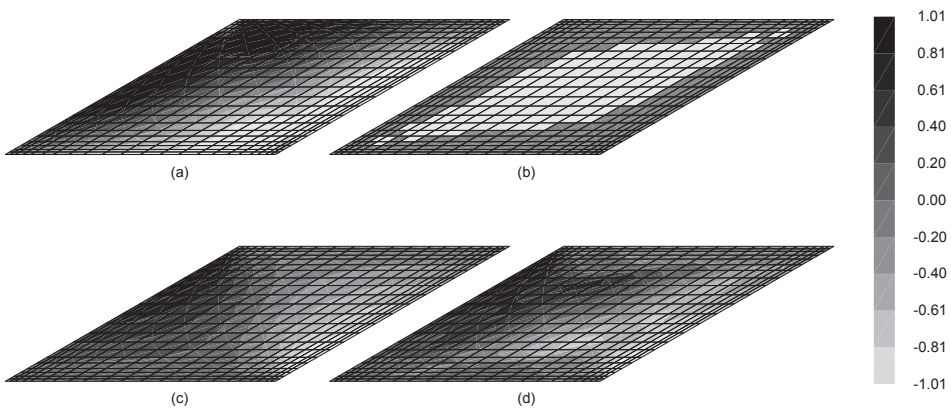

Figure 8.2.16: Stress resultant q_x computed with: (a) DKQ, (c) P3Q and (d) DKQ-P3Q model. The modelisation of (d) is presented in (b), where dark areas represent P3Q and light ones DKQ model.
Slika 8.2.16: Rezultante napetosti q_x (a) DKQ, (c) P3Q in (d) DKQ-P3Q model. Mešan model (d) je predstavljen v (b), kjer temnejša področja prikazujejo P3Q in svetlejša DKQ model.

8.3 Chapter summary and conclusions

We have presented a detailed development for plate model adaptivity procedure capable of selecting automatically the best suitable plate finite element between the two plate models, the first for thin Kirchhoff plate and the second for thick Reissner/Mindlin plate. The model adaptivity computation is carried out on the element basis, and it starts with the finite element mesh which is first passed through the standard mesh adaptivity procedure in order to achieve the acceptable discretization errors throughout the mesh. We addressed in detail the particular case of two low-order plate finite element models, represented with discrete Kirchhoff quadrilateral (DKQ) and Reissner/Mindlin quadrilateral (P3Q); but the same procedure would carry over to higher-order plate models that capture more accurately local 3D effects.

It is the key advantage of the presented approach to plate model adaptivity to remain uncoupled with respect to the mesh adaptivity procedure employed to reduce the discretization error, and thus can be combined with any already available mesh adaptivity procedure to ensure the optimal overall accuracy. This advantage stems from the proposed special choice of the finite element interpolations for both P3Q and DKQ plate elements, which results with the same quality of the discrete approximation for bending moments.

Numerical examples illustrate clearly that the proposed procedure is capable of capturing any significant contribution of shear deformations. The case in point concerns the shear layers which typically occur for different kinds of boundary conditions.

Chapter 9

Conclusions

The thesis is related to adaptive modeling of plates. Although the finite element modeling of plates reached a mature phase, the reflection shows that the fundamental questions of accuracy and reliability are still open and need to be properly addressed.

Before addressing the subject of adaptive modeling, two basic and one new plate theories are first studied in detail in chapters 2-4. The phenomena intrinsic to the plate modeling are identified and studied. The corresponding finite element formulation are presented in a way which respects the natural hierarchy present in modeling of plate structures. A Discrete Kirchhoff element, which is one of the most popular elements for the analysis of thin plates, was reformulated using an alternative notation, which enables general treatment of triangular and quadrilateral formulations. Moreover, the presented formulation for the DK elements enables the hierarchic (in a model sense) construction of the finite elements based on Reissner/Mindlin theory. The elements, denoted P3, are constructed as the hierarchic extension of the DK elements. The elements built on the higher-order theory including through-the-thickness stretch are further built on the basis of P3 elements. This type of hierarchic construction helps to maintain the physical insight despite the increasing complexity of the finite element formulation.

Additionally, conforming triangular plate element for thin plates is presented as well as incompatible modes finite elements for Reissner/Mindlin plates. All presented plate elements were implemented in finite element analysis computer codes and tested. Systematic comparison of the element performance through a series of numerical tests is performed. This comparison in itself presents a valuable contribution to the subject of finite element modeling of plate structures.

The research on discretization error estimates for finite element computation is active and today many results are available regarding the general treatment of the subject. In

this work some of the results are applied to the case of finite element modeling of plate structures. When using dimensionally reduced models, specific numeric issues (locking) appear. Phenomena intrinsic to plates require deeper understanding of the subject of error estimates. The application of the existing error estimation methods to the plate elements is thus not straightforward. A large part of the research work presented in thesis is related to the successful implementation of the equilibrated residual method (EqR) for the DK plate element. The implementation of the EqR method is challenging, among other things, mostly from the technical point of view. The computation process involves several steps: (i) computation of equilibrated boundary traction from the original finite element solution, (ii) setup of local element problems loaded with boundary tractions, (iii) solution of local problems with enhanced interpolation space and (iv) computation of the discretization error estimate from the local solution.

Several variations of the EqR method were implemented: the local computations were performed with various enhanced interpolations. Enhancing the interpolation space with the subdivision of existing element proved to be an efficient alternative to the more involved computation using the conforming element. This type of study has not been attempted before and thus presents a new contribution to the subject of discretization error estimates for plates. The comparison of the performance of EqR method and commonly accepted superconvergent patch recovery (SPR) method is presented by several numerical examples. Additionally, an adaptive construction of a mesh based on the estimation of discretization error is illustrated on a numerical example. Both methods have its own advantages: the EqR method provides noticeable higher local accuracy of the error estimates, while the SPR is significantly easier to implement. The EqR method proved to be a reasonable alternative to the SPR method.

Model error concept is discussed in chapters 7-8. Following the general treatment of the principles of model error estimation, a method of model error estimation based on the EqR method is proposed. Specific issues related to the construction of local problems for the plate elements are addressed in chapter 8. Several numerical tests illustrate the performance of the proposed method. The proposed method proved to be capable of detecting the areas with increased model error.

The work presented in this thesis showed another important conclusion: the hierarchy of the plate finite element models involved in the model error estimation procedure is the key to the successful model error estimation. It is only the use of hierarchic (in the model sense) family of plate elements which enabled the successful implementation of model

error estimates based on EqR.

An illustration of iterative adaptive construction of the optimal finite element model based on the computation of the model error indicator is presented. The example shows, that the proposed model error indicator is capable of driving the adaptive procedure.

Another important conclusion that was found out during the study of model error estimates is the fact that the maxim: 'build the model from coarse to fine' has its limits. It was shown namely that it is impossible to detect the boundary layer phenomena using the results of the coarse model only. It is therefore not realistic to expect from the proposed model error estimation method to detect phenomena which intrinsically depend on the complexity of the model itself. The coarse model just does not carry enough information to be able to detect a possible higher order phenomena. In order to capture all the important phenomena in a certain plate model using adaptive modeling, the initial model should not be too coarse.

To summarize: the main goal of the thesis was to implement and test the key element of the concept of adaptive modeling of plates: error estimates. Some of the most promising methods were explored and tested. The results presented in this thesis show that the studied error estimates are suitable for the purpose of adaptive modeling. This work thus indicates that it would be possible to construct a fully automated procedure for the determination of the optimal finite element model of a given plate problem.

Chapter 10

Razširjeni povzetek

10.1 Motivacija

Razumevanje obnašanja konstrukcij pod različnimi obremenitvami ima že od nekdaj velik pomen za človekov razvoj. Zgodovinsko gledano, je večji del znanja o konstrukcijah človek pridobil s preskušanjem. Vendar pa je zaradi naraščajoče kompleksnosti grajenih objektov kmalu postalo jasno, da ni mogoče in tudi ne ekonomično, da bi s preskušanjem določili odpornost konstrukcije v vseh možnih obtežnih primerih. Spoznanje je vodilo v razvoj modelov fizikalnih procesov, s katerimi je mogoče računsko napovedati obnašanje konstrukcij. Ker so modeli zgrajeni na podlagi eksperimentalnih rezultatov, njihova natančnost ne more preseči natančnosti, s katero izvajamo preskus. Natančnost modelske napovedi je hkrati omejena s končno računsko močjo, ki neposredno vpliva na raven podrobnosti, ki jo je moč opisati z danim računskim modelom.

V zgodnjih letih razvoja je bil analitični način reševanja računskih modelov edini dosegljiv način. Z njim je bilo mogoče obravnavati le probleme s preprosto geometrijo in snovnimi zakoni. Metode za približno računsko reševanje modelov so bile sicer kmalu razvite, vendar so bile bistveno omejene z računsko močjo reševalca (v tem času je bil to večinoma človek). Svoj silovit vzpon so doživele šele s pojavom sodobnih računalnikov. Sorazmerno kmalu po začetku uporabe je bilo mogoče z njimi reševati tudi kompleksne inženirske probleme. Dandanes so računski modeli postali sestavni del projektiranja. Na podlagi izračunov se sprejemajo kritične odločitve in zaključki. Iz tega razloga je definicija zanesljivosti in natančnosti modelskih napovedi posebnega pomena.

Razumevanje izbranega fizikalnega pojava je popolno šele, ko lahko izračunamo oziroma napovemo izid preskusa, s katerim ga preverjamo. Model določenega fizikalnega pojava je sprejet, ko se njegove napovedi ujemajo z izidi nadzorovanih preskusov. Ker inženirski pristop k modeliranju temelji na paradigmi: "tako preprosto, kot je le mogoče in le

tako zapleteno, kot je potrebno", je zahtevana raven kompleksnosti modela izbranega fizikalnega pojava določena s zahtevano natančnostjo napovedi.

Razliko med izmerjeno fizikalno stvarnostjo in modelskimi napovedmi lahko pripišemo enemu od dveh razlogov: (i) bodisi je model grajen na napačnih predpostavkah in/ali (ii) je rešitev modela je le približna. Napaki modelske napovedi, katere vzrok so napačne predpostavke, običajno pravimo *modelska napaka*. Približno reševanje modela je vzrok *diskretizacijski napaki*.

10.1.1 Verifikacija in validacija

Skupna napaka napovedi je tako vedno vsota modelske in diskretizacijske napake. Če je modelska napaka posledica približkov, storjenih pri zapisu sistema enačb, ki opisujejo izbran fizikalni pojav, je diskretizacijska napaka tista, ki nastane zaradi približnega reševanja teh istih enačb. Za študij natančnosti izbranega modela je bil razvit koncept verifikacije in validacije: *verifikacija* je primerjava približne rešitve (diskretizirane različice) modela s točno rešitvijo, validacija pa je primerjava modelskih napovedi z izidom preskusov.

Model je matematična idealizacija fizikalnega modela, ki je zgrajen na določenih predpostavkah in poenostavitvah. Pri definiciji modela je tako vedno prisotna določena stopnja abstrakcije, ki običajno vsebuje koncept zveznosti. Ta predpostavlja, da je rešitev znana v vsaki točki območja. Tak model računsko ni rešljiv, saj je število točk v sistemu (in s tem neznank) neskončno. Da bi dobili računsko rešljiv sistem, model diskretiziramo s končnim številom neznank. Široko uveljavljena metoda diskretizacije zveznih matematičnih modelov, ki jih opisujejo parcialne diferencialne enačbe, je metoda končnih elementov (MKE). Diskretizacija sistema prinese dodatno napako, ki ji pravimo *diskretizacijska napaka*.

Metoda končnih elementov je bila zasnovana s strani inženirjev in matematikov predvsem za reševanje problemov s področja linearne elastičnosti. Tudi dandanes metoda končnih elementov ostaja zlasti na področju linearne mehanike konstrukcij. V isto področje spada tudi žarišče tega dela: analiza upogiba ploskovnih konstrukcij z metodo končnih elementov.

10.1.2 Prilagodljivo modeliranje - optimalni model

Da bi našli optimalni model za analizo izbrane ploskovne konstrukcije, moramo najprej določiti primerne kriterije. Če je edini kriterij natančnost modelske napovedi, je najprimernejši model polni trirazsežni model. Vendar pa zaradi velike računske zahtevnosti

taka izbira ni posebej racionalna. Optimalnost modela zato definiramo v inženirskem smislu: optimalni model je najpreprostejši model, ki še dosega zahtevano natančnost.

Plošče so osnovni konstrukcijski elementi in za opis njihovega obnašanja je bilo razvitih več modelov. Ker je tretja razsežnost plošč znatno manjša kot preostali dve, uporabljamo za modele plošč načelo dimenzijske redukcije. Računska prednost uporabe dvorazsežnih modelov pred trirazsežnimi je očitna. Čeprav modeli plošč asimptotično konvergirajo k trirazsežnemu modelu, niso vsi zgrajeni na načelih asimptotične analize. Več uspešnih modelov plošč je bilo razvitih na podlagi a-priori predpostavk, ki so izšle iz globokega inženirskega uvida. Kljub temu je mogoče, glede na konvergenco k polnemu trirazsežnemu modelu, vzpostaviti hierarhijo med modeli. Mogoče je oblikovati družino hierarhično urejenih modelov plošč - vrsto modelov, katerih rešitve konvergirajo k točni trirazsežni rešitvi problema upogiba plošč. Konvergenca k točni trirazsežni rešitvi se kaže, med drugim, v zmožnosti opisa posebnih robnih pojavov, ki so značilni za trirazsežne rešitev.

Predpostavke, na katerih slonijo modeli plošč, so običajno povezani s kinematiko deformacije. Ta je močno odvisna od robnih pogojev, koncentrirane obtežbe in skokovitih sprememb v debelini ali snovnih lastnostih. Ker je kinematika krajevno odvisna, enako velja tudi za veljavnost modelskih predpostavk. Model je optimalen le v območju, kjer veljajo njegove predpostavke. Iz tega izhaja, da je optimalni model odvisen od kraja, vendar pa enotnega modela, ki bi bil optimalen po celotnem območju, običajno ni. Območje zato razdelimo v področja. Vsakega od področij modeliramo s svojim optimalnim modelom. Cilj prilagodljivega modeliranja je prepoznati ta področja in za vsakega od njih določiti svoj optimalni model.

Krajevno odvisen optimalni model ploskovne konstrukcije lahko zgradimo iterativno, v več korakih. Inženirski pristop h gradnji optimalnega modela sloni na načelu: od grobega proti bolj podrobnemu. Prvo analizo problema izvedemo z najbolj grobim modelom po celotnem območju. Z obdelavo rešitve dobimo oceno modelske napake. Glede na predpisano natančnost prepoznamo območja, kjer je napaka večja od predpisane in bi morali uporabiti boljši, bolj rafiniran model. Zgradimo nov mešan model, in izračunamo novo rešitev. Spet ocenimo modelsko napako in določimo področja, kjer je potrebno uporabiti boljši model. Postopek ponavljamo tako dolgo, dokler ne dosežemo zahtevane natančnosti po celotnem območju. Ključni element tega postopka je učinkovita in točna ocena modelske napake.

Ko izberemo krajevno odvisen optimalni model, ga diskretiziramo, da dobimo računsko rešljiv sistem enačb. Diskretizacija po metodi končnih elementov razdeli računsko območje

na končne elemente. Na vsakem od elementov zgradimo približek rešitve, ki je odvisen od končnega števila prostostnih stopenj. Kakovost približka je odvisna od velikosti elementa in razgibanosti rešitve - bolj, ko je rešitev spremenljiva, manjše elemente potrebujemo, da jo zadovoljivo opišemo. Pri optimalni diskretizaciji je diskretizacijska napaka enakomerno razdeljena po celem območju in je približno enaka za vse elemente, ne glede na velikost. Diskretizacijsko napako uravnavamo s spreminjanjem velikosti elementov. Gradnja optimalne diskretizacije (ali mreže) je običajno iterativna. Najprej izračunamo rešitev na sorazmerno grobi mreži in izračunamo oceno diskretizacijske napake. Ker je odvisnost diskretizacijske napake od velikosti elementa poznana a-priori, lahko, če je določena zahtevana natančnost rešitve, na podlagi ocene diskretizacijske napake ocenimo velikost elementa. Na tak način dobimo oceno porazdelitve velikosti elementov po območju in z upoštevanjem te ocene zgradimo novo mrežo. To ponavljamo tako dolgo dokler ne dosežemo predpisane natančnosti in zagotovimo enakomerno porazdelitev diskretizacijske napake po elementih.

Optimalni model, v smislu modelske in diskretizacijske napake, je prilagojen izbranemu problemu. Glavna prednost prilagodljivega modeliranja ni toliko v občutnem povečanju računske učinkovitosti, kolikor je v nadzoru nad natančnostjo modelskih napovedi. Samodejni postopek za izbiro optimalnega modela preprečuje neizkušenemu uporabniku neupravičene poenostavitve, ki lahko zabrišejo morebitne koncentracije napetosti. Po drugi strani pa je, zaradi vedno večje računske moči, skušnjava po izbiri preveč podrobnih modelov vedno večja. Čeprav ti zajamejo vse podrobnosti, jih je bistveno težje interpretirati in mnogokrat prav podrobnosti zasenčijo bistvene značilnosti rešitve.

10.1.3 Napaka diskretizacije, modelska napaka

Prilagodljivo modeliranje je iterativni proces, ki temelji na ocenah modelske in diskretizacijske napake. Pri obravnavi napake je potrebno jasno ločiti med oceno in cenilko napake. Cenilke običajno podajajo zgornjo in spodnjo mejo napake. Ker je mogoče dokazati, da napaka leži znotraj napovedanih meja, so cenilke precej konzervativne. Slaba stran jamstva, ki ga dajejo cenilke se odraža v bistveno precenjeni napaki. Po drugi strani ocene napake ne dajejo nobenih jamstev, temveč omogočajo precej natančno indikacijo napake. Namen računa napake določa izbiro med cenilkami in ocenami. V primerih, kjer je glavni cilj računa napake vodenje postopka prilagodljivega modeliranja, se uporabljajo ocene napake.

Za uspešno gradnjo optimalnega modela je ključen učinkovit izračun zanesljive ocene

napake: tako diskretizacijske, kot tudi modelske. Čeprav slednja lahko bistveno preseže diskretizacijsko napako, jo je precej težje oceniti. To se odraža v majhnem številu obstoječih metod za izračun ocene modelske napake. Ker obstoječe metode oceno modelske napake obravnavajo na precej splošni ravni, se v tem delu osredotočamo na izračun ocene modelske napake za primer modeliranja plošč. Razvoj postopka za oceno modelske napake za primer analize plošč s končnimi elementi predstavlja enega glavnih dosežkov tega dela.

Učinkovit postopek za izračun ocene modelske napake izhaja iz naslednje zamisli: modelska napaka meri razliko med rešitvijo z obstoječim modelom in rešitvijo z referenčnim modelom - polnim trirazsežnim modelom. Globalni račun točne rešitve z referenčnim modelom - samo zato, da bi rešitev primerjali z obstoječo rešitvijo - je seveda predrag. Zato poskusimo izračunati rešitev z referenčnim modelom na manjših območjih - najbolje kar na končnih elementih. Pri tem moramo poskrbeti, da lokalni izračuni čim bolj verno nadomestijo globalni izračun. Pri tem si predstavljamo, da območja, na katerih izvajamo lokalni izračun, izločimo iz kontinuuma in delovanje okolice predstavimo z robno obtežbo. Zato so robni pogoji za lokalne izračune Neumannovega tipa.

Osrednje vprašanje ocene modelske napake tako postane: "Kako oceniti robne pogoje za lokalne izračune?", če bi poznali točno rešitev, bi robne pogoje lahko določili iz napetosti s pomočjo Cauchijevega principa. Ker pa točne rešitve seveda ne poznamo, se pri oceni napetosti opremo na edino dosegljivo informacijo: trenutno rešitev s končnimi elementi. Ker rešitev s končnimi elementi predstavlja približek točne rešitve, lahko iz nje ocenimo napetosti, ki so podlaga za izračun robnih pogojev. Razvoj metod za izračun najboljše ocene robnih pogojev za lokalne izračune, je tako ključen del izračuna ocene modelske napake.

Uporaba te preproste zamisli na primeru modeliranja plošč ni zelo preprosta, saj je potrebno smiselno upoštevati posebne pojave, ki so značilni le za modeliranje plošč. Zahtevnost implementacije povečuje tudi dejstvo, da je večina končnih elementov za plošče nekompatibilnih.

10.2 Cilji

Glavni cilji naloge se nanašajo na koncept prilagodljivega modeliranja ploskovnih konstrukcij. Prvi cilj naloge je zato razvoj hierarhične družine (v modelskem smislu) dobro delujočih trikotnih in štirikotnih končnih elementov za plošče.

Ker je koncept prilagodljivega modeliranja ključno odvisen od zanesljivih ocen napak, se drugi cilj naloge nanaša predvsem na oceno napake diskretizacije: cilji so izpeljava, implementacija ter testiranje nekaj najbolj uveljavljenih a-posteriori metod za oceno napake. Pri tem se osredotočamo na dve najbolj prepoznavni metodi: SPR (*supercovergent patch recovery*) in EqR (*method of equilibrated residuals*). Metodi sta implementirani za primer DK in RM ploščnih elementov, ki so najbolj pogosto uporabljeni za analizo ploskovnih konstrukcij z metodo končnih elementov.

Trenutno je za oceno napake diskretizacije razvitih bistveno več metod kot za oceno modelske napake. V tem delu se za oceno modelske napake zanašamo na metodo, ki temelji na EqR metodi. Tretji cilj te naloge je pojasniti in izpeljati uporabo EqR metode za oceno modelske napake.

Zadnji cilj naloge je izpeljati proceduro za prilagodljivo modeliranje plošč. Ta naj bi sledila naslednjim korakom: izračunaj začetno rešitev izbranega problema s končnimi elementi, oceni modelsko napako in napako diskretizacije, na podlagi ocene napak konstruiraj boljši model (s končnimi elementi) problema. Prilagodljivo modeliranje naj bi sledilo konceptu gradnje od spodaj navzgor: od sorazmerno grobega modela in mreže do modela, ki je sposoben opisati vse pomembne pojave in pri tem nadzorovati skupno napako, kakor tudi njeno porazdelitev po območju.

10.3 Zgradba naloge

Nalogo sestavlja devet poglavij. V prvem poglavju sta podana pregled in trenutno stanje področja.

V poglavjih 2 do 4 je predstavljen pregled teorije plošč. Teorije so razvrščene od bolj preprostih do "kvazi" tridimenzionalnih. Teoretična obravnava plošč razkriva nekatere pojave, ki so tipični le zanje: singularnosti ter robna območja. Opis teorij, ki jih je mogoče hierarhično urediti, je dopolnjen z nekaj mogočimi diskretizacijami: končnimi elementi. Predstavljenih je nekaj najpomembnejših in uveljavljenih končnih elementov. Poglavja so zaključena z obravnavo nekaj testnih primerov, ki ilustrirajo različne vidike modeliranja plošč s končnimi elementi.

Poglavje 5 se začne s pregledom najpomembnejših metod za oceno napake diskretizacije. Splošnemu opisu sledi podrobnejša obravnava metod SPR in EqR. Implementaciji EqR metode je namenjena posebna pozornost v poglavju 6. Implementacija je nekoliko zahtevnejša za primer ne-konformnih končnih elementov in v literaturi še ni bila podrobneje

opisana. Več numeričnih primerov prikazuje razlike med posameznimi metodami ocene napake diskretizacije.

Poglavji 7 in 8 se ukvarjata z vprašanjem modelske napake. Splošni obravnavi modelske napake sledi opis načina ocene modelske napake, ki sloni na metodi uravnoteženih residualov. Posebna pozornost je namenjena implementaciji metode za primer končnih elementov za plošče, ki so predstavljeni v poglavjih 2-4. Učinkovitost metode je prikazana z več izbranimi numeričnimi primeri.

Zaključki in povzetek so podani v poglavju 9.

10.4 Plošče

Ploskovne konstrukcije so konstrukcije, katerih debelina je bistveno manjša od razpona. Povsem jih določata v ravnini ležeča nevtralna ploskev in njihova debelina. V nadaljevanju se bomo osredotočili na študij odziva ploskovnih konstrukcij na delovanje prečne obtežbe. Krajše ploskovne konstrukcije imenujemo kar plošče.

Obnašanje plošč pri delovanju prečne obtežbe prvenstveno določa razmerje med razponom in debelino plošče. Med tanke plošče štejemo plošče, pri katerih je to razmerje okvirno med 100 in 20. Zanje je značilno, da je mogoče prečne strižne deformacije zanemariti. Pri ploščah z razmerjem med 20 in 5, ki jih imenujemo srednje debele, je strižna deformacija končna in jo moramo upoštevati pri izračunu. Pri debelih ploščah, pri katerih je razmerje med razponom in debelino manjše od 5, moramo upoštevati tudi deformacije vzdolž debeline plošče. Deformacijsko polje takih plošč je tako že zelo blizu polnemu tri-dimenzionalnemu deformacijskemu stanju.

10.4.1 Tanke plošče

Model

V drugem poglavju obravnavamo upogib linearno elastičnih tankih plošč, pri čemer se opremo na glavno predpostavko t.i. Kirchhoffovega modela: ravna vlakna, ki pred deformacijo ležijo pravokotno na nevtralno ravnino, ostanejo ravna in pravokotna nanjo tudi po deformaciji. Nevtralno ploskev sestavljajo točke, ki se premaknejo le v smeri z. Pomik točke $P(x, y, 0)$ na nevtralni ploskvi je določen s prečnim pomikom $w(x, y)$. Pomik poljubne točke $P(x, y, z)$, ki leži na razdalji z od nevtralne ravnine, je določen z naslednjim izrazom (glej tudi Sliko 2.2.1):

$$u_x = +z\theta_y; \quad u_y = -z\theta_x; \quad u_z = w$$

Pri tem je s $\boldsymbol{\theta} = [\theta_x, \theta_y]^T$ označena rotacija vlakna, na katerem leži izbrana točka. Ker je vlakno pravokotno na nevtralno ravnino, je njegova rotacija določena z nagibom nevtralne ploskve (2.2.1):

$$\theta_x = +\frac{\partial w}{\partial y}; \quad \theta_y = -\frac{\partial w}{\partial x}$$

Deformacijsko polje, ki ustreza Kirchhoffovi predpostavki, je naslednje oblike (2.2.2):

$$\varepsilon_{xx} = -\frac{\partial^2 w}{\partial x^2}; \quad \varepsilon_{yy} = -\frac{\partial^2 w}{\partial y^2}; \quad \varepsilon_{xy} = -\frac{\partial^2 w}{\partial x \partial y}$$
$$\varepsilon_{zz} = 0; \quad \varepsilon_{xz} = 0; \quad \varepsilon_{yz} = 0$$

Za bolj kompaktni zapis uvedemo vektor ukrivljenosti (2.2.8)

$$\boldsymbol{\kappa} = [\frac{\partial^2 w}{\partial x^2}, \frac{\partial^2 w}{\partial y^2}, 2\frac{\partial^2 w}{\partial x \partial y}]^T$$

in zapišemo (2.2.5)

$$\varepsilon_{xx} = -z\kappa_{xx}; \quad \varepsilon_{yy} = -z\kappa_{yy}; \quad \gamma_{xy} = 2\varepsilon_{xy} = -z\kappa_{xy}$$

Predpostavimo ravninsko napetostno stanje ($\sigma_z z = 0$), iz česar dobimo (2.2.10). Z uvedbo rezultant napetosti (2.2.11) v obliki vektorja $\boldsymbol{m} = [m_{xx}, m_{yy}, m_{xy}]^T$ dobimo naslednjo relacijo (2.2.12)

$$\boldsymbol{m} = \mathbf{C}_B \kappa$$

kjer je konstitutivna matrika oblike (2.2.13)

$$\mathbf{C}_B = D \begin{bmatrix} 1 & \nu & 0 \\ \nu & 1 & 0 \\ 0 & 0 & \frac{1}{2}(1-\nu) \end{bmatrix}$$

s konstanto $D = \frac{1}{12}Et^3/(1-\nu^2)$, ki predstavlja izotropno togost plošče.

Ravnotežje diferencialnega elementa (glej Sliko 2.2.2) je določeno z enačbama (2.2.16) in (2.2.17). Z eliminacijo strižne sile $\boldsymbol{q}$ zapišemo ravnotežje v obliki (2.2.19) :

$$\frac{\partial^2 m_{xx}}{\partial x^2} + 2\frac{\partial^2 m_{xy}}{\partial x \partial y} + \frac{\partial^2 m_{yy}}{\partial y^2} = f$$

kjer je f prečna obtežba plošče.

Zgornje enačbe združimo v znano biharmonično enačbo(2.2.26)

$$\frac{\partial^4 w}{\partial x^4} + 2\frac{\partial^4 w}{\partial x^2 \partial y^2} + \frac{\partial^4 w}{\partial x^4} = f/D$$

Diferencialna enačba skupaj z robnimi pogoji predstavlja matematično formulacijo upogiba tankih plošč v močni obliki.

Ker je diferencialna enačba četrtega reda, sta na robu po dva robna pogoja, kar je v navideznem nasprotju s tremi količinami, ki so konjugirane h komponentam pomika na robu: (i) k prečnemu pomiku w - prečna strižna sila q, (ii) k zasuku v smeri roba θ_s - rezultanta momenta v smeri roba m_s in k pravokotnemu zasuku na rob θ_n - rezultanta momenta pravokotno na rob m_n (glej Sliko 2.2.4). Obravnava šibke formulacije problema (2.2.43) pokaže, da je nasprotje le navidezno, ker zaradi Kirchhoffove predpostavke zasuk pravokotno na rob $\theta_n = \frac{\partial w}{\partial s}$ ni neodvisen, temveč enolično določen s potekom pomika po robu. Na robu tanke plošče sta zato dve neodvisni komponenti obtežbe: (i) efektivna prečna sila $q_e f$, ki je konjugirana k prečnemu pomiku, ter (ii) moment vzdolž roba m_s, ki je konjugiran k zasuku, ki vrti vzdolž roba. Efektivna prečna sila je definirana z izrazom (2.2.44).

$$q_{ef} = q - \frac{\partial m_n}{\partial s}$$

Na prostem robu tako velja $q_e f = 0$ in $m_s = 0$, kar pomeni, da sta na prostem robu lahko različni od nič tako prečna sila $q \neq 0$, kakor tudi rezultanta momenta $m_n \neq 0$.

Posledica Kirchhoffove predpostavke, ki veže zasuk plošče s pomikom, je tudi pojav t.i. "koncentrirane" sile v nepodprtih vogalih plošče. Integracija per partes (po robu od točke A do točke B) v (2.2.43), ki pripelje do efektivne strižne sile, povzroči dodatni člen oblike $[um_n]_A^B$. Po upoštevanju zveznosti prečnega pomika, dodatni člen skupaj prispeva vsoto $\sum_I u_I(m_{n,I}|_B - m_{n,I}|_A)$, kjer so z I označene točke na robu. Členi vsote so različni od nič le v tistih točkah I vzdolž roba $\Gamma_{N,AB}$, kjer velja nezveznost $m_{n,I}|_B \neq m_{n,I}|_A$. Pri tem smo uporabili oznako $m_{n,I}|_A$ za vrednost m_n v točki I pri približevanju s strani točke A. Te členi, ki k virtualnemu delu zunanjih sil prispevajo $\sum_I u_I F_{C,I}$, kjer $F_{C,I} = [m_{n,I}]_A^B$, razumemo kot koncentrirano silo v točki I. Če se omejimo na reakcije, je koncentrirana sila različna od nič le v točkah prosto podprtega roba, kjer se smer robu nezvezno spremeni (kjer ima plošča vogal) (2.2.47). V primeru, ko je vogal togo vpet ali prost, je koncentrirana sila $F_{C,I}$ enaka 0.

Princip virtualnega dela za tanke plošče se glasi: v ravnovesju je virtualno delo zunanjih sil $\delta\Pi^{ext}$ enako virtualnemu delu notranjih sil $\delta\Pi^{int}$: $\delta\Pi^{int} = \delta\Pi^{ext}$ za poljuben virtualni pomik δw, ki ustreza Kirhhoffovi predpostavki ter robnim pogojem (Tabela 2.1), pri čemer je

$$\delta\Pi^{int} = \int_\Omega \delta\boldsymbol{\kappa}^T \boldsymbol{m}\, \mathrm{d}\Omega; \quad \delta\Pi^{ext} = \int_\Omega \delta w\, f\, \mathrm{d}\Omega + \int_\Gamma (\overline{q}_{ef}\delta w - \overline{m}_s \frac{\delta\partial w}{\delta n})\, \mathrm{d}s$$

Virtualna pomika na robu plošče δw in $\frac{\delta \partial w}{\delta n}$ sta neodvisna. K njima sta konjugirani obtežbi $\overline{q}_{ef}$ in $\overline{m}_s$. Z uporabo konstitutivne relacije $\boldsymbol{m} = \mathbf{C}_B \boldsymbol{\kappa} = \mathbf{C}_B \boldsymbol{\mathcal{L}} \boldsymbol{\kappa}$ lahko pokažemo, da je princip virtualnega dela ekvivalenten biharmonični enačbi.

Zanimiva posledica Kirchhoffove predpostavke je obstoj "singularnosti", ki nastane v določenih primerih krivega roba, ko je ta interpoliran z lomljenim robom. Zaradi Kirchhoffove predpostavke je na vogalu takega roba, normalna komponenta rotacije θ_n definirana dvakrat - v dveh smereh, zaradi česar je vogal efektivno vpet. To lahko povzroči singularnost v rezultantah napetosti. Vodilni člen, ki določa, kako izrazita je singularnost, opišemo z izrazom $r^{\lambda-2}$ za rezultante momentov ter $r^{\lambda-3}$ za strižne sile. Eksponent λ je odvisen od robnih pogojev ter obratno sorazmeren kotu α, ki ga oklepa vogal. Singularnost za rezultante momentov nastopi, kadar je $\lambda < 2$ (oziroma $\lambda < 3$ za strižne sile). Kritični koti, kjer nastopi singularnost, so podani v Tabeli 2.2. Za primer dvakrat prosto podprtega vogala tako preberemo, da singularnost strižnih sil nastopi, ko je $\alpha > 60°$ in za rezultante momentov, ko je $\alpha > 90°$.

Končni elementi

Iz principa virtualnega dela za tanke plošče vidimo, da v njem nastopajo največ drugi odvodi w. Interpolacija w mora biti zato najmanj zvezno odvedljiva $\mathcal{C}^1$, hkrati mora tudi točno opisati vse polinome do vključno drugega reda. Izkaže se, da je končne elemente, ki ustrezajo obema zahtevama, težko konstruirati. Običajno se za modeliranje odziva tankih plošč uporabljajo končni elementi, ki kršijo zahtevo po zvezni odvedljivosti, zaradi česar jim pravimo *nekompatibilni* v nasprotju s *kompatibilnimi* ali *konformnimi* elementi, ki tej zahtevi zadostijo.

V nadaljevanju je najprej predstavljen trikotni konformni element imenovan ARGY ([Argyris et al., 1968]). Zaradi velikega števila prostostnih stopenj, ki nimajo prave fizikalne interpretacije, se element zelo redko uporablja za praktične izračune. Nasprotje so nekompatibilni elementi tipa DK [Dhatt, 1970], [Batoz et al., 1980], [Batoz, 1982], ki uporabljajo interpolacijo pomika, ki ni zvezno odvedljiva. Ime DK (Diskretni Kirchhoff) izhaja iz dejstva, da interpolacija zadosti Kirchhoffovi predpostavki le v diskretno mnogo točkah. Konvergenca elementov tega tipa je zagotovljena, ker prestanejo t.i. "patch test". Kljub omenjenim lastnostim, so elementi DK zelo priljubljeni, saj so v mnogo primerih bolj učinkoviti od konformnih elementov.

Konformni trikotni element (2.3.4)

Interpolacija za trikotni konformni element ARGY predstavlja popolni polinom petega reda (z 21 parametri). To je najnižja stopnja, ki še zadošča pogoju zvezne odvedljivosti pri prehodu čez rob elementa. Interpolacija je zapisana v naravnem trikotniškem koordinatnem sistemu (2.3.21) $(\zeta_1, \zeta_2, \zeta_3)$:

$$w_h = \boldsymbol{\omega}^T \hat{\boldsymbol{p}}$$

kjer je $\hat{\boldsymbol{p}}$ vektor vozliščnih parametrov in $\boldsymbol{\omega}$ množica interpolacijskih funkcij, ki vsebuje 21 elementov :

$$\begin{aligned}\boldsymbol{\omega} = [&\zeta_1^5, \zeta_2^5, \zeta_3^5,\\ &\zeta_1\zeta_2^4, \zeta_2\zeta_3^4, \zeta_3\zeta_1^4, \zeta_2\zeta_1^4, \zeta_3\zeta_2^4, \zeta_1\zeta_3^4,\\ &\zeta_1^3\zeta_2^2, \zeta_2^3\zeta_3^2, \zeta_3^3\zeta_1^2, \zeta_2^3\zeta_1^2, \zeta_3^3\zeta_2^2, \zeta_1^3\zeta_3^2,\\ &\zeta_1^3\zeta_2\zeta_3, \zeta_1\zeta_2^3\zeta_3, \zeta_1\zeta_2\zeta_3^3, \zeta_1^2\zeta_2^2\zeta_3, \zeta_1^2\zeta_2\zeta_3^2, \zeta_1\zeta_2^2\zeta_3^2]^T\end{aligned}$$

Prostostne stopnje elementa se nanašajo na 3 vozlišča v ogliščih ter 3 vozlišča na sredini stranic. Vsako oglišče ima 6 prostostnih stopenj: prečni pomik, njegove prve odvode, ter druge odvode glede na smeri x in y. Vozlišče v sredini stranice ima eno prostostno stopnjo, ki se nanaša na odvod pomika v smeri normale stranice. Množica prostostnih stopenj elementa $\hat{\boldsymbol{w}}$ je tako (Slika 2.3.7):

$$\begin{aligned}\hat{\boldsymbol{w}} = [&\hat{w}_1, \hat{w}_2, \hat{w}_3,\ \hat{w}_{1,x}, \hat{w}_{1,y},\ \hat{w}_{2,x}, \hat{w}_{2,y},\ \hat{w}_{3,x}, \hat{w}_{3,y},\\ &\hat{w}_{1,xx}, \hat{w}_{1,xy}, \hat{w}_{1,yy},\ \hat{w}_{2,xx}, \hat{w}_{2,xy}, \hat{w}_{2,yy},\ \hat{w}_{3,xx}, \hat{w}_{3,xy}, \hat{w}_{3,yy},\\ &\hat{w}_{,n_{12}}, \hat{w}_{,n_{23}}, \hat{w}_{,n_{31}}\ ]^T\end{aligned}$$

Da bi določili povezavo med prostostnimi stopnjami $\hat{\boldsymbol{w}}$ ter parametri $\hat{\boldsymbol{p}}$, moramo izračunati odvode v vozliščih. Kot vmesni korak vpeljemo prostostne stopnje $\hat{\boldsymbol{w}}_\rho$, ki se nanašajo na trikotniške koordinate:

$$\begin{aligned}\hat{\boldsymbol{w}}_\rho = [&\ \hat{w}_1, \hat{w}_2, \hat{w}_3,\ \hat{w}_{1,12}, \hat{w}_{1,31},\ \hat{w}_{2,23}, \hat{w}_{2,12},\ \hat{w}_{3,31}, \hat{w}_{3,23},\\ &\hat{w}_{1,12^2},\ \hat{w}_{1,31^2},\ \hat{w}_{1,23^2}, \hat{w}_{2,12^2},\ \hat{w}_{2,31^2},\ \hat{w}_{2,23^2}, \hat{w}_{3,12^2},\ \hat{w}_{3,31^2},\ \hat{w}_{3,23^2},\\ &\hat{w}_{,n_{12}}, \hat{w}_{,n_{23}}, \hat{w}_{,n_{31}}]^T\end{aligned}$$

Povezavo med $\hat{\boldsymbol{p}}$ ter $\hat{\boldsymbol{w}}_\rho$ dobimo tako, da izvrednotimo odvode v trikotniškem koordinatnem sistemu v vozliščih elementa (pri tem uporabimo (2.3.30), (2.3.31) ter (2.3.36)).

Povezavo strnjeno zapišemo kot (2.3.40):

$$\hat{\boldsymbol{w}}_\rho = \mathbf{A}^{-1}\hat{\boldsymbol{p}}$$

pri čemer je $\mathbf{A}^{-1}$ matrika linearnega sistema enačb zapisana iz (2.3.38) ter (2.3.39). Preko transformacije odvodov iz globalnega v trikotniški koordinatni sistem

$$\begin{bmatrix} w_{,12} \\ w_{,23} \\ w_{,31} \end{bmatrix} = \begin{bmatrix} x_{12} & y_{12} \\ x_{23} & y_{23} \\ x_{31} & y_{31} \end{bmatrix} \begin{bmatrix} w_{,x} \\ w_{,y} \end{bmatrix}$$
$$\begin{bmatrix} w_{,12^2} \\ w_{,31^2} \\ w_{,23^2} \end{bmatrix} = \begin{bmatrix} x_{12}^2 & y_{12}^2 & -x_{12}y_{12} \\ x_{31}^2 & y_{31}^2 & -x_{31}y_{31} \\ x_{23}^2 & y_{23}^2 & -x_{23}y_{23} \end{bmatrix} \begin{bmatrix} w_{,xx} \\ w_{,yy} \\ 2w_{,xy} \end{bmatrix}$$

dobimo še:

$$\hat{\boldsymbol{w}}_\rho = \mathbf{X}_T\hat{\boldsymbol{w}}$$

kjer je $\mathbf{X}_T$ matrika linearne transformacije. Z upoštevanjem teh rezultatov dobimo:

$$\hat{\boldsymbol{p}} = \mathbf{X}\hat{\boldsymbol{w}}; \mathbf{X} = \mathbf{A}\mathbf{X}_T$$

Interpolacijo pomika končno izrazimo s prostostnimi stopnjami $\hat{\boldsymbol{w}}$ kot

$$w_h = \boldsymbol{\omega}^T\mathbf{X}\hat{\boldsymbol{w}}$$

Odtod izračunamo interpolacijo ukrivljenosti $\boldsymbol{\kappa}_h$, ki jo izrazimo preko interpolacije ukrivljenosti v trikotniških koordinatah:

$$\boldsymbol{\kappa}_h = \mathbf{T}\boldsymbol{\kappa}_{h,\rho}; \quad \boldsymbol{\kappa}_{h,\rho} = [w_{h,12^2}, w_{h,23^2}, w_{h,31^2}]^E = \omega_{,\rho}^T\hat{\boldsymbol{w}}$$

kjer je $\boldsymbol{\omega}_{,\rho} = [\boldsymbol{\omega}_{,12^2}, \boldsymbol{\omega}_{,23^2}, \boldsymbol{\omega}_{,31^2}]^T$ matrika dvojnih odvodov interpolacijskih funkcij v smereh stranic (glede na (2.3.31)).

Togostno matriko elementa določimo iz (2.3.46). Z uporabo (2.3.48) lahko integrale izračunamo analitično. Obtežni vektor izračunamo iz (2.3.51).

DK elementi za plošče

Dejstvo, da je izredno težavno skonstruirati zvezno odvedljivo interpolacijo za pomike, je vodilo k razvoju nekompatibilnih elementov. Ti običajno zgradijo ločeno interpolacijo za pomik w in zasuke $\boldsymbol{\theta}$, pri čemer mora biti izpolnjena Kirchhoffova predpostavka o ničelni strižni deformaciji $\boldsymbol{\gamma} = \nabla w - \boldsymbol{\theta} = 0$. Tako zahtevo je še vedno zelo težko izpolniti, zato

DK elementi za plošče uporabljajo interpolacijo, ki Kirchhoffovemu pogoju zadosti le v diskretnih točkah in še to le v določeni smeri: vzdolž vsakega roba elementa (ki je določen s smernim vektorjem $\boldsymbol{s}$) velja

$$\boldsymbol{\gamma}_h \cdot \boldsymbol{s} = 0$$

Pri tem je $\boldsymbol{\gamma}_h$ interpolacija strižne deformacije, ki izhaja iz $\boldsymbol{\gamma}_h = \nabla w_h - \boldsymbol{\theta}_h$, kjer je w_h interpolacija pomika in $\boldsymbol{\theta}_h$ interpolacija zasukov.

Zgled za konstrukcijo interpolacije te vrste najdemo pri elementih za Euler Bernoullijeve nosilce. Začnemo z neodvisnima interpolacijama za pomik w_h^{EB} ter zasuk θ_h^{EB}

$$\begin{aligned} w_h^{EB} &= \hat{w}_1 N_1 + \hat{w}_2 N_2 + \hat{w}_3 N_3 + \hat{w}_4 N_4 \\ \theta_h^{EB} &= \hat{\theta}_1 N_1 + \hat{\theta}_2 N_2 + \hat{\theta}_3 N_3 \end{aligned}$$

kjer so hierarhične interpolacijske funkcije (glej Sliko 2.3.8):

$$\begin{aligned} &N_1 = (1-\xi)/2; && N_2 = (1+\xi)/2 && \xi \in [-1,+1] \\ &N_3 = (1-\xi^2); && N_4 = \xi(1-\xi^2) \end{aligned}$$

Iz zahteve, da želimo zgraditi take interpolacije, pri kateri strižne deformacije ne bo, dobimo naslednji pogoj:

$$\gamma_h^{EB} = \frac{\partial w_h^{EB}}{\partial x} - \theta_h^{EB} = 0$$

Z njegovo pomočjo iz interpolacije izločimo prostostne stopnje $\hat{w}_3, \hat{w}_4$ ter $\hat{\theta}_3$ (glej (2.3.56)). To nas vodi do znane interpolacije za Euler Bernoullijev element (2.3.57), ki v vsakem vozlišču vsebuje le prostostni stopnji $\hat{w}_I$ in $\hat{\theta}_I$.

Pri gradnji interpolacije za DK elemente se opremo na zgornja spoznanja. Interpolaciji pomika in zasuka vdolž roba ustrezata interpolaciji (2.3.57), pri čemer upoštevamo, da je zasuk vzdolž roba θ enak zasuku $\theta_n = \boldsymbol{\theta} \cdot \boldsymbol{n}$.

Interpolacijo pomika zapišemo kot vsoto po ogliščih I in vozliščih na sredini stranic elementa, ki jih označimo z IJ:

$$w_h = \sum_I \hat{w}_I N_I + \sum_{IJ} (\hat{w}_{3,IJ} N_{IJ} + \hat{w}_{4,IJ} M_{IJ})$$

Pri tem smo z N_I označili interpolacijske funkcije, ki se nanašajo na vozlišče I, z N_{IJ} in M_{IJ} pa interpolacijske funkcije, ki se nanašajo na stranico IJ. Tako označevanje je nekoliko nekonvencionalno vendar koristno, saj z njim lahko opišemo tako trikotne kot tudi štirikotne elemente. Podobno zapišemo tudi interpolacijo zasukov:

$$\boldsymbol{\theta}_h = \begin{bmatrix} \theta_{x,h} \\ \theta_{y,h} \end{bmatrix} = \sum_{I=1}^{3} \hat{\boldsymbol{\theta}}_I N_I + \sum_{IJ} \hat{\boldsymbol{\theta}}_{3,IJ} \boldsymbol{n}_{IJ} N_{IJ}$$

kjer je $\hat{\boldsymbol{\theta}}_I = [\hat{\theta}_{xI}, \hat{\theta}_{yI}]$ ter $\boldsymbol{n}_{IJ}$ normala na stranico med vozliščema I in J. Ker mora vzdolž stranic elementa veljati

$$\boldsymbol{\gamma}_h \cdot \boldsymbol{s} = (\nabla w_h - \boldsymbol{\theta}_h) \cdot \boldsymbol{s} = 0$$

izločimo prostostne stopnje $\hat{w}_{3,IJ}$, $\hat{w}_{4,IJ}$ ter $\hat{\theta}_{3,IJ}$:

$$\begin{aligned}
\hat{w}_{3,IJ} &= \frac{L_{IJ}}{8} \boldsymbol{n}_{IJ} \cdot (\hat{\boldsymbol{\theta}}_I - \hat{\boldsymbol{\theta}}_J); \\
\hat{w}_{4,IJ} &= \frac{L_{IJ}}{4} \left(\frac{\hat{w}_J - \hat{w}_I}{L_{IJ}} - \frac{1}{2} \boldsymbol{n}_{IJ} \cdot (\hat{\boldsymbol{\theta}}_I + \hat{\boldsymbol{\theta}}_J) \right) \\
\hat{\theta}_{3,IJ} &= \frac{6}{L} \hat{w}_{4,IJ}
\end{aligned}$$

Taka interpolacija vsebuje le vozlišča v ogliščih elementa, kjer se nahajajo prostostne stopnje $\hat{\boldsymbol{w}}_I = [w_I, \hat{\theta}_{xI}, \hat{\theta}_{yI}]^T$. Interpolacije zapišemo v kompaktni obliki kot

$$\begin{aligned}
w_h &= \mathbf{N}_w \hat{\boldsymbol{w}} = \sum_I \mathbf{N}_{w,I} \hat{\boldsymbol{w}}_I; \quad \boldsymbol{\theta}_h = \mathbf{N}_\theta \hat{\boldsymbol{w}} = \sum_I \mathbf{N}_{\theta,I} \hat{\boldsymbol{w}}_I; \\
\boldsymbol{\kappa}_h &= \mathbf{B}_\kappa \hat{\boldsymbol{w}} = \sum_I \mathbf{B}_{\kappa,I} \hat{\boldsymbol{w}}_I
\end{aligned}$$

kjer je $\hat{\boldsymbol{w}} = [\hat{\boldsymbol{w}}_1, \hat{\boldsymbol{w}}_2, \cdots, \hat{\boldsymbol{w}}_{nen}]$ ter nen število vozlišč elementa. Eksplicitna oblika $\mathbf{N}_{w,I}$ ter $\mathbf{N}_{\theta,I}$ je podana v (2.3.64), (2.3.65) ter (2.3.66), kjer je številčenje predstavljeno na Sliki 2.3.11. Vektor ukrivljenosti $\boldsymbol{\kappa}_h$ določimo iz

$$\boldsymbol{\kappa}_h = [-\frac{\partial \theta_{y,h}}{\partial x}, \frac{\partial \theta_{x,h}}{\partial y}, \frac{\partial \theta_{x,h}}{\partial x} - \frac{\partial \theta_{y,h}}{\partial y}]$$

kjer je $\mathbf{B}_{\kappa,I} = [\mathbf{B}_{\kappa_{xx},I}, \mathbf{B}_{\kappa_{yy},I}, \mathbf{B}_{\kappa_{xy},I}]^T$:

$$\mathbf{B}_{\kappa_{xx},I} = -\frac{\partial \mathbf{N}_{\theta_y,I}}{\partial x}; \quad \mathbf{B}_{\kappa_{yy},I} = +\frac{\partial \mathbf{N}_{\theta_x,I}}{\partial y}; \quad \mathbf{B}_{\kappa_{xy},I} = +\frac{\partial \mathbf{N}_{\theta_x,I}}{\partial x} - \frac{\partial \mathbf{N}_{\theta_y,I}}{\partial y}$$

Togostno matriko $\mathbf{K}$ DK elementa izračunamo s pomočjo diskretizacije šibke oblike (2.2.51). Zapisana je v obliki bločne matrike $\mathbf{K} = [\mathbf{K}_{IJ}]$:

$$\begin{aligned}
a_{K,e}(w_h; u_h) &= \int_{\Omega_h^e} \boldsymbol{\kappa}^T(u_h) \boldsymbol{m}(w_h) \, \mathrm{d}\Omega = \\
&= \sum_{I,J} \hat{\boldsymbol{u}}_I^T \, \mathbf{K}_{IJ} \hat{\boldsymbol{w}}_J; \quad \mathbf{K}_{IJ} = \int_{\Omega_h^e} \mathbf{B}_{\kappa,I}^T \mathbf{C}_B \mathbf{B}_{\kappa,J} \, \mathrm{d}\Omega
\end{aligned}$$

Prav tako iz šibke oblike določimo konsistentni obtežni vektor $\boldsymbol{f} = [\boldsymbol{f}_I]^T$, kjer je $\boldsymbol{f}_I =$

$\boldsymbol{f}_{f,I} + \boldsymbol{f}_{t,I}$:

$$l_{K,e}(u_h) = \sum_I \hat{\boldsymbol{u}}_I^T \boldsymbol{f}_I = \hat{\boldsymbol{u}}^T \boldsymbol{f} =$$

$$= \int_{\Omega_h^e} f\, u_h \mathrm{d}\Omega + \sum_{\Gamma_{IJ}^e} \left[\int_{\Gamma_{IJ}^e} (\bar{q}_{ef}\, u_h + \overline{m}_s\, \boldsymbol{\theta}_h(u_h) \cdot \boldsymbol{s})\, \mathrm{d}s + [\overline{m}_n u_{h,\Gamma}]_I^J \right]$$

$$\boldsymbol{f}_{f,I} = \int_{\Omega_h^e} f\, \mathbf{N}_{w,I} \mathrm{d}\Omega; \quad \boldsymbol{f}_{t,I} = \sum_{\Gamma_{e,IJ}} \int_{\Gamma_{e,IJ}} (\bar{q}_{ef} \mathbf{N}_{w,I} + \overline{m}_s\, \boldsymbol{s}^T \mathbf{N}_{\theta,I})\, \mathrm{d}s$$

Trikotni DK element ima tri vozlišča v ogliščih trikotnika s prostostnimi stopnjami $\hat{\boldsymbol{u}}_I = [\hat{w}_I, \hat{\theta}_{xI}, \hat{\theta}_{yI}]$. Interpolacijske funkcije so definirane v trikotniškem koordinatnem sistemu

$$N_I = \zeta_I; \quad N_{IJ} = 4\zeta_I\zeta_J; \quad M_{IJ} = 4\zeta_I\zeta_J(\zeta_J - \zeta_I)$$

Interpolacijske funkcije (2.3.71) se na robovih ujemajo s hierarhičnimi funkcijami (2.3.55). Za integracijo se uporablja 4 točkovna integracijska shema (Tabela 2.3).

Štirikotni DK element ima štiri vozlišča v ogliščih štirikotnika s prostostnimi stopnjami $\hat{\boldsymbol{u}}_I = [\hat{w}_I, \hat{\theta}_{xI}, \hat{\theta}_{yI}]$. Interpolacijske funkcije so definirane v koordinatnem sistemu $(\xi, \eta) \in [-1, +1] \times [-1, +1]$:

I	1	2	3	4
IJ	12	23	34	41
r	ξ	η	ξ	η
s	η	ξ	η	ξ
p_r	+1	+1	-1	-1
p_s	+1	-1	-1	+1

$$N_I = (1 - p_r r)(1 - p_s s)/4;$$
$$N_{IJ} = (1 - r^2)(1 - p_s s)/2;$$
$$M_{IJ} = p_r r(1 - r^2)(1 - p_s s)/2$$

Koordinate in uteži w_i Gaussove integracijske sheme 2×2, ki se uporablja za izračun togostne matrike in obtežnega vektorja, so navedene v Tabeli 2.4.

V razdelku 2.4 so predstavljeni izbrani računski primeri, ki prikazujejo učinkovitost razvitih končnih elementov za opis glavnih značilnosti rešitev upogiba tankih plošč.

10.4.2 Srednje debele plošče

Teorija upogiba srednje debelih plošč v nasprotju s teorijo, ki velja za tanke plošče, ne gradi na predpostavki, da je prečna strižna deformacija plošč zanemarljiva. V tem smislu dopušča dodatne deformacijske načine. Sprostitev predpostavk Kirchhoffove teorije sta prva izvedla [Reissner, 1945] in [Mindlin, 1951]. Teorijo srednje debelih plošč zato imenujemo Reissner/Mindlinova teorija. Pri tem obstaja analogija med Euler-Bernoullijevo in Timošenkovo teorijo nosilcev ter Kirchhoffovo in Reissner/Mindlinovo teorijo plošč.

Najpomembnejša razlika je, da zasuki niso več popolnoma določeni s pomikom nevtralne ploskve, temveč so od pomika neodvisni. Ena od posledic je, da ni več zahtevana zveznost zasukov. Mogoče najzanimivejša posledica te dodatne svobode je obstoj t.i. robnih območij, področij blizu roba plošče, kjer prihaja do hitrih in velikih sprememb rezultante momenta m_n in strižnih sil. Robna območja pa niso le posledica predpostavk Reissner/Mindlinove teorije plošč, temveč so dejanski fizikalni pojav.

Glavne predpostavke Reissner/Mindlinove teorije so: (i) normala na prvotno referenčno nevtralno ploskev ostaja ravna tudi po deformaciji, čeprav ni več nujno pravokotna na deformirano nevtralno ploskev, (ii) debelina plošče se med deformacijo ne spremeni in (iii) normalne napetosti so zanemarljive. Zadnji dve predpostavki se izključujeta, kar je lahko preveriti. Da bi obšla to nasprotje, sta Reissner in Mindlin vsak na svoj način prilagodila teorijo. Čeprav se teoriji konceptualno razlikujeta, pa obe dajeta praktično enake rezultate za prečne pomike, strižne sile in rezultante momentov v vseh realnih konstrukcijskih problemih. Osnovna posledica zgornjih predpostavk je dejstvo, da deformacije srednje debelih plošč ni mogoče opisati le s prečnim pomikom w in njegovimi odvodi. Kot neodvisno spremenljivko moramo vpeljati tudi zasuk materialnega vlakna $\boldsymbol{\theta}$.

Model

V nadaljevanju namesto zasukov $\boldsymbol{\theta}$ vpeljemo rotacijo $\boldsymbol{\phi}$ (glej Sliko 2.2.1), ki je definirana kot $\boldsymbol{\phi} = [\phi_x, \phi_y]^T = [-\theta_y, \theta_x]^T$. Kinematične relacije, ki povezujejo pomik w in zasuk $\boldsymbol{\phi}$ z ukrivljenostjo $\boldsymbol{\kappa}$ in prečnimi strižnimi deformacijami $\boldsymbol{\gamma}$ so:

$$\boldsymbol{\kappa} = [\kappa_{xx}, \kappa_{yy}, \kappa_{xy}]^T = [\frac{\partial \phi_x}{\partial x}, \frac{\partial \phi_y}{\partial y}, (\frac{\partial \phi_y}{\partial x} + \frac{\partial \phi_x}{\partial y})]^T$$
$$\boldsymbol{\gamma} = [\gamma_x, \gamma_y]^T = [\frac{\partial w}{\partial x} - \phi_x, \frac{\partial w}{\partial y} - \phi_y]^T$$

Ravnotežna enačba je bila izpeljana že v prejšnjem poglavju in tu samo ponovimo glavni rezultat:

$$\nabla \cdot \boldsymbol{q}_{eq} = -f$$

kjer so strižne sile izpeljane iz ravnotežja označene s $bmq_{eq} = [q_{x,eq}, q_{y,eq}]^T$. Hkrati velja (glej (2.2.18)):

$$\nabla \cdot \mathbf{M} = -\boldsymbol{q}_{eq}; \quad \mathbf{M} = \begin{bmatrix} m_{xx} & m_{xy} \\ m_{xy} & m_{yy} \end{bmatrix}$$

Konstitutivna zveza med ukrivljenostjo $\boldsymbol{\kappa}$ in momentom $\boldsymbol{m}$ je

$$\boldsymbol{m} = \mathbf{C}_B \boldsymbol{\kappa}$$

Strižne deformacije, ki jih izračunamo iz kinematičnih predpostavk so konstantne po debelini. Ravnotežne enačbe po drugi strani kažejo, da variacija strižnih napetosti po debelini mora obstajati. Pri homogenem preseku je variacija po debelini parabolična funkcija z. Strižne deformacije, ki izhajajo iz kinematike, so torej v nasprotju z ravnotežjem diferencialnega elementa. Za preseganje tega nasprotja se uvede strižni korekcijski faktor c, ki konstitutivni zakon, ki veže strižne sile in deformacije spremeni tako, da je zagotovljen korekten izračun strižne deformacijske energije:

$$\boldsymbol{q}_c = \mathbf{C}_S \boldsymbol{\gamma}; \quad \mathbf{C}_S = cGt\mathbb{1} = \frac{cEt}{2(1+\nu)}\mathbb{1} = \tilde{c}/t^2 D\mathbb{1}; \quad \mathbb{1} = \begin{bmatrix} 1 & 0 \\ 0 & 1 \end{bmatrix}$$

kjer je $G = E/2(1+\nu)$ strižni modul in $\tilde{c} = 6c(1-\nu)$. Za strižni korekcijski faktor c običajno vzamemo vrednost 5/6.

Reissner/Mindlinova teorija omogoča bogatejšo množico robnih pogojev, kot pri Kirchhoffovi teoriji. Najpomembnejša razlika je, da lahko na vsakem robu definiramo tri neodvisne komponente robne obtežbe (prečno strižno silo q ter rezultanti momenta m_n in m_s). Nekatere od možnosti so navedene v Tabeli 2.1.

Deformacija srednje debelih plošč je določena s sistemom sklopljenih diferencialnih enačb

$$\begin{aligned} \triangle\triangle w &= f/D - \frac{t^2}{D\tilde{c}}\triangle f \\ +\frac{t^2}{12c}\triangle\triangle\phi_x - (\phi_{x,y} - \phi_{y,x})_{,y} &= f_{,x}/D \\ +\frac{t^2}{12c}\triangle\triangle\phi_y + (\phi_{x,y} - \phi_{y,x})_{,x} &= f_{,y}/D \end{aligned}$$

Poznavajoč f, D, t in c in ustrezne robne pogoje, lahko iz zgornjega sistema izračunamo prečni pomik w in rotaciji ϕ_x ter ϕ_y.

Z uvedbo Marcusovega momenta $\underline{m} = D(\frac{\partial\phi_x}{\partial x} + \frac{\partial\phi_y}{\partial y})$, za katerega velja $\triangle\underline{m} = f$ ter zvitja, ki ga definiramo kot $\Omega = \frac{\partial\gamma_y}{\partial x} - \frac{\partial\phi_x}{\partial y}$ in za katerega lahko pokažemo, da velja $\Omega = \frac{\partial\phi_y}{\partial x} - \frac{\partial\phi_x}{\partial y} = \frac{t^2}{12c}\Omega$, dobimo alternativni sistem diferencialnih enačb za w, Ω ter $\underline{m}$

$$\triangle\triangle w = f/D - \frac{t^2}{D\tilde{c}}\triangle f; \quad \Omega = \frac{\partial\phi_y}{\partial x} - \frac{\partial\phi_x}{\partial y} = \frac{t^2}{12c}\Omega; \quad \triangle\underline{m} = f$$

ki je sklopljen preko robnih pogojev.

Rešitev Reissner/Mindlinove teorije lahko prikažemo kot razširitev rešitve Kirchhoffove teorije. Povezavo obravnavamo v razdelku 3.2.2.

Princip virtualnega dela za srednje debele plošče je izpeljan iz sistema diferencialnih enačb. V ravnovesju velja

$$\delta\Pi^{int}(w, \boldsymbol{\theta}; \delta w, \delta\boldsymbol{\theta}) = \delta\Pi^{ext}(\delta w, \delta\boldsymbol{\theta})$$

kjer je

$$\delta\Pi^{int}\left(w,\boldsymbol{\theta};\delta w,\delta\boldsymbol{\theta}\right)=\int_{\Omega}\left(\delta\boldsymbol{\kappa}^{T}\boldsymbol{m}+\delta\boldsymbol{\gamma}^{T}\boldsymbol{q}\right)\,\mathrm{d}\Omega$$

in

$$\delta\Pi^{ext}\left(\delta w,\delta\boldsymbol{\theta}\right)=\int_{\Omega}f\,\delta w\,\mathrm{d}\Omega+\int_{\Gamma_q}\overline{q}\,u\mathrm{d}s+\int_{\Gamma_{m_n}}\overline{m}_n\vartheta_n\,\mathrm{d}s+\int_{\Gamma_{m_s}}\overline{m}_s\vartheta_s\,\mathrm{d}s$$

Robna območja

Robna območja so območja ob robu plošče, kjer se zasuki in rezultante napetosti hitro spreminjajo. Pojav je bil v literaturi obširno raziskan, zato na tem mestu povzemamo le glavne rezultate.

Bistvena razlika med Reissner/Mindlinovo in Kirchhoffovo teorijo je, da je rešitev slednje neodvisna od debeline plošče (razen seveda za konstantni faktor). Odvisnost rešitve Reissner/Mindlinove teorije od debeline plošče je kompleksna, vendar jo lahko obravnavamo kot perturbirano Kirchhoffovo rešitev. Iz relacij, zapisanih v razdelku 3.2.2, hitro prepoznamo, da je vir hitrih sprememb v rešitvi lahko le funkcija $\Omega=\phi_{x,y}-\phi_{y,x}$. Preostali funkciji Ψ in Φ, ki prispevata k razliki, sta namreč harmonični ($\triangle\Psi=0,\triangle\Phi=0$). Iz enačbe $\Omega=\frac{t^2}{12c}\triangle\Omega$ je razvidno, da člen na desni konvergira proti 0, ko gre $t\to 0$. V limiti velja Kirchhoffova predpostavka $\phi_{x,y}=\phi_{y,x}$. Hkrati je razvidno, da je širina robnega območja sormazmerna s $t/\sqrt{12c}$. Prečni pomik w kljub prisotnosti robnih območij ne izkazuje hitrih sprememb, saj ni neposredno odvisen od funkcije Ω, ki je edini izvor za hitre spremembe v robnem območju. Rešitev za prečni pomik w ter zasuka $\boldsymbol{\phi}$ lahko razvijemo v potenčno vrsto po debelini (3.2.38). Vodilni členi v razvoju so prikazani v Tabeli 3.2 in so odvisni od robnega pogoja. Mogoče nekoliko presenetljivo se pokaže, da je robno območje najizrazitejše pri prostem in mehko prosto podprtem robu. Druga skrajnost je vpeti rob, pri katerem robnega območja ni. Klub velikim gradientom pri tankih ploščah pa so vrednosti rezultant napetosti vedno končne in robno območje ni vzrok dodatnim singularnostim.

Podobno kakor pri tankih ploščah, tudi pri srednje debelih ploščah v določenih primerih pride do singularnosti v rezultantah napetosti. Običajno do singularnosti pride v vogalih plošče, ko je kot večji od nekega mejnega kota, ki je odvisen od robnih pogojev, ki veljajo v opazovanem vogalu. Mejni kot je sicer neodvisen od debeline plošče. Singularnost je omejena na neposredno okolico vogalne točke. Tabela 3.3 prikazuje eksponenta λ_1 in λ_2 za različne kote vogala za trdo in mehko prosto podprto ploščo.

Končni elementi

Končne elemente, ki ustrezajo Reissner/Mindlinovi teoriji, je bistveno lažje konstruirati, kot tiste, ki ustrezajo Kirchhoffovi teoriji in morajo ustrezati zahtevi po zvezni odvedljivosti interpolacije pomika. Bistvena razlika je tudi v dejstvu, da sta pomik w in zasuk $\boldsymbol{\phi}$ interpolirana neodvisno. Neodvisnost obeh interpolacij znatno olajša gradnjo končnega elementa. Hkrati morata biti interpolaciji izbrani zelo skrbno, da ne pride do pojava, ki mu običajno rečemo blokiranje ("locking"). Interpolacije, ki niso usklajene, namreč ne zmorejo opisati stanja z ničelno strižno deformacijo, kar povzroči, da v limiti tankih plošč, strižni deformacijski način prevlada nad upogibnim. Strižna deformacijska energija je namreč premosorazmerna debelini plošče, medtem ko je upogibna deformacijska energija sorazmerna tretji potenci debeline. V limiti tankih plošč je zato strižna deformacijska energija bistveno večja od upogibne. Prevladujoč del minimizacije potencialne energije je zato zmanjšanje strižne deformacijske energije, kar v limiti neskončno tanke plošče privede do pretogega odziva.

V nadaljevanju sta predstavljena trikotni in štirikotni element za plošče z oznako P3T in P3Q, ki sta grajena kot hierarhično nadaljevanje DK elementov. Elementa sta bila prvič predstavljena v [Ibrahimbegović, 1992] and [Ibrahimbegović, 1993]. V tem delu sta elementa izpeljana na novo, pri čemer je posebna pozornost namenjena skrbi, da se P3 elementa predstavi kot hierarhično nadgradnjo DK elementov.

Interpolacijo za pomik in rotacijo zapišemo po zgledu interpolacij za DK elemente. Spet se opremo na analogijo z nosilci. Tokrat namesto zahteve po ničelni strižni deformaciji vzdolž nosilca, predpišemo konstantno vrednost $\gamma_h = \frac{\partial w_h}{\partial x} - \theta_h = \hat{\gamma}_0 = const$. To nas pripelje do naslednjih vrednosti za parametre interpolacije 3.3.8:

$$\hat{w}_3 = +\frac{L}{8}(\hat{\theta}_1 - \hat{\theta}_2); \quad \hat{w}_4 = \frac{L}{4}(\frac{\hat{w}_2 - \hat{w}_1}{L} - \frac{1}{2}(\hat{\theta}_1 + \hat{\theta}_2)) - \frac{L}{4}\hat{\gamma}_0; \quad \hat{\theta}_3 = \frac{6}{L}\hat{w}_4$$

Interpolacijo pomika in zasuka za Timošenkov (TM) nosilec lahko predstavimo kot hierarhično razširitev interpolacije za Euler Bernoullijev (EB) nosilec:

$$w_h^{TM} = w_h^{EB} - \frac{L}{4}\hat{\gamma}_0 N_4; \qquad \theta_h^{TM} = \theta_h^{EB} + \frac{3}{2}\hat{\gamma}_0 N_3$$

kjer je interpolacija za EB podana v (2.3.57)-(2.3.58).

Po analogiji zapišemo interpolacijo za P3 elemente kot hierarhično razširitev interpo-

lacije za DK elemente (2.3.63):

$$w_h = w_h^{DK} - \sum_{IJ} \frac{1}{4} L_{IJ} \hat{\gamma}_{IJ} M_{IJ};$$
$$\boldsymbol{\theta}_h = \boldsymbol{\theta}_h^{DK} + \sum_{IJ} \frac{3}{2} \boldsymbol{n}_{IJ} \hat{\gamma}_{IJ} N_{IJ}$$

Strig vzdolž stranice IJ je označen z $\hat{\gamma}_{IJ}$, L_{IJ} je dolžina stranice IJ in $\boldsymbol{n}_{IJ}$ je normala na stranico IJ, glej Sliko 2.3.11. Podobnost med (3.3.9) in (3.3.10) je očitna.

P3 elementi imajo poleg vozlišč v ogliščih, kjer so definirane prostostne stopnje enake tistim za DK elemente $\hat{\boldsymbol{u}}_I = [\hat{w}_I, \hat{\theta}_{x,I}, \hat{\theta}_{y,I}]^T$, tudi vozlišča na sredini stranic, kjer so definirane prostostne stopnje $\hat{\boldsymbol{u}}_{IJ} = [\hat{\gamma}_{IJ}]$. Prostostna stopnja $\hat{\gamma}_{IJ}$ je enaka vrednosti strižne deformacije vzdolž stranice IJ. Elementi imajo nen vozlišč v ogliščih in nen vozlišč na sredini stranic (nen=4 za štirikotnike, in $nen = 3$ za trikotne elemente). Oglišča so oštevilčena z $I = 1, \ldots, nen$, vozlišča na sredini stranic pa od $IJ = (nen + 1), \ldots, 2\,nen$. Prostostne stopnje elementa so zbrane v $\hat{\boldsymbol{u}} = [\hat{\boldsymbol{u}}_1^T, \cdots, \hat{\boldsymbol{u}}_{nen}^T, \hat{\boldsymbol{u}}_{nen+1}^T, \cdots, \hat{\boldsymbol{u}}_{2\,nen}]^T$.

V matrični notaciji interpolacije P3 elementov zapišemo z

$$w_h = \mathbf{N}_w \hat{\boldsymbol{u}} = \sum_I \mathbf{N}_{w,I} \hat{\boldsymbol{u}}_I + \sum_{IJ} \mathbf{N}_{w,IJ} \hat{\boldsymbol{u}}_{IJ}; \qquad \mathbf{N}_{w,IJ} = -\frac{L_{IJ}}{4} M_{IJ}$$
$$\boldsymbol{\theta}_h = \mathbf{N}_\theta \hat{\boldsymbol{u}} = \sum_I \mathbf{N}_{\theta,I} \hat{\boldsymbol{u}}_I + \sum_{IJ} \mathbf{N}_{\theta,IJ} \hat{\boldsymbol{u}}_{IJ}; \qquad \mathbf{N}_{\theta,IJ} = +\frac{3}{2} \boldsymbol{n}_{IJ} N_{IJ}$$

kjer so $\mathbf{N}_{w,I} = \mathbf{N}_{w,I}^{DK}$, $\mathbf{N}_{\theta,I} = \mathbf{N}_{\theta,I}^{DK}$ matrike, ki so bile definirane pri obravnavi DK elementov, glej (2.3.63)-(2.3.66). Dodatni členi interpolacij (3.3.11) in (3.3.12) so odvisni le od prostostnih stopenj na sredini stranic, ki so zbrane v $\hat{\boldsymbol{u}}_{IJ}$. Vektor ukrivljenosti $\boldsymbol{\kappa}_h$ izračunamo direktno iz $\boldsymbol{\theta}_h$:

$$\boldsymbol{\kappa}_h = \mathbf{B}_\kappa \hat{\boldsymbol{u}} = \sum_I \mathbf{B}_{\kappa,I} \hat{\boldsymbol{u}}_I + \sum_{IJ} \mathbf{B}_{\kappa,IJ} \hat{\boldsymbol{u}}_{IJ}$$

Matrika $\mathbf{B}_{\kappa,I}$ je enaka matriki DK elementa, ki je definirana v (2.3.68): $\mathbf{B}_{\kappa,I} = \mathbf{B}_{\kappa,I}^{DK}$. Interpolacijo ukrivljenosti tako lahko zapišemo: $\boldsymbol{\kappa}_h = \boldsymbol{\kappa}_h^{DK} + \tilde{\boldsymbol{\kappa}}_h$, kjer je $\tilde{\boldsymbol{\kappa}}_h$ del, ki je odvisen le od $\hat{\boldsymbol{u}}_{IJ}$:

$$\tilde{\boldsymbol{\kappa}}_h = \sum_{IJ} \mathbf{B}_{\kappa,IJ} \hat{\boldsymbol{u}}_{IJ};$$
$$\mathbf{B}_{\kappa,IJ} = \frac{3}{2} \left[-n_{IJ,y} N_{IJ,x}, +n_{IJ,x} N_{IJ,y}, n_{IJ,x} N_{IJ,x} - n_{IJ,y} N_{IJ,y}\right]^T$$

Čeprav so bile interpolacije za w_h in $\boldsymbol{\theta}_h$ konstruirane tako, da je strižna deformacija vzdolž stranic konstantna in kot taka lahko tudi enaka nič, kljub temu ni sposobna opisa

čiste upogibne deformacije brez dodatnih motenj v obliki strižne deformacije. Zato je blokiranje elementa še vedno prisotno. Robustno in učinkovito zdravilo za blokiranje elementa je pristop s predpostavljenim poljem strižne deformacije (assumed shear strain approach). Strižno deformacijo interpoliramo kot bilinearno interpolacijo

$$\boldsymbol{\gamma}_h = \sum_I N_I \hat{\boldsymbol{\gamma}}_{h,I} = \sum_{IJ} \mathbf{B}_{\gamma,IJ} \hat{\boldsymbol{u}}_{IJ} = \mathbf{B}_\gamma \hat{\boldsymbol{u}}$$

kjer so $\hat{\boldsymbol{\gamma}}_{h,I}$ vozliščni parametri interpolacije prečne strižne deformacije in N_I standardne Lagrangeove interpolacijske funkcije. Parametri $\hat{\boldsymbol{\gamma}}_{h,I}$ so izbrani tako, da so v skladu z vrednostmi $\hat{\gamma}_{IJ}$, ki določajo konstantno vrednost strižne deformacije vzdolž stranice IJ. V vozlišču I, kjer se stikata stranici IJ in IK, so vozliščni parametri $\hat{\boldsymbol{\gamma}}_{h,I}$ izbrani tako, da projekcije $\hat{\boldsymbol{\gamma}}_{h,I}$ na stranici IJ in IK ustrezajo vrednostim $\hat{\gamma}_{IJ}$ in $\hat{\gamma}_{IK}$ zaporedoma (glej Sliko 3.3.1):

$$\hat{\boldsymbol{\gamma}}_{h,I} \cdot \boldsymbol{s}_{IJ} = \hat{\gamma}_{IJ}; \quad \hat{\boldsymbol{\gamma}}_{h,I} \cdot \boldsymbol{s}_{IK} = \hat{\gamma}_{IK}$$

Rešitev linearnega sistema je:

$$\hat{\boldsymbol{\gamma}}_{h,I} = \frac{\hat{\gamma}_{IK} \boldsymbol{n}_{IJ} - \hat{\gamma}_{IJ} \boldsymbol{n}_{IK}}{\boldsymbol{n}_{IJ} \cdot \boldsymbol{s}_{IK}}$$

Vozliščne vrednosti strižne deformacije $\hat{\boldsymbol{\gamma}}_{h,I}$ so odvisne le od vrednosti $\hat{\gamma}_{IJ}$. Posledično je interpolacija $\boldsymbol{\gamma}_h$ odvisna le od $\hat{\boldsymbol{u}}_{IJ}$:

$$\boldsymbol{\gamma}_h = \sum_{IJ} \mathbf{B}_{\gamma,IJ} \hat{\boldsymbol{u}}_{IJ}$$

Strižna togostna matrika $\mathbf{K}^S$ je definirana v 3.3.21 in 3.3.23.

Eksplicitna oblika matrike $\mathbf{B}_{\gamma,IJ}$, ki se nanaša na stranico IJ, je:

$$\mathbf{B}_{\gamma,IJ} = \left(N_J \frac{\boldsymbol{n}_{JK}}{\boldsymbol{n}_{JK} \cdot \boldsymbol{s}_{IJ}} - N_I \frac{\boldsymbol{n}_{HI}}{\boldsymbol{n}_{IJ} \cdot \boldsymbol{s}_{HI}} \right)$$

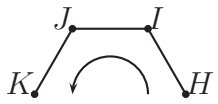

Zgornja izvajanja veljajo tako za štirikotne, kot tudi trikotne elemente. Interpolacijske funkcije N_I, N_{IJ} ter M_{IJ} so enake tistim, ki so uporabljene pri DK elementih.

Parametri $\hat{\boldsymbol{\gamma}}_{IJ}$, ki so definirani v vozliščih na sredini robov, otežujejo praktično uporabo P3 elementov. Zato jih obravnavamo kot neodvisne količine in jih odstranimo s pomočjo statične kondenzacije.

Parametri $\hat{\boldsymbol{\gamma}}_{IJ}$ pa ne vplivajo le na interpolacijo $\boldsymbol{\gamma}_h$, temveč tudi na $\boldsymbol{\kappa}_h$, saj velja

$$\boldsymbol{\kappa}_h = \mathbf{B}_\kappa \hat{\boldsymbol{u}} = \sum_I \mathbf{B}_{\kappa,I} \hat{\boldsymbol{u}}_I + \sum_{IJ} \mathbf{B}_{\kappa,IJ} \boldsymbol{n}_{IJ} \hat{\boldsymbol{\gamma}}_{IJ};$$

Prepoznamo, da so dodatni deformacijski načini definirani z $\mathbf{B}_{\kappa,IJ}\boldsymbol{n}_{IJ}$ in tedaj $\hat{\gamma}_{IJ}$ lahko interpretiramo kot njihove amplitude. Dodatne deformacijske načine obravnavmo kot nekompatibilne in jih izločimo s statično kondenzacijo. Da bi zagotovili, da element opravi "patch" test (glej [Ibrahimbegović, 1992]), moramo matriko $\mathbf{B}_{\kappa,IJ}$ spremeniti na naslednji način

$$\mathbf{B}_{\kappa,IJ} \mapsto \mathbf{B}_{\kappa,IJ} - \frac{1}{\Omega^e}\int_{\Omega^e} \mathbf{B}_{\kappa,IJ}\mathrm{d}\Omega$$

Togostno matriko elementa reduciramo s standardnim postopkom statične kondenzacije. Tako konstruirani elementi so označeni s PIT/PIQ.

Razdelek 3.4 obravnava vrsto različnih računskih primerov, ki prikazujejo učinkovitost izpeljanih končnih elementov P3 in PI. Posebna pozornost je namenjena računskim primerom, kjer je opazen razvoj robnih območij.

10.4.3 Debele plošče

Logični naslednik Reissner/Mindlinovega modela v hierarhiji modelov za upogib elastičnih izotropnih plošč, je model višjega reda, ki upošteva tudi deformacije vzdolž debeline. Model, ki je predstavljen v nadaljevanju, je poseben primer modela lupine, ki je predstavljen v [Brank, 2005] in [Brank et al., 2008]. Ploščo obravnava kot 2d ploskev v polnem trirazsežnem napetostnem stanju. To je ugodno, ker ni več potrebno uporabljati poenostavljenih 3d konstituvnih relacij, ki izhajajo iz predpostavke ravninskega napetostnega stanja. Prav tako so robna območja, ki so polni 3d pojav, bistveno bolje obravnavana z modeli višjega reda. Model za debele plošče je umeščen med Reissner/Mindlinov model in 3d model, zaradi česar je primeren za uporabo v postopku prilagodljivega modeliranja. V nadaljevanju je predstavljen model višjega reda za opis deformacij debelih plošč in končni element, ki temelji na razvitem modelu.

Model

Gradnjo interpolacije začnemo z opustitvijo predpostavke o ničelni normalni napetosti: $\sigma_{zz} \neq 0$. V primeru 3d linearne elastičnosti tako velja:

$$\sigma_{zz} = (\lambda + 2\mu)\varepsilon_{zz} + \lambda(\varepsilon_{xx} + \varepsilon_{yy}) \neq 0$$

z $\lambda = \frac{\nu E}{(1+\nu)(1-2\nu)}$, $\mu = \frac{E}{2(1+\nu)}$ kot Lamé-jevimi koeficienti. Kakorkoli, v limiti $t \to 0$ velja predpostavka o ravninskem napetostnem stanju

$$\varepsilon_{zz} = -\frac{\lambda}{\lambda + 2\mu}(\varepsilon_{xx} + \varepsilon_{yy})$$

Tovrstno limitno obnašanje je mogoče le, če so vse komponente deformacije ε_{xx}, ε_{yy}, ε_{zz} enakega reda glede na koordinato z. Le v tem primeru se lahko v zgornjem izrazu za σ_{zz} členi medsebojno odštejejo. Če sta npr. ε_{xx}, ε_{yy} linearni funkciji koordinate z, mora biti taka tudi komponenta ε_{zz}. Če naj bo ε_{zz} linearna funkcija z, potem mora biti pomik v smeri u_z najmanj kvadratična funkcija z, ker velja $\varepsilon_{zz} = \frac{\partial u_z}{\partial z}$.

Kinematiko pomikov debele plošče zapišemo z

$$\boldsymbol{u} = \boldsymbol{u}^{RM} + \boldsymbol{u}^{S}$$

kjer $\boldsymbol{u}^{RM}$ označuje kinematiko Reissner/Mindlinovega modela

$$\boldsymbol{u}^{RM} = w\boldsymbol{n}_\Omega - z\boldsymbol{\phi}; \quad \boldsymbol{n}_\Omega = [0,0,1]^T$$

in $\boldsymbol{u}^S$ označuje pomike, ki povzročijo deformacije po debelini (glej Sliko 4.2.1)

$$\boldsymbol{u}^S = \left((\bar{t}/t - 1)z - \kappa_{zz}z^2/2\right)\boldsymbol{n}_\Omega = \left(\varepsilon_{zz}^{(0)}z - \varepsilon_{zz}^{(1)}z^2/t\right)\boldsymbol{n}_\Omega$$

Komponenta $\boldsymbol{u}^S$ je kvadratična funkcija z koordinate: $\bar{t}$ je debelina deformirane plošče, t je debelina plošče pred deformacijo in $\kappa_{zz} = \varepsilon_{zz}^{(1)}2/t$ je parameter deformacije, kjer je $\boldsymbol{n}_\Omega$ normala na nevtralno ploskev pred deformacijo. Smer $\boldsymbol{u}^S$ ustreza smeri $\boldsymbol{n}_\Omega$. Relativna sprememba debeline je označena z $\varepsilon_{zz}^{(0)} = \bar{t}/t - 1$.

Komponente pomika $w = [u_x, u_y, u_z]^T$ so tako:

$$u_x = -z\phi_x; \quad u_y = -z\phi_y; \quad u_z = w + \varepsilon_{zz}^{(0)}z - \varepsilon_{zz}^{(1)}z^2/t$$

in deformacije, ki iz njih izhajajo (4.2.3) so

$$\begin{aligned}
\varepsilon_{xx} &= -z\kappa_{xx}; & 2\varepsilon_{xy} &= -z\kappa_{xy} \\
\varepsilon_{yy} &= -z\kappa_{yy}; & 2\varepsilon_{xz} &= \gamma_x + \varepsilon_{zz,x}^{(0)}z - \varepsilon_{zz,x}^{(1)}z^2/t \\
\varepsilon_{zz} &= \varepsilon_{zz}^{(0)} - 2z\varepsilon_{zz}^{(1)}/t = \varepsilon_{zz}^{(0)} - z\kappa_{zz}; & 2\varepsilon_{yz} &= \gamma_y + \varepsilon_{zz,y}^{(0)}z - \varepsilon_{zz,y}^{(1)}z^2/t
\end{aligned}$$

kjer so uporabljene definicije iz poglavij o tankih in srednje debelih ploščah:

$$\begin{aligned}
\kappa_{xx} &= \phi_{x,x}; & \gamma_x &= w_{,x} - \phi_x \\
\kappa_{yy} &= \phi_{y,y}; & \gamma_y &= w_{,y} - \phi_y \\
\kappa_{xy} &= \phi_{x,y} + \phi_{y,x}
\end{aligned}$$

Po analogiji z upogibnimi deformacijskimi členi, ki so sorazmerni s koordinato z, smo v (4.2.4) uvedli "ukrivljenost" κ_{zz}:

$$\kappa_{zz} = \varepsilon_{zz}^{(1)}/(t/2)$$

Hookove relacije za linearno elastični material so:

$$\sigma_{xx} = (\lambda + 2\mu)\varepsilon_{xx} + \lambda\varepsilon_{yy} + \lambda\varepsilon_{zz}; \qquad \sigma_{xy} = 2\mu\varepsilon_{xy}$$
$$\sigma_{yy} = (\lambda + 2\mu)\varepsilon_{yy} + \lambda\varepsilon_{xx} + \lambda\varepsilon_{zz}; \qquad \sigma_{xz} = 2\mu\varepsilon_{xz}$$
$$\sigma_{zz} = (\lambda + 2\mu)\varepsilon_{zz} + \lambda\varepsilon_{xx} + \lambda\varepsilon_{yy}; \qquad \sigma_{yz} = 2\mu\varepsilon_{yz}$$

Ravnotežne enačbe upoštevamo v šibki obliki z uporabo rezultant napetosti:

$$m_{xx} = \int_{-t/2}^{t/2} z\sigma_{xx}\mathrm{d}z; \qquad m_{yy} = \int_{-t/2}^{t/2} z\sigma_{yy}\mathrm{d}z; \qquad m_{xy} = \int_{-t/2}^{t/2} z\sigma_{xy}\mathrm{d}z$$
$$q_x = \int_{-t/2}^{t/2} \sigma_{xz}\mathrm{d}z; \qquad q_y = \int_{-t/2}^{t/2} \sigma_{yz}\mathrm{d}z$$
$$m_{zz} = \int_{-t/2}^{t/2} z\sigma_{zz}\mathrm{d}z; \qquad n_{zz} = \int_{-t/2}^{t/2} \sigma_{zz}\mathrm{d}z$$

Virtualno delo notranjih sil, ki upošteva tako kinematične kot tudi konstitutivne relacije, je definirano z

$$\delta\Pi^{int}(w, \boldsymbol{\phi}, \varepsilon_{zz}^{(0)}, \kappa_{zz}; \delta w, \delta\boldsymbol{\phi}, \delta\varepsilon_{zz}^{(0)}, \delta\kappa_{zz}) = \int_V \delta\boldsymbol{\varepsilon}^T\boldsymbol{\sigma}\mathrm{d}\Omega =$$
$$\int_\Omega \int_{-t/2}^{t/2} (\sigma_{xx}\delta\varepsilon_{xx} + \sigma_{yy}\delta\varepsilon_{yy} + \sigma_{zz}\delta\varepsilon_{zz} + \sigma_{xy}2\delta\varepsilon_{xy} + \sigma_{xz}2\delta\varepsilon_{xz} + \sigma_{yz}2\delta\varepsilon_{yz})\,\mathrm{d}z\mathrm{d}\Omega$$

kjer so $\boldsymbol{\sigma} = [\sigma_{xx}, \sigma_{yy}, \sigma_{zz}, \sigma_{xy}, \sigma_{xz}, \sigma_{yz}]^T$ definirani preko (4.2.4), (4.2.5) in (4.2.7) s kinematičnimi količinami in $\delta\boldsymbol{\varepsilon} = [\delta\varepsilon_{xx}, \delta\varepsilon_{yy}, \delta\varepsilon_{zz}, 2\delta\varepsilon_{xy}, 2\delta\varepsilon_{xz}, 2\delta\varepsilon_{yz}]^T$ so virtualne deformacije, ki so definirane z virtualnimi kinematičnimi količinami $\delta w, \delta\boldsymbol{\phi}, \delta\varepsilon_{zz}^{(0)}, \delta\kappa_{zz}$ na enak način, kot so realne deformacije definirane z realnimi kinematičnimi količinami (4.2.4), (4.2.7).

Po integraciji po debelini (4.2.8) dobimo naslednji izraz za virtualno delo notranjih sil (4.2.11)

$$\delta\Pi^{int} = \int_\Omega \left(\delta\tilde{\boldsymbol{\kappa}}^T\tilde{\boldsymbol{m}} + \delta\tilde{\boldsymbol{\gamma}}^T\tilde{\boldsymbol{q}} + \delta\varepsilon_{zz}^{(0)}n_{zz}\right)\mathrm{d}\Omega$$
$$\delta\Pi^{int} = \delta\Pi_\kappa^{int} + \delta\Pi_\gamma^{int} + \delta\Pi_{zz}^{int}$$
$$\delta\Pi_\kappa^{int} = \int_\Omega \delta\tilde{\boldsymbol{\kappa}}^T\tilde{\boldsymbol{m}}\,\mathrm{d}\Omega; \quad \delta\Pi_\gamma^{int} = \int_\Omega \delta\tilde{\boldsymbol{\gamma}}^T\tilde{\boldsymbol{q}}\,\mathrm{d}\Omega; \quad \delta\Pi_{zz}^{int} = \int_\Omega \delta\varepsilon_{zz}^{(0)}n_{zz}\,\mathrm{d}\Omega$$

kjer sta $\tilde{\boldsymbol{m}} = [m_{xx}, m_{yy}, m_{xy}, m_{zz}]^T$ in $\delta\tilde{\boldsymbol{\kappa}} = [\delta\kappa_{xx}, \delta\kappa_{yy}, \delta\kappa_{xy}, \delta\kappa_{zz}]^T$. Vektorja $\delta\tilde{\boldsymbol{\gamma}}$ in $\delta\tilde{\boldsymbol{q}}$ predstavljata virtualne deformacije in strižne sile.

Komponente $\tilde{\boldsymbol{m}}$ so povezane z ukrivljenostjo $\tilde{\boldsymbol{\kappa}} = [\kappa_{xx}, \kappa_{yy}, \kappa_{xy}, \kappa_{zz}]^T$ preko (konstitutivne (4.2.14) in kinematične (4.2.4) enačbe uporabimo v (4.2.9), (4.2.10))

$$
\begin{aligned}
m_{xx} &= \frac{t^3}{12}\left((\lambda+2\mu)\kappa_{xx} + \lambda\kappa_{yy} + \lambda\kappa_{zz}\right)\\
m_{yy} &= \frac{t^3}{12}\left((\lambda+2\mu)\kappa_{yy} + \lambda\kappa_{xx} + \lambda\kappa_{zz}\right)\\
m_{zz} &= \frac{t^3}{12}\left((\lambda+2\mu)\kappa_{zz} + \lambda\kappa_{xx} + \lambda\kappa_{yy}\right)\\
m_{xy} &= \frac{t^3}{12}\mu\kappa_{xy}
\end{aligned}
$$

Rezultanta napetosti n_{zz} je povezana z $\varepsilon_{zz}^{(0)}$ preko

$$
n_{zz} = t(\lambda+2\mu)\varepsilon_{zz}^{(0)} = \mathrm{C}_Z\varepsilon_{zz}^{(0)}; \quad \mathrm{C}_Z = t(\lambda+2\mu)
$$

Konstitutivne relacije zapišemo v kompaktni matrični obliki

$$
\tilde{\mathbf{C}}_B = \frac{t^3}{12}\begin{bmatrix} (\lambda+2\mu) & \lambda & 0 & \lambda \\ \lambda & (\lambda+2\mu) & 0 & \lambda \\ 0 & 0 & \mu & 0 \\ \lambda & \lambda & 0 & (\lambda+2\mu) \end{bmatrix}
$$

kar omogoča, da izrazimo (4.2.12) strnjeno kot:

$$
\tilde{\boldsymbol{m}} = \tilde{\mathbf{C}}_B\tilde{\boldsymbol{\kappa}}
$$

Virtualno delo notranjih sil (4.2.11) izrazimo kot hierarhično razširitev:

$$
\delta\Pi^{int} = \delta\Pi_{\kappa}^{int} + \delta\Pi_{\gamma}^{int} + \delta\Pi_{zz}^{int} = \delta\Pi^{int,RM} + \delta\Pi_{\kappa}^{int,\Delta} + \delta\Pi_{\gamma}^{int,\Delta} + \delta\Pi_{zz}^{int}
$$

kjer je

$$
\delta\Pi^{int,RM} = \int_{\Omega}\left(\delta\boldsymbol{\kappa}^T\mathbf{C}_B\boldsymbol{\kappa} + \delta\boldsymbol{\gamma}^T\mathbf{C}_S\boldsymbol{\gamma}\right)\mathrm{d}\Omega = \delta\Pi_{\kappa}^{int,RM} + \delta\Pi_{\gamma}^{int,RM}
$$

$\delta\Pi_{\gamma}^{int,\Delta}$ je podan v (4.2.28), $\delta\Pi_{\kappa}^{int,\Delta}$ v (4.2.8) in $\delta\Pi_{zz}^{int}$ v (4.2.11).

Zunanje sile delujejo na površine plošče: zgornjo in spodnjo površino (označeni sta z Ω^+ in Ω^-) ter stransko površino, ki jo označimo z Γ. Virtualno delo zunanjih sil je tako

$$
\delta\Pi^{ext} = \delta\Pi^{ext,\Omega} + \delta\Pi^{ext,\Gamma}
$$

Predpostavimo, da je robna obtežba $\overline{\boldsymbol{t}}$ konstantna po debelini, zato jo lahko integriramo in predstavimo kot rezultante momenta $\overline{m}_n$, $\overline{m}_s$ in strižne sile $\overline{q}_n$:

$$
\delta\Pi^{ext,\Gamma}(\delta w, \delta\boldsymbol{\phi}) = \int_{\Gamma}\int_{-t/2}^{t/2}\delta\boldsymbol{u}^T\overline{\boldsymbol{t}}\,\mathrm{d}z\,\mathrm{d}s =
$$

$$
\int_{\Gamma}(\delta w\overline{q}_n + \delta\theta_n\overline{m}_n + \delta\theta_s\overline{m}_s)\mathrm{d}s = \int_{\Gamma}(\delta w\bar{q}_n + \delta\boldsymbol{\theta}\,\overline{\boldsymbol{m}})\,\mathrm{d}s
$$

Ker v modelu višjega reda razlikujemo zgornjo (+) in spodnjo površino (-) plošče, ploskovna obtežba v splošnem lahko deluje na obe površini (upoštevajoč, da velja $u_z = w + \varepsilon_{zz}^{(0)} z - \frac{1}{2}\kappa_{zz} z^2$)

$$\delta\Pi^{ext,\Omega}(\delta w, \delta\varepsilon_{zz}^{(0)}, \delta\kappa_{zz}) = \int_{\Omega^+} f^+ \delta u_z^+ \,\mathrm{d}\Omega + \int_{\Omega^-} f^- \delta u_z^- \,\mathrm{d}\Omega + =$$
$$\int_{\Omega^+} f^+(\delta w + \frac{t}{2}\delta\varepsilon_{zz}^{(0)} - \frac{t^2}{8}\delta\kappa_{zz})\mathrm{d}\Omega + \int_{\Omega^-} f^-(\delta w - \frac{t}{2}\delta\varepsilon_{zz}^{(0)} - \frac{t^2}{8}\delta\kappa_{zz})\mathrm{d}\Omega$$

Končni element

Iz principa virtualnega dela izpeljemo končni element, ki ga označimo z oznako PZ, katerega interpolacija je grajena na osnovi interpolacije P3 elementa.

Prečni pomik w ter zasuk $\boldsymbol{\phi}$ interpoliramo na popolnoma enak način kot pri P3 elementu. Dodatno je potrebno interpolirati polji $\varepsilon_{zz}^{(0)}$ in $\kappa_{zz}^{(1)}$. Za obe uporabimo bilinearno interpolacijo:

$$\varepsilon_{zz,h}^{(0)} = \sum_I N_I \hat{\varepsilon}_{zz,I}^{(0)}; \quad \kappa_{zz,h}^{(1)} = \sum_I N_I \hat{\kappa}_{zz,I}^{(1)}$$

kjer so $\hat{\varepsilon}_{zz,I}^{(0)}$ in $\hat{\kappa}_{zz,I}^{(1)}$ dodatne vozliščne prostostne stopnje. PZ element ima v vozliščih, ki se nahajajo v ogliščih elementa naslednje prostostne stopnje $\hat{\boldsymbol{u}}_I = [w_I, \theta_{x,I}, \theta_{y,I}, \varepsilon_{zz,I}^{(0)}, \kappa_{zz,I}^{(1)}]^T$. V vozliščih na sredini stranic ostaja prostostna stopnja $\hat{\boldsymbol{u}}_{IJ} = [\gamma_{IJ}]$. Elementi imajo nen vozlišč v ogliščih in nen na sredini robov (nen=4 za štirikotne elemente, in $nen = 3$ za trikotne elemente). Vozlišča v ogliščih so označena z $I = 1, \ldots, nen$, tista na sredini stranic pa z $IJ = (nen + 1), \ldots, 2\,nen$. Prostostne stopnje elementa uredimo v vektor $\hat{\boldsymbol{u}} = [\hat{\boldsymbol{u}}_1^T, \cdots, \hat{\boldsymbol{u}}_{nen}^T, \hat{\boldsymbol{u}}_{nen+1}^T, \cdots, \hat{\boldsymbol{u}}_{2\,nen}^T]^T$.

Interpolacije izrazimo v strnjeni obliki kot:

$$\boldsymbol{\kappa}_h = \sum_I \mathbf{B}_{\kappa,I}\hat{\boldsymbol{u}}_I + \sum_{IJ} \mathbf{B}_{\kappa,IJ}\hat{\boldsymbol{u}}_{IJ}; \qquad \boldsymbol{\gamma}_h = \sum_{IJ} \mathbf{B}_{\gamma,IJ}\hat{\boldsymbol{u}}_{IJ};$$
$$\varepsilon_{zz,h}^{(0)} = \sum_I \mathbf{B}_{\varepsilon_{zz}^{(0)},I}\hat{\boldsymbol{u}}_I; \qquad \boldsymbol{\gamma}_h^{(1)} = \sum_I \mathbf{B}_{\gamma^{(1)},I}\hat{\boldsymbol{u}}_I;$$
$$\kappa_{zz,h}^{(1)} = \sum_I \mathbf{B}_{\kappa_{zz}^{(1)},I}\hat{\boldsymbol{u}}_I; \qquad \boldsymbol{\gamma}_h^{(2)} = \sum_I \mathbf{B}_{\gamma^{(2)},I}\hat{\boldsymbol{u}}_I + \sum_{IJ} \mathbf{B}_{\gamma^{(2)},IJ}\hat{\boldsymbol{u}}_{IJ}$$

kjer je

$$\boldsymbol{\kappa}_h = [\kappa_{xx,h}, \kappa_{yy,h}, \kappa_{xy,h}]^T; \quad \boldsymbol{\gamma}_h = [\gamma_{x,h}, \gamma_{y,h}]^T$$
$$\boldsymbol{\gamma}_h^{(1)} = \frac{t}{2}\left[\frac{\partial\varepsilon_{zz,h}^{(0)}}{\partial x}, \frac{\partial\varepsilon_{zz,h}^{(0)}}{\partial y}\right]^T; \quad \boldsymbol{\gamma}_h^{(2)} = \frac{t}{2}\left[\frac{\partial\varepsilon_{zz,h}^{(1)}}{\partial x}, \frac{\partial\varepsilon_{zz,h}^{(1)}}{\partial y}\right]^T$$

Pri uporabimo definicije iz razdelka 4.3.1.

Togostno matriko $\mathbf{K}$ PZ elementa dobimo z vstavljanjem diskretizacije (4.3.2) v (4.2.11), pri čemer upoštevamo konstitutivne relacije (4.2.13), (4.2.15) in (4.2.24). Sestavljena je iz treh delov, ki ustreza upogibni, strižni togosti in togosti pri deformaciji vzdož debeline:

$$\mathbf{K} = \mathbf{K}^B + \mathbf{K}^S + \mathbf{K}^Z$$

Togostno matriko izrazimo kot bločno matriko, kjer $\mathbf{K} = [\mathbf{K}_{ij}]$, kjer bloki $\mathbf{K}_{ij}$ ustrezajo interakciji prostostnih stopenj vozlišč i in j. Indeksi, ki se nanašajo na vozlišča v ogliščih, so označena z I in J. Z indeksoma IJ in KL so označena vozlišča na sredini stranic. Togostna matrika je organizirana kot:

$$\mathbf{K} = \begin{bmatrix} [\mathbf{K}_{I,J}] & [\mathbf{K}_{I,KL}] \\ [\mathbf{K}_{IJ,J}] & [\mathbf{K}_{IJ,KL}] \end{bmatrix}$$

Obtežni vektor je sestavljen iz treh delov $\boldsymbol{f} = \boldsymbol{f}_{f^+} + \boldsymbol{f}_{f^-} + \boldsymbol{f}_{\bar{t}}$, kjer je

$$\boldsymbol{f}_{f^\pm} = \int_{\Omega^e} f^\pm \left(\mathbf{B}_w \pm \frac{t}{2}\mathbf{B}_{\varepsilon_{zz}^{(0)}} + \frac{t^2}{8}\mathbf{B}_{\kappa_{zz}}\right)\mathrm{d}\Omega;$$
$$\boldsymbol{f}_{\bar{t}} = \int_{\Gamma_{Ne}} \left(\bar{q}\mathbf{B}_w + \overline{\boldsymbol{m}}^T\mathbf{B}_\theta\right)\mathrm{d}s$$

V razdelku 4.5 so obravnavani nekateri različni računski primeri, ki prikazujejo učinkovitost formulacije končnega elementa PZ za izračun odziva debelih plošč na zunanjo obtežbo.

10.5 Ocene napak

10.5.1 Napaka diskretizacije

Metoda končnih elementov je računska metoda, ki daje le približno rešitev danega robnega problema ([Zienkiewicz Taylor, 2000], [Ibrahimbegović, 2009]). Približek rešitve $\boldsymbol{u}_h$, ki ga dobimo z metodo končnih elementov, v nadaljevanju imenujemo *računska rešitev*.

Želja po oceni kvalitete računske rešitve v primerjavi s točno rešitvijo je zato dokaj naravna. Glavna razloga za oceno, kako blizu točni rešitvi je računska rešitev, sta: (i) nadzor nad natančnostjo računske rešitve in (ii) vodenje prilagodljive gradnje mreže, ki za dano število končnih elementov zagotovi optimalno rešitev po celotnem območju (glej [Ainsworth Oden, 2000], [Ladevèze Pelle, 2006], [Stein Ramm, 2003]). Nadzor na natačnostjo potrebujemo, da uspemo zagotoviti, da je računska rešitev znotraj vnaprej določenih meja napake. V kolikor želimo določiti stroge meje napake, za katere lahko jamčimo, govorimo o ocenah napake. Čeprav je poznavanje točnih meja napake zelo

zaželjeno, so po drugi strani take ocene običajno zelo konzervativne in lahko precenijo napako za več redov velikosti. Zelo dobro oceno velikosti napake dobimo s tako imenovanimi indikatorji napake ([Babuška Rheinboldt, 1978]), ki pa ne jamčijo meja. Ne le, da je izračun indikatorjev napake veliko lažji od izračuna strogih meja, se indikatorji napake bistveno bolje približajo dejanski napaki. Zato predstavljajo učinkovito in zanesljivo osnovo za prilagodljivo gradnjo mreže. Z drugimi besedami: indikatorje napake uporabljamo za učinkovit nadzor nad algoritmi za prilagodljivo mreženje, da dobimo optimalno natačnost računske rešitve z minimalnim številom prostostnih stopenj. V nadaljevanju se ocene napake vedno nanašajo le na indikatorje napake in ne razlikujemo striktno med ocenami meja napake in indikatorji napake.

Druga klasifikacija ocen napake diskretizacije zadeva način ocene: a priori ocene napake proti a posteriori načinom ocene napake. *A priori error ocene* se ukvarjajo z asimptotično oceno obnašanja napake glede na velikost končnih elementov h in stopnjo polinomske aproksimacije p. Ne zagotavljajo informacije od dejanski napaki računske rešitve. *A posteriori ocene* se za oceno napake zanašajo na postprocesiranje računske rešitve $\boldsymbol{u}_h$. V osnovi ločimo dve veliki skupini a posteriori ocen, ki temeljijo na (i) izračunu izboljšanih gradientov računske rešitve ter (ii) na izračunu residuala računske rešitve.

Ocene, ki temeljijo na izračunu izboljšanih gradientov računske rešitve so veliko popularnejše, predvsem na račun lažje implementacije. Posebej razširjena je metoda SPR (Superconvergent Patch Recovery), ki se zanaša na obstoj t.i. superkonvergenčnih točk, to je točk, kjer je konvergenca k točni rešitvi hitrejša kot sicer. Iz vrednosti računske rešitve, vzorčenih v teh točkah, se zgradi izboljšano (zvezno) polje gradientov rešitve. Tako izboljšano polje služi kot približek polju gradientov prave rešitve. Kot indikator napake služi energijska norma razlike med izboljšanimi gradienti in gradienti računske rešitve.

Metode, ki temeljijo na izračunu residuala računske rešitve so bodisi eksplicitne ali implicitne ([Ainsworth Oden, 2000], [Ladevèze Pelle, 2006], [Ladevèze Leguillon, 1983], [Stein Ramm, 2003], [Becher Rannacher, 2001]). Eksplicitne metode ocenijo napako z neposrednim izračunom norme residualov v notranjosti elementov ali z oceno gradientnih skokov na robovih elementov. Implicitne metode vključujejo tudi formulacijo ter izračun pomožnih robnih problemov, katerih rešitev je približek dejanske napake. Pomožni problemi so lokalni v smislu, da so definirani na končnih elementih ali krpah končnih elementov. Ključna pri ocenah te vrste je zagotovitev ustreznih robnih pogojev (Neumannovega tipa) za lokalne probleme.

Klasifikacija različnih a posteriori metod za oceno napake diskretizacije je prikazana na Sliki 5.1.1.

Zgoraj omenjene napake se vse ukvarjajo z globalno energijsko normo napake. Pri analizah s končnimi elementi je večkrat slučaj, da nas posebej zanima določena količina (npr. napetost v določeni točki). Za oceno napake teh količin so bili razvite metode za ciljno-orientirane ocene napake [Ainsworth Oden, 2000]. Ključna za oceno napake ciljne količine je definicija pomožnega problema, ki je dualen primarnemu problemu. Pomožni problem na nek način filtrira potrebno informacijo za točen izračun ocene napake ciljne količine. Kljub nedavnemu razmahu teh metod, ta metoda ocene napake ni obravnavana v tem delu.

Napaka diskretizacije je definirana kot razlika med točno rešitvijo $\boldsymbol{u}$ ter računsko rešitvijo $\boldsymbol{u}_h$

$$\boldsymbol{e}_h = \boldsymbol{u} - \boldsymbol{u}_h$$

Ta definicija je lokalna, saj se nanaša na določeno točko območja. Da bi dobili globalno oceno napake, izračunamo energijsko normo napake:

$$\|\boldsymbol{e}_h\|_E^2 = a(\boldsymbol{e}_h, \boldsymbol{e}_h)$$

Integral po območju Ω_h razdelimo v prispevke po elementih Ω_h^e:

$$\|\boldsymbol{e}_h\|_E^2 = \sum_e \|\boldsymbol{e}_{e,h}\|_E^2$$

SPR in EqR metodi za oceno napake diskretizacije

V nadaljevanju je podan kratek povzetek dveh metod za oceno napake diskretizacije, ki ju podrobneje obravnavamo v nadaljevanju. Napako v obeh primerih ocenimo iz ocene za gradiente točne rešitve $\boldsymbol{\sigma}^*$ (napetosti) po

$$\|\boldsymbol{e}^*\|_E^2 = \int_{\Omega_h} (\boldsymbol{\sigma}^* - \boldsymbol{\sigma}_h)^T \mathbf{C}^{-1} (\boldsymbol{\sigma}^* - \boldsymbol{\sigma}_h)\, \mathrm{d}\Omega$$

kjer so $\boldsymbol{\sigma}$ gradienti točne rešitve in matrika $\mathbf{C}$ predstavlja splošno konstitutivno matriko. Integral v (5.3.3) razbijemo v prispevke po elementih

$$\|\boldsymbol{e}^*\|_E^2 = \sum_e \eta_e^2; \quad \eta_e^2 = \sum_e \int_{\Omega_h^e} (\boldsymbol{\sigma}^* - \boldsymbol{\sigma}_h)^T \mathbf{C}^{-1} (\boldsymbol{\sigma}^* - \boldsymbol{\sigma}_h)\, \mathrm{d}\Omega$$

kjer je $\|\boldsymbol{e}^*\|_E^2$ indikator globalne napake, izražen kot vsota lokalnih ocen napake η_e^2.

Bistvena značilnost metode SPR je, da zgradi izboljšano rešitev za gradiente rešitve na podlagi vrednosti, ki jih iz računske rešitve odčita v t.i. superkonvergenčnih točkah $\boldsymbol{\sigma}_h(\boldsymbol{\xi}_{gp})$. V okolici vsakega vozlišča po metodi najmanjših kvadratov določimo polinomsko aproksimacijo, ki je najbližje izračunanim vrednostim v superkonvergenčnih točkah, ki so izbranemu vozlišču najbližje. Izboljšano vrednost gradientov v vozlišču $\boldsymbol{\sigma}_i^*$ odčitamo iz tako zgrajene polinomske aproksimacije. Zvezno interpolacijo gradientov $\boldsymbol{\sigma}^*$ v poljubni točki določimo tako, da na vsakem elementu zgradimo linearno interpolacijo, katerih parametri so izboljšane vrednosti $\boldsymbol{\sigma}_i^*$ v vozliščih $\boldsymbol{\sigma}^* = \sum_i \boldsymbol{\sigma}_i^* N_i$. Povzetek izračuna ocene napake diskretizacije po metodi SPR je podan v Algoritmu 1:

1. Določi računsko rešitev $\boldsymbol{u}_h$ problema (5.2.4) ter izračunaj $\boldsymbol{\sigma}_h(\boldsymbol{x}_{gp})$ v superkonvergenčnih točkah $\boldsymbol{x}_{gp}$
2. Izberi interpolacijo (5.3.10) vsake komponente $\bar{\sigma}_k^*$ v okolici vozlišča i
3. Izračunaj $[M_{ij}]$ ter $[b_i]$ iz (5.3.14)
4. Reši (5.3.14) za $\boldsymbol{a}_k$
5. Določi $\boldsymbol{\sigma}_i^*$ iz (5.3.12)
6. Iz interpolacije (5.3.2) določi $\boldsymbol{\sigma}^*$

Pri EqR metodi izboljšano rešitev določimo na podlagi rešitev lokalnih robnih problemov. Lokalne robne probleme običajno formuliramo na končnih elementih, ki so po robu obremenjeni z Neumannovimi robnimi pogoji. Ključni element EqR metode je določitev robnih pogojev za posamezne končne elemente. Določimo jih tako, da je lokalna rešitev na izbranem elementu z danimi robnimi pogoji enaka originalni računski rešitvi na istem elementu, če računamo z istim končnim elementom. S to zahtevo hkrati poskrbimo za to, da so robni pogoji zvezni na vsakem robu in uravnoteženi z delovanjem zunanje obtežbe. Preostane še zadnji korak: izračun rešitev lokalnih robnih problemov z izboljšano diskretizacijo. Glavni koraki metode EqR so definirani v Algoritmu 2:

1. Določi računsko rešitev $\boldsymbol{u}_h$ problema (5.2.4)
2. Izračunaj uravnoteženo robno obtežbo lokalnih problemov $\boldsymbol{t}_\Gamma^e$ za vsak rob $\Gamma \subset \Gamma^e$ vsakega elementa e (glej Algoritem 3)
3. Približno reši lokalni problem (5.4.28) za $\tilde{\boldsymbol{u}}_{e,h^+}$ z uporabo testnega prostora $\mathcal{V}_{h^+}$ kot izboljšanega približka k testnemu prostoru $\mathcal{V}_h$

4. Izračunaj lokalni indikator napake η_e^2 iz (5.4.24) in $\boldsymbol{\vartheta}_{e,h} = \tilde{\boldsymbol{u}}_{e,h^+} - \boldsymbol{u}_{e,h}$

Izračun uravnotežene robne obtežbe za lokalne robne probleme na elementih poteka posamično po vseh krpah elementov okrog vseh vozlišč mreže. Najprej izračunamo vozliščne residuale elementov (vozliščne reakcije elementa) $\boldsymbol{R}_I^e$ iz računske rešitve $\boldsymbol{u}_h$. Na podlagi preproste ocene določimo prvi približek obtežbe po robovih elementov $\tilde{\boldsymbol{t}}_\Gamma^e$, ki jo integriramo po principu virtualnega dela v projekcije $\tilde{\boldsymbol{r}}_{I,\Gamma}^e$. Izberemo vozlišče I in iz $\boldsymbol{R}_I^e$ ter projekcij $\tilde{\boldsymbol{r}}_{I,\Gamma}^e$ za vse elemente krpe elementov, ki se stikajo v vozlišču I, zgradimo linearni sistem za neznane projekcije $\boldsymbol{r}_{I,\Gamma}^e$. Ko rešimo vse linearne sisteme za vsa vozlišča mreže, dobimo za vsak rob (med vozliščema I in J) projekciji $\boldsymbol{r}_{I,\Gamma}^e$ te $\boldsymbol{r}_{J,\Gamma}^e$. Projekciji izhajata iz še neznane robne obtežbe $\boldsymbol{t}_{IJ}^e$ iz principa virtualnega dela zunanjih sil. Ko izberemo primerno diskretizacijo $\boldsymbol{t}_{IJ}^e$, izračunamo projekcije obtežbe, ki jih izrazimo s parametri diskretizacije. Ker projekciji poznamo, lahko izračunamo parametre diskretizacije robne obtežbe in s tem določimo iskano robno obtežbo. Glavni koraki postopka uravnoteženja robnih obtežb so povzeti v (3):

1. Izračunaj $\boldsymbol{R}_I^e$ iz $\boldsymbol{u}_h$ in (5.4.32)
2. Konstruiraj $\tilde{\boldsymbol{t}}_\Gamma^e$ iz (5.4.40) ter (5.4.39)
3. Izračunaj projekcije $\tilde{\boldsymbol{r}}_{I,\Gamma}^e$ obtežbe $\tilde{\boldsymbol{t}}_\Gamma^e$ iz (5.4.37)
4. Oblikuj sisteme enačb za krpe elementov okrog vsakega vozlišča (5.4.35) in jih reši za neznanke $\boldsymbol{r}_{I,\Gamma}^e$ s pomočjo (5.4.38)
5. Izberi interpolacijski funkciji ψ_k^I, ψ_k^J za robno obtežbo $\boldsymbol{t}_\Gamma^e$ ter določi vozliščne parametre interpolacije $\boldsymbol{p}_{\Gamma,I}^e$ iz (5.4.43)
6. Izračunaj robne obtežbe iz (5.4.40)

V nadaljevanju poglavja 5 sta SPR in EqR metodi ilustrirani na preprostem 1d modelnem problemu viseče palice.

Poglavje 6 obravnava implementacijo EqR metode za DK in RM elemente. Podrobno so obravnavani vsi koraki EqR metode. Posebna pozornost je namenjena primerni izbiri diskretizacije robne obtežbe ter reševanju lokalnih robnih problemov. Pomembno spoznanje je, da mora biti diskretizacija, ki jo uporabimo pri reševanju lokalnih problemov, izboljšana glede na diskretizacijo, ki je bila uporabljena za določitev prvotne računske rešitve. Izboljšavo, oz. razširitev diskretizacije lahko izvedemo tako, da razdelimo element na manjše elemente, kjer uporabimo prvotno diskretizacijo. Tak pristop z različnimi

delitvami je bil preiskušen na primeru DK elementov (glej razdelek 6.2.3). Alternativno lahko za izboljšano diskretizacijo uporabimo tudi različen element, katerega stopnja polinomske aproksimacije je višja od prvotno uporabljenega. Tak pristop je bil preskušen s trikotnim elementom ARGY. Element uporablja polinomsko aproksimacijo petega reda z 21 prostostnimi stopnjami, kar je znatno več od 9 prostostnih stopenj pri DKT elementu, ki je bil uporabljen za originalni izračun.

Računski primeri prikazujejo izračun ocene napake po SPR in EqR metodi za izbrane probleme. Pri tem je analiziranih več različic metode EqR. Prikazana je primerjava ocen napake s pravo napako, ki jo izračunamo na podlagi primerjave računske rešitve s točno rešitvijo. Analiza pokaže, da so metode po učinkovitosti primerljive med seboj in nobena bistveno ne odstopa. Indeks učinkovitosti je blizu 1 za vse obravnavane metode.

Poglavje se zaključi z računskim primerom, ki za izbran problem prikazuje prilagodljivo generiranje mreže, katerega osnova so različne ocene napake. Učinkovitost različnih metod za oceno napake pri kontroliranju procesa prilagodljivega mreženja primerjamo z razporeditvijo napake po elementih. V idealnem primeru bi bila razporeditev napake po elementih enakomerna. Rezultati analize pokažejo, da različne metode ocene napak med seboj praktično nerazločljive, saj so histogrami razporeditve napak po elementih po prilagodljivem mreženju med seboj, vsaj na kvalitativni ravni, zelo podobni.

10.5.2 Ocena modelske napake

Za modeliranje izbranega fizikalnega pojava običajno ne uporabimo najpopolnejše obstoječe teorije, čeprav bi bila s stališča natančnosti najprimernejša. Vodilo pri izbiri modela je učinkovitost glede na zahtevano natančnost. Preden zgradimo model, moramo poznati zahteve za natančnost njegovih napovedi. Te namreč preverjamo z preskusi, katerih natančnost je vedno omejena. Izbira primernega modela je tesno povezana z inženirskim pristopom, ki zagovarja, da mora biti izbrani model preprost, kot je le mogoče in le tako zapleten, kot je potrebno. Ker vsak model sloni na določenih predpostavkah, moramo zagotoviti, da so njegove predpostavke izpolnjene z vnaprej predpisano natančnostjo. Veljavnost predpostavk je funkcija kraja, kar pomeni, da je veljavnost modela krajevno omejena. Cilj prilagodljivega modeliranja je identifikacija območij veljavnosti posameznega modela in določitev najprimernejšega modela (glede na predpisano natančnost) za vsako območje.

Ideja za postopno gradnjo optimalnega modela temelji na hierarhično urejeni družini modelov. čeprav modeli niso nujno zgrajeni na podlagi asimptotičnih principov, temveč

so večkrat skonstruirani na podlagi inženirskega uvida, Vsi modeli izhajajo iz iste teorije. Urediti jih je mogoče glede na število predpostavk, ki jih uporabljajo in posledično glede na ujemanje njihovih rezultatov z rezultati, ki jih napove teorija.

Pri gradnji optimalnega modela začnemo od spodaj navzgor z najpreprostejšim modelom ter poiščemo njegovo računsko rešitev. Iz rešitve na vsakem elementu ocenimo veljavnost njegovih predpostavk in s tem ocenimo modelsko napako. Na območju, kjer je napaka večja od predpisane napake, model zamenjamo z naslednjim modelom iz družine hierarhično urejenih modelov. Postopek ponavljamo, dokler v celotnem območju modelska napaka ne pade pod predpisano mejo. Ključen element opisane strategije za prilagodljivo modeliranje je ocena modelske napake. Ocena modelske napake mora biti čim natančnejša in učinkovita.

Modelsko napako najbolj neposredno in natančno ocenimo tako, da primerjamo izračun izbranega modela z izračunom referenčnega modela/teorije. Ker je reševanje referenčnega modela drago, se zadovoljimo s primerjavo z naslednjim boljšim modelom iz urejene družine modelov. Tak pristop je sprejemljiv, ker se zadovoljimo z oceno napake. Kljub temu je predlagan način ocene modelske napake neučinkovit, ker predvideva dvakratno reševanje celotnega problema. Namesto tega račun z izboljšanim modelom ponovimo le na posameznih manjših območjih - elementih. Pri tem moramo poskrbeti, da je rešitev lokalnih robnih problemov na elementih čim bližje globalni rešitvi. Robni pogoji za lokalne probleme so Neumannovega tipa in predstavljajo obtežbo po robu elementa. Osrednje vprašanje takega pristopa postane, kako določiti robno obtežbo lokalnih problemov na način, da bodo ti čim natančneje replicirali rezultate globalnega izračuna.

Idejo za konstrukcijo robnih obtežb lokalnih problemov najdemo pri EqR metodi, ki smo jo obravnavali v okviru ocene diskretizacijske napake. Spomnimo, da EqR metoda zgradi robne obtežbe za elemente tako, da rešitev lokalnih problemov natanko ustreza globalni rešitvi, če so za izračun lokalnih rešitev uporabljeni isti končni elementi, ki so bili uporabljeni za globalni izračun rešitve. Tak pristop uporabimo tudi za račun modelske napake, le da lokalni problem, namesto z izboljšano diskretizacijo, rešujemo z izboljšanim modelom.

V 7. poglavju je natančno opisan predstavljen koncept ocene modelske napake. Splošno so obravnavani vsi koraki konstruiranja lokalnih problemov po zgledu EqR metode. Bistvena je jasna ločitev med projekcijami obtežbe ter dejansko robno obtežbo, ki omogoča boljše razumevanje omejitev in morebitnih potencialov predlaganega pristopa.

V 8. poglavju je splošni koncept izračuna modelske napake implementiran za primer

ocene modelske napake za Kirchhoffov model. Ker je končni element DK, ki temelji na Kirchhoffovi teoriji, nekompatibilen, je dobro razumevanje postopka izračuna robnih obtežb za lokalne probleme ključno. Poglavje 8.2 je namenjeno predstavitvi celotnega postopka izračuna indikatorja modelske napake za DK elemente. Začne se z obravnavo interpolacij DK elementa po robovih elementa, ki so pomembne za izračun projekcij robnih obtežb. S parametrizacijo robne obtežbe (8.2.6) lahko zapišemo bistveno relacijo, ki preslikuje robno obtežbo (oz. njene parametre) $\boldsymbol{t}_\Gamma^e$ v projekcije v vozliščih (8.2.14).

Da bi dobili robno obtežbo, ki je čim bližje dejanski robni obtežbi, sistem enačb za izračun projekcij robne obtežbe (7.2.20) regulariziramo po postopku, ki je opisan v 8.2.1.

Lokalne probleme rešujemo z RM modelom, s P3 elementi. Ker so elementi DK in P3 delijo iste interpolacijske funkcije, obtežni vektor lokalnih problemov posebej preprost (8.2.24). Izkaže se, da obtežba v vozliščih, ki se nahajajo v ogliščih elementov, ostaja enaka obtežbi DK elementov, dodatna je le obtežba v sredini robov, ki je definirana v (8.2.25).

Ko izračunamo novo izboljšano rešitev na elementu, izračunamo deformacijsko energijo v skladu z

$$\begin{aligned} E^{RM,e} &= \int_\Omega^e \boldsymbol{m}^{RM,T}\, \mathbf{C}_B{}^{-1} \boldsymbol{m}^{RM}\, d\Omega + \int_\Omega^e \boldsymbol{q}^{RM,T}\, \mathbf{C}_S{}^{-1} \boldsymbol{q}^{RM}\, d\Omega \\ &= E_B^{RM,e} + E_S^{RM,e} \end{aligned} \tag{10.5.1}$$

kjer je $\boldsymbol{m}^{RM} = [m_{xx}, m_{yy}, m_{xy}]^T$ in $\boldsymbol{q}^{RM} = [q_x, q_y]^T$.

Tako DK kot tudi P3 elementa dajeta zelo podobne napovedi za rezultante momentov. Bistvena razlika med njima je v oceni strižnih sil, saj DK element striga ne vsebuje. Zato lahko strižno deformacijsko energijo $E_S^{RM,e}$ uporabimo za oceno veljavnosti predpostavke Kirchhoffovega modela. Indikator modelske napake v obliki

$$\eta_e^M = E_S^{RM,e} / E^{RM,e}$$

, ki meri delež strižne deformacijske energije v celotni deformacijski energiji, je zato smiseln, saj dobro povzema bistvene razlike med modeloma.

V nadaljevanju so predstavljeni nekateri računski primeri (razdelek 8.2.4, 8.2.4), ki obravnavajo nekaj problemov upogiba plošč, pri čemer je glavna pozornost namenjena izračunu indikatorja modelske napake. Primeri prikazujejo robustnost predlagane metode glede na različne mreže in debeline plošče. Izkaže se, da indikator modelske napake, čeprav sicer kaže dobro ujemanje z dejansko modelsko napako, ne zmore zaznati robnih območij, kjer pride do hitrih sprememb rezultant napetosti.

Zadnji računski primeri (razdelek razdelek 8.2.4, 8.2.4) prikazujejo primer prilagodljivega modeliranja, kjer je bil na podlagi ocene modelske napake zgrajen model, ki vsebuje tako DK, kot tudi P3 elemente. Območja, kjer so uporabljeni P3 elementi, so tista, kjer je presežen postavljen kriterij modelske napake. Z mešanim modelom je bila izračunana nova rešitev, ki smo jo primerjali s prvotno rešitvijo z DK elementi in rešitvijo, dobljeno s P3 elementi. Pri gradnji mešanega modela je bilo potrebno ustrezno obravnavati prostostne stopnje na stiku DK in P3 elementov.

10.6 Zaključek

Naloga se ukvarja z vprašanjem prilagodljivega modeliranja plošč. Čeprav je področje modeliranja plošč s končnimi elementi v svoji zreli fazi, razmislek pokaže, da so še vedno odprta fundamentalna vprašanja točnosti in zanesljivosti.

Pred obravnavo prilagodljivega modeliranja smo v poglavjih 2 in 3 najprej obravnavali dve osnovni teoriji plošč. V nadaljevanju je v poglavju 4 predstavljena nova teorija upogiba debelih plošč, ki je bila razvita z namenom gradnje hierarhično urejene družine modelov za plošče. Posebej so obravnavani pomembnejši pojavi, ki so značilni za upogib plošč. Na podlagi predstavljenih modelov je bila na novo razvita družina končnih elementov.

Diskretni Kirchhoffov element (DK), ki je med najpopularnejšimi elementi za analizo tankih plošč, smo reformulirali z uporabo alternativne formulacije, ki omogoča splošno obravnavo tako trikotnih kot tudi štirikonih elementov. Dodatno predstavljena formulacija DK elementov omogoča hierarhično (v modelskem smislu) konstrukcijo končnih elementov, ki so zasnovani na Reissner/Mindlinovi teoriji. Elementi, označeni s P3, so zgrajeni ko hierarhična razširitev DK elementov. Končni elementi, ki so zasnovani na teoriji višjega reda in dopuščajo deformacije po debelini plošč, pa so bili razviti na osnovi P3 elementa. Hierarhična konstrukcija omogoča, da se kljub naraščajoči kompleksnosti modelov, ohrani fizikalni vpogled v mehanizem deformacije.

Predstavljena sta tudi konformni trikotni element za plošče, kot tudi različica P3 elementa za Reissner/Mindlinov model, ki strižne deformacijske načine obravnava kot nekompatibilne načine. Vse predstavljene elemente smo implementirali v več računalniških programih in jih tudi testirali. Z več računskimi primeri je bila opravljena sistematična primerjava učinkovitosti elementov. Že sama primerjava tako predstavlja doprinos k področju modeliranja plošč s končnimi elementi.

Področje raziskave na področju ocene napake diskretizacije je aktivno in dandanes je na voljo veliko rezultatov, ki se ukvarjajo z napako na splošni ravni. V tem delu smo nekaj teh rezultatov uporabili na primeru modeliranja plošč s končnimi elementi. Pri uporabi dimenzijsko reduciranih modelov, ki so značilni za plošče, se pojavijo specifični numerični problemi (blokiranje). Pojavi, značilni za plošče, zahtevajo globlje razumevanje teorije ocene napak. Uporaba obstoječih metod za oceno napak v problemih upogiba plošč zato ni brez težav. Velik del raziskovalnega dela, ki je predstavljen v tem delu, se zato ukvarja z uspešno implementacijo metode EqR za DK končni element za plošče. Implementacija je zahtevna, med drugim tudi na povsem tehnični ravni: računski postopek vsebuje več korakov: (i) izračun uravnotežene robne obtežbe iz prvotne računske rešitve, (ii) definicija lokalnih robnih problemov na elementih, ki so obteženi po robu, (iii) rešitev lokalnih problemov z izboljšano diskretizacijo in (iv) izračun napake diskretizacije iz lokalnih rešitev.

Implementiranih je bilo več različic EqR metode: lokalni izračuni so bili izvedeni z več različnimi diskretizacijami. Izboljšanje diskretizacije z delitvijo prvotnega elementa se je pokazala kot učinkovita alternativa bolj zapletenemu izračunu, kjer se za izboljšano diskretizacijo uporablja konformni element. Taka primerjava doslej še ni bila izvedena in predstavlja prispevek k področju ocene napake diskretizacije za plošče. Primerjava učinkovitosti EqR metode s splošno uveljavljeno SPR metodo je predstavljena na več računskih primerih. Prikazan je tudi postopek prilagodljivega mreženja, ki se opira na oceno napake diskretizacije. Obe metodi imata svoje prednosti: EqR metod zagotavlja večjo lokalno natančnost ocene napake, po drugi strani je implementacija SPR metode znatno lažja. Računski primeri so pokazali, da EqR metoda predstavlja učinkovito alternativo SPR metodi.

Modelska napaka je obravnavana v poglavjih 7-8. Po splošni obravnavi principov ocene modelske napake, je obravnavana metoda, ki sloni na EqR metodi. Specifična vprašanja, ki so povezana s konstrukcijo lokalnih problemov za končne elemente za plošče, so obravnavana v poglavju 8. Več računskih primerov prikazuje učinkovitost obravnavane metode. Primeri pokažejo, da je metoda sposobna zaznati področja s povečano modelsko napako.

To delo prinaša še en pomemben sklep: hierarhija končnih elementov, ki jih uporabljamo v proceduri za oceno modelske napake je ključna za uspešno oceno modelske napake. Le hierarhija med končnimi elementi, ki vsi izhajajo iz iste interpolacijske baze, omogoča uspešno implementacijo ocene napake na osnovi EqR metode.

Prikazan je primer prilagodljivega modeliranja, kjer za izbiro modela uporabljamo

oceno modelske napake. Primeri kažejo, da je predlagan postopek ocene modelske napake sposoben voditi postopek prilagodljivega modeliranja.

Ukvarjanje z oceno modelske napake je pripeljajo do naslednjega sklepa: maksima 'model gradimo od najbolj grobega proti bolj kompleksnemu' ima svoje meje. Pokazali smo namreč, da je samo iz rezultatov grobega modela, nemogoče zaznati robna območja. Od predlaganega postopka ocene modelske napake ni realno pričakovati, da bo zaznal pojave, ki so v svojem bistvu odraz kompleksnosti modela. Grobi model preprosto ne vsebuje dovolj informacije, da bi bil sposoben zaznati prisotnost morebitnih pojavov višjega reda. Da bi s prilagodljivim modeliranjem zajeli vse relevantne pojave v določene modelu, začetni model ne sme biti pregrob.

Glavni cilj tega dela je bil implementirati in testirati ključni element koncepta prilagodljivega modeliranja plošč: ocene napak. Raziskali in preskusili smo nekaj najbolj obetavnih metod. Rezultati, predstavljeni v tem delu kažejo, da so preskušene metode primerne za namen prilagodljivega modeliranja. To delo potrjuje, da bi bilo mogoče zgraditi popolnoma samodejno proceduro za konstrukcijo optimalnega računske modela izbranega problema upogiba plošč.

Bibliography

Adini, A., Clough, R.W. 1960. Analysis of plate bending by the finite element method. NSF report for Grant G-7337, Dept. of Civil Engineering, University of California, Berkeley.

Ainsworth, A., Oden, J.T. 2000. A posteriori error estimation in finite element analysis. Wiley Inter-Science.

Argyris, J., Fried, I., Scharpf, D. 1968. The TUBA family of plate elements for the matrix displacement method. The aeronautical journal of the royal aeronautical society, 72:701–709.

Arnold, D.N., Falk, R.S. 1989. Edge effects in the reissner/mindlin plate theory. Proc. Symp. Analyt. Comput. Models Shells, San Francisco, ASME Winter Annual Meeting, pages 71–89.

Babuška, I., Li, L. 1990. Hierarchic modeling of plates. Technical report, Maryland Univ College Park Inst For Physical Science and Technology.

Babuška, I., Li, L. 1992. The problem of plate modeling. theoretical and computational results. Computer Methods in Applied Mechanics and Engineering, 100:249–273.

Babuška, I., Miller, A. 1987. A feedback finite element method with a posteriori error estimation: Part i. the finite element method and some basic properties of the a posteriori error estimator. Computer Methods in Applied Mechanics and Engineering, 61(1):1–40. ISSN 0045-7825.

Babuška, I., Miller, A., Vogelius, M. 1983. Adaptive methods and error estimation for elliptic problems of structural mechanics. Maryland Univ College Park Inst For Physical Science and Technology.

Babuška, I., Pitkaranta, J. 1990. The plate paradox for hard and soft simple support. SIAM J. Numer. Anal., 21:551–576.

Babuška, I., Rheinboldt, W.C. 1978. Error estimates for adaptive finite element computations. SIAM J. Numer. Anal., 15:736–754.

Babuška, I., Schwab, C. 1993. A posteriori error estimation for hierarchic models of elliptic boundary value problem on thin domains, Technical note BN-1148. Technical report.

Bank, R.E., Weiser, A. 1985. Some A Posteriori Error Estimators for Elliptic Partial Differential Equations. Mathematics of Computation, 44(170):283–301. ISSN 0025-5718.

Batoz, J.L. 1982. An explicit formulation for an efficient triangular plate-bending element. International Journal of Numerical Methods in Engineering, 18:1077–1089.

Batoz, J.L., Bathe, K.J., Ho, L.W. 1980. A study of Three-node Triangular Plate Bending Elements. International Journal of Numerical Methods in Engineering, 15:1771–1812.

Bazeley, G.P., Cheung, Y.K., Irons, B., Zienkiewicz, O.C. 1965. Triangular elements in plate bending, conforming and nonconforming solutions. In Proceedings of the Conference on Matrix Methods in Structural Mechanics, pages 547–576.

Becher, R., Rannacher, R. 2001. An optimal control approach to a posteriori error estimation in finite element methods. Acta Numerica, pages 1–102.

Bell, K. 1969. A refined triangular plate bending finite element. International Journal for Numerical Methods in Engineering, 1(1):101–122. ISSN 1097-0207.

Bernadou, M. 1996. Finite element method for the shell problem. John Wiley.

Bogner, F.K., Fox, R.L., Schmidt Jr, L.A. 1966. The generation of interelement compatible stiffness and mass matrices by the use of interpolation formulas. Proc. Conf. on Matrix Methods in Structural Mechanics, WPAFB, Ohio, 1965, 66-80:397Ĭ444.

Bohinc, U., Brank, B., Ibrahimbegović, A. 2006. Prilagodljivo modeliranje plošč z metodo končnih elementov = adaptive finite element modelling of plates. In Kuhljevi dnevi 2006, Lipica, 21.-22. september 2006. Zbornik del. Ljubljana: Slovensko društvo za mehaniko, pages 9–16.

Bohinc, U., Ibrahimbegovic, A., Brank, B. 2009. Model adaptivity for finite element analysis of thin or thick plates based on equilibrated boundary stress resultants. Engineering Computations, 26(1/2):69–99. ISSN 0264-4401.

Bosshard, W. 1968. Ein neues, vollverträgliches endliches Element für Plattenbiegung. Internationaler Verein für Brückenbau und Hochbau, Abhandlungen, 28:1.

Brank, B. 2005. Nonlinear shell models with seven kinematic parameters. Computer methods in applied mechanics and engineering, 194(21-24):2336–2362. ISSN 0045-7825.

Brank, B. 2008. On boundary layer in the Mindlin plate model: Levy plates. Thin-walled Structures, 46(5):451–465. ISSN 0263-8231.

Brank, B., Bohinc, U. 2006. Robni efekti pri upogibu pravokotnih mindlinovih plošč = edge effects in bending of rectangular mindlin plates. In Kuhljevi dnevi 2006, Lipica, 21.-22. september 2006. Zbornik del. Ljubljana: Slovensko društvo za mehaniko, pages 25–32.

Brank, B., Ibrahimbegovic, A., Bohinc, U. 2008. On Prediction of 3d Stress State in Elastic Shell by Higher-Order Shell Formulations. CMES-Computer Modeling in Engineering and Sciences, 33(1):85–108. ISSN 1526-1492.

Ciarlet, P. 1991. Basic error estimates for elliptic problems. Handbook of numerical analysis, 2:17–351. ISSN 1570-8659.

Clément, P. 1975. Approximation by finite element functions using local regularization. Rev. Française Automat. Informat. Recherche Opérationnelle Sér. Rouge Anal. Numér, 9:77–84.

Clough, R.W., Tocher, J.L. 1965. Finite element stiffness matrices for analysis of plate bending. Proc. Conf. on Matrix Methods in Structural Mechanics, WPAFB, Ohio.

De Veubeke, B. 1968. A conforming finite element for plate bending. International Journal of Solids and Structures, 4(1):95–108. ISSN 0020-7683.

Dhatt, G. 1970. An efficient triangular shell element. Journal of AIAA, 8:2100–2102.

Felippa, C.A. 2009. Advanced Finite Element Methods - course materials. University of Colorado at Boulder.

Felippa, C.A., Clough, R.W. 1965. A refined quadrilateral element for analysis of plate bending. Proc. Conf. on Matrix Methods in Structural Mechanics, WPAFB, Ohio.

Flajs, R., Cen, S., Saje, M. 2010. On convergence of nonconforming convex quadrilateral finite elements AGQ6. Computer Methods in Applied Mechanics and Engineering, 199(25-28):1816–1827. ISSN 0045-7825.

Geuzaine, C., Remacle, J. 2009. Gmsh: A 3-d finite element mesh generator with built-in pre-and post-processing facilities. International Journal for Numerical Methods in Engineering, 79(11):1309–1331. ISSN 1097-0207.

Grätsch, T., Bathe, K. 2005. A posteriori error estimation techniques in practical finite element analysis. Computers & Structures, 83(4-5):235–265. ISSN 0045-7949.

Guide, M. 1998. The MathWorks. Inc., Natick, MA, 5.

Häggblad, B., Bathe, K. 1990. Specifications of boundary conditions for reissner/mindlin plate bending finite elements. International Journal for Numerical Methods in Engineering, 30(5):981–1011. ISSN 1097-0207.

Hughes, T.J.R. 2000. The Finite Element Method: Linear Static and Dynamic Finite Element Analysis. Dover publications.

Ibrahimbegović, A. 1992. Plate quadrilateral finite element with incompatible modes. Communications in Applied Numerical Methods, 8:497–504.

Ibrahimbegović, A. 1993. Quadrilateral finite elements for analysis of thick and thin plates. Computer Methods in Applied Mechanics and Engineering, 110:195–209.

Ibrahimbegović, A. 2009. Nonlinear solid mechanics: Theoretical Formulations and Finite element Solution Methods. Springer, Berlin.

Johnson, C., Hansbo, P. 1992. Adaptive finite element method in computational mechanic. Comp. Methods Appl. Mech. Eng., 101:21–58.

Kettil, P., Wiberg, N.E. 1999. Adaptive fe-analysis of column supported reissner-mindlin plate. Computers and Structures, 72(28-30):605–626.

Korelc, J. 2006. AceGen and AceFEM user manuals.

Ladevèze, P., Leguillon, D. 1983. Error estimate procedure in the finite element method and applications. SIAM Journal of Numerical Analysis, 20(3):485–509.

Ladevèze, P., Maunder, E. 1996. A general method for recovering euilibrium element tractions. Computer Methods Mech. Eng., 137:111–151.

Ladevèze, P., Pelle, J.P. 2006. La maîtrise du calcul en mécanique linéare et non linéare. Hermes Science - Lavoisier.

Lee, C.K., Hobbs, R.E. 1998. Automatic adaptive refinement for plate bending problems using reissner/mindlin plate bending elements. International Journal for Numerical Methods in Engineering, 41:1–63.

Lee, K.H., Lim, G.T., Wang, C.M. 2002. Thick levy plates re-visited. International Journal of Solids and Structures, 39:127–144.

Marcus, H. 1932. Die Theorie Elasticher Gewebe. Springer-Verlag, Berlin, Germany.

Melzer, H., Rannacher, R. 1980. Spannungskonzentrationen in Eckpunkten der Kirchhoffschen Platte. Bauingenieur, 55:181–184.

Mindlin, R.D. 1951. Influence of rotary inertia and shear on flexural vibrations of isotropic, elastic plates. J. Appl. Mech., 18:31–38.

Morley, L.S.D. 1963. Skew plates and structures. Pergamon press.

Oden, J.T., Cho, J.R. 1997. Local a posteriori error estimation of hierarchical models for plate- and shell-like structures. Computer in Mathematics with Applications, 149:33–48.

Park, K.C., Felippa, C.A. 1998. A variational framework for solution method developments in structural mechanics. Journal of Applied Mechanics, 1(65):242–249.

Reissner, E. 1945. The effect of transverse shear deformation on the bending of elastic plates. J. Appl. Mech., 12:69–77.

Sander, G. 1964. Bornes supérieures et inférieures dans lĺanalyse matricielle des plaques en flexion-torsion. Bull. Soc. Royale Sciences Liege, 33:456–494.

Selman, A., Hinton, E., Atamaz-Sibai, W. 1990. Edge effects in mindlin-reissner plates using adaptive mesh refinement. Engng. Comput., 7:217–226.

Stein, E., Ohnimus, S. 1997. Coupled model- and solution adaptivity in the finite element method. Computer Methods in Applied Mechanics and Engineering, 150:327–350.

Stein, E., Ohnimus, S. 1999. Anisotropic discretization- and model-error estimation in solid mechanics by local neumann problems. Computer Methods in Applied Mechanics and Engineering, 176:363–385.

Stein, E., Ramm, E. 2003. Error-controlled adaptive finite elements in solid mechanics. Wiley. ISBN 0471496502.

Stein, E., Ruter, M., Ohnimus, S. 2004. Adaptive finite element analysis and modelling of solids and structures. findings, problems and trends. International Journal for Numerical Methods in Engineering, 60:103–138.

Szabó, B.A., Sahrmann, G.J. 1988. Hierarchic plate and shell models based on p-extension. International Journal for Numerical Methods in Engineering, 26(8):1855–1881. ISSN 1097-0207.

Taylor, R. . FEAP-A Finite Element Analysis Program, Programmer Manual. University of California, Berkeley. http://www. ce. berkeley. edu/rlt.

Taylor, R. 2000. FEAP–a finite element analysis program-Version 7.3. University of California at Berkeley.

Taylor, R.L., Govindjee, S. 2002. Solution of clamped rectangular plate problems. Technical Report: UCB/SEMM-2002/09.

Timoshenko, S., Vojnovski-Kriger, S. 1959. Theory of plates and shells. McGraw-Hill book company.

Verfürth, R. 1994. A posteriori error estimation and adaptive mesh-refinement techniques. Journal of Computational and Applied Mathematics, 50(1-3):67–83. ISSN 0377-0427.

Visser, W. 1968. The finite element method in deformation and heat conduction problems. Delft.

Wang, C., Lim, G., Reddy, J., Lee, K. 2001. Relationships between bending solutions of Reissner and Mindlin plate theories. Engineering structures, 23(7):838–849. ISSN 0141-0296.

Wilson, E. 1997. SAP2000: Integrated finite element analysis and design of structures. Analysis reference. Computers and Structures.

Wolfram, S. 1988. Mathematica: a system for doing mathematics by computer. Addison-Wesley Longman Publishing Co., Inc. Boston, MA, USA. ISBN 0201193302.

Zienkiewicz, O.C., Taylor, R.L. 2000. Finite element method. Elseiver.

Zienkiewicz, O.C., Zhu, J.Z. 1992. The superconvergent patch recovery and a posteriori error estimates. part 1: The recovery technique. International Journal of Numerical Methods in Engineering, 33:1331–1364.